

# Generalized Advanced Propeller Analysis System (GAPAS)

## Volume I – Final Report

December 1986

Prepared by  
L. Glatt  
D.R. Crawford  
J. B. Kosmatka  
R. J. Swigart  
E. W. Wong

**TRW Space & Defense Sector**  
Redondo Beach, CA

Prepared for  
**National Aeronautics and Space Administration**  
NASA-Lewis Research Center  
Contract NAS3-22251

N94-71798

Unclas

Z9/07 0002852

(NASA-CR-185276) GENERALIZED  
ADVANCED PROPELLER ANALYSIS SYSTEM  
(GAPAS), VOLUME 1 Final Report  
(TRW Space and Defense Sector)  
345 p



# **Generalized Advanced Propeller Analysis System (GAPAS)**

## **Volume I – Final Report**

**December 1986**

Prepared by  
L. Glatt  
D.R. Crawford  
J. B. Kosmatka  
R. J. Swigart  
E. W. Wong

**TRW Space & Defense Sector**  
Redondo Beach, CA

Prepared for  
**National Aeronautics and Space Administration**  
NASA-Lewis Research Center  
Contract NAS3-22251





## SUMMARY

A Generalized Advanced Propeller Analysis System (GAPAS) has been developed under NASA Lewis Research Center Funding to provide a unified propeller analysis capability for analyzing advanced technology propellers. The technology areas incorporated in GAPAS include propeller aerodynamic performance, airfoil loading, acoustics, and structural analysis. These propeller analysis tools include the most fully developed technologies in a modular but unified system. GAPAS will treat multibladed propellers having straight or swept blades operating on aircraft up to Mach 0.8 and altitudes to 40,000 feet (12 km).

As verification of the analysis system, GAPAS has been used to analyze two propellers. The first is the SR-3 propeller operating at Mach 0.8 and is characteristic of an advanced technology propeller for application to high speed transport aircraft. The second is the Hartzell H101/16 propeller operating at Mach 0.35 and is characteristic of a General Aviation propeller. The results of these calculations are compared with available data. Current model limitations are discussed as well as recommendations for model improvements and additional verification requirements.

**PRECEDING PAGE BLANK NOT FILMED**



## CONTENTS

	Page
1. INTRODUCTION	1-1
2. TASK 1: EVALUATION OF ANALYSIS PROCEDURES	2-1
2.1 Guidelines for Evaluation of Analysis Procedures	2-1
2.2 Evaluation of Individual Analysis Procedures	2-2
2.2.1 Geometry Generator Module	2-2
2.2.1.1 Summary of Requirements	2-2
2.2.1.2 Section Profiles Perpendicular to the Line of Shear Centers	2-11
2.2.1.3 Evaluation of Candidate Geometry Generator Modules	2-17
2.2.2 Aircraft Flowfield Module	2-17
2.2.2.1 Summary of Requirements	2-17
2.2.2.2 Evaluation of Candidate Aircraft Flow Field Programs	2-19
2.2.3 Propeller Aerodynamic Performance	2-20
2.2.3.1 Summary of Requirements	2-21
2.2.3.2 UTRC High Speed Propeller-Nacelle Aerodynamic Performance Prediction Procedure	2-22
2.2.3.3 Chang-Sullivan - Theoretical Performance of High-Efficiency Propellers	2-24
2.2.3.4 Aljabri - Prediction of Propeller Performance and Loading in Uniform and Nonuniform Flowfields	2-26
2.2.3.5 Crigler - Application of Theodorsen Theory to Propeller Design	2-27
2.2.3.6 S.B.A.C Standard Method of Propeller Performance Estimation	2-28
2.2.3.7 Results of Review of Propeller Aerodynamic Performance	2-29
2.2.3.8 Summary	2-38
2.2.4 Airfoil Loading Module	2-43
2.2.4.1 Summary of Requirements	2-43
2.2.4.2 Garabedian and Korn (G&K)	2-45
2.2.4.3 Carlson (TRANSEP)	2-45
2.2.4.4 Smetana	2-46

PRECEDING PAGE BLANK NOT FILMED

## CONTENTS (Continued)

	Page
2.2.4.5 Eppler	2-47
2.2.4.6 Comparison of Prediction Methods	2-48
2.2.4.7 Airfoil Data Banks	2-57
2.2.5 Propeller Acoustic Signature	2-57
2.2.5.1 Acoustic Signature Technical Requirements	2-57
2.2.5.2 Method of Woan and Gregorek	2-58
2.2.5.3 Method of Succi	2-58
2.2.5.4 Method of Martin-Farassat (PROPFAN-Formulation I)	2-61
2.2.5.5 Method of Martin-Farassat (PROPFAN-Formulation II)	2-65
2.2.5.6 SAE AIR 1407 - Prediction Procedure for Propeller Noise	2-65
2.2.6 Structural Analysis	2-65
2.2.6.1 Beam Model Structural Analysis Requirements	2-65
2.2.6.1.1 Evaluation of Existing Beam Structural Analysis Methods	2-67
2.2.6.1.2 New Beam Model Structural Analysis Computer Code Development	2-69
2.2.6.2 Plate Model Structural Analysis Requirements	2-70
2.2.7 Aeroelastic Analysis Procedures	2-74
2.2.7.1 UTRC-G400PROP Aeroelastic Computer Code	2-75
2.2.7.2 Bell/NASTRAN Propeller Flutter Computer Code	2-76
2.2.7.3 Modification of Existing Aeroelastic Computer Codes	2-77
2.2.7.4 New Aeroelastic Computer Code Development	2-78
2.3 Recommendation of Analysis Procedures for Incorporation into GAPAS	2-79
2.3.1 Geometry Generator Module	2-79
2.3.2 Aircraft Flow Field Module	2-79

## CONTENTS (Continued)

	Page
2.3.3 Propeller Aerodynamic Performance	2-82
2.3.4 Airfoil Loading Module	2-82
2.3.5 Propeller Acoustic Signature	2-83
2.3.6 Structural Analysis Module	2-84
2.3.7 Aeroelasticity Module	2-85
2.4 Evaluation of Procedural Systems	2-86
2.4.1 Procedural System Requirements	2-86
2.5 Candidate Procedural Systems	2-87
2.5.1 ANOPP Procedural System	2-87
2.5.2 JCL Procedural System	2-90
2.6 Recommendation of Procedural System for Use in GAPAS	2-92
3. TASK 2: MODIFICATION AND DEVELOPMENT OF ANALYSIS PROCEDURES	3-1
3.1 Geometry Generator Module	3-1
3.2 Aircraft Flowfield Module	3-16
3.3 Propeller Aerodynamic Module	3-26
3.3.1 Modifications/New Developments	3-26
3.3.2 Verification of Propeller Aerodynamic Procedures	3-26
3.4 Airfoil Loading Module	3-35
3.4.1 Summary of Airfoil Loading Verification	3-55
3.5 Propeller Acoustic Module	3-56
3.5.1 Propeller Acoustic Modification/New Developments	3-56
3.5.2 Propeller Acoustic Verification	3-56
3.6 Structural Beam Module	3-76
3.6.1 Basic Assumptions Used in the Analysis	3-79
3.6.2 Geometric Preliminaries	3-80
3.6.3 Ordering Scheme for a Long Slender Beam	3-85
3.6.4 Development of Strain Components	3-87
3.6.5 Verification of Beam Model	3-95
3.6.5.1 Sample Calculations	3-95

## CONTENTS (Continued)

	Page
3.7 Aeroelasticity Module	3-107
3.7.1 Structural Twist and Sweep	3-108
3.7.1.1 Principal Assumptions	3-108
3.7.1.2 Basic Modeling Characteristics	3-111
3.7.2 Aerodynamic Sweep	3-112
3.7.2.1 Principal Assumptions	3-112
3.7.2.2 Basic Modeling Characteristics	3-113
3.7.3 Unsteady Stalled Airloads	3-113
3.7.3.1 Overview of Dynamic Stall Model Methodology	3-115
3.7.3.2 Parameters Influencing Dynamic Stall	3-115
3.7.4 Unsteady Unstalled Subsonic Aerodynamics	3-116
3.7.5 Sample Calculations	3-118
3.7.5.1 Description of Blade Configuration and Operating Conditions	3-119
3.7.5.2 Stall Flutter Correlation Cases	3-119
3.7.6 Recommendations	3-126
4. FORMULATION OF SYSTEM FRAMEWORK	4-1
4.1 Familiarization of ANOPP Procedural System	4-1
4.2 ANOPP System Checkout	4-2
4.3 Design of an Overall Data Base for GAPAS	4-7
4.3.1 Input/Output Procedures	4-7
4.3.2 System Interactions	4-8
4.3.3 GAPAS Data Base	4-10
5. SYSTEM INTEGRATION	5-1
5.1 Operation/Programming Standards	5-1
5.2 GAPAS Data Base Access Methods	5-1
5.2.1 Utilization of User Parameter	5-2
5.2.2 Utilization of Data Unit	5-3

## CONTENTS (Continued)

	Page
5.3 Functional Module Incorporation Technique	5-5
5.3.1 User Parameter Implementation	5-5
5.3.2 Data Unit Implementation	5-6
5.4 GAPAS Functional Modules and its Capabilities/Limitations	5-8
6. TASK 5: ANALYSIS SYSTEM VERIFICATION	6-1
6.1 Propeller Test Cases	6-1
6.1.1 SR-3 Propeller Test Case	6-1
6.2 Hartzell Propeller Test Case	6-47
6.3 Computer Resources Requirements	6-57
7. RECOMMENDATIONS	7-1
7.1 Module Improvements	7-1
7.1.1 Geometry Generator Module	7-1
7.1.2 Aircraft Flow Field Module	7-1
7.1.3 Airfoil Loading Module	7-1
7.1.4 Propeller Performance Module	7-2
7.1.5 Propeller Acoustic Module	7-2
7.1.6 Structural Analysis Module	7-3
7.1.7 Aeroelasticity Module	7-5
7.1.8 Option Module	7-5
7.2 Additional Calculations	7-5
REFERENCES	R-1

## ILLUSTRATIONS

		Page
1-1	Performance Mode - Single Pass Functional Description	1-3
1-2	Performance Mode - Iterative Pass Functional Description	1-4
1-3	Design Mode Functional Description	1-5
1-4	GAPAS Development Plan	1-6
2.1-1	Candidate Analysis Procedure Evaluation Factors	2-3
2.2-1	Airfoil Section Local Coordinate System (LCS)	2-5
2.2-2	Global Coordinate Systems (GCS-1: X'Y'Z'; GCS-2: XYZ)	2-6
2.2-3	Geometric Sweep angle Definitions	2-8
2.2-4	Geometry Generator Module - Aerodynamic Application	2-10
2.2-5	Geometry Generator Module - Acoustics Application	2-12
2.2-6	Geometry Generator Module - Structural Application (Mid-Chord Line)	2-13
2.2-7	Geometry Generator Module - Structural Application (Elastic Axis)	2-14
2.2-8	Candidate Propeller Internal Structures	2-15
2.2-9	Aerodynamic Performance Requirements Satisfaction Summary	2-30
2.2-10	Comparison of Predicted Performance for SR-2 Propeller. M = 0, $\beta = 58^\circ$ , CD = 0 (Uniform In-Flow)	2-33
2.2-11	Lifting Surface Calculation of Spanwise Bound Circulation for Rectangular, AR=6 Wing	2-33
2.2-12	Comparison of Lifting Line Spanwise Lift Distribution with that Calculated by the Weissinger-L Method. Rectangular Wing, AR=6	2-34
2.2-13	Comparison of Codes with Experiment SR-1 Prop; M = 0.8; Codes for $\beta = 61.2^\circ$ ; Purdue Code with Uniform In-Flow; Points are Experimental	2-34
2.2-14	Efficiency Versus J, Propeller 6129, M=0, 3 Blades, Ref. NACA R 642	2-37



# ILLUSTRATIONS (Continued)

	Page
2.2-15 Thrust Coefficient Versus J Propeller 6129, M=0, 3 Blades, Ref. NACA R 642	2-37
2.2-16 Effects of Thickness and Camber Corrections on Predicted CP for Propeller 6129	2-39
2.2-17 SR-2 Propeller Vortex Theory Versus Experiment, M = 0.6, $\beta = 58^\circ$ , for Theory	2-39
2.2-18 Effect of Corrections on Power M = 0, $\beta = 58^\circ$	2-40
2.2-19 Corrections to Local Alpha for Thickness and Flow Curvature	2-40
2.2-20 CP versus CT SR-2 Propeller, M = 0, $\beta = 58^\circ$	2-41
2.2-21 SR-2 Propeller Theory versus Experiment, M = 0.8, Lines are Theory for $\beta = 58^\circ$	2-41
2.2-22 Comparison of Results of Airfoil Analysis Codes with Experimental Data for the NACA 0012 Airfoil	2-50
2.2-23 Comparison of Results of Airfoil Analysis Codes with Experimental Data for the NASA LS(1)-0413 Airfoil	2-53
2.2-24 Drag versus Mach Number for NASA LS(1)-0413	2-56
2.2-25 Comparison with Data - Method of Woan and Gregorek	2-59
2.2-26 Comparison with Data - Method of Woan and Gregorek	2-60
2.2-27 Comparison with Experimental Data - Method of Succi	2-62
2.2-28 Comparison of Calculated and Measured Near-Field Propeller Noise Using Method of Martin and Farassat (Propfan I)	2-63
2.2-29 Comparison with Data - Method of Martin-Farassat (Propfan I) SR-1 Propeller, $M_{TH} = 1.03$	2-64
2.3-1 Wing Vortex Lattice Model	2-80
2.3-2 Wing Upwash as a Function of Longitudinal Position	2-81
2.3-3 Upwash 10% Semispan Ahead of Leading Edge as a Function of Number of Chordwise Divisions, Rectangular Wing, AR = 6	2-81

## ILLUSTRATIONS (Continued)

	Page
2.5-1 Schematic Layout of Core Storage	2-89
2.5-2 Sample Case Using ANOPP Internal Control Statement	2-91
2.5-3 Schematic TRW External JCL Procedure System	2-93
2.5-4 Sample External - JCL Procedure System	2-94
3.1-1 SR-3 Propeller-Nacelle Geometry	3-2
3.1-2 SR-3 Structural Model Line of Shear Centers and Profiles Perpendicular	3-4
3.1-3 SR-2 Structural Model Showing Problem at Tip with Line of Shear Centers	3-5
3.1-4 Three-View of SR-3 Propeller Blade Cuts Perpendicular to Line of Shear Centers	3-6
3.1-5 SR-3 Propeller-Nacelle Geometry Cuts Perpendicular to 1/4-Chord	3-7
3.1-6 SR-3 Propeller-Nacelle Geometry Cuts Perpendicular to 1/4-Chord	3-8
3.1-7 SR-3 Blade Geometry Cuts Perpendicular to 1/4-Chord	3-9
3.1-8 SR-3 - Airfoil Sections Perpendicular to 1/4-Chord	3-10
3.1-9 TRW Hartzell 101/16 Propeller-Nacelle Geometry Aerodynamic Cuts	3-12
3.1-10 TRW-Hartzell 101/16 Nacelle Geometry	3-13
3.1-11 TRW Hartzell 101/16 Structural Model Line of Shear Centers and Profiles Perpendicular	3-14
3.1-12 TRW-Hartzell 101/16 Propeller Blade	3-15
3.2-1 Neumann Code Element Geometry	3-17
3.2-2 Ellipsoid of Revolution at Angle of Attack	3-18
3.2-3 Tangential Velocity Factor for an Ellipsoid of Revolution in Cross-Flow	3-19
3.2-4 Surface Pressure Coefficient on an Ellipsoid of Revolution	3-20

## ILLUSTRATIONS (Continued)

	Page
3.2-5 TRW-Hartzell 101/16 Nacelle Geometry	3-21
3.2-6 Body Pressure Coefficient for 101-16 Test Case	3-22
3.2-7 Calculated Axial Velocity Ratio in Plane of the Propeller for 101-16 Test Case as Computed with Jumper Code	3-23
3.2-8 SR-3 Nacelle Geometry	3-24
3.2-9 Potential Flow Calculations for SR-3 Test Case	3-25
3.3-1 Aerodynamic Performance of 101/16 Propeller	3-28
3.3-2 Aerodynamic Performance of 101/16 Propeller	3-29
3.3-3 Aerodynamic Performance of 101/16 Propeller	3-30
3.3-4 Aerodynamic Performance of SR-3 Propeller	3-32
3.3-5 Aerodynamic Performance of SR-3 Propeller	3-33
3.3-6 Aerodynamic Performance of SR-3 Propeller	3-34
3.4-1 Lift-Coefficient Correction Due to Separation	3-36
3.4-2 Lift Coefficient Versus Angle of Attack for H101/16 at Station 10.282 ( $M_H = 0.379$ , $Re_L = 7.64 \times 10^5$ )	3-38
3.4-3 Boundary Layer Transition Point Versus for H101/16 at Station No. 10.282 ( $M_H = 0.379$ , $Re_L = 7.64 \times 10^5$ )	3-39
3.4-4 Boundary Layer Separation Point Versus Angle of Attack for H101/16 at Station No. 10.282 ( $M_H = 0.379$ , $Re_L = 7.64 \times 10^6$ )	3-40
3.4-5 Drag Coefficient Versus Angle of Attack for H101/16 at Station No. 10.282 ( $M_H = 0.379$ , $Re_L = 7.64 \times 10^5$ )	3-41
3.4-6 Pressure Coefficient Distribution for H101/16 at Station 10.282 ( $M_H = 0.378$ , $Re_L = 7.64 \times 10^5$ , $\alpha = 4^\circ$ )	3-42
3.4-7 Lift Coefficient Versus Angle of Attack for H101/16 at Station No. 17.042 ( $M_H = 0.45$ , $Re_L = 8.36 \times 10^5$ )	3-43
3.4-8 Boundary Layer Separation Point Versus Angle of Attack for H101/16 at Station 17.042 ( $M_H = 0.45$ , $Re_L = 8.36 \times 10^5$ )	3-45

# ILLUSTRATIONS (Continued)

	Page
3.4-9 Boundary Layer Transition Point Versus Angle of Attack for H101/16 at Station 17.042 ( $M_H = 0.45$ , $Re_L = 8.36 \times 10^5$ )	3-46
3.4-10 Drag Coefficient Versus Angle of Attack for H101/16 at Station 17.042 ( $M_H = 0.45$ , $Re_L = 8.36 \times 10^5$ )	3-47
3.4-11 Pressure Coefficient Distribution for H101/16 at Station 17.042 ( $M_H = 0.45$ , $Re_L = 8.36 \times 10^5$ , $\alpha = 40^\circ$ )	3-48
3.4-12 Lift Coefficient Versus Angle of Attack for H101/16 at Station No. 23.803 ( $M_H = 0.51$ , $Re_L = 8.79 \times 10^5$ )	3-50
3.4-13 Boundary Layer Transition Point Versus Angle of Attack for H101/16 at Station 23.803 ( $M_H = 0.51$ , $Re_L = 8.79 \times 10^5$ )	3-51
3.4-14 Boundary Layer Separation Point Versus Angle of Attack for H101/16 at Station 23.803 ( $M_H = 0.51$ , $Re_L = 8.79 \times 10^5$ )	3-52
3.4-15 Drag Coefficient Versus Angle of Attack for H101/16 at Station No. 23.803 ( $M_H = 0.51$ , $Re_L = 8.79 \times 10^5$ )	3-53
3.4-16 Pressure Coefficient Distribution for H101/16 at Station No. 23.803 ( $M_H = 0.51$ , $Re_L = 8.79 \times 10^5$ , $\alpha = 40^\circ$ )	3-54
3.5-1 Wing-Mounted Microphone Position 101/16 Propeller Acoustic Measurements Near Field	3-58
3.5-2 Acoustic Pressure Signature 101/16 Propeller Near Field (Run No. 11 of Ref. 3.5-2)	3-60
3.5-3 Overall Noise Spectra 101/16 Propeller Near Field (Run No. 11 of Ref. 3.5-2)	3-61
3.5-4 Acoustic Pressure Signature 101/16 Propeller Near Field (Run No. 12 of Ref. 3.5-2)	3-62
3.5-5 Overall Noise Spectra 101/16 Propeller Near Field (Run No. 12 of Ref. 3.5-2)	3-63
3.5-6 Acoustic Pressure Signature 101/16 Propeller Near Field (Run No. 13 of Ref. 3.5-2)	3-64
3.5-7 Overall Noise Spectra 101/16 Propeller Near Field (Run No. 13 of Ref. 3.5-2)	3-65

## ILLUSTRATIONS (Continued)

		Page
3.5-8	Comparison with Experimental Data SR-3 Propeller, $M_{TH} = 0.86$ Case	3-68
3.5-9	Acoustic Verification Results SR-3 Propeller	3-69
3.5-10	Microphone Locations - UTRC Wind Tunnel Near and Far Field	3-71
3.5-11	Propeller Plane Near-Field Pressure Signature at 0.8 D Tip Clearance Radial Location; SR-3 Propeller, $B = 2$ , $M_0 = 0.203$ , 6700 rpm, $M_{TH} = 0.687$	3-72
3.5-12	8P Harmonic Sound Pressure Level at 0.8D Tip Clearance; SR-3 Propeller, $B = 2$ , $M_0 = 0.203$ , 6700 rpm, $M_{TH} = 0.687$	3-73
3.5-13	8P Harmonic Sound Pressure Level at 4.40 Tip Clearance; SR-3 Propeller, $B = 4$ , $M_0 = 0.321$ , 8550 rpm, $M_{TH} = 0.901$	3-74
3.5-14	8P Harmonic Sound Pressure Level at 4.40 Tip Clearance; SR-3 Propeller, $B = 2$ , $M_0 = 0.203$ , 7500 rpm, $M_{TH} = 0.671$	3-75
3.6-1	Advanced Propeller (Prop-Fan)	3-77
3.6-2	Propeller Fixed and Beam Element Coordinate Systems	3-78
3.6-3	Inertial and Hub-Fixed Coordinate Systems	3-81
3.6-4	Hub-Fixed and Propeller-Fixed Coordinate Systems Including Sweep ( $\beta_s$ ), Precone ( $\beta_c$ ), and Pitch ( $\beta_p$ ) Adjustments	3-82
3.6-5	Element and Curvilinear Coordinate System of Pretwisted Beam Element	3-83
3.6-6	Beam-Type Finite Element	3-92
3.6-7	Tip-Loaded Analysis of Curved Cantilever Beam	3-96
3.6-8	Tip Displacements for a Tip-Loaded Curved Cantilever Beam	3-97
3.6-9	Tip Displacements for a Tip Loaded Curved Cantilever Beam	3-98
3.6-10	Tip Displacements for a Tip Loaded Curved Cantilever Beam	3-99

## ILLUSTRATIONS (Continued)

		Page
3.6-11	Natural Frequency Calculation of a Clamped-Clamped Circular Arc Beam	3-101
3.6-12	Natural Frequency Calculation of a Cantilever Beam with In-Plane Curvature	3-102
3.6-13	Natural Frequency Calculation of a Cantilever Beam with Out-of-Plane Curvature	3-103
3.6-14	Natural Frequency Calculation of a Pretwisted Cantilever Beam	3-104
3.6-15	Uniform Cantilevered Beam Under Transverse Loading	3-106
3.7-1	Basis for Use of Beam Theory for Structurally Swept Blade	3-109
3.7-2	Geometric Details of Typical Aerodynamically Swept Section	3-114
3.7-3	Example of Unsteady Aerodynamic Airfoil Characteristics and Associated Pade Approximation	3-117
3.7-4	Planform of SR-2 Model Prop-Fan Blade	3-120
3.7-5	Analytical Predictions of the Variation of SR-2 Blade Natural Frequencies with Tip Speed, Uncoupled Modes	3-123
3.7-6	Stall Flutter Correlation Results for the SR-2 Blade and G400PROP Calculations	3-125
4.2-1	Schematic ANOPP System Checkout Case	4-3
4.2-2	Input File for First ANOPP System Checkout Case	4-5
4.2-3	Input File for Second ANOPP System Checkout Case	4-6
4.3-1	Analysis Mode for GAPAS	4-9
4.3-2	Schematic of GAPAS Data Base	4-11
6.1-1	Three View Sketch of SR3 Showing Relative Location of Tip Airfoil and Pitch Change Axis	6-2
6.1-2	SR-3 Propeller Blade Characteristics	6-3
6.1-3	Geometric Blade Sweep as a Function of Blade Fractional Radius	6-4

# ILLUSTRATIONS (Continued)

	Page
6.1-4 SR-3 1/4 Chord Geometry	6-6
6.1-5 SR-3 Camber Line from Airfoil Loading Module (Z/C = 0.5837)	6-7
6.1-6 SR-3 Camber Line from Airfoil Loading Module (Z/C = 0.7673)	6-8
6.1-7 SR-3 Camber Line from Airfoil Loading Module (Z/C = 0.955)	6-9
6.1-8 Velocity in Propeller Plane of SR-3	6-11
6.1-9 SR-3 Power Coefficient and Efficiency Comparison of Calculations and Experiment as a Function of $\Delta\beta$	6-13
6.1-10 Normal Mach Number vs. Radial Distance for SR-3 Propeller $M_0 = 0.8$ , $J = 3.06$ , $C_p = 1.71$	6-14
6.1-11 Variation of Lift and Drag Coefficients with Radial Location for SR-3 Propeller $M_0 = 0.8$ , $J = 3.06$ , $C_p = 1.71$	6-15
6.1-12 Variation of Calculated Thrust and Power Coefficient Gradients with Blade Fractional Radius $M_0 = 0.80$ , $J = 3.06$ , $C_p = 1.71$ , $B = 8$	6-16
6.1-13 Meaning of Camber-Line Loading Parameter, $a$	6-18
6.1-14 Pressure Transducer Positions, SR-3 Propeller	6-19
6.1-15 Acoustic Pressure Signature SR-3 Propeller Near Field (Station No. 1) ( $M_0 = 0.80$ , $J = 3.06$ , $C_p = 1.71$ , $B = 8$ , $M_{TH} = 1.14$ , $a = 1$ )	6-20
6.1-16 Overall Noise Spectra SR-3 Propeller Near Field (Station No. 1) ( $M_0 = 0.80$ , $J = 3.06$ , $C_p = 1.71$ , $B = 8$ , $M_{TH} = 1.14$ , $a = 1$ )	6-21
6.1-17 Acoustic Pressure Signature SR-3 Propeller Near Field (Station No. 2) ( $M_0 = 0.80$ , $J = 3.06$ , $C_p = 1.71$ , $B = 8$ , $M_{TH} = 1.14$ , $a = 1$ )	6-22
6.1-18 Overall Noise Spectra SR-3 Propeller Near Field (Station No. 2) ( $M_0 = 0.80$ , $J = 3.06$ , $C_p = 1.71$ , $B = 8$ , $M_{TH} = 1.14$ , $a = 1.0$ )	6-23

# ILLUSTRATIONS (Continued)

	Page
6.1-19 Acoustic Pressure Signature SR-3 Propeller Near Field (Station No. 3) ( $M_0 = 0.80$ , $J = 3.06$ , $C_p = 1.71$ , $B = 8$ , $M_{TH} = 1.14$ , $a = 1.0$ )	6-24
6.1-20 Overall Noise Spectra SR-3 Propeller Near Field (Station No. 3) ( $M_0 = 0.80$ , $J = 3.06$ , $C_p = 1.71$ , $B = 8$ , $M_{TH} = 1.14$ , $a = 1.0$ )	6-25
6.1-21 Acoustic Pressure Signature SR-3 Propeller Near Field ( $M_0 = 0.80$ , $J = 3.06$ , $C_p = 1.71$ , $B = 8$ , $M_{TH} = 1.14$ , $a = 1$ )	6-26
6.1-22 Overall Noise Spectra SR-3 Propeller Near Field (Station No. 4) ( $M_0 = 0.80$ , $J = 3.06$ , $C_p = 1.71$ , $B = 8$ , $M_{TH} = 1.14$ , $a = 1.0$ )	6-27
6.1-23 Overall Sound Pressure Level SR-3 Propeller Near Field ( $M_0 = 0.80$ , $J = 3.06$ , $C_p = 1.71$ , $n = 8495$ rpm, $M_{TH} = 1.14$ , $a = 1.0$ )	6-28
6.1-24 Solution Results of Retarded Time Equation	6-29
6.1-25 Solution Results of Retarded Time Equation	6-30
6.1-26 NASA-SR-3 Advanced Turbopropeller	6-32
6.1-27 SR-3 Structural Model Line of Shear Centers and Profiles Perpendicular to Line of Shear Centers	6-33
6.1-28 Finite Element Model and Test Setup of NASA SR-3 Propeller	6-34
6.1-29 Analysis of a NASA SR-3 Advanced Propeller Cross Section Located at a Point 25% from Blade Root	6-35
6.1-30 Warping Function Distribution of a NASA SR-3 Cross Section Located at a Point 25% from Blade Root	6-36
6.1-31 Analysis of a NASA SR-3 Advanced Propeller Root Cross Section	6-37
6.1-32 Analysis of a NASA SR-3 Advanced Propeller Tip Cross Section	6-38
6.1-33 Comparison of Current Finite Element Predictions and Experimental Results for the First Mode Shape of NASA SR-3 Propeller	6-40



## ILLUSTRATIONS (Continued)

		Page
6.1-34	Comparison of Current Finite Element Predictions and Experimental Results for the Second Mode Shape of NASA SR-3 Propeller	6-41
6.1-35	Comparison of Current Finite Element Predictions and Experimental Results for the Third Mode Shape of the NASA SR-3 Propeller	6-42
6.1-36	Comparison of Current Finite Element Predictions and Experimental Results for the Fourth Mode Shape of the NASA SR-3 Propeller	6-43
6.1-37	Comparison of Test and Predicted Natural Frequencies for the NASA SR-3 (Campbell Diagram)	6-44
6.1-38	Undeformed and Deformed Line of Shear Centers for the SR-3 Propeller	6-46
6.2-1	Hartzell 101/16 Propeller Blade Characteristics	6-48
6.2-2	OASPL Results - 101/16 Propeller Near Field Conditions	6-49
6.2-3	TRW-Hartzell 101/16 Structural Model Line of Shear Centers and Profiles Perpendicular	6-51
6.2-4	Finite Element Model and Test Setup of Hartzell 101/16 Propeller	6-52
6.2-5	Comparison of Predicted and Experimental of First Mode Shape for the Hartzell 101/16 Propeller	6-53
6.2-6	Comparison of Predicted and Experimental Second Mode Shape for Hartzell 101/16 Propeller	6-54
6.2-7	Comparison of Predicted and Experimental Third Mode Shape for Hartzell 101/16 Propeller	6-55
6.2-8	Comparison of Test and Predicted Natural Frequencies for the Hartzell 101/16 (Campbell Diagram)	6-56

## TABLES

		Page
2.2-1	Summary of Airfoil Loading Computational Capability	2-44
3.3-1	Aerodynamic Performance Verification Requirements	3-27
3.5-1	Acoustics Verification Requirements	3-57
3.5-2	OASPL Results - 101/16 Propeller Near Field Conditions	3-66
3.7-1	SR-2 Model Prop-Fan Physical Parameters	3-121
3.7-2	Predicted and Measured Values of PTP Torsion Stress at Selected Operating Conditions for SR-2 Prop-Fan $a_{\infty}$ = 1155 ft/s = 352 in/s	3-122
6.2-1	GAPAS Limitations and Requirements	6-57

## 1. INTRODUCTION

The Propeller Research Program being pursued by NASA has the potential to exert a significant impact on the design of future subsonic aircraft. The potential gains in fuel economy with propeller propulsion will allow these aircraft to expand their role in an era of dwindling energy resources. TRW has been supporting NASA in these efforts through the development of a Generalized Advanced Propeller Analysis System (GAPAS).

The objective of the GAPAS program is the development of a unified analysis system applicable to advanced propellers for a wide range of applications. The range of operating conditions and parameters are described as follows: (1)  $M \leq 0.8$ , (2)  $7 \leq \text{altitude} \leq 40\text{K ft (12 km)}$ , (3)  $100 \leq \text{SHP} \leq 6000$ , (4)  $2 \leq \text{blade diameter} \leq 15 \text{ ft (0.6-4.6 m)}$ , (5)  $2 \leq \text{number of blades} \leq 8$ , (6)  $0^\circ \leq \text{sweep angles} \leq 45^\circ$ , (7)  $600 \leq \text{tip velocity} \leq 850 \text{ ft/s (180-260 m/s)}$ . In addition, GAPAS is to have the capability of analyzing metal or composite material blades of solid or spar-shell construction.

The guidelines followed in meeting the basic requirements of GAPAS were that state-of-the-art analysis tools would be used, where available, and that advanced state-of-the-art techniques would be developed for those capabilities that were either nonexistent or where current methods were found to be inappropriate. In addition, these existing analytical tools were not to be company proprietary. The analysis tools to be incorporated into the GAPAS program were to encompass the areas of (1) aerodynamics, (2) acoustics, (3) structures, and (4) aeroelasticity. One of the primary requirements of the GAPAS software architecture was the modular design of the system in order that different parts of the analysis system could be developed, operated, modified or replaced independently from the rest of the analysis system. An additional requirement was to allow GAPAS to operate in either a performance mode, i.e., a given propeller would be analyzed to predict the aerodynamic, structural, acoustic, and aeroelastic performance or in a limited design mode, i.e., the propeller would be optimized from an aerodynamic standpoint, subject to both acoustic and structural/aeroelastic constraints.

The required interaction between the various disciplines during both analysis and design modes of operation can be seen in Figures 1-1 through 1-3. In the performance mode of operation, the propeller performance and loading calculations are performed first, after which the resulting loading is input to the structural, aeroelasticity and acoustic analysis codes. In the iterative pass functional description shown in Figure 1-2, the effect of finite steady-state deflections are accounted for by modifying the original propeller geometry. The procedure is repeated between aerodynamic and structural modules until convergences occur. At this point, the results are used in both acoustic, and aeroelastic stability and response analyses.

In the design mode (Figure 1-3) the basic interactive capability between aerodynamics and structures still exists. However, capabilities must be included for modifying airfoil thickness-to-chord ratio ( $t/c$ ), as well as skin thickness, in order to accommodate both stress and frequency requirements. Thus, the looping back to the aerodynamic branch must now occur in order to account for changes in  $t/c$ , in addition to the deflection effects. Once convergence is achieved, an aeroelasticity analysis is performed in order to determine both aeroelastic stability and response.

Although both the performance and design modes have been discussed, the current version of GAPAS addresses only the single pass mode for solid propellers (Figure 1-1). The capability for analyzing composite propellers as well as the incorporation of both the iterative pass and design modes will be considered for future upgrades to the existing version of GAPAS.

The overall strategy in the development of GAPAS is shown in Figure 1-4. It is divided into five separate tasks. Task 1 consists of the review and evaluation of existing analysis procedures used in the calculation of aerodynamic, acoustic, structural and aeroelastic performance of advanced propellers operating in the range of conditions previously described. The evaluation procedures were based on such key items as: (1) degree of sophistication, (2) accuracy, (3) computational efficiency, (4) user friendliness, (5) availability of documentation, and (6) ease of modification. In addition, this task also involved the review and evaluation of existing procedures which were appropriate for

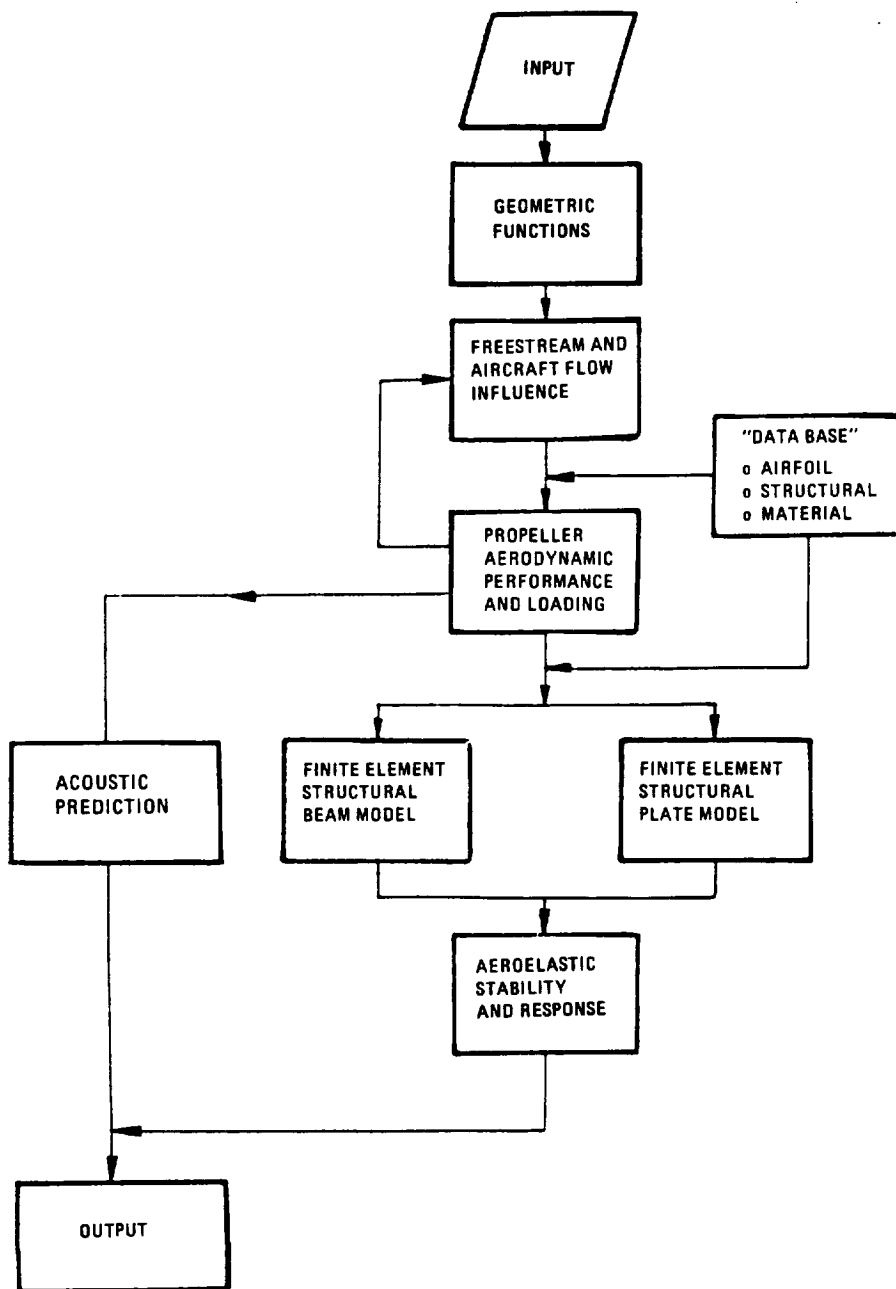


Figure 1-1. Performance Mode - Single Pass Functional Description

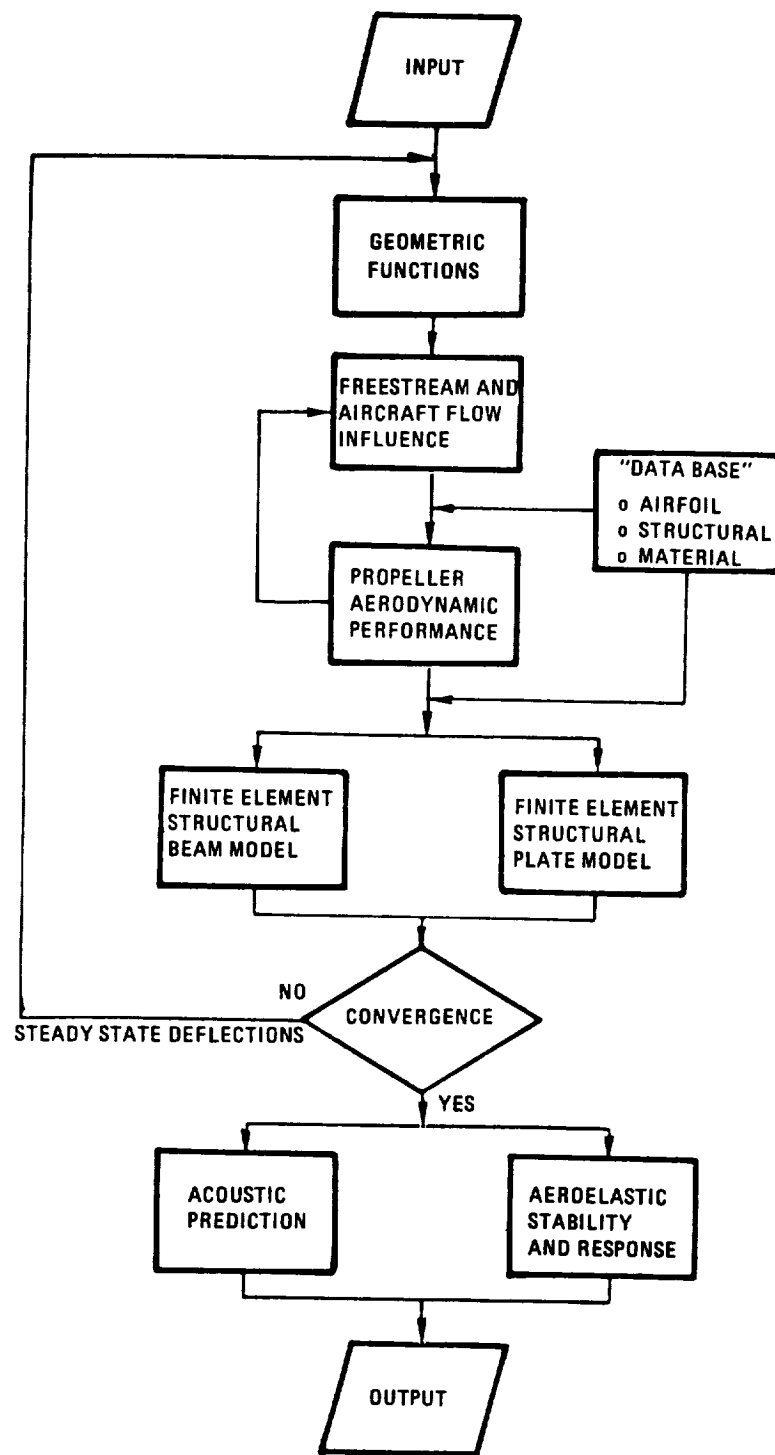


Figure 1-2. Performance Mode - Iterative Pass Functional Description

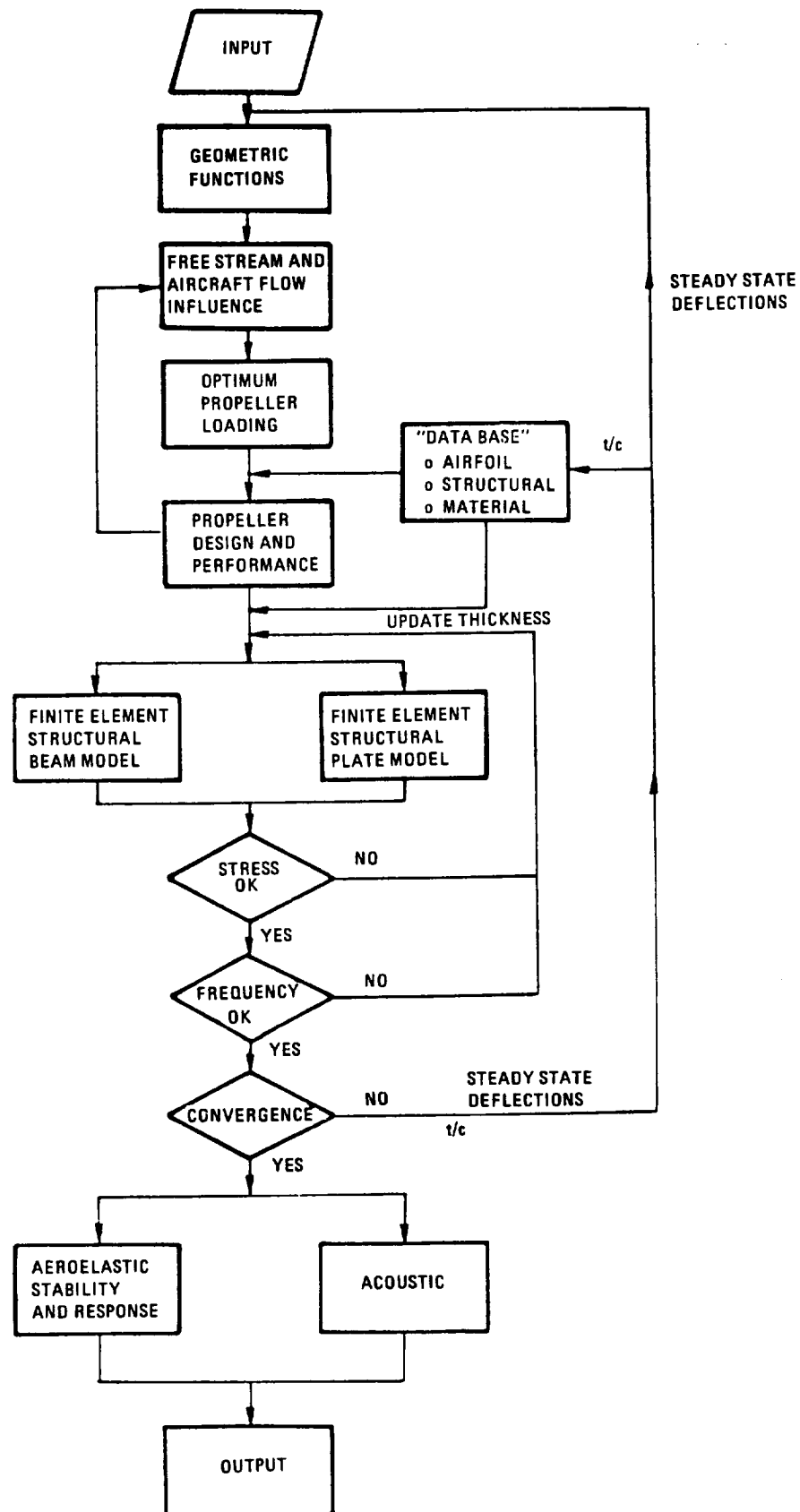


Figure 1-3. Design Mode Functional Description

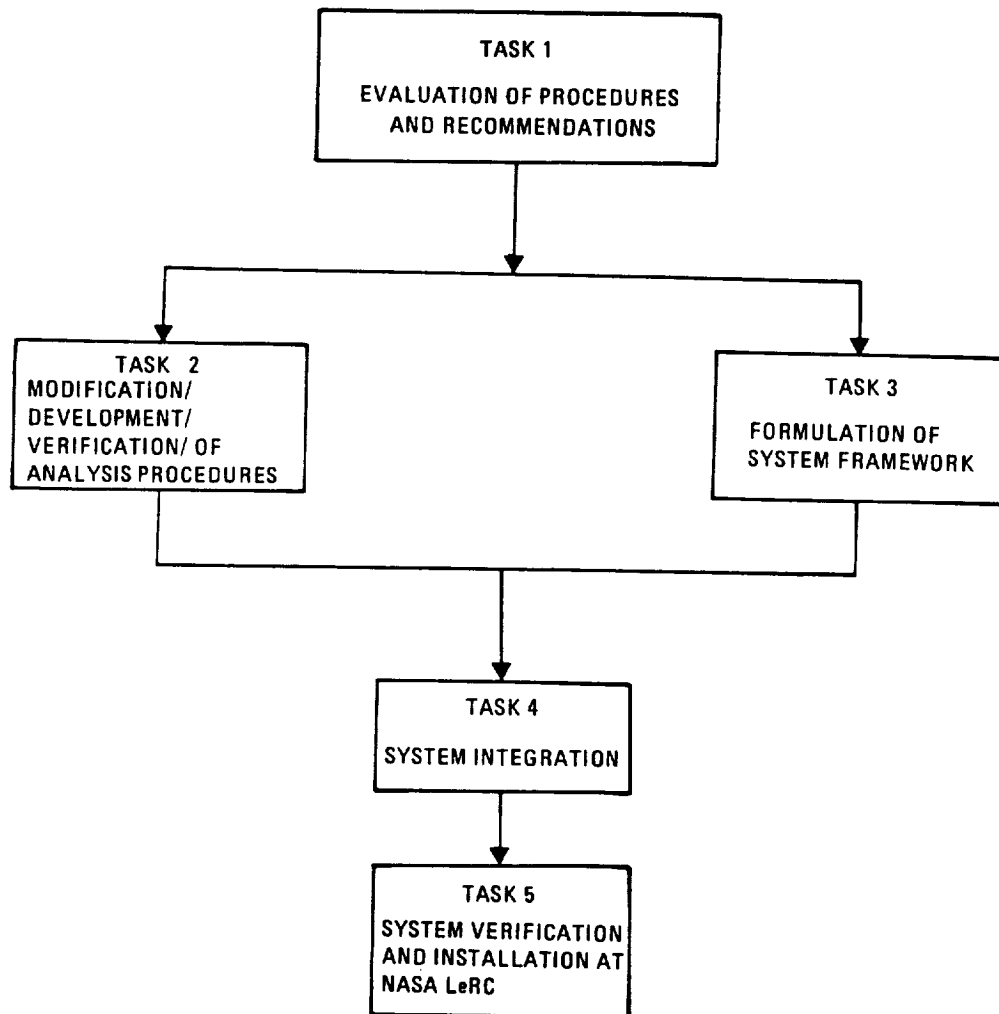


Figure 1-4. GAPAS Development Plan



incorporation of the analyses tools into a unified system. Some of the evaluation factors considered were capabilities for: (1) modular design, (2) interaction of individual modules occurring only through the procedural system, (3) data base management system for transfer of information between modules, (4) program software adaptable to generally available computers, (5) user control in batch or interactive modes, and (6) ability to operate in either a performance mode or a design mode. At the completion of Task 1, the selection of specific analysis tools to be incorporated in GAPAS, as well as the choice of the procedural system for unifying these analysis tools, was made.

After selection of analysis tools and procedural system, a concentrated effort on Tasks 2 and 3 was initiated. Task 2 encompassed the modification of existing analysis tools recommended from Task 1, as well as the development of analysis capabilities for those analytical tools that were previously unavailable. In addition, verification of individual modules was also performed. Task 3 involved the formulation of a logical framework used to unify the analysis tools, including the specification of all required interaction between modules. In addition, input/output procedures were developed to ensure that the common data flow required for different modules would be performed in an efficient manner. The capability for obtaining intermediate results at various stages of the calculation procedure was also included. This was necessary in order to allow for potential modifications of the analytical tools during the calculation procedure. Rather than rerun the entire procedure afterward, a restart capability was also included at key points in the procedure.

After completion of Tasks 2 and 3, the integration of the individual modules was performed. During the course of the integration task, it became apparent that, from the standpoint of both resources and schedule, the capability for the performance and design modes of operation could not be implemented. Therefore, it was decided to incorporate only the single pass performance mode into the prototype version of GAPAS and include the design mode in a later version. After incorporation of the analytic tools necessary for use in the performance mode was completed, Task 5, the verification and installation of GAPAS on the NASA Langley Computer, was

initiated. During this task, two propellers were analyzed; one, typical of a high speed commuter aircraft (SR-3 propeller) and the other, typical of a general aviation aircraft (Hartzell 101/16 propeller).

This final report is divided into seven sections. Sections 2, 3, 4, and 5 describe Tasks 1, 2, 3, and 4, respectively. Section 6 describes the results of the verification study and comparison with available data. Section 7 discusses recommendations for future work, including additional calculations necessary for further verification, as well as module improvements, and the need for experimental data to aid in the verification.

## 2. TASK 1: EVALUATION OF ANALYSIS PROCEDURES

This chapter discusses the evaluation task required to select analysis procedures for incorporation into GAPAS.

### 2.1 GUIDELINES FOR EVALUATION OF ANALYSIS PROCEDURES

Prior to the selection of the appropriate analysis procedures, it was necessary to establish a formal set of evaluation criteria based on the stated objectives and requirements of GAPAS. In general, the evaluation was based on the modeling analyses, solution methodology, and available computer program.

The analytical modeling was evaluated based on rigor, sophistication, comparisons with data, and flight regimes of applicability to GAPAS. The technical requirements satisfied and not satisfied were delineated. Potential modifications to extend the analytical modeling were identified. The additional technical effort required, the payoff in terms of added technical requirements satisfied, and risks which could affect success were also determined.

The numerical solution methodology was evaluated for efficiency, and alternate approaches were identified. Alternate approaches were assessed for amount of effort required, the payoff in terms of efficiency (savings in storage requirements, computer time, and improvements in reliability), and the risks involved in successfully achieving an alternate solution approach.

The computer program had many characteristics that needed to be identified and assessed for compatibility with GAPAS requirements. These included program language, computer system compatibility, execution time, disc file requirements, overlays, input format, output format, etc. The existence and adequacy of code documentation (including a user's manual), the reliability of successful execution, the degree of user familiarity required for application, and the amount of effort required to achieve compatibility with GAPAS code requirements were also determined. Finally, the effort required to implement modifications in the modeling analysis and/or numerical solution approach was evaluated.

This evaluation approach to the analysis procedures is summarized and illustrated in Figure 2.1-1.

It is evident that these evaluations not only provide technical assessment of the current procedure, but also an assessment of potential modifications, i.e., work required, benefits to GAPAS, cost, and risks. This data was needed to provide a basis for the selection of procedures to be recommended to NASA at the end of Task 1. The evaluation of each analysis procedure is described in Section 2.2.

## 2.2 EVALUATION OF INDIVIDUAL ANALYSIS PROCEDURES

The analysis procedures necessary to satisfy the GAPAS objectives fall into seven specific categories. These are (1) propeller geometry generation, (2) aircraft flowfield effects on propeller performance, (3) propeller aerodynamic performance, (4) airfoil loading distributions, (5) propeller acoustic performance, (6) propeller structural analysis, and (7) propeller aeroelastic and structural dynamics. Each category is considered a separate module in GAPAS.

### 2.2.1 Geometry Generator Module

#### 2.2.1.1 Summary of Requirements

The geometry generator module is necessary to define the shape of the propeller and to calculate quantities that are passed to the aircraft flow field, propeller performance, airfoil loading, acoustics, structures and aeroelasticity modules through the data base.

The geometry generator module should be applicable in both the "performance mode" and the "design mode". In the performance mode, the blade geometry is specified, whereas in the design mode, the sweep, twist, and thickness distributions are determined as part of the optimization and structural analyses procedures. Therefore, in the design mode it is preferable to keep the original propeller geometry (which would correspond to the first guess) as well as a file for the "current geometry", which would be the "original geometry" modified by sweep, twist, and thickness (i.e., for the latest iteration).

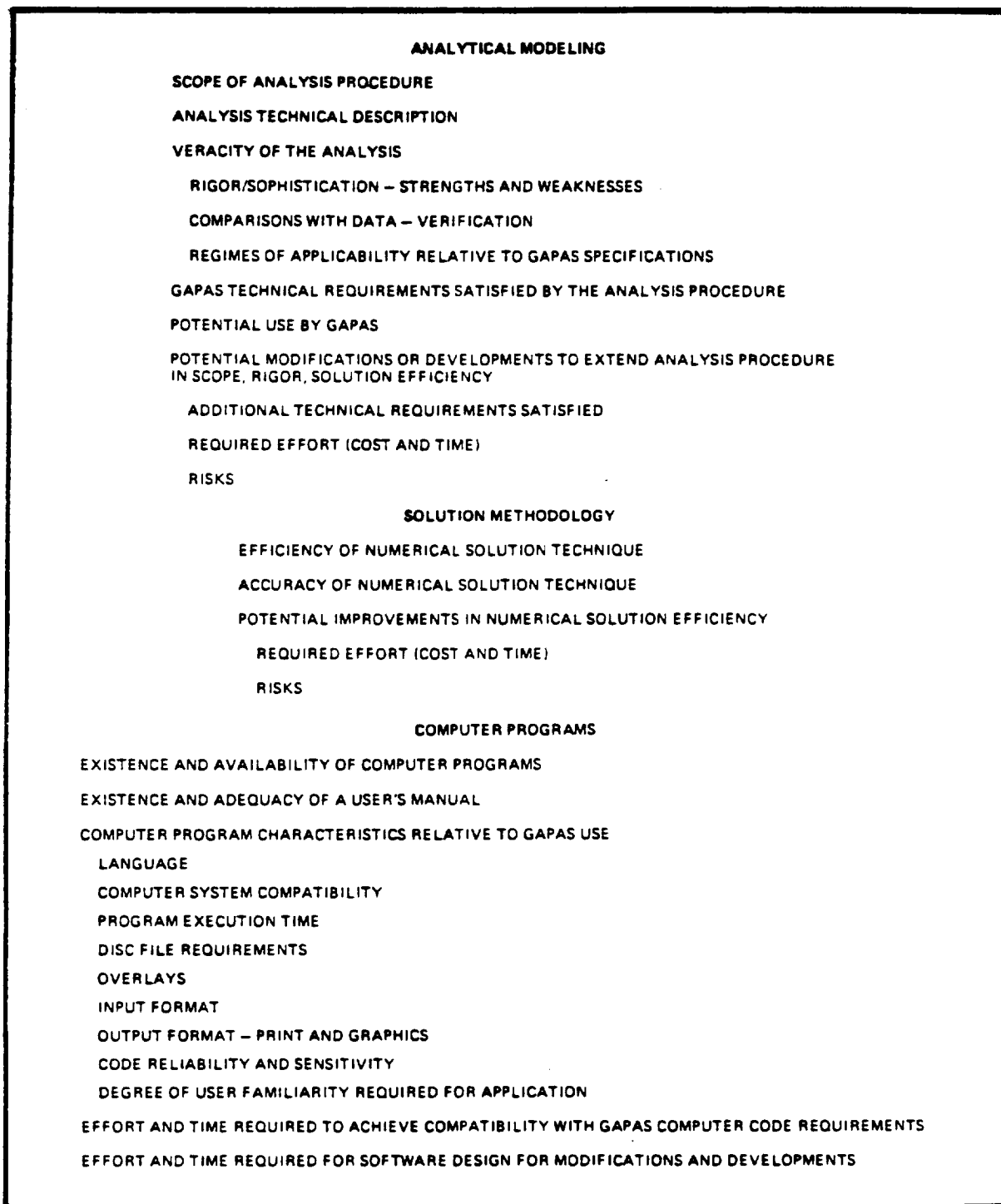


Figure 2.1-1. Candidate Analysis Procedure Evaluation Factors

The geometry generator module should specify the external (and, if applicable, the internal) coordinates of the blade section geometry in at least three cartesian coordinate systems. The coordinate systems are: (1) local coordinate system (LCS), which lies in a plane sliced through the propeller at an arbitrary angle, wherein  $x = 0$ ,  $y = 0$  corresponds to the leading edge of the airfoil section (Figure 2.2-1); (2) a global coordinate system fixed to the propeller blade (GCS-1) and designated by  $X'Y'Z'$  coordinates (Figure 2.2-2). Here, the  $Z'$  axis lies along the pitch change axis (PCA), the  $Y'$  axis is forward along the axis of rotation, and the  $X'$  axis orthogonal to both  $Y'$  and  $Z'$  axes and in the direction as determined by the right-hand rule; (3) a second global coordinate system (GCS-2) which is fixed in space (Figure 2.2-2) and has coordinates  $XYZ$ . The GCS-1 and GCS-2 are identical when the propeller is at the 12 o'clock position ( $\phi = 0$ ). The angle  $\phi$  is measured in the CCW direction of rotation. The GCS-2 is necessary when the flow field in the propeller plane is nonuniform in the azimuthal direction ( $0 \leq \phi \leq 2\pi$ ).

The geometry generator module will be used by the aerodynamic, acoustics and structural modules. Because each of these analyses require different output from the geometry generator module, a list of input and the required output for each different module is described below.

Input: The input parameters to the geometry generator module should include at least:

- (1) Number of input stations along the PCA wherein the propeller blade geometry is specified. (A minimum of 12 for the performance mode and 5 for the design mode) =  $N_i$

Corresponding to each  $N_i$

- (2) Distance along PCA =  $R_i/R$ , where  $R$  is the propeller radius
- (3) Chord length =  $c/R$ , where  $c$  is the longest chord length
- (4) Maximum thickness to chord ratio =  $(t/c)$
- (5) Blade pitch angle =  $\beta$  (degrees)
- (6) Horizontal reference axis height =  $H_a/R$

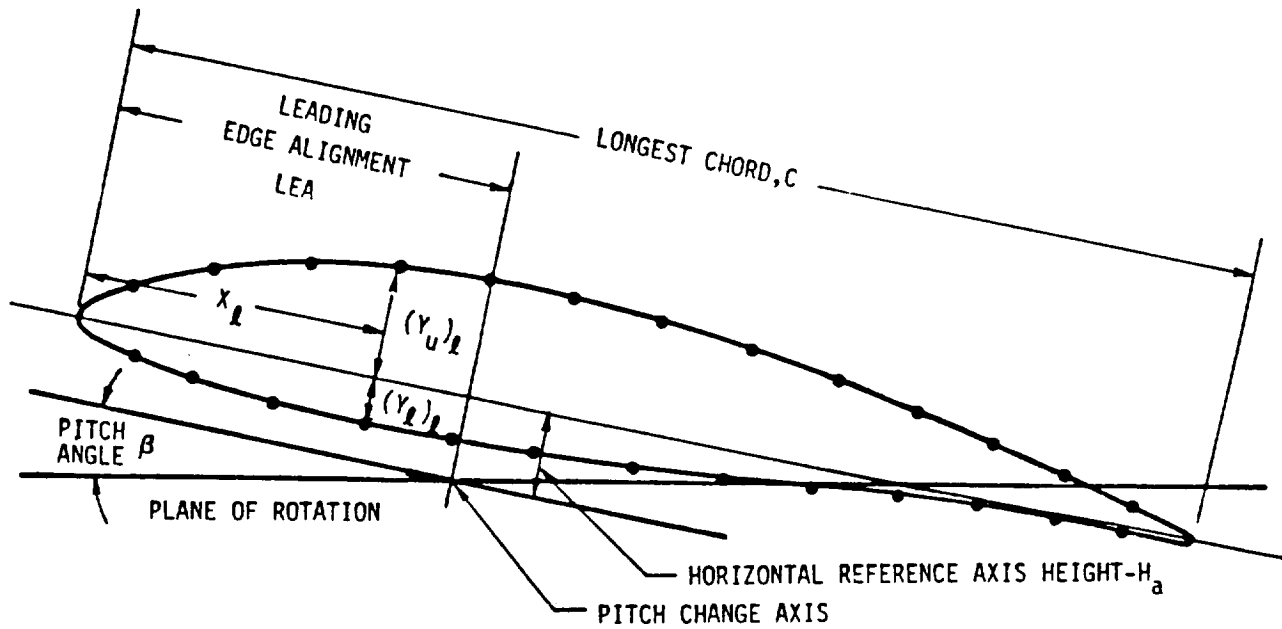


Figure 2.2-1. Airfoil Section Local Coordinate System (LCS)

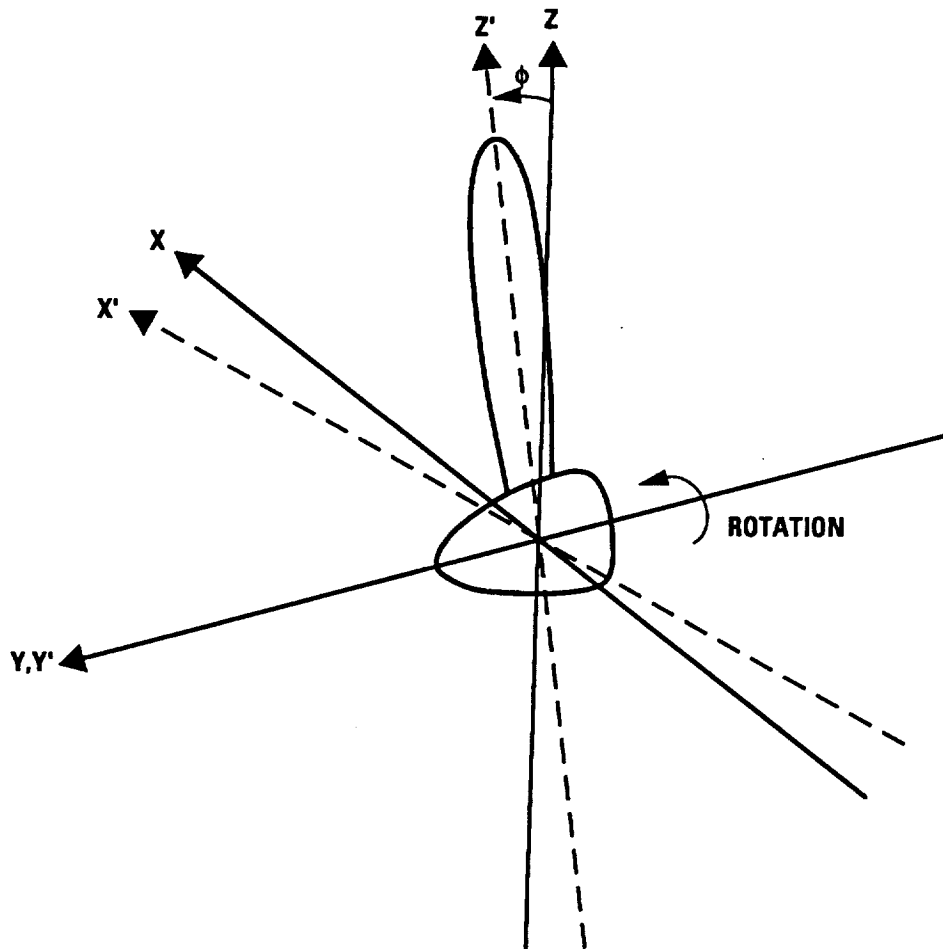


Figure 2.2-2. Global Coordinate Systems (GCS-1:  $X'Y'Z'$ ; GCS-2:  $XYZ$ )



- (7) Leading edge alignment =  $LEA/c$
- (8) Coordinates of the upper and lower surfaces in the LCS =  $(x/c, y/c)$ . If specifying a family of airfoils, specify the equations of camber and thickness (or in case of Clark Y, specify thickness or  $C_{L_D}$ ).
- (9) Center of gravity location in the LCS =  $(x/c)_{c.g.}, (y/c)_{c.g.}$
- (10) Number of stations where airfoil blade section geometry is required to be output =  $N_0$
- (11) Distance along the PCA corresponding to each of the  $N_0$  locations =  $R_0/R$
- (12) Flag indicating whether output is required for airfoil loading, acoustics or structural analyses
- (13) Equation of the arbitrary line (expressed in GCS-1) or the X'Y'Z' coordinates of the arbitrary line (expressed in GCS-1) through which planes normal to this line will be constructed that slice through the propeller blade.
- (14) Number of azimuthal stations (in GCS-2) where the coordinates of the leading and trailing edge of the airfoil section are required (i.e., 36 for  $10^\circ$  spacing in  $\phi$ ).
- (15) Flag describing distribution of the type of propeller structure.

Calculations: Parameters that are to be calculated in the geometry generator module are

- (1) Center of gravity location in the LCS
- (2) Cross-sectional area of airfoil section
- (3) Moments of inertia ( $I_x, I_{xy}, I_y, J$ ) in the LCS
- (4) Transformation of (1) and (3) to the GCS-1
- (5) Using spline fits, obtain leading and trailing edge coordinates in the GCS-2 for each of the desired airfoil sections at the required  $\phi$  locations.
- (6) Sweep angle, defined as the angle between the PCA and the tangent to the leading edge or the tangent to the mid-chord (include both computations). See Figure 2.2-3.
- (7) If camber and thickness are input (either in equation or table format), compute the airfoil coordinates in both LCS and GCS-1.

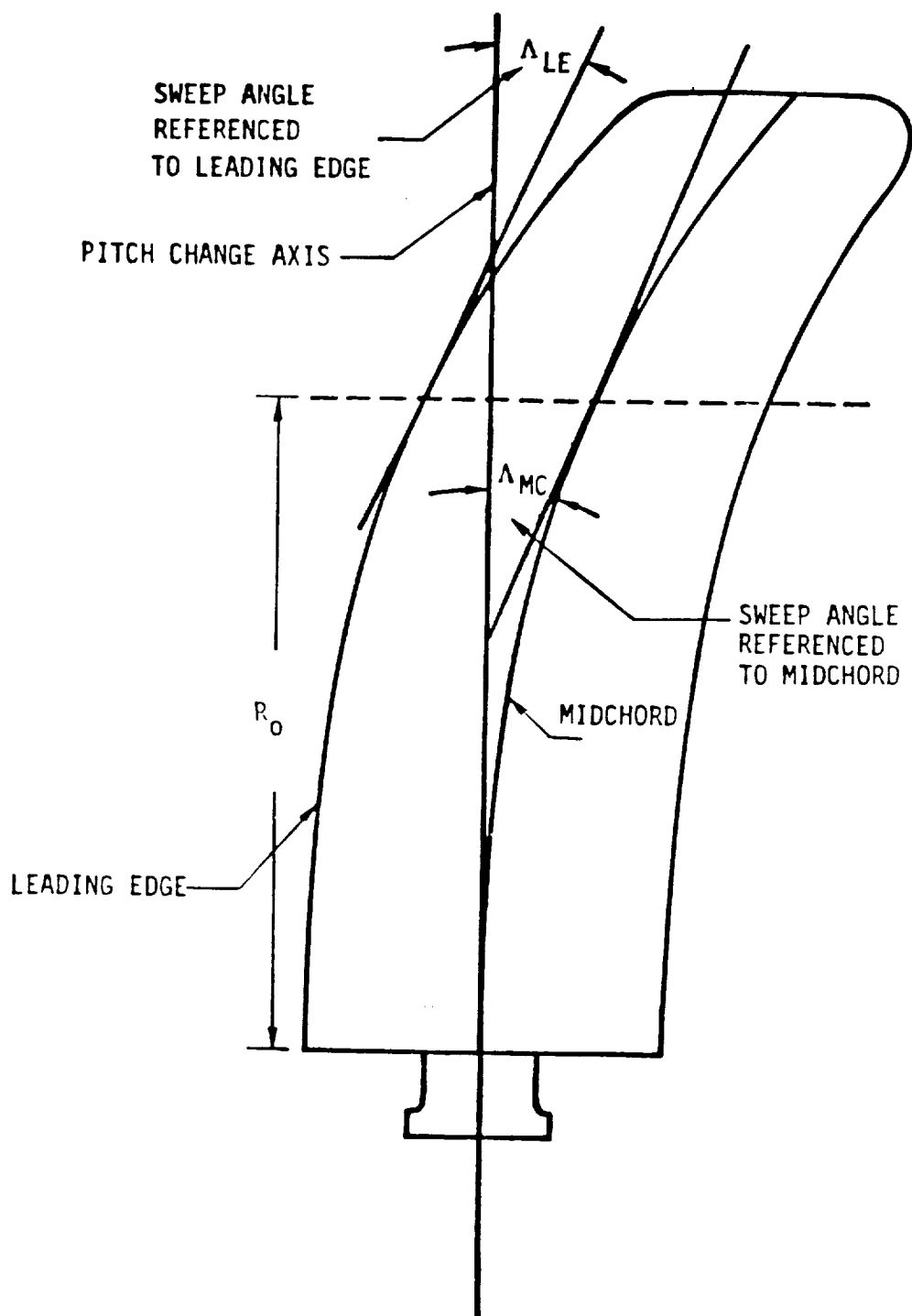


Figure 2.2-3. Geometric Sweep angle Definitions

- (8) The coordinates of the airfoil geometry in the plane perpendicular to the arbitrary line specified in the input. These coordinates should be in both the LCS and GCS-1. For the aerodynamic module, this line will be either the leading edge or the mid-chord. For the acoustic module, the line will be the pitch change axis. However, in the structural module this line cannot be specified a priori, but must be computed. This computation requires interaction with the geometry generator module as proposed in Section 2.2.1.2.

Output: Parameters that are required to be output will depend on which of the modules (airfoil loading, acoustics, or structures) are using the geometry generator module. Listed below are the output parameters required for each of the three modules accessing the geometry generator module. Output variables should be in nondimensional form, consistent with the input.

a. Aerodynamics: For each of the required output stations:

- (1) Radius measured along the PCA corresponding to the airfoil section to be output =  $R_0/R$
- (2) Coordinates of the airfoil section in the plane normal to the specified line (either leading edge or mid-chord, see Figure 2.2-4. A minimum of 64 points around the airfoil should be output. These coordinates should be in the LCS and GCS-1 (include  $dy_1/dx_1$  and  $d^2y_1/dx_1^2$ ).
- (3) Sweep angle of leading edge and mid-chord line referenced to the PCA ( $\Delta_{LE}$ ,  $\Delta_{MC}$ ) = degrees.
- (4) Coordinates of the leading edge and trailing edge points in GCS-2 of each of the airfoil sections corresponding to each of the required azimuthal positions of the propeller blade.
- (5) Comparative blade weight will be an integrated weight starting from some initial radius near the propeller shank and ending at the tip.

b. Acoustics: For each of the required output stations:

- (1) Radius measured along the PCA corresponding to the airfoil section to be output =  $R_0/R$
- (2) Camber =  $y/c$
- (3) Maximum thickness =  $t/c$
- (4) Leading edge alignment =  $LEA/c$

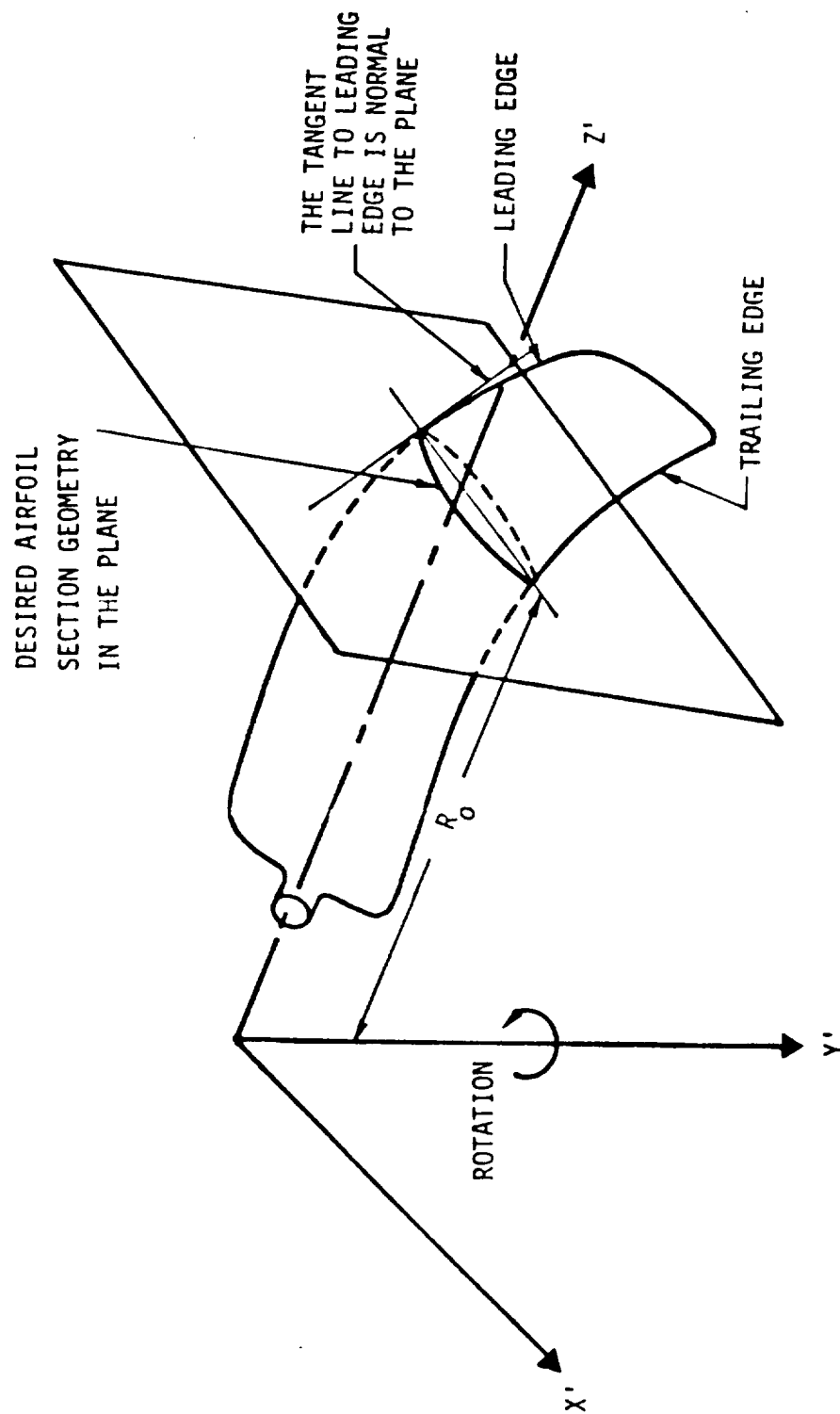


Figure 2.2-4. Geometry Generator Module - Aerodynamic Application

- (5) Chord =  $c/R$
- (6) Propeller section pitch angle = degrees

Parameters (2)-(6) are measured in a plane normal to the PCA (Figure 2.2-5).

c. Structures: For each of the required output stations:

- (1) Radius measured along the PCA corresponding to the airfoil section to be output =  $R_o/R$
- (2) Center of gravity location in LCS =  $(x/c)_{c.g.}$ ,  $(y/c)_{c.g.}$
- (3) Moments of inertia ( $I_x$ ,  $I_y$ ,  $I_{xy}$ ,  $J$ ) with respect to LCS
- (4) Coordinates of the airfoil section in a plane perpendicular to the specified line (Figures 2.2-6 and 2.2-7). These coordinates should be in both LCS and GCS-1.
- (5) Cross-sectional area and location of area centroid
- (6) Horizontal reference axis height =  $H_a/R$
- (7) Blade pitch angle = degrees
- (8) Specific material corresponding to each airfoil section coordinate in the required plane as well as information on the material direction of each orthotropic material with respect to the normal to the direction of this plane passing through the blade.
- (9) In regard to internal geometry, the module should be able to handle, in addition to the solid blade, hollow, UTRC spar shell (central metallic spar surrounded with composite skin), and semi-monocoque structures (e.g., using ribs for support). Similar information as in (8) will be required for cases involving internal geometry. (See Figure 2.2-8 for examples.)

#### 2.2.1.2 Section Profiles Perpendicular to the Line of Shear Centers

##### Finding the Elastic Axis (Center of Twist) of the Propeller Blade

The elastic axis of a straight blade is defined as the line of shear centers. For a straight blade the elastic axis will be straight. For a curved blade, the assumption will still be used that it is the line of shear centers, but the elastic axis will be defined by a polynomial in three-dimensional space.

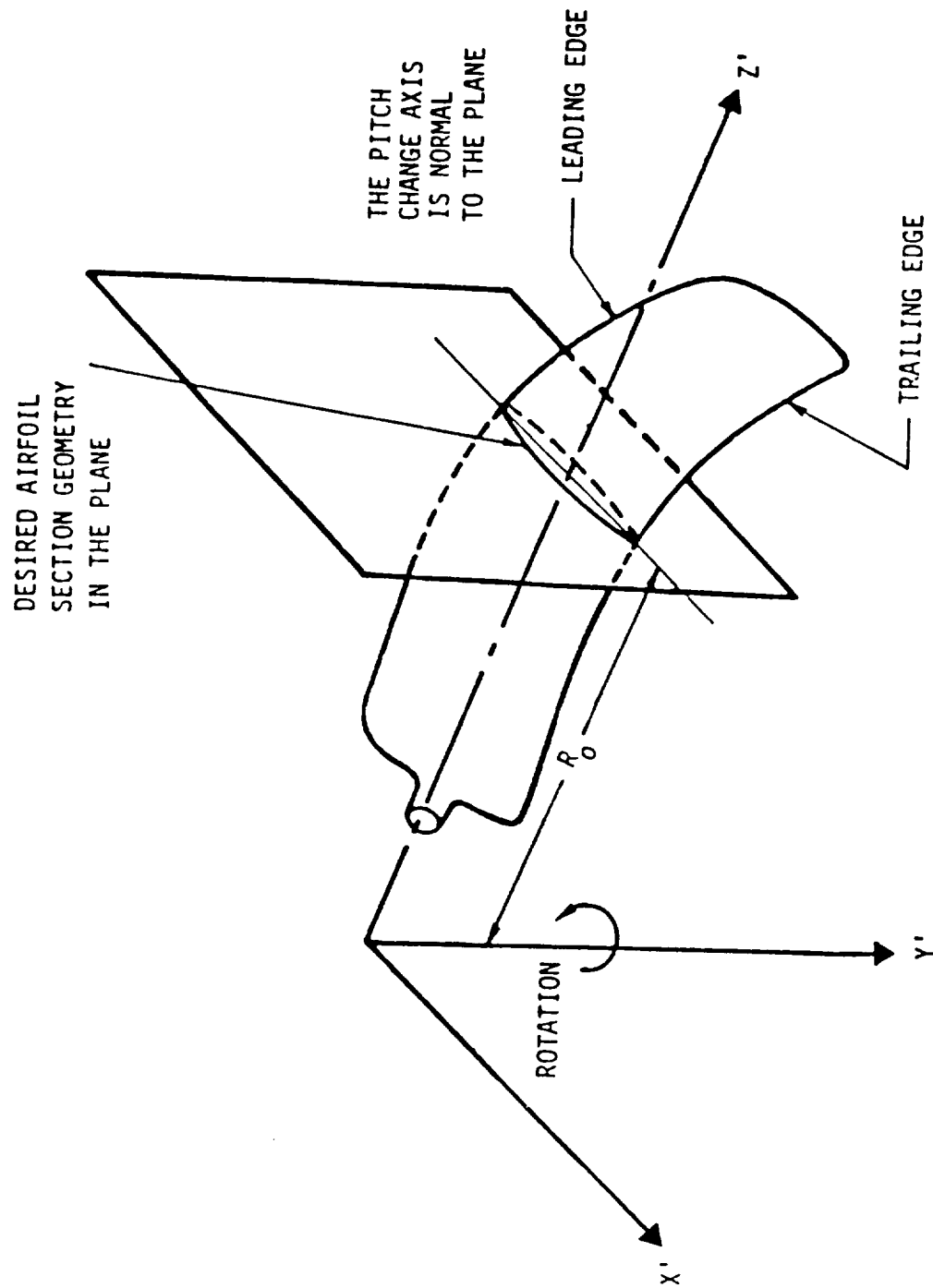


Figure 2.2-5. Geometry Generator Module - Acoustics Application

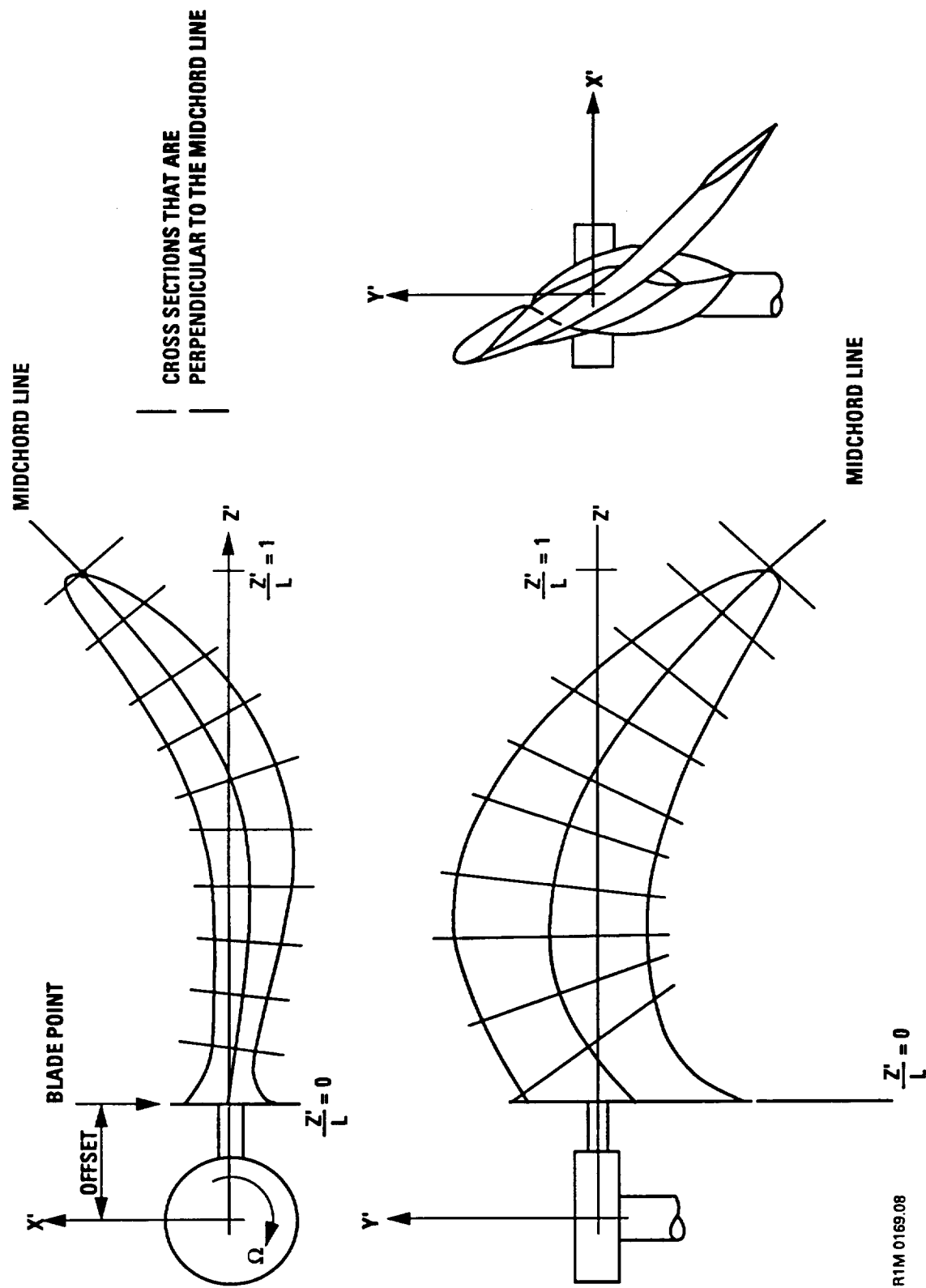


Figure 2.2-6. Geometry Generator Module - Structural Application (Mid-Chord Line)

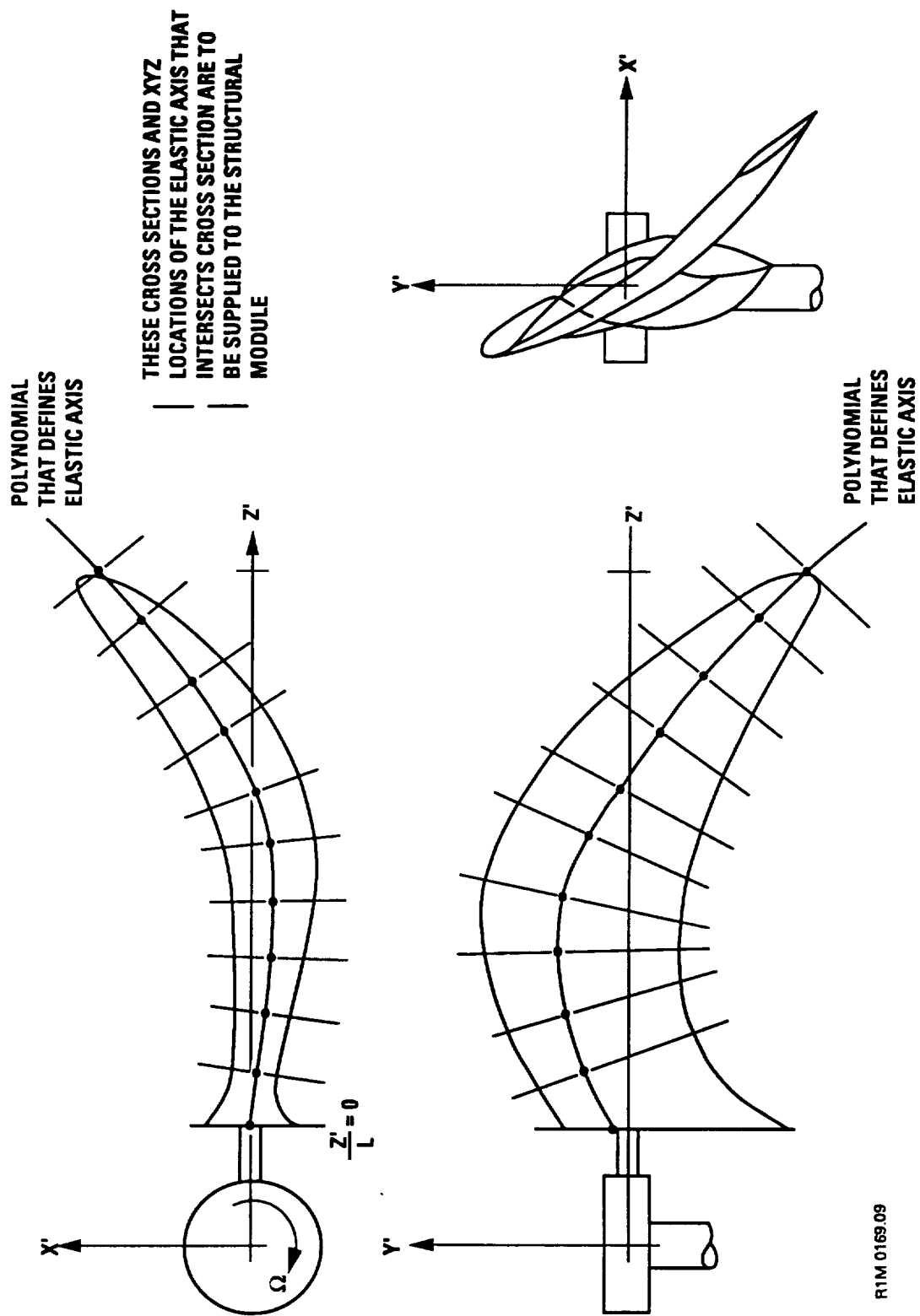


Figure 2.2-7. Geometry Generator Module - Structural Application (Elastic Axis)



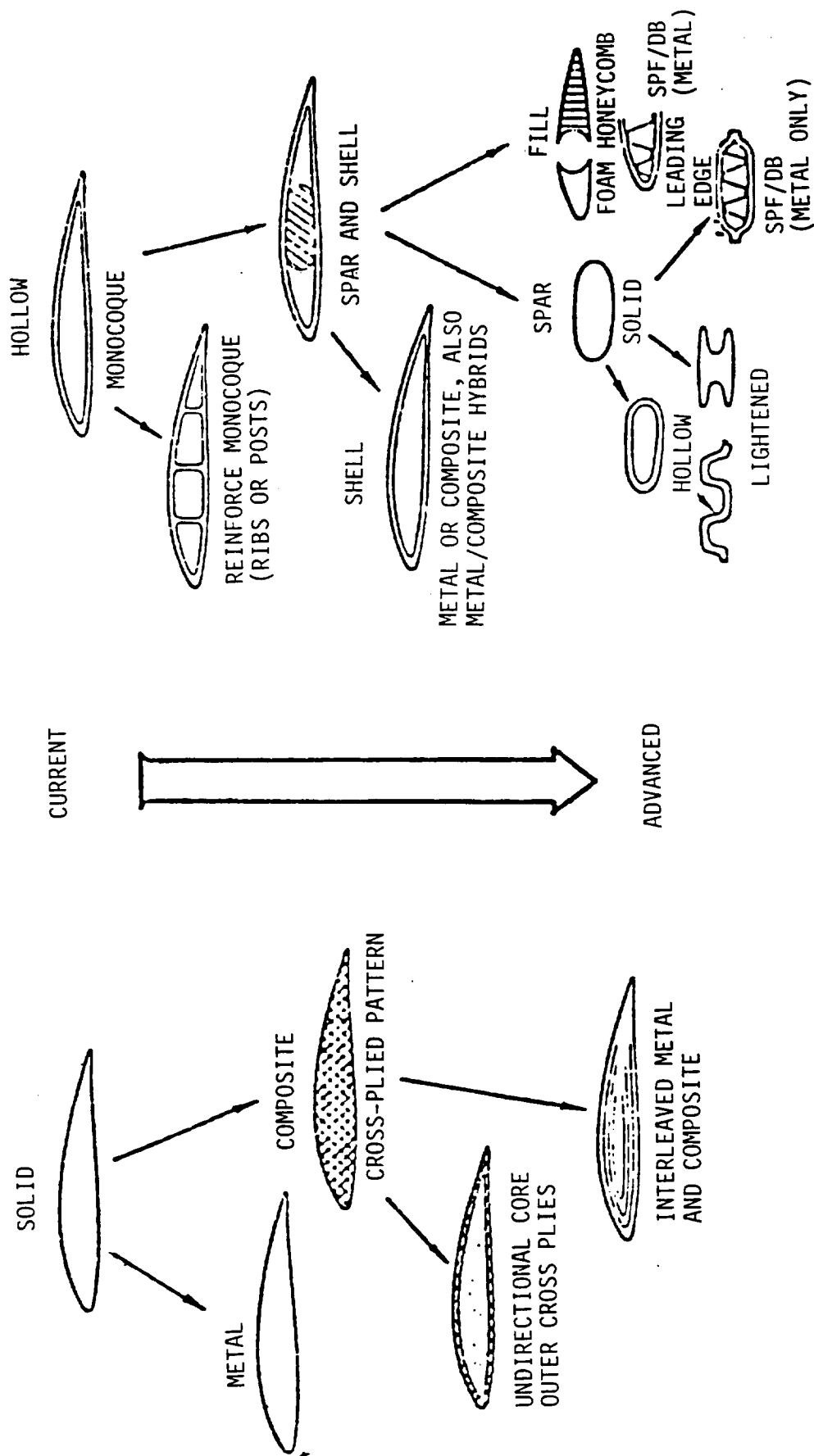


Figure 2.2-8. Candidate Propeller Internal Structures

### Procedures for Determining the Elastic Axis

- (1) The geometry generator will give 11 equally spaced cross sections perpendicular to the mid-chord line (at  $Z'/L = 0, 0.1, 0.2, 0.3, 0.4, 0.5, 0.6, 0.7, 0.8, 0.9, 1.0$ ).
- (2) Using these 11 cross sections, the shear center program will calculate the shear center of each cross section (11 shear centers performed in structural module).
- (3) The geometry generator will define a polynomial that follows these shear center points (first guess of elastic axis).
- (4) The geometry generator will give 11 equally spaced cross sections perpendicular to this polynomial
- (5) Using these 11 cross sections, the shear center program will calculate the shear center of each cross section (performed in structural module).
- (6) The geometry generator will define a polynomial that follows these shear center points. (This is the polynomial that will be used for the elastic axis definition.)

### Determination of Blade Properties with Respect to the Defined Elastic Axis

Using the polynomial that defines the elastic axis of the blade, the beam finite elements and the blade's area and mass properties will be calculated.

- (1) The geometry generator will divide the elastic axis polynomial into 10 equal lengths. ( $Z'/L = 0, 0.1, 0.2, 0.3, 0.4, 0.5, 0.6, 0.7, 0.8, 0.9$ , and  $1.0$ ; 11 point locations needed for 10 divisions.) The  $X', Y', Z'$  locations of these 11 points will need to be supplied to the structural module.
- (2) Cross sections perpendicular to the elastic polynomial at these 11 point locations will also be supplied to the structural module.
- (3) These cross sections must have adequate definition so as to describe inside and outside geometry, mass properties of all material, and stiffness properties of all material used in the cross section.
- (4) Using this cross section definition, a structural program will be used to calculate the area centroidal point, mass center points, and all area properties (performed in structural module).

### 2.2.1.3 Evaluation of Candidate Geometry Generator Modules

There are no readily available geometry generator modules that have the capability to match the requirements of Sections 2.2.1.1 and 2.2.1.2. The geometrical requirements that are needed by the candidate programs for the aircraft flow field, propeller performance, airfoil loading, acoustics, structures and aeroelasticity modules drive the design of the Geometry Generator Module. Therefore, it is necessary to develop a new Geometry Generator Module.

### 2.2.2 Aircraft Flowfield Module

#### 2.2.2.1 Summary of Requirements

The aircraft flowfield in which the propeller operates is to be calculated in order to define the radial and azimuthal variations of the velocity in the propeller plane which, in turn, are used to calculate propeller aerodynamic performance, including noise and forced excitations.

Input: Aircraft characteristics shall include the following:

- (1) Angle of attack
- (2) Sideslip
- (3) Fuselage and nacelle shapes
- (4) Wing characteristics:
  - (a) Quarter chord coordinates
  - (b) Wing lift coefficient as a function of angle of attack
  - (c) Span length
  - (d) Root chord length (assumes no taper)
  - (e) Dihedral
  - (f) Sweep.

Propeller plane characteristics shall include the following:

- (1) Center coordinates and vertical and side tilt angles referenced to aircraft

- (2) Locations for which velocities shall be calculated in terms of azimuthal angle and radial location increments.

Output: Along with the specified input parameters, the output shall include the following:

- (1) Fuselage and nacelle characteristics:
  - (a) Panel geometry used for potential flow calculation
  - (b) Panel source strengths
  - (c) Surface velocities referenced to free stream velocity
  - (d) Surface pressure coefficients
- (2) Wing characteristics:
  - (a) Geometry of bound vortex along quarter chord
  - (b) Geometry of the trailing vortices
- (3) Propeller plane characteristics:
  - (a) Radial, azimuthal and axial velocity components
  - (b) Velocity components relative to aircraft coordinate system
  - (c) Flow angles relative to propeller coordinate system
  - (d) Flow angles relative to aircraft coordinate system.

Requirements of Analysis Capabilities: The calculation procedures shall include the following capabilities:

- (1) Incompressible potential flow paneling methods shall be used to model wing-fuselage combinations representing single-engine aircraft or wing-nacelle-fuselage combinations representing multi-engine aircraft.
- (2) The wing shall be modeled by a single horseshoe vortex placed along the quarter chord line.
- (3) The influence of the wing on the aircraft fuselage and nacelles shall be considered, but it shall be assumed that these bodies do not influence the wing.

- (4) Computational efficiency shall be maximized by taking advantage of the
  - (a) Use of aircraft symmetry.
  - (b) Development of guidelines for required number of panels, panel size and distribution.
  - (c) Identification of aircraft components that do not strongly influence flow in the propeller plane, and development of simple modeling rules or criteria for ignoring them.
- (5) Paneled models for the aircraft shall consist of quadrilateral and triangular elements as solid boundaries (i.e., velocity tangent to surface). Some panels shall be specified as relaxed boundaries to model inlets and outlets by matching their flows (i.e., specified velocity).

#### 2.2.2.2 Evaluation of Candidate Aircraft Flow Field Programs

GAPAS is intended to be a modular set of programs interacting through a common data base and executive system. As better modules become available, they can be incorporated with minimal disruption of the other subprograms. With this in mind, we chose to incorporate the simplified potential flow program by Jumper (Refs. 2.2-1 and 2.2-2) which was easily modified to run as a GAPAS module. It can calculate the velocity components in the plane of the propeller using source panels to model the nacelle and a horseshoe vortex for the lifting wing.

Other programs considered for incorporation into the aircraft flow field module were:

- (1) NEUMANN, code for axisymmetric bodies at angle of attack using the ideas of References 2.2-3, 2.2-4, and 2.2-5.
- (2) UTRC, which computes viscous axisymmetric flow with a center body, as described by Reference 2.2-6.
- (3) USSAERO, a source-vortex panel method (Ref. 2.2-7).
- (4) DANAIR, a three-dimensional higher order panel method described by Reference 2.2-8.
- (5) SOUSSA, a three-dimensional Green's Function Method ... see References 2.2-9 through 2.2-12.
- (6) VSAERO, a three-dimensional Green's Function Method ... see References 2.2-13 through 2.2-16.

For the panel methods described above, the body, wing, wake, etc. are divided into panels with singularity distributions of unknown strength – source, doublet, vortex. The assumed distributions – constant, linear, etc. – and panel description – quadrilateral, hyperboloid – depend on which method is used. The body boundary conditions (normal velocity component equal to zero) are satisfied at the control points with provision for relaxed flow conditions at the inlet/outlet panels resulting in a system of linear equations. Matrix methods are used to solve the system of equations for the unknown singularity strengths. Then, when the distribution of singularity strengths is known, the velocity components can be determined at any point within the flow field – in particular, the propeller plane.

The evaluation of the candidate procedures for calculation of the aircraft flow field were based on the modeling analysis, the solution methodology, and the computer program. In general, the programs that were based on more sophisticated analytical modeling tended to be too large for incorporation into GAPAS. These included VSAERO, SOUSSA, PANAIR, USSAERO and UTRC, which are all large stand-alone programs with the flexibility (and added complication) to analyze general flow field problems. The risk involved in modifying one of these programs for application to the propeller flow field problem was judged to be greater than the limitations of the easily converted JUMPER and NEUMANN codes. The initial decision was made to incorporate the JUMPER and NEUMANN codes, with modifications to the latter for axisymmetric bodies at angle of attack.

### 2.2.3 Propeller Aerodynamic Performance

Five aerodynamic performance procedures were evaluated for possible inclusion in the GAPAS Propeller Aerodynamic Performance Module. Each procedure included an operating computer code. Procedures evaluated were developed at United Technology Research Center (Ref. 2.2-6) (referred to as the UTRC code); Purdue University (Ref. 2.2-17) (Chang-Sullivan Code); Pennsylvania State University (Ref. 2.2-18) under the guidance of B.W. McCormick (Aljabri code); NACA (Ref. 2.2-19) (Crigler code); and the Society of British Aircraft Constructors (Ref. 2.2-20) (the S.B.A.C. code). The UTRC code is based on lifting-line theory, whereas the Chang-Sullivan code is based on a vortex lattice method. The Aljabri code is based on a

classical vortex analysis, whereas the Crigler code is based on Theodorsen's method (Ref. 2.2-21), and the S.B.A.C. code is based on a semi-empirical method.

#### 2.2.3.1 Summary of Requirements

These above procedures were evaluated against the contractual propeller aerodynamic performance technical requirements; namely, the calculation procedures are to have the capability to:

- (1) Account for blade sweep and/or proplets utilizing a curved lifting-line approach; the cosine rule shall be applied to airfoil data to account for blade sweep;
- (2) Represent the vortex wake by a finite number of helical vortex filaments, and calculate the induced flow at any radial location on the blade by summing over the wake filaments and propeller lifting line;
- (3) Account for supersonic effects by (a) limiting the related induced flow in the region of influence of the rotating Mach cone, and (b) reducing the airfoil lift for sections within the tip Mach cone;
- (4) Calculate propeller performance for the following four basic modes; with:
  - (a) Radially varying velocities input in the propeller plane
  - (b) Mode (a) type input plus a specified angle of attack to the propeller plane
  - (c) Radial and azimuthal variations of velocity input in the propeller plane(Note, (a) - (c) do not include the effects of wake deflection.)
  - (d) Inviscid flow calculated around an axisymmetric nacelle; results of this calculation shall be used to place the wake vortex filaments along stream surfaces conforming to the shape of the nacelle, and to determine the velocities in the propeller plane as a function of radial location;
- (5) Account for variation of airfoil type along the propeller span; in particular, the analysis shall be capable of calculations for different specified airfoil types in the inboard and outboard sections of the propeller, with a procedure for computing airfoil characteristics in the transition region by interpolation;
- (6) Account for cascade effects of multiblade propellers;

- (7) Account for drag and spinner-blade shank interference drag of typical round shank general aviation propellers.

The methods and codes were evaluated against a set of evaluation factors shown in Figure 2.1-1. Each procedure will be discussed in relation to these factors and the technical requirements delineated above.

#### 2.2.3.2 UTRC High Speed Propeller-Nacelle Aerodynamic Performance Prediction Procedure

The UTRC aerodynamic performance prediction procedure is based on a lifting-line analysis that is combined with a viscous compressible center-body interaction program originally developed for duct and compressor applications (Refs. 2.2-22 and 2.2-23). The procedure first calculates the inviscid and viscous flow about the nacelle only. For the inviscid flow an axisymmetric potential-flow solution that utilizes conformal mapping based on a Schwartz-Christoffel transformation is used. For the viscous flow an implicit forward-marching numerical integration technique for solving the parabolized Navier-Stokes equations between the inviscid-flow streamlines is utilized. The propeller-nacelle wake flow is then represented by a finite number of vortex filaments that are placed along stream surfaces to conform to the shape of the nacelle, and the results of the nacelle flow calculation are used to locate the wake vortex filaments around the nacelle and to determine the inflow velocity at the propeller as a function of radial location. Each propeller blade is represented by a segmented bound vortex lifting line along the propeller blade quarter-chord line. The induced velocity due to the blade-bound vortex and wake trailing vortex elements at any blade radial location is then determined by applying the Biot-Savart law. This information, combined with the nacelle-flow solution, defines the inflow and the effective angle of attack. Coupling the angle-of-attack with two-dimensional airfoil and cascade data then allows the local lift and drag to be determined. These lift and drag forces are then resolved into thrust and torque components and integrated over the blade to allow calculation of thrust, power, and propeller efficiency. A final optional step is to use the blade forces in a circumferentially averaged (axisymmetric) viscous compressible flow calculation to ensure that the velocities between the blades and downstream of the propeller do not become high enough to result in large losses due to



shock waves, and to determine the drag of the nacelle in the presence of the propeller.

Evaluation of the UTRC analysis and computer code against the contractual analysis capabilities delineated in Section 2.1 indicates that the procedure utilizes a curved lifting-line to account for blade sweep but is not currently able to handle proplets (Item 1). In addition, the wake representation and calculation of induced flow conform to the requirement of Item 2 (representation of vortex wake by finite number of helical vortex filaments and calculation of induced flow by summing over them and the propeller lifting line). With regard to a means of accounting for supersonic effects (Item 3), the UTRC methodology limits the related induced flow in the region of influence of the rotating Mach cone (Item 3(a)) by discriminating between vortices within and outside the Mach cone and, for those within, between those which affect a blade segment at a particular time and those which do not. Moreover, with regard to the reduction of airfoil lift for sections within the tip Mach cone, the UTRC methodology takes this into account using correction factors developed by Borst (Ref. 2.2-24) based on the tip relief model of Evvard for fixed wings (Ref. 2.2-25). A modification of this correction to include sweep is currently underway by UTRC. With regard to propeller performance calculation capabilities (Item 4), the methodology does not treat unsteady effects; it is only capable of handling cases 4(a) (radially varying velocities input at the propeller plane) and 4(d) (with inviscid flow around an axisymmetric nacelle). With regard to Item 5, the UTRC methodology allows for variation of airfoil type along the propeller span and includes a procedure for computing airfoil characteristics in the transition region by interpolation. Regarding Item 6 (cascade effects for multiblade propellers), these effects are currently included for NASA 65 series airfoils for a gap-to-chord ratio greater than 0.8; blade width and finite-thickness effects are not presently included, although the code is currently being modified by UTRC to include an alternate cascade correction based on the method of G.L. Mellor (Ref. 2.2-26). Regarding Item 7 (drag and spinner-blade shank interference drag), although nacelle and propeller blade drag are accounted for, there is currently no provision for calculation of interference drag.

In summary, the strengths of the UTRC analysis procedure include the extensive capability for calculation of the nacelle flow field, the discrimination of vortices within and outside the Mach cone, the cascade and supersonic tip corrections, and the flexibility of prescribing the wake. This latter item, however, may be argued to be an uncertainty and actually a weakness in the method.

The greatest shortcoming of the method lies in the use of a lifting line model which corrects only the section angles of attack for the induced effects of the wake. The wake actually induces a curved flow field which can have a significant effect on the section lift coefficients for wide blades.

The computer code (PANPER) based on the UTRC methodology is written in Fortran V for the Univac 1110 computer. The code is also running on the IBM 3030 system at NASA-Lewis, but has not been completely implemented on the CDC Cyber 175 system. A highly-detailed user's manual is available (Ref. 2.2-27).

#### 2.2.3.3 Chang-Sullivan - Theoretical Performance of High-Efficiency Propellers

The next analysis procedure evaluated was that developed by Chang (Ref. 2.2-17) and Sullivan (Ref. 2.2-28) at Purdue University. This procedure utilizes the vortex-lattice method (also known as first-order lifting-surface method; Weissinger-L method) to solve for propeller performance. In this methodology, the propeller blade and wake are represented by a system of segmented bound and trailing vortices, with the bound vortex segments placed at the quarter-chord points of the blade. The strengths of the bound- and wake-vortex filaments are determined using the Biot-Savart law and the condition that the flow be tangent to the blade mean camber line along the three-quarter chord line. Application of the Kutta-Joukowski law at any radial location then determines the lift coefficient of the blade at that point. Blade drag is determined from correlations based on blade camber, thickness, Mach number, and lift, including viscosity and compressibility effects. Resolving lift and drag into thrust and torque components and integrating over the blade then allows calculation of propeller thrust, power, and efficiency. Moreover,

the analysis includes sweep and proplets, and treats the nacelle in approximate fashion by representing it as an infinite cylinder. Cascade effects are included for thin blades only, but there is no correction for finite-thickness effects and no provision for supersonic tip effects.

Evaluation of the Chang-Sullivan aerodynamic performance procedure against the contractual analysis capabilities indicates that the procedure utilizes a curved lifting line and accounts for both blade sweep and proplets. Moreover, the propeller wake is represented by a finite number of helical vortex filaments and the induced flow at any radial location is calculated by summing over the wake filaments and the propeller lifting line. However, supersonic flow effects are not accounted for. In addition, as in the case of the UTRC methodology, only propeller performance cases 4(a) (radially varying) velocities at the propeller plane) and 4(d) (with inviscid flow around an axisymmetric nacelle) can be handled by the Chang-Sullivan procedure because the methodology does not treat unsteady effects. The Chang-Sullivan procedure does allow for variation of airfoil type along with propeller span, however, and is capable of performing calculations for different specified airfoil types in the inboard and outboard sections of the propeller. As previously mentioned, cascade effects are included only for thin blades, and the procedure accounts for blade drag but not spinner-blade shank interference drag.

In summary, the strength of the Chang-Sullivan methodology lies in its use of the vortex-lattice method. It is thus capable of modeling sweep, proplets, and low-aspect-ratio blades. Cascade effects (for thin blades) are also accounted for by this method.

There are several shortcomings of the Chang-Sullivan procedure, however. These include: (1) a simplified modeling of the wake geometry, (2) unsteady aerodynamic effects are not treated, (3) no provision for supersonic tip effects, (4) the method for obtaining airfoil section properties at high Mach numbers is not clear, and (5) no corrections for finite thickness effects.

Another shortcoming of this code is the lack of any correction to the section lift coefficients for compressibility. Having calculated lift coefficient on the basis of the incompressible first-order lifting surface theory, the code then determines a section drag coefficient adjusted for Mach number. However, a correction is needed for lift coefficient as well.

The computer code based on the Chang-Sullivan analysis is written in Fortran IV and is operational on the IBM 3030 and CDC Cyber 175 computers. However, a detailed user's manual has not been developed.

#### 2.2.3.4 Aljabri – Prediction of Propeller Performance and Loading in Uniform and Nonuniform Flowfields

In addition to the UTRC and Chang-Sullivan methods, the aerodynamic performance procedure developed by A.S. Aljabri under the guidance of B.W. McCormick (Ref. 2.2-18) was evaluated. The Aljabri methodology is based on classical vortex theory applied to a lifting-line model of the blades which, strictly speaking, is valid only for straight unswept blades. Under the assumption that the induced velocity in the propeller plane is half that in the ultimate wake, the circulation at any blade radial location is determined from a line integral of the tangential velocity over the circumference of the blade plane at that radial location. Application of the Kutta-Joukowski equation then allows calculation of lift as a function of radial location. Airfoil section data are utilized to obtain lift-curve slope (which enters into determination of tangential velocity). Compressibility effects are accounted for in the section data via the Prandtl-Glauert rule, and nacelle effects are treated only in terms of introducing a nonuniform inflow at the propeller plane. Once lift and drag are determined as a function of radial position, integration over the blade allows calculation of propeller thrust, power, and aerodynamic efficiency. The methodology utilizes Prandtl's tip-loss factor to account for a finite number of blades, and corrects for finite blade width and thickness effects. The computer program, as originally set up, can handle Clark Y, NACA 4-digit-series (24xx), and NACA 16-series airfoil sections through a range of Mach numbers and angles of attack. Other section types can be handled if section lift and drag data are available. In addition, the methodology allows the calculation of unsteady flows by two alternative

methods, a quasi-steady method and a two-dimensional unsteady method. In the quasi-steady method, the assumption is made that the lift and drag at a given azimuthal position are the same as if the flow were steady at the flow conditions corresponding to that azimuthal location. In the two-dimensional unsteady method, in which Theodorsen's method is utilized, the blades are assumed to be two-dimensional, independent of each other, and each blade element is assumed to undergo a pure heaving motion.

Evaluation of the Aljabri procedure against the contractual analysis capabilities indicates that the methodology does not account for blade sweep and/or proplets, nor does it represent the vortex wake by a finite number of helical vortex filaments. In addition, the procedure has no provision to account for supersonic tip effects. The methodology is capable of handling unsteady as well as steady flows, however, and can perform calculations for basic modes 4(a) (radially varying velocities input in the propeller plane), 4(b) (mode (a) type input plus a specified angle of attack to the propeller plane), and 4(c) (radial and azimuthal variations of velocity input in the propeller plane). As previously indicated, however, the methodology only treats nacelle effects in terms of introducing a nonuniform inflow at the propeller plane. It does allow for variation of propeller type along the propeller span, accounts for cascade effects of multibladed propellers, and blade drag. Spinner-blade shank interference drag is not accounted for, however.

The computer code is operational on the CDC Cyber 175, and has an execution time of about 5 seconds for a typical case. A user's manual has been developed for this code (Ref. 2.2-29).

#### 2.2.3.5 Crigler - Application of Theodorsen Theory to Propeller Design

The next analysis procedure evaluated was that based on Crigler's application (Ref. 2.2-19) of Theodorsen's theory (Ref. 2.2-21) to propeller design. The methodology relates conditions in the ultimate wake to those in the propeller plane through a mass coefficient, and yields the same result as conventional vortex theory with Goldstein's tip correction for single-rotating propellers. Basically, expressions are developed relating section lift coefficient, flow angle with respect to the propeller plane, the so-called "fictitious impact velocity", and the mass coefficient (which

is related to Theodorsen's circulation function). Utilization of airfoil data to obtain lift coefficient as a function of flow angle completes the system for a given radial location. Airfoil data are also utilized to obtain drag, and resolution into thrust and torque components and integration over the blade enable propeller performance to be calculated.

When evaluated against the contractual propeller aerodynamic performance technical requirements, it is noted that Crigler's procedure has no provision for blade sweep and/or proplets, nor is the vortex wake represented by a finite number of helical vortex filaments. Also, supersonic effects are not accounted for. Moreover, the procedure has no provisions for unsteady-flow or nacelle effects, and thus is only applicable to the calculation of propeller performance for basic mode 4(a) (with radially varying velocities input in the propeller plane). Additionally, the method does not account for cascade effects for multibladed propellers, or spinner-blade shank interference drag. Blade drag is accounted for, however.

The computer code based on Crigler's methodology is currently running on the CDC Cyber 175. The code is available in Basic as well as Fortran versions, but does not have a user's manual.

#### 2.2.3.6 S.B.A.C Standard Method of Propeller Performance Estimation

The last aerodynamic performance analysis procedure evaluated is an empirical method based on the Society of British Aircraft Constructor's (S.B.A.C.) standard method of propeller performance estimation (Ref. 2.2-20). This is a semi-empirical procedure based on the fundamental assumption that the propeller efficiency can be expressed as the product of the induced efficiency, which takes into account the induced losses caused by the effect of a finite number of blades, and a factor of merit which takes into account low-speed profile drag, compressibility drag, and root drag. In addition, the method accounts for nacelle and fuselage flow, but has no means of taking into account blade sweep or supersonic tip effects, and treats only Clark-Y section blades. Thus, when evaluated against the contractual propeller aerodynamic performance technical requirements, it is to be noted that the S.B.A.C. methodology neither accounts for blade sweep and/or proplets nor represents the vortex wake by a finite number of

helical vortex filaments or accounts for supersonic flow effects. The computer code is, however, applicable to calculation of propeller performance for basic modes 4(a) (with radially varying velocities input in the propeller plane) and 4(d) (with inviscid flow calculated around an axisymmetric nacelle). In addition, as mentioned, the methodology treats only Clark-Y airfoil section blades and thus does not account for variation of airfoil type along the propeller span. Also, it does not account for cascade effects of multiblade propellers, but does take into account low-speed profile drag, compressibility drag, and root drag.

A computer code for programmable calculators based on the S.B.A.C. method and developed by Korkan and Ruff (Ref. 2.2-58) has been implemented at TRW. References 2.2-20 and 2.2-58 provide sufficient information to serve as user's manuals.

#### 2.2.3.7 Results of Review of Propeller Aerodynamic Performance Procedures

Results of the evaluation of the aerodynamic performance analysis procedures in terms of the contractual technical requirements are summarized in Figure 2.2-9.

In addition, a comparison of results of the UTRC lifting-line method and the Chang-Sullivan vortex-lattice method was carried out by B.W. McCormick. Both the lifting-line (UTRC) and vortex-lattice (Chang-Sullivan) methods replace the propeller blade by a single bound vortex line and a trailing helical vortex wake. Both have the problem of defining the wake and both require the added inclusion of section profile drag and compressibility effects. In addition, both require the solution of a system of  $N$  simultaneous algebraic equations to satisfy boundary conditions at  $N$  points along the blade. Thus, the computational time and the effort required to run each mode should be about the same, all other aspects of the problem being treated the same.

Although similar, the two methods are basically different. The lifting line model calculates the induced angle of attack,  $\alpha_i$ , at each station so that the section lift coefficient,  $C_{\ell}$ , is given by:

Candidate Codes	Sweep and/or Proplets	Wake Representation of Finite Number of Helical Vortex Filament	Supersonic Tip Effects	Compressibility Correction	Prop. Perf. Modes*	Airfoil Variation Along Span	Up to 8 Airfoil Types	Cascade Effects	Drag	Spinner Blade Shape Interference Drag
UTRC	X	X	X	X	A, B			X	X	
Chang-Sullivan	X	X		Drag coefficient only	A, B			X	X	
Aljabri				Airfoil data	A, B, C				Airfoil data	
Crigler				Airfoil data	A				Airfoil data	
S.B.A.C.				X	A, B				X	

\*Mode A) Rapidly varying velocities input in propeller plane

Mode B) Mode A) plus specified angle of attack of propeller plane

Mode C) Radial and azimuthal variations of velocity at propeller plane

Mode D) Inviscid flow around antisymmetric nacelle, including effects of wake deflection

Figure 2.2-9. Aerodynamic Performance Requirements Satisfaction Summary



$$C_L = C_{L_\alpha} (\alpha - \alpha_i) \quad (2.2-1)$$

where  $\alpha$  is the local angle of attack and  $C_{L_\alpha}$  is the lift curve slope. But from the Kutta-Joukowski relationship,

$$L = \rho V \Gamma \quad (2.2-2)$$

with  $V$  being the local velocity and  $\Gamma$  the bound circulation; it follows that

$$\Gamma = 1/2 c C_L V \quad (2.2-3)$$

where  $c$  is the section chord length. Since  $\alpha_i$  is a function of  $\Gamma$ , Equations (2.2-1) and (2.2-2) can be combined to give a single equation for  $\Gamma$  or  $C_L$ . Actually,  $\alpha_i$  at any station depends upon the distribution of  $\Gamma$  since the radial gradient of  $\Gamma$  results in the trailing vortex system. Thus, the above relationships must be satisfied at  $N$  points along the blade to obtain  $N$  simultaneous equations for  $\Gamma$  at each point.

Unfortunately, the correction to  $\alpha$ , namely  $\alpha_i$ , is only part of the difference between two- and three-dimensional flows around a lifting surface. For high aspect ratios,  $\alpha_i$  is the major correction, so that a lifting line model applies fairly well to conventional propeller blades. In addition to changing the direction of the flow at a blade section, the trailing vortex system induces a flow curvature which effectively reduces the camber of the section. As the aspect ratio of a lifting surface decreases, this camber correction becomes increasingly important.

On the other hand, the vortex lattice (Wessinger's L) method is really a first-order lifting surface theory and, as such accounts for all induced effects from the trailing vortex system. It does this by determining the strengths of the trailing vortices, and hence the bound vortex strength distribution, to assure that the resultant of the free stream and induced velocities is tangent to the section mean camber lines at  $N$  points along the locus of the section 3/4-chord points. Again,  $N$  simultaneous equations for  $\Gamma$  are obtained.  $C_L$  can then be obtained from Equation (2.2-3) followed by an estimated  $C_d$ .

To illustrate the basic differences in the lifting line model and the Weissinger-L method as applied to propellers, the UTRC and Chang-Sullivan codes were run using identical wake geometries and section properties ( $C_d$  and  $C_l$  versus  $\alpha$  and Mach number). Figure 2.2-10 presents such a comparison and also includes results from a vortex theory code that was written specifically for this study. The points labeled UTRC and Chang/Sullivan were taken directly from Reference 2.2-30. The vortex theory results will be discussed later.

From Figure 2.2-10, it can be seen that the UTRC code predicts results which are about 10% higher than the Chang-Sullivan code for this case. Probably this basic difference is even greater since the UTRC code uses airfoil data to obtain  $C_l$  whereas the Chang-Sullivan code uses the value of  $C_l$  obtained from a potential flow solution. Typically, the most exact potential flow solutions predict  $C_l$  values which are 3 to 8% too high.

A vortex-lattice code was written specifically for this study to examine the validity of the Weissinger-L method for finite wings and to compare it with a lifting line model. Results of a lifting-surface calculation are presented in Figure 2.2-11 and results of the Weissinger-L method code are shown in Figure 2.2-12, along with the results of lifting-line theory. For this rectangular wing having an aspect ratio of 6, two important observations can be made. First, the Weissinger-L method gives spanwise load distribution in close agreement with distributions calculated by lifting surface theory. Second, the lifting-line model overpredicts the wing lift by about 8% for this aspect ratio. As the aspect ratio decreases, this difference can be expected to become even greater.

Figure 2.2-13 taken from Reference 2.2-31 shows the UTRC code to overpredict the value of power coefficient,  $C_p$ , at a given advance ratio when compared with experimental data for the SR-1 propeller at a Mach number of 0.8. While this is reasonable to expect in light of Figure 2.2-12, there are other factors which may explain this difference such as blade twist due to centrifugal effects. Reference 2.2-30 shows about a 1 degree decrease in the blade pitch angle at the 3/4 radius when operating at the design rpm for the SR-3 propeller. Although SR-1 probably has less deflection, the experimental data for an angle of 62.5 degrees is seen to agree better with the UTRC predictions for 61.2 degrees.

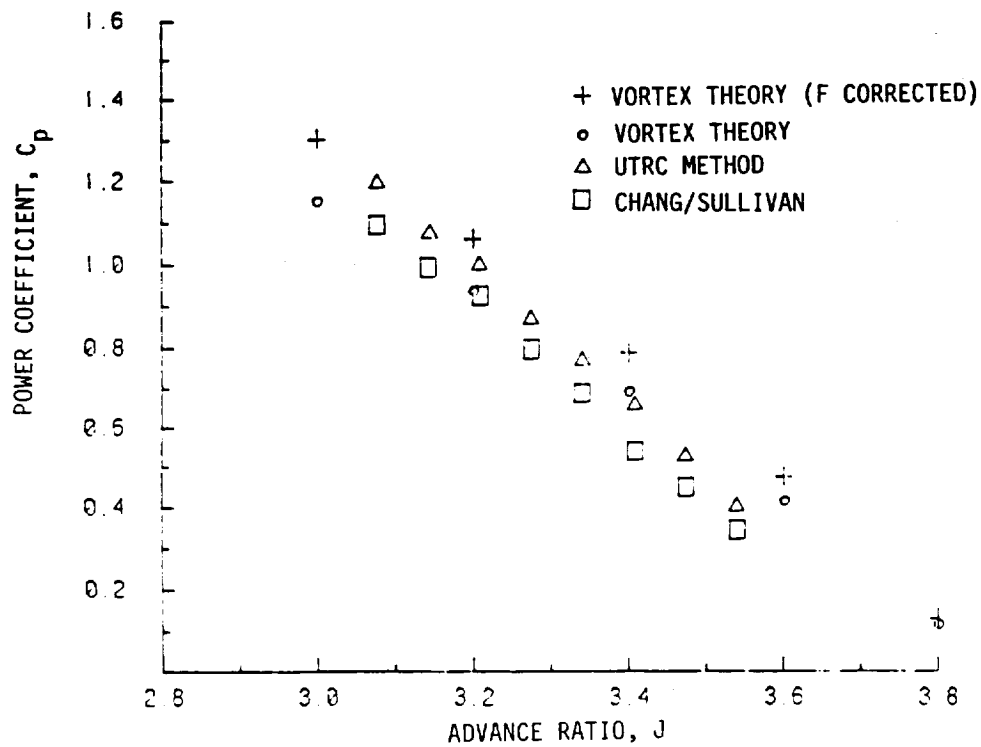


Figure 2.2-10. Comparison of Predicted Performance for SR-2 Propeller.  
 $M = 0$ ,  $\beta = 58^\circ$ ,  $C_D = 0$  (Uniform In-Flow)

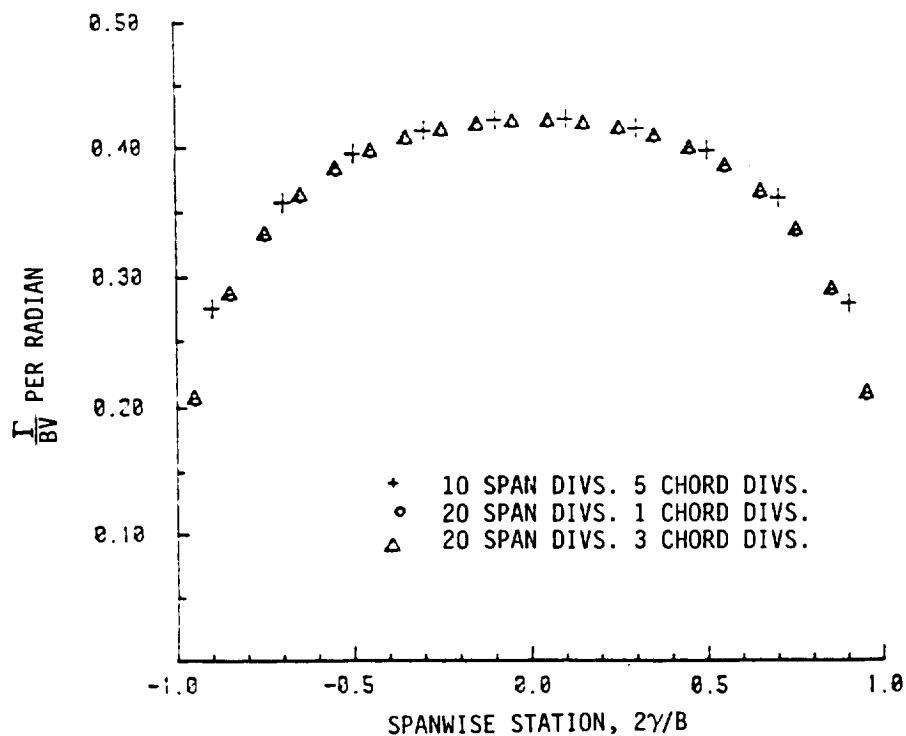


Figure 2.2-11. Lifting Surface Calculation of Spanwise Bound Circulation for Rectangular, AR=6 Wing

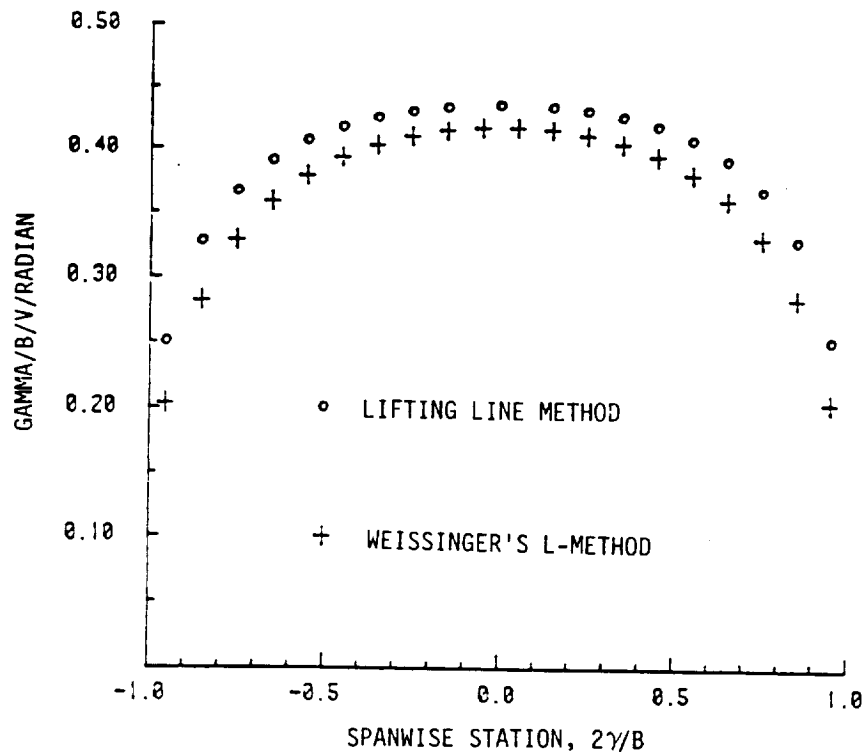


Figure 2.2-12. Comparison of Lifting Line Spanwise Lift Distribution with that Calculated by the Weissinger-L Method. Rectangular Wing, AR=6

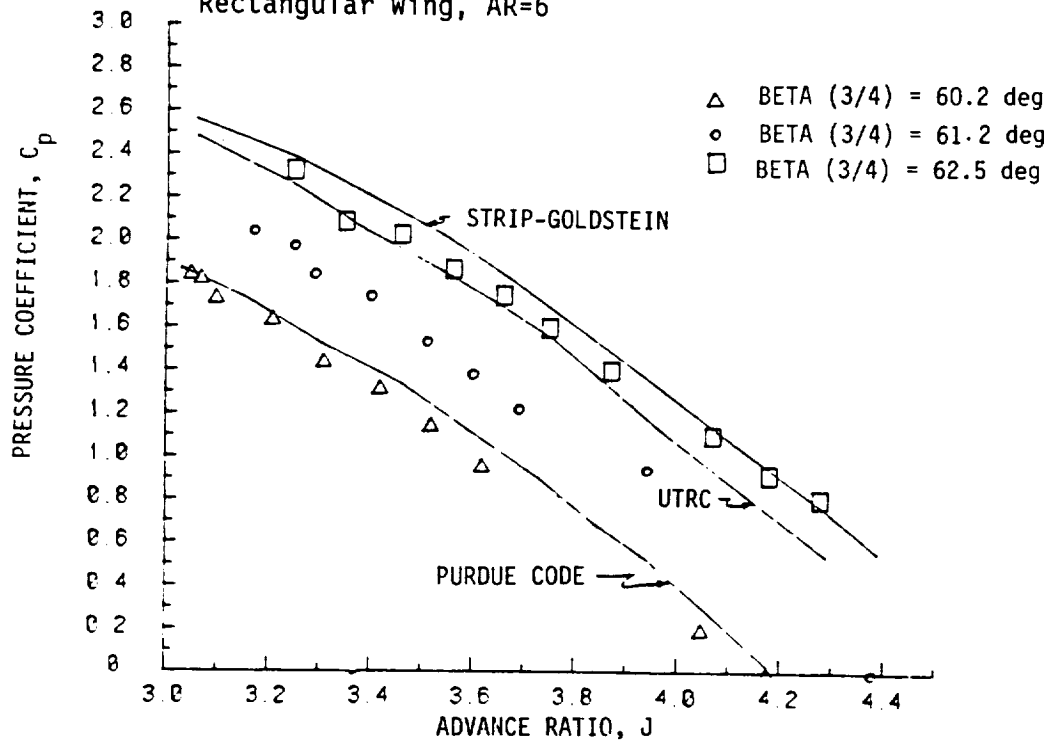


Figure 2.2-13. Comparison of Codes with Experiment SR-1 Prop;  $M = 0.8$ ; Codes for  $\beta = 61.2^\circ$ ; Purdue Code with Uniform In-Flow; Points are Experimental

Figure 2.2-13 suggests close agreement between predictions of the Chang-Sullivan code with experimental data. The word "suggests" is used because the predicted results were made using a uniform inflow. The reference states that the difference between a uniform and nonuniform inflow is equivalent to a pitch change of about 1 degree. It may be noted that the Chang-Sullivan calculation for  $\beta = 61.2$  degrees shows good agreement with experimental data at 60.2 degrees. Such a correction is, of course, only approximate and there is also the question of whether or not the pitch should not be changed again by about 1 degree for centrifugal stiffening. One could argue, therefore, that the Chang-Sullivan predictions made at 61.2 degrees for a uniform inflow would be compared to the experimental results at 61.2 degrees because of compensating effects from the nonuniform inflow and twisting of the blades due to centrifugal forces.

In addition to uncertainties raised by blade twisting and nonuniform inflow, it is difficult to compare the basic aerodynamic theories on which the two codes are based because of the significant influences that section profile drag has on predicted thrust and power at high Mach numbers and advance ratios. One should really be certain that both codes are using identical equations or tables to define section lift and drag coefficients.

Also, the slope of an airfoil lift curve varies significantly in the transonic flow regime. The Weissinger-L method, however, cannot reflect any change in  $\Gamma$  with Mach number. Thus, the agreement between theory and experiment shown in Figure 2.2-13 for the Chang-Sullivan code may be simply fortuitous for this particular case.

In addition to the above comparisons between results of the UTRC and Chang-Sullivan codes, a code based on vortex theory was written which uses the same basic equations as Reference 2.2-18 but without any unsteady effects or elaborate modeling of airfoil data. The code, which includes corrections for finite thickness and flow curvature, requires no solution of simultaneous equations and runs efficiently on a Tektronix 4051 computer in Basic language. The code was checked against Reference 2.2-18 for the SR-2 propeller at low Mach numbers and the two codes were found to give nearly identical results. Thus, the simpler code written in BASIC was used for the evaluations given here.

To begin, vortex theory is in effect a lifting line model using a prescribed wake shape. For a nonoptimum propeller, the theory assumes that Goldstein's kappa function (or Prandtl's F-function) can be used to relate the bound circulation to the induced velocities. Depending upon how one defines the wake helix angle, whether or not a lightly loaded propeller is assumed, and depending on how one relates the direction of the induced velocity to the resultant velocity (normality condition at the propeller plane or in the ultimate wake), and other details, different predictions based on vortex theory will be obtained by different investigators.

The method used here, and by Reference 2.2-18, takes the wake helix angle as equal to the blade tip pitch angle at all radial stations. It also assumes that the resultant induced velocity is normal to the helical surface at the propeller plane. In addition, corrections can be made for finite thickness and flow curvature to improve upon the lifting-line approximation.

Reference 2.2-18 shows good agreement, even at slightly supersonic tip Mach numbers, between predictions and experimental measurements for conventional propellers. To check this, additional calculations were performed and the results are presented in Figures 2.2-14 and 2.2-15. It can be seen from these figures that the variation of power coefficient and efficiency with advance ratio is predicted closely for the three-bladed, conventional propeller considered.

This particular adaptation of vortex theory includes several corrections intended as refinements to the classical approach. These include corrections to:

- (1) Section angles of attack to account for the effect of finite thickness;
- (2) Effective camber of a section due to the local flow curvature produced by the trailing vortex system;
- (3) Goldstein's kappa factor (or Prandtl's F-factor) to account for a finite hub radius (this correction is not in Reference 2.2-18, but can easily be added).

The first two corrections are discussed in Reference 2.2-32. The third correction was first derived in Reference 2.2-33. An approximate closed-

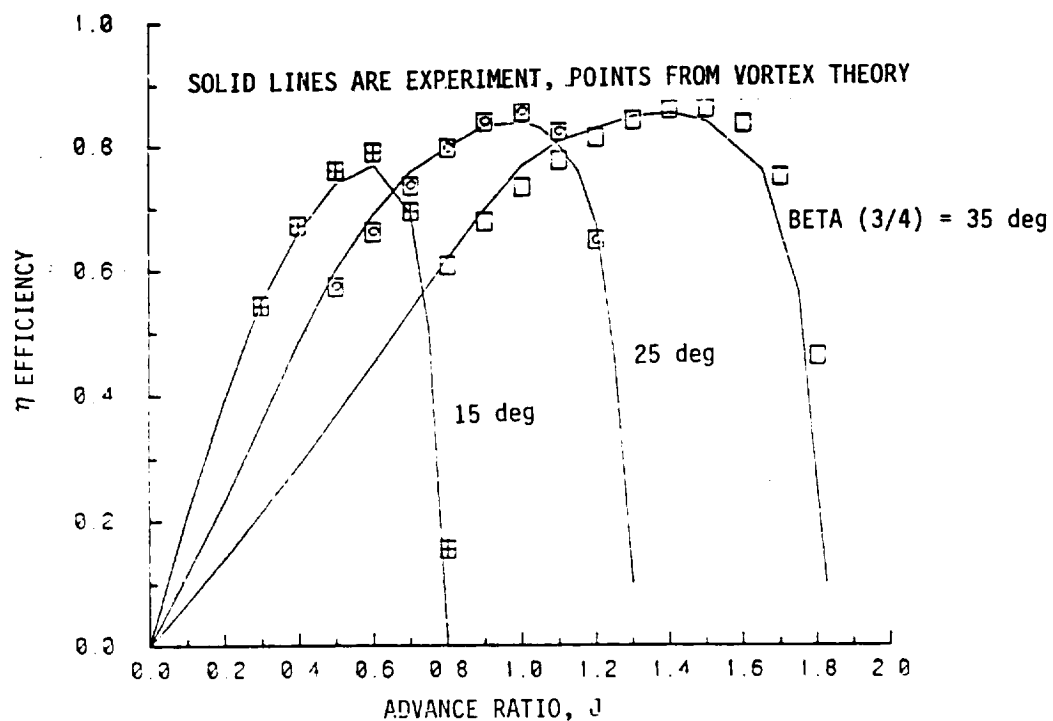


Figure 2.2-14. Efficiency Versus J, Propeller 6129, M=0, 3 Blades, Ref. NACA R 642.

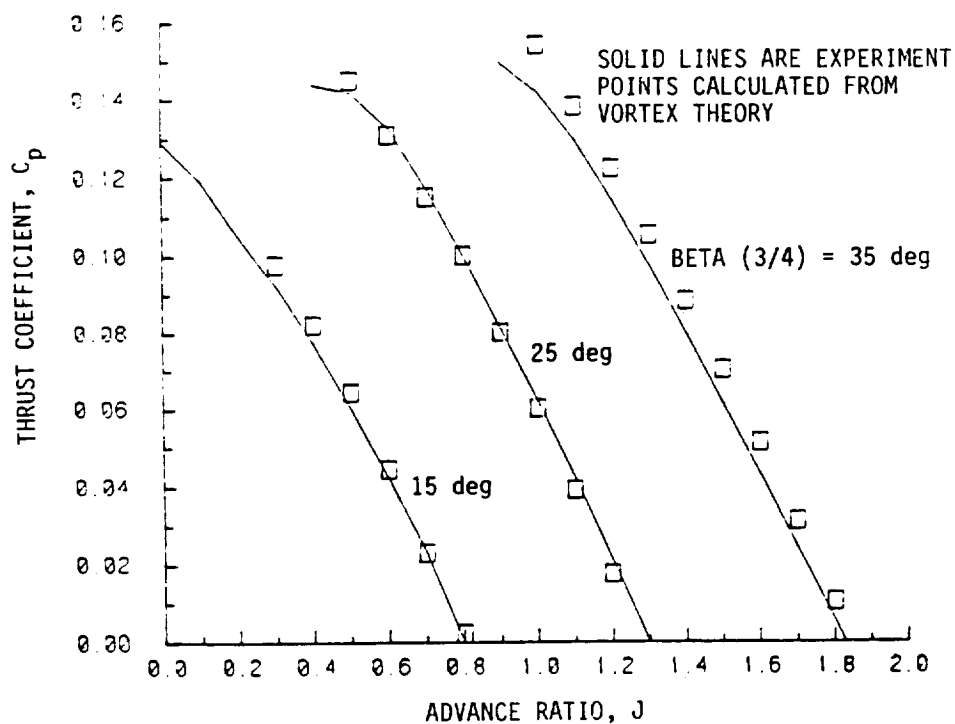


Figure 2.2-15. Thrust Coefficient Versus J, Propeller 6129 M=0, 3 Blades, Ref. NACA R 642.

form expression, similar to Prandtl's F-factor, was derived in Reference 2.2-34 and is used here. The influence of the first two corrections on the conventional propeller 6129 is shown in Figure 2.2-16. They are seen to decrease the predicted  $C_p$  values by about 3 or 4%. Plotting  $C_p$  versus thrust coefficient,  $C_T$ , the percentage change is even smaller.

A comparison of vortex theory with experiment for the SR-2 propeller is presented in Figure 2.2-17. Here the thickness and camber corrections are seen to be more significant for this propeller having wider blades and a higher solidity. The predicted  $C_p$  versus the advance ratio,  $J$ , is seen to agree fairly well with the experimental data for a blade angle of 59 degrees and tends to confirm the need for such corrections. The correction for a finite hub is not included in this figure, but from Figure 2.2-10 one would infer that the corrected  $C_p$  values in Figure 2.2-17 would be increased by approximately 11% at the lower values of  $J$  and varying linearly to no increase at higher  $J$  values, which would place the final values close to the  $\beta = 59$  degrees points.

To study these corrections further, Figures 2.2-18, 2.2-19, and 2.2-20 were prepared for the SR-2 propeller at a low Mach number to avoid the uncertainties in modeling airfoil properties. Again, the total effect on the predicted  $C_p$  is significant, approximately 20%, at a given  $J$ . From Figures 2.2-17 and 2.2-19, it is apparent that the thickness correction is relatively minor and that most of the correction arises from the flow curvature. Again, from Figure 2.2-18 for a given  $C_T$ , there is not too much of an effect on  $C_p$ .

The UTRC and Chang-Sullivan codes are compared to the SR-2 data at a Mach number of 0.8 in Figure 2.2-21. This comparison is taken from Reference 2.2-30. Keeping in mind possible blade twist, it appears that the predictions from the UTRC code may be in better agreement with experimental results than the Chang-Sullivan code, at least for this particular example.

#### 2.2.3.8 Summary

In summary, a single code alone will not meet all the requirements of GAPAS, namely;



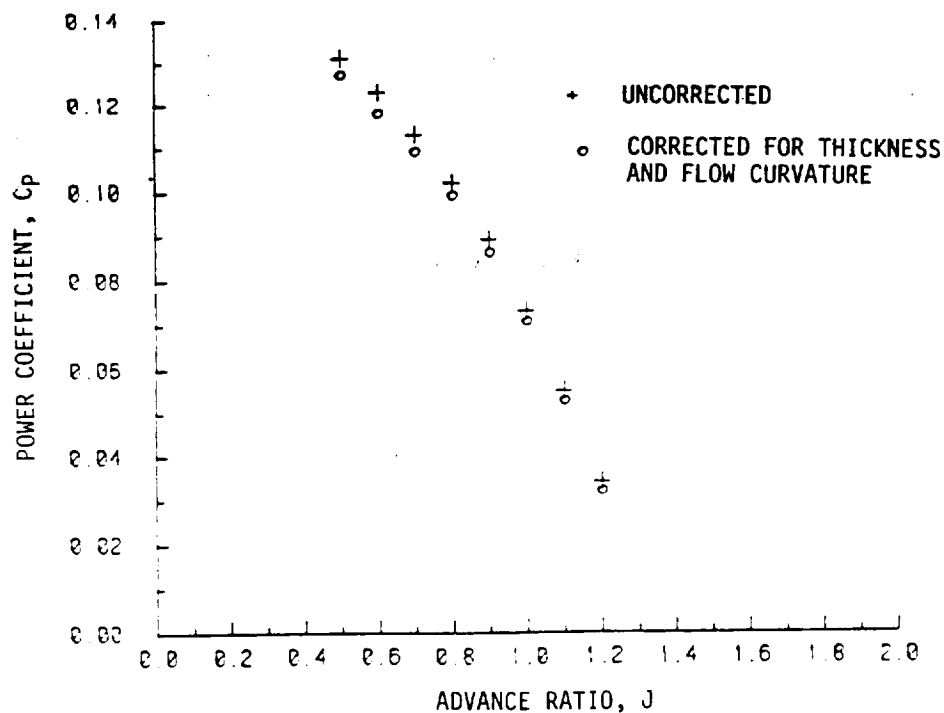


Figure 2.2-16. Effects of Thickness and Camber Corrections on Predicted CP for Propeller 6129

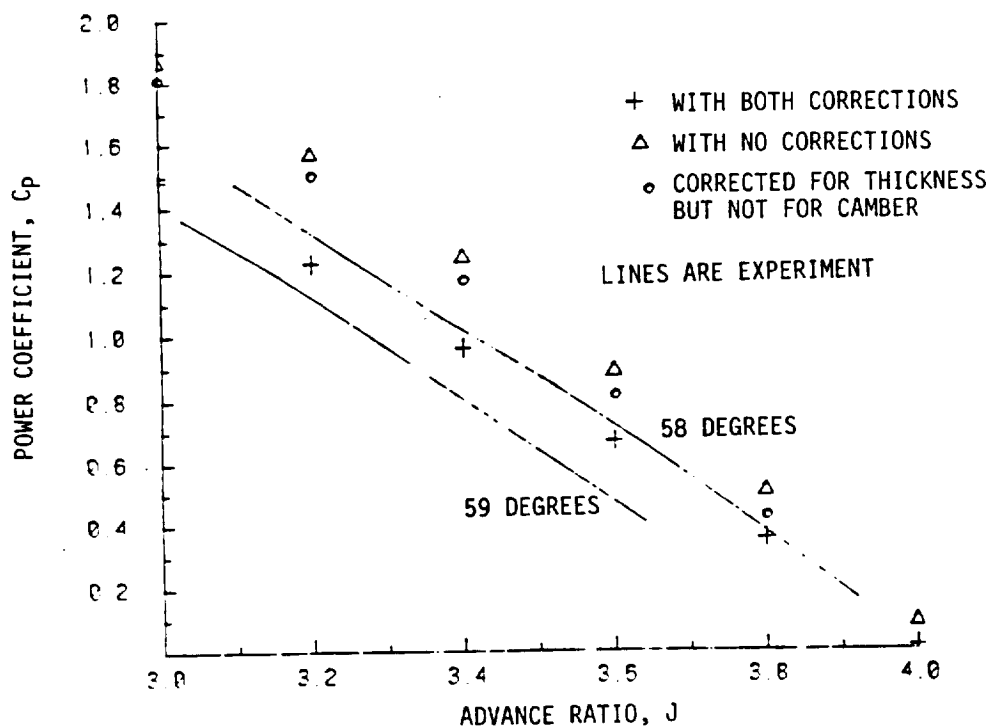


Figure 2.2-17. SR-2 Propeller Vortex Theory Versus Experiment,  $M = 0.6$ ,  $\beta = 58^\circ$ , for Theory

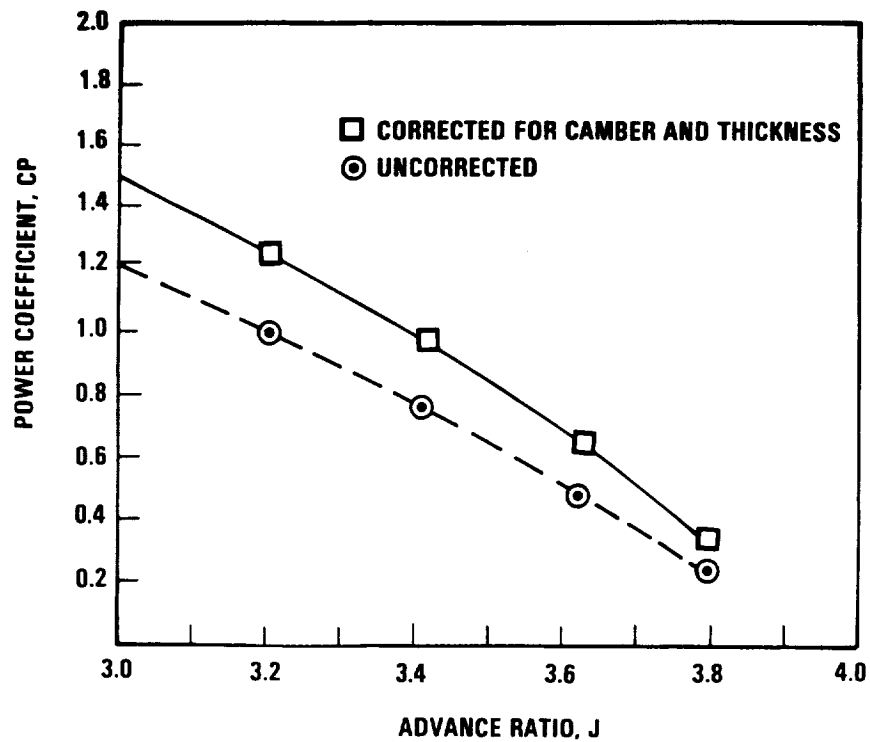


Figure 2.2-18. Effect of Corrections on Power  $M = 0$ ,  $\beta = 58^\circ$

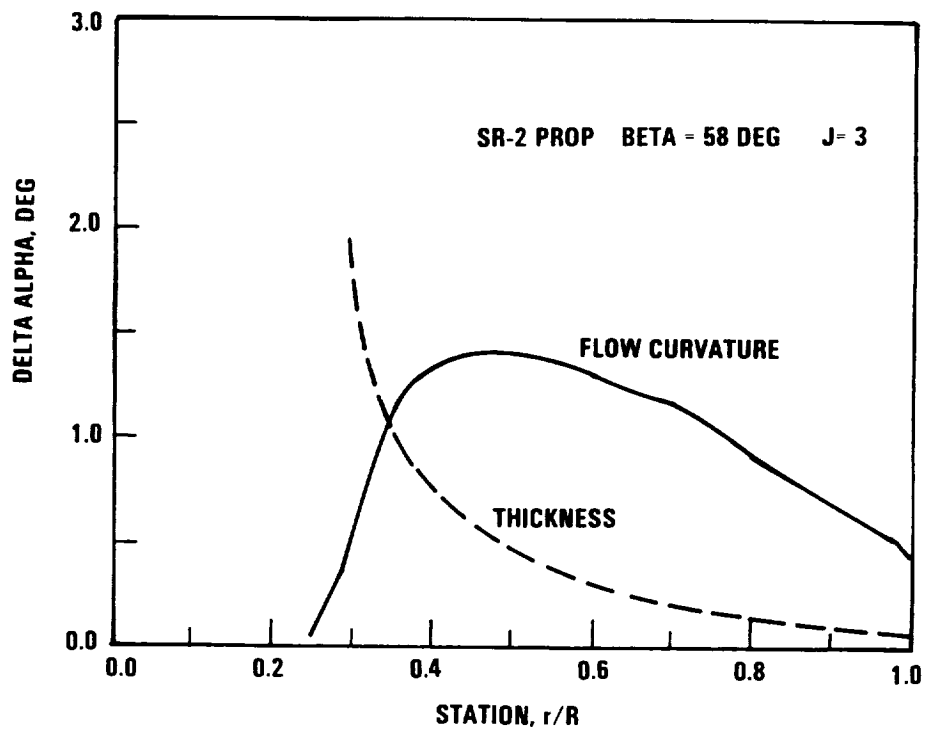


Figure 2.2-19. Corrections to Local Alpha for Thickness and Flow Curvature

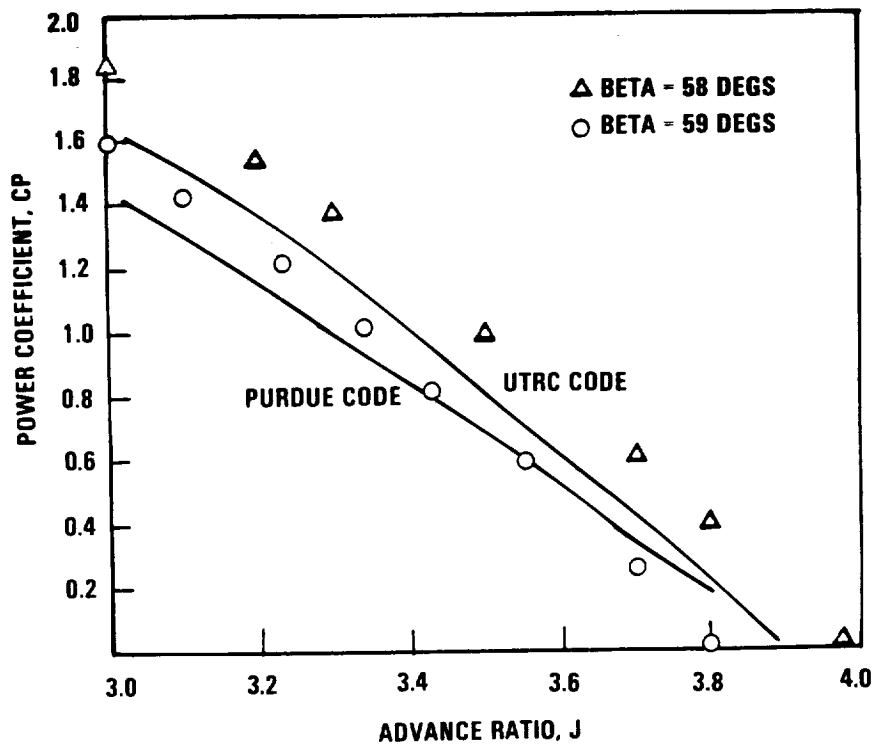


Figure 2.2-20. CP versus CT SR-2 Propeller,  $M = 0$ ,  $\beta = 58^\circ$

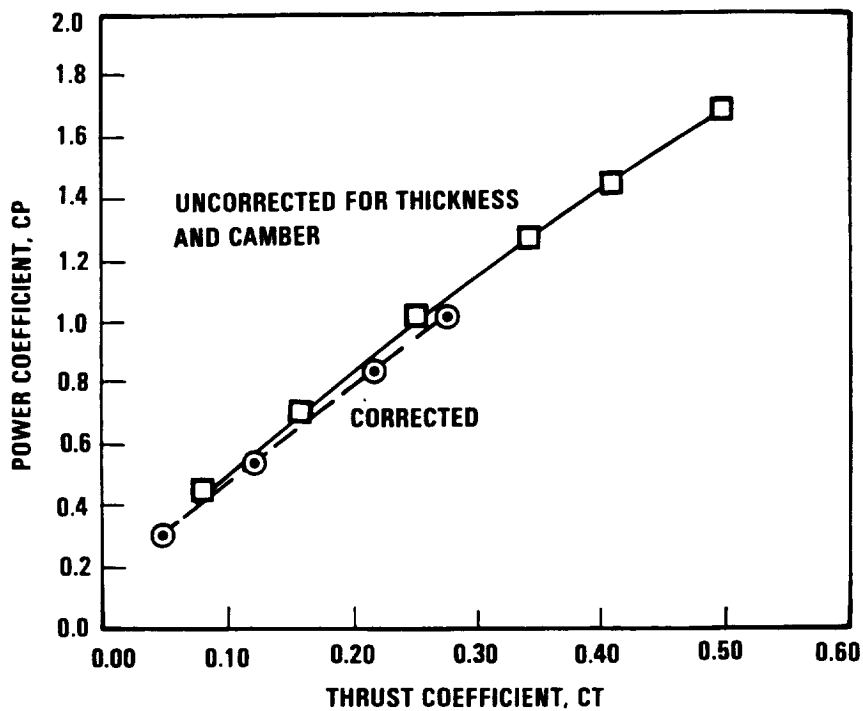


Figure 2.2-21. SR-2 Propeller Theory versus Experiment,  $M = 0.8$ , Lines are Theory for  $\beta = 58^\circ$

- Sweep
- Proplets
- Unsteady effects
- Accurate predictions of performance.

All of the codes suffer from a lack of exactness, but in different areas and each could be improved. The Aljabri code is limited by the restrictions of classical vortex theory, and while it might be possible to modify this theory to include sweep in Prandtl's F-factor, the inclusion of proplets appears highly doubtful. From a computing efficiency viewpoint, it is probably the fastest of the three codes and probably as accurate as if all the corrections mentioned previously are included.

The Chang-Sullivan code is a lower order Weissinger's L-method but otherwise is deficient in several ways. It does not consider any unsteady effects; it neglects any compressibility effects on the L-method and, hence, on the lift. There is no correction for blade thickness or finite hub and the wake is prescribed in a very approximate way.

The UTRC code is an elaborate lifting-line model with cascade corrections and a supersonic tip relief factor. The propeller analysis is combined with a fairly sophisticated nacelle-flow code. Despite a statement to the contrary in Reference 2.2-6, none of the corrections in the code account for the basic difference between a lifting-surface and lifting line model. The use of cascade data compares to the finite thickness corrections in the Aljabri code and corrects for the presence of the bound circulation of adjacent blades. The code still lacks a correction for flow curvature produced by the wake over wide blades. It should be noted that the Aljabri code does not contain any cascade corrections and probably should. The Chang-Sullivan code, except for finite thickness effects, does not need any cascade corrections because of the use of Weissinger's L-Method.

## 2.2.4 Airfoil Loading Module

### 2.2.4.1 Summary of Requirements

The calculations for the overall propeller aerodynamic performance do not require detailed pressure and skin friction distributions. The necessary input to the performance calculation are  $C_L$  and  $C_D$  versus angle-of-attack. This information can be obtained from two-dimensional airfoil data corresponding to the airfoil family, specific geometry, angle-of-attack, local Mach number, and local Reynolds number. In addition to the  $C_L$  and  $C_D$  coefficients, the moment coefficient,  $C_M$ , may be required for a structural analysis of the propeller using a simple beam theory. Therefore, airfoil data banks will be required in GAPAS for different families that make up the specific propeller (i.e., NACA-16, Clark Y, NACA 65/CA) to be analyzed.

In other types of propeller analysis, detailed distribution of the normal and tangential stresses are required (i.e., acoustic analysis or detailed structural analysis). In addition, where no airfoil data banks are available, detailed calculations will be required to generate  $C_L$ ,  $C_D$ , and  $C_M$ . Determination of the latter quantities should necessarily include the capability to accurately calculate compressible flows, transonic subcritical and supercritical flows, and viscous effects, including both laminar and turbulent boundary layers, and the transition of one to the other. For the analysis of propeller blade sections embodying these capabilities, computer codes based on the following four analyses can be used extensively in both the design and analysis of airfoils suitable for propeller application:

- (1) Bauer, Garabedian, and Korn Analysis (Refs. 2.2-35 through 2.2-37)
- (2) Carlson Analysis/Design (Refs. 2.2-38 through 2.2-40)
- (3) Smetana, Summey, Smith, and Carden Analysis (Refs 2.2-41 and 2.2-42)
- (4) Eppler Analysis (Refs. 2.2-43 through 2.2-46).

These computer programs have been in routine use in the aircraft industry and are discussed below. A summary of these methods is given in Table 2.2-1.

Table 2.2-1. Summary of Airfoil Loading Computational Capability

Computer Code	Where Applicable	Inviscid Flow Methodology	Laminar	Boundary Layer Transition	Turbulent	Iteration on $\delta^*$	Design Mode	Plot Capability	Core Storage (Octal)	Run Times (sec)
Carlson	Transonic	Finite difference solution of full inviscid potential flow equation for airfoil in stretched Cartesian coordinate	Thwaite	$\bar{K}$ model	Nash-Macdonald	Yes	Yes	Yes printer plot	107,000	90
G&K	Transonic	Finite difference of full inviscid potential flow equation for conformally mapped airfoil	No	fixed	Nash-Macdonald	Yes	No (separate design mode available)	Yes hard copy	107,000	120
Smetana	Subcritical	Distributed vorticity ( $\gamma_l$ ) over airfoil shape approximated by closed polygon	Pohlhausen	Natural or fixed	Goradia and Truckenbrodt	Yes	No	Yes hard copy	57,000	36
Eppler	Subcritical	Distributed vorticity over airfoil shape approximated by curved panels	Hartree	Natural only variable roughness	Empirical	No	Yes	Yes hard copy	77,000	5

#### 2.2.4.2 Garabedian and Korn (G&K)

The G&K method (Refs. 2.2-35 through 2.2-37) calculates the flow field around the airfoil based on a weak viscous-inviscid interaction methodology. The inviscid flow calculation is based on the solution of the steady, two-dimensional, irrotational full potential equation. The solution algorithm is based on a relaxation finite difference scheme used on a grid conformally mapped into a unit circle. The viscous effects are calculated using an integral boundary layer method based on Nash-Macdonald (Ref. 2.2-47). The version of the G&K program that was evaluated did not have a capability for computing the laminar portion of the boundary layer, and thus, the flow is assumed inviscid until the boundary layer becomes turbulent at a specified point on the airfoil. The viscous-inviscid interaction is accounted for by computing the displacements effects of the boundary layer and then adding this to the actual airfoil shape. The calculation is repeated until the method converges.

The G&K method becomes inaccurate as the local Mach number on the airfoil exceeds approximately 1.4. This is due to the irrotationality assumption and thus, cannot account for proper entropy production across the shock waves. In order to accelerate the convergence of the method, the calculations are performed first on a coarse grid (80 x 15 meshpoints) for a specified number of cycles, and then repeated on a finer grid (160 x 30 meshpoints). In addition, the method does not properly account for separation at the trailing edge or when massive separation occurs on the airfoil.

The G&K code utilizes about 2 minutes of CPU time to execute on a CDC CYBER 175 and requires 107K octal for core storage. A detailed user's manual is also available for the computer code.

#### 2.2.4.3 Carlson (TRANSEP)

The Carlson method (Refs. 2.2-39 and 2.2-40) calculates the flow field around the airfoil based on a weak viscous-inviscid interaction methodology. The inviscid flow calculation is based on the solution of the steady, two-dimensional, irrotational full potential equation. The equation is solved using a rotated finite difference scheme based on Jameson and South (Ref. 2.2-48). This method avoids difficulties in the

supersonic region associated with nonalignment of the flowfield and the coordinate system. The coordinate system utilized is based on a stretched cartesian system. The solution is obtained using column relaxation sweeping from upstream to downstream. An improved rate of convergence is obtained by the use of a coarse, then medium, and then fine grid solution.

The viscous effects are determined by utilization of boundary layer integral methods. The laminar region is calculated based on the compressible Thwaites method, whereas, the turbulent boundary layer is calculated based on the method of Nash-Macdonald. The transition from the laminar regime to the turbulent regime is determined from a method based on a Pohlhausen  $\bar{K}$  parameter in conjunction with the data correlation of Granville (Ref. 2.2-43). The viscous-inviscid interaction is accounted for through the displacement thickness effects on the airfoil shape. A highly empirical incompressible analysis is incorporated in the model to address extensive upper surface separation.

The computer program also has a design option built in whereby the airfoil downstream of the nose region is computed based on a prescribed pressure distribution in that region. The code requires 107K octal core storage and executes in about 90-120 seconds of CPU time on the CDC CYBER 175 per case wherein three different grid schemes are utilized during the calculation (i.e.,  $13 \times 7$ ,  $25 \times 13$ , and  $49 \times 25$  grid point).

The program calculates and outputs  $C_p$ ,  $C_L$ ,  $C_{D_{total}}$ ,  $C_{D_f}$ ,  $C_{M_{1/4}}$ , and  $C_{M_{L.E}}$ . A detailed user's manual is also available.

#### 2.2.4.4 Smetana

The method of Smetana (Ref. 2.2-41) calculates the flowfield around the airfoil based on a weak viscous-inviscid interaction methodology. The inviscid flow is based on a steady, two-dimensional, subcritical distributed vorticity method. Here, the airfoil is approximated by a closed polygon with the airfoil surface represented by distributed vortices of unknown intensity. With the assumption that the airfoil surface is a streamline and also satisfies the Kutta condition, the strength of the distributed vortices is determined and thus, so is the pressure distribution on the airfoil. Compressibility effects are modeled through a Karman-Tsien transformation.



The viscous effects are calculated using integral methods. The laminar flow portion is calculated using a Pohlhausen fourth-order velocity profile, whereas the turbulent flow is computed based on a choice of two different methods. The first method is that of Goradia (Ref. 2.2-42). This method has been shown to give good results in regions of strong adverse pressure gradients. The second method is that of Truckenbrodt (Ref. 2.2-49) and is a refined method which can be used when the pressure gradients are not too adverse and for accurately determining the separation point. The transition from laminar flow to turbulent flow is based on either a prescribed transition point or a natural transition criteria based on Blasius flat plate boundary layer stability theory and correlation of Reynolds number based on momentum thickness versus integrated shape factor.

The coupling between the viscous and inviscid flow is through the boundary layer displacement effects. Since the inviscid equations are linear, the correction is obtained by evaluating the thickness and camber effects separately. The effect of camber due to boundary layer displacement is calculated first and the thickness effects are then calculated for a symmetric airfoil at zero angle of attack for the basic thickness and for the same symmetric airfoil with displacement effects included. The total solution for the velocity is then given by one solution for camber plus the solution for thickness with displacement effects, minus one solution for the basic airfoil thickness.

The Smetana code requires 57K octal core storage and executes in about 15 seconds of CPU time on the CDC CYBER 175. A user's manual is available, however there is a learning curve required in using this code since the calculated values of  $C_L$  and  $C_M$  are sensitive to the density of the airfoil coordinates input. This sensitivity is related to the local slope of the airfoil.

#### 2.2.4.5 Eppler

The method of Eppler (Refs. 2.2-43 and 2.2-46) calculates the flow-field around the airfoil using an inviscid, steady, two-dimensional distributed vorticity method. The viscous effects are computed using a combination of integral methods and semiempirical correlations. The version of the code evaluated did not provide for viscous-inviscid interaction.

The inviscid methodology allows for both sharp trailing edges as well as blunt trailing edges. In the case of the sharp trailing edge, the Kutta condition is satisfied, whereas, in the case of a blunt trailing edge, a rear stagnation point is enforced in addition to excluding any singularities at the two trailing edge points. The boundary condition of zero velocity normal to the airfoil surface is satisfied on the vorticity panels. Rather than exclude one point in order to enforce the Kutta condition (i.e., Sharp T.E.) and thus have the number of equations equal to the number of unknowns, all equations are kept and the Kutta condition also satisfied. Since this leads to more equations than unknown, the system of equations is solved in a least-squares sense. The calculation for arbitrary angle of attack is obtained by a superposition of the  $\alpha = 0^\circ$  and  $\alpha = 90^\circ$  case. Compressibility effects are accounted for by using a Karman-Tsien transformation.

The viscous effects in the laminar region are calculated using a Hartree velocity profile (power law) and solves both the momentum integral equation and kinetic energy integral equations. In the turbulent region, empirical expressions are used for the skin friction, shape factor, and dissipation coefficient. If separation occurs in the laminar region, the model switches to turbulent in an attempt to simulate reattachment. In addition, the profile drag coefficient is calculated using the method of Squire-Young. The version of the Eppler code that was evaluated incorporated a correction to  $C_L$  when separation occurs on the airfoil. This produced better agreement for  $C_{L_{\max}}$  when compared to available data.

The Eppler code requires 77K octal core storage and executes in about 5 seconds of CPU time on the CDC CYBER 175 for each case. Documentation and a user's manual are available. The code also has a design option available to the user.

#### 2.2.4.6 Comparison of Prediction Methods

The resulting four computer programs have been used to make theoretical predictions of the NACA 0012 and LS(1)-0413 (GA(W)) airfoils for comparison with experimental data (Ref. 2.2-51) taken in the Ohio State University (OSU) Airfoil Transonic Facility. Specifically, pressure

distribution comparisons for both the sub- and supercritical regimes for these airfoils can be used to examine how well each computer program compares with the experimental data and to determine any deficiencies in the theoretical predictions.

#### NACA 0012 Comparisons

The first series of numerical calculations were carried out for the NACA 0012 airfoil (Figure 2.2-22A) for the following subcritical flow conditions:

<u>Mach No.</u>	<u>Reynolds No.</u>	<u><math>\alpha</math></u>
0.351	$3.65 \times 10^6$	0.00
0.345	$3.24 \times 10^6$	3.93
0.342	$3.39 \times 10^6$	7.88

The results are shown in Figure 2.2-22B for the  $\alpha = 3.93$  degrees and indicate relatively good agreement between all four computer programs and test data. Note, however, that the Eppler code tends to underpredict the  $C_p$  values in comparison to experimental data in the leading edge upper surface region resulting in a greater pressure suction peak. This effect was further pronounced at  $\alpha = 7.88$  degrees. It may also be noted that all programs in this subcritical comparison for the angles of attack considered overpredict the base pressure coefficient, resulting in a much higher pressure recovery than was measured in the wind tunnel.

In the next series of numerical calculations carried out for the NACA 0012 airfoil, zero-degree angle of attack was maintained while the free-stream Mach number was increased for the following conditions:

<u>Mach No.</u>	<u>Reynolds No.</u>	<u><math>\alpha</math></u>
0.575	$4.68 \times 10^6$	0.00
0.725	$5.34 \times 10^6$	0.00
0.808	$6.12 \times 10^6$	0.00

For the lower two Mach numbers, subcritical conditions were maintained and comparisons between theory and experiment for these two cases were considered acceptable with the exception of the region about the leading edge suction peak and failure to recover the proper pressure at the

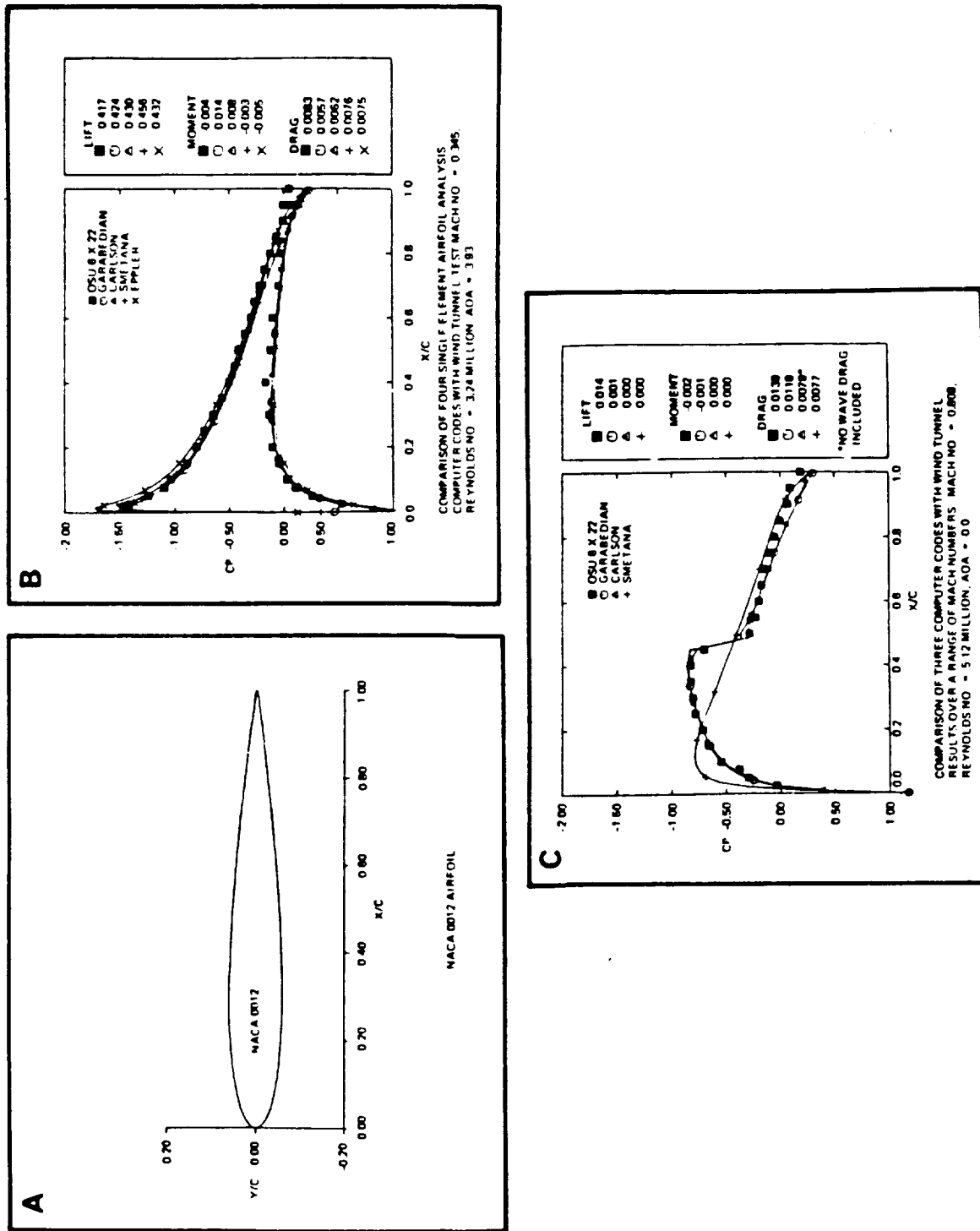


Figure 2.2-22. Comparison of Results of Airfoil Analysis Codes with Experimental Data for the NACA 0012 Airfoil

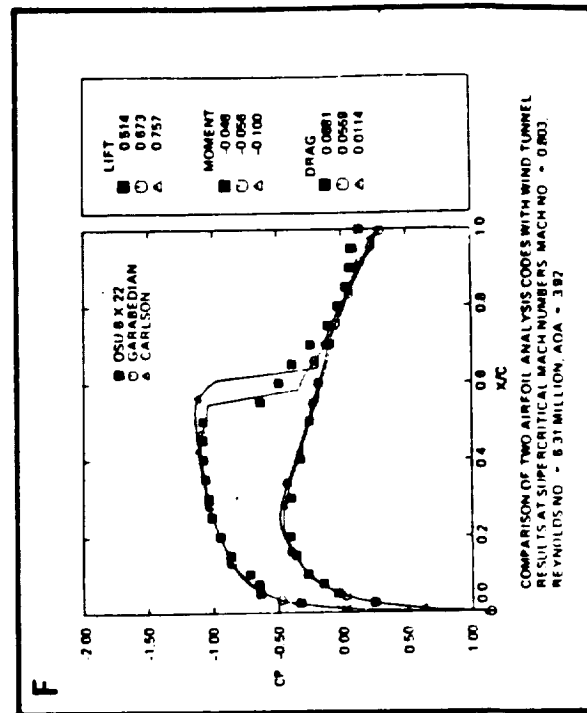
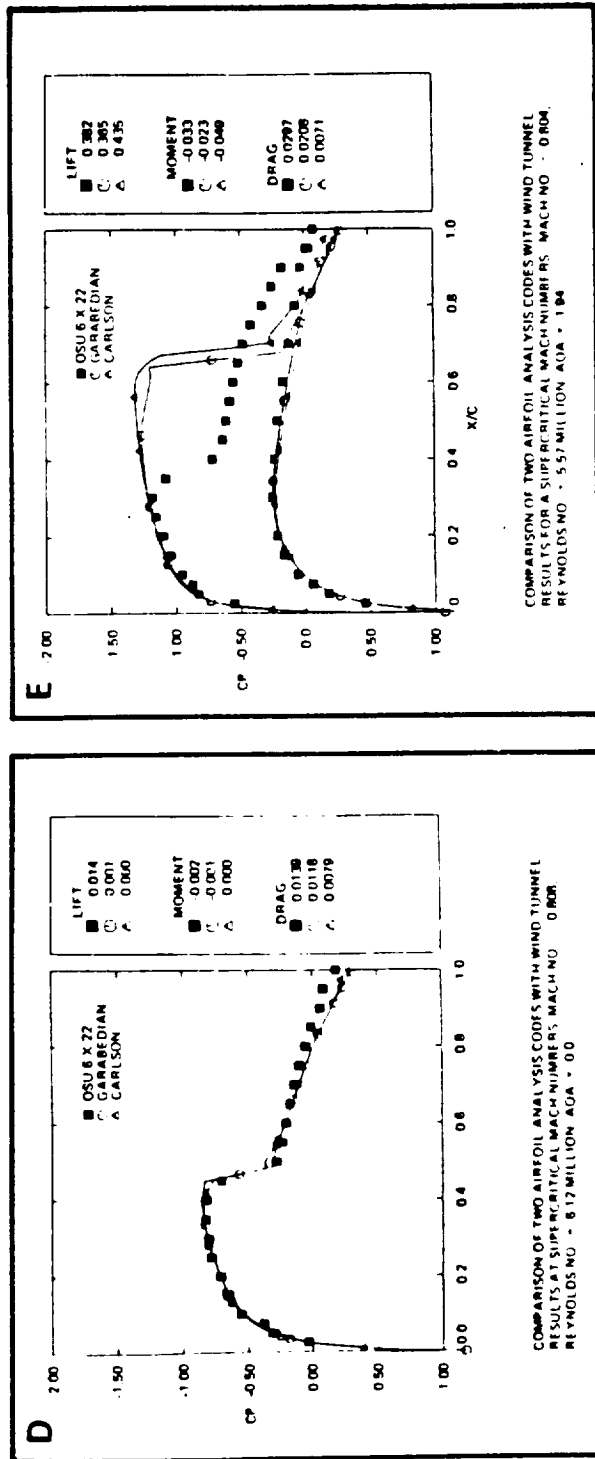


Figure 2.2-22. Comparison of Results of Airfoil Analysis Codes with Experimental Data for the NACA 0012 Airfoil (Continued)

trailing edge. However, comparisons of the lift, drag, and moment showed these pressure differences to have a significant effect on the prediction of the pertinent coefficients. Moreover, increasing the Mach number to the third condition in this series of comparisons ( $M = 0.808$ ) has produced a supercritical flow condition as shown in Figure 2.2-22C. This emphasizes that Smetana, et al. does not predict the existing shock wave because of its solution methodology, whereas Garabedian, et al. and Carlson successfully predict not only the magnitude of the pressure rise but also the position of the shock wave.

Consideration of the more severe comparisons, i.e., the supercritical test conditions for the NACA 0012 airfoil, are shown in Figures 2.2-22D, E, and F for the following test conditions:

<u>Mach No.</u>	<u>Reynolds No.</u>	<u><math>\alpha</math></u>
0.808	$6.12 \times 10^6$	0.00
0.804	$5.57 \times 10^6$	1.94
0.803	$6.31 \times 10^6$	3.92

The zero-degree angle of attack,  $M = 0.808$  case (Figure 2.2-22D), shows good agreement between predictions and data over both the upper and lower surface of the airfoil with the exception of the recovery pressure at the trailing edge. As the angle of attack is increased to 1.94 degrees (Figure 2.2-22E), the deviation from experiment of both the Garabedian and Carlson codes in terms of shock wave location, drag and moment can be easily seen. Increasing the angle-of-attack further to 3.92 degrees for the nominal Mach number of 0.8 results in the comparisons shown in Figure 2.2-22F. The large discrepancy in the shock wave location between theory and experiment in this case may be attributed to the strong shock wave, which is difficult to model analytically, and possible departure from two-dimensional flow in the OSU Airfoil Transonic Flow Facility.

#### NASA LS(1)-0413 Comparisons

The LS(1)-0413 airfoil was selected to illustrate the cambered supercritical type of airfoils which differ from the symmetric NACA 0012 airfoil shape. As shown in Figure 2.2-23A, the LS(1)-0413 airfoil is a cambered section that was designed for general aviation applications and

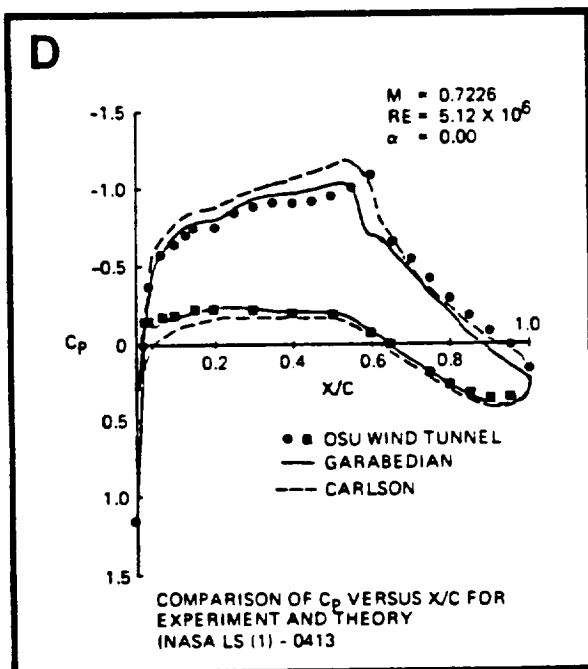
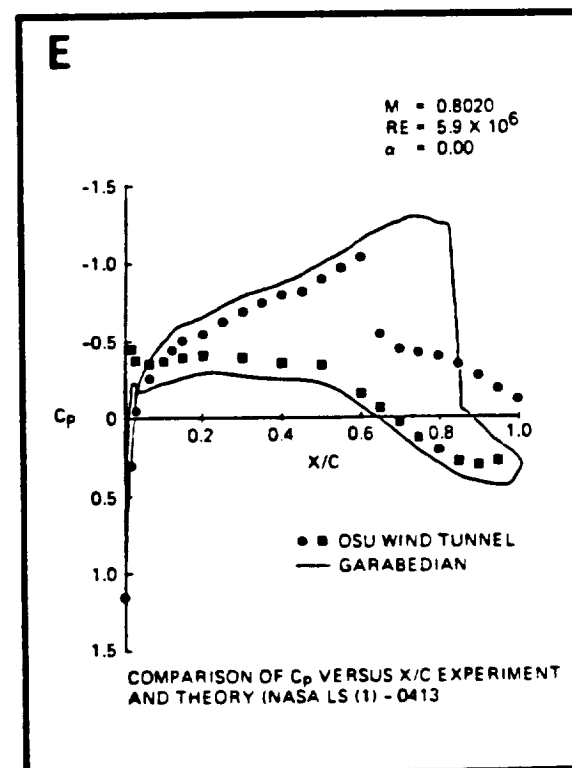
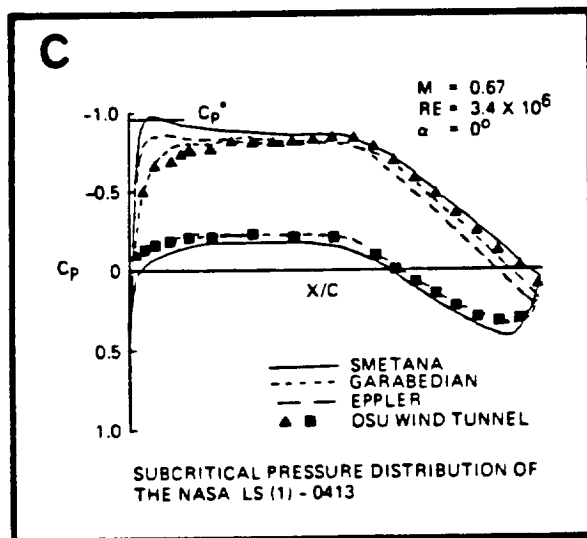
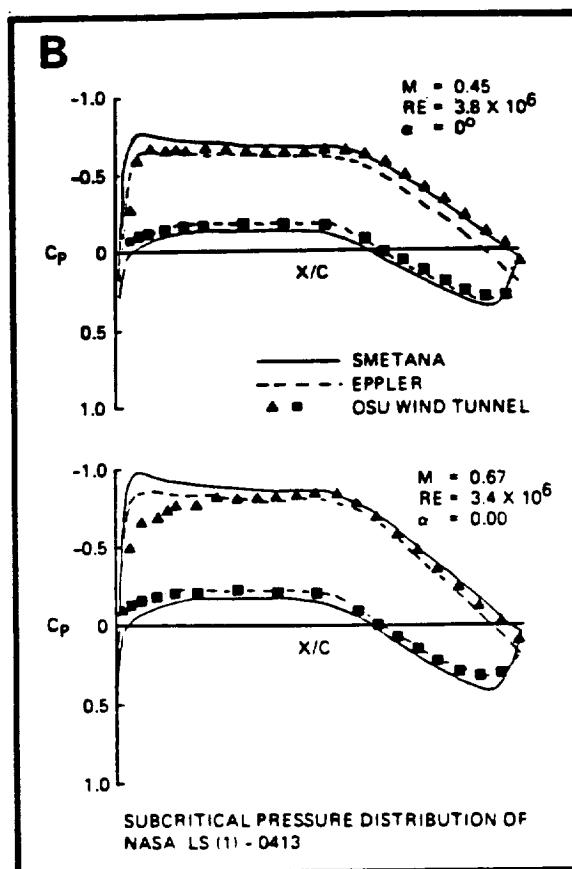
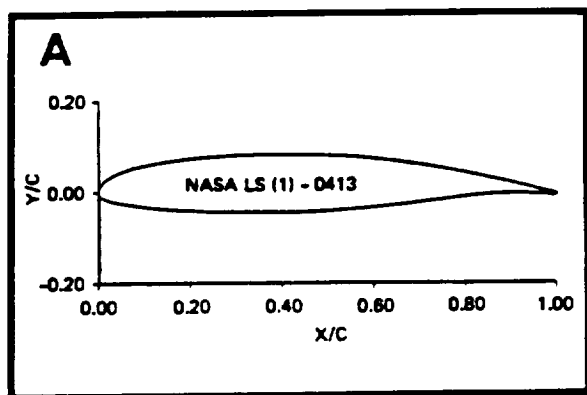


Figure 2.2-23. Comparison of Results of Airfoil Analysis Codes with Experimental Data for the NASA LS(1)-0413 Airfoil

originally termed the GA(W)-2. The airfoil contains the trailing edge region cusp characteristics of the GA(W) series and of the supercritical type airfoils. This airfoil, with a maximum thickness-to-chord ratio of 0.13, may be contrasted to the 12% thick symmetrical NASA 0012 section shown in Figure 2.2-22A.

The subcritical cases were initially considered and results are shown in Figures 2.2-23B and C for the following conditions:

<u>Mach No.</u>	<u>Reynolds No.</u>	<u><math>\alpha</math></u>
0.45	$3.8 \times 10^6$	0.00
0.67	$3.4 \times 10^6$	0.00

Figure 2.2-23B indicates that, for these two cases, the theoretical predictions of Smetana, et. al, and Eppler do compare well with experimental data. However, the deficiencies of Eppler are evident in terms of recovery pressure at the trailing edge for Mach numbers of 0.45 and 0.67, whereas for this airfoil, Smetana, et. al. predictions are accurate. The leading edge suction peak disagreement experienced earlier during the NACA 0012 comparisons is also present in this comparison, being prominent for the Mach 0.67 case. The Garabedian computer program predictions for this case are shown in Figure 2.2-23C and, as can be seen, are sufficiently valid over both the upper and lower surface of the airfoil. As noted in the discussion on per-case run times, this program is considerably more expensive than that of Smetana or Eppler because of its methodology.

The next series of numerical calculations considered the following test conditions:

<u>Mach No.</u>	<u>Reynolds No.</u>	<u><math>\alpha</math></u>
0.7226	$5.12 \times 10^6$	0.00
0.7552	$5.11 \times 10^6$	0.00
0.8020	$5.90 \times 10^6$	0.00

Comparisons of the computer program theoretical predictions with experimental results at OSU Transonic Airfoil Facility for the first case are shown in Figure 2.2-23D. Here, the prediction of shock wave location by both Garabedian, et. al. and Carlson are acceptable. Carlson's prediction



shows increased suction on the upper surface upstream of the shock location when compared to the experimental data, which indicates that the specified angle-of-attack may be incorrect. Therefore, the lift coefficient should be matched in these cases rather than  $\alpha$ , an option which is available only in the Garabedian code at the present time. Considering a higher Mach number case, Figure 2.2-23E, indicates that the Garabedian computer program capabilities have been exceeded, which is possible for the present theoretical codes when the shock Mach number exceeds 1.4. Although TRANSEP was not run during this previous study, one would expect similar problems when the local Mach number exceeds about 1.4.

Consideration of the drag divergence properties of any airfoil is an important factor in the airfoil analysis. Drag coefficient calculations have been carried out for the LS(1)-0413 airfoil and compared to the experimental results of the OSU Transonic Airfoil Facility. The results, shown in Figure 2.2-24, indicate excellent agreement between Garabedian and experimental measured drag values. Figure 2.2-24 also indicates the magnitude of the wave drag experienced beyond the drag divergence Mach number. Additional comparisons between the OSU experimental data and Garabedian theoretical results may be made by referring to the work of McGhee and Beasley (Ref. 2.2-52).

The results of the limited comparisons contained here for both airfoils indicate that at  $M < 0.3$  and  $\alpha < 3$  degrees, acceptable agreement is arrived at between experiment and theory for all four methods. However, as both the Mach number and  $\alpha$  are increased, the Smetana and Eppler codes depart from experimental results with lower pressures at the leading edge and higher pressures near the trailing edge. In supercritical flow, the theoretical predictions of both Garabedian, et al. and Carlson satisfactorily agree with experimental data for moderate values of lift coefficient in terms of pressure distribution, shock wave location, and magnitude of shock pressure increase. However, as the angle of attack is increased, the pressure distribution computed by the Carlson code does not agree well with the experimental data and is indicative of an improper angle-of-attack input.

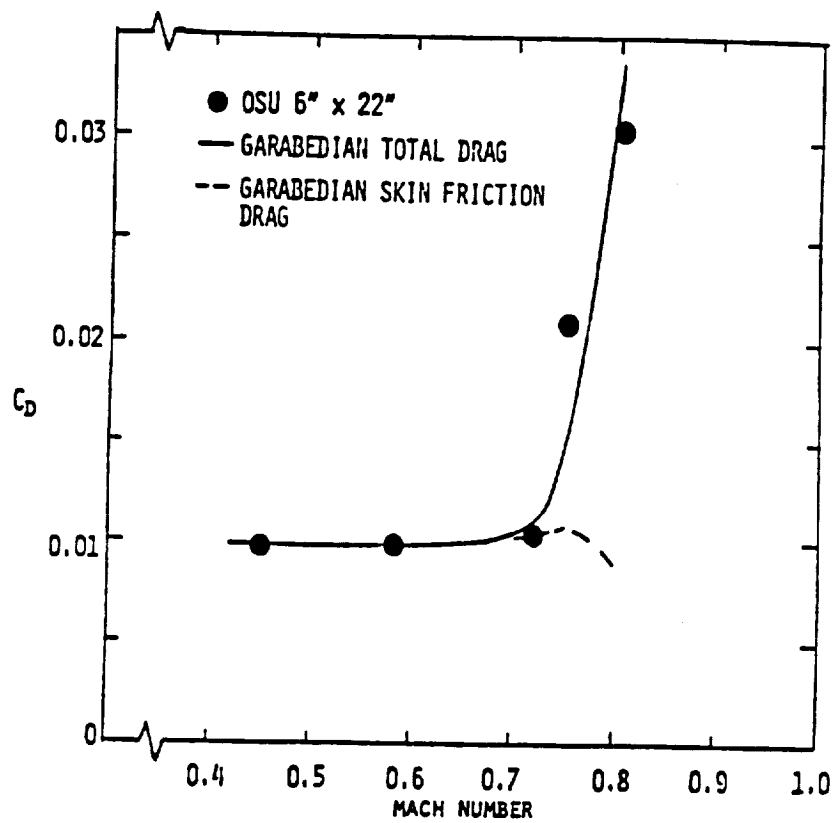


Figure 2.2-24. Drag versus Mach Number for NASA LS(1)-0413

#### 2.2.4.7 Airfoil Data Banks

For cases wherein the detailed loading on the propeller is not required, airfoil data banks can be implemented in order to obtain  $C_L$ ,  $C_D$  and  $C_{M_{1/4}}$ . These data banks would be developed based on airfoil type. The user would input the airfoil type, chord length, thickness-to-chord ratio, freestream Mach number, freestream Reynolds number, angle of attack, and altitude. The resultant output would contain  $C_L$ ,  $C_D$ , and  $C_{M_{1/4}}$ .

At the time of the evaluation, three data banks were available. The first two were developed by Korkan at Texas A&M University and include the Clark Y airfoil series and a NACA 16 airfoil series. A separate NACA 16 data bank is also included in the UTRC propeller-nacelle code. Work is also underway (Korkan) for the development of the NACA 65/CA series and the four-digit series of airfoils. Additional airfoil data banks can be developed using theoretical prediction methods discussed previously. This would allow for the potential expansion of the airfoil data banks.

#### 2.2.5 Propeller Acoustic Signature

Four propeller acoustic analysis procedures were evaluated for possible inclusion in the GAPAS acoustics module. These procedures and resulting computer codes were those developed by Woan and Gregorek (Ref. 2.2-53) at Ohio State, Succi (Refs. 2.2-54 and 2.2-55) at MIT, Martin and Farassat (Refs. 2.2-54 and 2.2-56) at NASA-Langley Research Center (two versions), and an empirical method developed at Hamilton-Standard (Ref. 2.2-58).

##### 2.2.5.1 Acoustic Signature Technical Requirements

The above noted acoustic procedures and computer codes were evaluated against the contractual propeller acoustic signature technical requirements; namely, that the calculation procedures are to have the capability to:

- (1) Calculate discrete-frequency noise for non-compact sources, including both loading and thickness noise components;
- (2) Calculate quadrupole thickness noise for transonic rotational speeds, with a contractor-provided criterion for application;

- (3) Calculate broad-band noise, with a contractor-provided criterion for application;
- (4) Account for blade sweep and/or proplet tip devices.

The acoustic analytical methods and codes were also evaluated based on the factors shown in Figure 2.1-1, and discussed in Section 2.1. Each procedure will be discussed in light of these factors and the technical requirements delineated above.

#### 2.2.5.2 Method of Woan and Gregorek

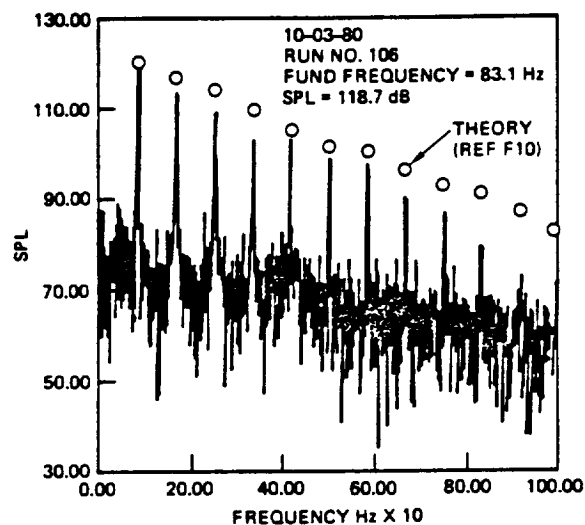
The method of Woan and Gregorek (Ref. 2.2-53) is a time-domain formulation for a noncompact source which accounts for thickness and steady pressure loading noise. To calculate the contributions of each blade to the thickness and loading noise, the blade is divided into panels, and contributions from each panel are summed over all panels. Calculations are performed for both the near and far field for the acoustic pressure signature and frequency spectra. The code provides thickness, loading, and total noise values, handles different airfoil families efficiently, is capable of handling in-plane sweep, and is user-oriented and numerically efficient. Moreover, results compare well with experimental data (see Figures 2.2-25 and 2.2-26). The formulation, however, is applicable to subsonic helical tip Mach numbers only, requires airfoil pressure coefficient distributions at each radial location, and does not include 1/3 octave band, sound power level, broad-band noise, and perceived noise level calculational capabilities.

With regard to the computer program, the code is currently operational on the CDC Cyber 175 system and has an execution time of about 140 CPU seconds for a typical case. The core storage requirement is approximately 130K octal words. A user's manual is not available for this code, however.

#### 2.2.5.3 Method of Succi

In contrast to the analysis of Woan and Gregorek, which is applicable for a non-compact source, Succi's method (Refs. 2.2-54 and 2.2-55) is a time domain formulation for compact noise sources only. The method takes into account both loading and thickness noise wherein the blades are divided into small segments and the thickness and steady pressure loading

**A** COMPARISON OF CALCULATIONS USING METHOD OF WOAN AND GREGOREK WITH NEAR-FIELD MEASUREMENTS FOR SINGLE-ENGINE BEECH SUNDOWNER C-23



**B** COMPARISON OF CALCULATIONS USING METHOD OF WOAN AND GREGOREK WITH NEAR-FIELD MEASUREMENTS FOR MIT LOW NOISE/HIGH PERFORMANCE 3-BLADE PROPELLER

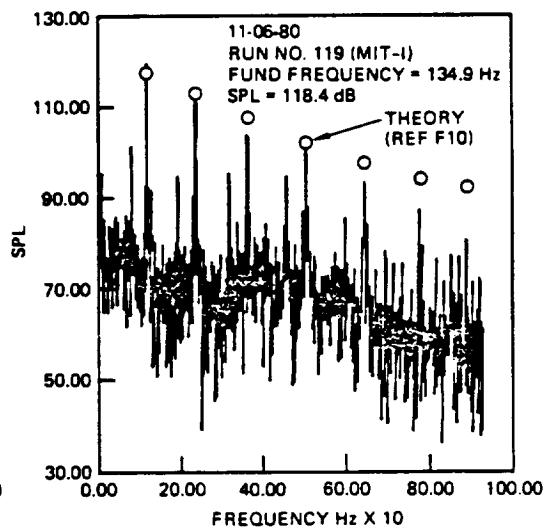
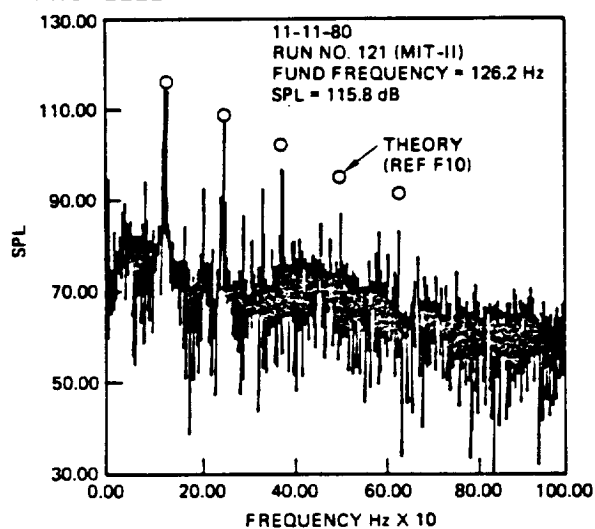


Figure 2.2-25. Comparison with Data - Method of Woan and Gregorek

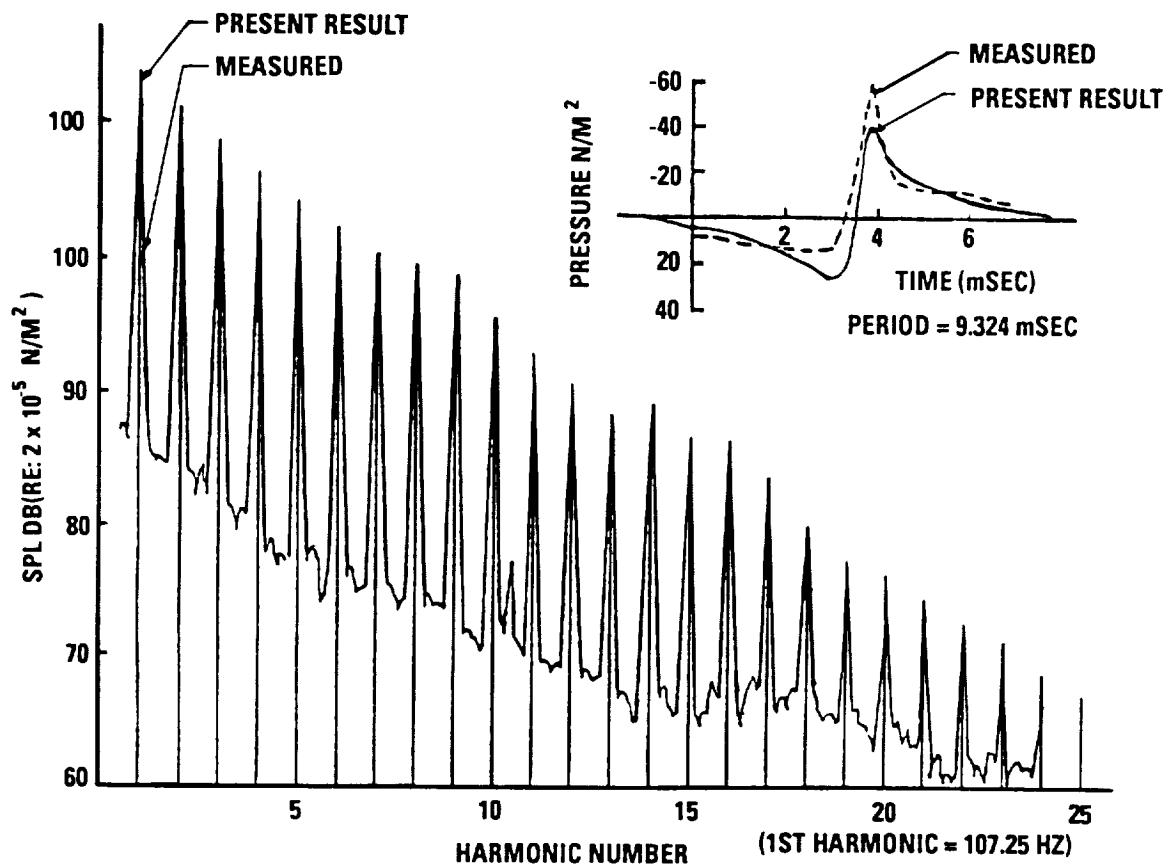


Figure 2.2-26. Comparison with Data - Method of Woan and Gregorek

contributions are summed over all segments. The code requires that a chordwise pressure distribution be input at each radial location, and outputs the acoustic pressure signature and frequency spectra for subsonic helical tip Mach numbers only. In addition, the code computes 1/3 octave band sound pressure level if desired. Broad-band noise, sound power level, and perceived noise level capabilities are not included, however. The code yields excellent agreement with experiment for in-plane measurements, but only fair agreement for out-of-plane measurements in the near field (Figure 2.2-27). In addition, the code handles different airfoil families and is numerically efficient.

With respect to the computer code, Succi's method is operational on the CDC Cyber 175. In addition, program documentation and a user's manual are available. For a typical case, the execution time of the code is approximately 14 CPU seconds, and the code requires a core storage of approximately 127K octal words.

#### 2.2.5.4 Method of Martin-Farassat (PROPFAN-Formulation I)

The Martin-Farassat code (PROPFAN-Formulation I) (Refs. 2.2.54 and 2.2-56) is based on a time domain formulation for non-compact sources which accounts for thickness and steady pressure loading contributions to the noise field for subsonic propellers. The code outputs both acoustic pressure signature and frequency spectra (i.e., sound pressure level as a function of specified number of harmonics), for thickness, loading and total noise contributions, and is capable of handling both in-plane and out-of-plane sweep. Reasonable agreement with experimental data is obtained in the near-field for in-plane and out-of-plane locations for both pressure signature and spectral distributions (Figures 2.2-28 and 2.2-29). The code does not include quadrupole noise source terms or the capability of calculating 1/3 octave band, sound power level, perceived noise level, or broad-band noise, however.

The subsonic module of PROPFAN I, also called SPN (Subsonic Propeller Noise) is operational on the CDC Cyber 175 computer system. The code is sufficiently documented to serve as its own user's manual. For a typical case, the execution time is approximately 25 CPU seconds, and the code requires a core storage of approximately 50K octal words.

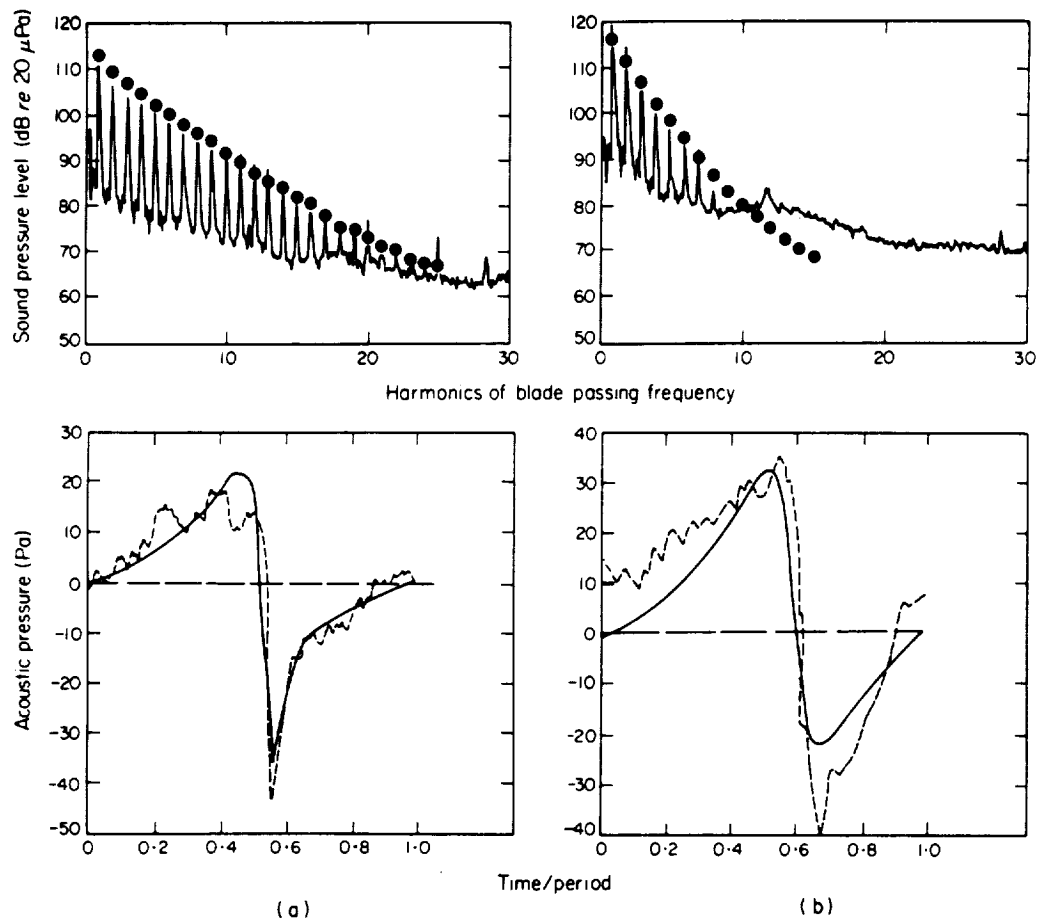


Figure 2.2-27. Comparison with Experimental Data - Method of Succi

Calculated and measured acoustic spectra (top) and pressure signatures (bottom) for a general aviation propeller. (a) In-plane microphone, period = 9.32 ms; (b) aft microphone. For spectra:       , experimental, theoretical; for pressure signatures:       , experimental,       , theoretical.



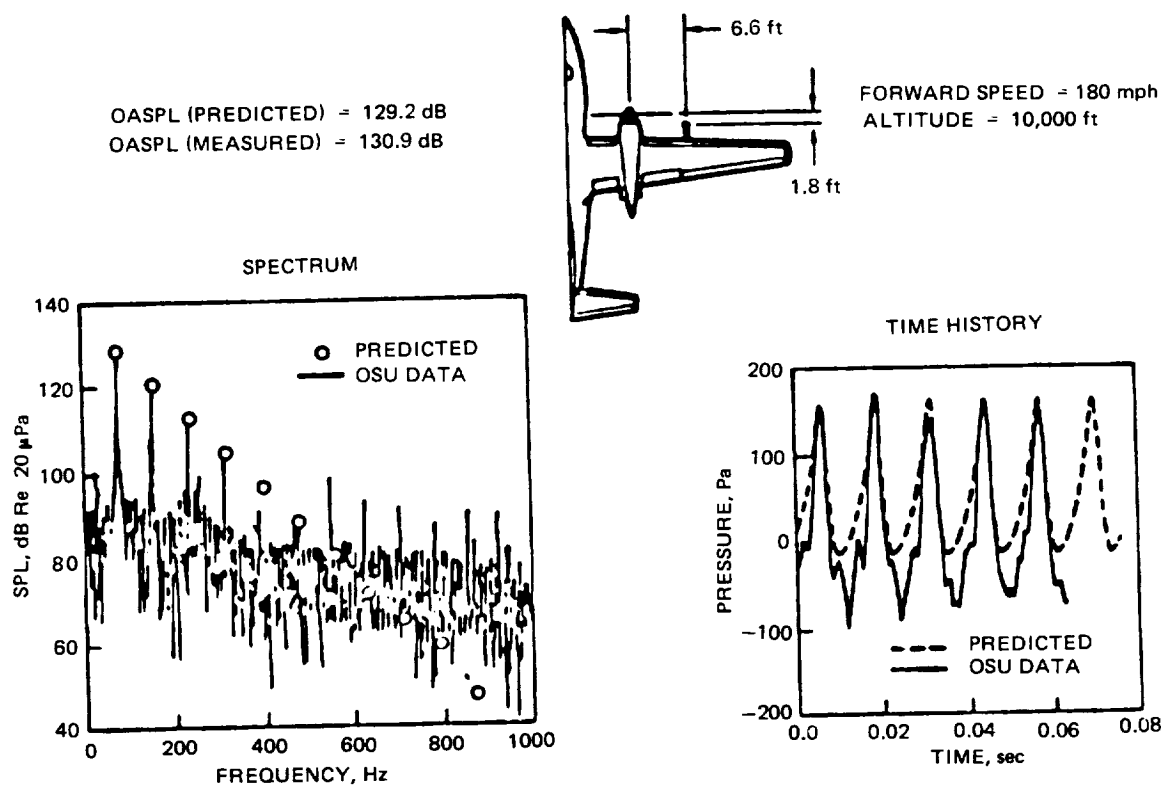


Figure 2.2-28. Comparison of Calculated and Measured Near-Field Propeller Noise Using Method of Martin and Farassat (Propfan I)

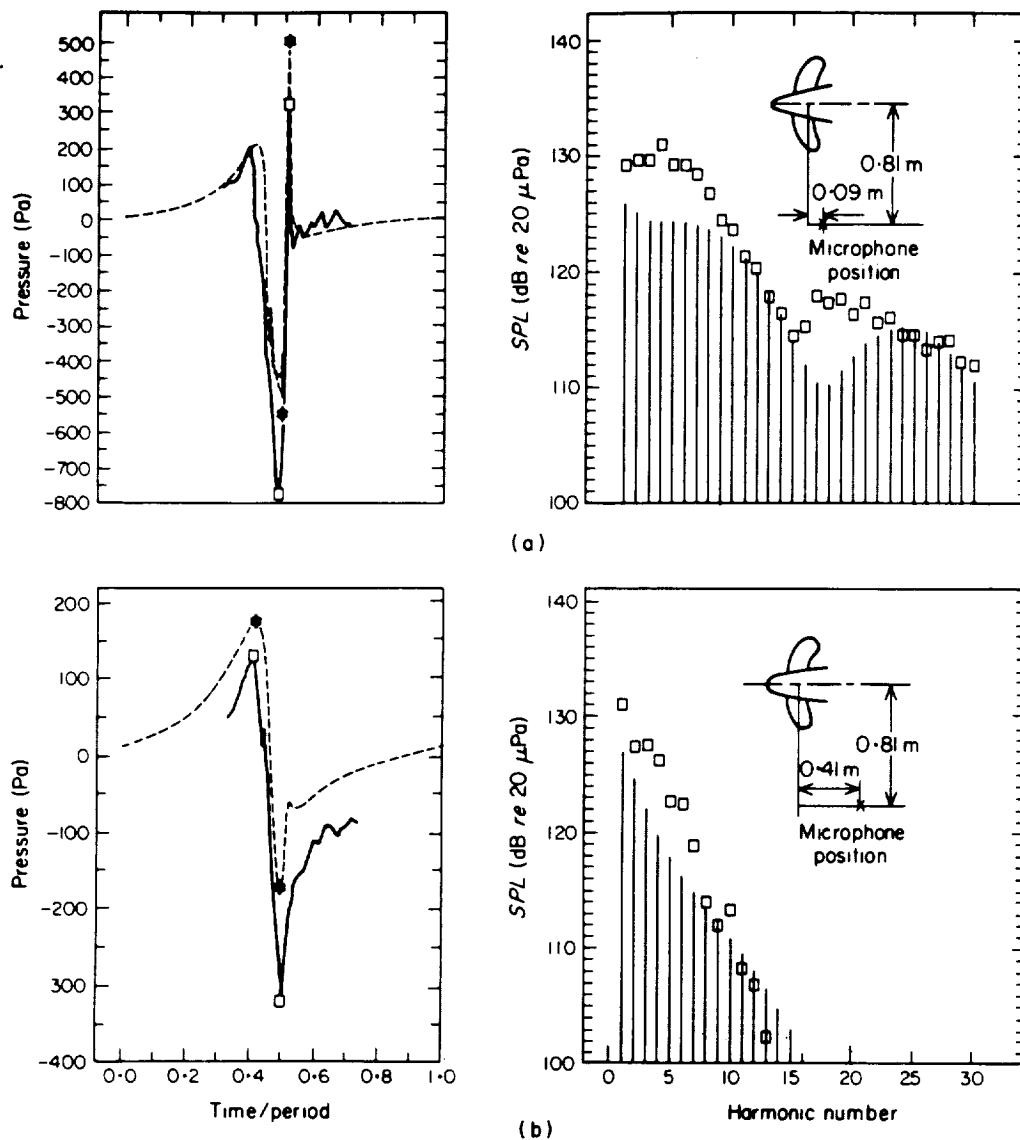


Figure 2.2-29. Comparison with Data - Method of Martin-Farassat (Propfan I) SR-1 Propeller,  $M_{TH} = 1.03$

Period, 2.667 ms; number of blades, 2. For signatures:  $\square$ , experimental;  $---$ \*, theoretical; for spectra:  $\square$ , experimental;  $|$ , theoretical. (a) Microphone position 0.09 m from propeller plane; experimental OASPL = 139.1; theoretical OASPL = 135.5; (b) microphone position 0.41 m from propeller plane; experimental OASPL = 135.2; theoretical OASPL = 130.9. All OASPL's dB re 20  $\mu$ Pa.

#### 2.2.5.5 Method of Martin-Farassat (PROPFAN-Formulation II)

This version of the Martin-Farassat methodology (Ref. 2.2-56) is also a time-domain formulation for non-compact sources but incorporates an improved formulation for the transonic and supersonic speed ranges. The code output is identical to that Formulation I, but reduced computer run times and greater accuracy are anticipated for transonic and supersonic helical tip Mach numbers. Again, as with Formulation I however, the code does not include the quadrupole noise source term or have the capability of calculating 1/3 octave band, sound power level, perceived noise level, or broad-band noise.

The computer code, called TPN (Transonic Propeller Noise), is fully operational at TRW and is sufficiently documented to serve at its own user's manual. For a typical case, the execution time is approximately 10 CPU seconds, and the code requires a core storage of approximately 100K octal words.

#### 2.2.5.6 SAE AIR 1407 - Prediction Procedure for Propeller Noise

This code is based on an empirical method developed by Hamilton-Standard (Ref. 2.2-57). It is based on static propeller test data and does not include nacelle effects. The method has been shown to yield good results in the far field for forward flight with a nacelle; however, since flight effects act to decrease the noise and nacelle effects act to increase it, the effects tend to cancel. The approach consists of determining a series of partial levels and correction factors from graphs and summing the partial contributions arithmetically. The graphical quantities have been curve fit by Korkan and Ruff (Ref. 2.2-58), and the code originally developed for a programmable calculator has been implemented on the TRW computer system. References 2.2-57 and 2.2-58 provide sufficient information to serve as user's manuals.

#### 2.2.6 Structural Analysis

##### 2.2.6.1 Beam Model Structural Analysis Requirements

The determination of the steady-state deflected shape, the stresses within the blade, and the natural frequencies of vibration (including mode shapes) of the rotating blade are quantities that are very difficult to

calculate for advanced propellers. A beam-type structural analysis model, if it is developed correctly, has the advantages that it can calculate these quantities using a minimum of computer storage and time. The beam-type structural model is applied by discretizing the blade into a series of beam-type segments along the line of shear centers of the blade. The cross sections of the blade, which are perpendicular to the line of shear centers, are used as the cross sections of the beam segments.

Studies have shown that a beam-type model can be successfully used to analyze helicopter rotors (Refs. 2.2-59 through 2.2-62) and wind turbine blades (Refs. 2.2-63 and 2.2-64). In these studies, the differential equations of motion that define the blade were derived with the following important capabilities: (1) A nonlinear strain-displacement relation is used that is based on small linear strains and finite rotations. This is important to correctly model the effects of the in-plane centrifugal forces with the changing of the blade stiffness. (2) Allowances are included for the mass center axis and the area center axis of the blade to be offset from line-of-shear centers. These offsets are important for accurately modeling the twisting and bending of the blade due to the centrifugal forces. (3) Warping of the cross section is included based on the work of Timoshenko (Ref. 2.2-65). (4) The centrifugal forces are derived using the deformed position of the blade using relations that are compatible with the nonlinear strain-displacement relations.

These equations can be derived using either Hamilton's Principle (Ref. 2.2-60) or Newton's force method (Ref. 2.2-59 through 2.2-61). The solution of these nonlinear differential equations can be solved by either the Galerkin method (Refs. 2.2-60, 2.2-62, and 2.2-64) or the finite element method (Ref. 2.2-66 through 2.2-68). The finite element method is preferred because it can be easily used to model propellers with irregular geometries.

The inclusion of a structural analysis procedure for advanced propellers, using a beam type model in the GAPAS program, can be accomplished by either of two alternatives. The first method is to modify one of the existing structural analysis computer codes so that rotational effects can be

included. The other alternative is to develop a new structural analysis computer code which is specifically designed for propellers.

#### 2.2.6.1.1 Evaluation of Existing Beam Structural Analysis Methods

Five structural analysis computer programs, based on a beam-type model, were considered as possible candidates for the GAPAS program. None of these codes could be used to analyze advanced propellers without extensive modifications. Four of the codes are general finite element codes that do not include rotational effects. These codes are excellent for the analysis of general beam-type structures, but they have never been used to analyze propellers. The fifth code is designed to statically analyze conventional propellers (straight), but it is incapable of advanced propeller analysis.

A review of the computer codes that were considered follows.

ADINA. The ADINA finite element code was investigated as a possible candidate for the structural analysis of advanced propellers utilizing a beam-type model. This code has an excellent nonlinear beam element with the capability to analyze large displacements. The overall size of the code is relatively small for efficient programming techniques and for using out-of-core equation and eigenvalue solvers. This program, which is not a public domain computer code, would require major modifications in three main areas before it could be used for propeller analysis. The first modification is the inclusion of the centrifugal and the Coriolis forces of the spinning blade. These forces are derived based on the deflected shape of the blade. The second modification is to alter the nonlinear capabilities so that a full moderate deflection theory (i.e., small strains, finite rotations) with nonlinear coupling between the displacements and the rotations is used. The final modification is to include a beam element composed of composite materials and cross section warping.

NASTRAN. A computer code developed by MacNeal-Schwendler Corporation, which was originally developed in the public domain (COSMIC/NASTRAN) and is also sold commercially (MSC-NASTRAN), was also investigated. This finite element computer code would require the same modifications as the

previously described ADINA before advanced propellers could be structurally analyzed. An additional task is required to reduce the overall size of the code so that it will not exceed the GAPAS executive system requirements. The only advantage of using this code is that it exists in the public domain and a full listing is available from COSMIC.

SAMIS. The Structural Analysis and Matrix Interpretative System (SAMIS) computer code was also considered as a possible candidate for the analysis of rotating propellers utilizing a beam-type model. This public domain finite element program is designed to perform the linear and nonlinear, static and dynamic analyses of structures. The use of this code within GAPAS would require the linear and nonlinear effects due to the centrifugal forces to be calculated and input at each load step of the solution process. These forces would be adjusted until the nonlinear solution process converged to the nonlinear static equilibrium position of the loaded blade. Modifications would also have to be performed to generate the mass, Coriolis force, and stiffness matrices about this equilibrium position.

SPAR. The SPAR finite element computer code was also considered as a possible candidate because a public domain version exists and its size is well within the requirements of the GAPAS executive system. This code, which has full nonlinear capabilities, requires a small core size because of its judicious use of out-of-core equation and eigenvalue solvers. The same modifications that are required for the ADINA would also have to be completed before it could be used to analyze advanced propellers.

TRW-HARTZELL "STEADY". A computer code developed by TRW-Hartzell, which was designed to analyze the static deflections and internal loads of a rotating straight propeller, was also considered. This code, STEADY, is based on the Galerkin method (not the finite element method) to solve for the nonlinear static equilibrium position of the blade due to steady aerodynamic and centrifugal forces. Although this code has the capability for analyzing propellers, there are still significant modifications that would have to be made before advanced propellers could be analyzed. These modifications would include allowances for blade sweep and pretwist, conversion of the code to a finite element code, and development of

structural dynamic capabilities (i.e., eigenvalue solvers) including derivation of the Coriolis force matrix.

#### 2.2.6.1.2 New Beam Model Structural Analysis Computer Code Development

The development of a new structural analysis computer code based on a beam-type model was also investigated. This code would require less work than modifying existing structural analysis computer codes (as previously described) and would produce a code that is specifically designed to analyze both conventional and advanced propellers. The procedure would include the development of a nonlinear beam-type finite element computer code that can calculate the nonlinear static equilibrium position and the natural frequencies of vibration of the rotating blade. The propeller would be modeled by a series of straight beam finite elements that are located along the line of shear centers of the blade. The finite element method is used because it has the versatility to analyze any arbitrarily swept propeller with or without proplets. The structural model developed for this code could be used in the development of an advanced propeller aeroelasticity code.

The nonlinear beam finite element can be derived by extending the work of previous authors (Refs. 2.2-59 through 2.2-61) to include the following capabilities: (1) The beam cross section has a general shape with allowances for offsets of the mass center and the area center from the shear center. (2) Constants due to warping of the cross section are derived based on the previous work of other authors (Refs. 2.2-69 and 2.2-70). (3) The nonlinear equations are derived using a moderate deflection theory (i.e., small strains, finite rotations) and an ordering scheme that is used to identify and neglect higher order terms.

The finite elements would be developed using the variation of Hamilton's principle, where the matrices associated with the kinetic energy (i.e., mass, Coriolis force, centrifugal stiffness and force) are derived with allowances for the deformed beam to be arbitrarily offset from the spin vector. The nonlinear static equilibrium position of the blade is calculated by neglecting the time-dependent terms and solving the nonlinear equations due to the steady rotational forces and aerodynamic forces. The hub forces and the stresses of the blade can then be calculated based on

this position. The natural frequencies of vibration and the mode shapes would be calculated by linearizing the nonlinear equations of motion about the nonlinear static equilibrium position.

#### 2.2.6.2 Plate Model Structural Analysis Requirements

A finite element structural plate module that can model propeller blades of low aspect ratio or high activity factor is requested for the GAPAS program. This module, which will use isoparametric plate-type finite elements to define the propeller, will calculate a refined representation of the stresses along the chordwise direction and calculate chordwise vibration modes or local modes along the propeller edge. The results are very important to designers of highly swept composite blades where local edge stresses may become large enough to cause material delamination.

The structural theory that is required to model the propeller using plate-type finite elements is a full two-dimensional moderate deflection theory that includes allowances for finite rotational deflections. This is required because finite rotational deflections (bending and twisting) have been recorded in the wind tunnel testing of highly swept advanced propellers. The two-dimensional moderate deflection theory requires the use of nonlinear strain-displacement relations that will produce a set of highly nonlinear differential equations of equilibrium. The inertial forces and aerodynamic forces are also derived so that they are fully compatible with the nonlinear strain-displacement relations. The linear and nonlinear finite elements are derived using an isoparametric formulation and the variation of Hamilton's principle.

A plate-type model structural analysis program for GAPAS which uses a full two-dimensional moderate deflection theory is currently beyond the scope of the commercially available finite element computer codes. Many nonlinear finite element codes exist that are based on a semi-moderate deflection theory (geometric stiffness matrices), but none of these contains the rotational effects that are derived to be compatible with the moderate deflection theory. There are two choices for the development of a structural plate module. The first is to modify an existing finite element code so that it includes the nonlinear and rotational effects and still fits within the GAPAS storage requirement. The second choice is to develop



a new plate-type structural analysis computer program that is based on a full two-dimensional moderate deflection theory and contains all of the rotational and aerodynamic effects modeled in a compatible fashion.

#### 2.2.6.2.1 Evaluation of Existing Plate Model Structural Analysis Methods

Five computer codes were considered as possible candidates for performing the plate-type analysis of advanced propellers for the GAPAS program. All of these programs have the capabilities for addressing a linear or nonlinear analysis, but only one is capable of analyzing rotating structures. These codes would require significant modification so that the rotational forces (i.e., Coriolis force matrix, centrifugal stiffening matrix, centrifugal force array) are correctly modeled and included. In order to make these modifications, the source code must be available.

A review of the five computer codes that were considered follows.

ADINA. The ADINA finite element computer code was considered as a possible candidate for the following reasons: (1) This code has an excellent family of plate and shell type finite elements that would require minimum modification in order to analyze advanced propellers. These elements were derived based on the DKT (discrete Kirchhoff theory) method and are extremely efficient and stable for very thin plates (Ref. 2.2-71). (2) The program has full nonlinear analysis and structural dynamic capabilities. (3) The equation and eigenvalue solvers are written out-of-core so that the program takes very little actual core space to run. The size of this program is well within the requirements of the GAPAS executive system.

The disadvantages associated with the ADINA computer code are that it is not available to the public domain (i.e., no source listing) and that modifications of the code would be required. These modifications include the development of all matrices associated with the rotational forces and the nonlinear moderate deflection.

AGGIE-I. A fully nonlinear finite element computer code (AGGIE-I), developed at Texas A & M, was considered for the GAPAS program because it exists in the public domain and is of minimum size due to the use of efficient programming techniques and out-of-core solvers. This code is a reworking of the NON-SAP computer code with additional capabilities such as: (1) linear or nonlinear orthotropic material properties, (2) nonlinearities due to large displacements or large strains, and (3) better behaved two-dimensional (plate) elements and three-dimensional (solid) elements.

The disadvantage of this code is that it is still under development and verification. Portions of the nonlinear static and the eigenvalue options have not been fully checked out. It would be difficult to make modifications to this code to include the rotational and nonlinear moderate deflection effects if the original code has not been debugged.

BELL/NASTRAN PROPELLER FLUTTER CODE. The COSMIC/NASTRAN finite element computer code, modified by the Bell Corporation for analyzing propellers, was studied as one of the possible options for the GAPAS program. This modified code includes all of the effects due to rotation (centrifugal stiffening matrix and force array) and a nonlinear strain theory (geometric stiffness matrix). This code is too large for the GAPAS executive system and significant modifications would have to be made to reduce the size before it could be considered for GAPAS.

SAMIS. The Structural Analysis and Matrix Interpretative System (SAMIS) finite element computer code was also considered because it is a public domain program that has linear and nonlinear, static and dynamic capabilities. This code has a constant thickness, isotropic plate-type element that is not very well-behaved for moderately thick applications. In order for this code to be considered for GAPAS the following modifications would be required: (1) install a better orthotropic plate or shell-type element that has improved convergence properties for thin plate applications (DKT element) and moderately thick applications (Mindlin element); (2) develop the nonlinear stiffness matrices for the new plate element using a moderate deflection theory; (3) develop the matrices associated with the rotational forces (i.e., Coriolis force matrix,

centrifugal stiffening matrix, centrifugal force array); (4) convert the appropriate routines so that orthotropic materials and rotational effects can be input.

SPAR. The SPAR finite element computer was also investigated as a possible candidate for the GAPAS program because it has the advantages of being a public domain program and requiring very small core space (100K octal). This computer code includes a wide range of capabilities including static and dynamic responses to concentrated and distributed loads, use of either a standard or complex eigenvalue solver for vibration analysis, and nonlinear analysis for beam elements and shear panels can be used for structural stability calculations or for the calculation of the nonlinear equilibrium position.

Although the SPAR computer code is a fine code for doing structural analysis, there are no allowances in the program for modeling of rotational dynamics, nonlinear bending of plate or shell type elements, or for an iteration scheme for calculating the nonlinear position of structures composed of plate-type elements. These matrices would have to be developed using a theory that is compatible with the plate and shell elements that currently exist in the program. Once these matrix subroutines are derived, an iteration scheme (Newton-Raphson method) would have to be incorporated into the program so that the nonlinear stiffness matrix can be updated after each load step.

Care must be taken to ensure that the addition of the subroutines and the iteration scheme would not make the code too large for the GAPAS executive system. If that were to occur, sections of the SPAR code would have to be removed (i.e., thermal loading routines, fluid element routines, shear panel routines).

#### 2.2.6.2.2 New Plate Model Structural Analysis Computer Code Development

The development of a new plate-type finite element analysis code that can be used in GAPAS would require that a complete two-dimensional moderate deflection theory be derived for the propeller. This moderate deflection theory would include allowances for finite rotational deflections and the use of higher order nonlinear strain-displacement effects in order to model

the nonlinear coupled bending-torsion deflections of the propeller. The material properties of the plate (or flat shell) would include allowances for a laminate construction composed of orthotropic materials. The modeling of the inertial loads and the aerodynamic loads must be done using the deformed shape of the blade in a way that is fully compatible with the two-dimensional moderate deflection theory. The triangular and quadrilateral finite elements associated with the plate-type element would be derived by the variation of Hamilton's principle using an isoparametric formulation. Because some of the matrices are nonlinear, a Newton-Raphson iteration scheme must be employed in order to adjust the nonlinear stiffness matrices during the calculation of the nonlinear static equilibrium position. A bandwidth minimizer and an out-of-core eigenvalue solver are required to ensure that the size of the program does not exceed the requirements for the GAPAS executive system.

The newly developed plate finite element computer code would follow the same solution methodology as the beam-type structural analysis procedure of GAPAS. By doing this, many of the routines that have been developed for the beam computer code can be directly incorporated. It would also be possible to combine the two codes so that propellers that are composed of both beam and plate-type finite elements could be analyzed.

#### 2.2.7 Aeroelastic Analysis Procedures

The development of prop-fan blades, which are highly swept and extremely thin, has led to a complex problem of predicting the aeroelastic stability boundaries, forced response, and vibratory characteristics. Most of the studies that have been performed in the area of aeroelastic predictions, during the past 20 years, have been concerned with helicopter rotors. The development of an aeroelastic model for advanced propellers requires that both the structural model and the aerodynamic model of the blade be more complex than the equivalent helicopter rotor model. The structural model must include allowances for nonlinear deflections, blade sweep and pretwist, and nonisotropic material behavior. The aerodynamic model must incorporate both the steady and unsteady aerodynamics of the swept blade rotating near transonic Mach numbers.

The aeroelastic model that is used for the advanced propeller must be capable of determining:

- (1) Eigensolutions of the structurally coupled mode shapes and natural frequencies
- (2) Steady-state blade displacements, moments, and stresses
- (3) Time history solutions of blade displacements, moments, and stresses.

There are a limited number of computer codes that have the capability of performing an aeroelastic analysis of advanced propellers. These codes, which have been written recently, are extensions of the work by investigators analyzing helicopter rotors. Four alternatives were evaluated as possible candidates for the propeller aeroelastic portion of the GAPAS program. They are:

- (1) Use of the G400-PROP aeroelastic code, which was developed by UTRC, to perform the aeroelastic analysis
- (2) Use of the Bell/NASTRAN propeller flutter code
- (3) Modification of an existing helicopter aeroelasticity computer code
- (4) Development of a new aeroelastic computer code specifically designed for advanced propellers.

#### 2.2.7.1 UTRC-G400PROP Aeroelastic Computer Code

A computer code was developed by United Technologies Research Corporation (UTRC) to perform the aeroelastic analysis of advanced propellers under NASA contract NASA 3-22753 (Ref. 2.2-72). This code, G400-PROP, is a modification of a previously developed helicopter rotor aeroelastic code (G400) with allowances for blade sweep, blade pretwist, and improved aerodynamics at high Mach numbers.

The structural model for the propeller is developed based on a linear straight beam-type model developed by Houbolt and Brooks (Ref. 2.2-73) with allowances for blade pretwist and blade sweep. The sweep of the blade is approximated by taking the undeformed curved line of shear centers of the blade and straightening it out so that an equivalent straight propeller can be analyzed. This approximation, which is only correct for very small

sweep angles, neglects the coupling effects that are introduced due to the geometric sweep of the blade. The nonlinear terms associated with a moderate deflection theory (i.e., small strains, finite rotations) are not included, which also limits the accuracy of the model.

The aerodynamic model, which is used in the code, is based on propeller aerodynamics and the original helicopter aerodynamic model has been removed. The new model is based on a two-dimensional strip theory with allowances for swept airfoil flow effects and coupling between propeller and nacelle. The aerodynamic load representation in the attached flow region (unstalled case) is based on time domain aerodynamics using Pade approximants. A model for dynamic stall, developed by Gangwani (Ref. 2.2-74), has been incorporated using curve-fitting of experimental data. This model represents the state of the art for propeller airfoil unsteady aerodynamics.

The differential equations of equilibrium are discretized using the global Galerkin method. The nonlinear static equilibrium position of the blade due to the steady aerodynamic forces and the centrifugal forces must be defined as a user input. Since this equilibrium position is not known and is unique for each operating condition, numerous errors will occur if the position is not correctly defined.

The initial version of this code was too large to operate on the computer system without overlay (440K octal words) and this could not be used as one of the candidates for GAPAS. A reduced version of the code has been developed (350K octal) however this version would have to be run as a stand-alone code and could not be an integral part of GAPAS.

#### 2.2.7.2 Bell/NASTRAN Propeller Flutter Computer Code

A computer code developed by Bell Corporation, which is capable of calculating the flutter boundaries of advanced propellers, was also considered as a possible candidate. This code was developed by making modifications to the COSMIC/NASTRAN finite element code to account for blade rotation (i.e., Coriolis and centrifugal force matrices) and steady aerodynamic loads. The modifications were derived based on a linear theory and were incorporated by adding five modules to the code. A geometric stiffness

matrix, which was derived based on a nonlinear strain theory (not a moderate deflection theory), is used to calculate the nonlinear equilibrium position of the blade due to the rotational and aerodynamic forces.

The following are the limitations of the BELL/NASTRAN code: (1) The current version of this code is not capable of analyzing an advanced propeller subjected to unsteady aerodynamic loads. In order to study this problem, the unsteady aerodynamic stiffness and damping matrices must be derived and input into the program by the user. (2) The time history solutions of the blade displacements and stresses cannot be determined without making considerable modifications to the code. (3) The code is too large for the GAPAS executive system and significant changes would have to be made in order to reduce the size.

#### 2.2.7.3 Modification of Existing Aeroelastic Computer Codes

A study was also done to determine the practicality of developing an aeroelasticity code by combining portions of existing aeroelasticity codes. This would include using a structural model from an aeroelasticity code that is based on the finite element method (Ref. 2.2-75) and using the dynamic stall model and the unsteady aerodynamic model from the G400-PROP computer code (Ref. 2.2-72). Two advantages can be identified when following this approach. First, a finite element structural model is capable of correctly accounting for sweep and pretwist of an advanced propeller. This model is derived based on the full moderate deflection theory (i.e., small strains and finite rotations) and includes all of the constants associated with cross-section warping. Second, the unsteady aerodynamic model from the G400-PROP is an excellent package that is derived in the time domain, using Pade approximants.

This approach has the advantage that the best portions of existing aeroelastic codes can be combined to create a hybrid computer code. Considerable time can be saved by using portions of these codes directly rather than rederiving them. The only disadvantage with this approach is that the actual programming of each code must be fully understood and that the new code must correctly access all the capabilities of the two existing codes.

#### 2.2.7.4 New Aeroelastic Computer Code Development

The development of a new aeroelastic computer code, which is specifically designed for advanced propellers, was also investigated. The advantage with this approach is that a code could be designed to be fully compatible with all of the other existing codes in GAPAS. The structural and aerodynamic models would be derived based on advanced propeller parameters instead of altering existing helicopter aeroelasticity codes (i.e., G400-PROP). A nonlinear structural model would be needed which is based on the finite element method and includes the effects due to cross section warping, large centrifugal forces, and nonisotropic material behavior. This model would be developed as part of the GAPAS structural analysis. Options would also be included so that actual experimental mode shapes could be used instead of the finite element mode shapes. The aerodynamic model would be derived based on the same assumptions as the structural model so that it is fully compatible. This model would follow the aerodynamic model of the G400-PROP, using Pade approximants for the time domain unsteady aerodynamics and a dynamic stall model developed by Gangwani (Ref. 2.2-74). Cascade effects would be incorporated in the unsteady unstalled aerodynamics, which is important for multibladed propellers.

The development of this code would be a major undertaking but would produce the best results for the analysis of advanced propellers.



## 2.3 RECOMMENDATION OF ANALYSIS PROCEDURES FOR INCORPORATION INTO GAPAS

The following summary describes the conclusion and recommendations for incorporation of analysis procedures into GAPAS as well as the modifications necessary to allow GAPAS to meet the operation requirements as discussed earlier.

### 2.3.1 Geometry Generator Module

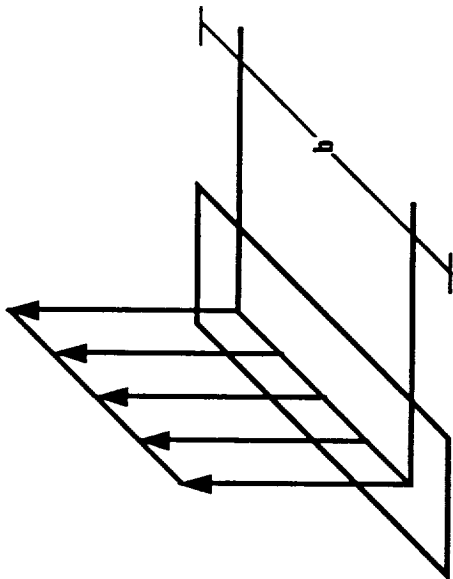
Since an adequate geometry computer code does not exist for incorporation into GAPAS, a new geometry generator module will be developed.

### 2.3.2 Aircraft Flow Field Module

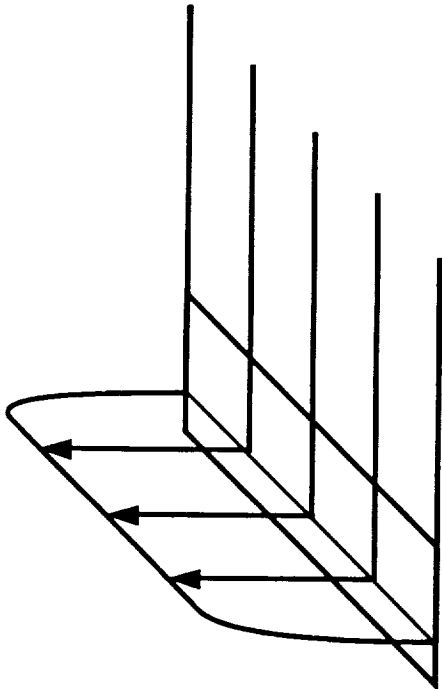
The inflow velocity components in the plane of the propeller are calculated by Jumper's code (Refs. 2.2-1 and 2.2-2) using incompressible potential flow methods. The fuselage/nacelle geometry is divided into source panels of unknown strength, while the wing is replaced by an equivalent lifting horseshoe vortex.

There was some concern that the influence coefficients, as calculated by JUMPER, should be computed more accurately for the effect of nearby panels using the ideas of Hess and Smith (Ref. 2.2-5). However, comparison of results in Figure 2.2-12 computed with the axisymmetric NEUMANN code show good agreement.

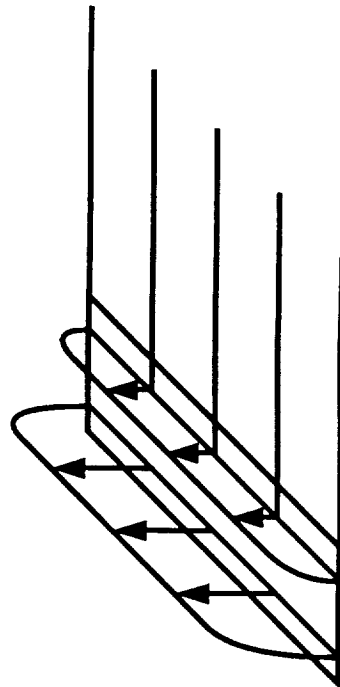
One drawback of JUMPER is the model of the wing – a single horseshoe vortex. Calculation of the upwash ahead of a wing modeled by a series of lifting lines is depicted in Figure 2.3-1. The results of a small stand-alone calculation of the upwash ahead of a finite span wing are shown in Figures 2.3-2 and 2.3-3. As can be seen, the single horseshoe vortex underpredicts the upwash by half compared to lifting line calculations with two or more chordwise divisions for propeller planes about 10% of the wing semispan ahead of the wing leading edge. The upwash will affect the local angle of attack at the propeller blade for various azimuth locations. The streamwise component of the inflow velocity should not be affected as much. This modification is not implemented into the current aircraft flow field module. Minor modifications would be required in the definition of sideslip and angle of attack to correspond to standard aircraft notation.



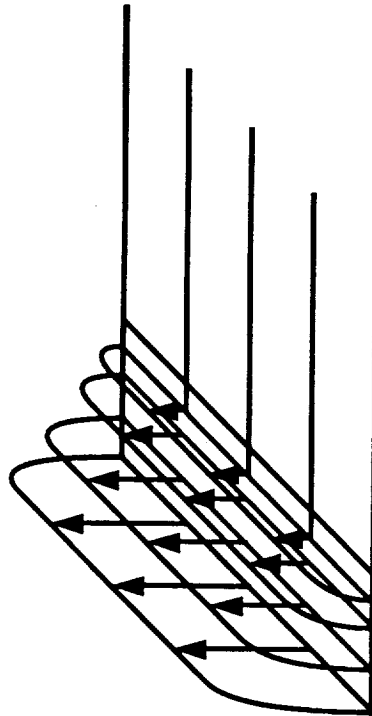
**HORSESHOE VORTEX**



**1 BOUND LINE VORTEX**



**2 BOUND LINE VORTEX**



**4 BOUND LINE VORTEX**

Figure 2.3-1. Wing Vortex Lattice Model

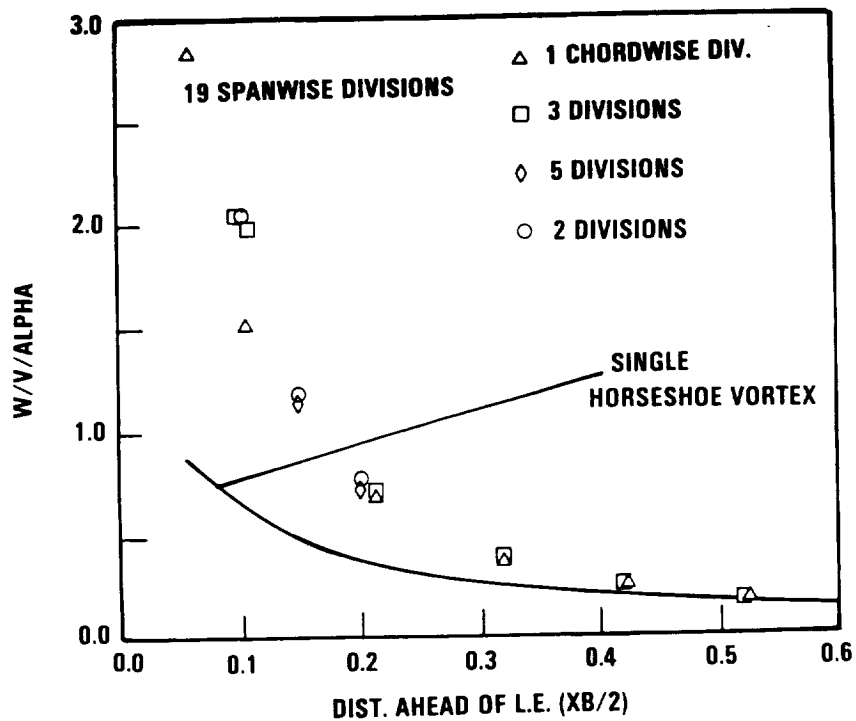


Figure 2.3-2. Wing Upwash as a Function of Longitudinal Position

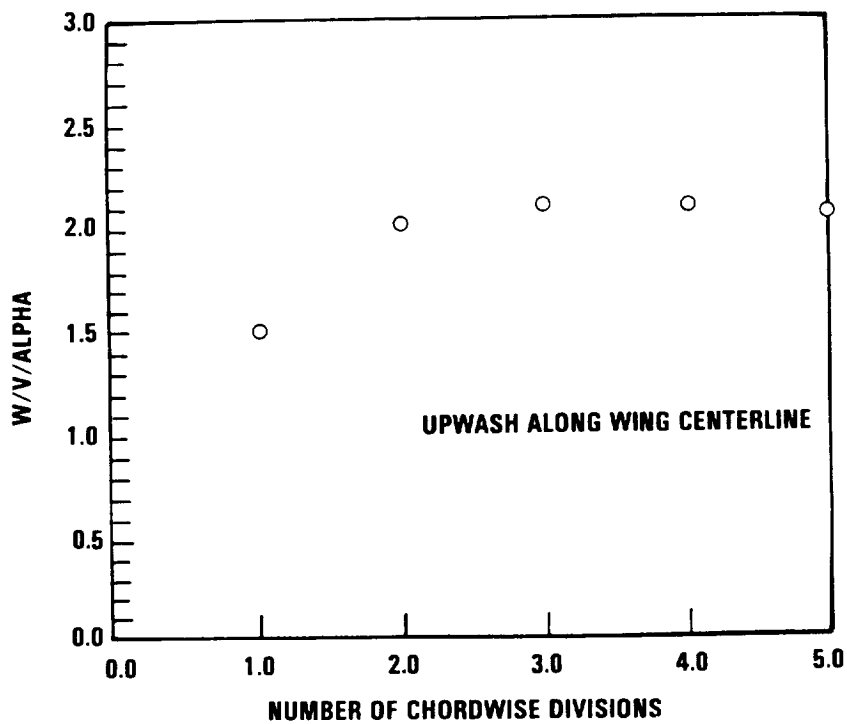


Figure 2.3-3. Upwash 10% Semispan Ahead of Leading Edge as a Function of Number of Chordwise Divisions, Rectangular Wing,  $AR = 6$

In addition, the propeller plane would be generalized so that a curved propeller could be considered. The input/output routines would also be modified to interact with the data base.

### 2.3.3 Propeller Aerodynamic Performance

Based on the detailed aerodynamic procedures review, it is recommended that the UTRC code be the primary code utilized in GAPAS for the steady-flow case, and that the Chang-Sullivan codes be implemented as a secondary code for the consideration of configurations with proplets. In addition, it was recommended that the Aljabri code be implemented into GAPAS to provide the capability for calculating unsteady effects. The required modifications to the above codes are described below:

- (1) The Chang-Sullivan and Aljabri codes required a change in the calls to the airfoil section data in the individual codes to calls to external data banks as defined in the airfoil loading module.
- (2) Improve the integration subroutines in the Aljabri code for the calculation of thrust and power coefficients in order to provide greater flexibility and accuracy.
- (3) In the area of new developments, an investigation of propeller aerodynamic optimization methods for use in a GAPAS limited design mode of operation.

### 2.3.4 Airfoil Loading Module

After review of the analysis procedures, the following recommendations for the airfoil loading module are made:

- (1) Incorporate the Eppler code into GAPAS for use in the propeller hub region (i.e.,  $M_\infty < 0.3$  and  $Re_\infty < 10^6$ ). This recommendation is based on Eppler's use of the code for thick airfoil sections. A modification to this code is also necessary in order to include the effect of weak viscous-inviscid interaction.
- (2) Incorporate the Smetana code into GAPAS for use in the propeller mid-section (i.e.,  $M_\infty < 0.6$ ,  $Re_\infty > 10^6$ ). Necessary modifications would involve the incorporation of the Eppler  $C_{L_{max}}$  model as well as cleaning up the code logic. In addition, a study would be necessary in order to select one of the two turbulent models for use in GAPAS.
- (3) Incorporate the TRANSEP code into GAPAS for use in the propeller tip region ( $M_\infty > 0.6$ ,  $M_{local} < 1.4$ )

- (4) Incorporation of the G&K code into GAPAS would require substantial modification such as the inclusion of a (1) laminar boundary layer capability; (2) transition criteria; and (3) massive separation model. Since initial comparisons show TRANSEP able to handle the supercritical cases, G&K will be used as a backup code.
- (5) Incorporate the Clark Y and NACA 16 airfoil data banks into GAPAS. As additional data banks become available, these can also be incorporated.
- (6) For the higher Mach number cases, wherein the Carlson code is unable to be utilized, airfoil data banks will be required.
- (7) Due to limited input data in describing the geometry of the propeller, spline-fit routines will be necessary in order to obtain a smooth set of airfoil coordinates. Results of using the previously described analysis codes show inaccurate results can be obtained for  $C_L$ ,  $C_D$ , and  $C_M$  if discontinuities in slopes exist in the airfoil shape.
- (8) Development of an algorithm for the selection of the proper airfoil code to be used. This will depend on freestream conditions, propeller locations, airfoil geometry. This will require an evaluation of these codes to determine consistency in the overlap regions.

In summary, specification of the airfoil coordinate geometric data after smoothing, angle-of-attack, Mach number, Reynolds number, and fixed or natural boundary layer transition with appropriate selection of the airfoil analysis code would then yield  $C_L$ ,  $C_D$ ,  $C_m(LE)$ , and  $C_m(c/4)$  along with the required pressure distribution. These pressure distributions would then be stored for each radial location on the propeller to be used in the propeller acoustic performance and structural analysis calculations.

### 2.3.5 Propeller Acoustic Signature

Based on review of the described methodologies, the Martin-Farassat code - Formulation II has been selected as the primary code to be utilized in GAPAS for acoustic calculations. This code has the capability of handling in-plane and out-of-plane blade sweep, as well as subsonic, transonic, and supersonic flow regions. Secondary codes for implementation are the Succi code and the SAE AIR 1407 method.

Modifications to the acoustic module require the inclusion of a noise source information routine to calculate:

- (1) Sound power level spectra (1/3 octave band)
- (2) Overall sound power level
- (3) Sound pressure level spectra (1/3 octave band)
- (4) Overall sound pressure level (1/3 octave band)
- (5) A-weight sound pressure level
- (6) 1/10, 1/3, and full octave sound pressure level
- (7) 1/10, 1/3, and full octave sound power level
- (8) Perceived noise level
- (9) Broadband noise.

#### 2.3.6 Structural Analysis Module

After evaluation of the beam analysis codes, it was recommended that a new structural analysis computer code, based on a nonlinear beam-type finite element model, be developed. This code would be derived using assumptions that are fully compatible with the other codes that are to be incorporated within GAPAS. In addition, a section properties and shear center computer code would be developed that would generate the line of shear centers of the propeller and all of the structural constants of the blade about this line of shear centers.

The line of shear centers of the blade is determined by: (1) calculating the shear center locations for a set of cross sections perpendicular to the initial guess of the line of shear centers, (2) fitting a polynomial through the calculated shear center locations, (3) recalculating the shear center locations based on cross sections perpendicular to the polynomial, and (4) fitting a new polynomial through the recalculated line of shear centers. This iteration process continues until the polynomial (i.e., line of shear centers) converges to a unique solution.

It is recommended that a new plate-type structural analysis program be developed as part of a follow-on effort after the initial version of GAPAS is verified. This program would be developed along the same lines as the beam-type program so that the two would be fully compatible. An additional advantage is that it would be an easier task to develop a plate-type aeroelasticity model using this plate-type structural model as a basis.

#### 2.3.7 Aeroelasticity Module

After evaluation of alternatives, it was decided that the reduced version of the G400-PROP computer code would be incorporated into GAPAS as a stand-alone code after it has been fully verified by UTRC. This would require all the necessary input to be generated by the GAPAS code and submitted as an input file to the G400-PROP code. A series of test cases would then be run to check the validity of the code by comparing the results from the code with experimental results. These test cases would include both stability and response calculations. The sensitivity of the user-defined equilibrium position and the simplicity of the structural would be investigated.

If, as a consequence of the tests, the G400-PROP program proves itself to be either unreliable or has severe limitations, it is recommended that a new aeroelastic analysis based upon the moderate deflection, swept, pretwisted, finite-element beam model be developed for the aeroelasticity module in GAPAS.

## 2.4 EVALUATION OF PROCEDURAL SYSTEMS

### 2.4.1 Procedural System Requirements

The selection of the procedural system is partially based on the requirements of the analysis procedures discussed previously. However, additional requirements are introduced when user friendliness and specific user options are introduced. A summary of the required capabilities of the procedural system is described below:

- (1) Generation of propeller, nacelle and airframe geometry characteristics in a common modular format for use by the various calculation procedures from simple user input options.
- (2) Modular design so that different parts of the analysis system can be developed, operated, modified or replaced independently.
- (3) An overall scheme for communication and interaction between the relatively independent modules only through the procedural system.
- (4) Data base management for the orderly transfer of information between modules.
- (5) Program software which is adaptable to generally available computers. In particular, subprograms that are unique to a specific computer and not adaptable to others, shall not be considered.
- (6) User control for simple input preparation and selective use of the calculation modules.
- (7) Single-pass, noninteractive analysis mode of operation for the aerodynamic, acoustic and structural branches of the system.
- (8) Multiple-pass, interactive analysis mode of operation for the aerodynamic, acoustic and structural branches of the system with a convergence criterion recommended by the contractor.
- (9) User control in batch or interactive modes.
- (10) Step-by-step problem solution without penalty for repeated problem setup.
- (11) Problem restart following either planned or unplanned interruptions.
- (12) Diagnostics and defaults to minimize user input data and identify procedural errors.



- (13) Translation of diagnostics to remedy procedural errors and print out explanatory messages.
- (14) A file security system to prevent accidental destruction of stored files.

These requirements may be satisfied with a software design for GAPAS consisting of two independent program segments: (1) the procedural system, and (2) the functional module library. The procedural system is an executive system that controls the flow of analysis modules calculations and provides errors handling. The functional module library simply contains all the incorporated analysis modules.

Two such systems, the NASA-Langley ANOPP and the TRW JCL system are potential candidates for GAPAS. The ANOPP system represents an internal system that controls the execution flow of analysis modules by using internally coded control language. The JCL system is an external system because it uses control language supported by a host computer operating system. A review of these two procedural systems is described below.

## 2.5 CANDIDATE PROCEDURAL SYSTEMS

### 2.5.1 ANOPP Procedural System

The ANOPP system, which stands for Aircraft Noise Prediction Program, was developed by NASA-Langley for the analysis of aircraft noise. The procedural system is one of the two parts of the overall system while performing three distinct functions. These functions are controlled by management systems which provide or handle executive, data base and dynamic storage services.

The executive management system controls the execution flow of analysis modules by using internally coded control statements. These statements, once processed, perform the following tasks:

- (1) Perform system initialization
- (2) Interpret all input control statements
- (3) Control the execution of functional modules by bringing them into the dynamic storage area one at a time, thus achieving the goal of modularity
- (4) Direct the action to be taken when a fatal error is encountered

- (5) Preserve the operating environment at user selected checkpoints during execution for subsequent restart runs
- (6) Re-establish the operating environment preserved in a previous execution by a user checkpoint request.

The ANOPP internal control statements are defined and monitored by the executive management system, just as job control cards are monitored by the host operating system. The control statements provide basic functions as job processing control, branching control, data base manipulation, etc.

The ANOPP data base management system has a hierarchical structure which, from top to bottom, consists of data units, data members, records, elements and words. A data unit is a collection of data members, and a member is a collection of records, etc. The system is controlled by various data structures, directories and tables, which in turn provide a means of storing and retrieving data on sequential and direct access storage devices. In particular, the following features are provided:

- (1) Creation of new data units on direct access devices
- (2) Access of existing data units
- (3) Direct and sequential access of data members
- (4) Binary or formatted data types
- (5) Reading and writing of data members and records.

The ANOPP dynamic storage management system provides basic allocation and deallocation of core storage within an execution. The dynamic core is defined as that portion of machine memory available within the program field length. The control of storage is accomplished by dividing the field length into two areas, the global and local dynamic storage areas. For a given execution run, the size (and therefore the boundary) of the global area is fixed and it contains all the permanent routines necessary to drive the executive system, internal data structures and directories. The local area houses the transient routines which may be part of the executive system or functional modules. Transient routines are constantly unloaded to provide space for other transient modules. There, the local area is of variable length depending on the size of the routine currently residing. A top-down diagram of the storage layout is illustrated in Figure 2.5-1.

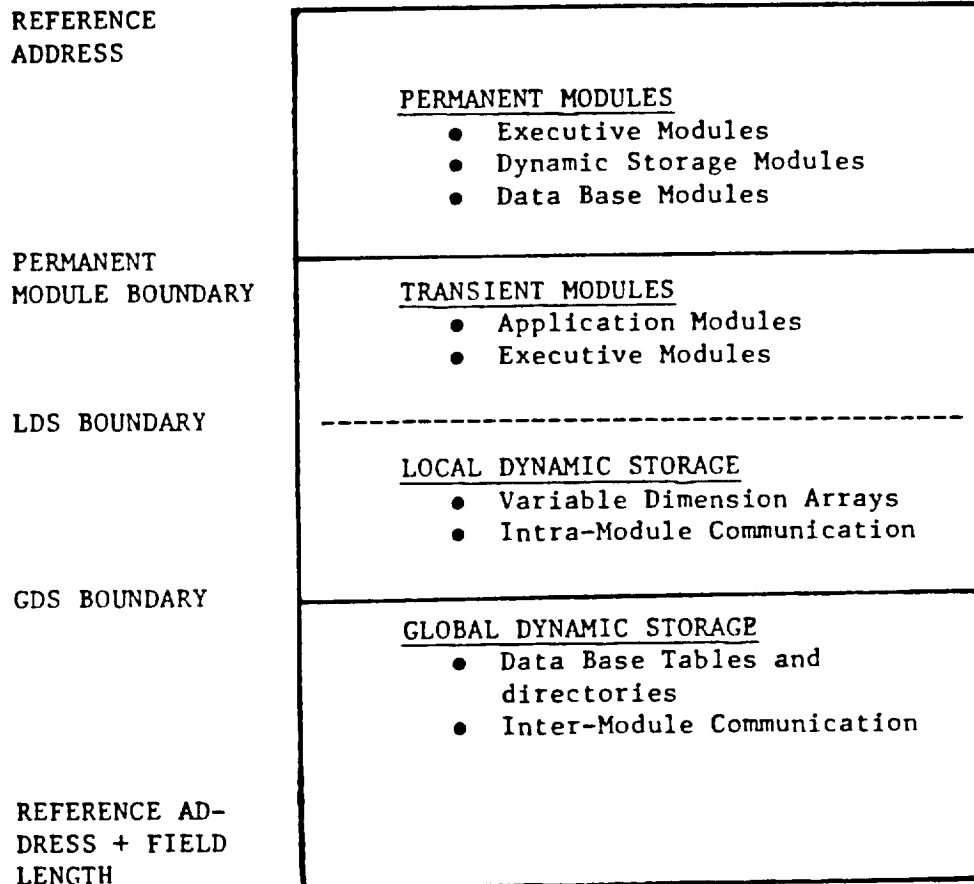


Figure 2.5-1. Schematic Layout of Core Storage

To demonstrate the capability and relative ease of using the ANOPP procedural system, a fictitious sample case is constructed as shown in Figure 2.5-2. The figure illustrates a typical ANOPP input file which activates the procedural system to perform a number of different tasks. First, the "STARTCS" control statement initializes the system. "CREATE" and "UPDATE" instruct the data base management system to open a new formatted data file with actual data following the "UPDATE" statement. Then two functional modules DIM and GGM are loaded separately into the local dynamic storage area for execution. Upon completion, two other modules, AFM and PAM are executed five times, one after another. This conditional branching mechanism is accomplished by using "PARAM" and "IF GOTO" statements. Finally, the ANOPP session is terminated by the "ENDCS" statement. It is clear the design of the control statements is based on the FORTRAN language. Because of this similarity, a first-time user can learn and subsequently master the system without much difficulty.

#### 2.5.2 JCL Procedural System

The TRW JCL system can be viewed as a concept or procedure that a programmer normally adopts when confronted with a need to link up a number of large and diversified computer codes through their input/output requirements. The approach is to treat each code as a stand-alone separate program. Each program is executed and the results required for other programs are written into a data file(s) and saved at the end of the current session. For fast data access, binary data files should be used. Formatted files should be created for those which may require user manipulation. Formatted files are preferred because of their readability. A collection of these data files forms a data base through which all modules interact. Therefore, each module is loaded in core one at a time using system job control cards. When the processing is completed, the module is unloaded from core thereby freeing up the resources for other modules. A schematic of the procedural system is shown in Figure 2.5-3. this figure shows a single-pass run with processing starting with module ECM and proceeding from left to right to PPM. For a multiple-pass or design run, program execution requires looping back and repeating the execution as shown.

```

JOB, ...
USER, ...
CHARGE, ...
ATTACH, ANOPP
RFL, 170000.
ANOPP.
7/8/9      (END OF RECORD CARD)
STARTC $
ANOPP, JECHO = TRUE. LENGL = 3500 $
$
$ DEMO PROBLEM FOR GAPAS, SINGLE PASS MODE
$ CREATE REQUIRED INPUT DATA BASE MEMBER
$
CREATE DIM $
UPDATE NEWU = DIM SOURCE = * $
      - ADDR  OLDM=*, NEWM=GEOM  FORMAT=3H4RSS
      0.0      0.0      0.0075    0.0179
      0.1      0.0      0.0080    0.0200
.
.
.
END* $
EXECUTE DIM $
EXECUTE GGM $
PARAM COUNTER = 0 FLAG = .FALSE. $
REPEAT  PARAM COUNTER = COUNTER + 1 $
        EXECUTE AFM $
        EXECUTE PAM
        IF (FLAG.EQ.TRUE) GOTO ENDLOOP $
        IF (COUNTER. NE. 5) GOTO REPEAT $
ENDLCOP CONTINUE $
        EXECUTE BSM $
.
.
.
ENDCS $
6/7/8/9      (END OF INFORMATION CARD)

```

Figure 2.5-2. Sample Case Using ANOPP Internal Control Statement

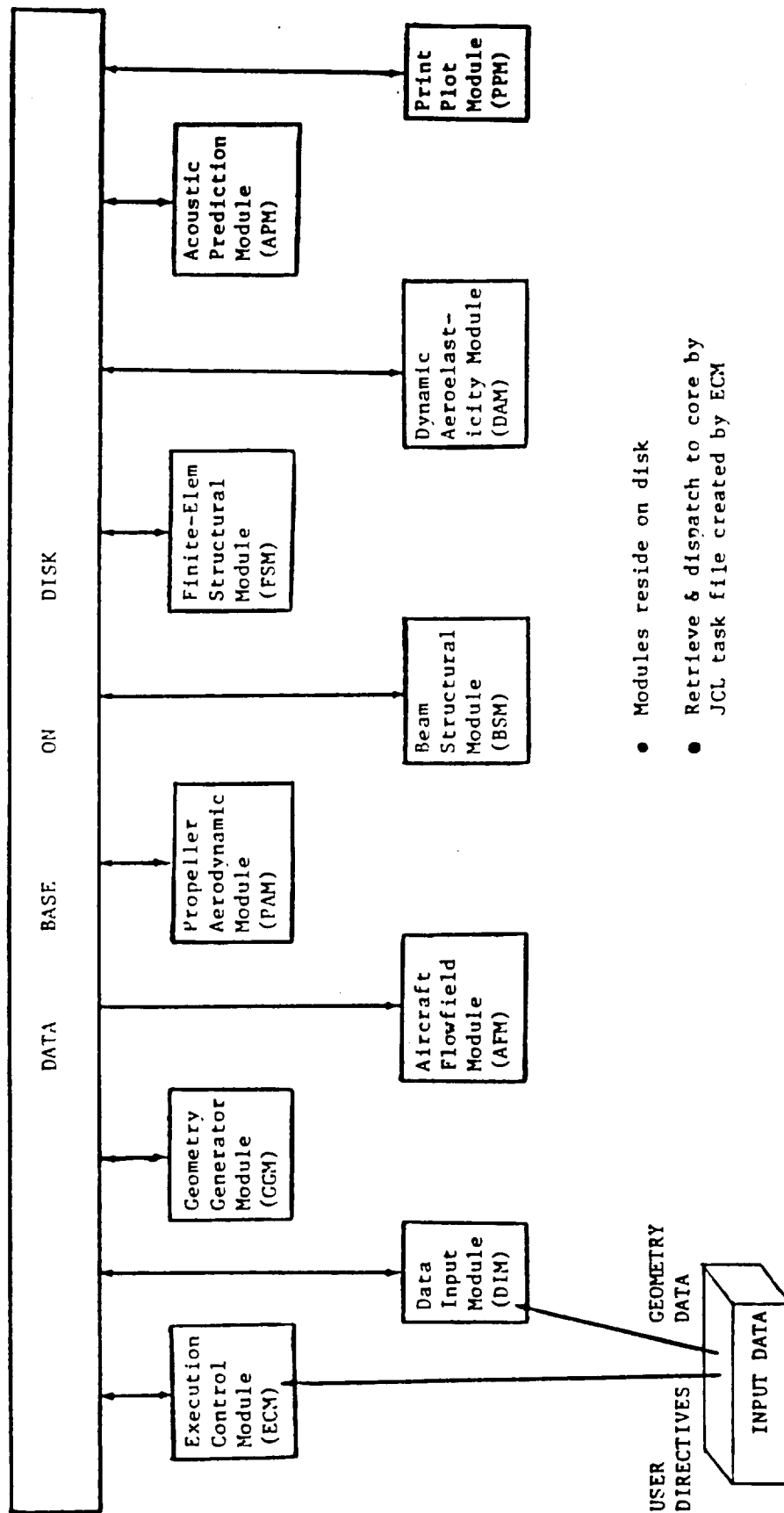
Constructing job control cards for a specific run may be tedious and prone to error. A software program can be written to alleviate such problems. The program, termed EXECUTION CONTROL MODULE (ECM) in Figure 2.5-3, reads user input which specifies single-pass, multiple-pass, design or a restart run. Depending on the processing mode available to a user, the ECM supported directives can be input in card form in a batch mode, or through a question-and-answer session in an interactive mode. After processing the user directives, ECM creates a file containing job control cards necessary to interact with the host computer system for a specific run.

Figure 2.5-4 demonstrates the concept of the JCL procedural system for a CDC computer system. The CDC control language is designed for simplicity, thereby eliminating the requirements for specifying any input/output devices as commonly encountered in IBM systems. The left-hand side of the figure shows the control card sequence required to run module ECM. After user directives are processed, ECM creates a file called JCLFILE which is subsequently processed by CDC control statement "BEGIN". The content of JCLFILE appearing on the right, contains a set of CDC control statements. These statements retrieve modules DIM and GGM for execution, then repeat execution of modules AFM and PAM five times. The counter mechanism is controlled by three control registers, R1, R2 and R3. Upon completion, processing continues with BSM and so on.

This simple example of the JCL system shows that such a system can be developed to satisfy some GAPAS requirements.

## 2.6 RECOMMENDATION OF PROCEDURAL SYSTEM FOR USE IN GAPAS

Although only two procedural systems have been examined, four different options exist because of host computer system differences. The issue of computer system differences arises because the ANOPP system is heavily CDC machine-dependent and the program requirement stipulates that GAPAS be developed for use on the NASA Lewis IBM TSS/370 system. These options are as follows:



- Modules reside on disk
- Retrieve & dispatch to core by JCL task file created by ECM

Figure 2.5-4. Sample External - JCL Procedure System

```

JOB, ...
USER, ...
CHARGE, ...
ATTACH, ECM.
FIN, ECM.
LGO.
RETURN, ECM.
REWIND, JCLFILE.
BEGIN, JCLFILE.
7/8/9 (END OF RECORD CARD)
DIRECTIVE 1.
DIRECTIVE 2.
      .
      .
      .
      } INPUT
      } FOR
      } ECM
EOR.
&NAME1ST1 L=1, J=10, ...
      .
      .
      .
      } INPUT
      } FOR
      } DIM
6/7/8/9 (END OF FILE CARD)

```

```

PROC, JCLFILE.
COMMENT. RETRIEVE DIM FOR EXECUTION.
ATTACH, DIM.
LOAD, DIM.
EXECUTE.
RETURN, DIM.
ATTACH, GGM.
LOAD, GGM.
EXECUTE, INPUT = GGMINPT.
RETURN, GGM.
COMMENT. SET CONTROL REGISTER R1, R2,
      AND R3.
SET (R1 = 0).
SET (R2 = 0).
SET (R3 = 5).
COMMENT. "WHILE" THROUGH "ENDW" DEFINES
      A LOOP.
WHILE (R2. LT. R3) FINISH.
ATTACH, AFM.
LOAD, AFM.
EXECUTE, INPUT = AFMINPT.
ATTACH, PAM.
LOAD, PAM.
EXECUTE, INPUT = PAMINPT.
SET (R2 = R2 + 1).
COMMENT. R1 SET INSIDE PAM.
IFE (R1. NE. 0) OUT.
ENDW, FINISH.
ENDIF, OUT.
RETURN, AFM.
RETURN, PAM.
ATTACH, BSM.
LOAD, RSM.
EXECUTE, INPUT = BSMINPT.
RETURN, BSM.
      .
      .
      .
ATTACH, PPM.
LOAD, PPM.
LGO, PPM. EXECUTE, INPUT = PPMINPT.
      .
      .
      .
REVERT.

```

Figure 2.5-4. Sample External - JCL Procedure System



- (1) JCL Procedural System on CDC/NOS Computer: This is a viable option due to system simplicity, but undesirable because the project requires that GAPAS be developed for the IBM TSS/370 computer. Furthermore, the risk of unforeseen development problems and the likelihood of GAPAS being expensive to execute makes this option even less attractive.
- (2) JCL Procedural System on IBM TSS/370: The TSS/370 system is a unique system that supports a control language entirely different from that of standard IBM systems. This system is rarely used in the aircraft industry. With this major shortcoming, this option is unacceptable.
- (3) ANOPP Procedural System on IBM TSS/370: This option would represent perhaps the best candidate from both system capability and program requirement standpoints. Unfortunately, ANOPP was written for a CDC machine and therefore using this system with an IBM machine would require extensive and often expensive code conversion. In fact, such undertaking has been estimated to take between 3 and 4 man-years. Undoubtedly, such a conversion effort would drain most GAPAS resources. Therefore, this option is unacceptable.
- (4) ANOPP Procedural System on CDC/NOS: This option is perhaps the best candidate currently available. ANOPP is a proven system and was developed for a CDC machine, thus, no conversion would be required. More importantly, CDC computers are widely used in the industry, thereby providing a common base for GAPAS.

In summary, two distinct procedural systems have been examined: (1) The JCL system, yet to be developed, can be designed to meet some GAPAS requirements. (2) The ANOPP system, which has already been built, meets most of the requirements. Based on these considerations, the following is recommended for GAPAS:

- (1) Develop GAPAS for operation on the CDC/NOS computer systems
- (2) Select ANOPP as procedural system for GAPAS.



### 3. TASK 2: MODIFICATION AND DEVELOPMENT OF ANALYSIS PROCEDURES

Analysis procedures and new developments as recommended in Section 2.7 will be discussed. Results of the verification of the operation of the modified or newly developed analysis procedures will be compared with available data from two propeller configurations. The first, the Hamilton-Standard SR-3 propeller, typical of a high-speed commuter-type aircraft, and the second, a Hartzell 101/16 propeller, representative of a small, moderate-speed General Aviation Aircraft. The verification calculations performed considered variations in Mach number, advance ratio and power coefficient.

Modifications and new developments for each of the individual modules are discussed below. In addition, individual module comparisons with available data are also discussed.

#### 3.1 GEOMETRY GENERATOR MODULE

The geometry generator module was developed at TRW to take the geometrical input information and calculate quantities required by the other analysis modules. In the development of a stand-alone version of this module, two small plot routines were written to display input data and section properties of cuts perpendicular to various spanwise arbitrary lines. The transformation matrices were used to construct multiple blades from the single blade information for display of the "wire-mesh" figures in an oblique view such as that in Figure 3.1-1 for the SR-3 propeller-nacelle geometry. The graphical output was a valuable tool for verification of input data and for understanding limitations of the code.

One of the most challenging aspects of the development of the geometry generator module was the calculation of the line of shear centers and the profiles perpendicular to it. This is an iterative process requiring an initial guess for the line of shear centers and a comparison of the shear center of profiles perpendicular to this line. The requirements are detailed in Sections 2.2.1.2 of this report and Section 2.1.1.7 of the User's Manual.

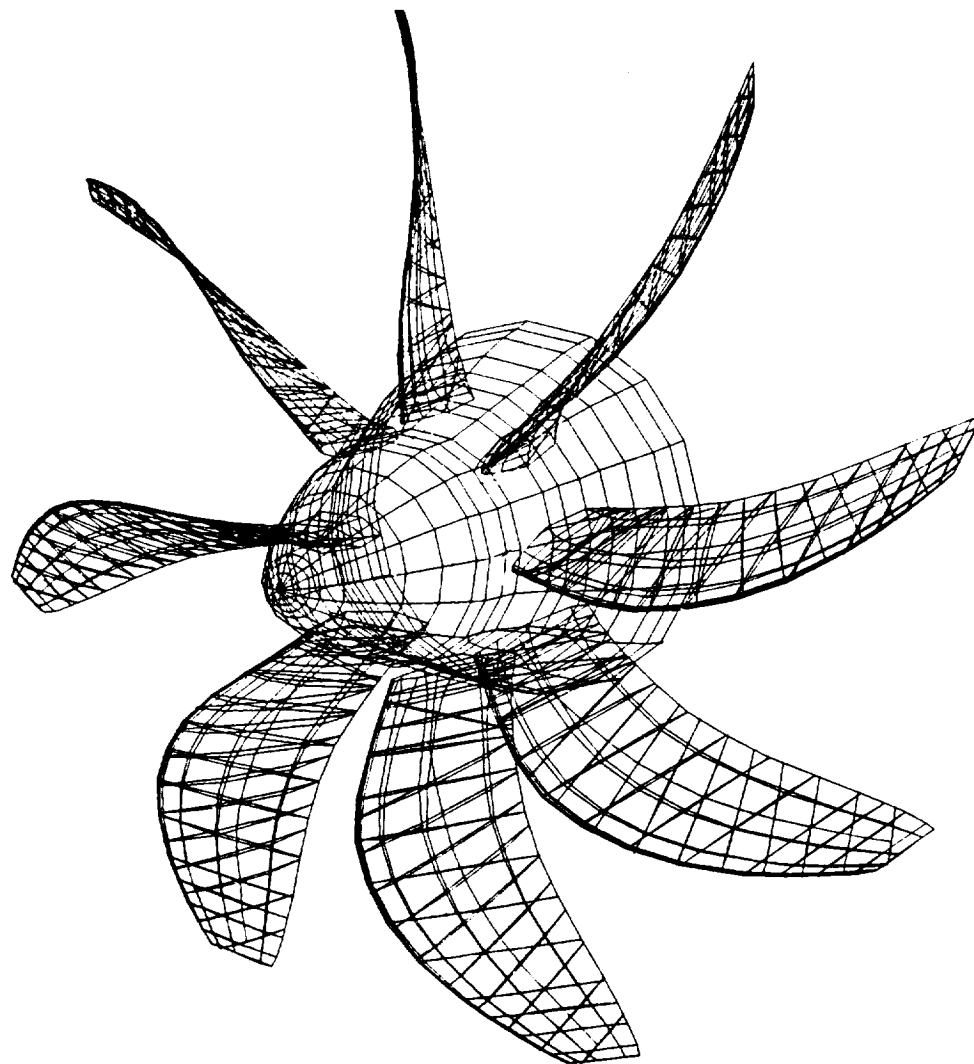


Figure 3.1-1. SR-3 Propeller-Nacelle Geometry

Typical results for the line of shear centers and the profiles perpendicular to this line are shown in Figure 3.1-2 for the SR-3 blade. The beam elements are constructed along this line using the section properties of the profile at both ends of the segment.

In the development of this model, problems were encountered with convergence at the propeller tip as indicated in Figure 3.1-3. The problem was traced to boundary conditions in the spline-fit solution. A modification in the spline-fit routine was made so that the slope at the tip was constrained to that of the initial guess during the iteration process. This allows convergence to occur without any additional problems.

The results for cuts perpendicular to the converged line of shear centers is given in Figure 3.1-4 for a single blade of the SR-3 propeller. Note that the trailing edges of some of the cuts are almost touching. It is important that these profiles are not allowed to cross; if they cross, the spline-fit coefficients become inaccurate and there are negative contributions to the volume of the beam element. The crossing of profiles can be avoided by observing the graphical output of the profiles and making the necessary adjustments.

For the propeller performance module the quarter-chord line must be identified so that the trailing vortices can be located. The relevant profiles are located at the midpoint of the bound vortex perpendicular to the quarter-chord line. The propeller-nacelle geometry of the SR-3 is shown in Figures 3.1-5 and 3.1-6 along with cuts perpendicular to the quarter-chord. In Figure 3.1-7 the details of the cuts show that the trailing edges of some of the profiles intersect. This does not cause a problem in the performance option, but when the pressures on the surface are to be interpolated for the acoustics module, the splines will not vary smoothly and the pressure may be triple-valued at a point. The best solution to this problem is to change the spacing to eliminate the crossing of the profiles. On the other hand, the more fundamental question of the adequacy of the strip theory, using two-dimensional airfoil sections, should be addressed. Wide, swept blades seem to be pushing the lifting-line performance theory to its limits. The airfoil loading module requires detailed information about the cuts perpendicular to the quarter-chord. The airfoil sections for the SR-3 are shown in Figure 3.1-8. The camber

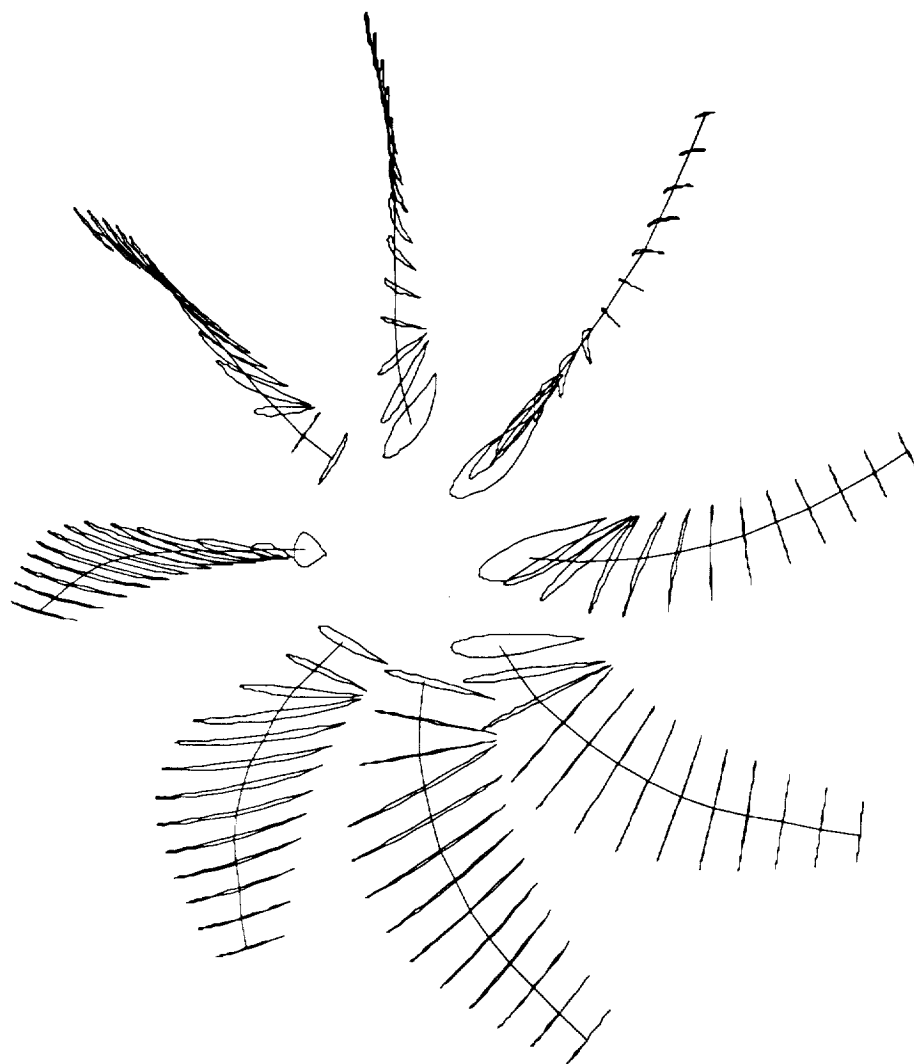


Figure 3.1-2. SR-3 Structural Model Line of Shear Centers and Profiles Perpendicular

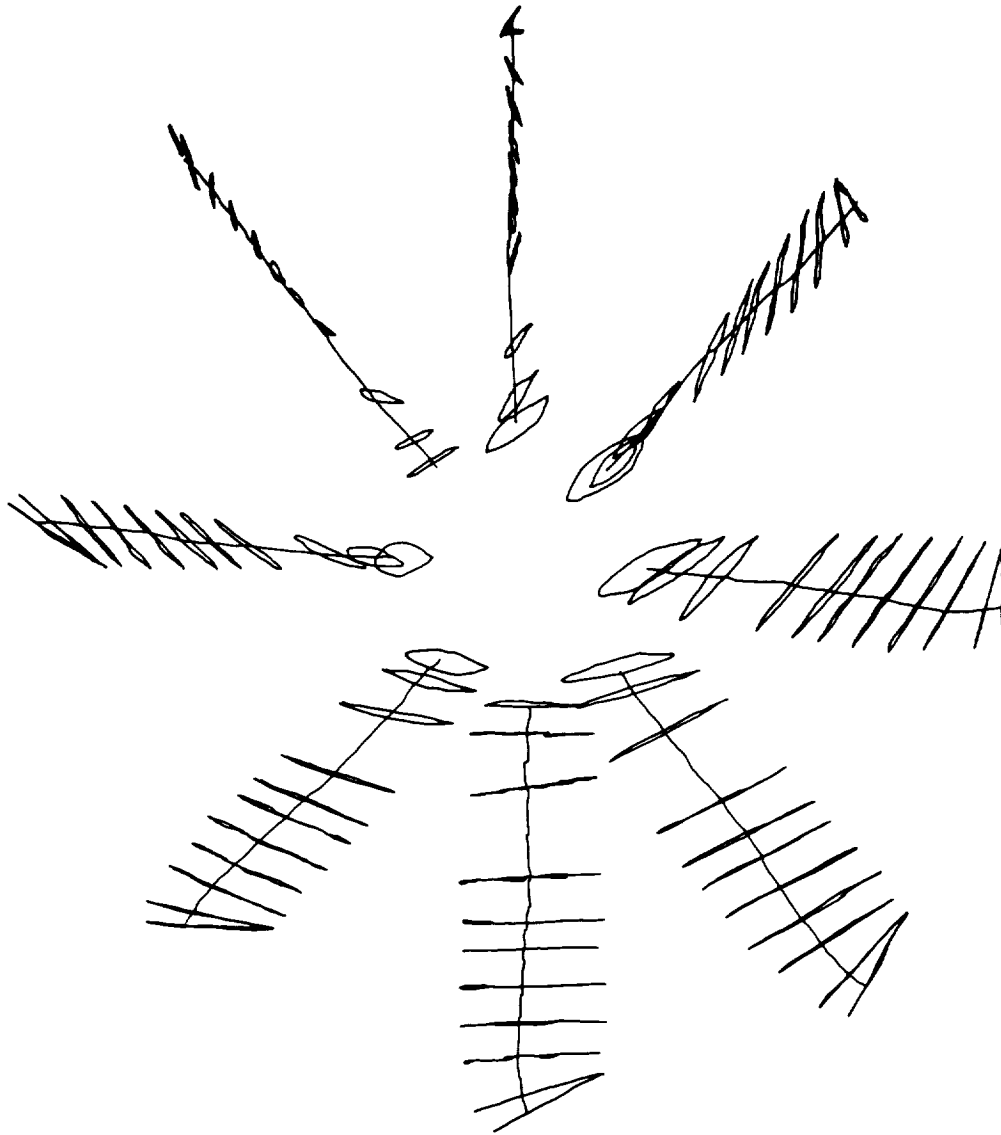


Figure 3.1-3. SR-2 Structural Model Showing Problem at Tip with Line of Shear Centers

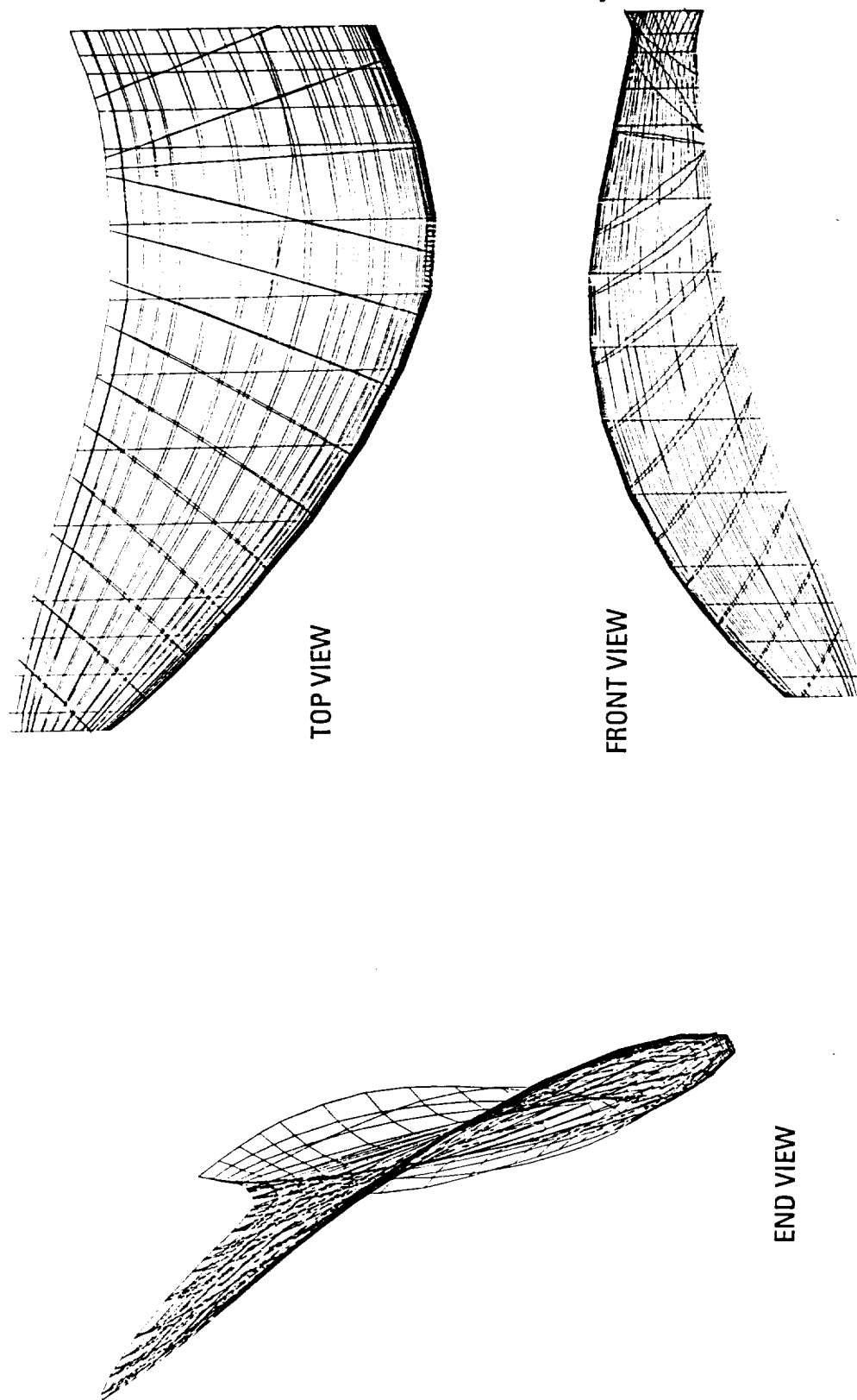


Figure 3.1-4. Three-View of SR-3 Propeller Balde Cuts Perpendicular to Line of Shear Centers



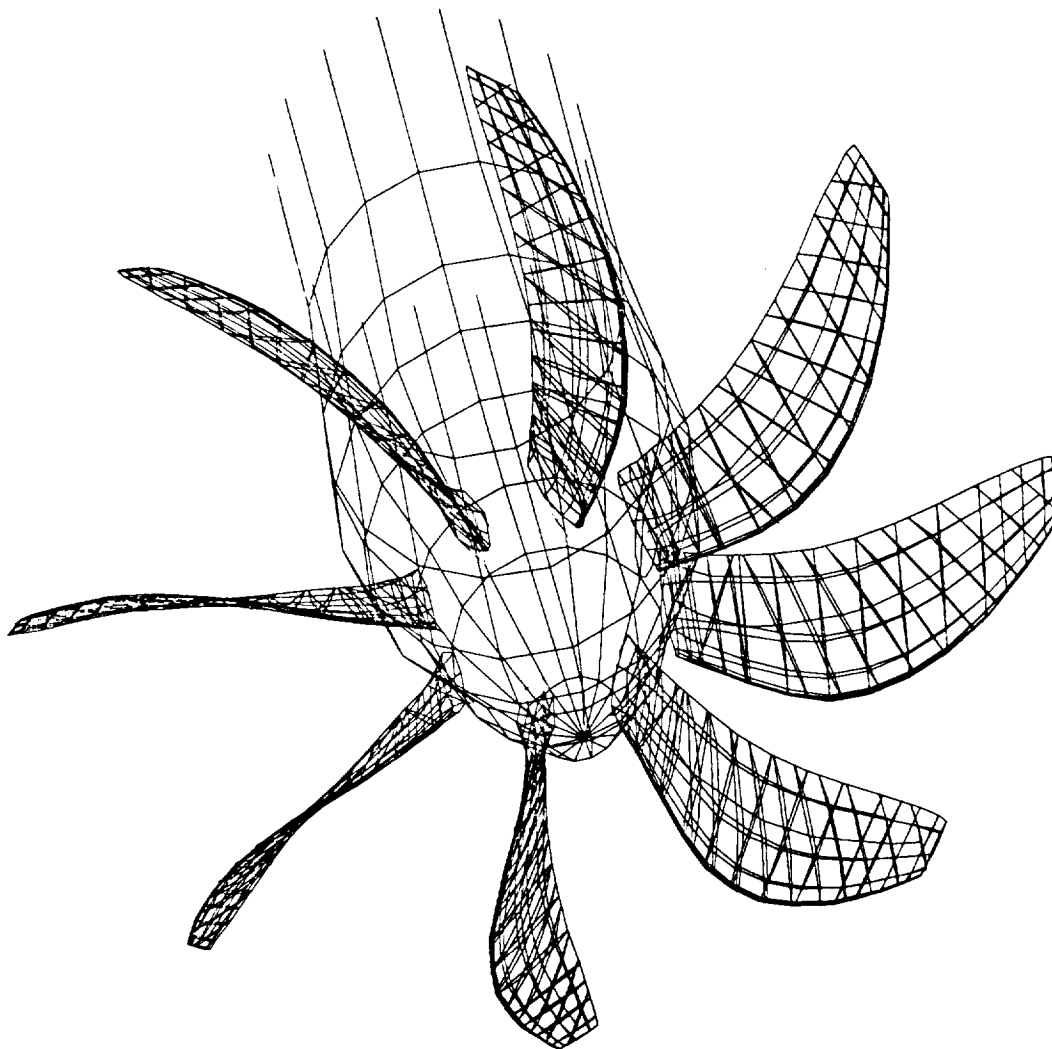


Figure 3.1-5. SR-3 Propeller-Nacelle Geometry Cuts  
Perpendicular to 1/4-Chord

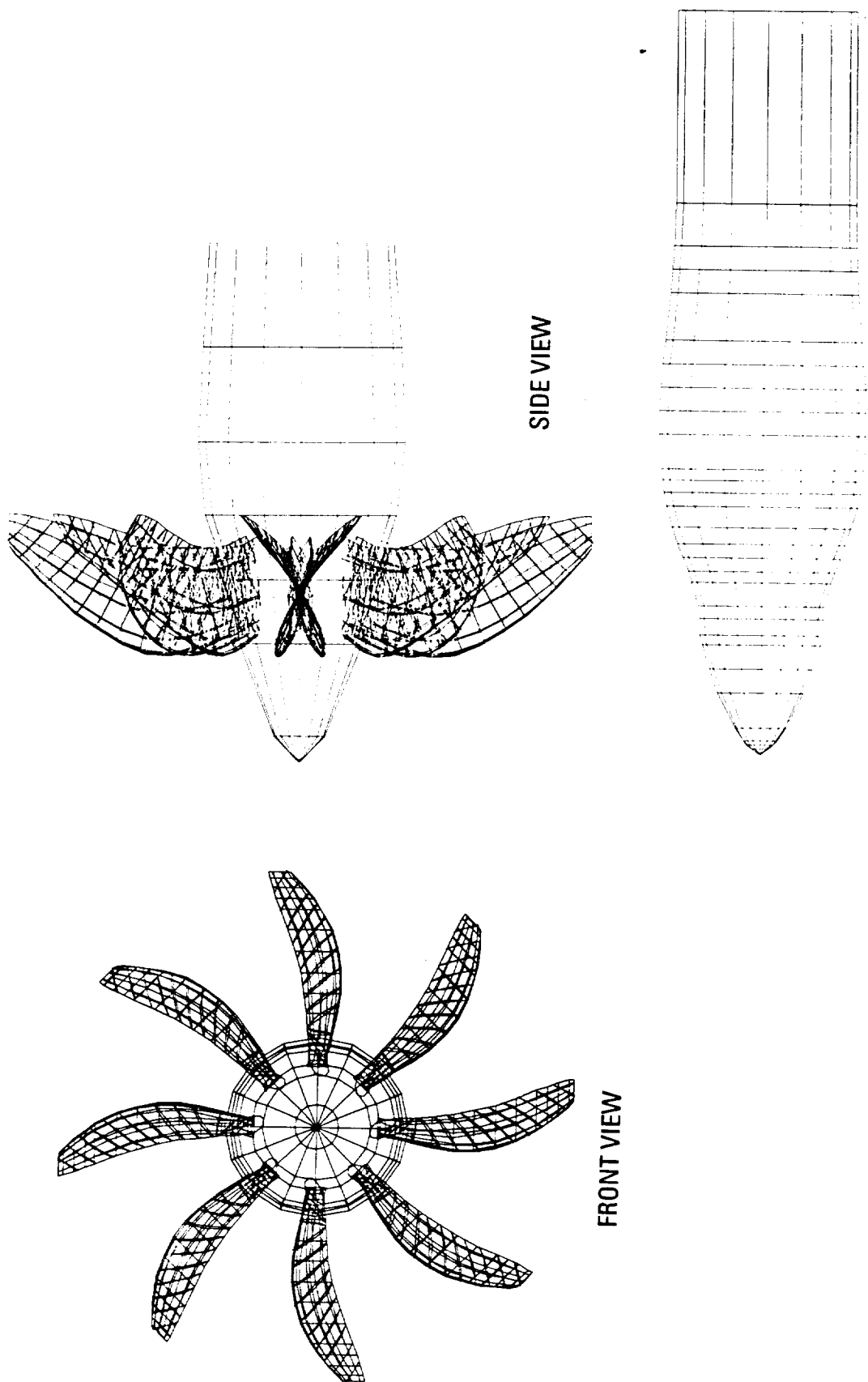
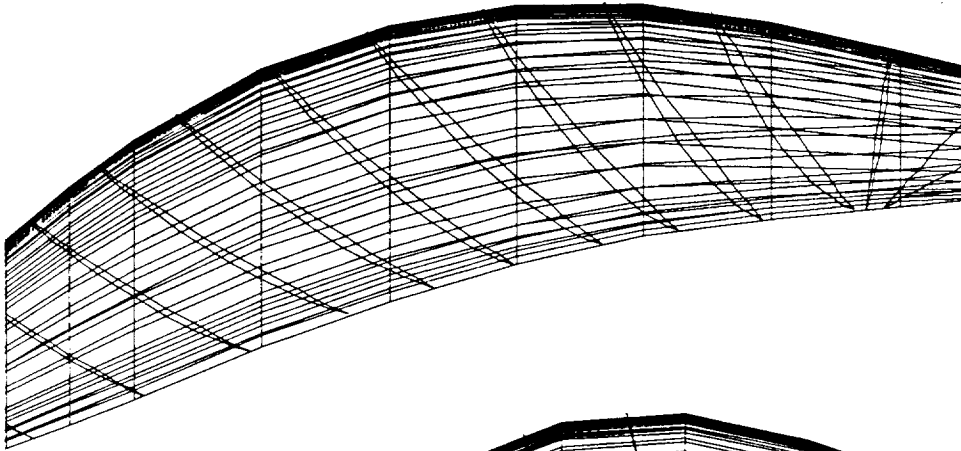


Figure 3.1-6. SR-3 Propeller-Nacelle Geometry Cuts Perpendicular to 1/4-Chord

Front View



Bottom View

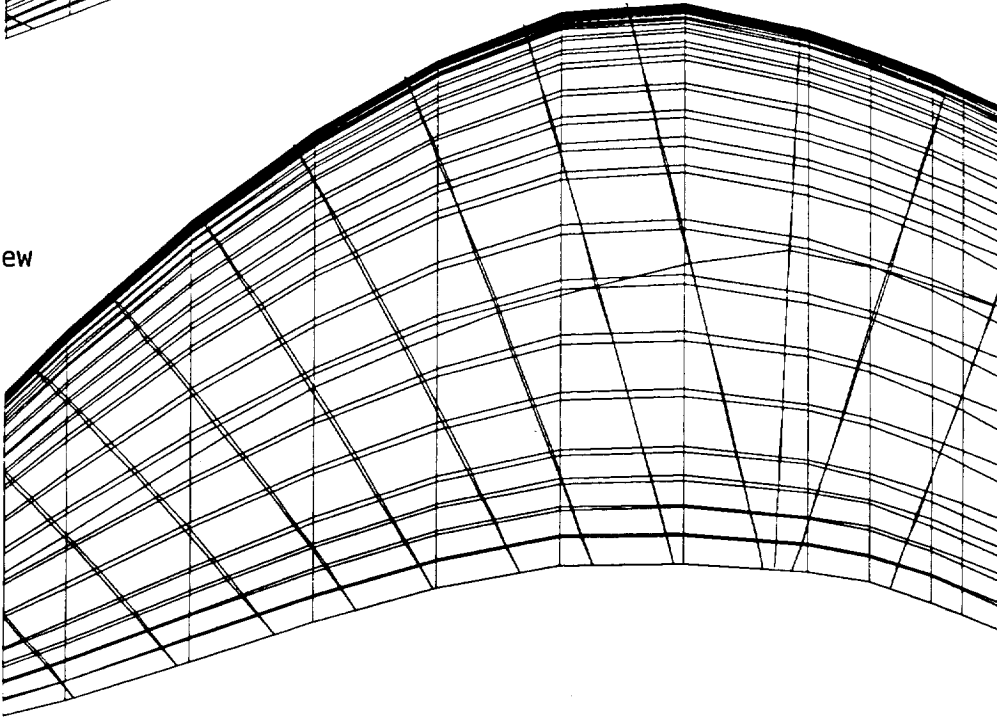


Figure 3.1-7. SR-3 Blade Geometry Cuts Perpendicular to 1/4-Chord

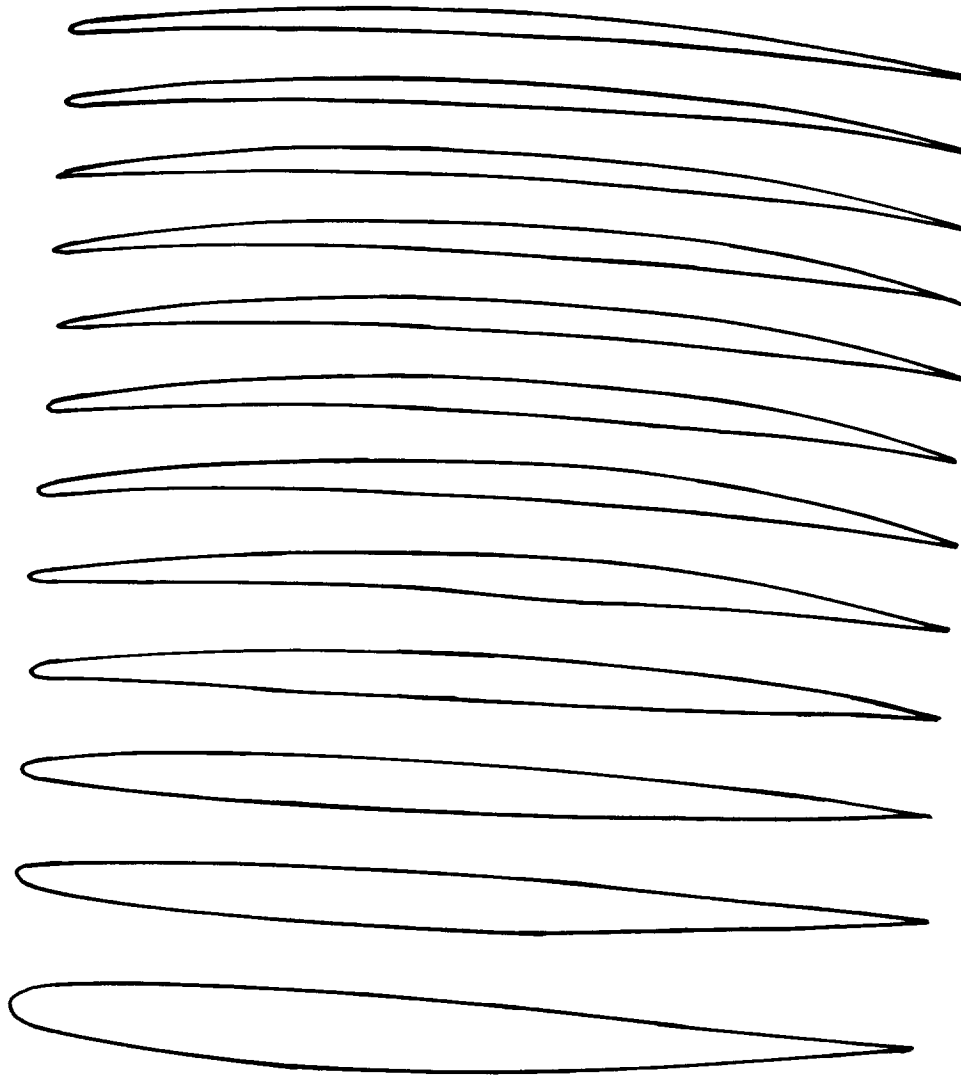


Figure 3.1-8. SR-3 - Airfoil Sections Perpendicular to 1/4 Chord

line and nose radius are two of the required quantities that are output for each profile (not shown on the figure).

The Hartzell 101/16 propeller-nacelle geometry is shown in Figures 3.1-9 and 3.1-10. Note that only the propeller from approximately 20 percent station outward has been included due to lack of propeller definition in the inner region. With the relatively straight blades of this configuration there are no problems with crossing profiles. The line of shear centers converges rapidly for this case and is shown in Figure 3.1-11. For performance calculations the profiles perpendicular to the quarter-chord are required. These are shown in Figure 3.1-12 for the Hartzell 101/16 blade.

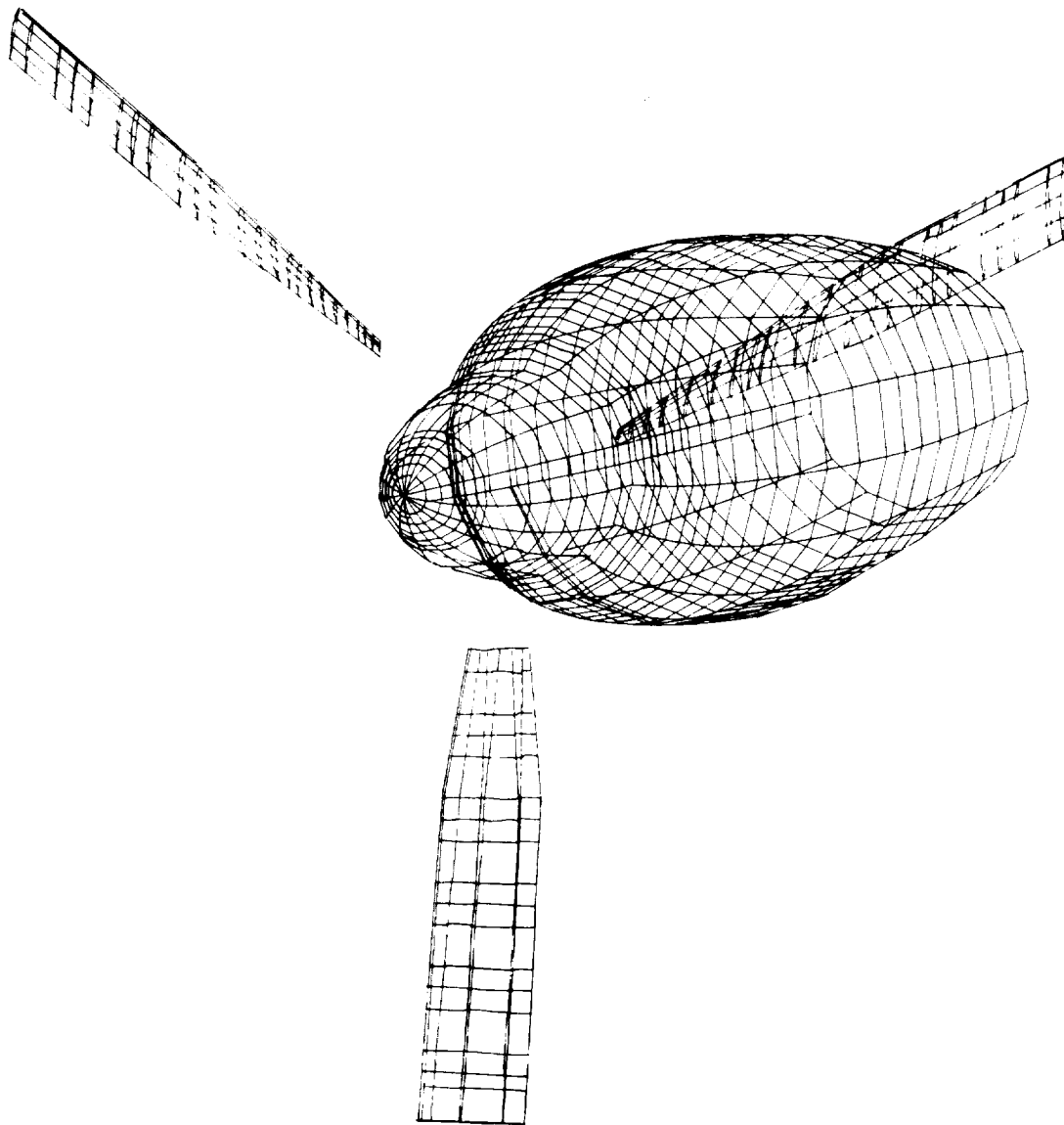


Figure 3.1-9. TRW Hartzell 101/16 Propeller-Nacelle Geometry  
Aerodynamic Cuts

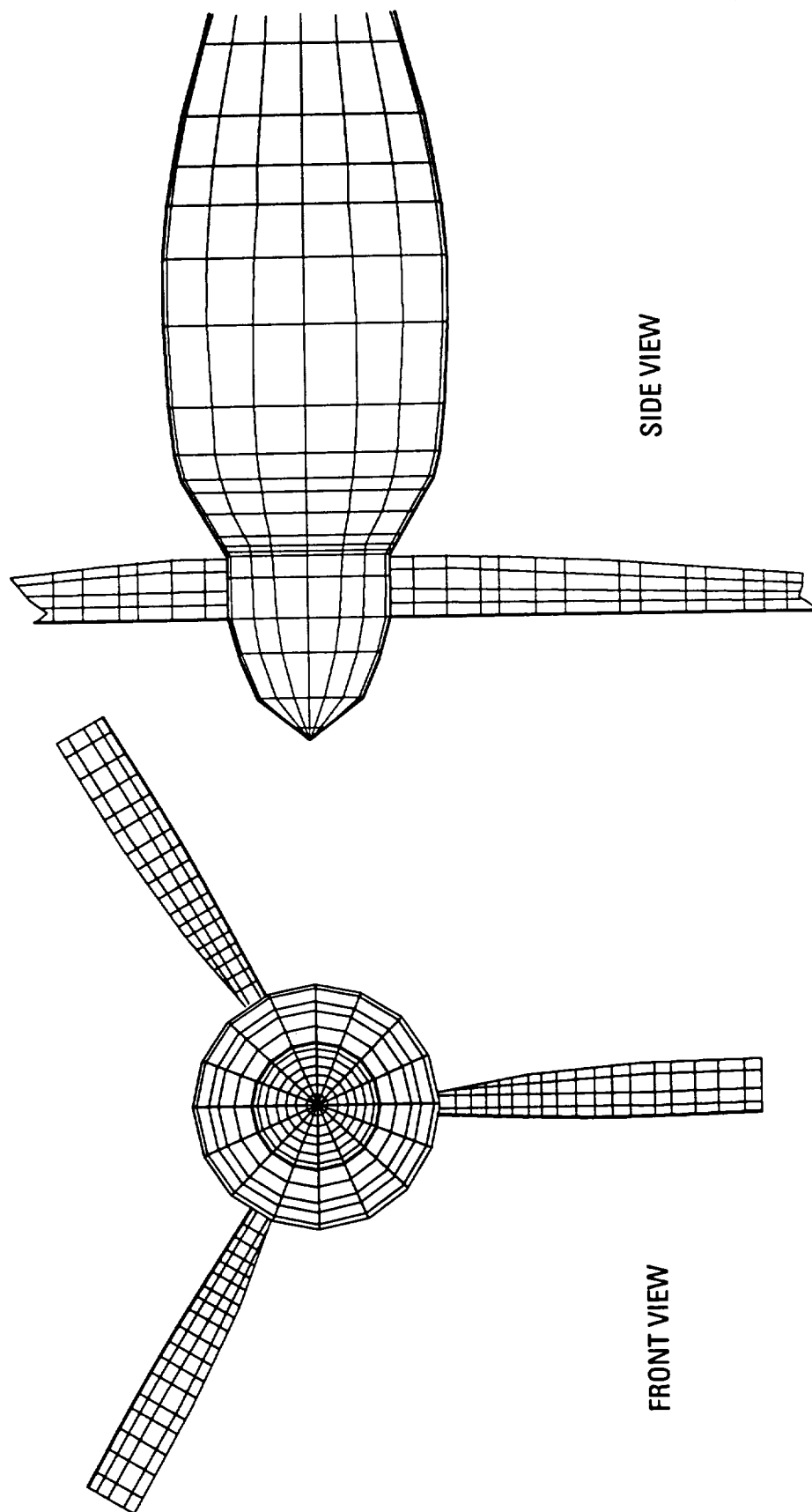


Figure 3.1-10. TRW-Hartzell 101/16 Nacelle Geometry

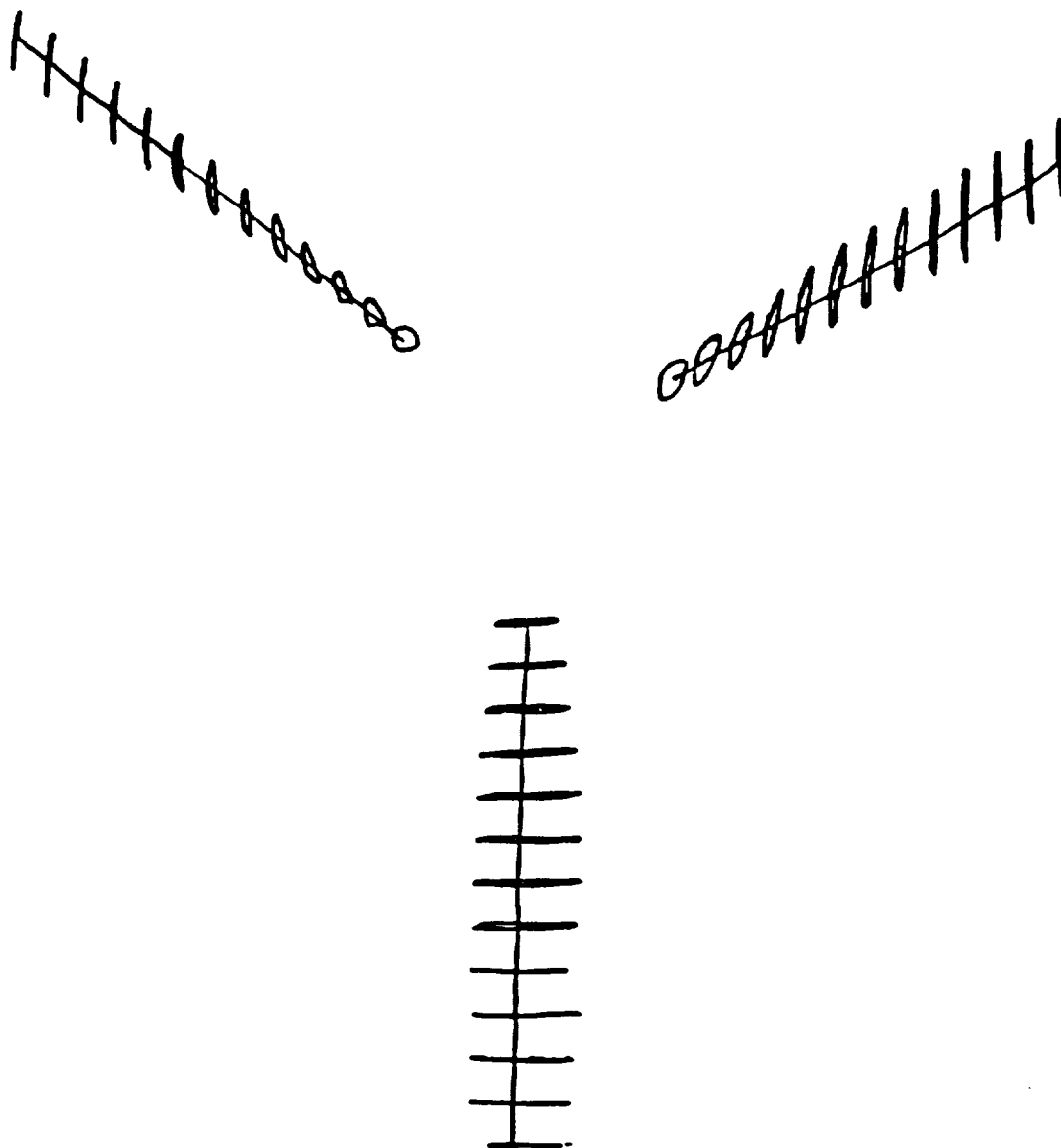
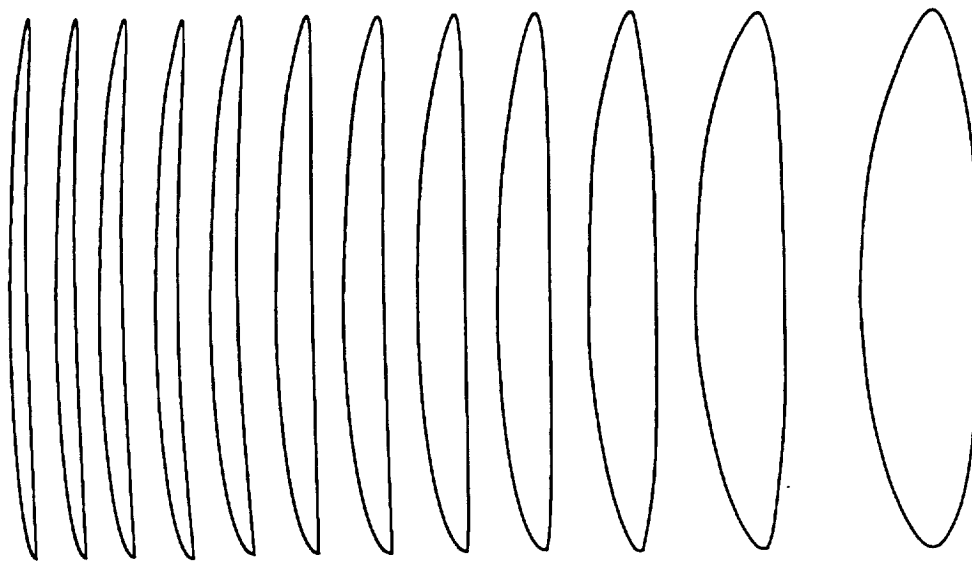


Figure 3.1-11. TRW Hartzell 101/16 Structural Model Line of Shear Centers and Profiles Perpendicular



AIRFOILS PROFILES PERPENDICULAR TO 1/4 CHORD



01M 90.439.03

FRONT VIEW



BOTTOM VIEW

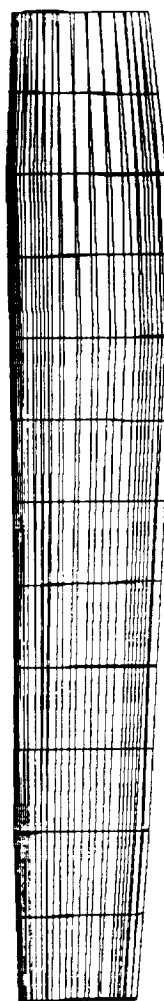


Figure 3.1-12. TRW-Hartzell 101/16 Propeller Blade

### 3.2 AIRCRAFT FLOWFIELD MODULE

Modifications were made to Jumper's code generalizing the propeller plane and slightly modifying the definition of the angle-of-attack and angle of sideslip.

The NEUMANN code is a low-order source panel method where ring source terms are integrated on conical frustum elements as indicated in Figure 3.2-1. The source terms are decomposed into constant terms on each element for the axial flow component and terms proportional to  $\cos \phi$  for the crossflow component. The flow field at arbitrary angle of attack is found by a linear combination of the axial and crossflow solutions.

The calculated results from the NEUMANN code compares favorably with experiments and with exact solutions such as that for crossflow over an ellipsoid (Figure 3.2-2). The exact solution described by Reference 2.2-4 and numerical results for the tangential component of the velocity at the surface of an ellipsoid in crossflow are shown in Figure 3.2-3. The surface pressure coefficient is shown in Figure 3.2-4 where we also present the results from JUMPER for a variety of mesh spacing. The NEUMANN code was a valuable tool for validation of the JUMPER code.

Sample calculations were made with the NEUMANN and JUMPER codes for flow over the H101/16 and SR-3 nacelles. The H101/16 nacelle geometry is shown in Figure 3.2-5 with the body pressure coefficient given in Figure 3.2-6. The corresponding axial velocity ratio in the plane of the propeller is shown in Figure 3.2-7.

For the SR-3 nacelle, the body pressure coefficient and geometry are shown in Figures 3.2-8 and 3.2-9. Comparison between the NEUMANN and JUMPER codes shows that the approximations made for the influence coefficients using point sources at the centroids of the elements does not lead to large differences in the body pressure.

After the above calculations were completed, it was decided to implement only the JUMPER code into GAPAS since it was capable of handling the case of both nacelle and lifting wing. For an axisymmetric body the NEUMANN code would be more efficient, but since it cannot handle the case with a wing or with a tilt of the propeller axis (i.e., thrust axis not

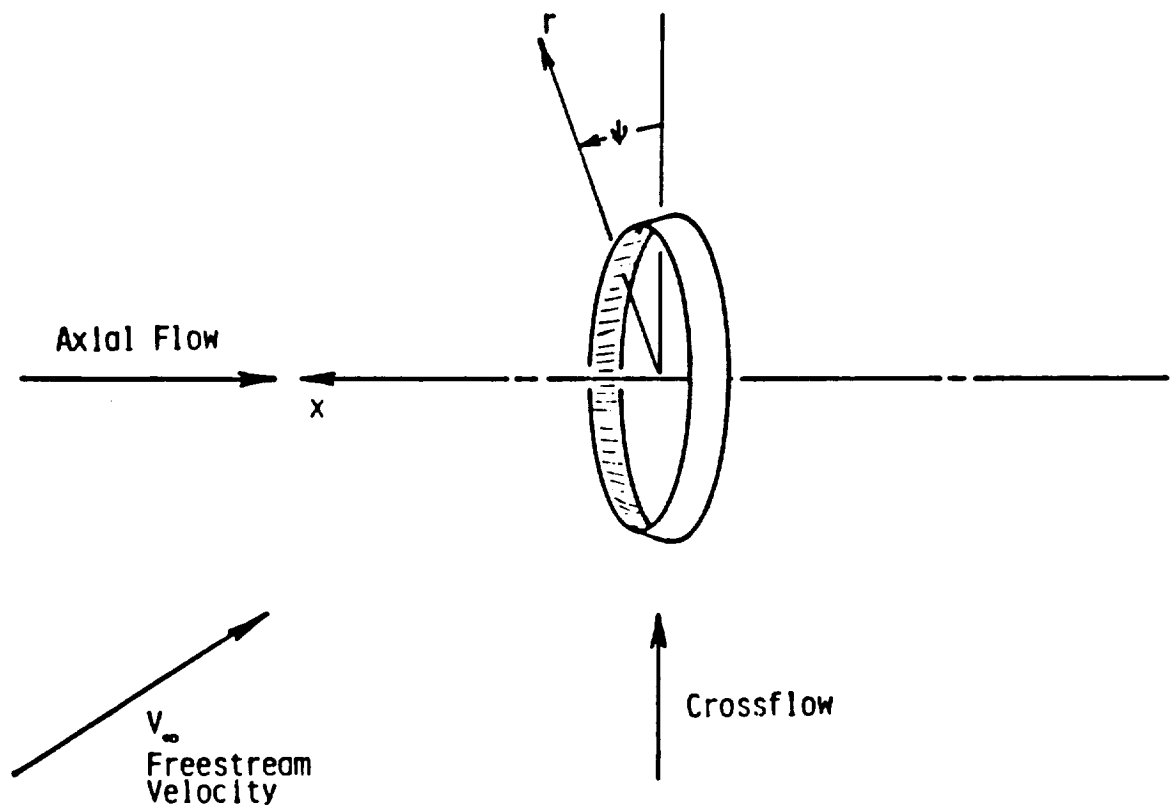


Figure 3.2-1. Neumann Code Element Geometry

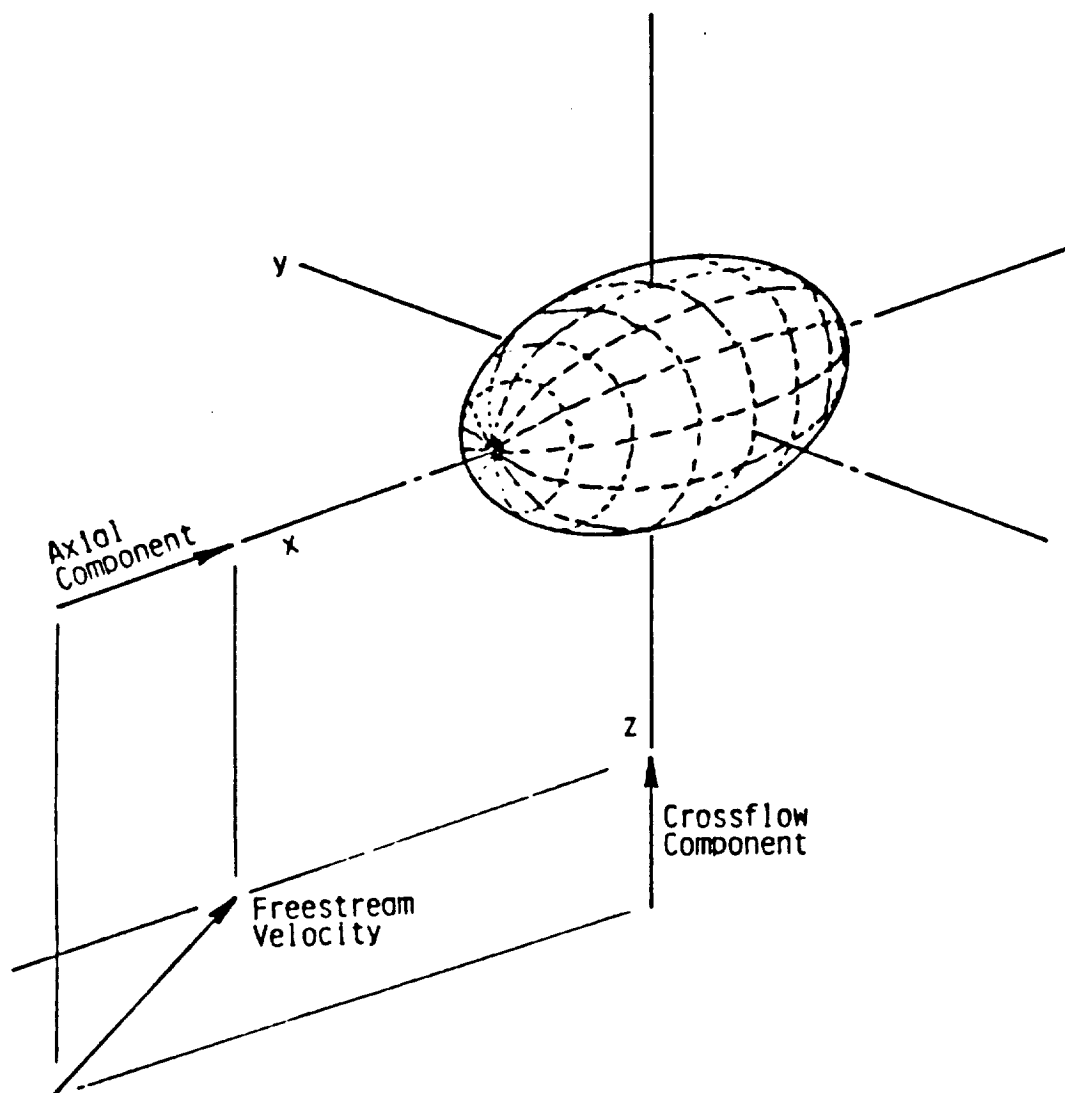


Figure 3.2-2. Ellipsoid of Revolution at Angle of Attack

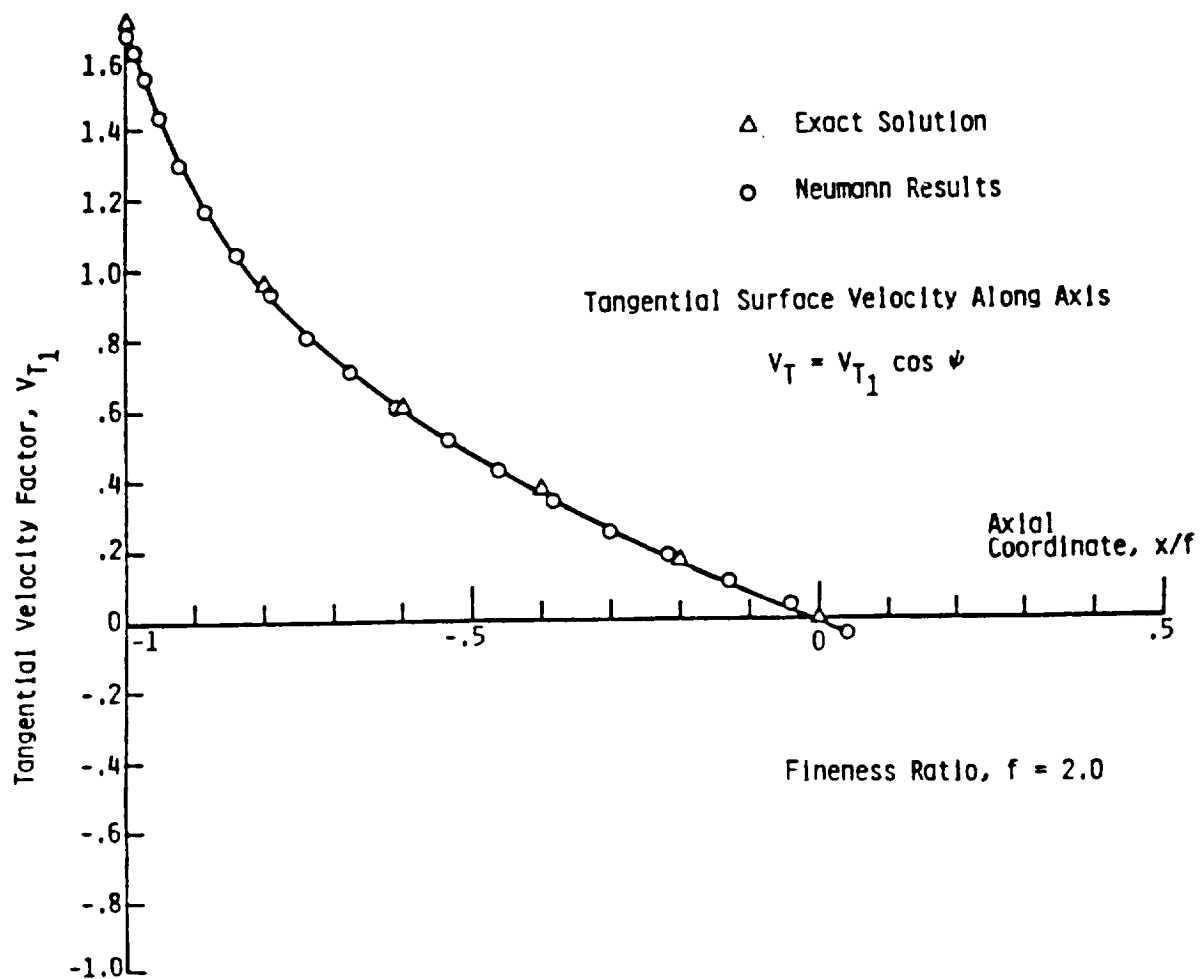


Figure 3.2-3. Tangential Velocity Factor for an Ellipsoid of Revolution in Cross-Flow

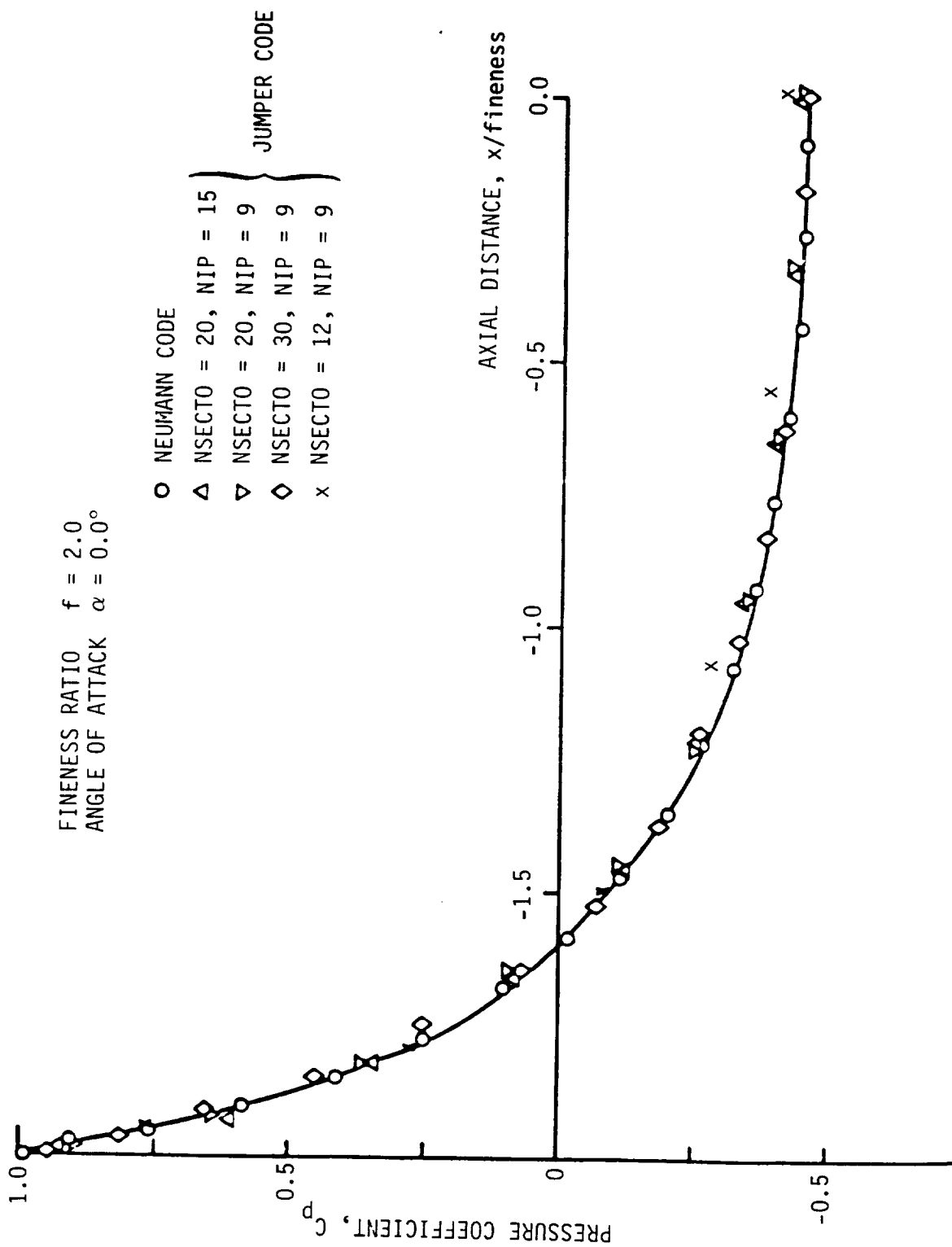


Figure 3.2-4. Surface Pressure Coefficient on an Ellipsoid of Revolution

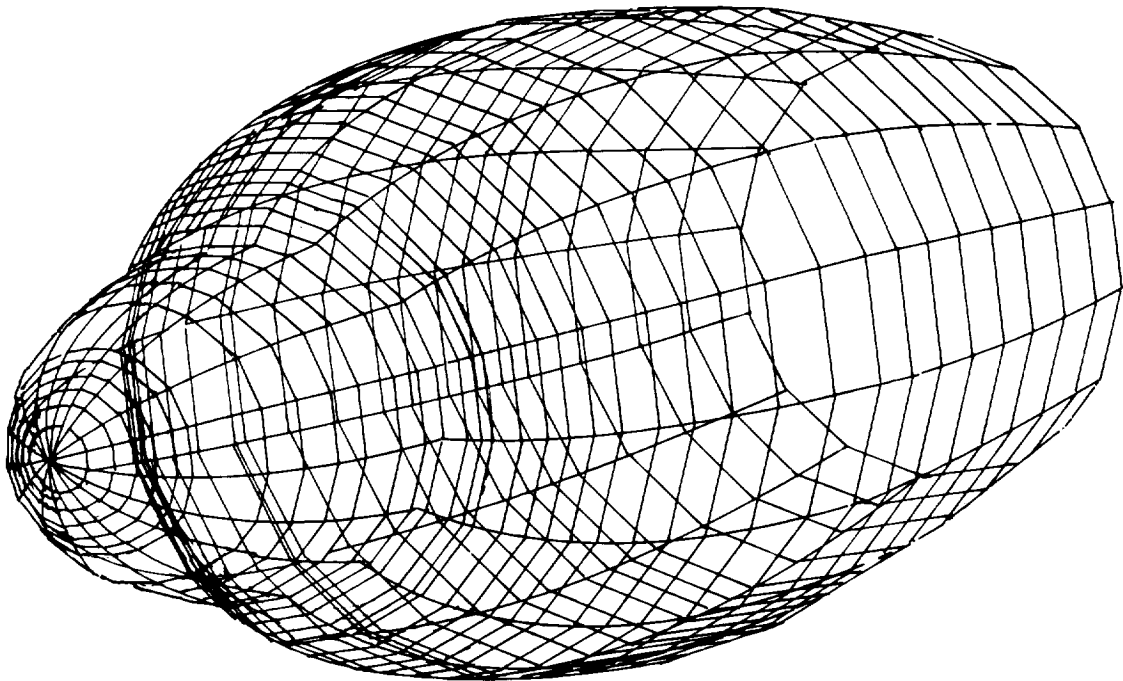


Figure 3.2-5. TRW-Hartzell 101/16 Nacelle Geometry

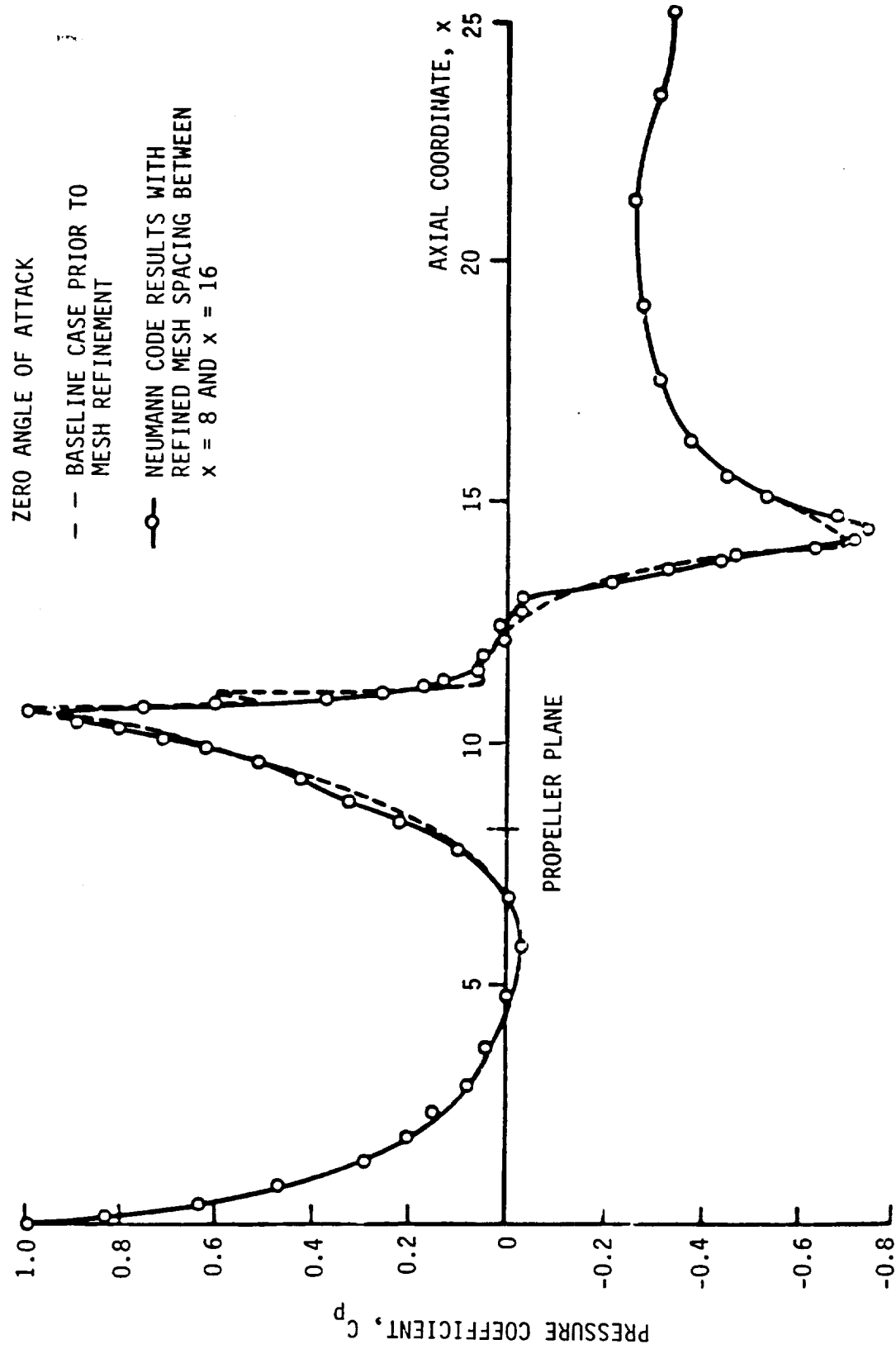


Figure 3.2-6. Body Pressure Coefficient for 101-16 Test Case



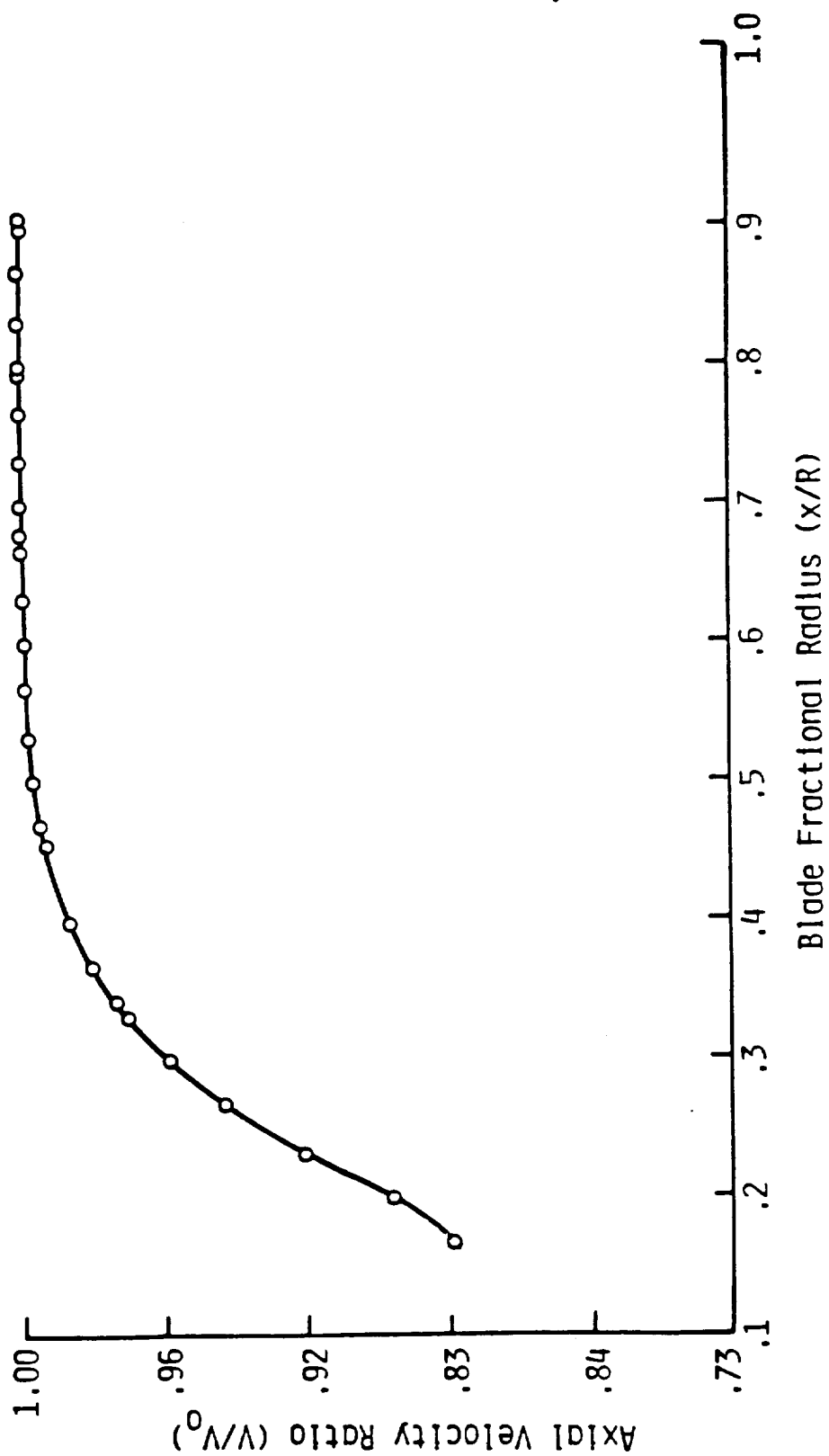


Figure 3.2-7. Calculated Axial Velocity Ratio in Plane of the Propeller for 101-16 Test Case as Computed with Jumper Code

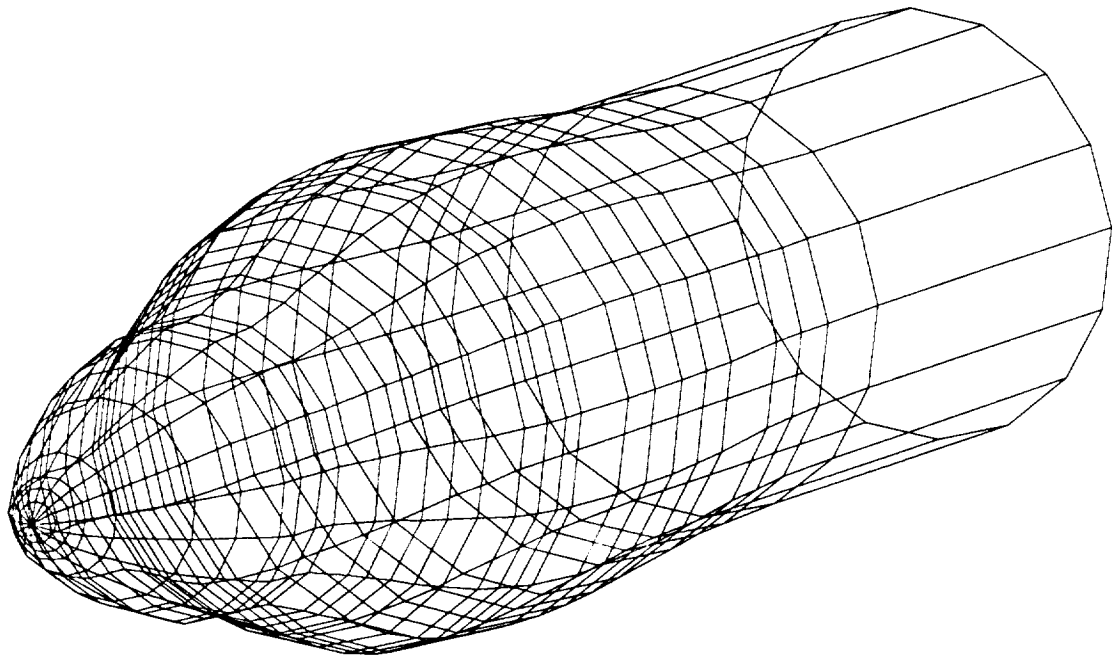


Figure 3.2-8. SR-3 Nacelle Geometry

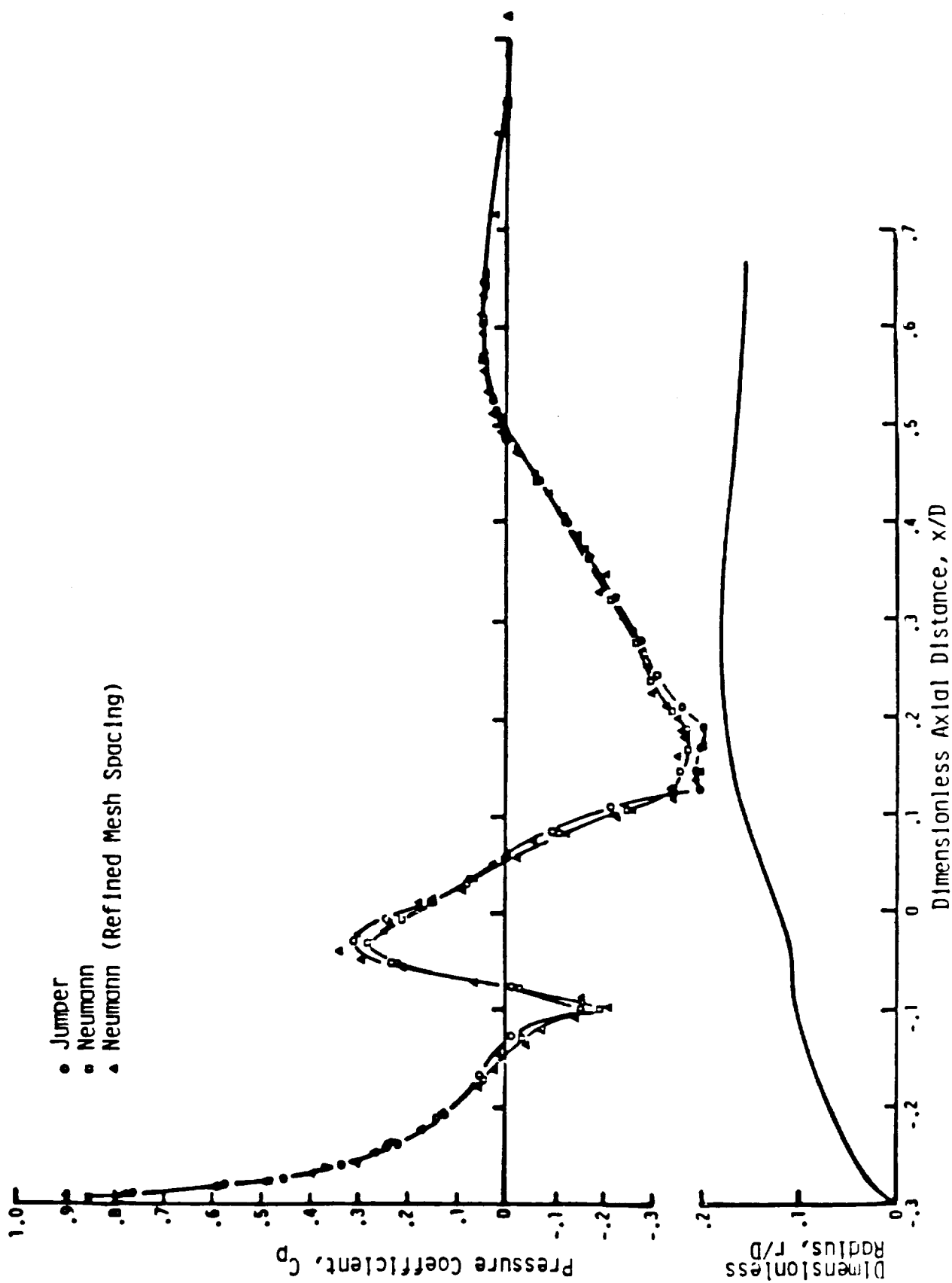


Figure 3.2-9. Potential Flow Calculations for SR-3 Test Case

aligned with longitudinal axis of nacelle), it was not incorporated into the Aircraft Flowfield Module.

### 3.3 PROPELLER AERODYNAMIC MODULE

#### 3.3.1 Modifications/New Developments

The aerodynamic performance analysis procedures recommended for implementation into GAPAS were, in order of priority, (1) UTRC, (2) Chang-Sullivan, and (3) Crigler procedures for the steady-flow cases, and (4) the Aljabri procedure for the unsteady flow case. Subsequent to NASA approval, difficulties were encountered in implementing the UTRC code on the TRW computer system, and the Chang-Sullivan code was made the first-priority code for the steady-flow case. Modifications to the Chang-Sullivan and Aljabri codes were carried out to change the calls to airfoil section data; internal calls were eliminated and replaced with external calls to the airfoil loading module. In addition, in the Aljabri code, improvements in the integration subroutines for calculation of thrust and power coefficient were carried out to provide greater flexibility and accuracy.

#### 3.3.2 Verification of Propeller Aerodynamic Procedures

Experimental data for the Hartzell 101/16 and SR-3 propellers were provided by NASA for use in the verification task. Table 3.3-1 summarizes the operating conditions for the aerodynamic performance verification task. Conditions selected for the H101/16 propeller were based on the data contained in Reference 3.3-1 and, for the SR-3 propeller, conditions correspond to data contained in References 3.3-2 and 3.3-3.

Calculation results for the 101/16 propeller are shown in Figures 3.3-1 through 3.3-3 for the Mach 0.11, 0.22, and 0.35 conditions, respectively. Since these are low-speed cases and the 101/16 is a straight-blade propeller, the calculational results shown were obtained using the Aljabri code. Results were obtained for thrust coefficient,  $C_T$ , power coefficient,  $C_p$ , and efficiency,  $\eta$ , as a function of advance ratio,  $J$ . For each Mach number condition, three additional advance ratios other than those required in Table 3.3-1 were calculated. Note that acceptable agreement (within 15%) is obtained for all quantities (efficiencies are obtained to within 5%) except for  $C_T$  and  $C_p$  at the lowest (0.526) advance-

Table 3.3-1. Aerodynamic Performance Verification Requirements

Flight Condition	Mach No.	Advance Ratio	Power Coefficient
101/16 Propeller			
Takeoff	0.11	0.526	0.192
Climb	0.22	1.103	0.204
Cruise	0.35	2.234	0.304
SR-3 Propeller			
Takeoff	0.20	0.877	1.007
Climb	0.45	1.870	1.695
Cruise	0.80	3.060	1.695

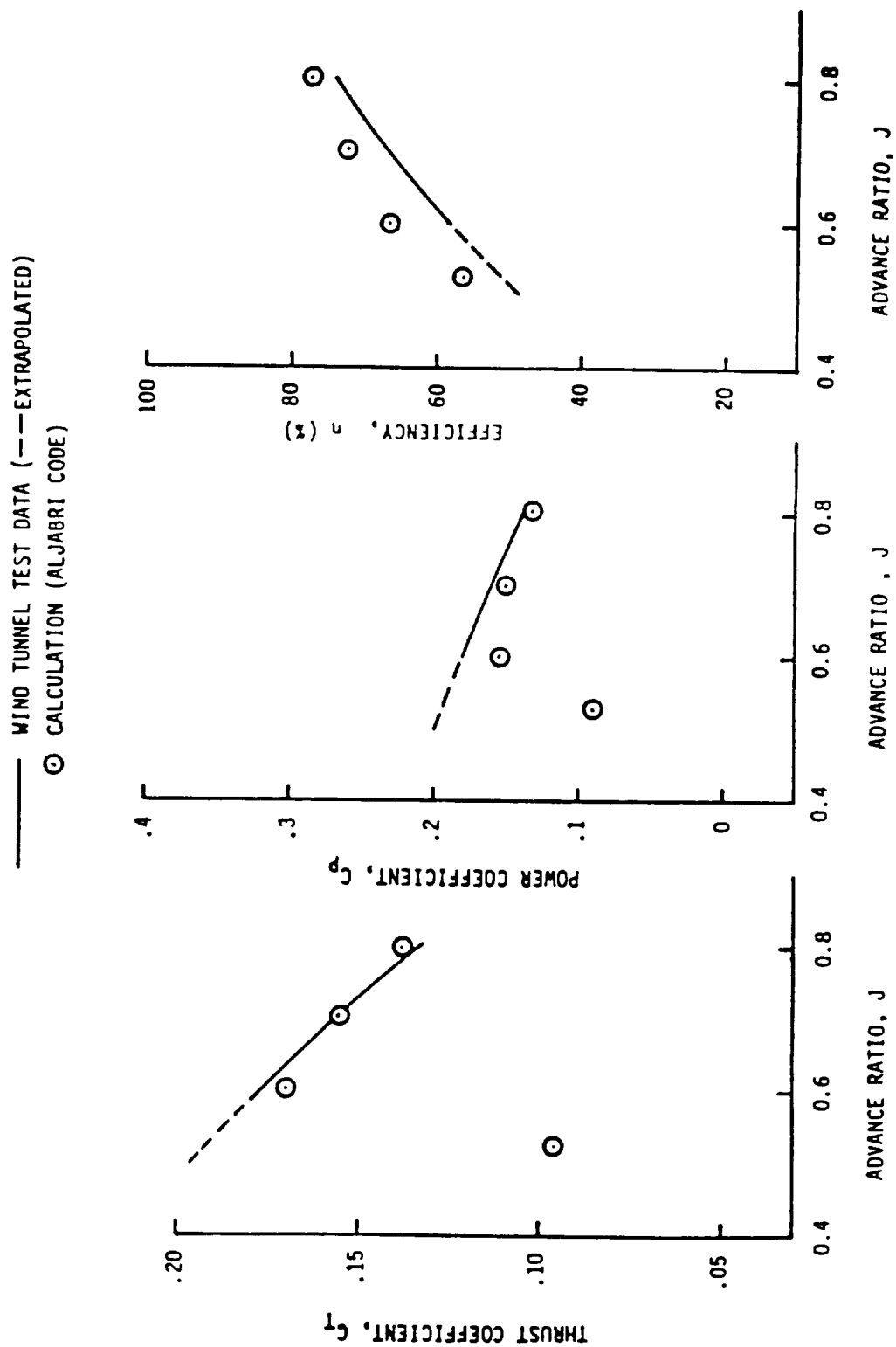


Figure 3.3-1. Aerodynamic Performance of 101/16 Propeller,  $M_0 = 0.11$

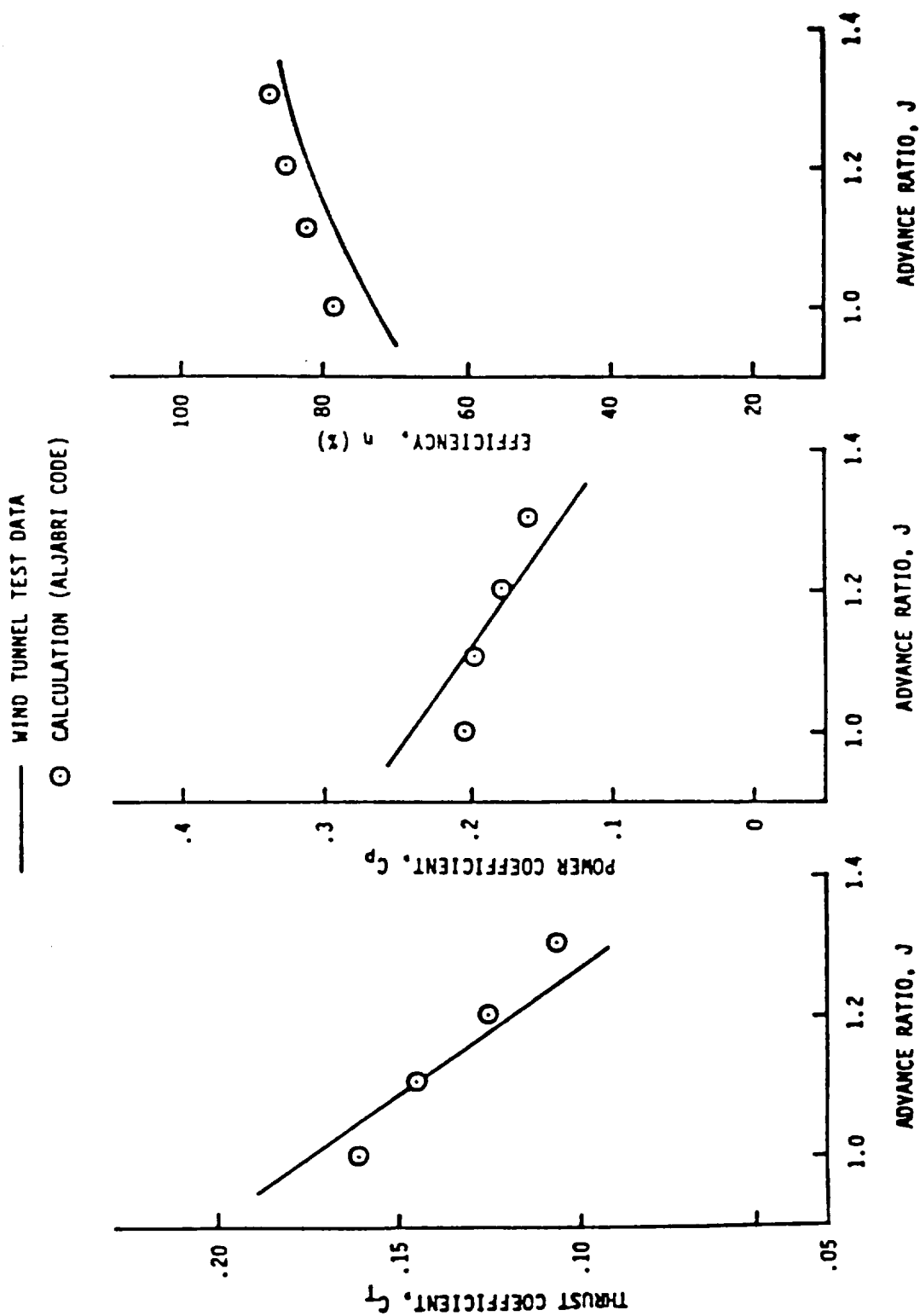


Figure 3.3-2. Aerodynamic Performance of 101/16 Propeller,  $M_0 = 0.22$

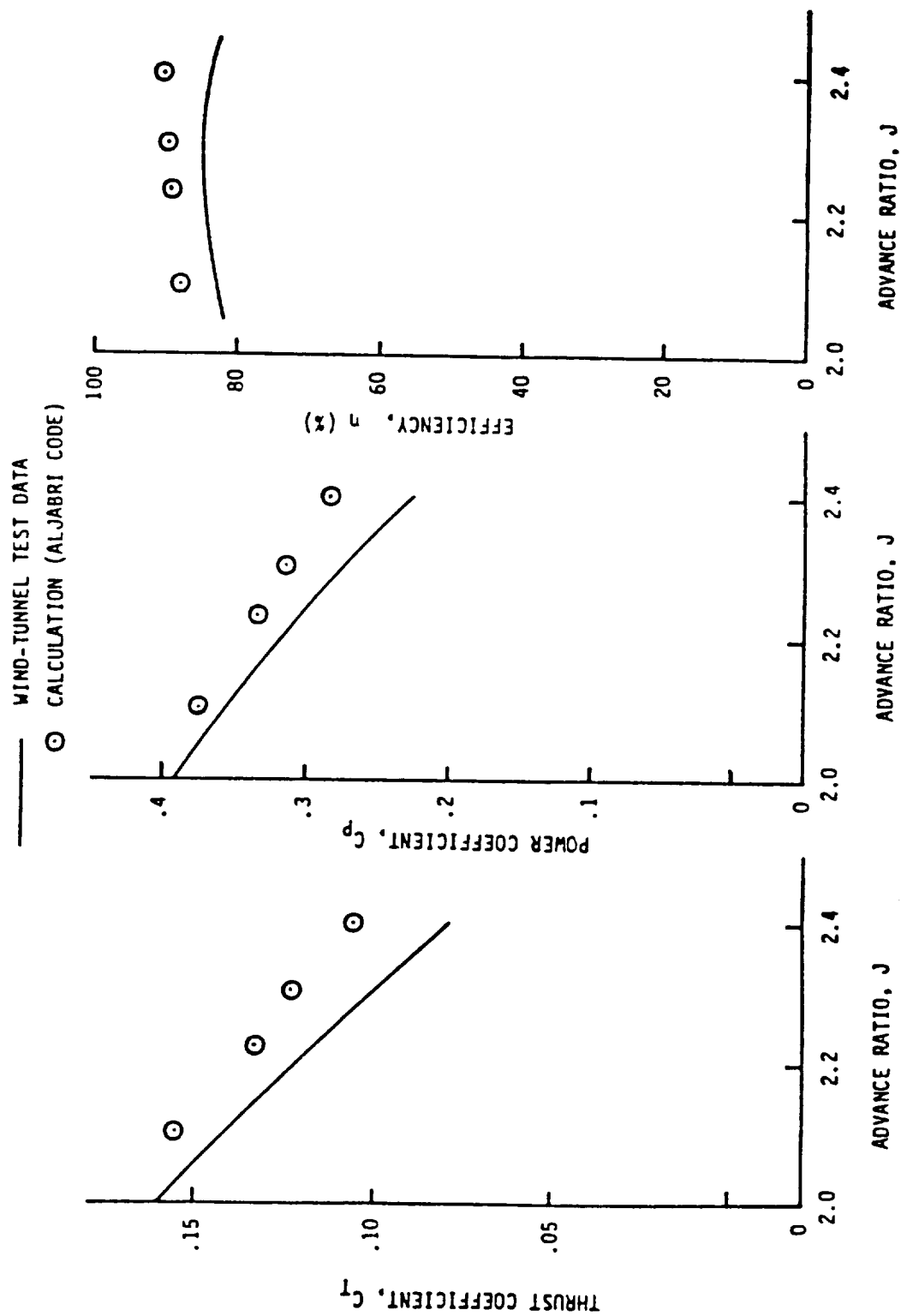


Figure 3.3-3. Aerodynamic Performance of 101/16 Propeller,  $M_0 = 0.35$



ratio condition for the Mach 0.11 case. Note that the data are shown extrapolated in this region, however, and for these calculations lift and drag coefficients were obtained using the North Carolina State (Smetana) code and/or the Eppler code which, due to high values of airfoil section angle of attack at this condition, indicate a possible flow-separation condition and thus a substantially reduced lift coefficient.

Calculations for the SR-3 propeller were obtained using the Chang-Sullivan code and are compared with experimental data in Figures 3.3-4 through 3.3-6. For this propeller  $C_p$  and  $\eta$  are shown as functions of  $J$ . (Sufficient information is available to obtain thrust coefficient since  $C_T$ ,  $C_p$ , and  $\eta$  are not independent functions of  $J$ , but are related through the expression  $\eta = JC_T/C_p$ ; also, both experimental and calculated efficiencies are net efficiencies, i.e., the data are corrected for increase in thrust due to mutual interaction between the propeller blades and the spinner and nacelle flow fields, and the calculation is for an isolated propeller). As in the case of the 101/16 propeller, calculations were carried out for a number of advance ratios surrounding the required values. Note the excellent agreement at Mach 0.45 (within 2%) and good agreement at Mach 0.80 (within 8%). At Mach 0.2, however, differences as large as 15% between calculation and experiment may be noted. Again, flow separation may be a contributing factor.

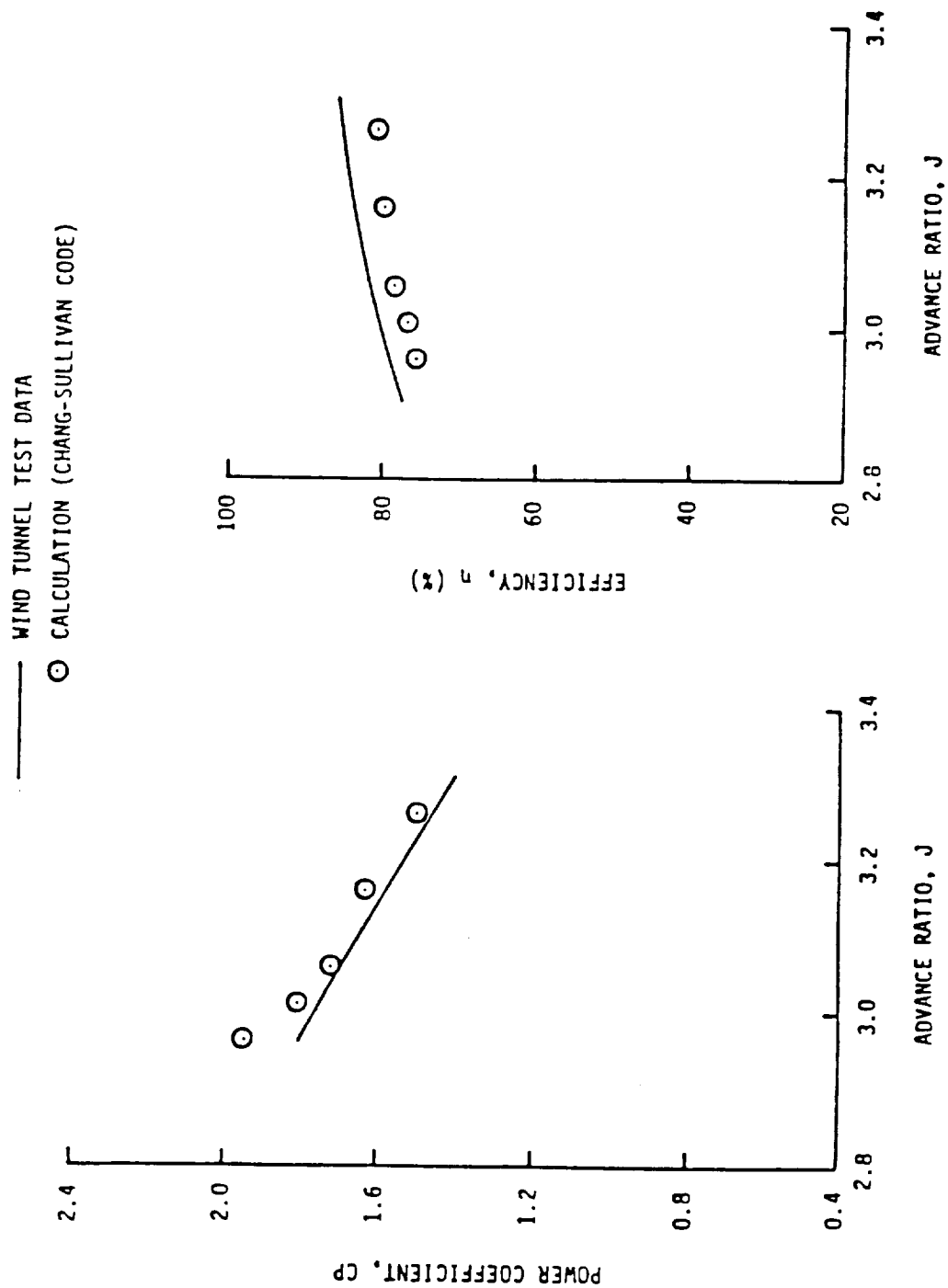


Figure 3.3-4. Aerodynamic Performance of SR-3 Propeller  
 $M_0 = 0.80$ ,  $\beta.75R = 60.95^\circ$

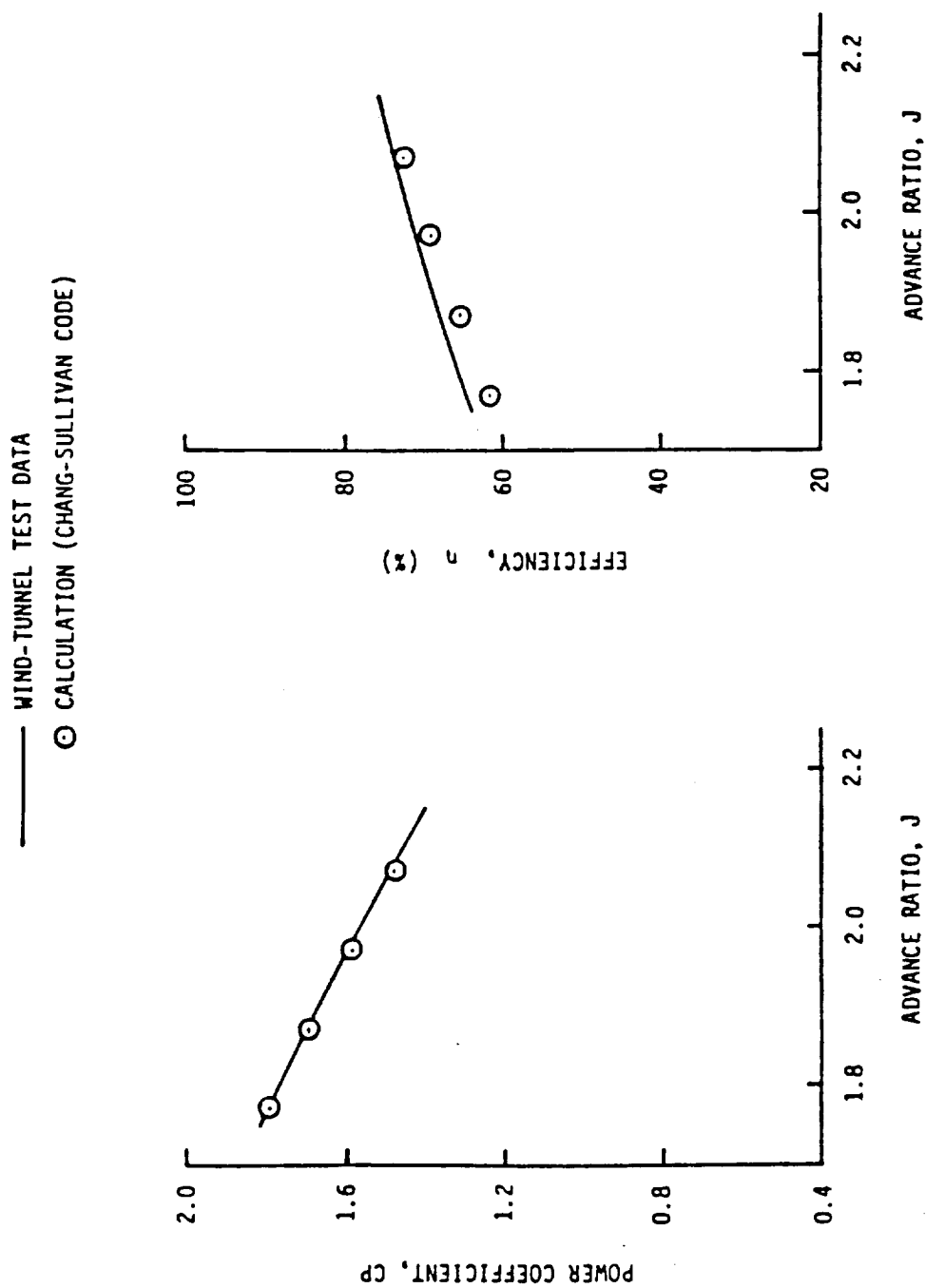
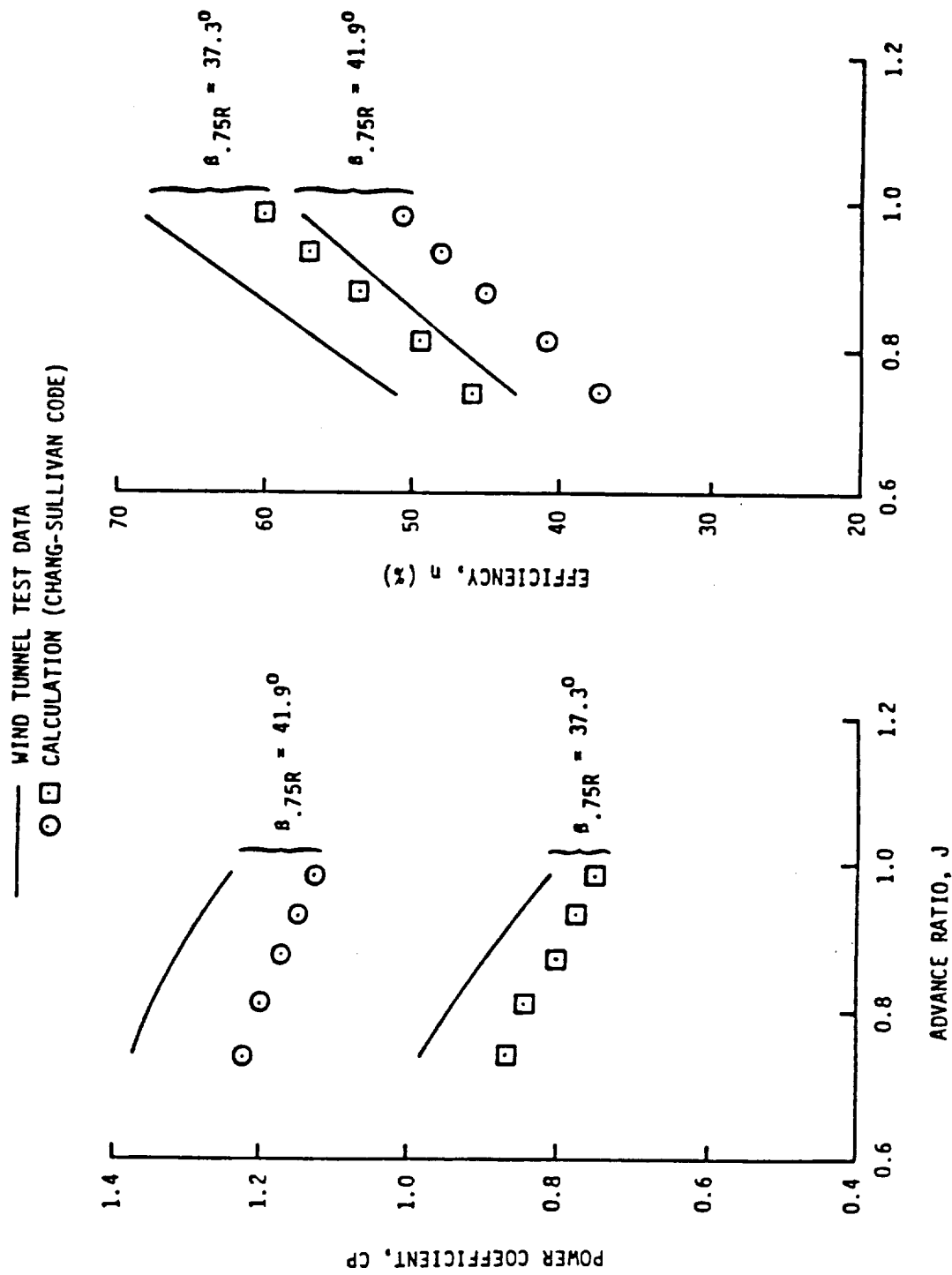


Figure 3.3-5. Aerodynamic Performance of SR-3 Propeller  
 $M_0 = 0.45$ ,  $\beta.75R = 53.5^\circ$

Figure 3.3-6. Aerodynamic Performance of SR-3 Propeller,  $M_0 = 0.2$

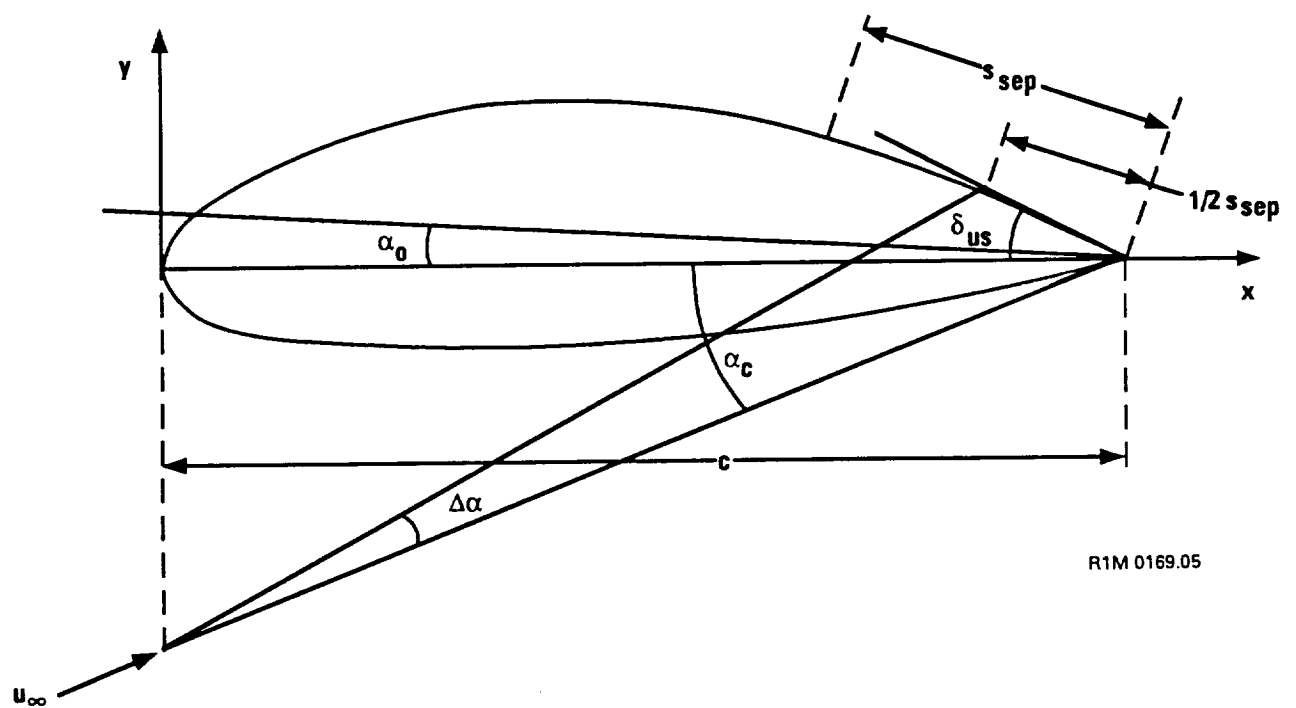
### 3.4 AIRFOIL LOADING MODULE

The major task required for this module is the development of the algorithm for determining the particular airfoil analysis code to be used in different regions of the propeller. At the higher freestream Mach number (i.e.,  $M > 0.5$ ), the TRANSEP code will be required along most of the propeller sections. Therefore, a study was performed in order to determine whether the Smetana code could be eliminated in place of the TRANSEP code even at the lower Mach numbers. This would allow for only two airfoil codes to be implemented into GAPAS. In addition, the study would also determine if TRANSEP could be utilized in the hub section, thereby reducing the required number of analysis codes to just TRANSEP.

In order to perform this study, the Hartzell H101/16 propeller was utilized. The freestream Mach number for this propeller was 0.11 during the take-off case, increasing to 0.35 during the cruise case. These operating conditions were analyzed using TRANSEP, Smetana, and Eppler. Since the propeller was composed of modified Clark Y sections in the mid-region and NACA 16 sections in the outer regions, the airfoil data banks were also used in the comparison. The study compared  $C_L$ ,  $C_D$ ,  $C_p$  distribution, location of boundary layer transition, and location of boundary layer separation.

The geometry of the Hartzell H101/16 propeller was developed using the definition of the airfoil shapes at seven spanwise stations. Due to the sparse input of the airfoil coordinates, a spline-fit smoothing routine was used to produce 57 points on both the upper and lower surfaces. The airfoil loading properties were computed at each of the seven stations for the freestream Mach numbers of 0.22 and 0.35, at angles-of-attack between 0 and 12 degrees in increments of 2 degrees. For these operating conditions the actual angles of attack ranged between 4 and 9 degrees. For the freestream Mach number of 0.11, only the TRANSEP code was utilized due to the large regions of separation present on the upper surface of the airfoil ( $10 \leq \alpha \leq 18^\circ$ ).

Prior to the initiation of this study, the Eppler  $C_{L_{\max}}$  correction was implemented into the Smetana code. The methodology for the correction is shown in Figure 3.4-1. The correction is ad hoc and corrects the angle of



R1M 0169.05

Figure 3.4-1. Lift-Coefficient Correction Due to Separation

attack by reducing its value by  $\Delta\alpha$ , where  $\Delta\alpha$  is calculated based on an upper surface which is shortened by one-half the distance of the separation point location from the trailing edge of the airfoil. Here  $c$  is the chord length  $\delta_{us}$  is the trailing edge angle of the upper surface,  $\alpha_c$  is the angle of attack,  $S_{sep}$  is the distance of the upper surface separation point from the trailing and thus the value of  $\Delta\alpha$  can be computed using the law of sines. In addition, a simple weak viscous-inviscid interaction methodology was incorporated into Eppler during this study.

Calculations were performed for all seven spanwise stations on the Hartzell H101/16 propeller at the three operating conditions. These operating conditions were: (1)  $M_\infty = 0.35$ ,  $J = 2.234$ ; (2)  $M_\infty = 0.22$ ,  $J = 1.103$ ; and (3)  $M_\infty = 0.11$ ,  $J = 0.526$ . For each case, the helical Mach number was computed as was the freestream Reynolds number based on the airfoil chord length. Results for stations 10.282, 17.042, and 23.803 at  $M_\infty = 0.35$  are discussed below. These sections correspond to a transition type airfoil in the inner region; a modified Clark Y airfoil in the mid-region; and a NACA 16 airfoil in the outer region. Figures 3.4-2 through 3.4-7 show comparisons of the resultant calculations at Station 10.282; the helical Mach number at this station is 0.379 and  $Re_L = 0.764 \times 10^6$ . Figure 3.4-2 shows the calculated values of  $C_L$  versus  $\alpha$ . The figure shows that TRANSEP and Eppler give nearly the same  $C_L$  as a function of  $\alpha$  up to  $\alpha = 6$  degrees. At this point Eppler calculates leading edge separation and thus the method cannot be used. The results of Smetana show a reasonable comparison up to about a 4-degree angle of attack. However, for  $\alpha > 4$  degrees, the results deviate significantly from the TRANSEP results. When the Eppler  $C_{L_{max}}$  correction is included, the computed  $C_L$  is lower than the uncorrected case. Figure 3.4-3 shows the location of transition from laminar to turbulent flow on both upper and lower surfaces. The results of Eppler and TRANSEP compare very well, whereas the Smetana results show an earlier transition at the lower angle of attack, and a delayed leading edge transition to turbulent flow at the higher angles of attack. Figure 3.4-4 shows the location of upper surface separation. All calculations are in close agreement up to  $\alpha = 6$  degrees. At higher angles of attack, the Eppler analysis breaks down showing leading edge separation, whereas the Smetana results show separation progressing forward toward  $X/C = 0.75$  at

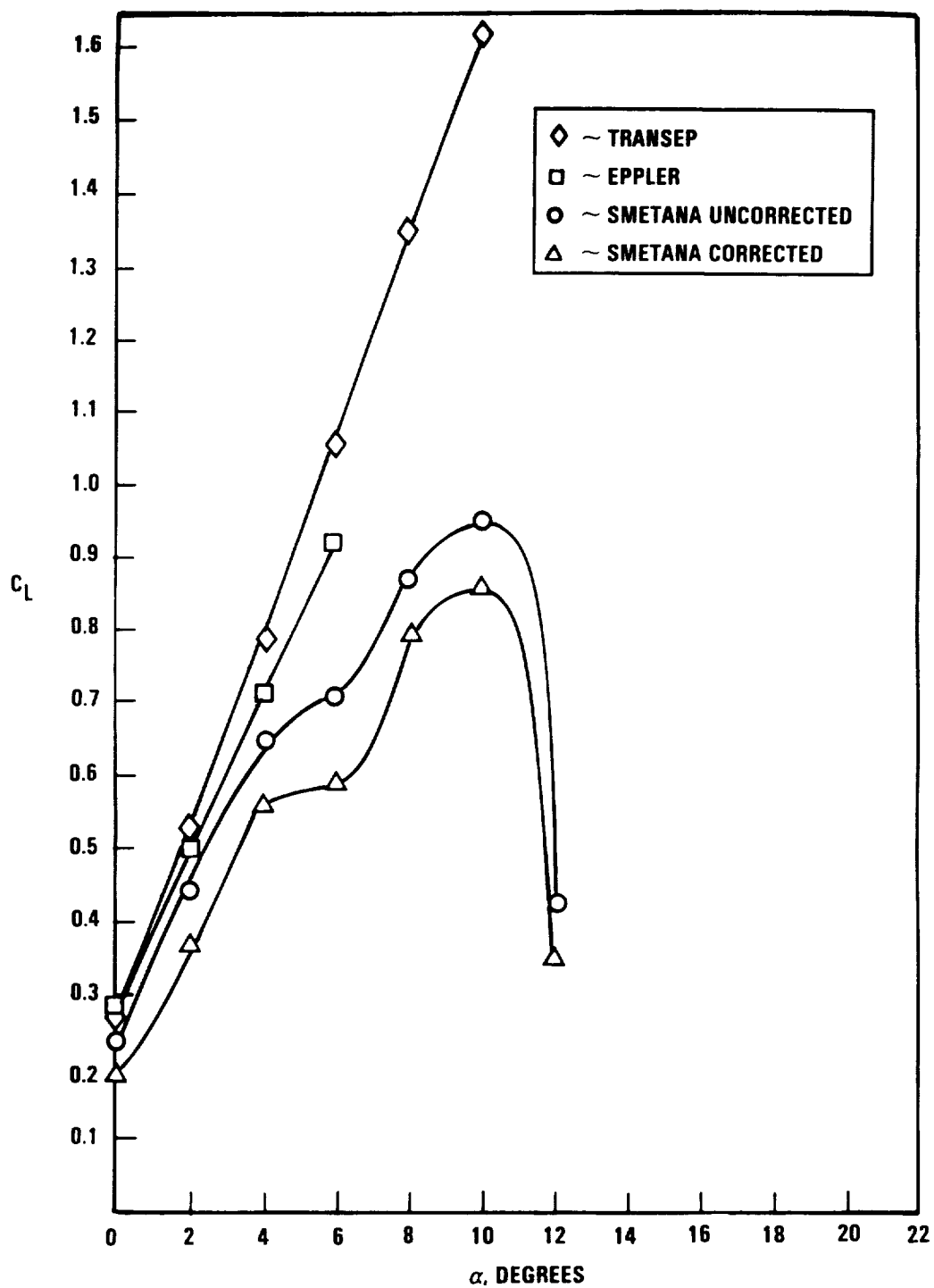


Figure 3.4-2. Lift Coefficient Versus Angle of Attack for H101/16 at Station 10.282 ( $M_H = 0.379$ ,  $Re_L = 7.64 \times 10^5$ )



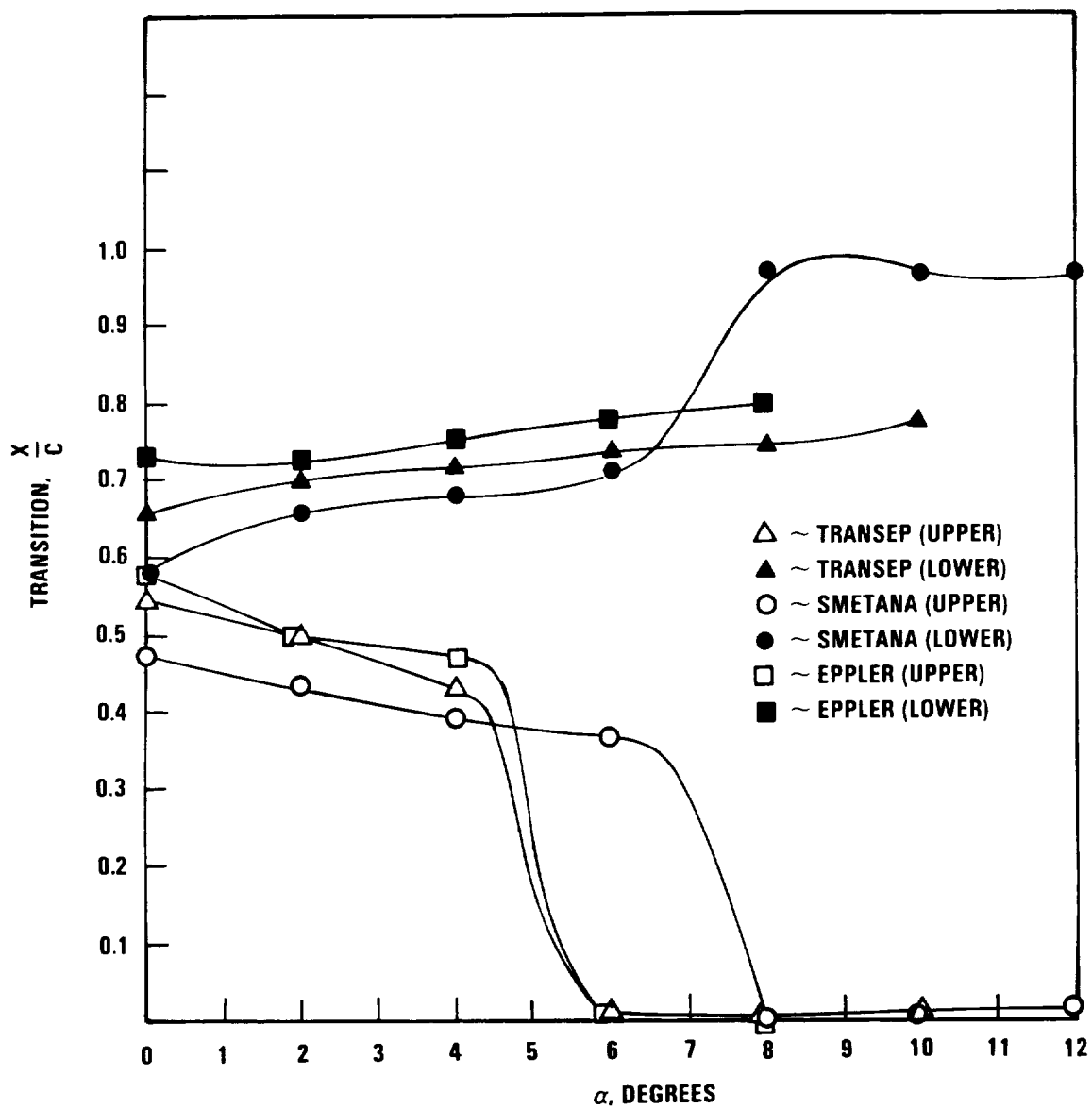


Figure 3.4-3. Boundary Layer Transition Point Versus for H101/16 at Station No. 10.282 ( $M_H = 0.379$ ,  $Re_L = 7.64 \times 10^5$ )

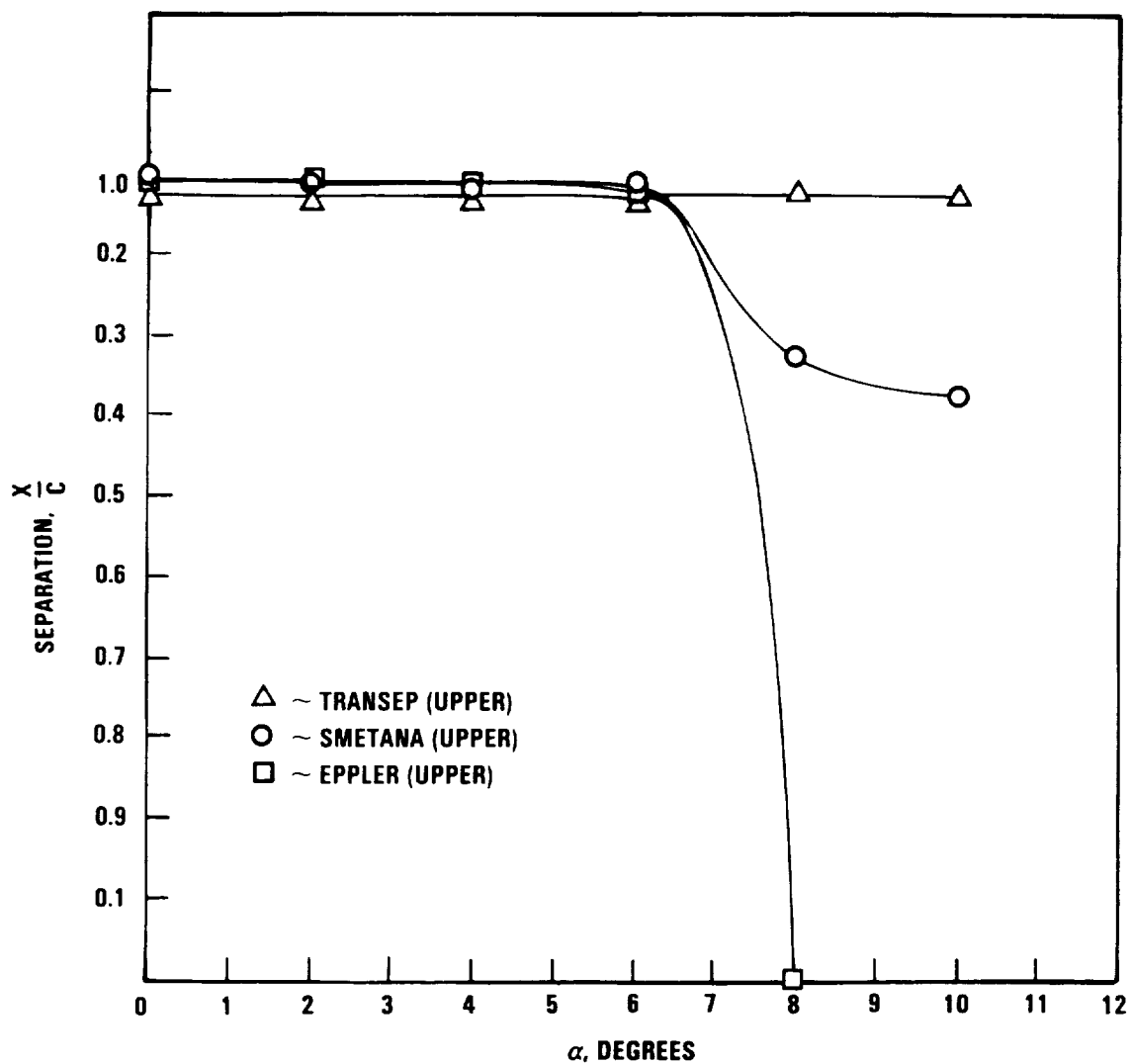


Figure 3.4-4. Boundary Layer Separation Point Versus Angle of Attack for H101/16 at Station No. 10.282 ( $M_H = 0.379$ ,  $Re_L = 7.64 \times 10^6$ )

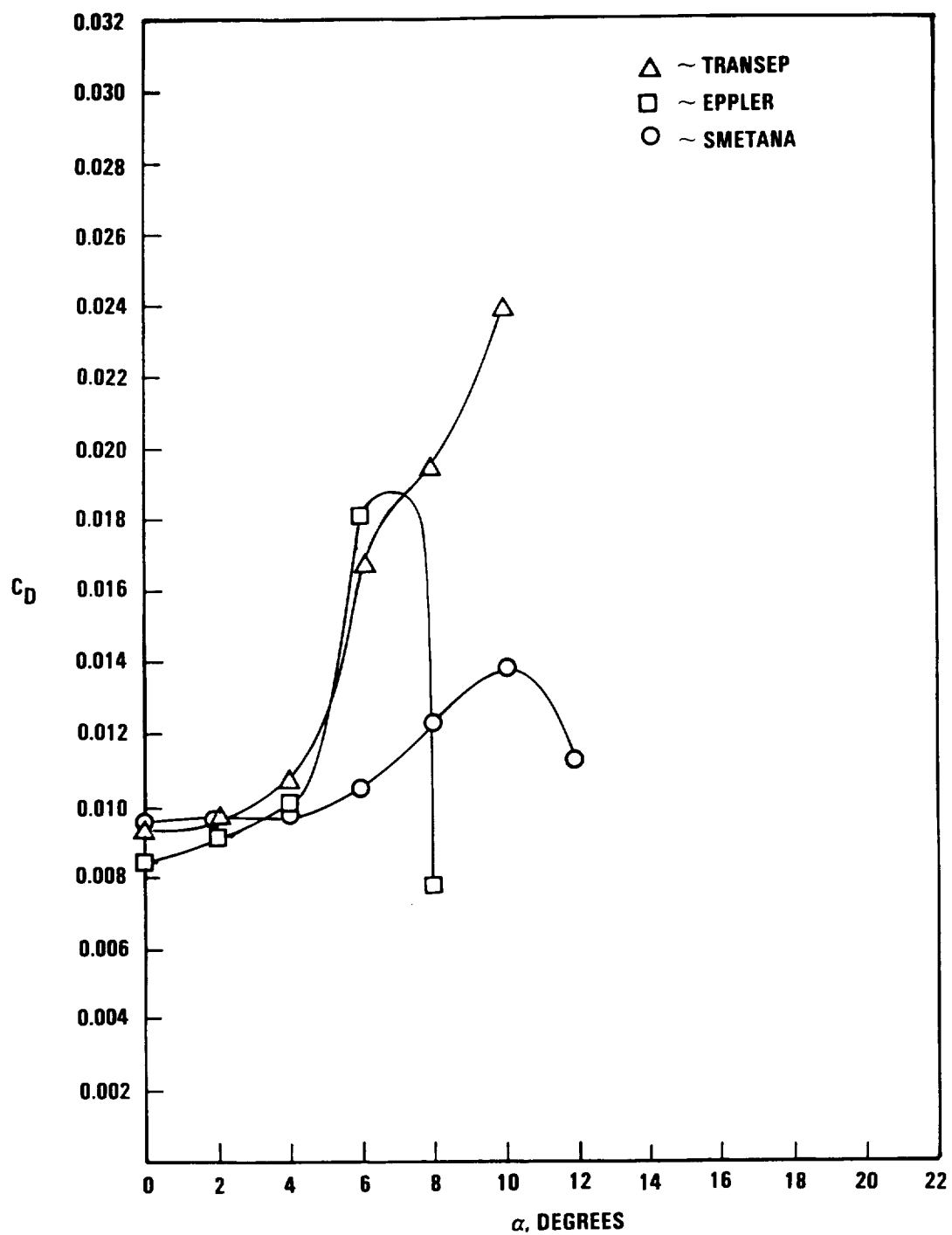


Figure 3.4-5. Drag Coefficient Versus Angle of Attack for H101/16 at Station No. 10.282 ( $M_H = 0.379$ ,  $Re_L = 7.64 \times 10^5$ )

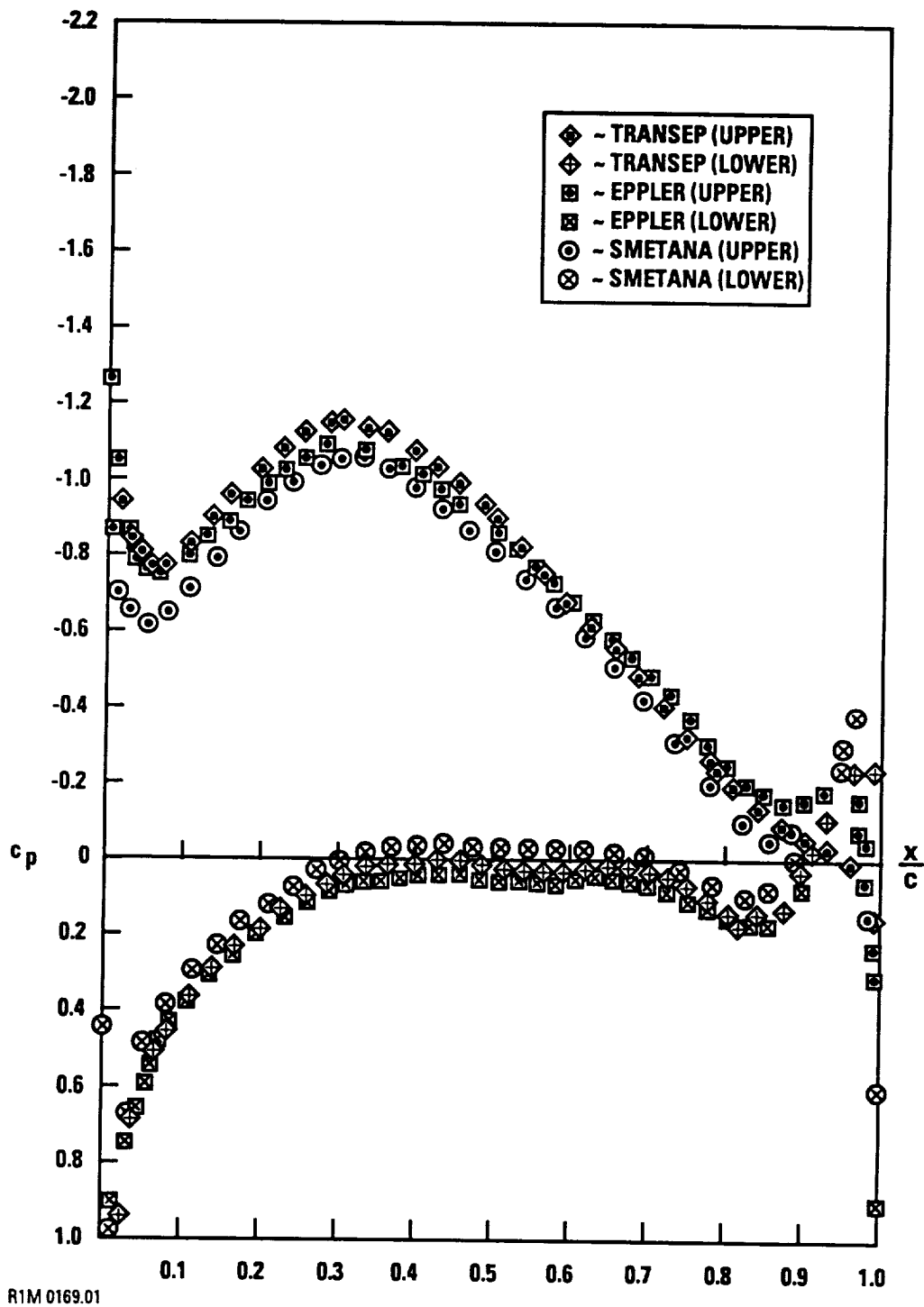


Figure 3.4-6. Pressure Coefficient Distribution for H101/16 at Station 10.282 ( $M_H = 0.378$ ,  $Re_L = 7.64 \times 10^5$ ,  $\alpha = 4^\circ$ )

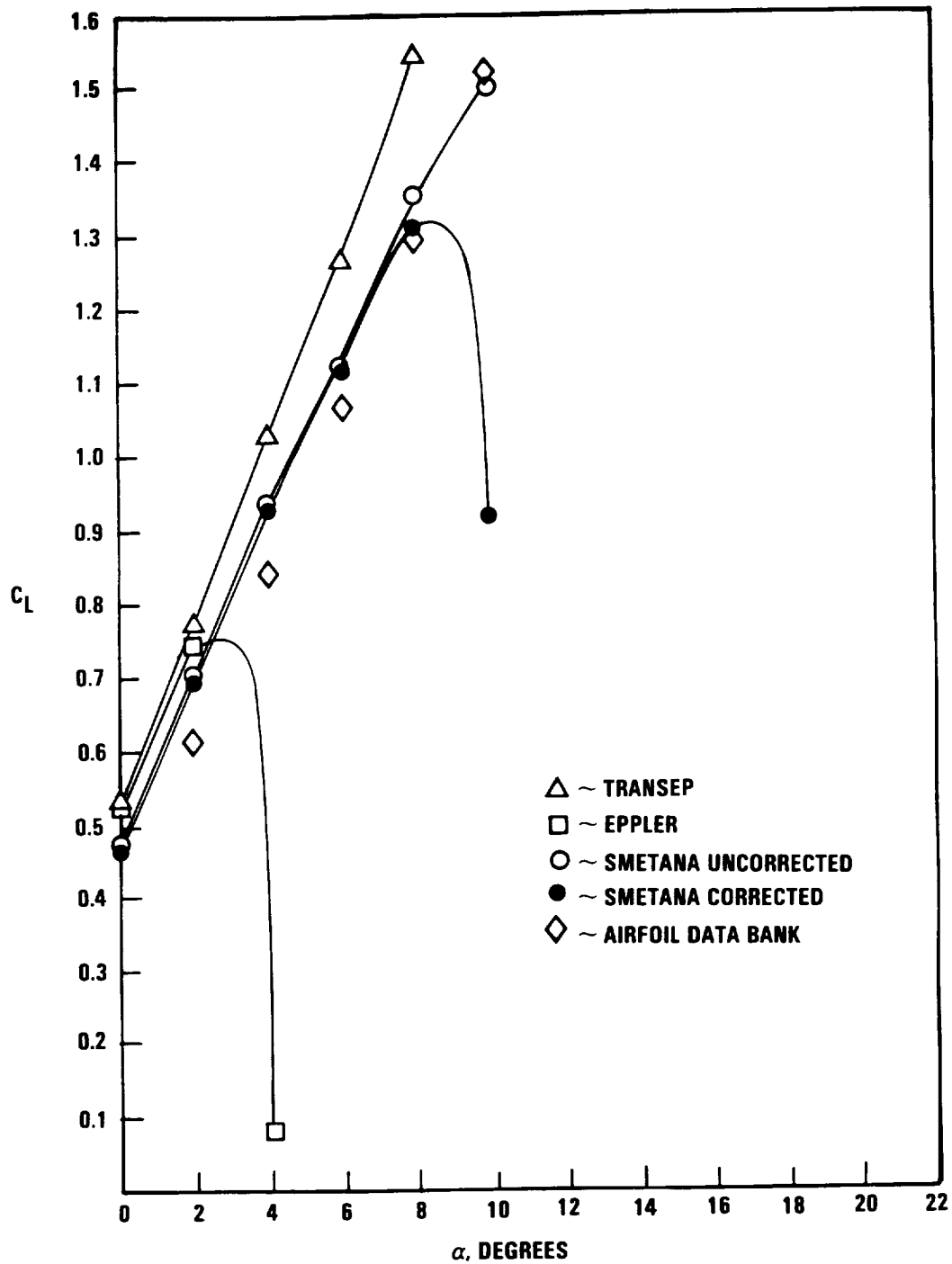


Figure 3.4-7. Lift Coefficient Versus Angle of Attack for H101/16 at Station No. 17.042 ( $M_H = 0.45$ ,  $Re_L = 8.36 \times 10^5$ )

$\alpha = 10$  degrees. The TRANSEP results indicate minor separation effects. Figure 3.4-5 shows the calculated values of  $C_D$  versus  $\alpha$ . Both TRANSEP and Eppler results agree very well up to  $\alpha = 6$  degrees, after which Eppler shows leading edge separation. Although Smetana compares favorably with TRANSEP at small  $\alpha$ , the values of  $C_D$  deviate significantly at the higher values of  $\alpha$ . Figure 3.4-6 shows the resultant  $C_p$  distribution at  $\alpha = 4$  degrees. Both Eppler and TRANSEP compare very well over most of the airfoil, except near the region of the trailing edge. However, there is some deviation in the Smetana results, especially near the leading edge on the upper surface.

The next set of comparisons is for the propeller mid-region, station 17.042. Here the helical Mach number is 0.45 and  $Re_L = 0.836 \times 10^6$ . Since this section is a modified Clark Y airfoil, we will also include in the comparison the resultant  $C_L$  and  $C_D$  as obtained from the airfoil data bank. Figure 3.4-7 shows the resultant  $C_L$  versus  $\alpha$  for TRANSEP, Smetana, Eppler, and the Clark Y airfoil data bank. The results of the Smetana code with the  $C_{L_{max}}$  correction indicate the flow has separated. At  $\alpha > 8$  degrees. The results of Eppler are in reasonable agreement with results up to  $\alpha = 2$  degrees, after which leading edge separation occurs (Figure 3.4-8). The  $C_L$  as obtained from the data banks is lower than that of the analysis codes at most conditions, however, it seems to be closer to that of Smetana. Figure 3.4-8 shows the location of the upper surface separation point. Both Smetana and TRANSEP are in agreement up to  $\alpha = 8$  degrees, whereas, Eppler shows leading edge separation at  $\alpha = 4$  degrees. Figure 3.4-9 shows the transition location obtained from the analysis methods. At  $\alpha = 0$ , Eppler shows leading edge transition on the lower surface; however at  $\alpha = 2$  and 4 degrees, the transition on the lower surface moves aft ( $X/C \approx 0.95$ ). Figure 3.4-10 shows the resultant  $C_D$  versus  $\alpha$ . Both Smetana and TRANSEP agree very well up to  $\alpha = 8$  degrees, whereas Eppler shows the leading edge separation problem as discussed above. The data bank values of  $C_D$  are in reasonable agreement up to  $\alpha = 4$  degrees. Above  $\alpha = 4$  degrees, the data bank results show a significantly lower value of  $C_D$ . Note that at  $\alpha = 10$  degrees, TRANSEP had convergence problems due to local Mach number effects exceeding the limitations of the code. Figure 3.4-11 shows the resultant  $C_p$  distribution on the airfoil at  $\alpha = 4$  degrees. Although the

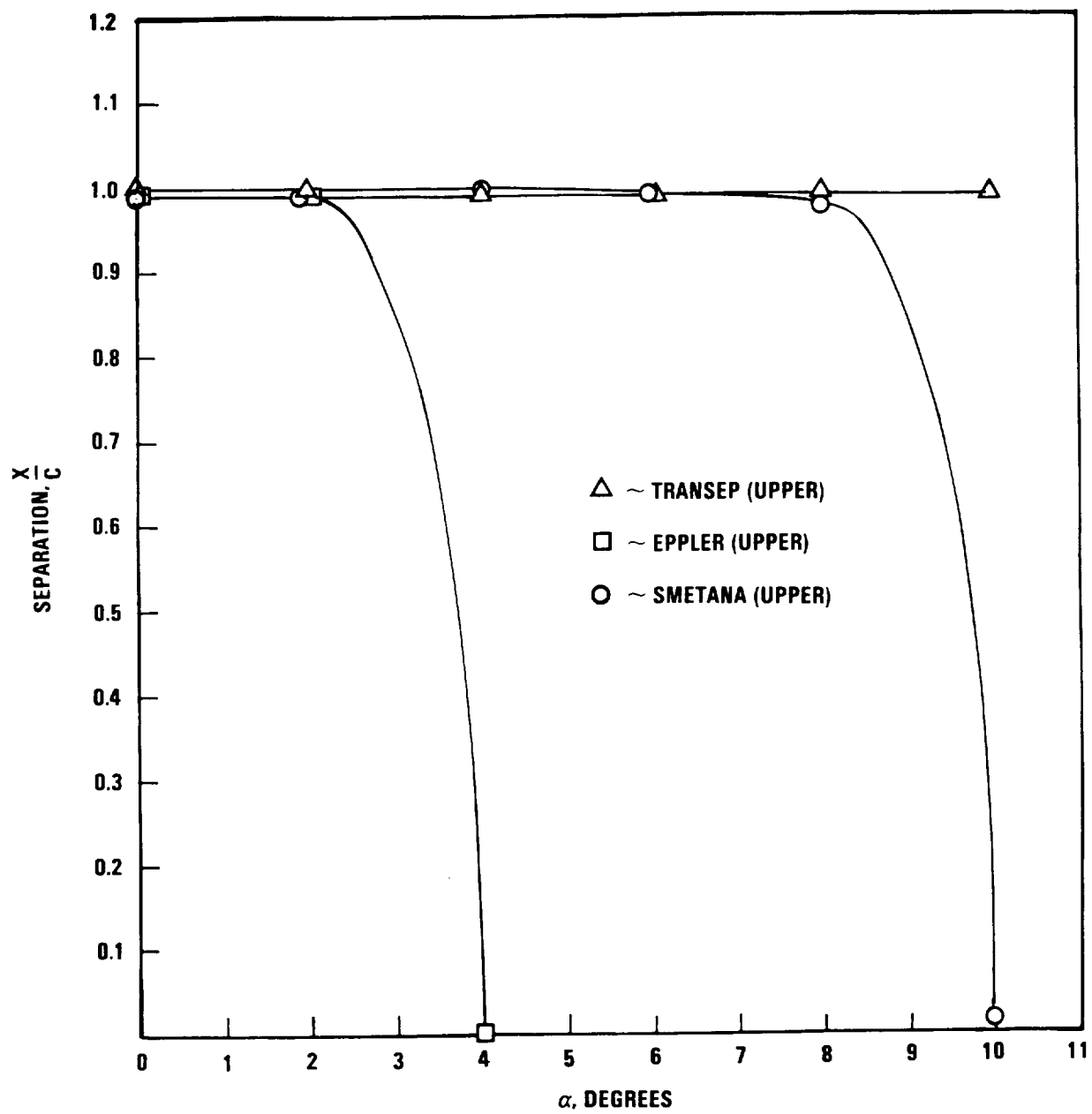


Figure 3.4-8. Boundary Layer Separation Point Versus Angle of Attack for H101/16 at Station 17.042 ( $M_H = 0.45$ ,  $Re_L = 8.36 \times 10^5$ )

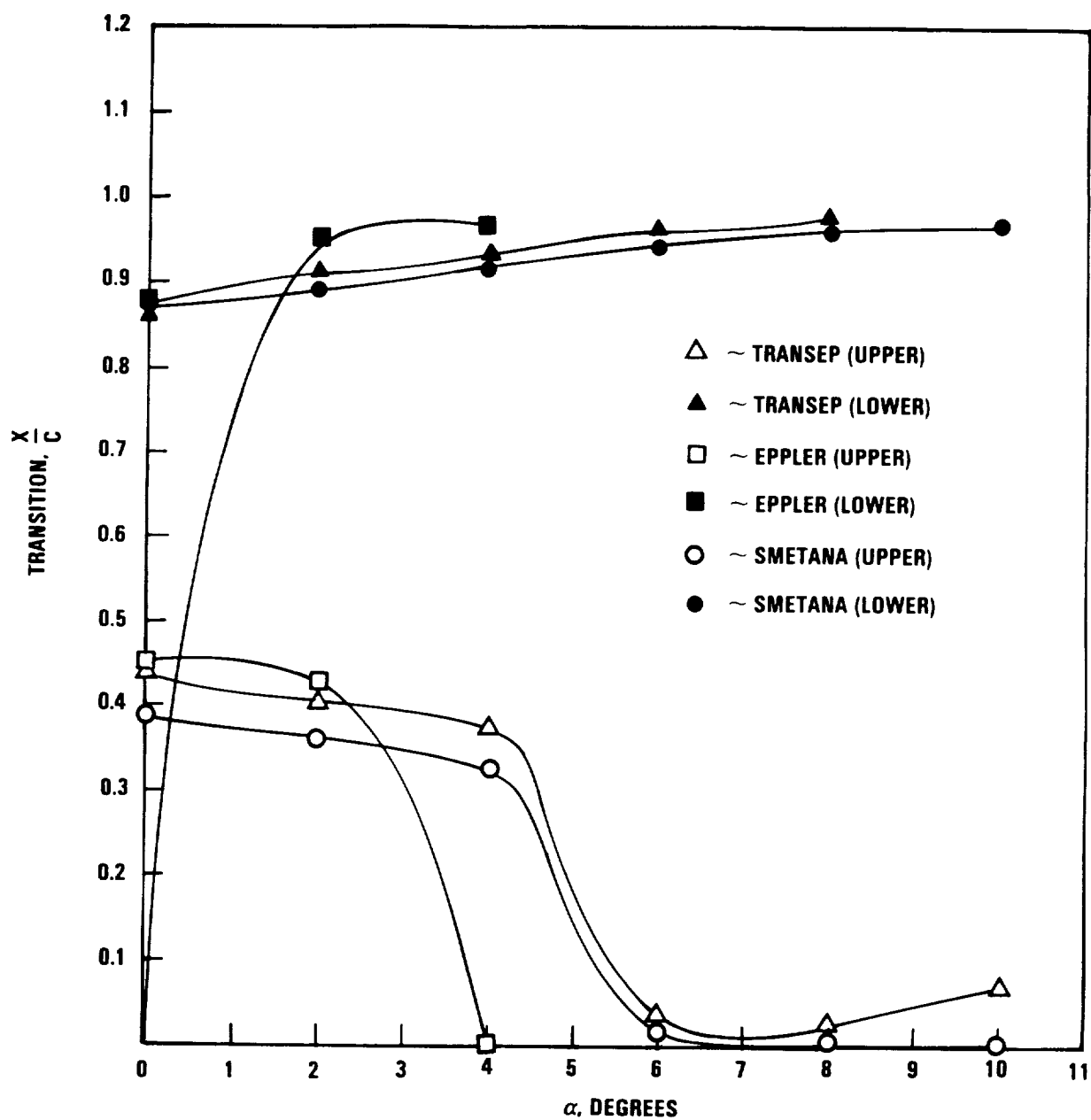


Figure 3.4-9. Boundary Layer Transition Point Versus Angle of Attack for H101/16 at Station 17.042 ( $M_H = 0.45$ ,  $Re_L = 8.36 \times 10^5$ )



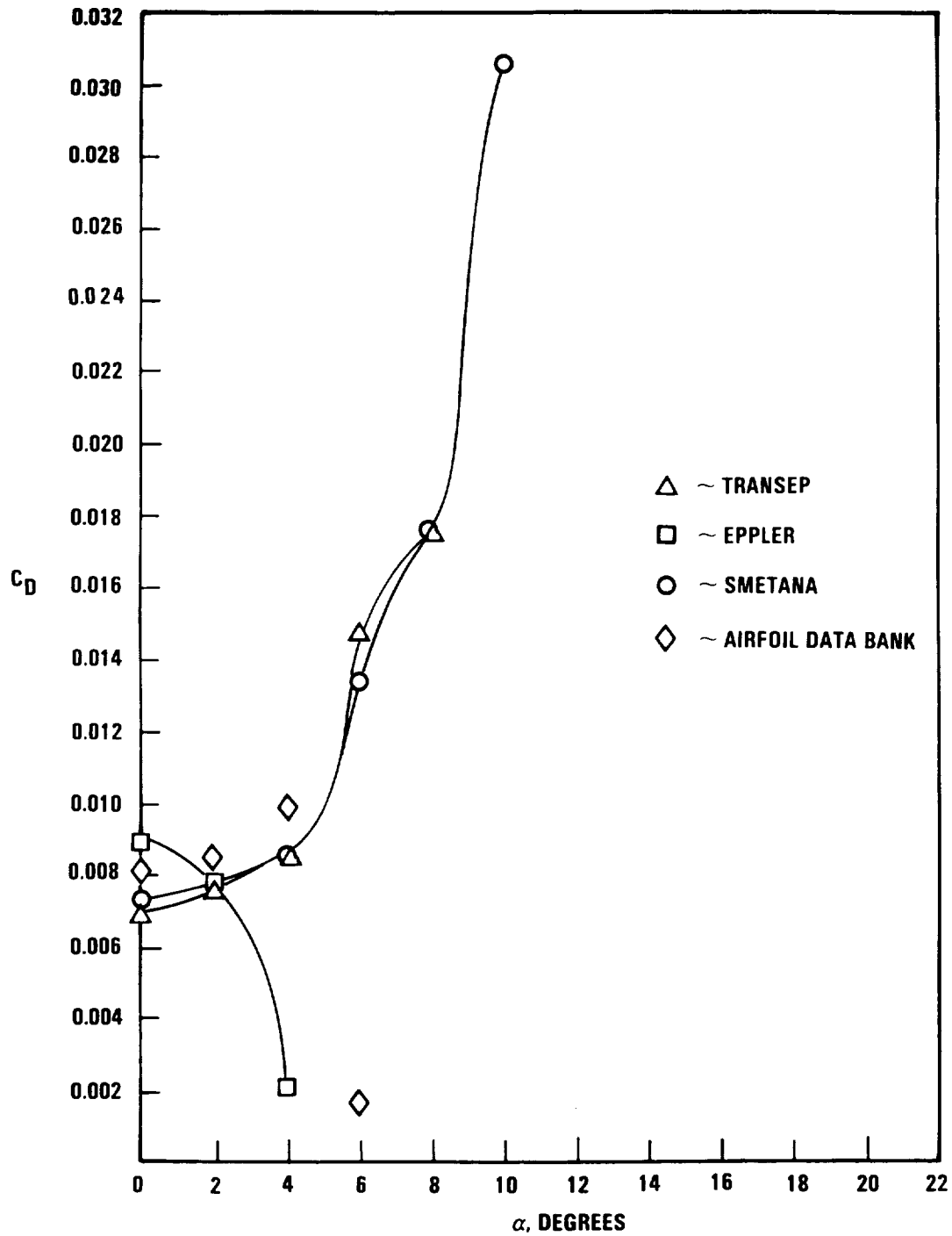
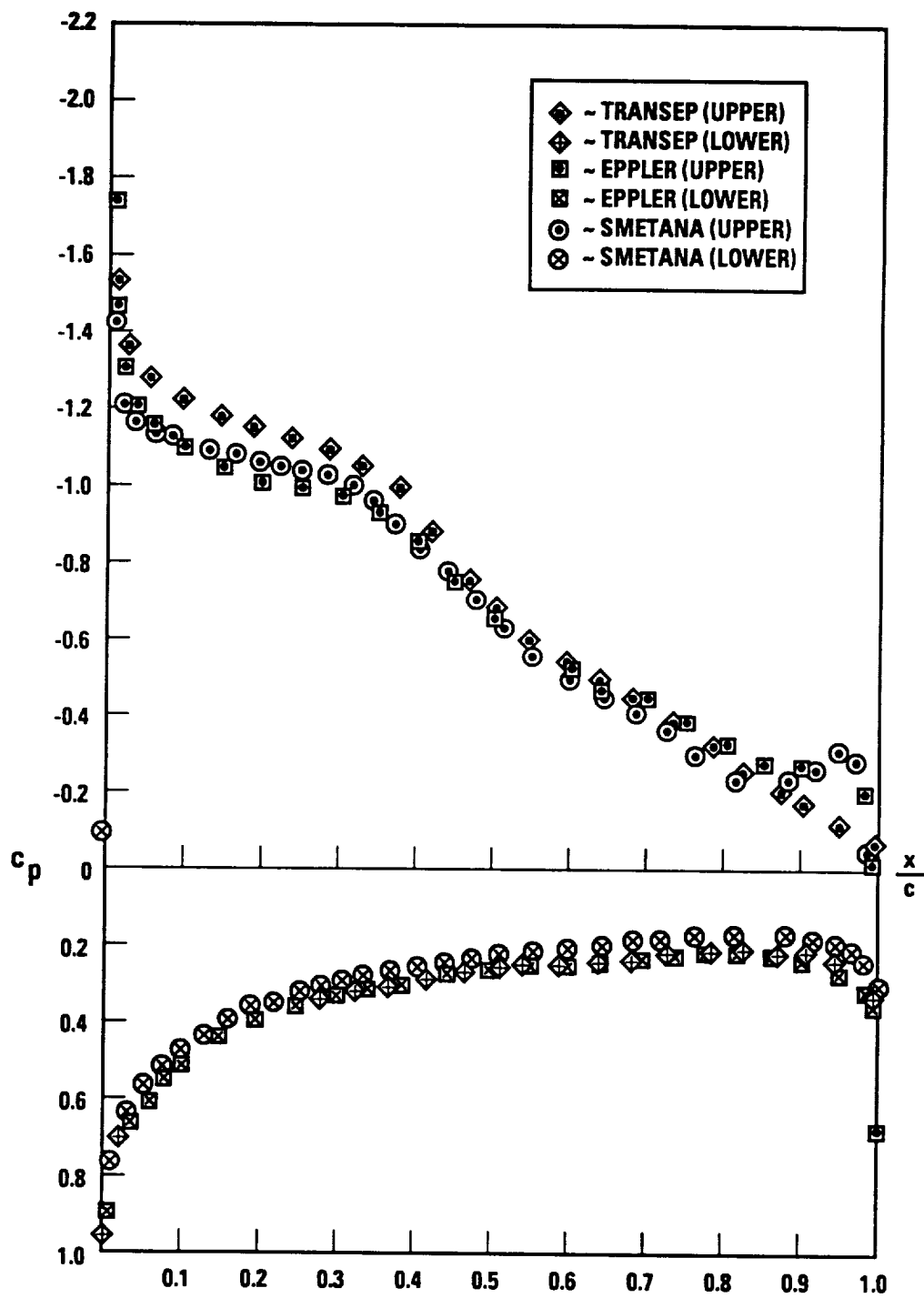


Figure 3.4-10. Drag Coefficient Versus Angle of Attack for H101/16 at Station 17.042 ( $M_H = 0.45$ ,  $Re_L = 8.36 \times 10^5$ )



R1M 0169.02

Figure 3.4-11. Pressure Coefficient Distribution for H101/16 at Station 17.042 ( $M_H = 0.45$ ,  $Re_L = 8.36 \times 10^5$ ,  $\alpha = 40^\circ$ )

subcritical codes are in reasonable agreement with each other, on the upper surface upstream of  $X/C = 0.4$ , they show a deviation from the TRANSEP results.

The final airfoil section corresponds to station 23.803 and is characteristic of a NACA 16 airfoil section. Here, the helical Mach number is 0.51 and the Reynolds number is  $0.879 \times 10^6$ . Since the NACA 16 airfoil data bank is available, we will also include in the comparison values obtained from it. Figure 3.4-12 shows the resultant  $C_L$  versus  $\alpha$ . As can be seen, the Eppler results are showing separation whereas the TRANSEP results are in excellent agreement with the NACA 16 data bank. The results of Smetana calculation corrected for  $C_{L_{\max}}$  show an early rollover in  $C_L$ . However, the uncorrected calculation of Smetana appears to give a value of  $C_{L\alpha}$  which is in closer agreement to both the airfoil data bank and TRANSEP, although at a slightly higher angle-of-zero-lift. Figures 3.4-13 and 3.4-14 show boundary layer transition and separation, respectively. The Smetana results show leading edge separation at  $\alpha = 8$  degrees, however TRANSEP shows very little separation on the upper surface. Figure 3.4-15 shows the  $C_D$  versus  $\alpha$ . For this helical Mach number, both TRANSEP and Smetana are in very good agreement between  $\alpha = 2$  and  $\alpha = 6$  degrees. The TRANSEP calculation encountered convergence problems at the higher angle of attack. At  $\alpha = 0$ , there is some disagreement between the two results. The value of  $C_D$  at  $\alpha = 0$  obtained from the data banks is significantly higher than any of the analysis methods predict. However, this can be attributed to the required extrapolation of  $C_D$  necessary when the input parameters (i.e.,  $C_{LD}$ ) are outside the range of the parameters built into the airfoil data bank. In the case of  $C_{LD} = 0.4$ , at the same helical Mach number, and thickness to chord ratio,  $C_D = 0.0049$  at  $\alpha = 0$ . Finally, Figure 3.4-16 shows the  $C_p$  distribution at  $\alpha = 4$  degrees. Although all three prediction methods have a problem in the trailing edge region, the overall pressure distributions from the three methods are in good agreement.

Additional calculations were run at  $M_\infty = 0.22$ , however the overall comparisons are similar as those discussed previously. At  $M_\infty = 0.11$ , a massive separation occurs and thus neither Eppler nor Smetana codes can be utilized. Based on the above comparisons, it was concluded that the

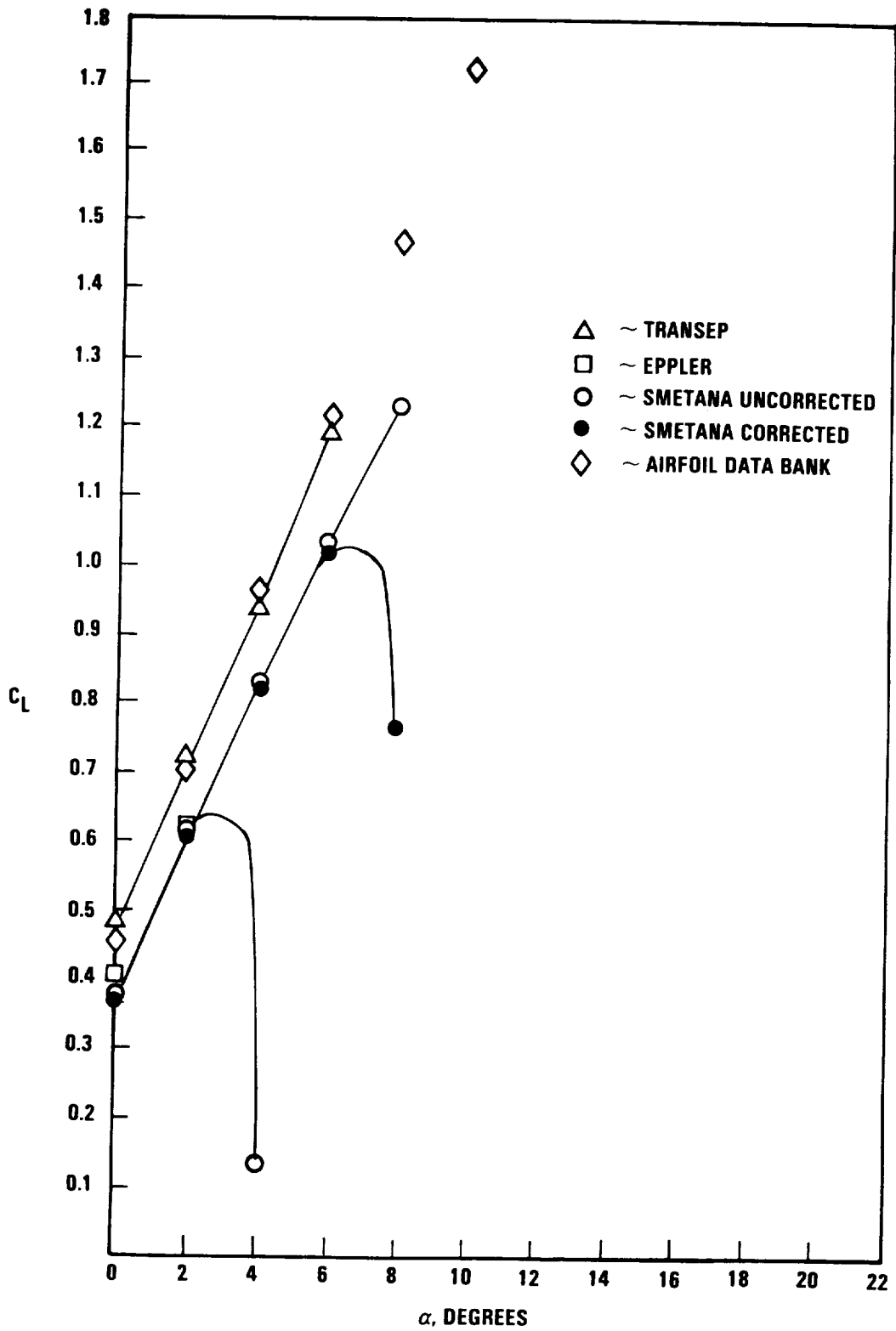


Figure 3.4-12. Lift Coefficient Versus Angle of Attack for H101/16 at Station No. 23.803 ( $M_H = 0.51$ ,  $Re_L = 8.79 \times 10^5$ )

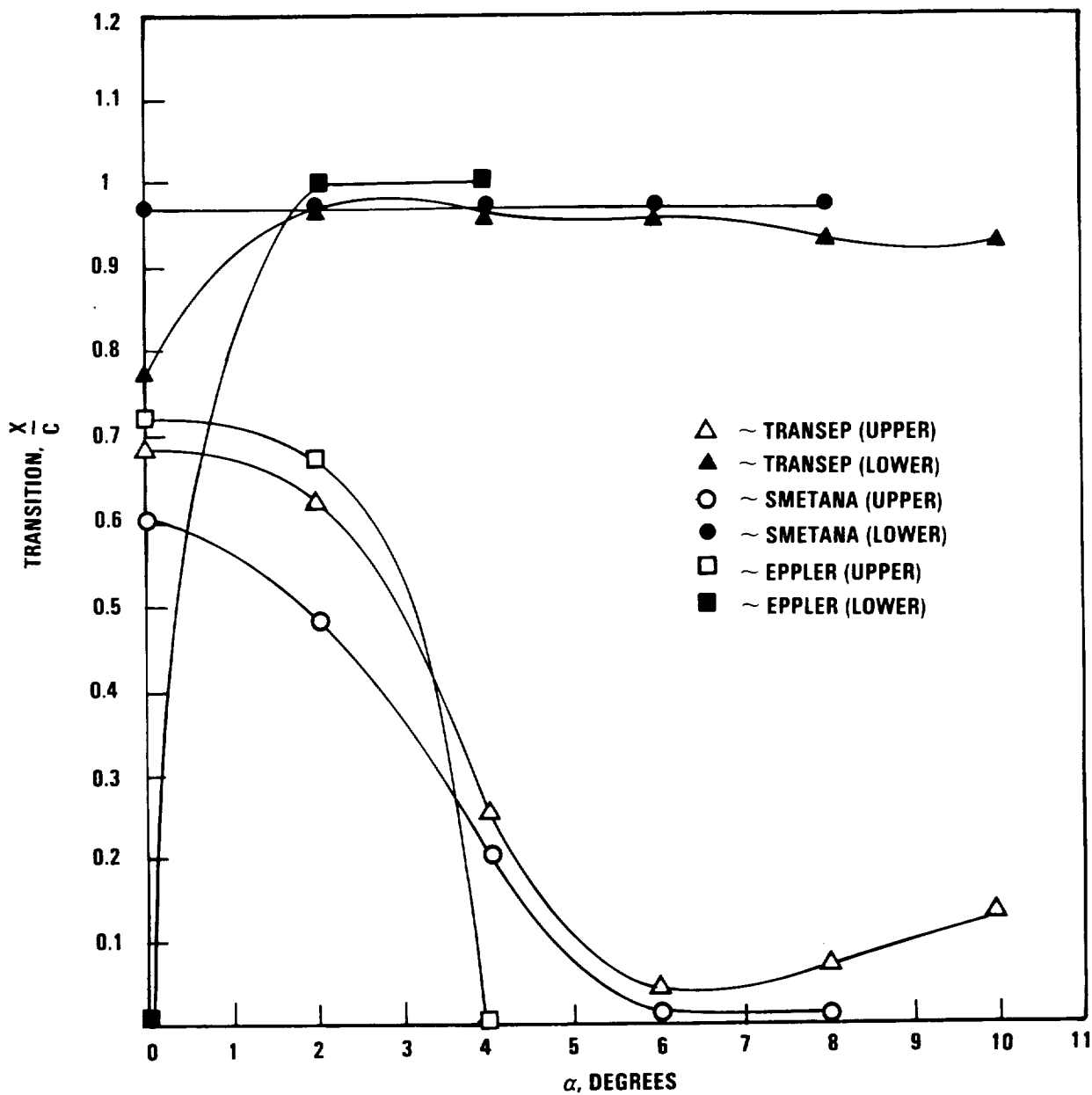


Figure 3.4-13. Boundary Layer Transition Point Versus Angle of Attack for H101/16 at Station 23.803 ( $M_H = 0.51$ ,  $Re_L = 8.79 \times 10^5$ )

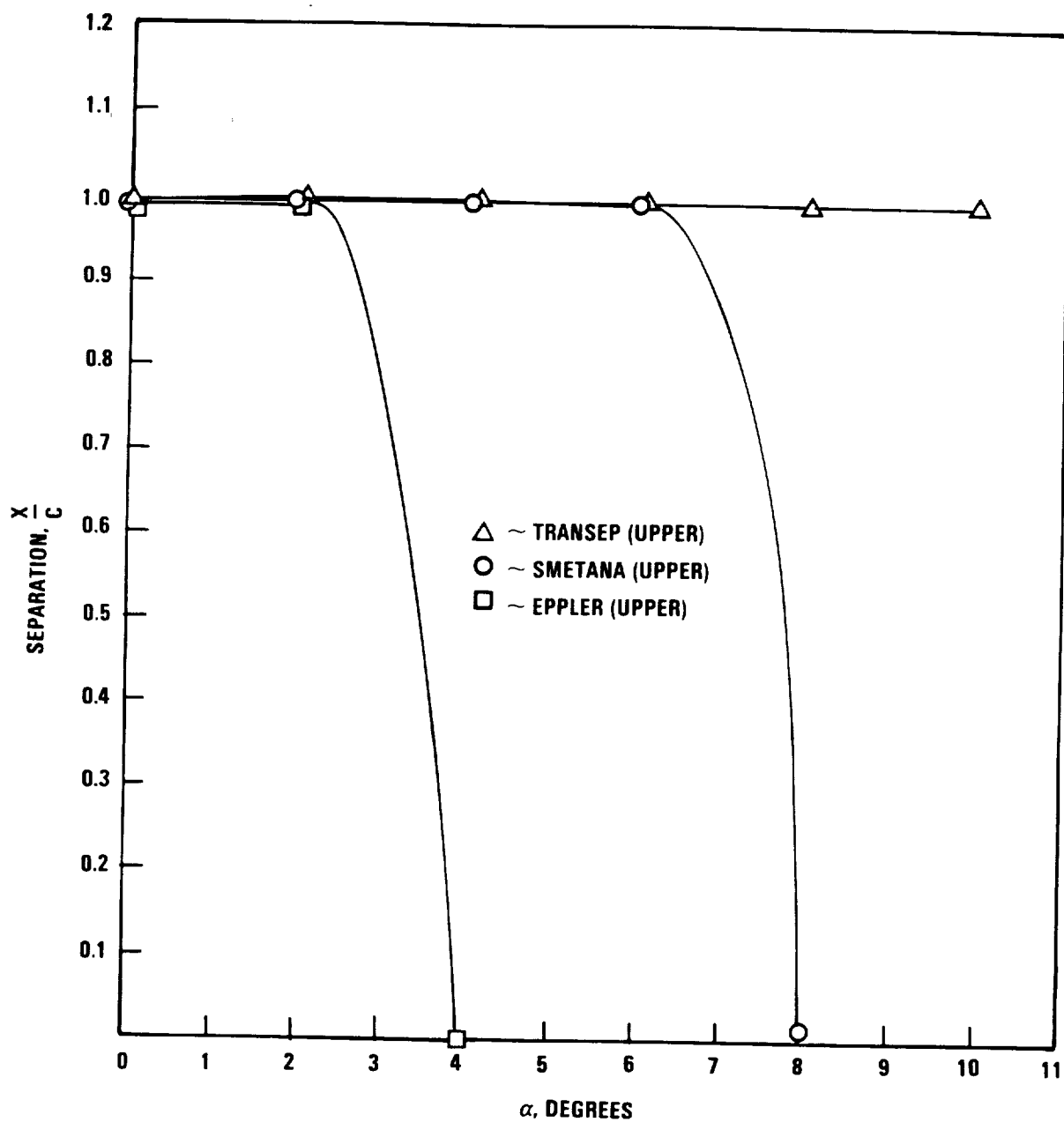


Figure 3.4-14. Boundary Layer Separation Point Versus Angle of Attack for H101/16 at Station 23.803 ( $M_H = 0.51$ ,  $Re_L = 8.79 \times 10^5$ )

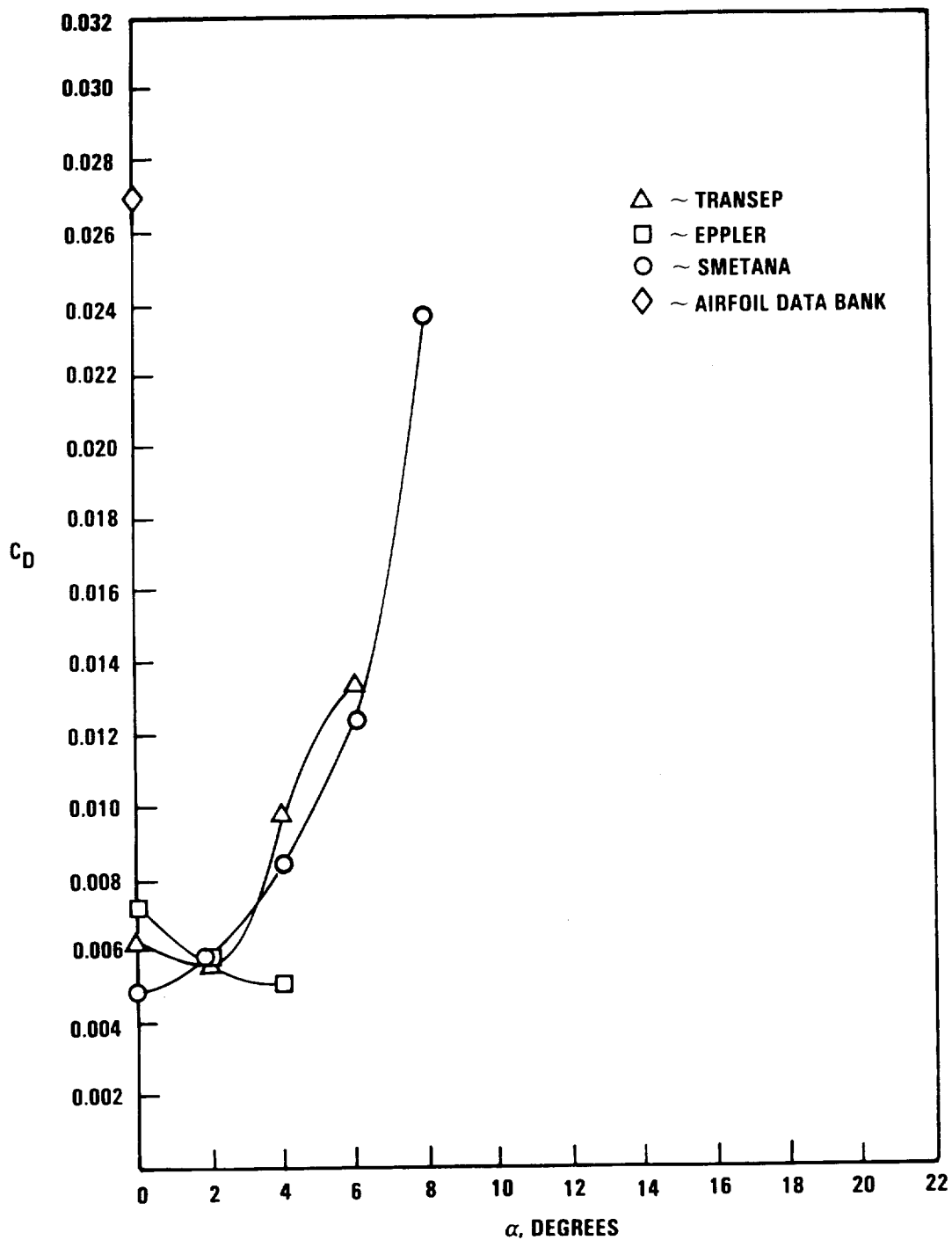


Figure 3.4-15. Drag Coefficient Versus Angle of Attack for H101/16 at Station No. 23.803 ( $M_H = 0.51$ ,  $Re_L = 8.79 \times 10^5$ )

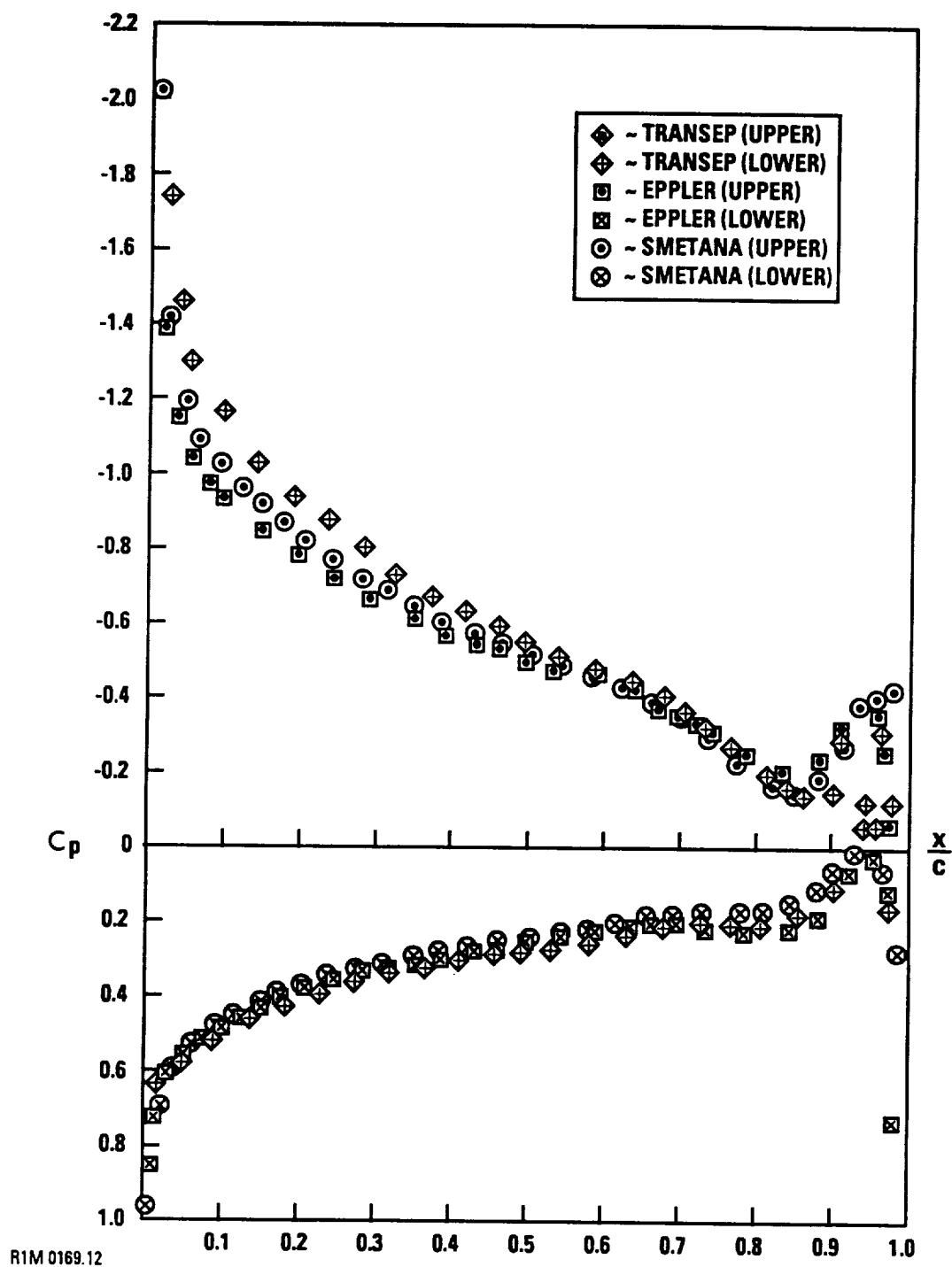


Figure 3.4-16. Pressure Coefficient Distribution for H101/16 at Station No. 23.803 ( $M_H = 0.51$ ,  $Re_L = 8.79 \times 10^5$ ),  $\alpha = 40^\circ$ )



Smetana code can be eliminated as a primary analysis code in GAPAS, thus reducing the number of analysis codes to no more than two. Since the Eppler code was essentially designed for use on thick sections, it will be utilized where TRANSEP is unable to calculate the flow in the hub section. At the high freestream Mach numbers and angles of attack where the local Mach numbers exceed the capability of the TRANSEP analysis method airfoil data banks will be utilized.

In order to investigate the massive separation model in the TRANSEP code, the case of  $M_\infty = 0.11$  was investigated. The TRANSEP (see GAPAS User's Manual) incorporates a flag to turn on the separation model during the calculation. During this study, a number of cases were run wherein separation occurred close to the trailing edge. For these calculations, it was anticipated that the results of running these calculations with and without the massive separation model should be in close agreement. However, the solutions obtained using the two methods were significantly different. In addition, the investigation of Blascovich (Ref. 3.4-1) also showed that the current massive separation model does not give correct trends for Reynolds numbers greater than  $2.58 \times 10^6$  and  $\alpha > 15.3$  degrees due to an incorrect calculation of the Nash-Macdonald separation parameter. Thus, additional work is necessary to correct this deficiency and thus, massive separation flag should be turned off when running TRANSEP.

#### 3.4.1 Summary of Airfoil Loading Verification

- (1) The Smetana code can be eliminated as a primary airfoil code in GAPAS
- (2) TRANSEP can be utilized for a substantial portion of the blade. However, further verification of TRANSEP is necessary in order to determine the limit on the thickness of sections as a function of Mach number and angle-of-attack wherein numerical problems arise, thereby allowing for the possible elimination of the use of Eppler in the GAPAS airfoil loading module.
- (3) In the thick regions of the propeller, where use of TRANSEP will not allow for a converged solution, utilize Eppler.
- (4) The massive separation in TRANSEP is not operational, and thus, large separation cannot be calculated properly with TRANSEP.
- (5) It is necessary to expand the airfoil data banks to cover the regimes that are beyond the capabilities of both TRANSEP and Eppler (i.e.,  $M_H > 0.5$  and  $\alpha \geq 6$  degrees).

### 3.5 PROPELLER ACOUSTIC MODULE

#### 3.5.1 Propeller Acoustic Modification/New Developments

At the completion of Task 1, acoustics calculation procedures approved by NASA for inclusion in the GAPAS computer code were, in order of priority, PROPFAN II (also called TPN) (Ref. 3.5-1), the Succi procedure, and the SAE AIR 1407 empirical method. Due to the initial unavailability of TPN from NASA-Langley, the SPN code was first implemented on the TRW computer system. TPN was subsequently received and has been implemented into the GAPAS system.

Modifications to both SPN and TPN included a noise source information routine which determined (1) broadband noise; (2) acoustic pressure as a function of time; (3) sound power level spectra (1/3 octave band); (4) overall sound power level; (5) sound pressure level spectra (1/3 octave band); (6) overall sound pressure level (OASPL); (7) A-weighted sound pressure level; (8) 1/10, 1/3, and full octave sound pressure and sound power level; and (9) perceived noise level, and (10) sound power level (point source, far field). The details of this routine are given in Volume II - User Manual.

#### 3.5.2 Propeller Acoustic Verification

In the verification of the acoustics analysis and calculational procedures, experimental data were provided by the NASA Project Manager for the Hartzell 101/16 and SR-3 propellers. The verification conditions for both the 101/16 and SR-3 propellers are given in Table 3.5-1. For the 101/16 propeller, data for three near-field and two far-field conditions were given as detailed in Reference 3.5-2. For the SR-3 propeller, data for the four near-field and two far-field conditions were given as detailed in Reference 3.5-3 through 3.5-5.

In the case of the 101/16 propeller near-field conditions, data were taken in flight using a wing-mounted microphone as shown in Figure 3.5-1. The propeller was three-bladed with a radius of 1.347 meters (53 inches) and had a fixed lateral distance from its hub to the microphone of 2.024 meters (79.68 inches). The aircraft flight Mach number was 0.317 and the propeller rotational speed was 1591 rpm, resulting in an advance ratio of

Table 3.5-1. Acoustics Verification Requirements

101/16 Propeller

3 Near-field conditions, 2 far-field

Near field - wing mounted microphone

$B = 3$ ;  $R = 1.347$  m (53");  $M_O = 0.317$ ,  $J = 1.52$

$\Omega = 1591$  rpm;  $M_{TH} = 0.727$

Far field - ground located microphone

$B = 3$ ;  $R = 1.347$  m (53");  $h = 762$  m (2500');  
 $M_O = 0.301$ ;  $J = 1.46$ ;  $\Omega = 1591$  rpm;  $M_{TH} = 0.714$

SR-3 Propeller

4 Near-field conditions, 2 far-field

Near field - wind tunnel data

$B = 8$ ;  $R = 0.311$  m (12.25") (NASA Lewis 8 by 6 tunnel)

$M_O$	$J$	$C_p$	RPM	$M_{TH}$
0.80	3.06	1.71	8495	1.14
0.70	3.06	1.89	7550	1.00
0.60	3.06	1.91	6573	0.86

$B = 2$ ,  $R = 0.311$  m (UTRC tunnel)

$M_O = 0.203$ ,  $J = 0.97$ ,  $\Omega = 6700$  rpm,  $M_{TH} = 0.687$

Far field - UTRC wind-tunnel

$B = 4$ ,  $R = 0.311$  m,  $M_O = 0.321$ ,  $J = 1.2$ ,  $\Omega = 8550$  rpm,  
 $M_{TH} = 0.901$

$B = 2$ ,  $R = 0.311$  m,  $M_O = 0.203$ ,  $J = 0.87$ ,  $\Omega = 7500$  rpm,  
 $M_{TH} = 0.761$

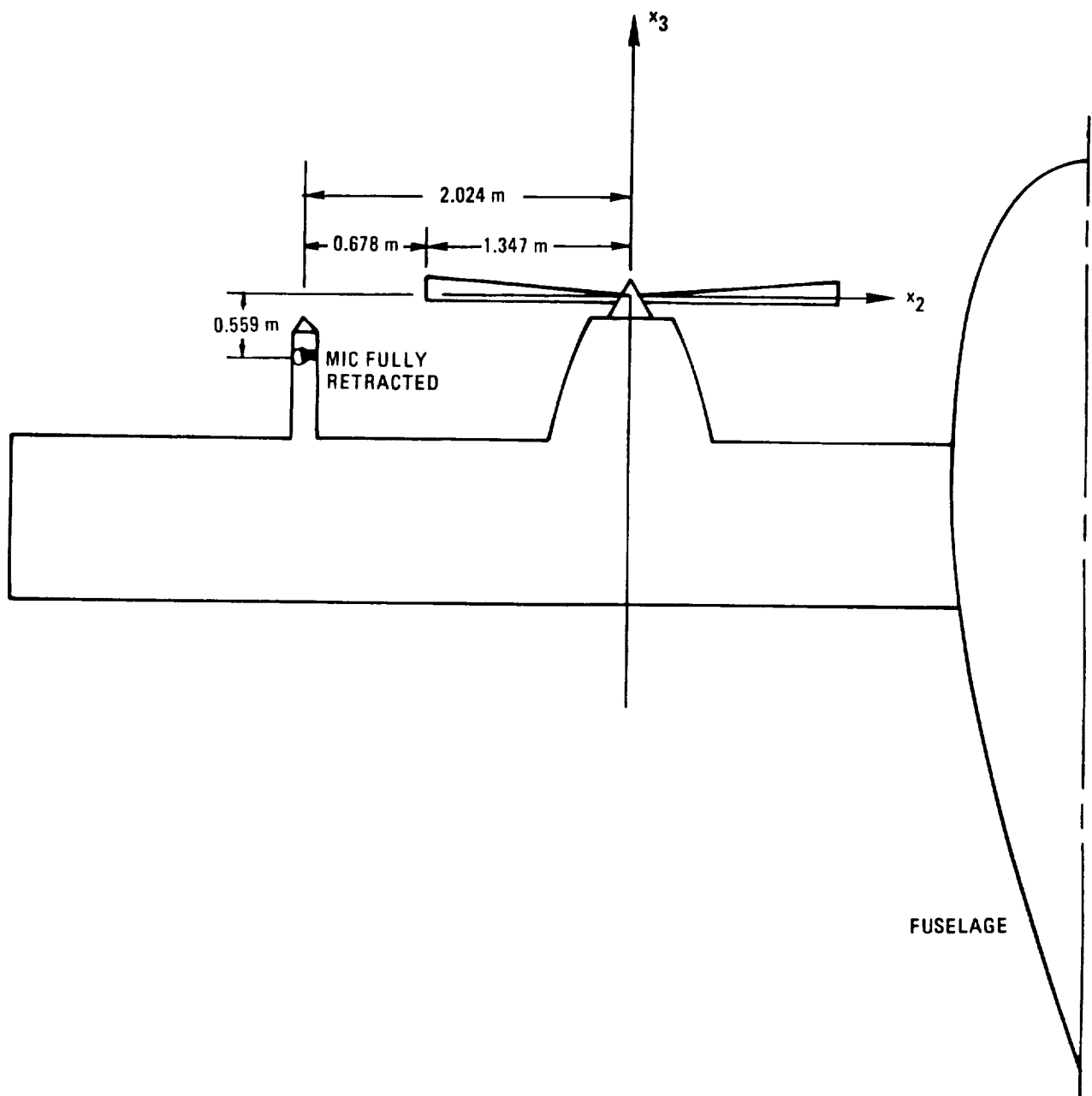


Figure 3.5-1. Wing-Mounted Microphone Position 101/16 Propeller  
Acoustic Measurements Near Field

1.52 and a helical tip Mach number of 0.727. Measurements were taken for distance between the propeller plane and microphone of 0.279 meter (11 inches), 0.406 meter (16 inches), and 0.559 meter (22 inches) (fully retracted position), respectively.

Comparisons of data with calculations using the SPN code for acoustic pressure signature and sound pressure level spectra are shown in Figures 3.5-2 and 3.5-3, respectively, for the 0.279 meter (11-inch) microphone (boom) position (cf, Figure 3.5-1 for boom position reference axes; coordinate  $x_1$  is normal to the  $x_2$ - $x_3$  plane, and axes  $x_1$ ,  $x_2$ ,  $x_3$  form a right-handed system). Also shown for comparison purposes are calculations carried out at Ohio State University using the Woan-Gregorek code. Note the overall good agreement of the SPN results with the measured data except in the vicinity of the peak, where overprediction on the order of 15% occurs. The pressure minimum is accurately predicted, however. In addition, agreement of the noise spectra results is excellent for the first five harmonics but decreases substantially for harmonic numbers greater than five. This is not of practical significance, however, since most of the acoustic energy is in the first few harmonics. Comparisons of calculational and experimental results for the 0.406-meter (16-inch) microphone position for acoustic pressure signature and overall noise spectra are shown in Figures 3.5-4 and 3.5-5. Note in this case that the peak overpressure is accurately predicted, but overall agreement for the pressure signature is not as good as in the previous case and the pressure minimum is about 50% underpredicted. Observations for the noise spectra (Figure 3.5-5) are similar to the previous case, namely that agreement for the first five harmonics is excellent but drops off substantially for harmonic numbers greater than five. Lastly, comparisons with experimental results for the 0.559-meter (22-inch) microphone position are shown in Figures 3.5-6 and 3.5-7. For this case the agreement for the pressure signature is only fair, overpredicting the peak by about 20% and underpredicting the trough by 70%. Again, however, agreement for the first five harmonics of the sound pressure level spectra is excellent, but decreases for harmonic numbers above 5. In addition, results for overall sound pressure level (OASPL) for the three 101/16 propeller near-field conditions are shown in Table 3.5-2. Note, there is excellent agreement of

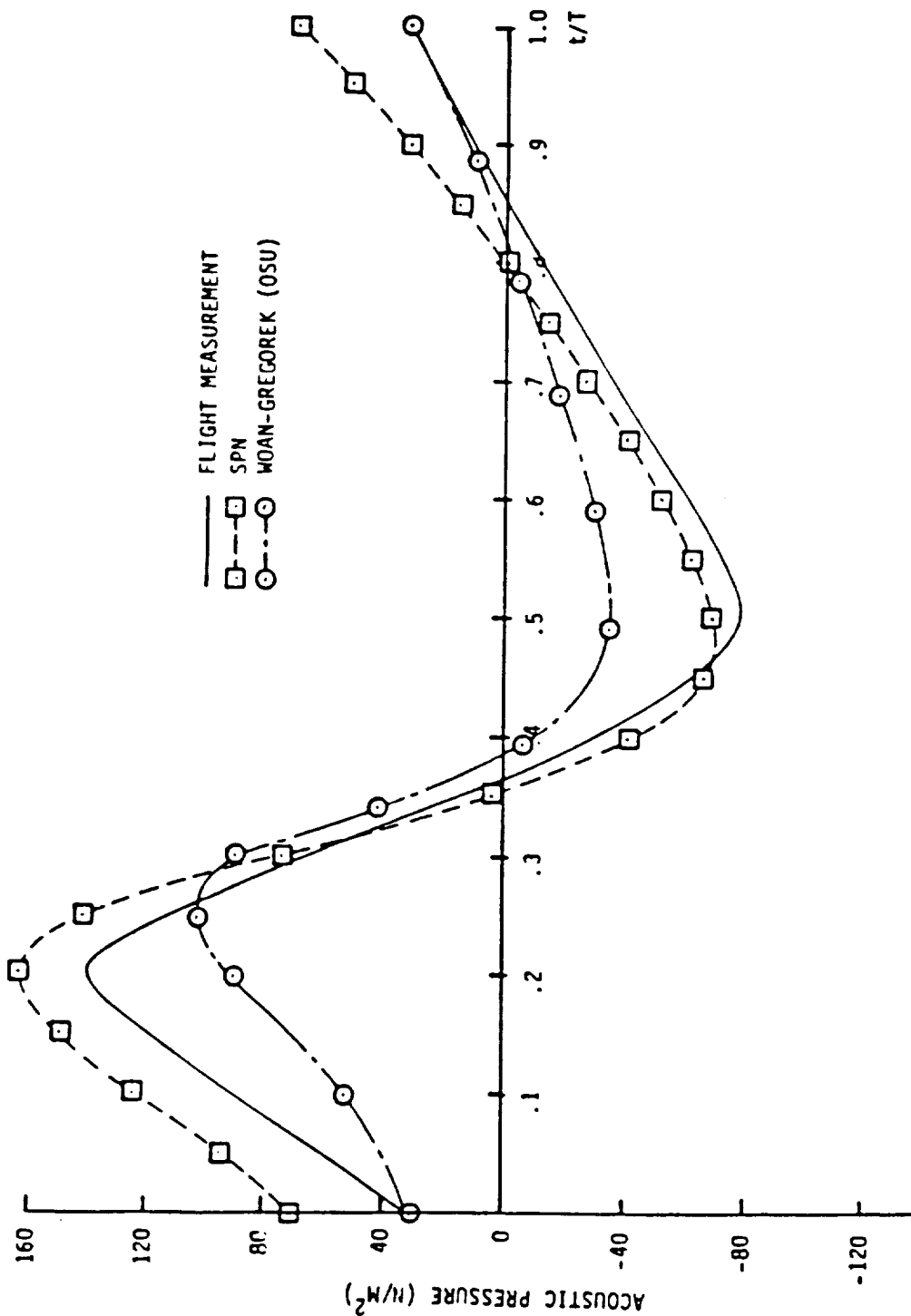


Figure 3.5-2. Acoustic Pressure Signature 101/16 Propeller Near Field  
 (Run No. 11 of Ref. 3.5-2)  $M_{\infty} = 0.317$ ,  $PALT = 3043$  M,  
 $B = 3$ ,  $n = 1591$  rpm, boom position (M)  
 $\frac{X1}{0.0} \frac{X2}{-2.024} \frac{X3}{-0.279}$

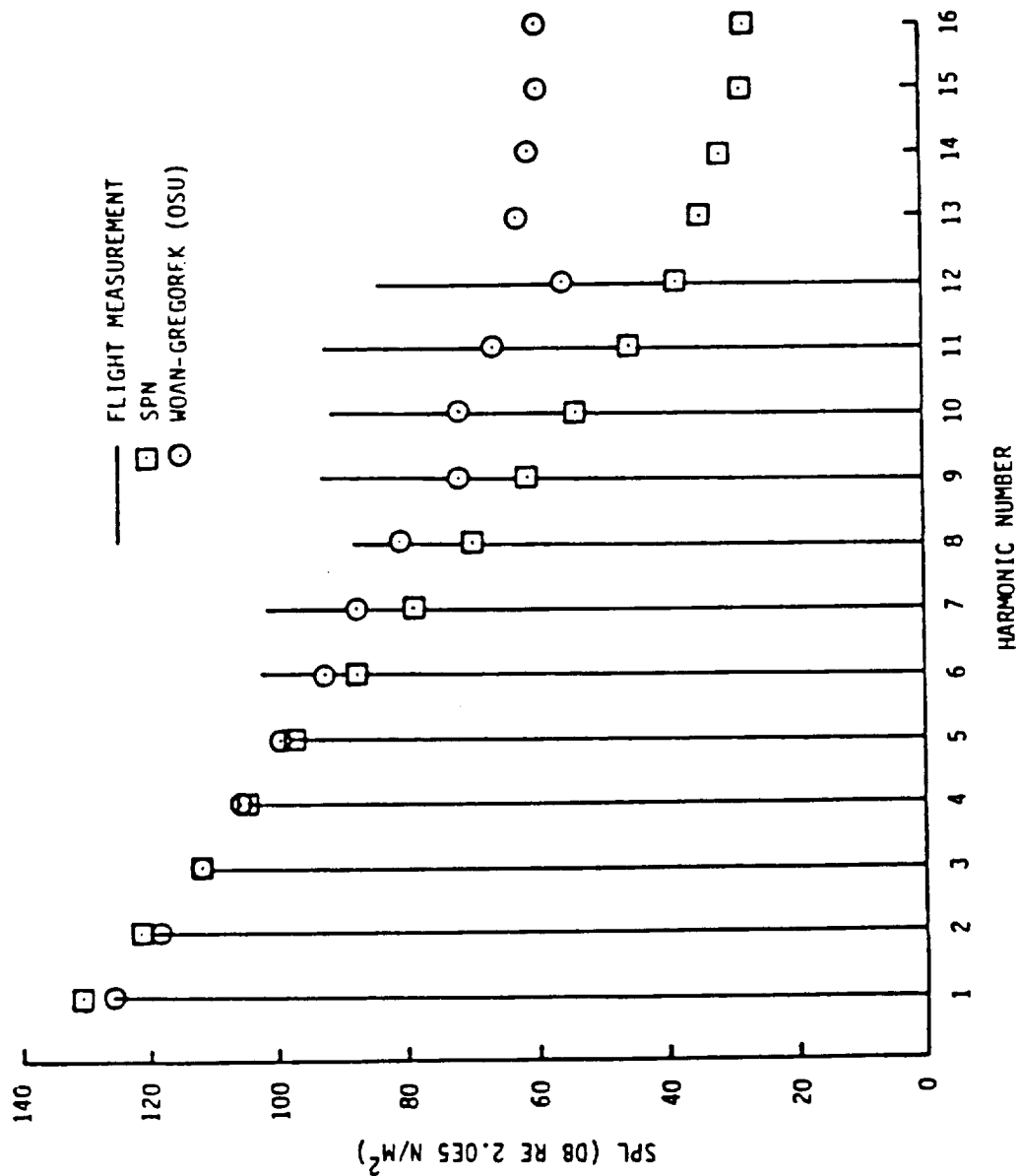


Figure 3.5-3. Overall Noise Spectra 101/16 Propeller Near Field (Run No. 11 of Ref. 3.5-2)  
 $M_{\infty} = 0.317$ ,  $PALT = 3043$  M,  $B = 3$ ,  $n = 1591$  rpm, boom position (M)  
 $X1 \quad X2 \quad X3$   
 $0.0 \quad -2.024 \quad -0.279$

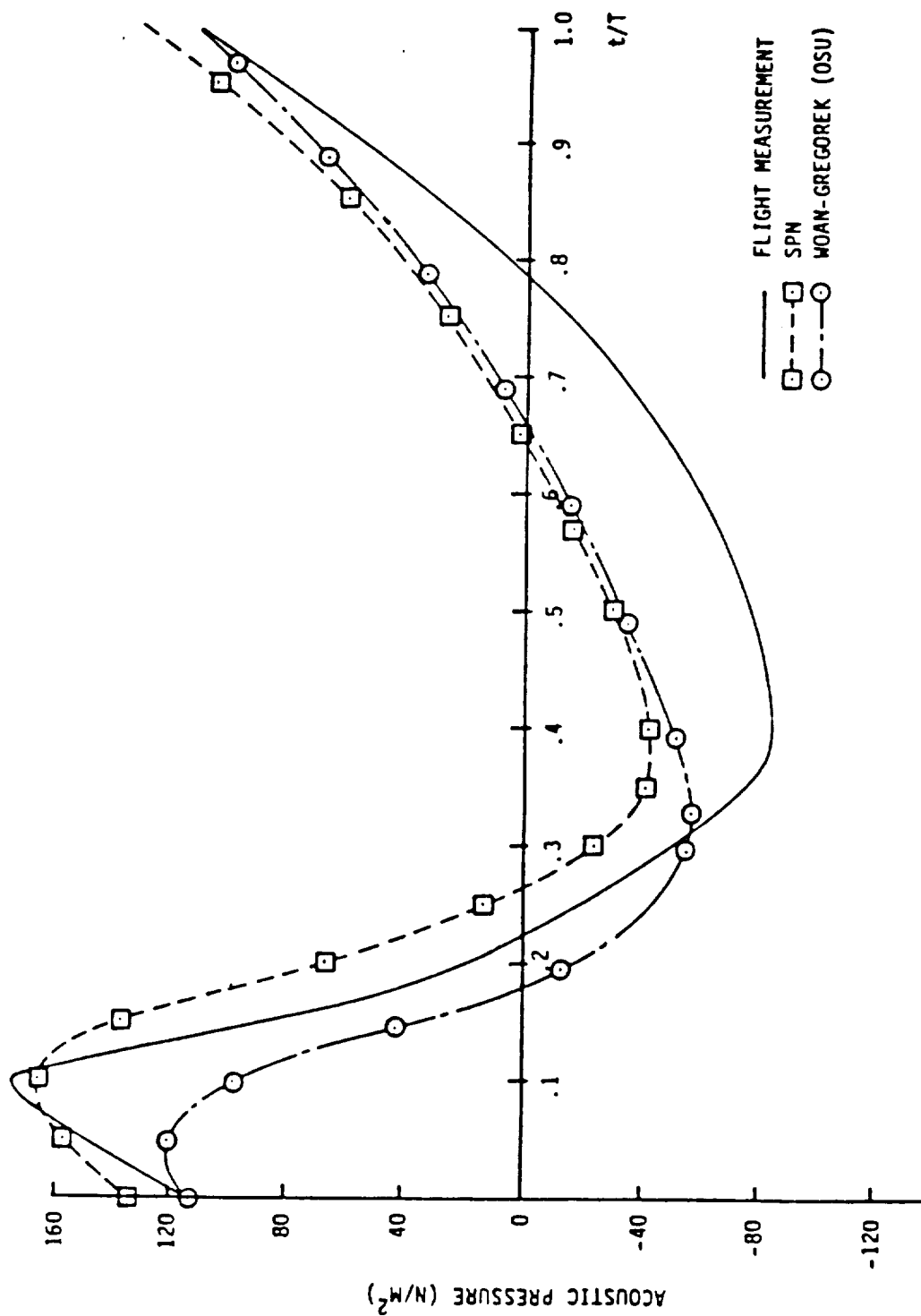


Figure 3.5-4. Acoustic Pressure Signature 101/16 Propeller Near Field  
(Run No. 12 of Ref. 3.5-2)  $M_\infty = 0.317$ , PALT = 3043 M,  
 $B = 3$ ,  $n = 1591$  rpm, boom position (M)  
 $\frac{X1}{0.0}$   $\frac{X2}{-2.024}$   $\frac{X3}{-0.406}$



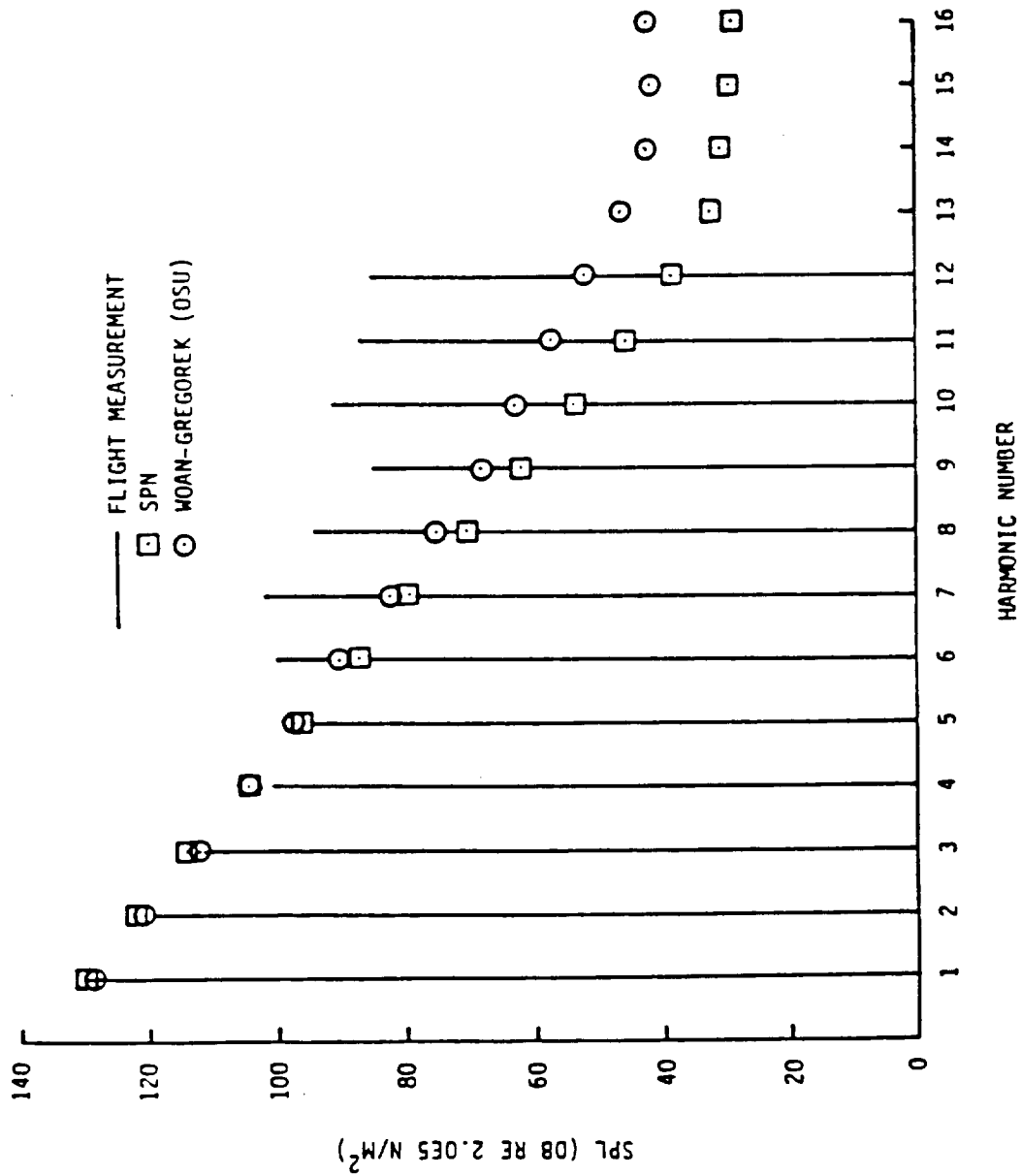


Figure 3.5-5. Overall Noise Spectra 101/16 Propeller Near Field (Run No. 12 of Ref. 3.5-2)  
 $M_{\infty} = 0.317$ ,  $PALT = 3043$  M,  $B = 3$ ,  $n = 1591$  rpm, boom position (M)  
 $X1 \quad X2 \quad X3$   
 $0.0 \quad -2.024 \quad -0.406$

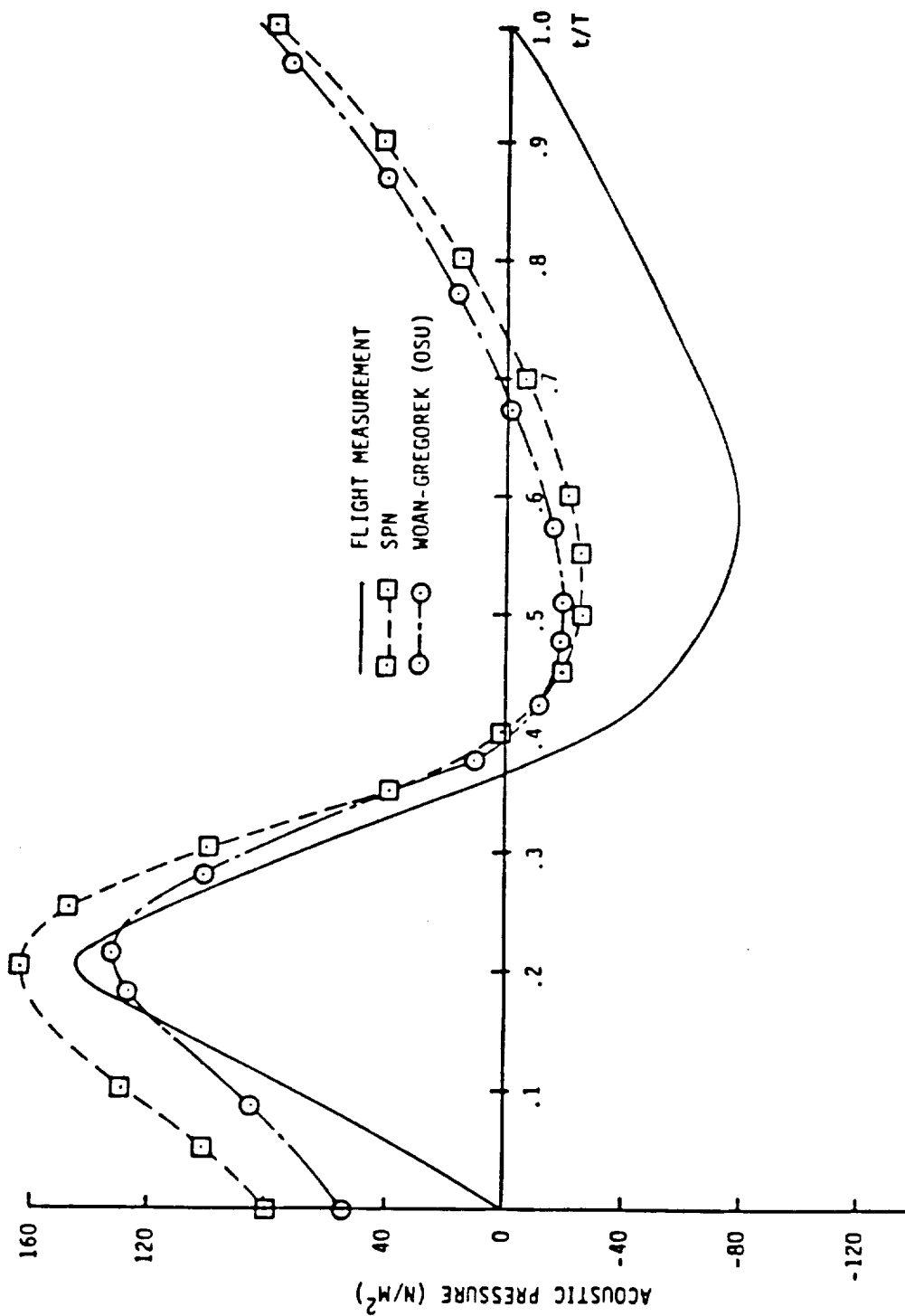


Figure 3.5-6. Acoustic Pressure Signature 101/16 Propeller Near Field  
 (Run No. 13 of Ref. 3.5-2)  $M_{\infty} = 0.317$ ,  $PALT = 3043$  M,  
 $B = 3$ ,  $n = 1591$  rpm, boom position (M)  
 $\frac{X1}{0.0}$   $\frac{X2}{-2.024}$   $\frac{X3}{-0.559}$

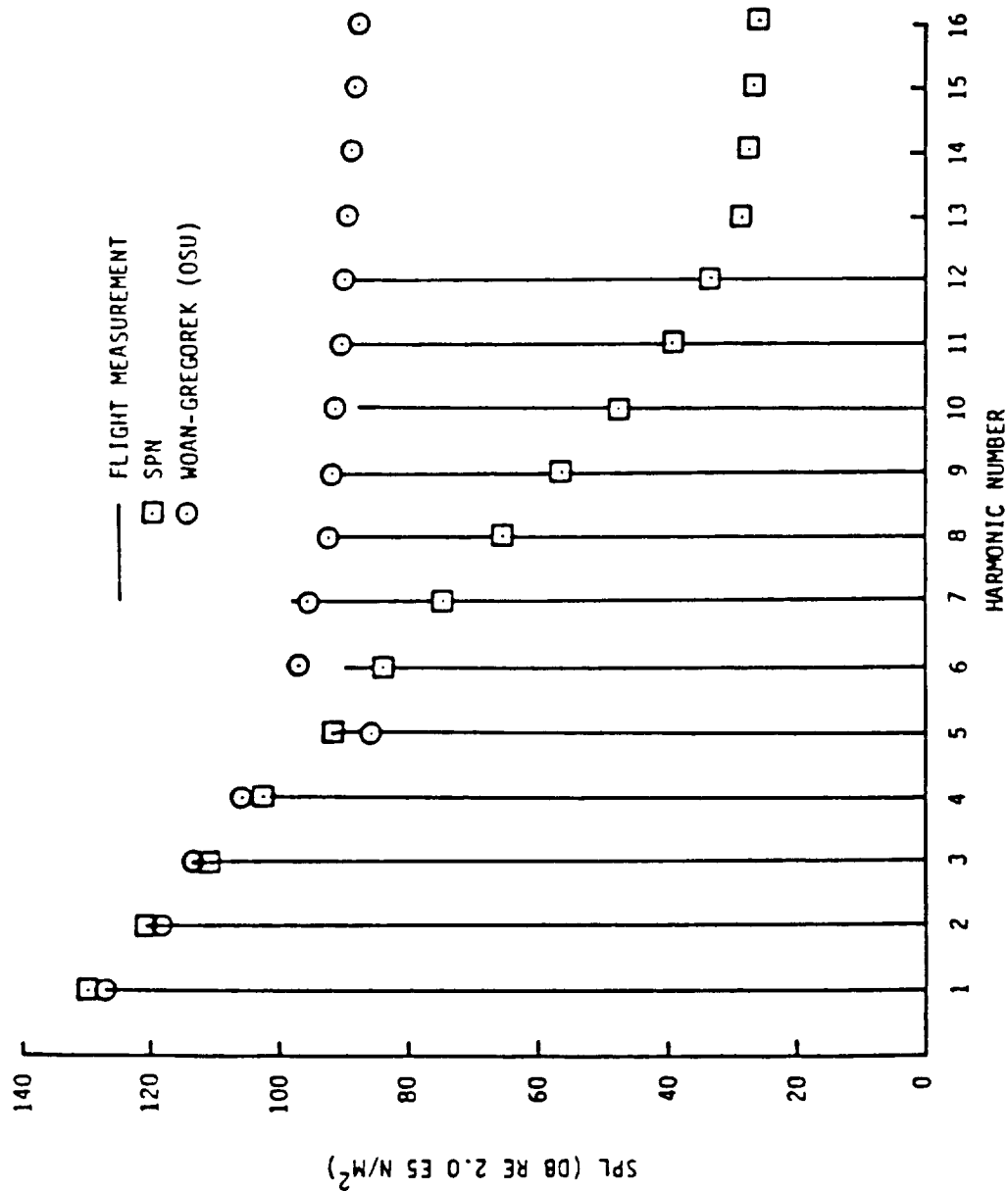


Figure 3.5-7. Overall Noise Spectra 101/16 Propeller Near Field (Run No. 13 of Ref. 3.5-2)  
 $M_{\infty} = 0.317$ ,  $PALT = 3043$  M,  $B = 3$ ,  $n = 1591$  rpm, boom position (M)  
 $X1 \quad X2 \quad X3$   
 $0.0 \quad -2.024 \quad -0.559$

Table 3.5-2. OASPL Results - 101/16 Propeller Near Field Conditions

$M_{\infty} = 0.317$ ,  $PALT = 3043$  m,  $B = 3$ ,  $n = 1591$  rpm

$$\left[ OASPL = 10 \log_{10} \sum_{n=1}^N (P_{rms}/P_{ref})_n^2; N = \text{Total number of harmonics} \right]$$

Run No. 11

(Boom 0.279 m aft of propeller plane)	Flight Data	131.15 dB
	SPN	131.54 dB
	Woan-Gregorek	126.85 dB

Run No. 12

(Boom 0.406 m aft of propeller plane)	Flight Data	130.86 dB
	SPN	130.67 dB
	Woan-Gregorek	129.18 dB

Run No. 13

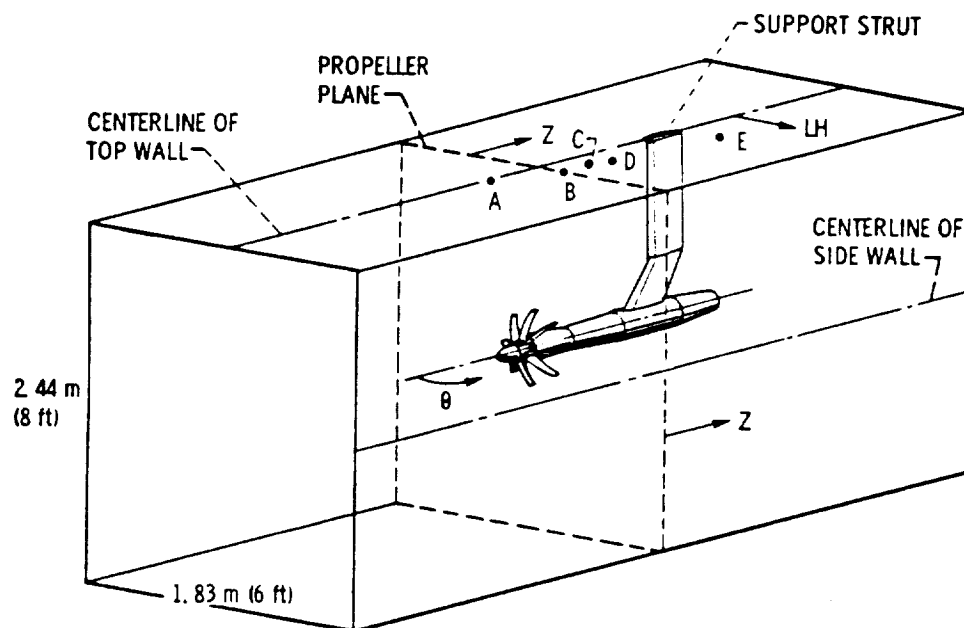
(Boom 0.559 m aft of propeller plane)	Flight Data	130.95 dB
	SPN	129.96 dB
	Woan-Gregorek	127.66 dB

the SPN result with data (within 1 dB for all cases). In addition, the OASPL results predicted by SPN, are substantially more accurate than those predicted by the Woan-Gregorek methodology.

With regard to verification of the far-field cases for the 101/16 propeller (Table 3.5-1), the data were taken using a ground-located microphone to measure propeller noise signatures generated by an aircraft flying overhead; thus the noise source and observer are in relative motion. The SPN code, as originally developed, can only handle the case of the observer fixed relative to the noise source. An additional module called TPM (Tone Propagation Module) developed for the NASA-Langley ANOPP (Aircraft Noise Prediction Program) computer code addresses the case of the noise source and observer in relative motion. At the present time, this module has not been incorporated into the GAPAS system and thus the 101/16 propeller far-field acoustics verification cases have not been carried out.

Turning now to verification of the SR-3 propeller cases, there are four near-field and two far-field cases as indicated in Table 3.5-2. Three of the near-field cases correspond to data taken in the NASA-Lewis 8' x 6' wind tunnel for an eight-bladed propeller having a radius of 0.311 meter (12.25 inches) and covering a helical tip Mach number range of 0.86 to 1.14 (subsonic to supersonic). The pressure-transducer locations in the 8' x 6' tunnel with which the near-field test data were taken for the helical Mach 0.86 case are shown in Figure 3.5-8. Note that all of the transducers are at a nominal distance of 1-1/2 blade diameters [3 feet (0.915 meter)] from the blade tip, that the transducers are offset at various lateral distances, LH, from the wall centerline, and that transducer B is nominally in the propeller plane. Results for sound pressure level are compared with SPN calculations for the helical tip Mach number 0.86 case in Figure 3.5-9. This figure also shows the results of the SPN calculation using both ANOPP aerodynamics and the aerodynamics as obtained from the GAPAS airfoil loading module which accounts for compressibility effects.

The helical tip Mach number cases corresponding to 1.0 and 1.14 could not be calculated accurately using SPN due to the transonic-supersonic nature of the flow over the propeller. Although TPN could address these cases, it was not available during the Task 2 verification and thus these



POSITION	TRANSDUCER				
	A	B	C	D	E
	TRANSDUCER POSITION, cm (in.)				
Z	-33.0(13.0)	0.953(0.375)	23.9(9.4)	45.2(17.8)	107.4(42.3)
LH	4.83(1.9)	10.2(4.0)	2.54(1.0)	7.62(3.0)	31.5(12.4)
NOMINAL ANGLE, $\theta$ , deg.	75	90	101	110	131

Figure 3.5-8. Comparison with Experimental Data SR-3 Propeller,  $M_{TH} = 0.86$  Case

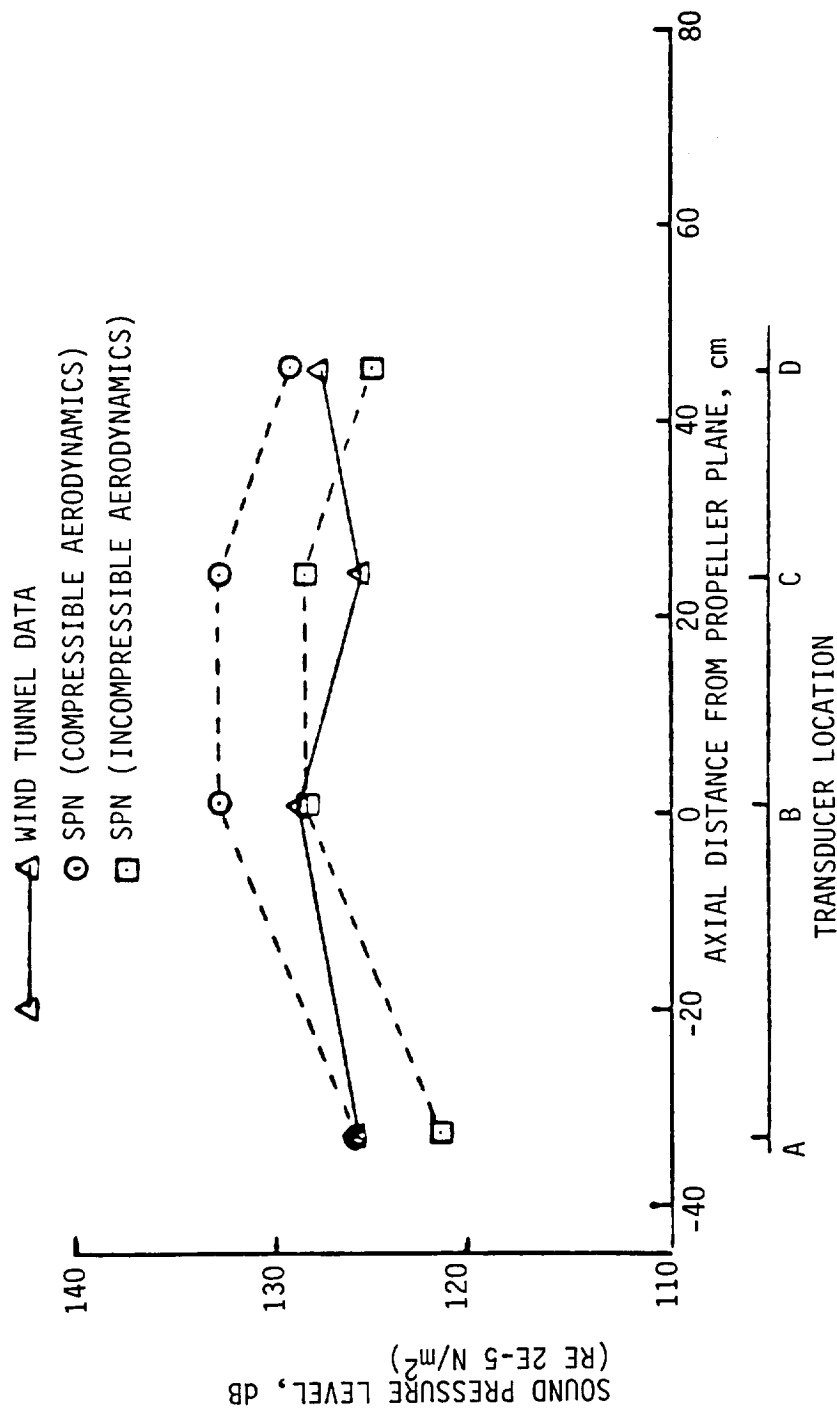


Figure 3.5-9. Acoustic Verification Results SR-3 Propeller  
 $B = 8$ ,  $\beta_{.75R} = 61.3^\circ$ ,  $M_0 = 0.60$ ,  $J = 3.06$ ,  $M_{TH} = 0.86$

cases were not verified during this task. Later availability of TPN, however, allowed these cases to be run and results for the SR-3 propeller at a helical tip Mach number of 1.14 were carried out under Task 5 and are described in Section 6.

For the near- and far-field measurements taken in the UTRC ART (Acoustics Research Tunnel), the microphone locations are shown in Figure 3.5-10. Near-field results for a two-bladed propeller at the 0.8 diameter location are shown in Figures 3.5-11 and 3.5-12 for the free-stream Mach 0.203, 6700 rpm (helical tip Mach number 0.687) case. Note the excellent agreement between the SPN calculations and data for both the acoustic pressure signature (Figure 3.5-11) and 8P harmonic sound pressure level (Figure 3.5-12). The 8P harmonic is that corresponding to the first fundamental blade passage harmonic of an eight-bladed propeller. This harmonic generally dominates all others and provides the major contribution to the overall noise level. This is due to the fact that the principle of linear superposition of acoustic data, which states that for linear sources the total acoustic field may be derived by summing the acoustic fields of all the individual sources, applies for prop-fan acoustic measurements despite the existence of nonlinear sources because the regions of the nonlinear sources from each blade do not overlap. Thus, the acoustic field of an eight blade prop-fan can be found from the two-blade test data by choosing multiples of the 8P harmonic and multiplying the acoustic pressure at each of these frequencies by four, the ratio of the number of blades. In terms of sound pressure level this is equivalent to adding 12 dB to the fourth harmonic from the two blade test data (Ref. 3.5-5).

With regard to the SR-3 far-field verification cases, calculational results using SPN for 8P harmonic sideline directivity at 4.4 diameters tip clearances are shown in Figures 3.5-13 and 3.5-14 for helical tip Mach numbers of 0.901 and 0.761, respectively. (A four-bladed propeller was utilized in Run 8, Figure 3.5-13, whereas a two-bladed propeller was used in Run 329, Figure 3.5-14.) The axial locations for these data are corrected for tunnel shear-layer refraction effects, which can be significant at the far-field locations. Note the excellent agreement



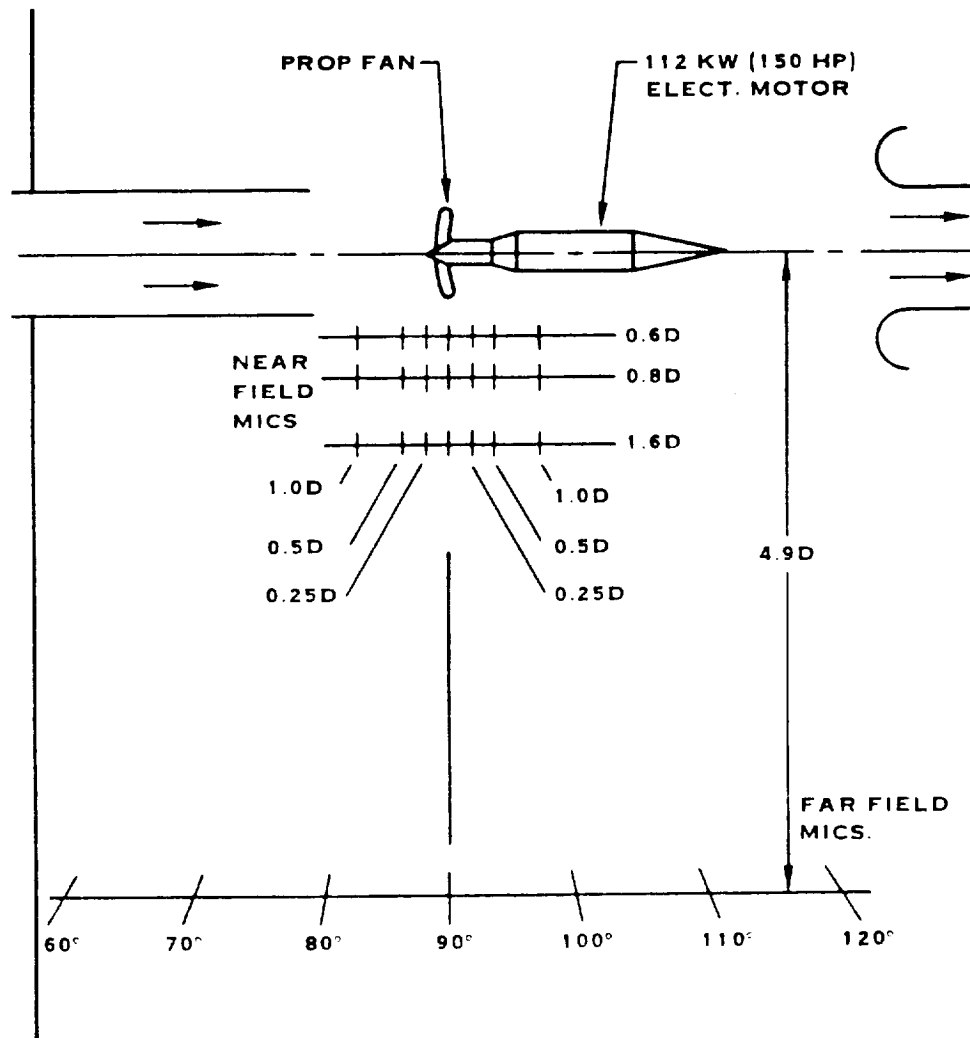


Figure 3.5-10. Microphone Locations - UTRC Wind Tunnel Near and Far Field

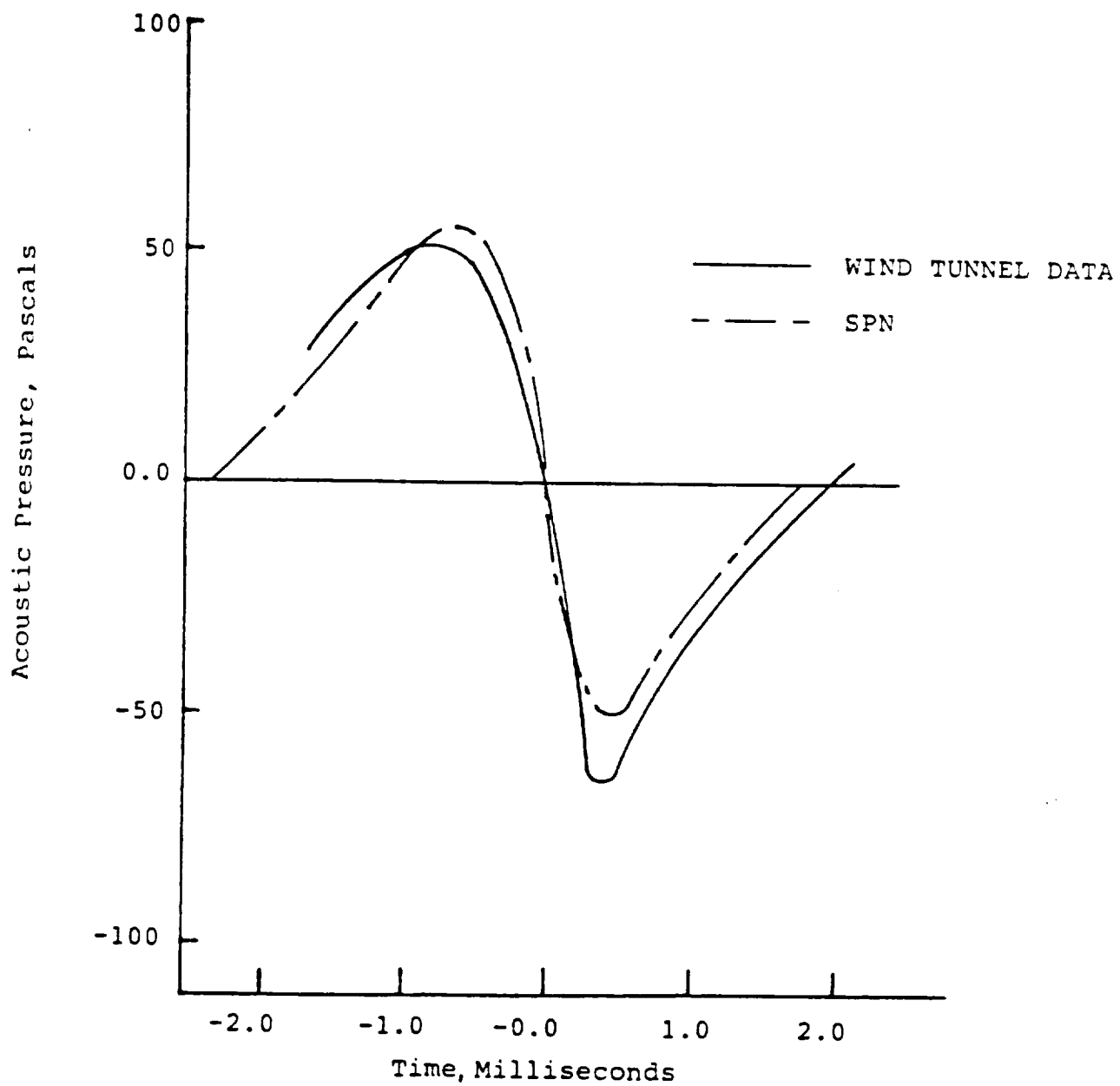


Figure 3.5-11. Propeller Plane Near-Field Pressure Signature at 0.8 D Tip Clearance Radial Location; SR-3 Propeller, B = 2,  $M_0 = 0.203$ , 6700 rpm,  $M_{TH} = 0.687$

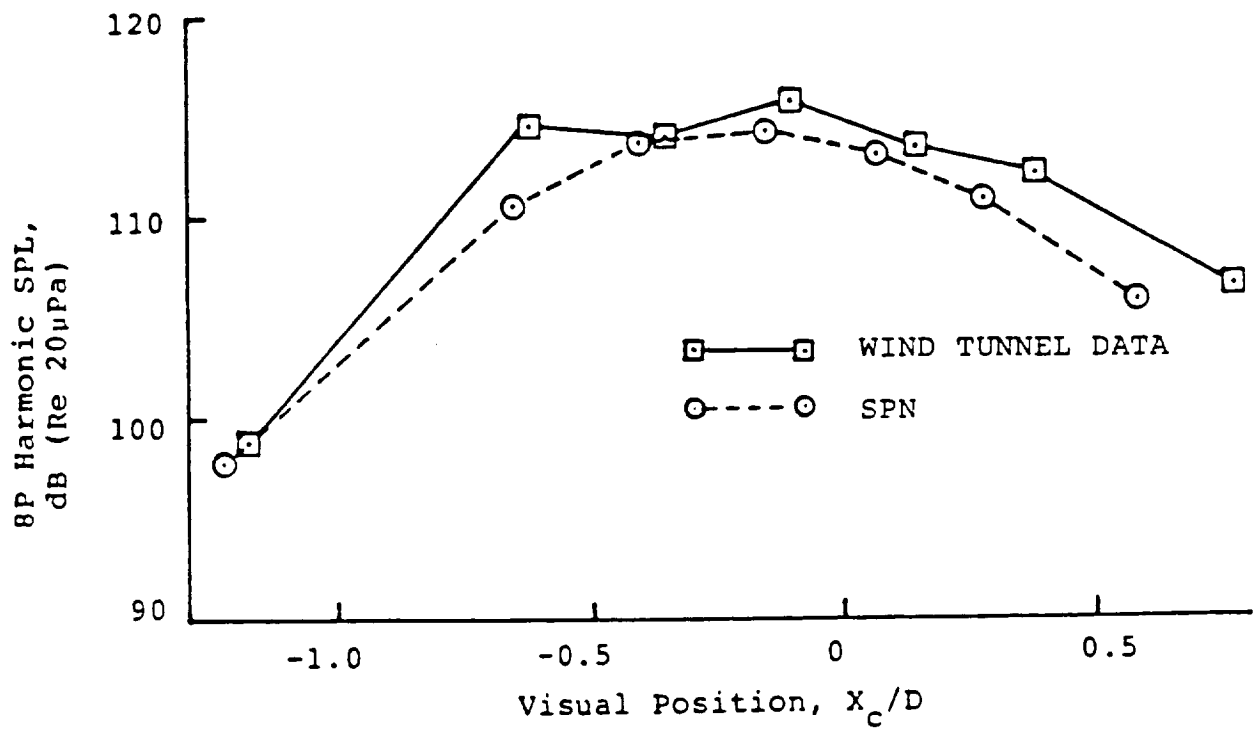


Figure 3.5-12. 8P Harmonic Sound Pressure Level at 0.8D Tip Clearance;  
SR-3 Propeller,  $B = 2$ ,  $M_0 = 0.203$ , 6700 rpm,  $M_{TH} = 0.687$

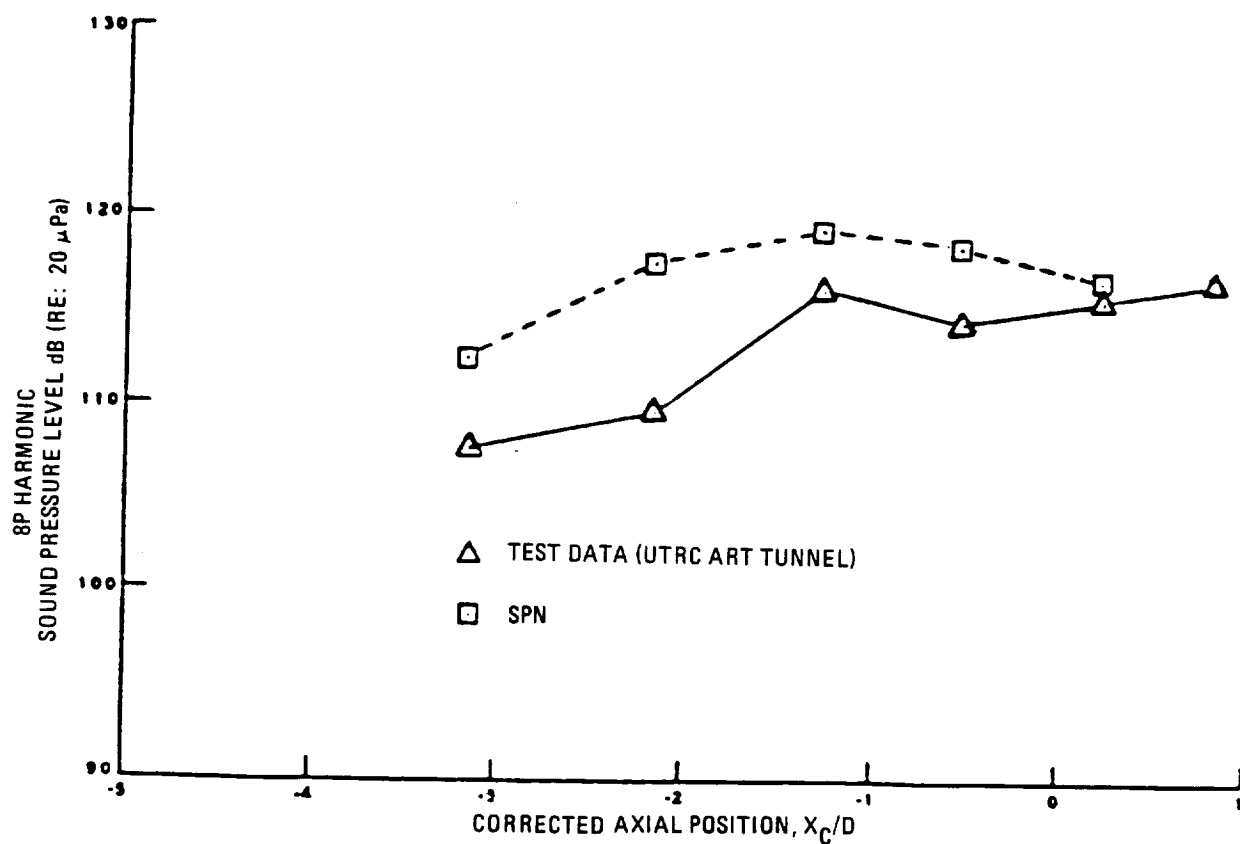


Figure 3.5-13. 8P Harmonic Sound Pressure Level at 4.40 Tip Clearance;  
SR-3 Propeller,  $B = 4$ ,  $M_0 = 0.321$ , 8550 rpm,  $M_{TH} = 0.901$

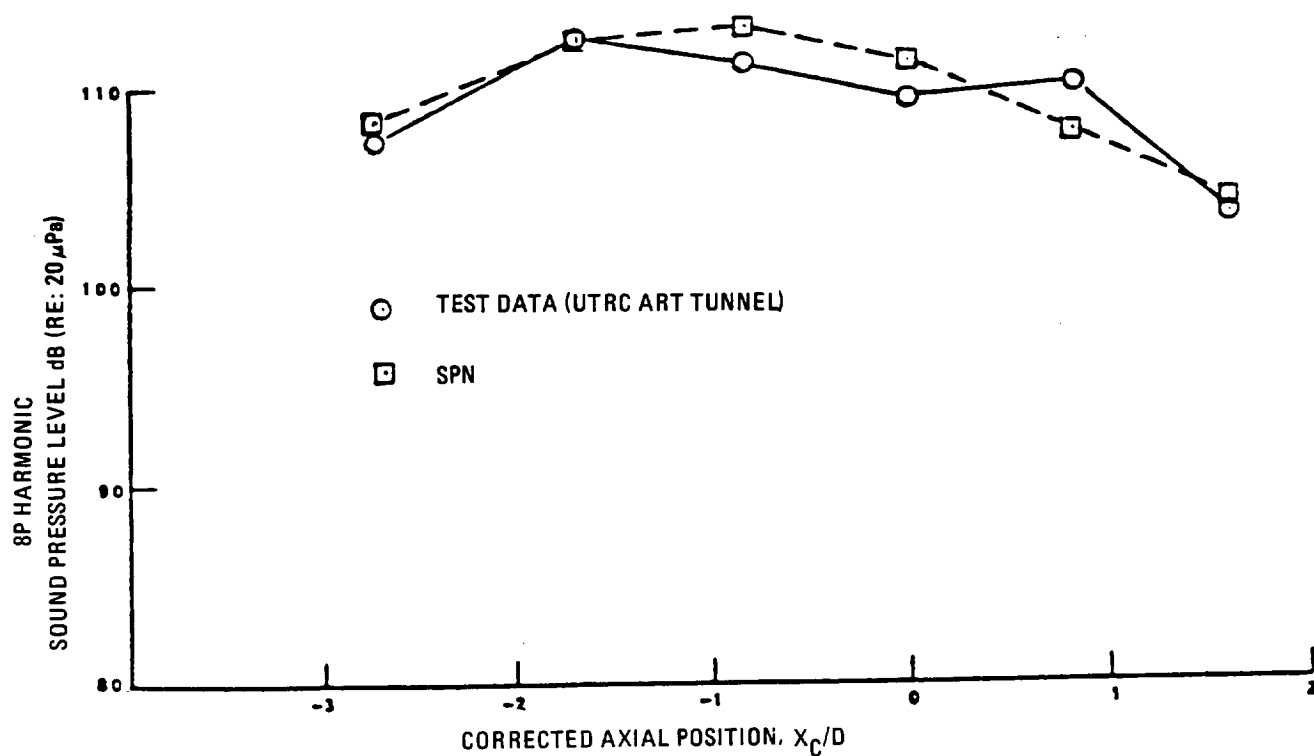


Figure 3.5-14. 8P Harmonic Sound Pressure Level at 4.40 Tip Clearance; SR-3 Propeller,  $B = 2$ ,  $M_0 = 0.203$ , 7500 rpm,  $M_{TH} = 0.671$

between calculation and data for the 0.761 helical tip Mach number case (within 2% for all axial positions), but lesser agreement (within 7%) for the 0.901 helical tip Mach number case. This is most likely due to transonic effects at the higher helical tip Mach number, which are not properly taken into account in SPN.

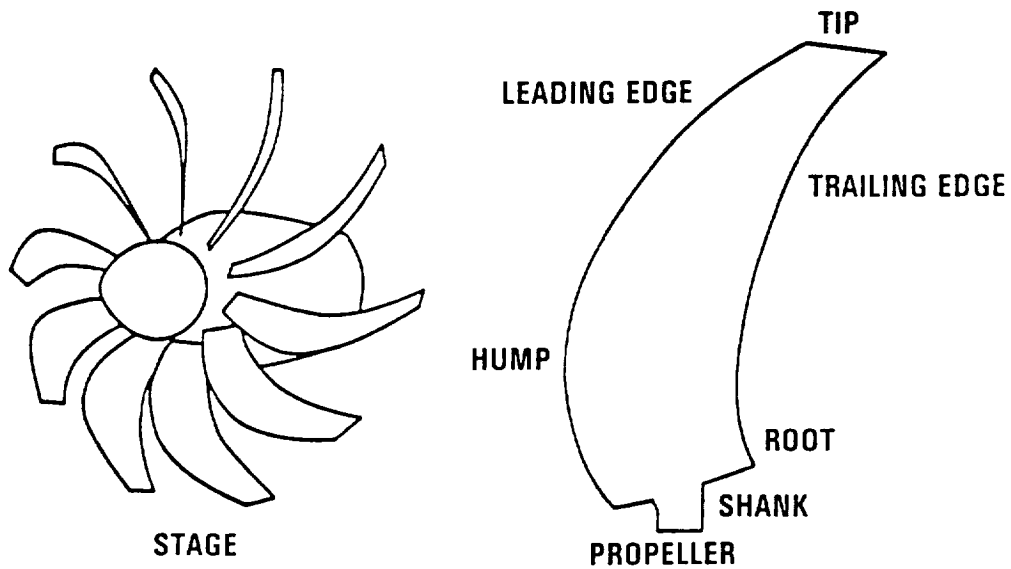
In summary, all required calculations for verification of the acoustics analysis procedure using SPN have been carried out with the exception of the far-field/ground-located microphone case for the 101/16 propeller and the near field/transonic supersonic helical tip Mach number cases for the SR-3 propeller. The former (101/16) case requires the addition of the tone propagation module (TPM) to SPN, which is not currently incorporated into GAPAS. The latter (SR-3) cases require exercising the transonic propeller noise (TPN) module in GAPAS. As previously indicated, the results of the calculation for the SR-3 propeller at a free stream Mach number of 0.8 and helical tip Mach number of 1.14 are discussed in Section 6, which describes the results of the overall GAPAS verification, Task 5.

### 3.6 STRUCTURAL BEAM MODULE

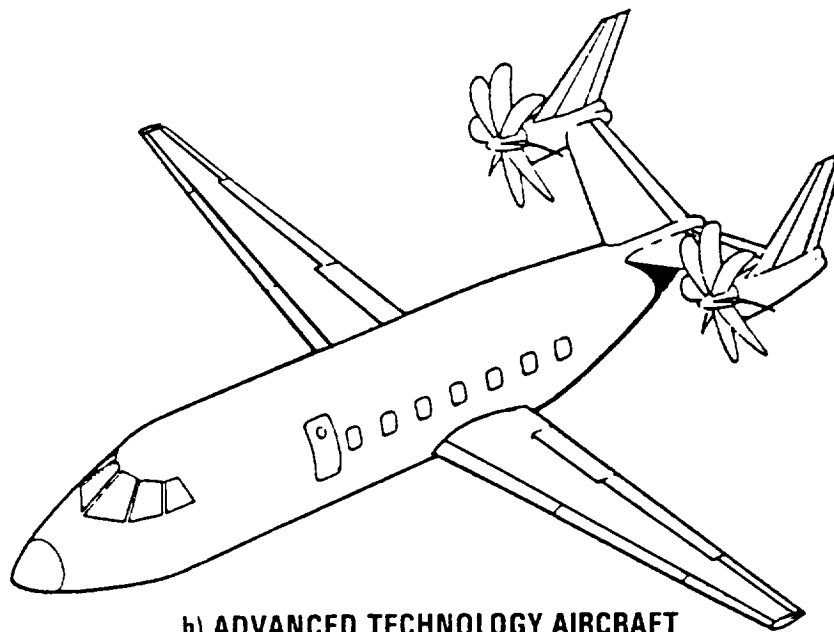
The free vibration analysis of a generally curved and pretwisted rotating blade is a complex problem that requires the development of a nonlinear analytical model. For conventional and advanced blades (advanced prop-fan, Figure 3.6-1), this model must be general enough to account for an arbitrary amount of blade curvature and pretwist, as well as blade cross sections with general prismatic shape. Allowances must also be included to account for changes in the blade orientation at the hub. These changes, which will alter the centrifugal forces of the blade, include a pitch setting for conventional propellers and a general pitch setting about an arbitrary vector for advanced prop-fans (i.e., pitch setting is a linear combination of pitch, precon, and sweep). These blades, which are quite flexible, require a nonlinear theory for deriving the equations of motion in order to properly account for the stiffening effects from the centrifugal forces.

Due to the complexities of this problem, an exact solution cannot be determined, and thus, approximate methods (for example, Ritz, Galerkin, finite element) must be used. The finite element method was chosen because it readily lends itself to the modeling of a curved and twisted blade. The other methods were unattractive because they either required knowing approximate deflection functions (Ritz method) or required deriving the full nonlinear partial differential equations of motion and natural boundaries of the Galerkin's method.

The finite element method, which is based on variational principles, is applied by dividing the blade into subregions, calculating the total dynamic potential ( $U - T - W_e$ ) for each subregion, and then deriving the finite elements by taking the variation of each subregion (Hamilton's principle). In this development, each subregion is defined with straight beam type finite elements which are located along the curved line of shear centers of the blade, Figure 3.6-2. The curved line of shear centers of the blade must be calculated before this analysis can be done. The finite elements for each straight beam are derived with allowances for; arbitrary cross section shape, beam pretwist, cross section warping (St. Venant type warping functions) and nonlinear behavior based on the moderate deflection

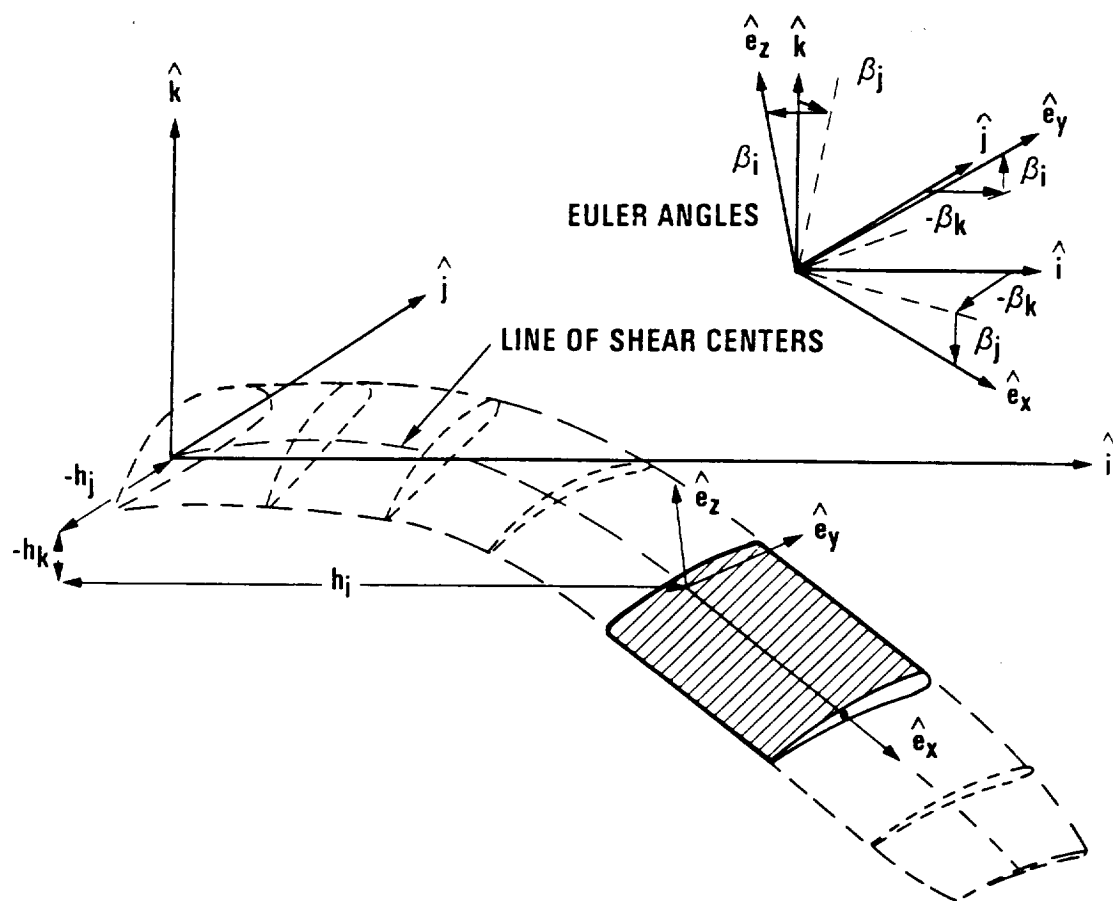


**a) TURBOPROP STAGE AND PROPELLER**



**b) ADVANCED TECHNOLOGY AIRCRAFT**

Figure 3.6-1. Advanced Propeller (Prop-Fan)



**Blade-Fixed ( $i, j, k$ ) and Beam Element ( $e_x, e_y, e_z$ ) Coordinate Systems**

Figure 3.6-2. Propeller Fixed and Beam Element Coordinate Systems



theory (small strains and finite rotations). All of the effects of blade rotation are properly included by allowing the beam element to be arbitrarily positioned within the blade coordinate system, Figure 3.6-2. An ordering scheme is developed to identify and neglect higher order terms which are produced during this development.

A model for the free vibration analysis of a generally curved and pretwisted rotating blade is developed by the following steps: (1) The curved blade is divided into a summation of straight beams which are laid end-to-end along the line of shear centers of the blade. (2) All of the transformation matrices associated with the blade and the straight beam element are derived. (3) The strain energy, kinetic energy, and work of external forces for a beam element are derived. (4) The finite elements associated with a single straight beam are derived by taking a variation of the total dynamic potential (Hamilton's principle). (5) The beam elements are assembled to form a structural model of the blade. (6) The free vibration analysis is calculated using the nonlinear finite element model of the blade.

### 3.6.1 Basic Assumptions Used in the Analysis

The following assumptions are used in the development of a beam finite element model capable of a nonlinear structural dynamic analysis of rotating blades.

- (1) The speed of rotation of the blade is constant.
- (2) The blade is modeled by a series of straight beam finite elements that are located along the line of shear centers of the blade. The cross section for each beam finite element is defined as the section perpendicular to the line of shear centers.
- (3) The shape of the blade cross section is arbitrary (i.e., no simplifying assumptions based on symmetry are made). There are three distinct points on the cross section.
  - (a) Shear center of the cross section. The beam finite element is defined using the shear centers of two adjacent cross sections of the blade. All cross-sectional properties of the beam are defined relative to this point.
  - (b) Area center of the cross section.
  - (c) Center of mass.

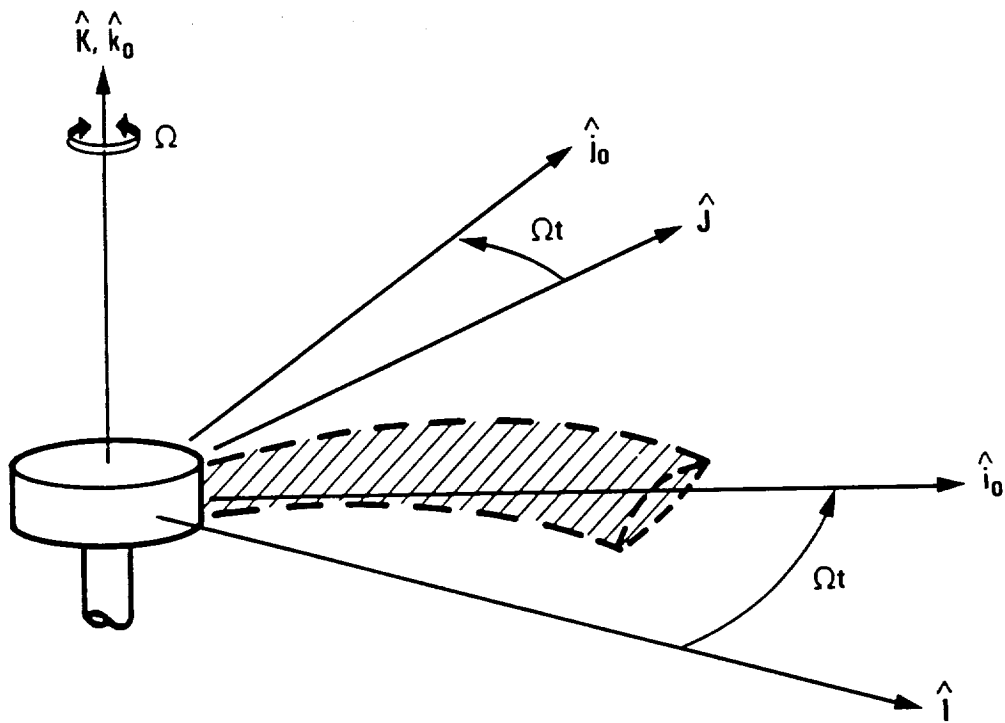
- (4) The beam element has an arbitrary amount of built in pretwist which is defined about the line of shear centers. Pretwist is defined as the change in the angular orientation of the principal axes of the cross section along the beam length.
- (5) The stresses within the cross section ( $\sigma_{yy}, \sigma_{zz}, \sigma_{yz}$ ) are equal to zero. The strains within the cross section ( $\epsilon_{yy}, \epsilon_{zz}, \gamma_{yz}$ ) are allowed to be nonzero, but small (negligible compared to 1).
- (6) The beam can bend in two mutually perpendicular directions normal to the line of shear centers of the beam, and can also twist about this line of shear centers.
- (7) The beam may undergo moderate deflections, which implies small strains and finite rotations.
- (8) An ordering scheme, based on beam theory, is used to identify and neglect higher order terms.
- (9) A warping function is used to model the axial deformation of the beam due to torsional twist.
- (10) The effects of damping (i.e., structural or viscous) have not been included.

### 3.6.2 Geometric Preliminaries

The development of a nonlinear beam finite element model for the analysis of a rotating, pretwisted, blade undergoing moderate deflections requires the use of five coordinate vector sets. The coordinate vector sets are: the element coordinate system ( $\hat{e}_x, \hat{e}_y, \hat{e}_z$ ), the curvilinear coordinate system ( $\hat{e}_x, \hat{e}_\eta, \hat{e}_\zeta$ ), a blade coordinate system, ( $\hat{i}, \hat{j}, \hat{k}$ ), a hub coordinate system ( $\hat{i}_0, \hat{j}_0, \hat{k}_0$ ), and an inertial reference frame ( $\hat{I}, \hat{J}, \hat{K}$ ). These coordinate systems are shown in Figures 3.6-3 through 3.6-5.

The beam finite element and the equations of motion are derived in the element coordinate system ( $\hat{e}_x, \hat{e}_y, \hat{e}_z$ ). This coordinate system is an orthonormal vector set with one vector,  $\hat{e}_x$ , defined along the undeformed line of shear centers of the beam, and the other two vectors,  $\hat{e}_y$  and  $\hat{e}_z$ , defined in the cross section of the beam, Figure 3.6-5. The applied forces of the beam are defined in this system.

The curvilinear coordinate system ( $\hat{e}_x, \hat{e}_\eta, \hat{e}_\zeta$ ) is also associated with the undeformed beam and it is used to account for the axial-bending-torsion coupling effects of a pretwisted beam. The vector,  $\hat{e}_x$ , is defined along



Inertial (I, J, K) and Hub-Fixed ( $i_0, j_0, k_0$ ) Coordinate Systems

Figure 3.6-3. Inertial and Hub-Fixed Coordinate Systems

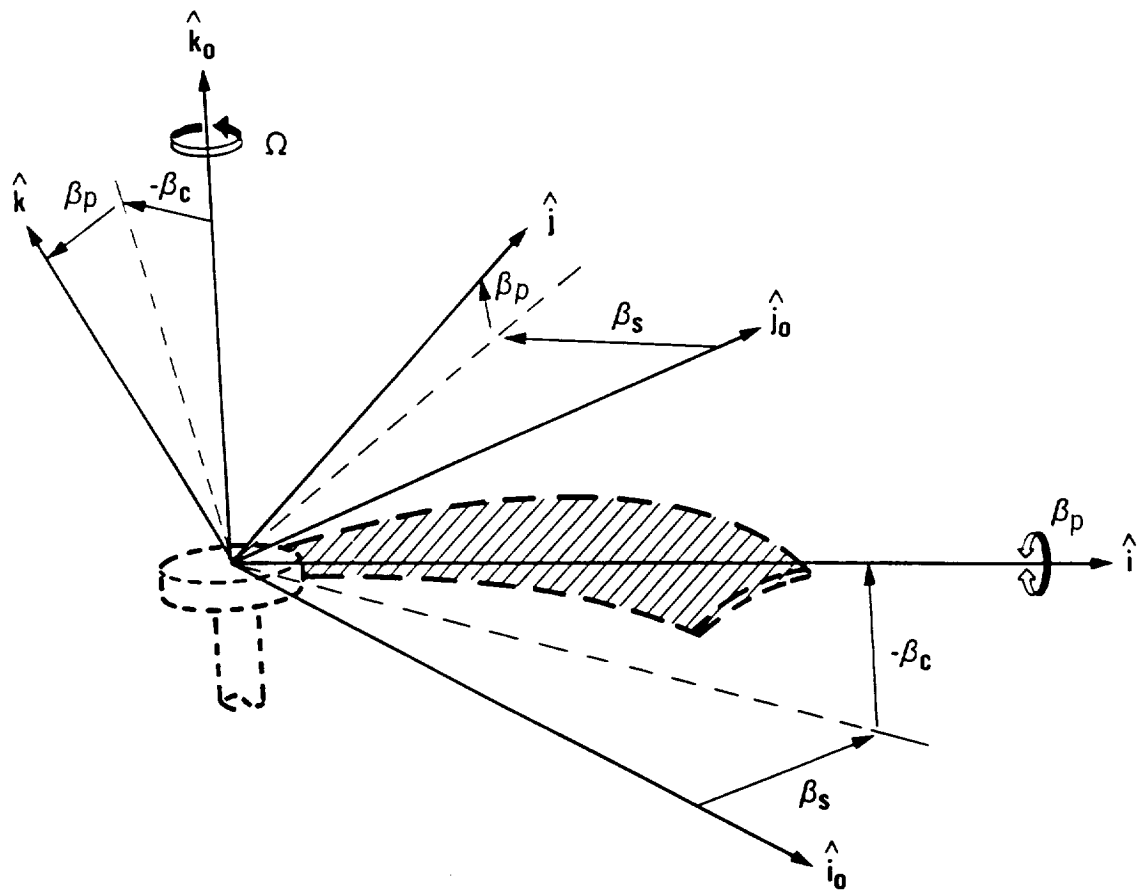


Figure 3.6-4. Hub-Fixed and Propeller-Fixed Coordinate Systems Including Sweep ( $\beta_s$ ), Precone ( $\beta_c$ ), and Pitch ( $\beta_p$ ) Adjustments

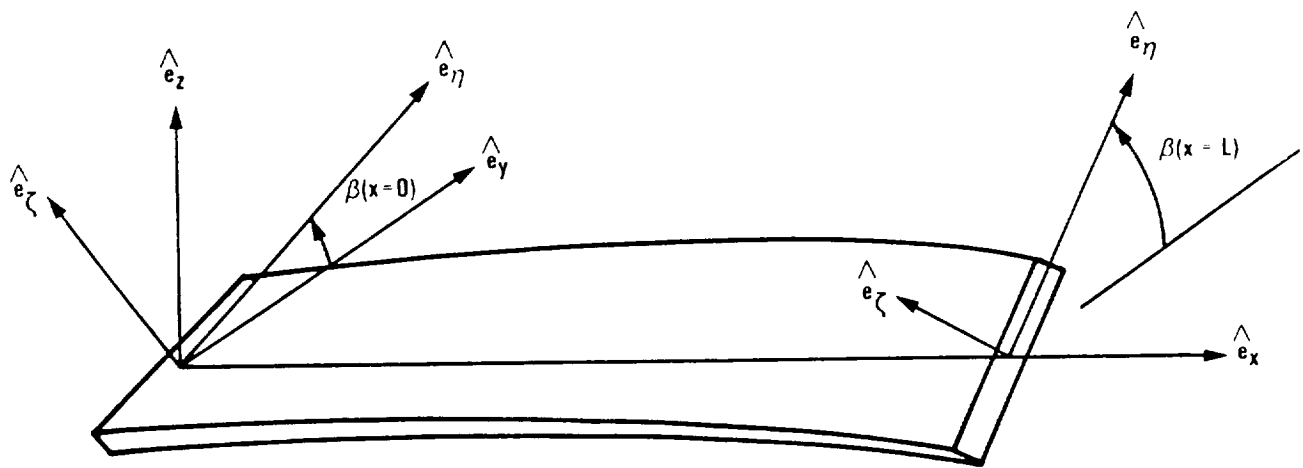


Figure 3.6-5. Element and Curvilinear Coordinate System of Pretwisted Beam Element

the undeformed line of shear centers of the beam element. The two remaining vectors,  $\hat{e}_\eta$  and  $\hat{e}_\zeta$ , are defined in the beam cross section and they rotate about the line of shear centers,  $\hat{e}_x$ , with the pretwist of the beam. These two vectors remain parallel to the principal axes of the beam cross section at any point over the beam length, Figure 3.6-5. The strain components, the material properties, and the cross section warping function are all derived in this system.

The blade coordinate system  $(\hat{i}, \hat{j}, \hat{k})$  rotates with the hub and it is used to define the coordinates and the displacements of the blade. The vector  $\hat{i}$  aligns with the pitch axis of the blade and the vectors  $\hat{j}$  and  $\hat{k}$  are associated with in-plane and out-of-plane displacements of the blade, respectively. All three vectors are orthogonal to each other. The beam finite elements, which are defined in the element coordinate system must first be transformed to this coordinate system before they are assembled along the line of shear centers of the blade.

The hub coordinate system  $(\hat{i}_0, \hat{j}_0, \hat{k}_0)$  is fixed to the rotating hub, where the  $\hat{k}_0$  axis aligns with the spin axis, the  $\hat{i}_0$  axis aligns with the pitch axis, and  $\hat{j}_0$  is perpendicular to both axes and is located in the spin plane. Changes in the pitch setting or precone of the blade are accomplished by changing the orientation of the blade coordinate system with respect to the hub coordinate system.

The inertial reference frame  $(\hat{I}, \hat{J}, \hat{K})$  is fixed in space and it is used to locate the rotating blade, where the  $K$  axis aligns with the spin axis of the hub. The transformations between all the above coordinate systems are required in order to perform the analysis.

### 3.6.3 Ordering Scheme for a Long Slender Beam

An ordering scheme is defined which is used to identify and delete higher order terms that are produced during the derivation of the nonlinear equations of motion for a straight rotating beam. This is accomplished by assigning relative magnitudes to all terms, and then neglecting terms which are considered small in comparison to the largest terms. This approach is in agreement with the ordering scheme developed by other authors (Refs. 3.6-1 and 3.6-2).

The guidelines, which are used for assigning the relative magnitudes, were determined by careful study of the geometry and the deflection patterns of tip-loaded straight cantilever beams. They are valid for most isotropic engineering materials (i.e., aluminum, steel, titanium, etc.) and most fiber-reinforced composite materials (i.e., orthotropic and anisotropic material behavior). The use of fiber-reinforced composite materials will alter the actual deflection patterns of the beam, but these patterns will not exceed the ordering scheme parameters for most engineering applications.

The geometric ratio of the cross section to the length ( $y/L$ ,  $z/L$ ) is taken as 0.2 for a long, slender beam. Defining this ratio as  $\epsilon$ , ( $\epsilon \approx 0.2$ ), and quantities of  $\epsilon^2$  are neglected with respect to unity. The axial coordinate ratio of the beam is taken as unity ( $x/L \approx 1$ ). The pretwist of the beam,  $\beta$ , is defined as a large angle ( $\beta \approx 1$ ). The large angle assumption for pretwist angle,  $\beta$ , will guarantee that all the axial-bending-torsion coupling effects are included in the derivation.

The maximum allowed axial deflection of a cantilever beam is determined by applying an axial tip load that will produce a stress state equal to the material yield stress. The nondimensional axial deflection ( $u/L$ ) is on the order of 0.001-0.008 for most engineering materials.

The maximum torsional deflection that a tip loaded cantilever beam can experience before yielding is calculated based on the octahedral shear stress theory. For a cantilever beam with an elliptical cross section, the maximum torsional deflection ( $\phi$ ) will be on the order of 0.1-0.2, ( $\epsilon$ ).

The maximum planar deflections are determined by applying a tip moment such that the stresses in the beam are equal to the material yield stress. For typical engineering materials, the nondimensional deflections ( $v/L$ ,  $w/L$ ) and slopes ( $v_{,x}$ ,  $w_{,x}$ ) at the tip will be on the order of 0.06-0.15, ( $\epsilon$ ).

The warping deflection ratio ( $\psi/L^2$ ) is defined to be the same order as the axial deflection,  $u$ . This assumption agrees with the exact solutions developed by other authors (Refs. 3.6-3 through 3.6-7), when the cross section exhibits symmetry. Based on this work, the derivatives of the warping function ( $\psi_{,\eta}/L$ ,  $\psi_{,\zeta}/L$ ) are defined as  $\epsilon$ .

A summary of the ordering parameter,  $\epsilon$ :

Order 1:

$$\left. \begin{array}{l} \frac{x}{L} \\ \beta \end{array} \right\} L ( )_{,x} \quad (3.6-1a)$$

Order  $\epsilon$ :

$$\left. \begin{array}{l} \frac{y}{L}, \frac{\eta}{L} \\ \frac{v}{L}, \frac{w}{L} \\ \phi \end{array} \right\} \begin{array}{l} \frac{z}{L}, \frac{\zeta}{L} \\ \frac{\psi_{,x}}{L}, \frac{\psi_{,y}}{L} \\ v_{,x}, w_{,x} \end{array} \quad (3.6-1b)$$

Order  $\epsilon^2$ :

$$\left. \begin{array}{l} \frac{u}{L}, u_{,x} \end{array} \right\} \frac{\psi}{L^2} \quad (3.6-1c)$$

The ordering scheme is applied by determining the relative magnitude of all of the terms of an energy expression. If the largest terms are of order ( $\epsilon^i$ ), then all of the terms of order ( $\epsilon^i$ ) are retained (first-order terms), all of the terms of order ( $\epsilon^{i+1}$ ) are retained (second-order terms), and all of the terms of order ( $\epsilon^{i+2}$ ) or higher are neglected (higher order terms). It is important to apply this ordering scheme to energy-type



expressions because if one equation is ordered differently than another, unbalanced matrices are produced.

#### 3.6.4 Development of Strain Components

A detailed development of the elastic strain components by either a linear or nonlinear approach can be found in many texts that cover the theory of elasticity. In this development, the elastic strain components are derived using a full nonlinear moderate deflection theory based upon the work of Wempner (Ref. 3.6-8). They are derived in a curvilinear coordinate system  $(\hat{e}_x, \hat{e}_\eta, \hat{e}_\zeta)$  so that the effects of beam pretwist are properly accounted for.

The equations of motion and boundary conditions are derived for a beam rotating about an arbitrary axis using Hamilton's principle. These equations are valid for a slender beam which is composed of a homogenous material. The beam is defined so that it can be arbitrarily offset and oriented with respect to the spin axis. This representation includes lengthwise variation in the following properties: beam pretwist, mass and stiffness properties, and mass centroid offset and area centroid offset from the line of shear centers. The external loads are represented by a set of generalized distributed loads and moments, which are defined in the element coordinates axes  $(\hat{e}_x, \hat{e}_y, \hat{e}_z)$ .

The strain energy,  $U$ , is obtained using the strain components and the constitutive relations defined in the curvilinear coordinate system  $(\hat{e}_x, \hat{e}_\eta, \hat{e}_\zeta)$ . The curvilinear coordinate system is chosen because for most applications, where the beam has a uniform cross section with varying pretwist, the cross section properties need only be defined once. If the element coordinate system was chosen, the cross section properties would need to be specified at each node location.

The kinetic energy,  $T$ , is developed by calculating the velocity vector of a point on the deformed beam and using the mass distribution of the cross section. The velocity vector is calculated by taking the time derivative of a position vector from the origin of the inertial reference to a point in the cross section on the deformed rotating beam. This position

vector is capable of modeling a beam with an arbitrary offset and orientation from the inertial reference frame.

The work of external forces,  $W_e$ , is derived by including the effects of the nonconservative forces (i.e., distributed loads and moments) acting through a displacement about the deformed equilibrium position.

Hamilton's principle represents a generalization of the principle of minimum potential energy to include dynamic effects. It is stated as an integral equation in which the total dynamic potential ( $U - T - W_e$ ) is an extremum over the time integral;  $t_1 \leq t \leq t_2$ . A discussion of the principle can be found in Refs. 3.6-9 and 3.6-10.21. Hamilton's principle can be stated in the following mathematical form:

$$\int_{t_1}^{t_2} (\delta U - \delta T - \delta W_e) dt = 0 \quad (3.6-2)$$

The partial differential equations of motion and the associated boundary conditions are calculated by substituting the variation of the strain energy,  $\delta U$ , the variation of the kinetic energy,  $\delta T$  and the virtual work of the external loads into Hamilton's principle. There are two requirements that must be met in order for Hamilton's principle to be identically equal to zero and thus, the total dynamic potential to be an extremum. First, all the terms inside the integral must be identically equal to zero. Since the variations of the displacements and twist are arbitrary over the length of the beam, then in order for all of the terms to be equal to zero, the functions multiplied by these variations must be zero. The four functions that are associated with the four variations are the equations of motion of the beam.

Second, the sum of the equilibrium conditions at the boundary due to the strain energy variation, the kinetic energy variation, and the virtual work, must also be zero at  $x = 0$  and  $x = L$ . These conditions are used to obtain the boundary condition of the beam element.

The resultant equations of motion are a set of nonlinear partial differential equations. They are nonlinear in terms of the space dependent variables. In order to perform the free vibration analysis of a rotating

propeller, these equations are solved by assuming that the displacements are a superposition of functions which are space-dependent and time-dependent. The space dependent displacement functions are determined by solving the time-independent nonlinear partial differential equations (i.e., neglect all time-dependent terms). Introducing this nonlinear space-dependent solution into the nonlinear partial differential equations results in a standard eigenvalue problem for the time-dependent function, the solution to which yields the natural frequencies and mode shapes of the rotating blade.

The solution of the nonlinear partial differential equations can be determined using approximate methods. Three methods that have been used successfully are the Ritz method, the Galerkin method, and the finite element method. A detailed discussion of these methods can be found in References 3.6-11 through 3.6-14. For this analysis, the finite element is applied.

The finite element method is a generalized form of the Ritz method with all of the advantages and few if any of the disadvantages. This method is a piecewise application of the variational method. The solution procedure is not based on solving the nonlinear differential equations of motion, but minimizing the total dynamic potential of the rotating blade. The variation of the total dynamic potential with respect to the displacements is equal to zero when the total dynamic potential is minimized (i.e., apply Hamilton's principle to each subregion).

Writing Hamilton's principle in discretized form,

$$\int_{t_1}^{t_2} \sum_{i=1}^n (\delta U_i - \delta T_i - \delta W_{ei}) dt = 0 \quad (3.6-3)$$

where;

- $n$  = number of finite elements in the model
- $\delta U_i$  = variation of the strain energy in the  $i$ th element
- $\delta T_i$  = variation of the kinetic energy in the  $i$ th element
- $\delta W_{ei}$  = virtual work of the external forces in the  $i$ th element.

The solution for the displacement function will solve the nonlinear differential equations of motion and the natural boundary conditions that are implicitly contained in the total dynamic potential. This has been shown using the calculus of variations (Ref. 3.6-9).

The blade is divided into subregions (beam type finite elements) and the variation of the total dynamic potential is applied to each subregion using a set of interpolation functions for the displacements. Since the interpolation functions are not defined over the entire domain, they are not required to solve the boundary conditions, but they have to satisfy convergence criteria (completeness and continuity).

Both the displacements and variations of displacements are expressed in terms of the product of space-dependent interpolation functions and time-dependent functions.

Substituting the displacements and the variations of the displacements into the  $i^{\text{th}}$  element of the discretized form of Hamilton's principle (Eq. 3.6-3) and carrying out the integration will produce a set of matrix equations.

All of the matrices that are produced represent a complete set of self-adjoint finite elements (i.e., symmetric linear and nonlinear Jacobian matrices and antisymmetric Coriolis matrix). This occurs because the ordering scheme is applied to each of the energies (strain energy, kinetic energy, potential energy) instead of the equations of motion.

Since the virtual displacements are arbitrary over the time integral, then the variation of the deformation array is also arbitrary in the discretized form of Hamilton's principle and the equations of motion can be written in the form:

$$[M]\{\dot{q}\} + [M^C]\{\dot{q}\} + \left( [K^T] + [K^{NL}\{q\}] \right) \{q\} + \{F^T\} = \{0\} \quad (3.6-4)$$

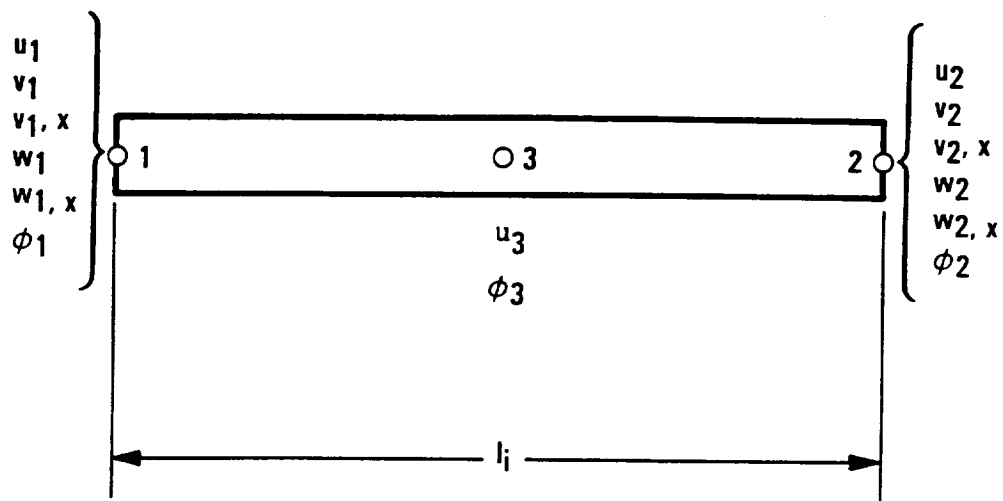
where  $[M]$  is the element mass matrix  $[M^C]$  the Coriolis damping matrix,  $[K^T]$  the linear stiffness matrix,  $[K^{NL}]$  the nonlinear stiffness matrix,  $\{F^T\}$  the force matrix, and  $\{q\}$  the nodal deformations.

In this development, the finite element matrices are generated using Hermite interpolation polynomials that are substituted into the variation of Hamilton's principle. A cubic Hermite interpolation polynomial is used for the planar deflections ( $v, w$ ) and a quadratic Hermite polynomial is used for the axial deflection ( $u$ ) and the torsional rotation ( $\phi$ ).

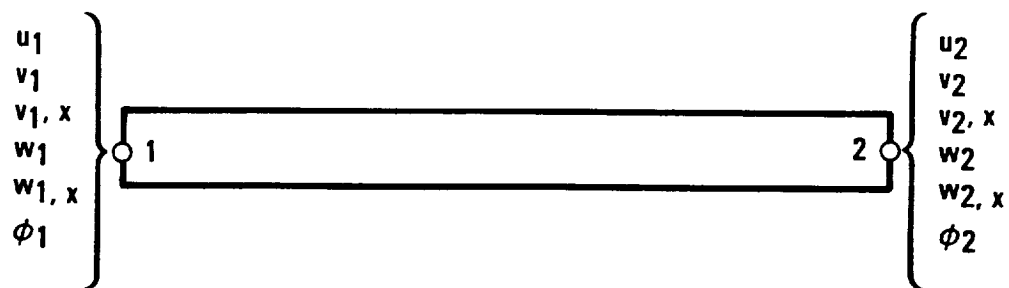
The cubic Hermite interpolation polynomial is ideally suited for the development of the beam bending finite element for the following reasons. It guarantees uniform convergence by having the required rigid body displacement, rigid body rotation, and constant curvature modes. The bending strains vary linearly over the element length, which goes beyond the requirement of a constant strain mode. The resulting elements using this polynomial will have interelement compatibility for both displacements and slopes. The nodal parameters are the displacements and slopes at either end of the beam.

The quadratic Hermite interpolation polynomial was chosen for the axial deflection ( $u$ ) and the torsional rotation ( $\phi$ ) because it has a higher level of accuracy than the linear Hermite interpolation polynomial. This same torsional model (i.e. quadratic polynomial) was used successfully in previous finite element studies of helicopter rotor aeroelasticity (Ref. 3.6-12). Both the linear and the quadratic polynomials satisfy all the convergence requirements, but the quadratic polynomial also has capability of modeling the linear variation of strain along the element length. The quadratic polynomial is used to generate an axial and a torsion element which has the same level of accuracy as the beam bending element. This allows the discretization of the model for torsion or axially loaded analysis to be the same as for a bending analysis. The nodal parameters for the axial element and the torsion element are chosen as the two element boundaries and the element mid-point.

The resulting beam finite element has 14 nodal parameters; 4 in-plane deflections, 4 out-of-plane deflections, 3 axial deflections and 3 torsion deflections. They are defined as 6 parameters (3 deflections, 3 rotations) at each end of the beam and 2 parameters (1 axial deflection, 1 torsion deflection) at the mid-point of the element (Figure 3.6-6). The mid-point node is condensed from the element after formation using the assumption



a) VIRGIN FORM—14 NODAL DEGREES OF FREEDOM



b) AFTER CONDENSATION—12 NODAL DEGREES OF FREEDOM

Figure 3.6-6. Beam-Type Finite Element

that the axial and torsion loads on the element can be fully described using the two end nodes only (i.e., external loads on the mid-point node are equal to zero). Condensing out the mid-point node will reduce size of the matrices and the bandwidth of the overall model without sacrificing the accuracy of the calculation.

The removal of the mid-point node is done by either static condensation (Ref. 3.6-13) or Guyan reduction (Ref. 3.6-15). In this study, static condensation is used to eliminate the element mid-point node from the static equations of equilibrium. Guyan reduction is used to eliminate the element mid-point node from the dynamic equations of motion. The beam finite element in its final form will have 12 nodal parameters; 3 deflections and 3 rotations at each end of the beam.

All of the beam finite elements are defined with a linear variation in properties and loads between the two end nodes. This will increase the convergence rate and reduce the number of elements that are required for modeling nonuniform blades.

Assembly of the finite elements into system matrices and enforcement of the geometric boundary conditions is handled as in the conventional finite element method (Ref. 3.6-14).

The solution of the structural dynamic analysis of the rotating propeller is accomplished in two steps. The first step is to solve for the nonlinear static equilibrium position of the blade using a Newton-Raphson iteration scheme; this procedure has been used in similar studies (Ref. 3.6-11 and 3.6-12). The second step is to solve for the natural frequencies of vibration of the nonlinear equations of motion by assuming that the motion is a small linear perturbation about the static equilibrium position. Details of the equations of methodology are given in the User's Manual.

The solution for the nonlinear static equilibrium position is accomplished by neglecting the time-dependent terms in the equations of motion and using a Newton-Raphson iteration scheme to solve the nonlinear equations of equilibrium. The Newton-Raphson scheme, which is based on a

Taylor series expansion, has proven itself as one of the best solution techniques available in geometrically nonlinear analyses (Ref. 3.6-16) and is used routinely in rotor blade dynamics (Refs. 3.6-11 and 3.6-12). This method is extremely accurate and possesses second order convergence. In this study, the iteration is considered to have converged when the absolute change of all the deformations is less than  $10^{-4}$  for each cycle.

For the case of free vibration for a rotating blade, the nonlinear equilibrium state of the blade can be considered to be independent of time. Thus the static equations of equilibrium of the rotating blade are obtained by neglecting the time dependent terms:

$$\{f(q)\} = \left[ [K^T] + [K^{NL}\{q\}] \right] \{q\} + \{F^T\} = \{0\} \quad (3.6-5)$$

The linear solution of the nonlinear equations of equilibrium is calculated during the first cycle of the iteration scheme, because the initial guess in the iteration is taken by setting all of the nonlinear effects equal to zero. Once the iteration converges to the steady-state equilibrium position, the element forces, the hub shear forces and moments, and the stresses are then calculated within the blade.

The calculation of the mode shapes and natural frequencies of vibration of the rotating blade are calculated by linearizing the nonlinear equations of motion. This is accomplished by assuming that the vibration is a small linear perturbation,  $\{\Delta q\}$ , about the nonlinear static equilibrium position, and neglecting products of the perturbation quantities (i.e.,  $\Delta q_i \Delta q_j = 0$ ).

$$[M] \{\dot{\Delta q}\} + [M^C] \{\Delta \dot{q}\} + \left[ [K^T] + [J^{NL}\{q\}] \right] \{\Delta q\} = \{0\} \quad (3.6-6)$$

$n$

Since the effects of structural damping have been neglected, the above equation will reduce to a standard eigenvalue problem (Ref. 3.6-17).

The linearized equations of motion can be written as:

$$[M] \{\dot{\Delta q}\} + \left[ [K^T] + [J^{NL}\{q\}] \right] \{\Delta q\} = \{0\} \quad (3.6-7)$$

$n$



Equations (3.6-7) are solved by standard eigenvalue techniques. The calculated eigenvalues are the squares of the natural frequencies of vibration and the corresponding eigenvectors are equal to the mode shapes.

### 3.6.5 Verification of Beam Model

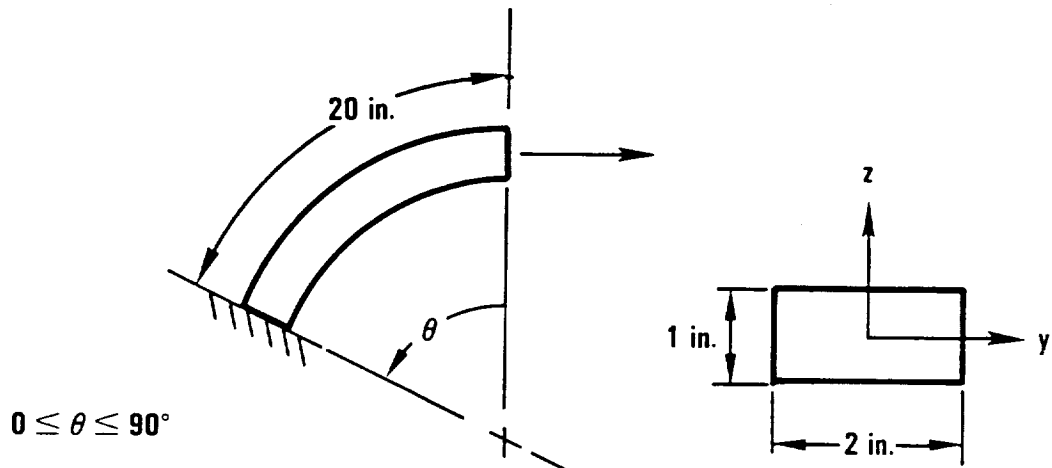
Numerical results aimed at illustrating the characteristics and behavior of the nonlinear rotating beam finite element model, will be presented. The results are divided into two separate groups. The first group of results are used to illustrate a few of the analyses that were done to verify the model. This included comparisons of linear and nonlinear, static and dynamic results with known analytical and experimental solutions. The second group of results is described in Section 6 wherein the methodology is applied to two propellers.

#### 3.6.5.1 Sample Calculations

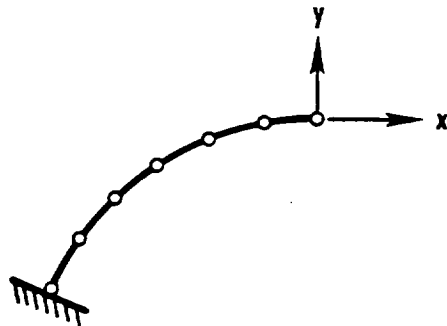
Part of the initial verification of this model was to test its ability to analyze curved beams. An analysis of a tip-loaded circular cantilever beam was done using the present finite element model, Figure 3.6-7. A series of tests were performed for different radii of curvature and the solutions were compared with known analytical results (Ref. 3.6-18). The beam finite element model consisted of six finite elements that were placed along the curved elastic axis of the beam. Six different tip loads (i.e., three tip forces, three tip moments) were applied separately to the model and the tip displacements were calculated for fixed values of beam curvature. Excellent results (Figures 3.6-8 through 3.6-10) were obtained as the curvature of the beam varied from zero degrees (straight cantilever beam) to 90 degrees (semicircular cantilever beam).

The calculation of the natural frequencies and mode shapes of a curved beam were performed and a comparison was made with known analytical solutions (Ref. 3.6-8). This part of the verification of the model was slightly more difficult since even though numerous results for straight beams are available, there are very few closed form results that exist for curved beams. This is because the mode shapes for curved beams are geometrically coupled together and their definition is usually described in either two- or three-dimensions.

**MATERIAL: ALUMINUM - 6061 T6**

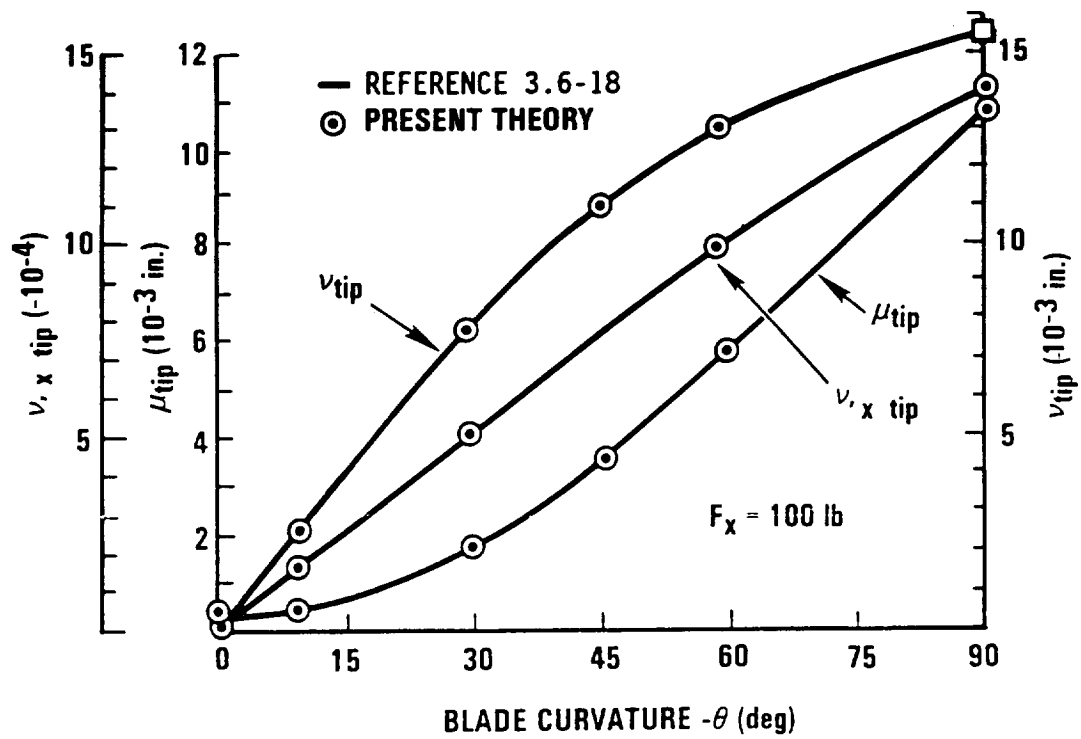


**A) DESCRIPTION OF CURVED BEAM**

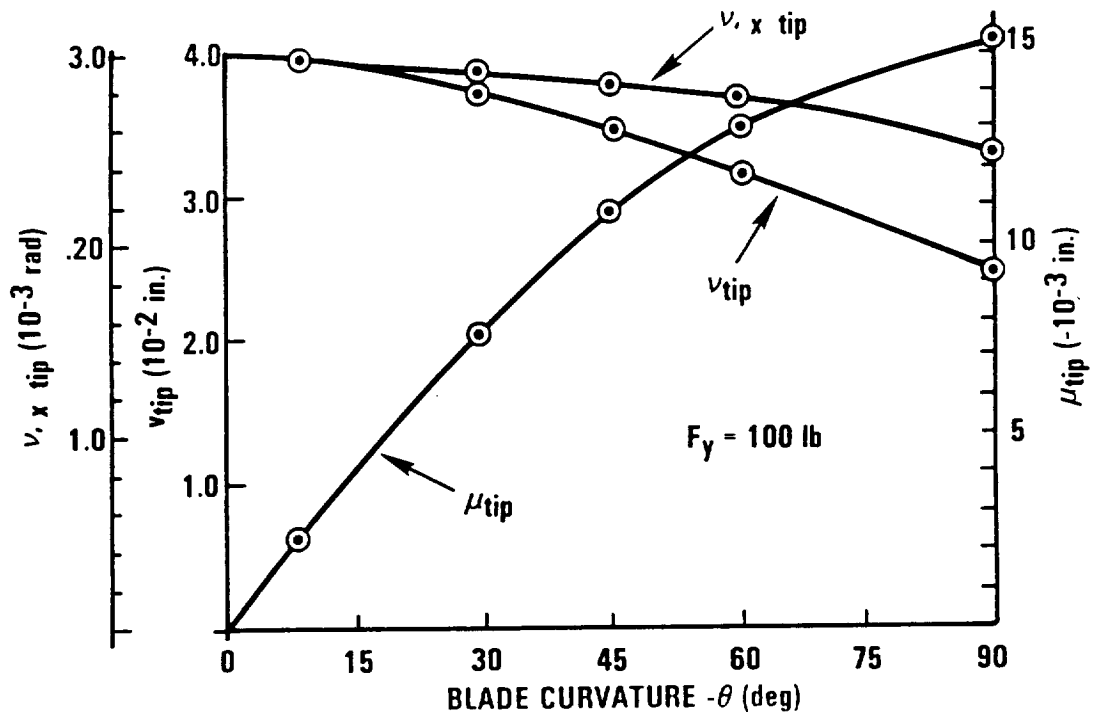


**B) FINITE ELEMENT REPRESENTATION (6 ELEMENTS)**

Figure 3.6-7. Tip-Loaded Analysis of Curved Cantilever Beam

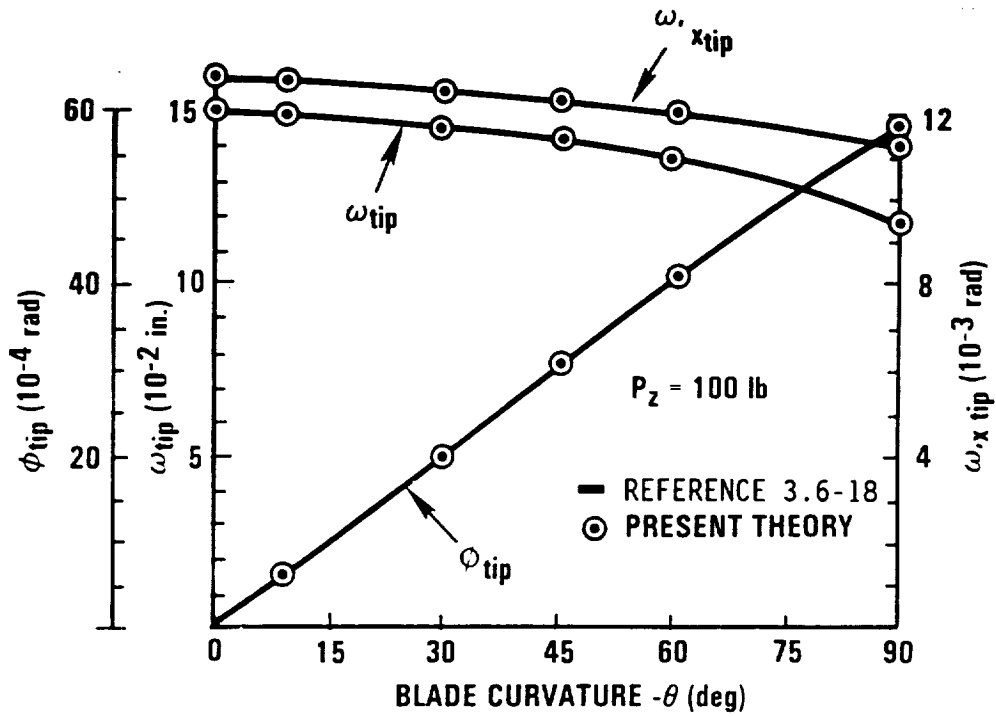


a) Applied axial force

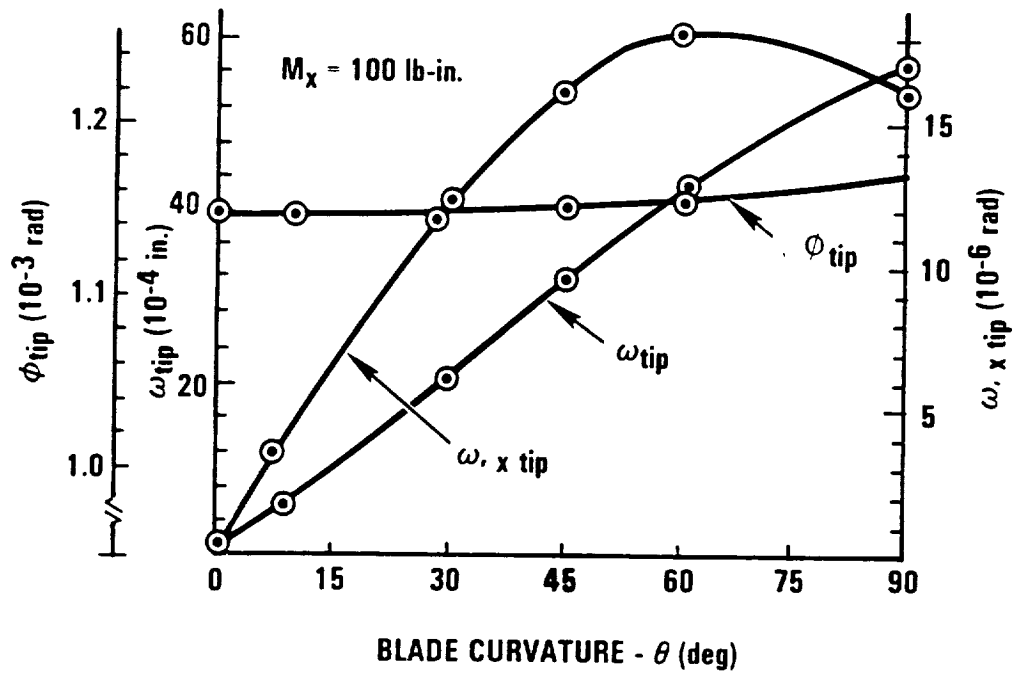


b) In-plane transverse shear force

Figure 3.6-8. Tip Displacements for a Tip-Loaded Curved Cantilever Beam

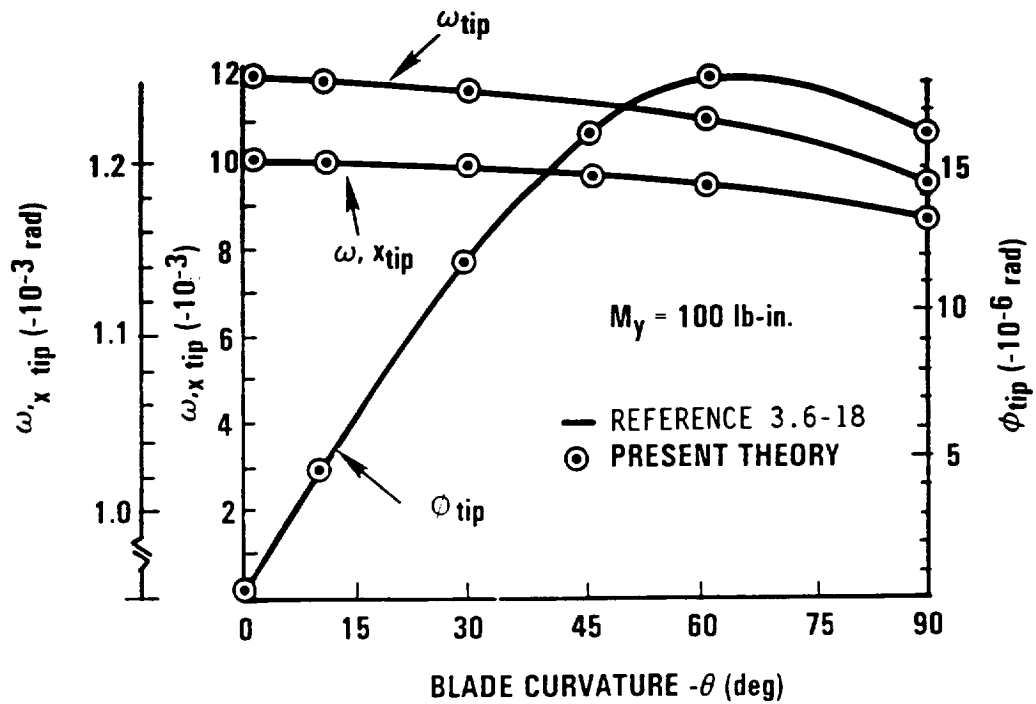


a) Applied out-of-plane transverse force

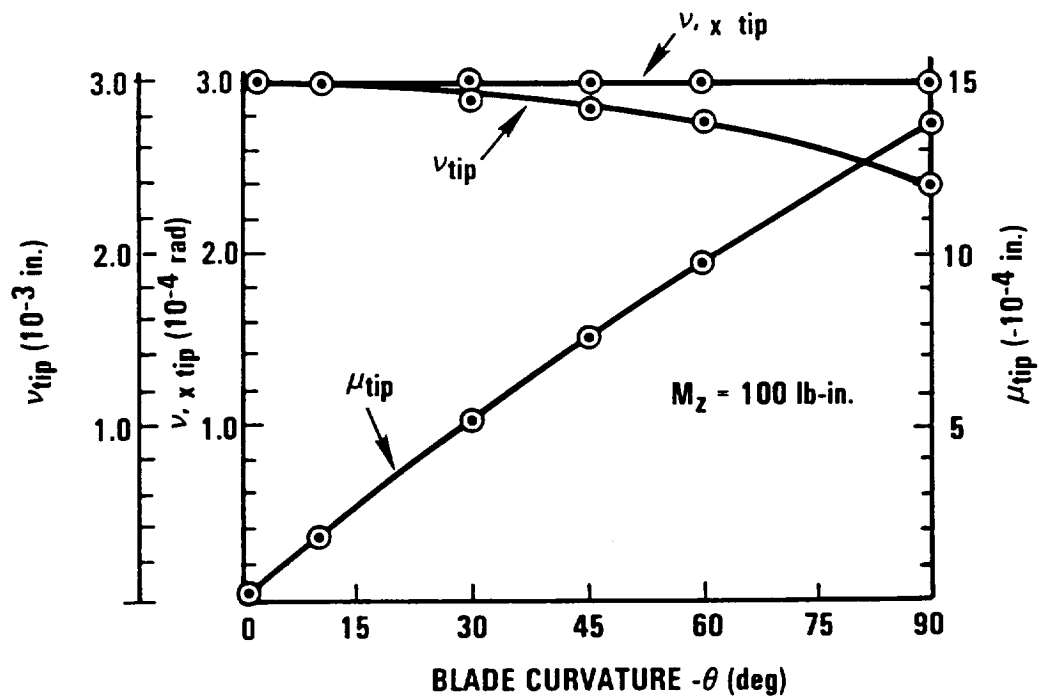


b) Torsion moment

Figure 3.6-9. Tip Displacements for a Tip Loaded Curved Cantilever Beam



a) Applied out-of-plane bending moment



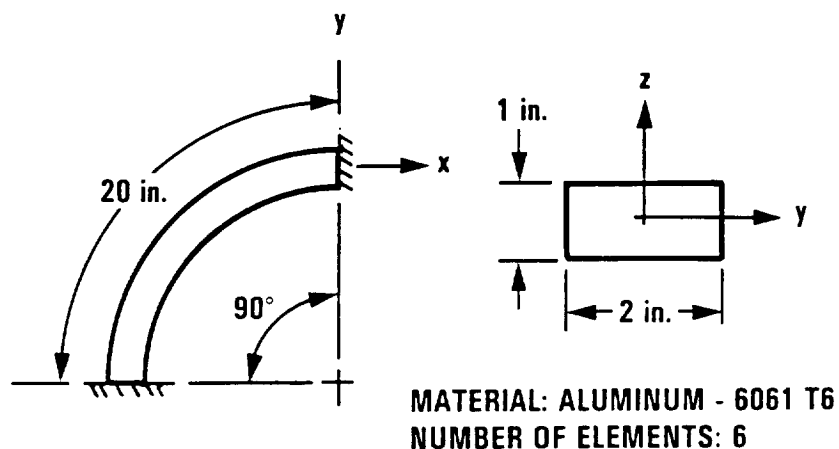
b) In-plane bending moment

Figure 3.6-10. Tip Displacements for a Tip Loaded Curved Cantilever Beam

The natural frequencies and mode shapes for a straight cantilever beam were calculated, using six finite elements, and a comparison was made with analytical results (Ref. 3.6-19, p. 108). Excellent agreement was obtained for the first 11 mode shapes and frequencies, errors of less than 0.5% were found between the analytical solution and the present model.

The natural frequencies and mode shapes of a clamped-clamped semi-circular arc were calculated and the solutions were compared with analytical results (Ref. 3.6-19, p. 207-208), see Figure 3.6-11. Six finite elements were placed along the curved elastic axis of the beam and the first eight eigenvalues and eigenvectors were determined. These mode shapes were compared with the analytical solutions for the in-plane flexural modes and the first out-of-plane flexure mode. From Figure 3.6-11 it can be observed that a good correlation between the finite element model and the analytical solution was obtained for very few finite elements. A comparison of the torsion modes and the higher order out-of-plane flexural modes could not be done because an analytical solution could not be found.

A study was also done to see how the natural frequencies and mode shapes of a cantilever beam would vary as in-plane, out-of-plane, and pre-twisted curvatures were introduced. The definition of the geometry of the beam and the results are presented in Figures 3.6-12 through 3.6-14. A series of analyses were performed by starting with a straight cantilever beam and increasing the in-plane curvature (Figure 3.6-12). The results of this study show that introducing in-plane curvature will cause a slight reduction in the natural frequencies of the out-of-plane modes (z direction) over the complete range of curvatures. This can be accounted for by noting that, as curvature is introduced into the beam, the beam is actually becoming shorter (in the x direction) and the mass effects are no longer evenly distributed, but are concentrated closer to the tip. This shortening of the beam and shifting of the mass center of the beam will lower the natural frequencies of the out-of-plane modes. A sharp increase in the first torsion natural frequency and a sharp decrease in the third z natural frequency in the region of high in-plane curvatures can be accounted for due to the geometric coupling.

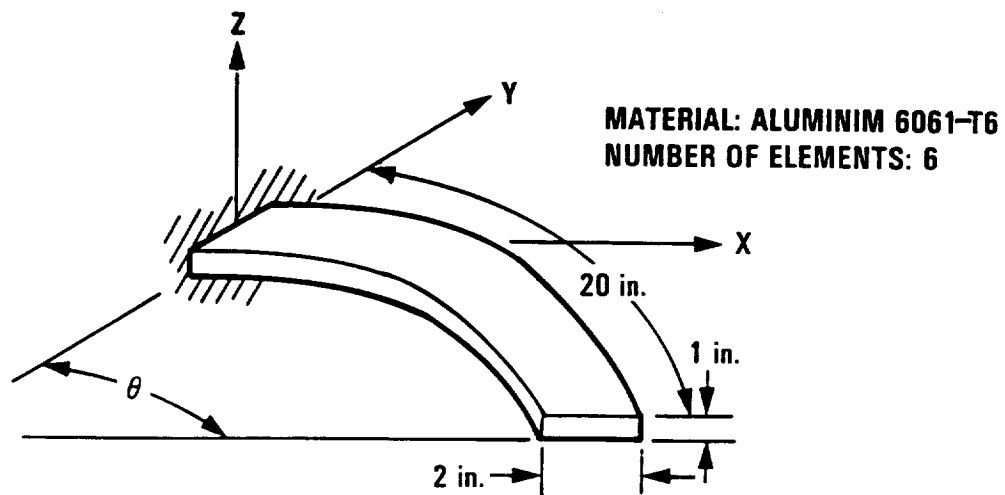


A) DESCRIPTION OF CURVED BEAM

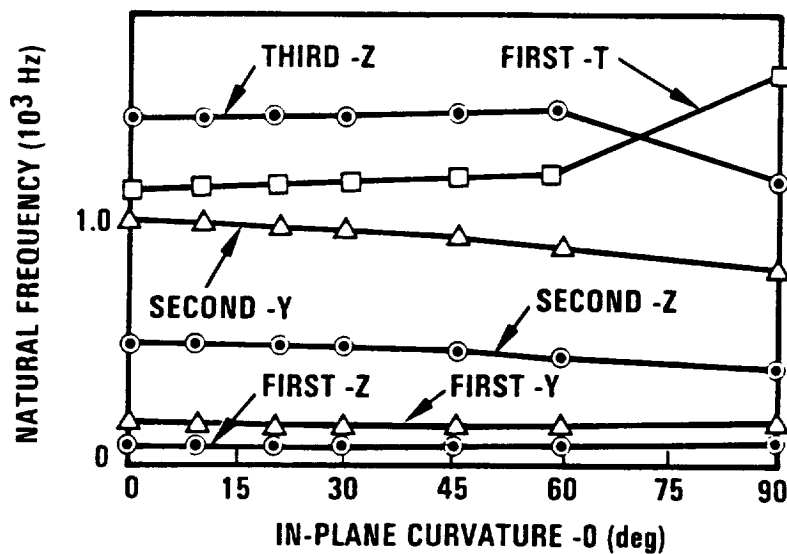
MODE DESCRIPTION	PRESENT THEORY EIGENVALUE (Hz)	REFERENCE 3.6-19 EIGENVALUE (Hz)	ERROR (%)
FIRST OUT-OF-PLANE FLEXURE	472.21	473.2	0.21
SECOND OUT-OF-PLANE FLEXURE	1343.8		
FIRST IN-PLANE FLEXURE (HOOP)	2237.26	2277.5	1.8
SECOND IN-PLANE FLEXURE	2494.7	2542.5	1.9
FIRST TORSION	2578.3		
THIRD OUT-OF-PLANE FLEXURE	2716.2		
FOURTH OUT-OF-PLANE FLEXURE	4537.6		
SECOND TORSION	4953.6		

B) COMPARISON OF PRESENT THEORY WITH PREVIOUS CLOSED FORM SOLUTIONS  
REFERENCE 3.6-19

Figure 3.6-11. Natural Frequency Calculation of a Clamped-Clamped Circular Arc Beam



A) DESCRIPTION OF CANTILEVER BEAM WITH IN-PLANE CURVATURE

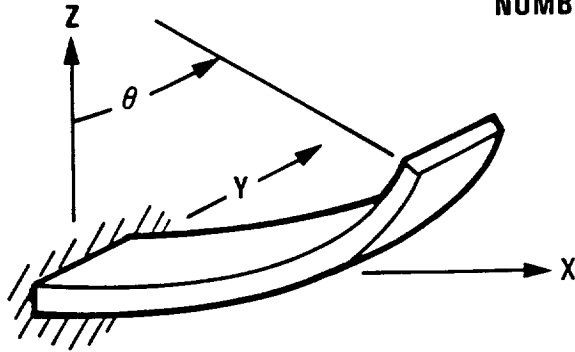


B) NATURAL FREQUENCY OF CANTILEVER BEAM

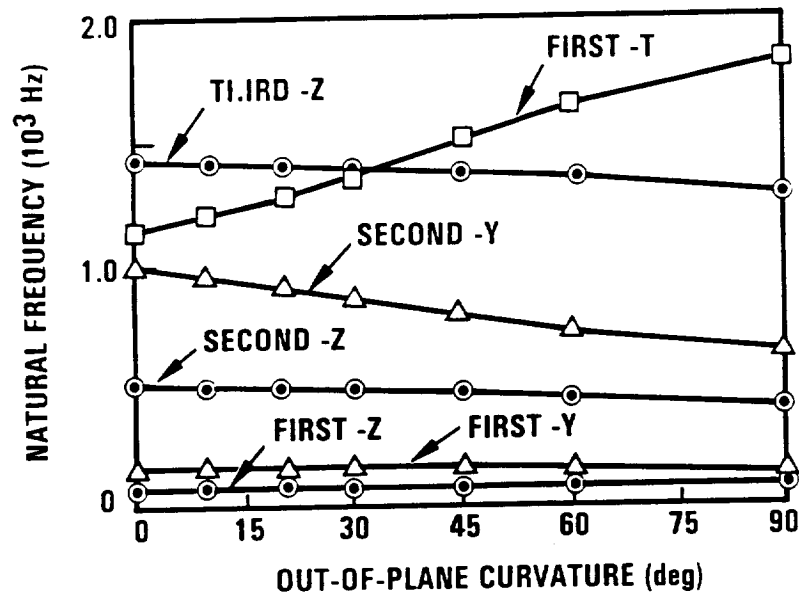
Figure 3.6-12. Natural Frequency Calculation of a Cantilever Beam with In-Plane Curvature



**MATERIAL: ALUMINIM 6061-T6**  
**NUMBER OF ELEMENTS: 6**



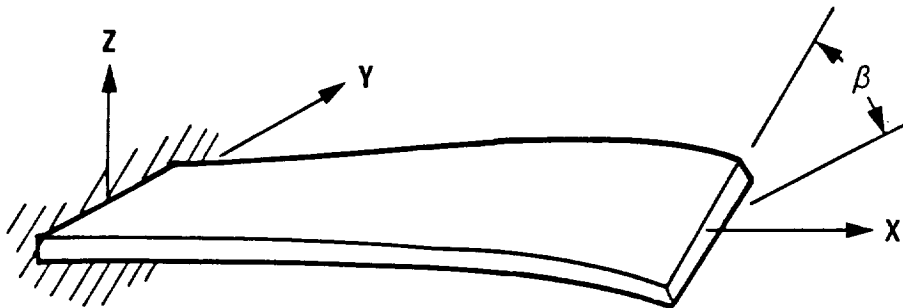
**A) DESCRIPTION OF CANTILEVER BEAM WITH OUT-OF-PLANE CURVATURE**



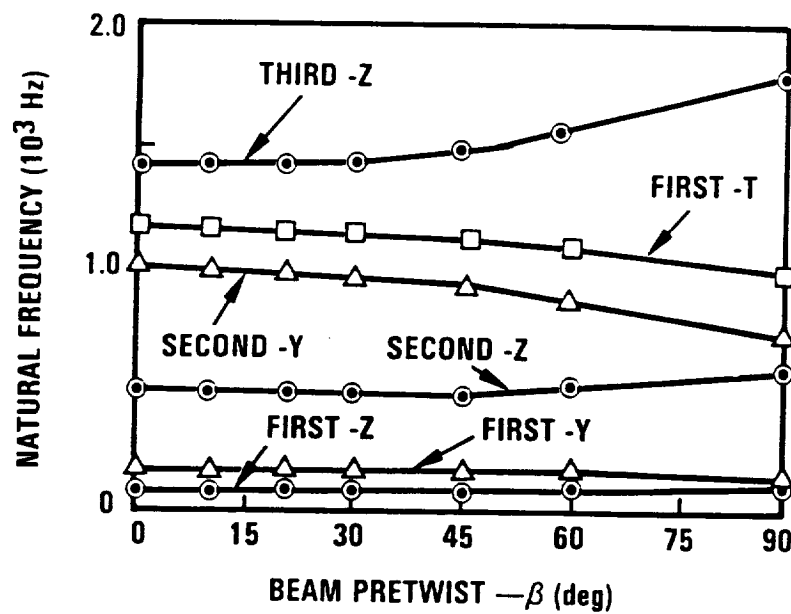
**B) NATURAL FREQUENCIES OF CANTILEVER BEAM**

Figure 3.6-13. Natural Frequency Calculation of a Cantilever Beam with Out-of-Plane Curvature

MATERIAL: ALUMINIM 6061-T6  
NUMBER OF ELEMENTS: 6



A) DESCRIPTION OF PRETWISTED CANTILEVER BEAM



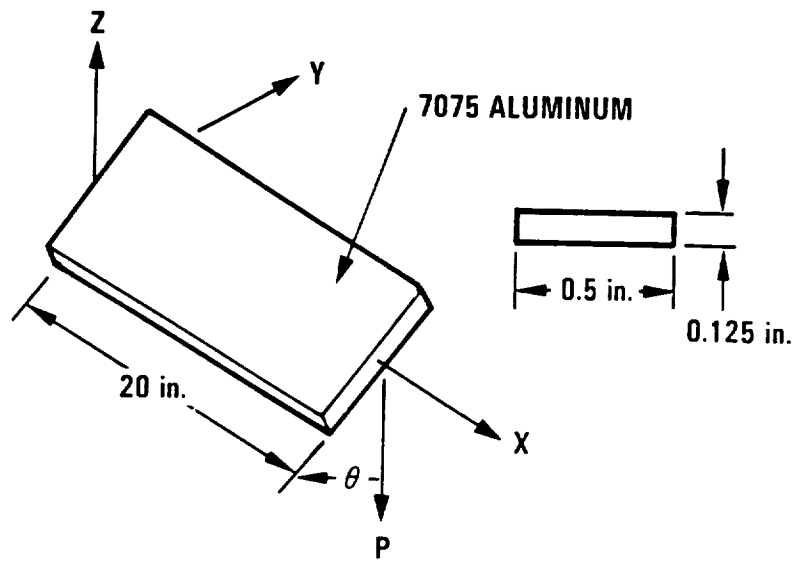
B) NATURAL FREQUENCIES OF CANTILEVER BEAM

Figure 3.6-14. Natural Frequency Calculation of a Pretwisted Cantilever Beam

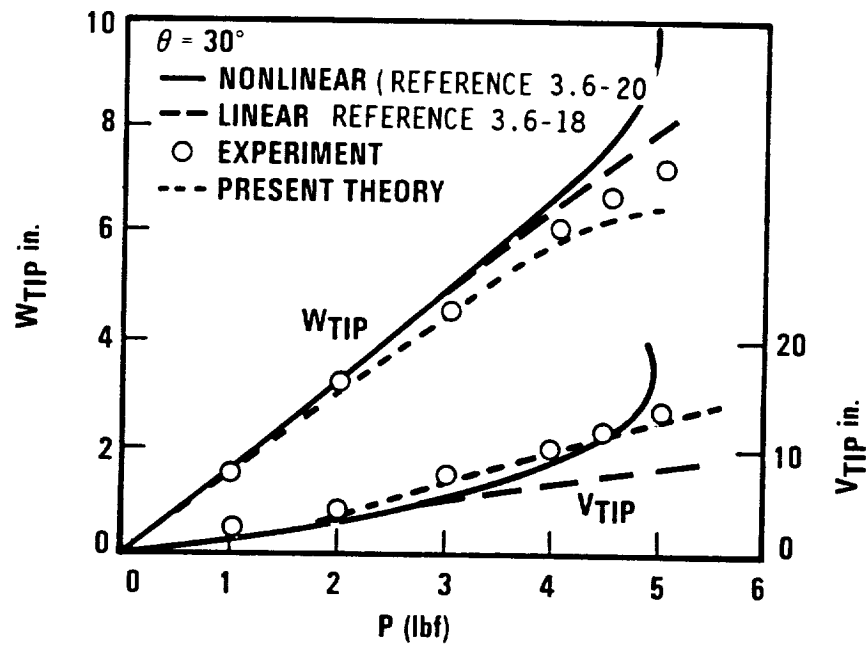
The introduction of out-of-plane curvature into the cantilever beam model will produce effects that are very similar to the effects of in-plane curvature (Figure 3.6-13). Out-of-plane curvature will generally lower both the in-plane and out-of-plane natural frequencies of the beam because of the geometric shortening and shifting of the mass center that is taking place. The natural frequency for the first torsion mode increases as out-of-plane curvature is added to this model, due to the geometric coupling between the torsion mode and the in-plane motion.

The incorporation of a uniform distribution of pretwist along the beam length will cause the in-plane and out-of-plane natural frequencies to coalesce, Figure 3.6-14. This can be accounted for due to the geometric coupling that is introduced between the in-plane and out-of-plane degrees of freedom. The first torsion natural frequency also decreases due to the incorporation of beam pretwist that reduces the torsional stiffness of the model.

The nonlinear terms associated with the moderate deflection theory were verified using experimental results that were obtained by loading a straight cantilever beam in the moderate deflection regime, Figure 3.6-15. The results of the calculations using this finite element model were identical to the results produced by Rosen and Friedmann (Refs. 3.6-2 and 3.6-20). This was expected because when the effects of beam pretwist and curvature are neglected, the equations developed by the present theory will reduce to the equations of Rosen and Friedmann (Ref. 3.6-2). One of the figures from their paper has been included to show how this theory compares with the other theories. From Figure 3.6-15b, it can be observed that the present theory follows the experimental results very closely in nonlinear range whereas as the linear theory falls away and theory developed by Hodges and Dowell (Ref. 3.6-1) appears to be unstable. Further discussion of the comparison between the different theories can be found in Reference 3.6-20.



A) DESCRIPTION OF CANTILEVER BEAM



B) TIP DEFLECTIONS OF THE BEAM

Figure 3.6-15. Uniform Cantilevered Beam Under Transverse Loading

### 3.7 AEROELASTICITY MODULE

The assurance of satisfactory structural dynamic behavior, in particular aeroelastic (flutter) stability, requires an accurate aeroelastic analysis specifically directed to the particular characteristics of advanced propeller designs. Prior to presenting the results of test cases using the G400-PROP code, an overview is given of the important details of the G400-PROP aeroelastic analysis procedure developed to satisfy the analysis requirements of advanced propeller designs. This code is a modification of the G400 Helicopter Rotor Aeroelastic Analysis. These modifications involved removing the modules specialized for helicopter analysis and adding modules for generating an equivalent "straightened-out" propeller (i.e., equivalent straight rotor) out of a swept advanced propeller. Significant work was also done to extend the aerodynamic modules for higher Mach numbers.

This code was originally too large to be considered as a possible option for GAPAS due to the size constraints of the executive system. A new version of this code has been written with all of the options of the original code, but with a significant reduction in size so that it can be utilized in GAPAS. The reduced version, however, is still too large to be part of the unified analysis system and thus the G400-PROP code will be used as a stand-alone code on the NASA computer. This would require appropriate input data to be generated by the GAPAS code in the form of an input file for the G400-PROP code. The "reduced" version of the code is still under development and debugging of the code is underway. The reduced version of the code is currently not able to reproduce the time-history results of the original version of G400-PROP. Calculations, which were performed using the original version of the code, are presented. Time-history and stability solutions were generated for an NASA SR-2 (straight) propeller at various rotational speeds.

The analysis of swept propellers using this code has not been investigated, because the original version of the G400-PROP code did not have a capability for generating the line of shear centers and the structural constants. The capability for generating these properties now exists (GAPAS Geometry Generator), however, a reliable version of the G400-PROP code is not available.

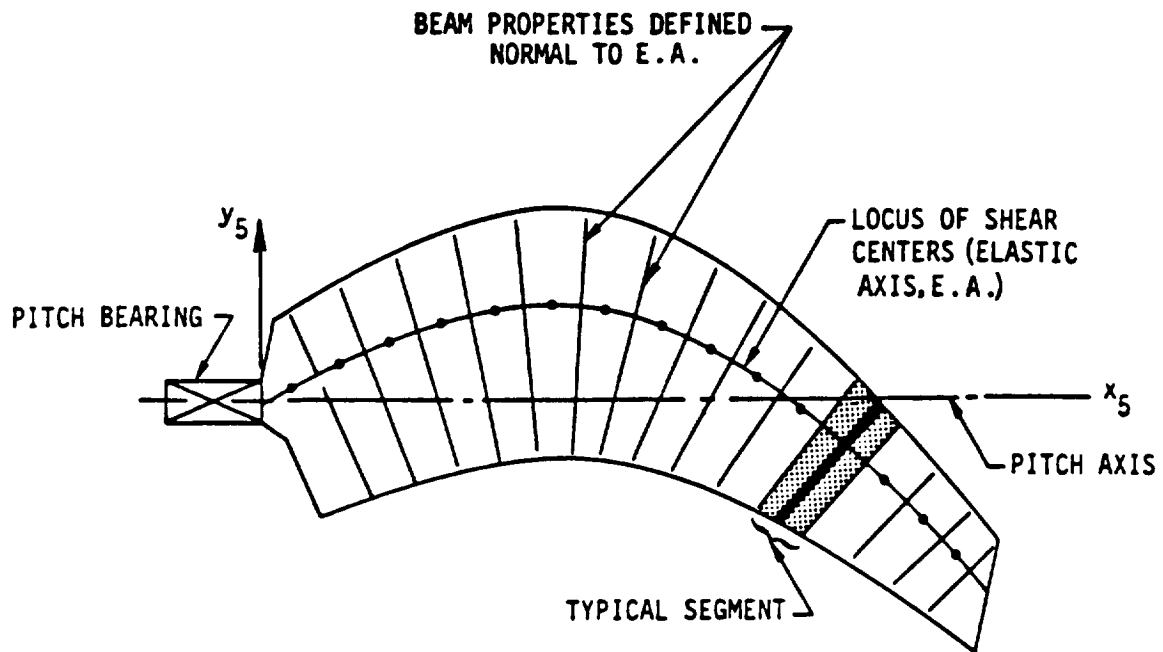
### 3.7.1 Structural Twist and Sweep

Modeling the structure of the blade is an extended version of what has been done in previous versions of G400 (Refs. 3.7-1 and 3.7-2). The most significant changes are those concerning sweep and twist associated with advanced propellers (i.e., prop-fan).

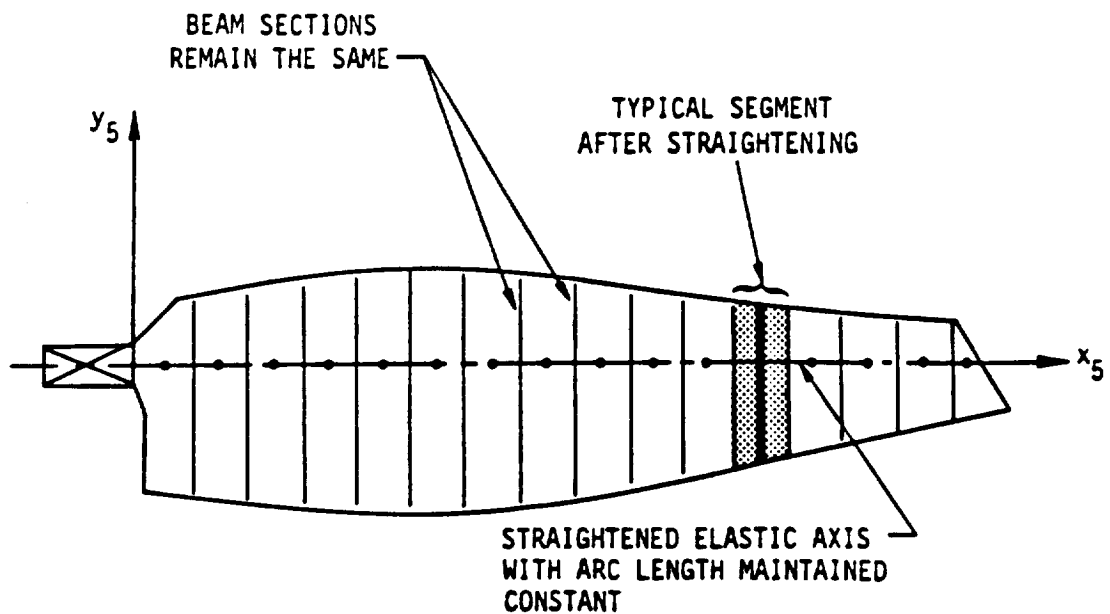
#### 3.7.1.1 Principal Assumptions

The principal assumptions associated with the derivation of the propeller model are presented:

- (1) The rotor is rotating at a constant velocity, has infinite impedance, and is in steady translational flight. The orientation of the rotor in space is specified by the appropriate Euler angles (pitch and roll). The orientation to the freestream is specified by means of a rotor angle-of-attack and a yaw angle.
- (2) The elastomechanics of the blade are described within a beam theory framework with corrections of a kinematic nature to account for the structural twist and sweep (Figures 3.7-1a and 3.7-1b).
- (3) The elastic (torsion) axis is defined as the spanwise locus of shear centers of the two-dimensional blade (beam) sections taken perpendicular to this spanwise locus. Note that this definition treats the elastic axis as an abstracted section property, as contrasted with what one would measure in a bench test of an actual curved beam. In such a test, the locus of points where bending loads produce no torsion deflection (at the points of load application) would conform to the usual interpretation of the "elastic axis". This axis, however, would be different from the herein usage of this term to denote the locus of section shear centers. The built-in structural sweep (elastic axis offset), together with the elastic bending deflections, defines an elastic axis which is generally a space curve about which the local torsion deflections must take place. Thus, as shown in Figure 3.7-1a, each spanwise beam segment generally will not be defined parallel to the other segments. For the analysis of the beam-like elastic properties, the structurally swept blade (Figure 3.7-1a) is assumed to have its so-defined elastic axis



a) LOCUS OF SHEAR CENTERS DEFINING ELASTIC AXIS



b) EQUIVALENT BEAM FOR DEFINING BEAM ELASTOMECHANICS

Figure 3.7-1. Basis for Use of Beam Theory for Structurally Swept Blade

"straightened out". This artificial straightening defines an "equivalent beam" whose (straight) elastic axis has the same arc length as the line of shear centers of the original swept blade (Figure 3.7-1b).

- (4) The bending elasticity is described by the conventional (linear) beam bending and (nonlinear) torsion characteristics, as formulated by Houbolt and Brooks (Ref. 3.7-3), for the above defined "equivalent beam". It is recognized that various deficiencies have been identified in these and other earlier formulations, both with respect to their adequacy for moderate to large bending deflections (Ref. 3.7-4 and 3.7-5) and with respect to the proper modeling of pretwisted beams under tension (Ref. 3.7-6 through 3.7-8). However, there is no well-established agreement either on the impact of these deficiencies on propeller aeroelasticity or more importantly, on a proper reformulation. Thus, the continued use herein of the Houbolt and Brooks elastic formulations must be viewed as an eventually correctable deficiency of uncertain importance, to be addressed at some future date.
- (5) The elastic bending and torsion deflections are "small" and respectively defined in a local sense normal to and along the space curve as defined by the built-in elastic axis. These deflections are defined as small (i.e., squares of these terms can be neglected with respect to one).
- (6) The elastic bending and torsion deflections can be described using the "uncoupled" normal bending and torsion modes of the "equivalent beam" (i.e., straightened-out beam). The uncoupled modes are calculated assuming zero precone, prelag, pitch, pretwist, center-of-gravity offset, and elastic axis offset. The use of these uncoupled modes is a major deficiency for analyzing highly swept pretwisted propellers (i.e., prop-fans) because the actual modes are always geometrically coupled.
- (7) Blade elastic bending is defined by the conventional beam bending differential equations (Ref. 3.7-3) wherein the usual independent spanwise variable is taken to be the arc length along the elastic axis. Within this context, the explicit elastic bending-torsion coupling due to structural sweep is omitted in favor of implicit coupling due to inertial, aerodynamic, and gravitational loadings taken with the appropriate sweep-related kinematics.
- (8) The blade aerodynamic and structural twist distributions are nonlinear. Additionally, the total (integrated) angle of structural twist is negligible beyond second order; however, cases of large local twist rates over short sections of span can still be addressed.



- (9) Local radial foreshortening is defined relative to the equivalent "straightened-out" beam (Figure 3.7-1). Contributions to radial foreshortening accrue from (a) the built-in structural sweep, (b) first-order (linear) functions of bending, arising from built-in structural sweep, (c) second-order (nonlinear) functions of bending each with elastic torsion arising from built-in structural sweep, and (d) second-order functions each of both flatwise and edgewise bending.
- (10) The elastic axis of the straightened-out beam is coincident with the feathering (pitch) axis at the root of the blade.
- (11) The blade flapping and lead-lag deflection degrees of freedom are assumed to be fixed at the hub.
- (12) The blade distributions of the center-of-gravity, aerodynamic center, and the center-of-tension (area center) are defined in two-dimensional sections normal to the curved "line of shear centers". It is assumed that these cross sections are symmetric about the chordline, and that all of the offsets lie along the chord. Most propellers do not have symmetric cross sections and neglecting the effects of asymmetry will lead to errors in the definition of the centrifugal loads.
- (13) The blade sections have finite thickness mass, but generally the thicknesswise location of the section center-of-gravity away from the chordwise principal axis is negligible.

#### 3.7.1.2 Basic Modeling Characteristics

The derivation of the structural model of the propeller is characterized by the following steps. (1) The line of shear centers (space curve) and the structural properties (elastic, inertial, and 1/4 chord location) of the blade must first be determined using either experimental or analytical techniques. These values are required input to the G400-PROP. (2) An equivalent straightened-out blade is defined in a manner such that it has an elastic axis with the same length as the curved line of shear centers and structural properties that are equivalent to the section properties of the curved blade. This straightening out of the blade will uncouple all of the in-plane and out-of-plane motion that is present in swept and pretwisted propellers. (3) The linear differential equations of motion, which were derived by Houbolt and Brooks (Ref. 3.7-3), are applied to the equivalent straightened-out blade. (4) These equations are solved using the global Galerkin method combined with a set of uncoupled mode shapes of

a nonrotating beam. These mode shapes are calculated assuming that the mass, area, and elastic axes are coincident.

Further development of the structural model and the mathematical formulation of the sweep angles can be found in Reference 3.7-9.

### 3.7.2 Aerodynamic Sweep

The unsteady airloads formulation incorporated in the G400-PROP analysis is based on aerodynamic concepts originally developed for helicopter rotor blades. A characteristic of the aerodynamics of helicopter rotor blades is the generally large variability in local air velocities due to combination of rotation with translational motion within the plane of the rotor. As a result, the aerodynamic formulations that have evolved are typically of a "strip theory" type with varying degrees of refinement to account for unsteady and swept flow effects. Such refinements are two-dimensional and applied in a heuristic manner based on the strip theory assumption.

#### 3.7.2.1 Principal Assumptions

In addition to the basic strip theory assumption, the assumptions related to the sweep of the blade are defined as follows:

- (1) The local aerodynamic section sweep angle is defined by the angle the local airflow direction makes with the blade section taken normal to the midchord line.
- (2) The section angle of attack is defined by the inflow and pitch angles measured with the section taken normal to the midchord line.
- (3) For those cases wherein the "quasi-static" option is invoked, the effective angle of attack is defined as the sum of the pitch and inflow angles. For this case, inflow angle is evaluated using local flow velocities at the 3/4 chord control point.
- (4) For those cases wherein either of the specific, more advanced unsteady methods of the next two sections are invoked, the angle of attack or plunge variables are also defined using Assumption (2), but with inflow angle evaluation at the 1/4 chord control point.
- (5) Airfoil drag is divided into two vectorial components (pressure drag and skin friction drag) which are vectorially added to give the total drag. Pressure drag is that generally associated with

compressibility and lift, and locally acts in the direction normal to the midchord line, whereas skin-friction drag acts in the direction of the local flow velocity (Fig. 3.7-2).

- (6) Skin friction drag varies with span (and hence Mach number) but is invariant with angle of attack.
- (7) Lift, pitching moment, and pressure drag coefficients are determined by the angle of attack and Mach number measured in the section normal to the midchord line. The lift, pitching moment, and pressure drag are determined by their so-defined coefficients and the dynamic pressure based on the velocity components normal to the midchord line.
- (8) Skin friction drag is determined by the Mach number and dynamic pressure based upon the vector sum of all components of the local flow.

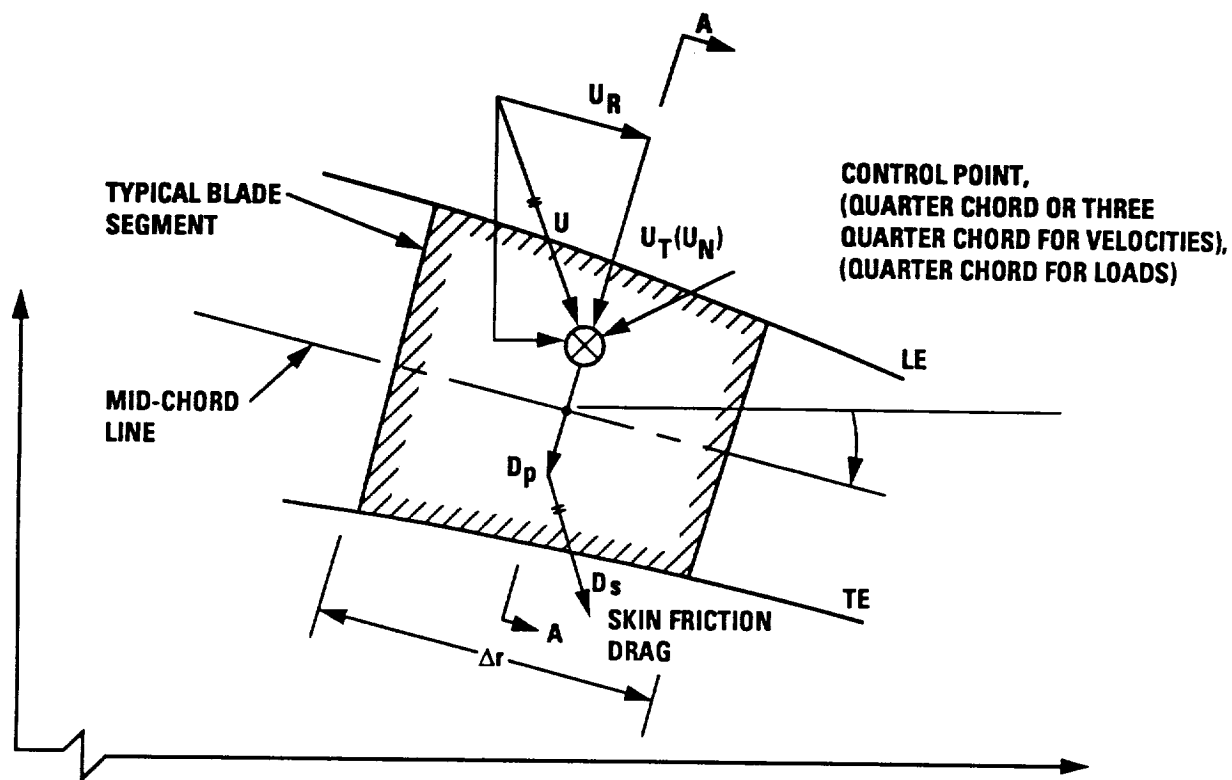
#### 3.7.2.2 Basic Modeling Characteristics

The airload distributions are derived using strip theory along with cross sections that are perpendicular to the "line of midchords". The sweep angles of this cross section are defined using Euler angles. The total velocity vector,  $U$ , is decomposed into vector components that are defined parallel (tangential) and perpendicular (radial) to the cross section. The local lift and the pressure drag are calculated based upon strip theory where the velocity vector parallel to the cross section and the local section angle of attack (difference of the total pitch angle and the inflow angle) are used. The skin friction drag is calculated using the total velocity vector.

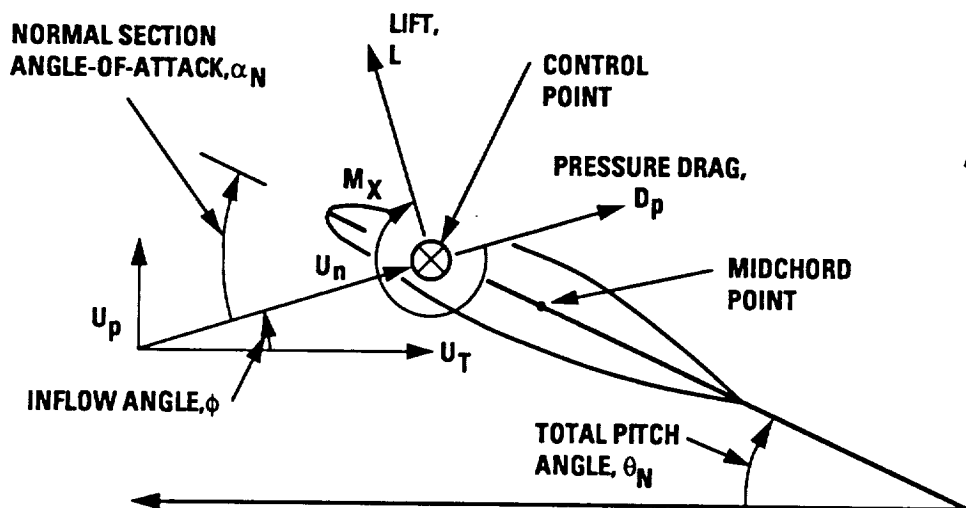
Further explanation of the development, including the mathematical derivation, can be found in Reference 3.7-9, pages 40-50.

#### 3.7.3 Unsteady Stalled Airloads

Detailed analysis of dynamic stall experiments has led to a semi-analytic methodology characterized by a set of relatively compact analytical expressions, called synthesized unsteady airfoil data, which accurately describe in the time-domain the unsteady characteristics of stalled airfoils (Ref. 3.7-10). Under the present study, the unsteady stalled airloads methodology was expanded for propeller applications by synthesizing similar unsteady loops at subsonic Mach numbers that are higher than helicopter rotor applications. More specifically, the high



**A. PLAN FORM VIEW**



**B. NORMAL AIRFOIL SECTION A-A**

R1M 0169.07

Figure 3.7-2. Geometric Details of Typical Aerodynamically Swept Section

Mach number data contained in References 3.7-11 and 3.7-12 were reduced to synthesized form within the established Reference 3.7-10 framework.

### 3.7.3.1 Overview of Dynamic Stall Model Methodology

When an airfoil experiences an unsteady increase in angle of attack beyond the static stall angle, a vortex starts to grow near the leading edge region. As the angle continues to increase, the vortex detaches from the leading edge and is convected downstream near the surface. The suction associated with the vortex normally causes an initial increase in lift. The magnitude of the increase depends on the strength of the vortex and its distance from the surface. The streamwise movement of the vortex depends on the airfoil shape and the pitch rate. The relative distance between the vortex and the airfoil varies according to the kinematics of the airfoil. That is, it depends on characteristics such as the pitch rate and the instantaneous angle of attack. As the vortex leaves the trailing edge, a peak negative pitching moment is obtained. The airfoil remains stalled until the angle-of-attack is sufficient so that reattachment of the flow can occur. The method used in the development of the G400-PROP incorporates all of these events.

### 3.7.3.2 Parameters Influencing Dynamic Stall

The unsteady lift, drag and pitching moment coefficients of the airfoils obtained from the two-dimensional oscillating airfoil test show a large degree of hysteresis when plotted as functions of angle of attack, particularly when the reduced frequency and the maximum angle of attack are sufficiently high. The amount of hysteresis and the shape of the loops vary in a highly nonlinear fashion with such test parameters as amplitude, mean angle, and reduced frequency.

The results of the oscillating airfoil test clearly indicate that the dynamic characteristics of an airfoil depend on the following main parameters: (1) airfoil shape and sweep, (2) Mach number, (3) Reynolds number, (4) mean angle of attack, (5) reduced frequency, and (6) oscillation amplitude.

The first four parameters affect both the static and the dynamic characteristics of the airfoil, while the last two are purely dynamic

parameters. Since this analysis will employ a time-history solution techniques for computation of the aerodynamic loading, frequency domain parameters (4-6) are inappropriate for time domain simulations. As a result, an alternative set of dynamic parameters, which are appropriate for time-domain simulations, is defined. The alternative parameters are: (4) the instantaneous angle of attack, (5) the nondimensional pitch rate, and (6) the unsteady decay parameter, which accounts for the time history effects of the change in instantaneous angle of attack and is based on the Wagner function.

The analytical expressions are obtained mostly by mathematical or empirical means and in general they represent simple quantitative approximations to the various observed physical features of the dynamic stall phenomenon. The mathematical derivation for the six parameters, including a means of predicting the dynamic stall events can be found in Reference 3.7-9.

#### 3.7.4 Unsteady Unstalled Subsonic Aerodynamics

The use of quasi-static airloads in the aeroelastic analysis of advanced propeller systems (i.e., prop-fans) lends itself to simplicity and, hence, economy rather than accuracy. For an accurate quantitative aeroelastic analysis, unsteady aerodynamic forces become indispensable. This can be seen by noting the lift coefficient variations with reduced frequency shown in Figure 3.7-3 for a two-dimensional airfoil at a subsonic Mach number typical of prop-fan operations. The reduced frequency range shown in Figure 3.7-3, moreover, is typical of the vibration modes of real prop-fans. The aerodynamic force lag is substantial as implied by the imaginary part of the lift coefficient.

The majority of the available unsteady aerodynamic lift and moment information for airfoils comes from theory or experiments in the (real) frequency domain instead of in the time domain. This is due to the simplicity in the mathematics and experimental efforts in working in the frequency domain. In order to perform time-history solutions for an aeroelastic problem, however, the frequency domain unsteady aerodynamic data must be properly transformed into the time domain. In order to overcome these difficulties, Pade approximants have been introduced as an

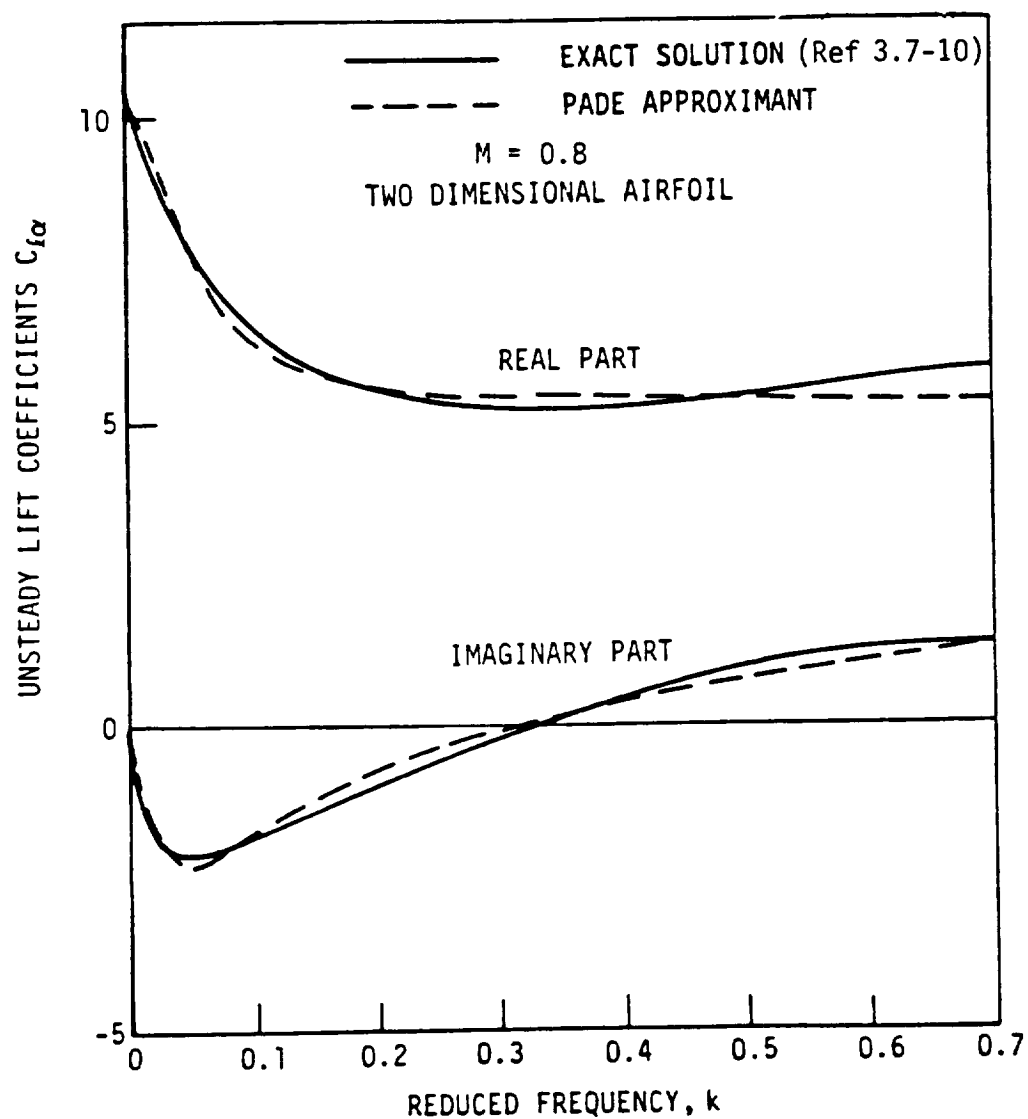


Figure 3.7-3. Example of Unsteady Aerodynamic Airfoil Characteristics and Associated Pade Approximation

approximate but consistent way to bridge the gap between the (real) frequency domain unsteady aerodynamic data and the time domain description of the unsteady aerodynamic forces (Ref. 3.7-13). An example of the application of the method is shown in Figure 3.7-3. As opposed to the generally transcendental nature of the unsteady aerodynamic data, Pade approximants are defined in terms of rational functions that are known to have simple Laplace transforms or inverse Fourier transforms. In addition to the mathematical advantage, the Pade approximant also provides a quick method for interpolating and/or extrapolating the frequency domain data, which is generally limited to a few discrete frequencies.

In Reference 3.7-9, the sources of unsteady aerodynamic data used in the G400-PROP study are described and the data synthesization procedures for rendering these data to Pade forms are described. The details of proceeding from the Pade forms to linear differential equations are also described.

#### 3.7.5 Sample Calculations

In this section, stall flutter calculations are presented that are used to provide an indication of the performance of the original version of the G400-PROP computer code (i.e., not the reduced version). These calculations were performed using the SR-2 propeller, which is a short, straight, isotropic blade with very little pretwist. This blade was selected for two reasons: First, a complete set of structural properties, including the line of shear centers location, exist. Second, results from NASA-conducted stall flutter tests of this blade exist and are readily accessible.

It should be noted that the performance of this code cannot be completely identified by these calculations, because this code was originally a helicopter rotor code that was designed to analyze straight blades. The modifications that were incorporated in this code, which include the capability of analyzing swept and pretwisted advanced propellers, are not being tested with these calculations. It is presumed that the results for a curved blade analysis would be no better than the results for a straight blade because the structural model for the blade is straight with correction factors that account for sweep.



#### 3.7.5.1 Description of Blade Configuration and Operating Conditions

The SR-2 prop-fan propeller model is constructed out of solid steel, has a 0.6223-meter diameter, and is configured with eight "shovel tipped" blades (no sweep). The planform of this model design is shown in Figure 3.7-4, and a summary of the pertinent geometric and other measured parameters is given in Table 3.7-1. Also included in this table are the various dynamic properties that were defined in Reference 3.7-9. Rough estimates of the equivalent viscous structural damping values were estimated from stall flutter tests (Ref. 3.7-9). The torsion stress/pitching moment  $\tau/M$ , at the 19.05 cm spanwise location was calculated using the blade geometry and appropriate formulas from Reference 3.7-14.

The nine different operating conditions that were chosen for the SR-2 propeller blade are described in Table 3.7-2. The first five cases are used to verify the analytical predictions of Reference 3.7-9 and to correlate with the experimental stall flutter results performed by UTRC.\* The last four cases were used to correlate the G400-PROP results with experimental stall flutter wind tunnel data. These four cases were run at 7000 rpm, but with different blade pitch angle settings, so that the predicted stall flutter point can be compared with the actual pitch setting that caused stall flutter.

Analytical predictions of the variations in uncoupled blade modal frequencies with tip speed are presented in Figure 3.7-5. These frequencies, of course, lack the coupling effects of pretwist, precone, prelead, etc., which the G400-PROP analysis provides when addressing swept propellers.

#### 3.7.5.2 Stall Flutter Correlation Cases

Table 3.7-2 and Figure 3.7-6 summarize the experimental and analytical stall flutter results for the statically thrusting SR-2 propeller blade. The experimental results are presented in Table 3.7-2 as pitch and speed settings of the propeller that produce stall flutter. The experimental

---

\*These tests were performed under Contract NAS3-2755 and are summarized in UTRC Report R81-335414, "Static Stall Flutter Tests of ASD Prop-fan Models."

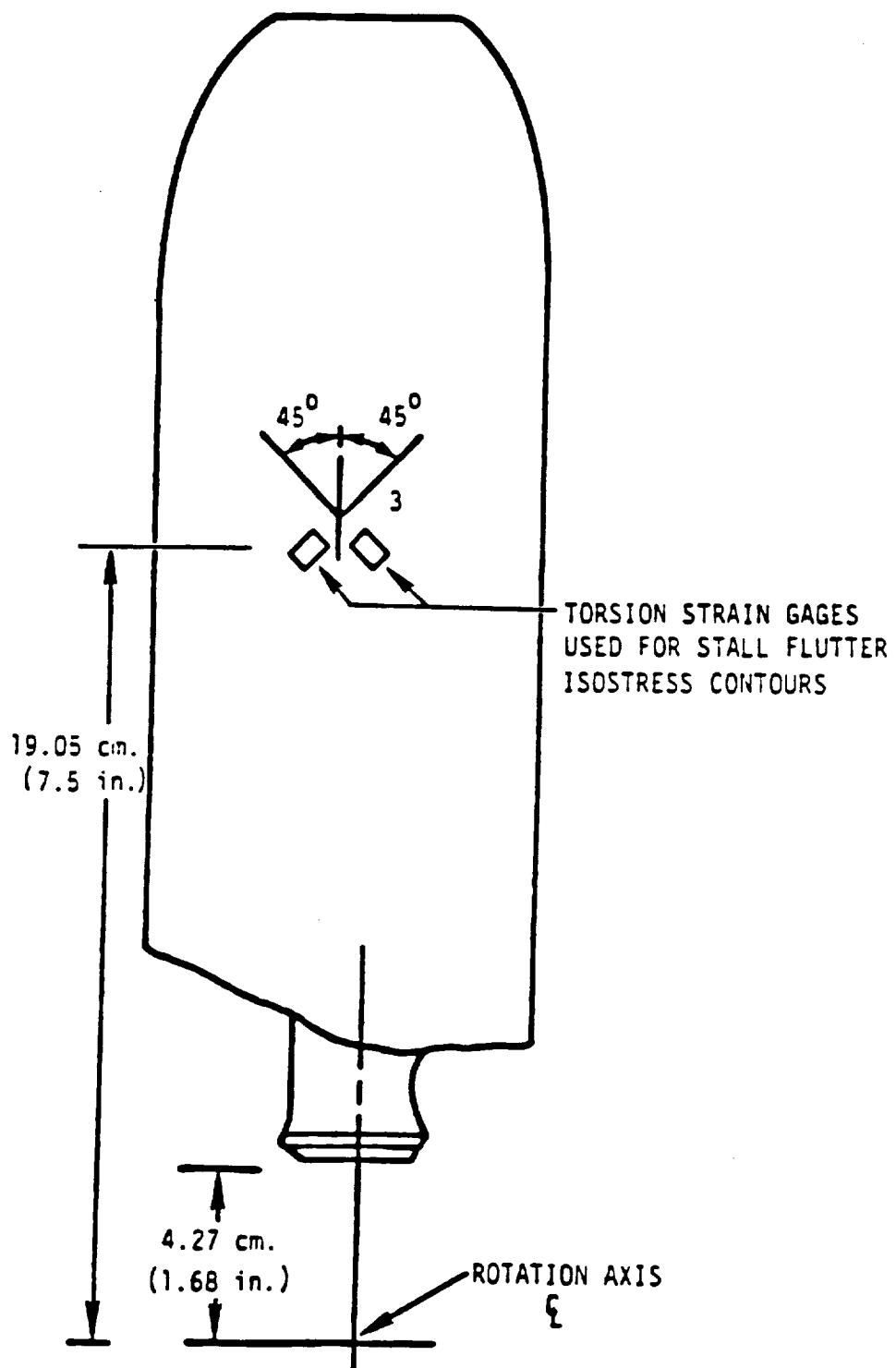


Figure 3.7-4. Planform of SR-2 Model Prop-Fan Blade

Table 3.7-1. SR-2 Model Prop-Fan Physical Parameters

<u>Design Parameters</u>	<u>Model Values</u>
Tip Speed, $\Omega R$ , m/s	277.01
Rotor Speed, $\Omega$ , rpm	8500
No. of Blades, $b$	8
Radius, $R$ , m	.3112
Solidity, $\sigma$	.565
Blade Root Offset, $e$	.1372R
Preconing, $\beta_B$ , deg	0.1
Prelead-lag, $\delta_B$ , deg	0.1
Fabrication Material	4340 stainless steel
<u>Parameters Calculated or Estimated</u>	
<u>Uncoupled Mode Natural Frequencies (Calculated)</u>	
1st Flatwise Natural Frequency, $\omega_{w_1}$ , Hz	233.34 (1.577P)
2nd Flatwise Natural Frequency, $\omega_{w_2}$ , Hz	541.94 (3.825P)
3rd Flatwise Natural Frequency, $\omega_{w_2}$ , Hz	1037.74 (7.325P)
1st Edgewise Natural Frequency, $\omega_{v_1}$ , Hz	1030.59 (7.274P)
1st Torsional Natural Frequency, $\omega_{\theta_1}$ , Hz	627.64 (4.430P)
2nd Torsional Natural Frequency, $\omega_{\theta_2}$ , Hz	1246.79 (8.801P)
<u>Structural Critical Damping Ratios (Estimated)</u>	
Flatwise Modes	0.008
Edgewise Mode	0.008
Torsion Modes	0.008
<u>Torsion Stress/Pitching Moment (Calculated)</u>	
$\tau/M$ (@ $r = 19.05$ cm)	3.89/cm <sup>3</sup> (63.77/in <sup>3</sup> )

Table 3.7-2. Predicted and Measured Values of PTP Torsion Stress at  
Selected Operating Conditions for SR-2 Prop-Fan  
 $a_{\infty} = 1155 \text{ ft/s} = 352 \text{ in/s}$

Case	Rotational Speed $\Omega$ , rpm	Blade Pitch $\beta$ , degree	Forward Flight Speed, m/s	G400-Prop Results		Experimental Results	
				1/2 Peak- to-Peak, psi	Comments	1/2 Peak- to-Peak, psi	Comments
1	2000	30	0	<500	No stall	<500	No stall
2	8500	20	0	<500	No stall	<500	No stall
3	8500	25	0	7537	Stall	<1000	No stall
4	8500	30	0	4345	Stall	5000	No stall
5	8500	32	0	1857	Stall	8000	Stall
6	7000	20	0	<500	No stall	<500	No stall
7	7000	24.1	0	10,000	Stall	<1000	No stall
8	7000	27.6	0	34,500	Stall	1000	No stall
9	7000	35.8	0	22,100	Stall	7000	Stall

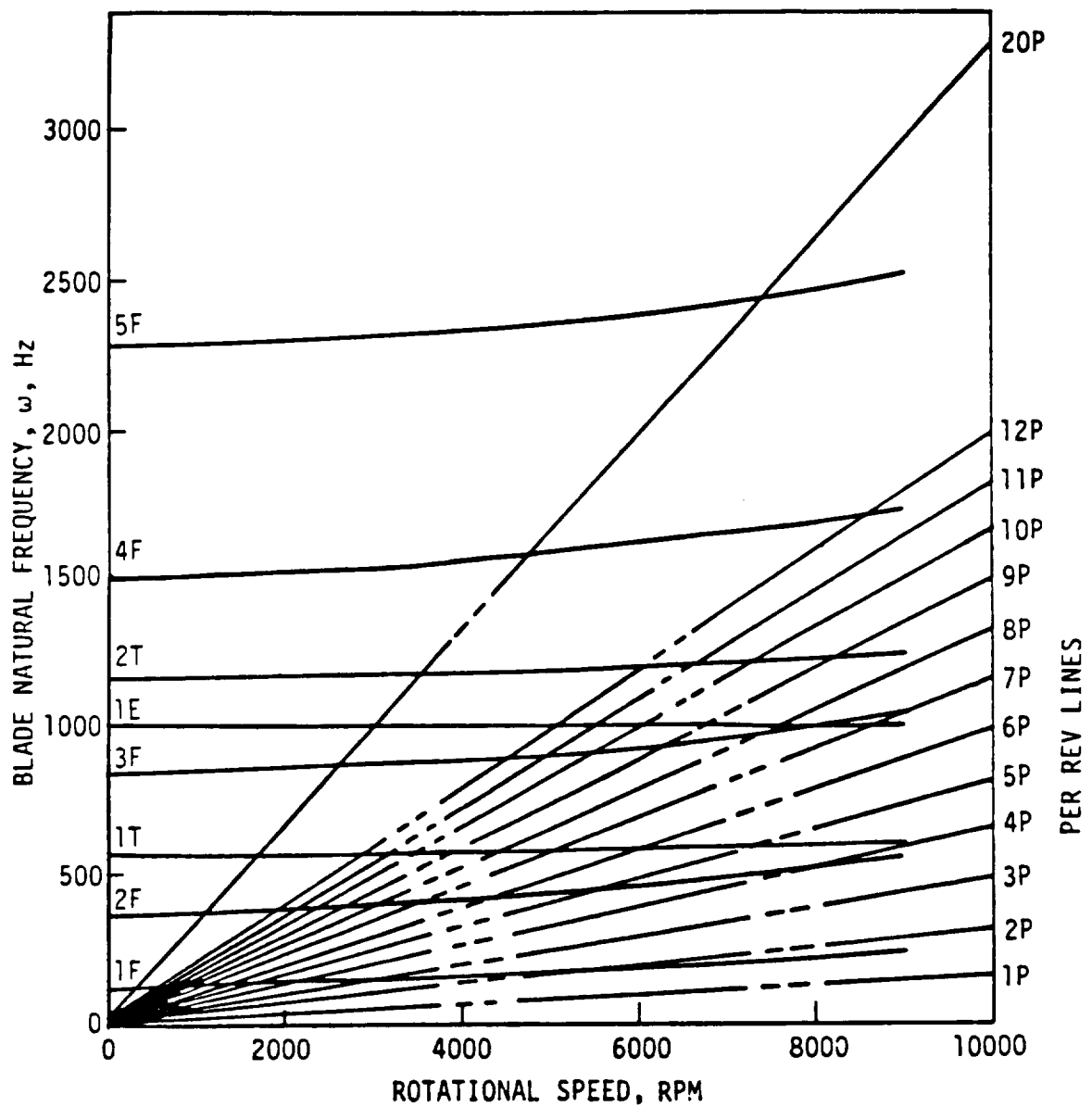


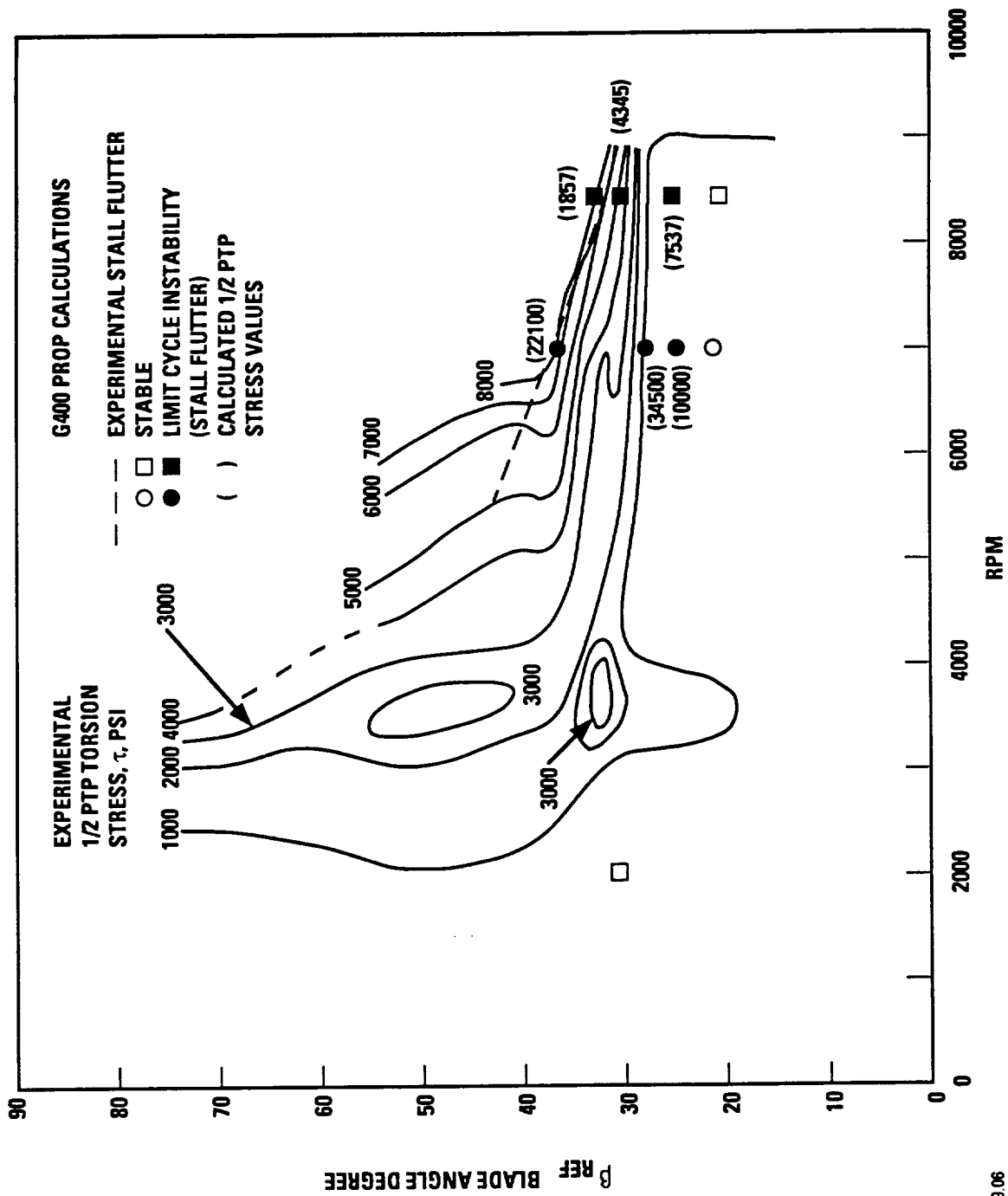
Figure 3.7-5. Analytical Predictions of the Variation of SR-2 Blade Natural Frequencies with Tip Speed, Uncoupled Modes

results of Figure 3.7-6 are presented as isostress curves for the 1/2 peak-to-peak (1/2PTP) torsion stresses which are calculated using strain gage data at the 19.05 cm spanwise location, as shown in Figure 3.7-4. The reduction of the test data to 1/2PTP torsion stresses was accomplished using the manufacturer's gage factors which were supplied by UTRC (Ref. 3.7-9).

The analytical G400-PROP calculations consist of Cases 1 through 9 given in Table 3.7-2 and are indicated in Figure 3.7-6 as open or closed square or circular symbols. If the symbols are open, then the calculation has predicted that the blade is stable. Likewise, a closed symbol indicates that the code has predicted stall flutter. The square symbols refer to calculations that were also performed by UTRC, while the circular symbols refer to calculations that were performed by TRW. The calculated values of the 1/2PTP torsion stresses are also listed.

Case 1 (2000 rpm,  $\beta_{\text{ref}} = 30^\circ$ ) was used as a reference point to check that the analytical model was well behaved and that the 1/2PTP stresses were small and in agreement with the experimental results. Cases 2 through 5 (8500 rpm,  $\beta_{\text{ref}} = 20^\circ, 25^\circ, 30^\circ, 32^\circ$ ) were used to compare the predicted stall flutter point, which agreed with the UTRC analytical predictions, with the experimentally derived stall flutter point (8500 rpm,  $\beta_{\text{ref}} = 31.8^\circ$ ). From Figure 3.7-6, it can be seen that the stall flutter point that was predicted by the G400-PROP analysis is 6.8 degrees less than what was recorded in the test ( $25^\circ$  versus  $31.8^\circ$ ). Another important observation is that the predicted 1/2PTP torsion stresses do not agree with the experimentally recorded results. The calculated torsion stresses are extremely high for low values of pitch, but are smaller for high values of pitch. This was not expected or recorded in the test because, as the pitch angle is increased, the blade is more unstable and the recorded torsion stresses are much larger.

Cases 6 through 9 (7000 rpm,  $\beta_{\text{ref}} = 20^\circ, 24.1^\circ, 27.6^\circ, 35.8^\circ$ ) were also used to compare the analytically predicted stall flutter point with the experimentally recorded point (7000 rpm,  $\beta_{\text{ref}} = 35.8^\circ$ ). The predicted stall flutter point is 11.7 degrees less than the experimentally recorded point ( $24.1^\circ$  versus  $35.8^\circ$ ). The experimental data of the blade operating



RIM 0169.06

Figure 3.7-6. Stall Flutter Correlation Results for the SR-2 Blade and G400PROP Calculations

at 7000 rpm and a pitch setting of 24.1 degrees is very clean with the recorded torsion stresses less than 500 psi and blade acting very stable. The analytical results, for this same operating condition, show the blade acting highly unstable with the torsion stresses equal to 10,000 psi. The predicted torsion stresses for these four cases do not look that much better than the previous four cases because the magnitude is at most 30 times too large and the trends are not in agreement with the experimentally recorded data.

Possible reasons for the disparity between the experimental data and the analytically predicted results are:

- (1) The inadequacy of using uniform inflow for the statically thrusting condition
- (2) The uncertainty in the static stall characteristics of the NACA 16-series airfoil data used
- (3) The unknown impact of cascading effects on the airfoil stall characteristics.

#### 3.7.6 Recommendations

Based on the above calculations, it was recommended that, prior to the G400-PROP aeroelasticity analysis being incorporated into GAPAS, a number of test cases should be run using the latest reduced version of the code. These cases are meant to evaluate the G400-PROP code using straight and swept advanced propellers.

- (1) Calculate the natural frequencies, mode shapes, and flutter points of a straight conventional propeller with pretwist. A comparison of this data with experimentally derived data (three bladed assembly) would be useful in determining how well the uncoupled modes of the G400-PROP predict the geometrically twisted modes of the actual blade. Expected agreement of the stall flutter points should be very good because cascade effects can be ignored.
- (2) Calculate the natural frequencies, mode shapes, and flutter points of an actual swept propeller (curved and pretwisted) and compare them with actual test data. These will test the sweep transformations that are included in the structural and the aerodynamic models. It is also useful in determining the importance of using a nonlinear structural model versus the current linear structural model.



- (3) Repeat the calculations in (2), by making a small perturbation to the defined line of shear centers of the swept blade. This calculation is necessary in order to access the sensitivity of the line of shear center location on the flutter calculations.



#### 4. FORMULATION OF SYSTEM FRAMEWORK

The objective of this task is to formulate the system framework for the design of the procedural system. Based on the evaluation of procedural systems performed in Task 1 the ANOPP system was recommended and subsequently adopted as the procedural system for GAPAS. Although the system has been developed and used extensively for aircraft noise prediction analysis, its applicability to GAPAS has yet to be determined. Therefore, the main objectives for this task are focused on: (1) familiarization of the ANOPP system for the preparation of GAPAS integration; (2) checking out system functions and checkpoint/restart capabilities; (3) identifying input/output requirements for the GAPAS functional modules.

##### 4.1 FAMILIARIZATION OF ANOPP PROCEDURAL SYSTEM

The objective of this subtask is to determine the mechanism through which users, functional modules, and the executive system interact. This is of utmost importance to functional module writers because modification to existing modules for integration must be compatible with the procedural system. An examination of the system shows that the mechanism is built upon the coordination of three sets of system routines. These routines perform separate functions which: (1) interpret user directives to determine the mode of execution desired, (2) transfer data between modules, and (3) dynamically manage the core storage for efficient operations.

User directives, or ANOPP control statements, are internally defined statements. These statements provide a means for user and system interactions. Because of the large core requirement, GAPAS is likely to be either I/O or CPU-bound, meaning that batch mode is the likely mode of operation. Therefore, user directives are to be assembled in the form of an input file and submitted in a batch process.

The ANOPP data transfer mechanism is controlled by a number of system routines normally residing in core. These routines perform basic functions of READ and WRITE for functional modules. The data base consists of two types of data, either in the form of a named disk file or single-value variables maintained in core. UPDATE and PARAMETER are the user directives provided for constructing these types of data. Typically, user parameters

are utilized for program control flags, single-valued operating conditions, and parameters frequently modified among modules. The advantage of having this type of data is in fast access time. Data files are designed for the storage of voluminous data generated by functional modules. These files are dynamically created at run time, therefore requiring no prior "open" or subsequent "close". This feature has the merit of efficient use of system resources thereby avoiding unnecessary I/O waits.

It is evident that a number of system routines must reside in core to perform the basic executive functions. Although the exact number changes from time to time, the average size of these routines is estimated to be 200K octal words. A CDC CYBER-175 machine has a maximum storage of 377K. The existence of the ANOPP procedural system reduces the field length otherwise available to functional modules. Therefore all modules are restricted to less than 177K words. All modules considered for GAPAS, except the aeroelasticity module, meet this storage constraint. For modules requiring slightly more memory, the system dynamic storage management system can be utilized. The system provides run-time dimensioning of arrays, thereby allocating and deallocating storage within a module.

#### 4.2 ANOPP SYSTEM CHECKOUT

The purpose of this task was to verify the operation of ANOPP under the TRW CDC/TSS computer system. This is necessary because the TRW system supports only some NOS features and ANOPP was developed under the generic CDC/NOS system. In addition, major features such as data transfer mechanism and checkpoint/restart must be checked to determine their operational status.

In the first exercise, two simple modules were incorporated. These modules required services from the data base manager which performs some read/write functions. User parameters were also employed. Data transfer between these modules was successful indicating that system routines handled the data base function properly under the TRW computer system.

In the second exercise, two potential GAPAS modules were used. These modules were the JUMPER code and ALJABRI code which are used for the aircraft flowfield and propeller performance calculations. Figure 4.2-1 shows

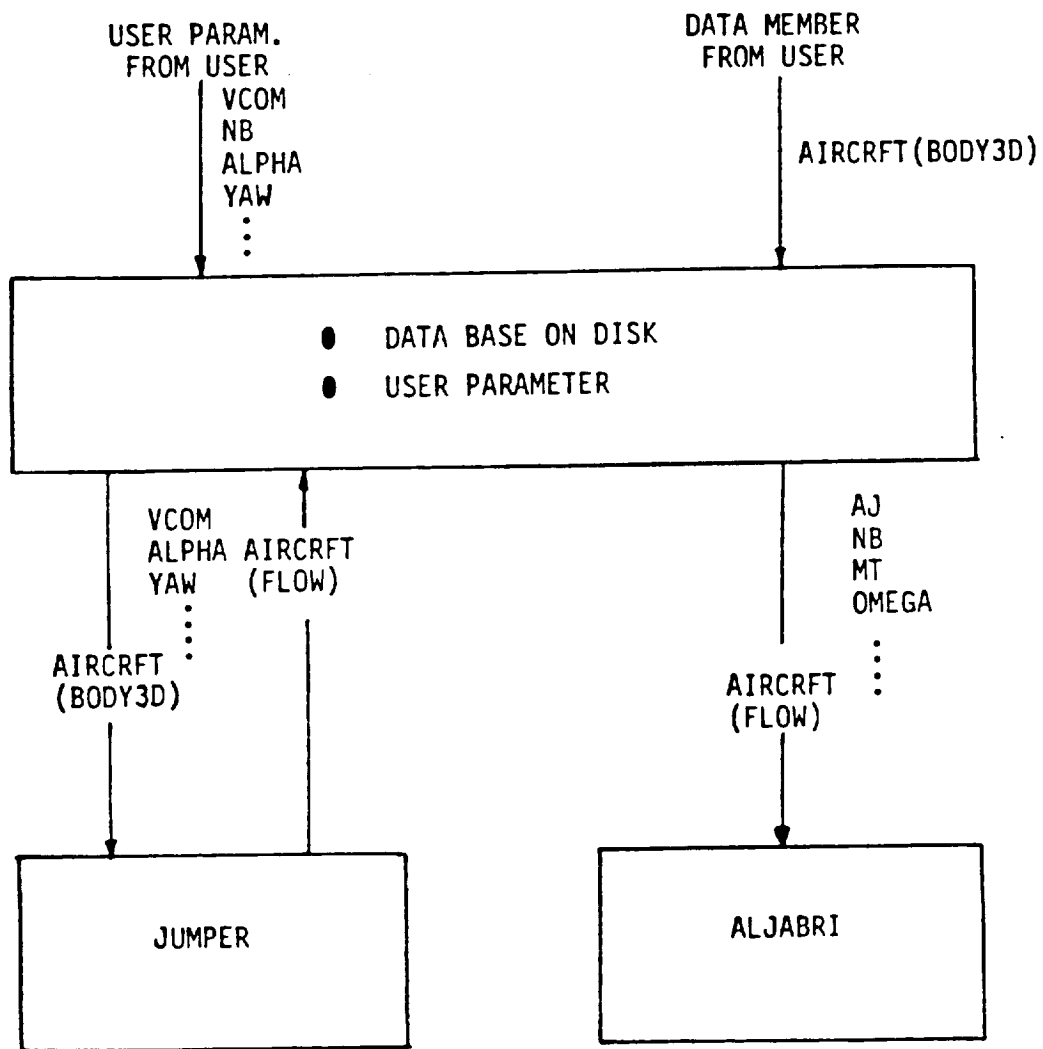


Figure 4.2-1. Schematic ANOPP System Checkout Case

the required interactions between the modules and a user. The user defines the geometry of the aircraft nacelle in the data unit called AIRCRFT(BODY3D) and the operating conditions (freestream velocity, number of blades, angle of attack, etc.) in user parameters (VCOM,BN,ALPHA). A data base is then created to store the user input and transfer the required data to the functional module JUMPER as the module is executed. Upon completion, JUMPER instructs the data base manager to store the three velocity components of the flow field in another data unit called AIRCRFT(FLOW). As JUMPER execution is completed, the ALJABRI module is loaded in core previously occupied by JUMPER. During the course of execution, retrieval of aircraft flowfield data is initiated and the data base routines are activated for such operation. Along with this data file, user parameters such as advance ratio (AJ) and rotational speed (OMEGA) are input by the user. In brief, this figure shows a conceptual construct for GAPAS.

Figure 4.2-2 shows the input file for the checkout case described above. The first two statements, ANOPP and STARTCS, simply signal the beginning of an ANOPP run, thereby initializing arrays and parameters. After the PARAM and UPDATE statements, the system constructs a data base with values as defined in the input stream. CKPNT sets up a checkpoint at this point of execution. The effect of setting up a checkpoint is to instruct the procedural system to unload all data in the current run environment into a disk file. This file will be used subsequently for a restart run. The EXECUTE statement moves a functional module into core for execution. After JUMPER and ALJABRI modules are completed, ANOPP will exit with the ENDCS statement.

Figure 4.2-3 shows typical input files for restart runs. As previously mentioned, checkpoint files must be constructed (by using the CKPNT statement) and saved. Every time a CKPNT statement is encountered in an input stream, a new version (cycle) of the checkpoint file will be written. To execute a restart run, the checkpoint file must be attached along with the rest of CDC job control statements. In this figure, the first example illustrates a restart run of Cycle 1 using the control statement RSTRT. Effectively, the checkpoint file attached will be loaded and the run environment at which the first CKPNT was encountered in a previous run is

ANOPP CKPNT=CKPOINT \$  
STARTCS \$

INITIALIZE AN ANOPP RUN

PARAM VCOM = 0.47, ALPHA=0.0, YAW=0.0 \$  
PARAM NSYMET = 0 \$

USER PARAMETERS FOR JUMPER

.  
. .

UPDATE NEWU = AIRCRAFT, SOURCE = \* \$  
-ADDR NEWM = body, . . . \$

6 \$  
1, 3, 0 \$  
0.0 0.0 0.0 \$  
0.0 0.0 0.0 \$

DATA BASE FILE FOR JUMPER

.  
. .

END\* \$

CKPNT \$

ESTABLISH FIRST CHECKPOINT

EXECUTE JUMPER \$

EXECUTE JUMPER

CKPNT \$

ESTABLISH SECOND CHECKPOINT

PARAM AJ = 2.372, NB = 3 \$  
PARAM MT = 707.09, R = 5.0 \$

USER PARAMETERS FOR ALJABRI

EXECUTE ALJABRI \$

EXECUTE ALJABRI

ENDCS \$

END ANOPP RUN

Figure 4.2-2. Input File for First ANOPP System Checkout Case

RSTRT RSTRT = CKPOINT, RSCYCL = 1	\$	}	ACTIVATE RESTART CAPABILITY
STARTCS	\$		
ENDCS	\$	}	START EXECUTION END

#### INPUT FILE FOR THE THIRD ANOPP SYSTEM CHECKOUT CASE

RSTRT RSTRT = CKPOINT, RSCYCL = 2	\$	}	ACTIVATE RESTART CAPABILITY
STARTCS	\$		
ENDCS	\$	}	START AND END

Figure 4.2-3. Input File for Second ANOPP System Checkout Case



re-established. This requires reading from the checkpoint file of all named data files and user parameters and storing these data either on disk or in core. In the second example, restart is desired at Cycle 2.

In summary, all the checkout cases ran successfully, indicating that the ANOPP procedural system functions properly under TRW CDC/TSS computers.

#### 4.3 DESIGN OF AN OVERALL DATA BASE FOR GAPAS

##### 4.3.1 Input/Output Procedures

The adoption of the ANOPP procedural system has severely limited the option of user input to GAPAS. As discussed earlier, the procedural system requires approximately 200K octal words. By the time functional modules are loaded, the storage resource of a typical CDC CYBER machine will be practically fully utilized. Furthermore, a full GAPAS run that involves a number of modules is likely to take more than 30 minutes of execution time. In view of these considerations, GAPAS would primarily operate in a batch processing mode.

In a batch mode process, a user must first perform three separate tasks before a program can be executed. First, the source FORTRAN code must be compiled, meaning that the code is to be converted into machine language code using a FORTRAN compiler. In this case, a FORTRAN IV compiler is required. The next step is to link all the compiled codes into an overall system, thereby assigning relative core addresses to each machine instruction and variable. For GAPAS, this step is accomplished by using the CDC SEGMENT LOADER. The segment loader, rather than the conventional loader, is used because the extremely large size of the system requires that it be overlayed. The segment loader provides a flexible overlay mechanism. Finally, as the overall program is linked, an executable code is produced and saved. This executable codes along with a user-constructed input file, will be submitted for a batch process. A typical user input contains a sequence of ANOPP control statements which define the logic of execution of each functional module.

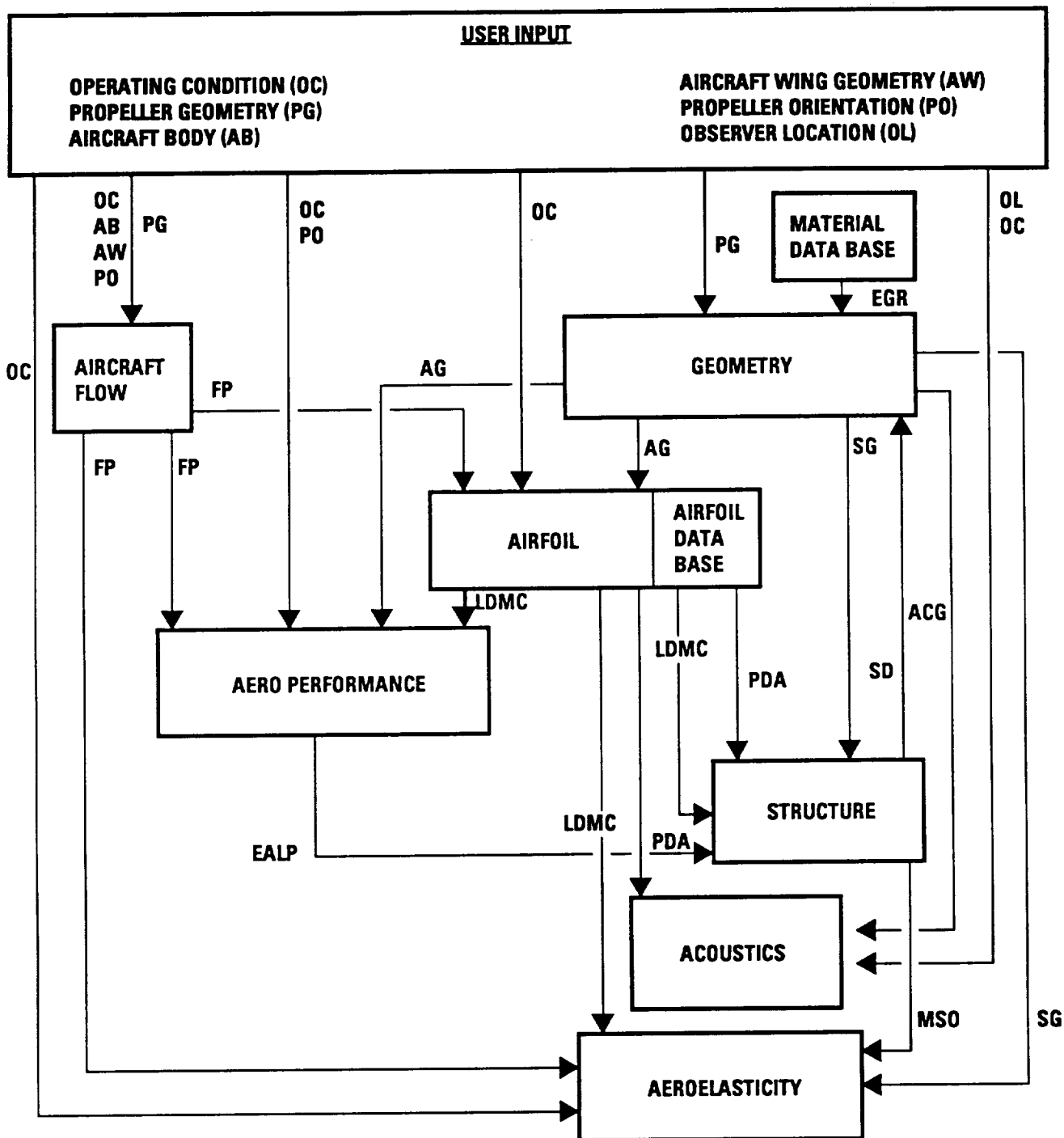
In each functional module, diagnostic messages will be coded and corrective action will be suggested. Furthermore, ANOPP provides extensive error processing and trace-back series. In case of system error(s), such

as retrieving data from a nonexistent data unit, messages including names of routines will be displayed. Although the system is basically designed for batch process, intermediate results may be obtained by using the checkpoint/restart capability, thereby achieving a fast turnaround processing.

#### 4.3.2 System Interactions

One of the basic requirements for the design of ANOPP is that of modularity. Specifically each module is regarded as an independent module. Interactions among these modules occur through a central data base. Therefore, no direct calls between modules are allowed. The advantage of having a modular design is evident. First, it allows clear input/output requirements, thereby making program debugging easy. Second, as new modules are developed, older modules can be readily replaced. Figure 4.3-1 shows the required interactions between functional modules required by GAPAS.

In the single-pass mode, a user defines the operating conditions, propeller geometry, aircraft nacelle geometry, propeller orientation and observer locations if the acoustic signature is desired. These data are stored into the GAPAS data base for the functional module manipulations. The geometry generator is processed and data required for aerodynamic, aeroacoustic and structural calculations are generated. In essence, data for sections perpendicular to the quarter-chord, pitch change axis and elastic axis are determined. Again, these data are stored in the data base. For retrieving geometry and operating data from the data base, the aircraft flow field module is executed to generate the velocity in the propeller plane to be used for airfoil loading calculations. The next step requires construction of a drag polar from repeated execution of an airfoil loading module. In certain cases, a drag polar may be obtained directly from a data bank, thereby avoiding lengthy calculations. The drag polar, along with operating conditions and geometry data, are then transferred into the aerodynamic performance module through the data base. This module determines the efficiency of a propeller and also prepares a loading distribution for the input of the structure and aeroacoustic modules. Blade deflections and internal stress are calculated in the structure



R1M 0169.10

AG - SECTION DATA FOR AERODYNAMICS  
 ACG - SECTION DATA FOR ACOUSTICS  
 SG - SECTION DATA FOR STRUCTURE  
 FP - FLOWFIELD IN PROPELLER PLANE  
 MSO - MODE SHAPES AND OTHER STRUCTURAL DATA  
 LDMC - LIFT, DRAG AND MOMENT COEFFICIENT

EALP - EFFECTIVE ANGLE ATTACK DISTRIBUTION  
 PDA - PRESSURE DISTRIBUTION  
 EGR - E, G AND P OF MATERIAL  
 SD - STEADY STATE DEFLECTION

Figure 4.3-1. Analysis Mode for GAPAS

module using the geometry data and loading information. To complete the system, aeroacoustic and aeroelasticity modules are executed. These two modules require different sets of geometry data and loadings, and generate no information required for other modules. In a multiple-pass mode, Figure 4.3-1, repeated executions of the geometry, aircraft flow field, airfoil loadings and performance modules are performed until a criterion on deflections is met. The acoustics and aeroelasticity modules that are outside this loop are to be processed upon convergence.

#### 4.3.3 GAPAS Data Base

Based on functional module interactions, a tentative data base has been worked out to provide a system framework for the integration of the final GAPAS system. The data base is shown graphically in Figure 4.3-2 with a set of named data units. Initially, the data base contains only data units defined by the user, namely GEOM(BLADE), GEOM(INTRNL), AIRCRFT(BODYAX), AIRCRFT(PROP), AIRCRFT(INLET), BEAM(DAMP), BEAM(WARP) and OBSERV(COORD). The convention of naming an ANOPP data file is designated as data unit name (data member name). These data units correspond to inputs required for the geometry generator, aircraft flowfield, structural and aeroacoustic modules. As modules are executed, more data units are generated. For example, the geometry generator generates various section profiles and its associated properties by performing cuts perpendicular to the quarter-chord line, pitch change axis, and elastic axis with designated names as GEOM(AERO), GEOM(NOISE), GEOM (STRUC1), GEOM(STRUC2), respectively. The required input for the aircraft flowfield module are the aircraft and propeller geometry data, such as AIRCRFT(BODYAX), AIRCRFT(PROP), etc. The execution of this module results in the three components of velocity in the propeller plane and is stored in AIRCRFT(FLOW). The airfoil loading module requires input stored in GEOM(AERO) and AIRCRFT(FLOW) and in turn generates a drag polar stored in AERO(CL), AERO(CD), and pressure distributions in AERO(PRESS). The aerodynamic performance module requires input of the airfoil section properties and freestream Mach number stored in GEOM(AERO) and AIRCRFT(FLOW) and generates the actual pressure loading stored in AEROP(PRESS). Finally, the structural beam module takes the data stored in AEROP(PRESS), GEOM(STRUC1), BEAM(DAMP) and BEAM(WARP)

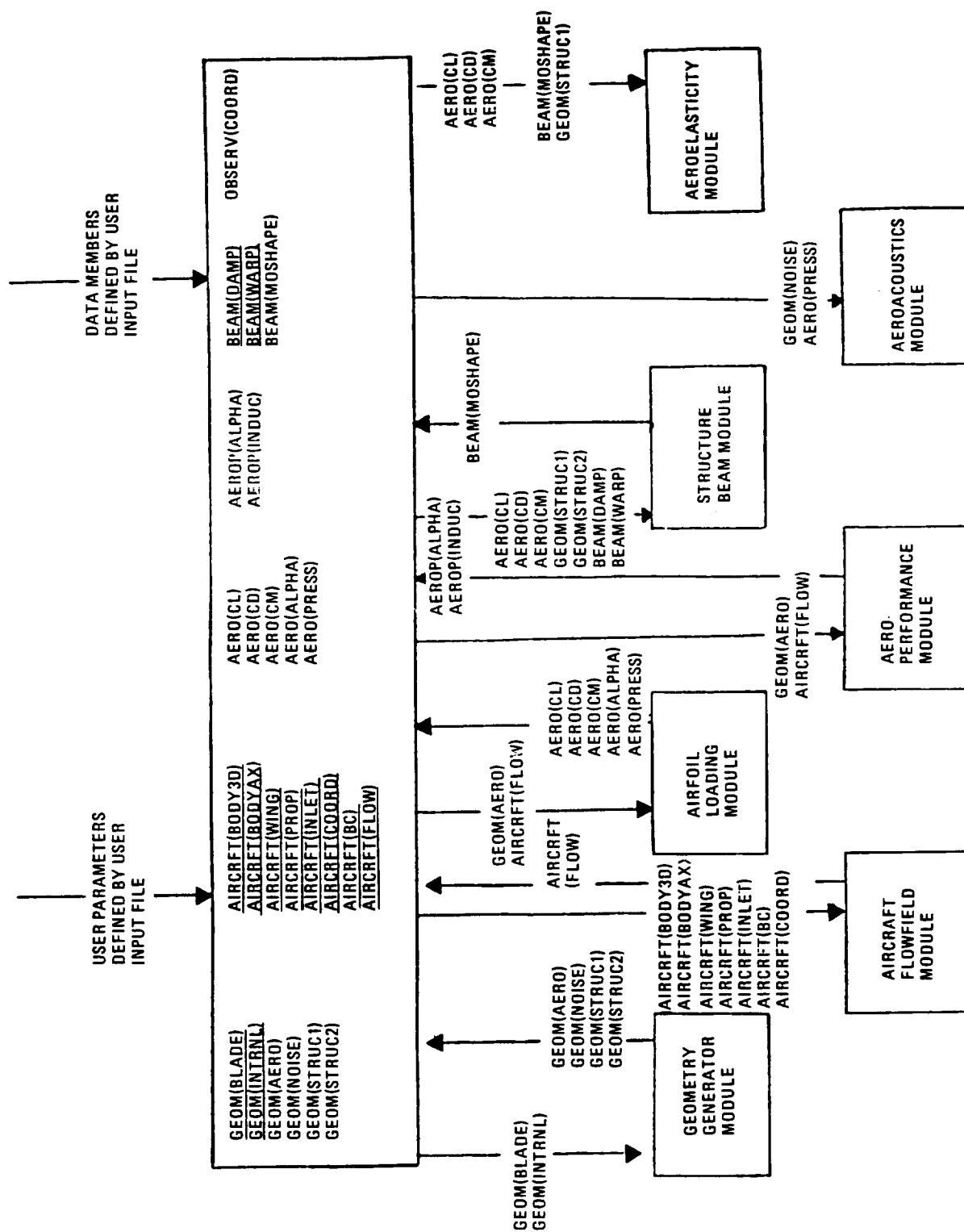


Figure 4.3-2. Schematic of GAPAS Data Base

for the analysis of stress and deflection stored in BEAM(XYZ). Up to this point, the data base for the operation of a single-pass mode has been described. In the interactive mode, the steady-state deflections of the blade are added to the original propeller geometry in order to produce a new propeller geometry and the above procedure is repeated until a converged steady-state deflection of the propeller is attained. The final version of the data base will undoubtedly consist of more data units for extra output of diagnostic purposes. As for the aeroacoustic module, propeller geometry data and pressure loading stored in GEOM(NOISE) and AEROP(PRESS) are required. No data files are needed to be generated for the interactions with other modules. The aeroelasticity module, which is not available at this time, will not be discussed but input data required to run such a module have been generated. Such data are stored in AERO(CL), AERO(CD), BEAM(MOSHAPE) etc. In addition, the design mode option has not been incorporated in this version of GAPAS. Section 5 discusses the system integration and the computer codes that have been implemented in this version of GAPAS.

## 5. SYSTEM INTEGRATION

### 5.1 OPERATION/PROGRAMMING STANDARDS

Because of the constraints stipulated by the ANOPP executive system, the source programs for GAPAS are written to execute on the CDC/CYBER NOS computer systems. In addition, FORTRAN IV compilers compatible to NOS systems are required. The size of the overall program also requires that overlay techniques must be used to keep the program within core storage limits. The CYBER segment loader (SEGLOAD) is selected because it offers flexibilities which allow multi-level, multi-tree structure overlay. These flexibilities are necessary for GAPAS because of its logical structure which separates its data base, executive system and functional modules in hierarchical levels. Certain programming rules are adopted for reasons of clarity and readability. These rules are designed to make subsequent maintenance of the GAPAS system relatively easy. These rules are outlined as follows:

- (1) All main modules and their submodules are to perform a specific task; for example, an aerodynamic loading module is to perform calculations of the drag polar only.
- (2) All intrinsic functions used are available from most standard system libraries.
- (3) Comment statements are included for modifications performed on any existing modules.
- (4) No non-standard FORTRAN statements will be used.
- (5) Data base access for functional modules is coded in self-contained routines, thus data transfer can be readily verified.

### 5.2 GAPAS DATA BASE ACCESS METHODS

The GAPAS data base consists of data separated broadly into two categories depending upon which devices they are stored on, namely, the user parameters and data units and their members. The following sections discuss the characteristics and the mechanics of implementing them.

### 5.2.1 Utilization of User Parameter

The user parameters represent single-value data stored in main memory. This type of data has the advantage of fast access, thereby making the overall execution time short. The disadvantage is that these data tend to take up precious main memory otherwise available for the process. In addition, user parameters are not transient data, meaning that they stay in core as long as the overall GAPAS is executing. These data remain even after the function module that creates them has been unloaded in core. Therefore, for a functional module writer who is to incorporate an existing module into the GAPAS system, careful consideration must be taken when input/output data are to be stored in the form of user parameters. User parameters should be utilized for data with a small number of elements and having to be accessed frequently.

Two methods are provided for accessing these data depending upon the user modes. For a programmer, ANOPP control statement "PARAM" is used. The format and its options will be discussed in the GAPAS User Manual. For a functional module writer, a number of ANOPP system utilities can be "CALL" to perform basic data base read/write functions. These utilities are summarized as follows:

- XGETP - This utility subroutine retrieves a user parameter value from the user parameter value table maintained in core. In a functional module, a "CALL XGETP" is issued for a specified parameter and its value is returned. If such a parameter cannot be found in core, a diagnostic message will be returned instead.
- FMPARI - This utility subroutine retrieves a number of specified user parameters in just one utility "CALL". Multiple values will be returned. The way XGETP and FMPARI are set up is similar, except that for the latter, two arrays defined with all the specified parameter names and their corresponding values must be set up in the module. The proper way to set these up will be illustrated in a subsequent section.
- XPUTP - This utility subroutine establishes (writes) or modifies a user parameter value in the user parameter value table maintained in core. A new parameter can be created and the value of an existing parameter can be changed by issuing a "CALL XPUTP" with a specified character name and value.



**FMPARO** - This utility subroutine establishes (writes) or modifies a number of user parameters. As for subroutine **FMPARI**, arrays or consecutive words in memory must be set up to pass the parameter names and values to the user parameter name table and value table.

Throughout the discussion of user parameter, the user parameter name table and value table have been mentioned. These tables are data structures required to be maintained in core for the operations of data retrieval and storage. The name table contains the names of all user parameters in alphanumeric data type, and a pointer for each parameter pointing at the address where its value can be found. The value of each parameter is stored in the value table whose address is indicated by the pointer. It is clear that the creation of a user parameter requires the maintenance of several words in memory. Caution must therefore be exercised to conserve storage in determining if an input/output datum be maintained as a user parameter.

#### 5.2.2 Utilization of Data Unit

The GAPAS data base manager (DBM) provides functional modules with a machine independent method of storing and retrieving data on direct access storage devices. The DBM provides a hierarchical data structure having direct and sequential accessing of logical records. The highest level of the hierarchy is called data base, which is defined as a collection of data units. During GAPAS execution the data base is created, expanded and modified via control statements such as **CREATE**, **ATTACH**, **LOAD**, and **UPDATE**. These statements are discussed in the User Manual. From the host operating system stand-point, a data unit is implemented as a file, physically stored on a direct access storage device. A data unit may consist of a number of logical segments termed "data member." Each member segment is uniquely named within a data unit and is comprised of a set of sequentially organized records. The combination of the data unit name and the data member name is required to reference a specific data segment. Analogous to the concept of a file, a data member may contain either formatted or unformatted data, fixed length or variable length records. Depending on the type of format, data may be retrieved in words or a full record.

The data base manager, as part of the GAPAS system, provides basic open/close, read/write, and position functions for module writers via calls to specific member manager routines. These routines are discussed as follows:

- (1) OPEN ROUTINES - The initial steps in opening a data unit are the validation of the name argument and the determination of whether the data member is in use. A valid name is specified as one to eight alphanumeric characters, with a leading alphabetic character. If the data member is not found, a data structure called member control block is established to keep track of the new member. The member name, record length, number of records, etc., will be written into the control block. Four opening routines are available for different applications:

- MMOPAP - open member to write append
- MMOPWD - open member to write directly
- MMOPWS - open member to write scratch
- MMOPRD - open member to read

- (2) WRITE ROUTINES - Typically, there are three levels of validation performed by these routines. First, the name argument is checked. Second, the member control block is checked to determine if the previous record is completed. Finally, the data member format type is checked to determine if the record to be written is consistent. When all required validations are completed, records are then written to the data unit residing on a disk. These write routines are available for writing either a full record or words:

- MMPUTR - write a record
- MMPUTW - write a partial record of n words
- MMPUTE - write a partial record of n elements

- (3) READ ROUTINES - Basically, two steps for validation are performed. First, the name argument is validated. Second, the member control block is checked to determine if the member is positioned within a record. If it is, the member is repositioned to the beginning of the next record. Upon completion of these validations, a record is read and stored into an array reserved for such purpose. Full record or partial record can be read by using the following routines.

- MMGETR - read a record
- MMGETW - read a partial record of n words
- MMGETE - read a partial record of n elements

- (4) CLOSE ROUTINE - If the member was open for reading, the member is logically closed. If it was open for writing, a number of data structures that are required for keeping track of the member are updated, and the member is logically closed.

MMCLOS - close a member

- (5) POSITION ROUTINES - These routines perform two steps for validation. First, the argument name is verified, and second, the determination of whether the data unit is open for read is performed. If it is not, the system will terminate with appropriate messages. If it is, the record position is then set either to the beginning of the member or skipped forward n records as specified. Positioning of records is accomplished by updating the current record counter in the member control block.

MMSKIP - skip n records

MMREW - rewind a member

MMPOSN - position member to record n

### 5.3 FUNCTIONAL MODULE INCORPORATION TECHNIQUE

In this section, examples are presented to show how the executive system routines discussed above are used in incorporating the functional modules in GAPAS. The geometry generator (GEOGEN) is selected for this purpose due to its extensive input/output requirements.

#### 5.3.1 User Parameter Implementation

In the following example, the retrieval of user parameters are coded in SUBROUTINE UPGEOM in GEOGEN. Since nine parameters are to be retrieved, a DIMENSION statement is required to set up arrays to receive data. Therefore, "DIMENSION NAME(9), IVALUE(9), NELEM(9), ITYPE(9)" is coded. The next step is to set up default values for each parameter by storing such values in the array designated to receive the parameter data. Therefore "IVALUE(1)=0", etc., are coded. The next step is to define the user parameter names to be retrieved which results in "NAME(1)=6HIGLOBE", etc. The next step defines the type of data (integer or real) and number of elements for each parameter. This is accomplished in a DO loop. Then "CALL FMPARI(NAME,IVALUE,ITYPE,NELEM,9)" is issued to perform the actual user parameter retrieval. Upon completion, the values are returned in array IVALUE. The last step is to store the retrieved value into the appropriate variables defined in COMMON blocks.

```

SUBROUTINE UPGEOM(IGLOBE, ISPACE, ISTART)
COMMON/OPCON/NPROP, PRESS, .... IROT..
COMMON/MXVAR/NIN, NSLICE, .....
.....
.....
DIMENSION NAME(9), IVALUE(9), NELEM(9), ITYPE(9), ..
.....
.....
IVALUE(1)=0
IVALUE(2)=1
.....
.....
NAME(1)=6HIGLOBE
NAME(2)=6HISPACE
.....
.....
DO 1 I=1,9
  ITYPE(I)=1
1  NELEM(I)=1
.....
.....
CALL FMPARI(NAME, IVALUE, ITYPE, NELEM, 9)
.....
.....
IGLOBE=IVALUE(1)
ISPACE=IVALUE(2)
.....
.....
RETURN
END

```

### 5.3.2 Data Unit Implementation

The next example illustrates the mechanics of reading a data unit by using the system routines outlined in Section 5.2. In the original geometry generator, three read statements are used to input the geometry of a propeller blade. The first read statement inputs the number of spanwise stations and number of points for each airfoil section. The second read statement inputs the local coordinates and a ply angle of all the points in a section. The last read statement inputs the leading edge alignment, horizontal length, chord length, twist angle and the global coordinates of the section. The second and third read statements are repeated for each section. The original codings are as follows:

```

.....
.....
10 READ(5,10) NIN, NWIRE
   FORMAT(2I5)

```

```

        DO 60 IN=1,NIM
        READ(5,20) ((XTIN(IWIRE,IN,I),I=1,4),IWIRE=1,NWIRE)
        READ(5,30) TLEA(IN),THA(IN),TCHORD(IN),TWIST(IN),
1  (XTIN(IN,1,I), I=1,3)
60  CONTINUE
20  FORMAT(4E14.7)
30  FORMAT(7F10.5)
        .....
        .....

```

Analogous to accessing a file, the open, read and close steps are required. As in user parameters, arrays must be set up for the name and temporary data storage area. For that, the "DIMENSION NAME(3), IHDR(2), TEMP(17)" is coded. These arrays are used as name definition, for the return of system flags, and a buffer area. The next step defines the data unit and member names resulting in "NAME(1)= 4HGEOM NAME(2)=6HMSLICE". Then the data member is opened for read by "MMOPRD(NAME,IHDR,STATUS)". The actual reading is performed by "MMGETR(NAME,TEMP,4,NWDS,STATUS)". Upon completion, data stored in the temporary buffer area are transferred in the array designated in the module's COMMON block.

```

SUBROUTINE GEOIN
        .....
        .....
COMMON/INPUT/STIN(53),XTIN(53,17,4),.....TLEA(17),THA(17),....
        .....
        .....
DIMENSION NAME(3),IHDR(2),TEMP(17)
        .....
        .....
NAME(1)=4HGEOM
NAME(2)=6HMSLICE
CALL MMOPRD(NAME,IHDR,STATUS)
DO 24 IN=1,NIN
CALL MMGETR(NAME,NWIRE,1,NWDS,STATUS)
DO 21 IWIRE=1,NWIRE
CALL MMGETR(NAME,TEMP,4,NWDS,STATUS)
XTIN(IWIRE,IN,1)=TEMP(1)
XTIN(IWIRE,IN,2)=TEMP(2)
XTIN(IWIRE,IN,3)=TEMP(3)
XTIN(IWIRE,IN,4)=TEMP(4)
21 CONTINUE
        .....
        .....
CALL MMGETR(NAME,TEMP,7,NWDS,STATUS)
TLEA(IN)=TEMP(1)
THA(IN)=TEMP(2)
TCHORD(IN)=TEMP(3)

```

.....  
.....  
RETURN  
END

The setup for writing data into data base is analogous to that of reading and the details will not be repeated here. For more information, the ANOPP Reference Manual is recommended.

#### 5.4 GAPAS FUNCTIONAL MODULES AND ITS CAPABILITIES/LIMITATIONS

The current version of GAPAS addresses the propeller performance mode. Only the basic codes necessary to determine the propeller geometry, aerodynamics, structure and acoustics have been incorporated at this time. For the completeness of the system an atmospheric module (ATM) has been incorporated to provide atmospheric properties as a function of altitude. Due to different demands for airfoil section calculations,, a geometry generator (GEOGEN) has been developed and included in the system for the determination of sections perpendicular to the quarter-chord, pitch change axis and elastic axis. For aerodynamic analysis, the system has included an aircraft flow field code (JUMPER), two airfoil data banks (NACA16 and CLARK-Y), an airfoil loading module (TRANSEP) and the Chang-Sullivan performance module (PROPCHG). The original NACA16 data bank, as developed at Texas A&M University, has been enhanced by including a transonic capability derived from AIR23. AIR23 was developed at UTRC. For structural analysis a beam module with the capability of performing both static and dynamic analysis for solid blades has been incorporated. Finally, two NASA Langley acoustics modules, one for subsonic flow (SPN) and one for transonic flow (TPN) have been included. To exercise these two modules a blade shape module (RBS) which transforms the airfoil section from a cartesian coordinate system into an elliptic coordinate system has also been incorporated. In addition, a pressure loading module (PLD) has been developed to evaluate loading for sections normal to pitch change axis from sections normal to quarter-chord. In short, a basic framework for propeller analysis has been developed.

A summary of GAPAS features and limitations is described below.

- (1) Each functional module is functionally independent and thus can be easily modified or replaced.
- (2) Checkpoint/restart capability has been used repeatedly. It has been particularly useful for intermediate output analysis as well as for storing results of previous module calculations so that it is unnecessary to repeat that part of the overall solution. This capability not only reduces the overall processing time but also enhances the turnaround time.
- (3) Error traceback has been provided particularly in system level. Any fatal or nonfatal error will trigger a traceback of all routines leading to the subsequent diagnostics.
- (4) Modules have been linked to operate in both single pass mode and aerodynamic/structural interaction mode.
- (5) Design mode capability does not exist in this version of GAPAS.
- (6) User is limited to only one set of spanwise and chordwise stations for aerodynamics, structures, and acoustics.
- (7) In the case of swept propellers, it has been assumed that strip theory for the section normal to the quarter-chord will provide the correct drag polar. This assumption must still be verified.
- (8) The moment coefficient used for the SR-3 propeller is obtained from the subsonic NACA-16 data bank. Transonic data needs to be included in this module.
- (9) TRANSEP is the only airfoil prediction code incorporated.
- (10) Structural module only addresses solid blades and thus GAPAS will not currently analyze composite blades or blades with internal structure.
- (11) Structural module only contains a beam model. In the case of high activity factor or low aspect ratio propellers, the existing beam module would not be appropriate and a plate analysis would be required.
- (12) Acoustic module (TPN) has been found to exhibit problems in obtaining a converged solution to the retarded time equation for some observation locations (see page 6-18).
- (13) Acoustic signature does not include the contribution from the skin friction. Although SPN includes skin friction, it is currently not transferred into the acoustic module.

- (14) The aeroelastic capability is not integrated within GAPAS and must be run as a stand-alone code.
- (15) GAPAS can only be run on CDC computers in a batch mode.
- (16) Current version of GAPAS does not contain a graphics capability.



## 6. TASK 5: ANALYSIS SYSTEM VERIFICATION

### 6.1 PROPELLER TEST CASES

In order to verify the operation of the computer code, two calculations have been performed using GAPAS. The first, an advanced technology SR-3 propeller, representative of a high-speed commercial transport, and the second, a Hartzell 101/16 propeller, representative of a small, moderate-speed general aviation aircraft. Although the original verification task was to encompass a series of calculations for the above propellers over various Mach numbers, advance ratios, and propeller pitch angles, substantial time and resources were expended uncovering numerous problems with functional modules that were acquired, as well as developed in-house, and thus, resources allowed for only one operating condition for each propeller.

In order to verify the operation of GAPAS and determine potential problem areas, all the analysis capabilities incorporated in GAPAS were exercised during the course of performing both calculations. In the case of the SR-3 propeller, the interactive mode was utilized, wherein the aerodynamics and structural modules were coupled together during the calculation. In the case of the SR-3 propeller, the airfoil loading was calculated using NACA 16 data banks, whereas, TRANSEP was used for the 101/16 propeller. In the acoustics calculation, SPN was used in the 101/16 calculation, whereas, TPN was used in the SR-3 calculation.

The results of the above calculation are described below. Comparisons between the calculations and available data are also shown.

#### 6.1.1 SR-3 Propeller Test Case

The SR-3 propeller is a 0.62-m (24.5-inch) diameter, variable pitch, 8-bladed advanced technology propeller (Figure 6.1-1). The blade is composed of a series of NACA 16 airfoils in the region beyond 53 percent of the blade radius, a NACA 65/CA series from the hub to the 37 percent blade radius, and a transition region between the two families (Ref. 6.1-1). Figure 6.1-2 describes details of the blade characteristics. The airfoil sections are laid out along streamlines which vary from conical lines at the spinner to cylindrical lines at the blade tip. Figure 6.1-3 shows the

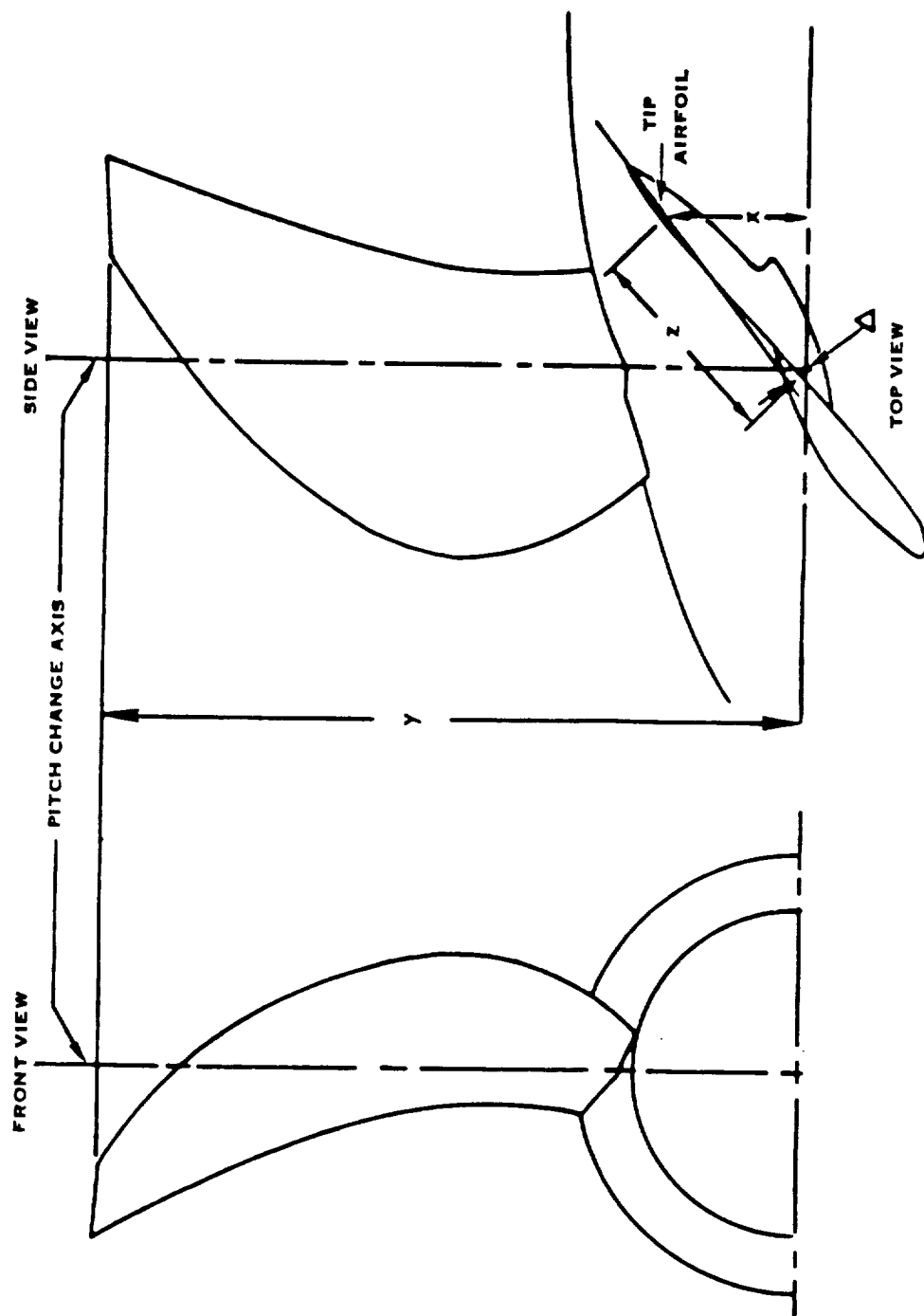


Figure 6.1-1. Three View Sketch of SR3 Showing Relative Location of Tip Airfoil and Pitch Change Axis

8 BLADES/235AF/0.241 CLI  
0.62 METER (24.5 INCH) DIAMETER

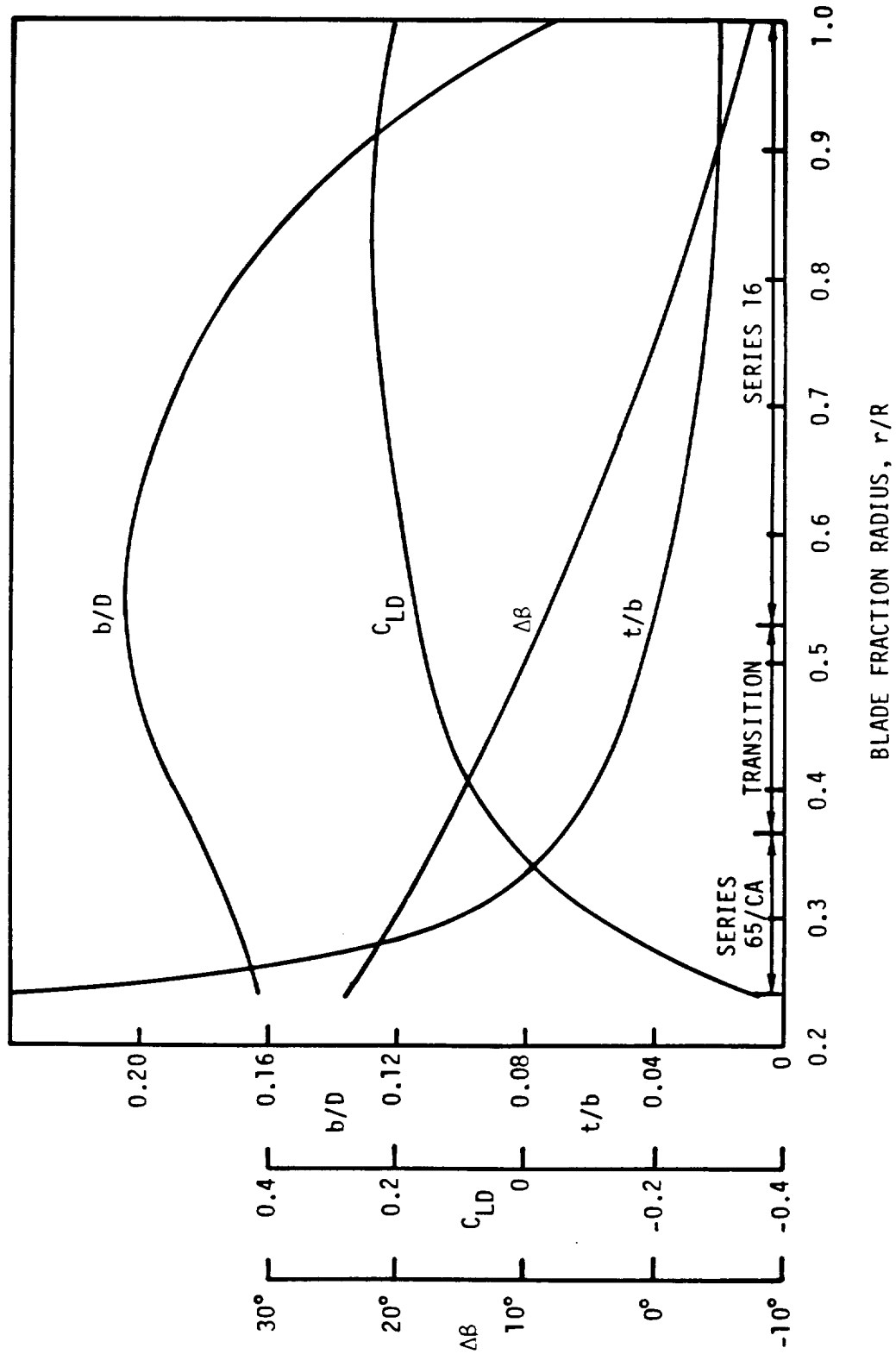
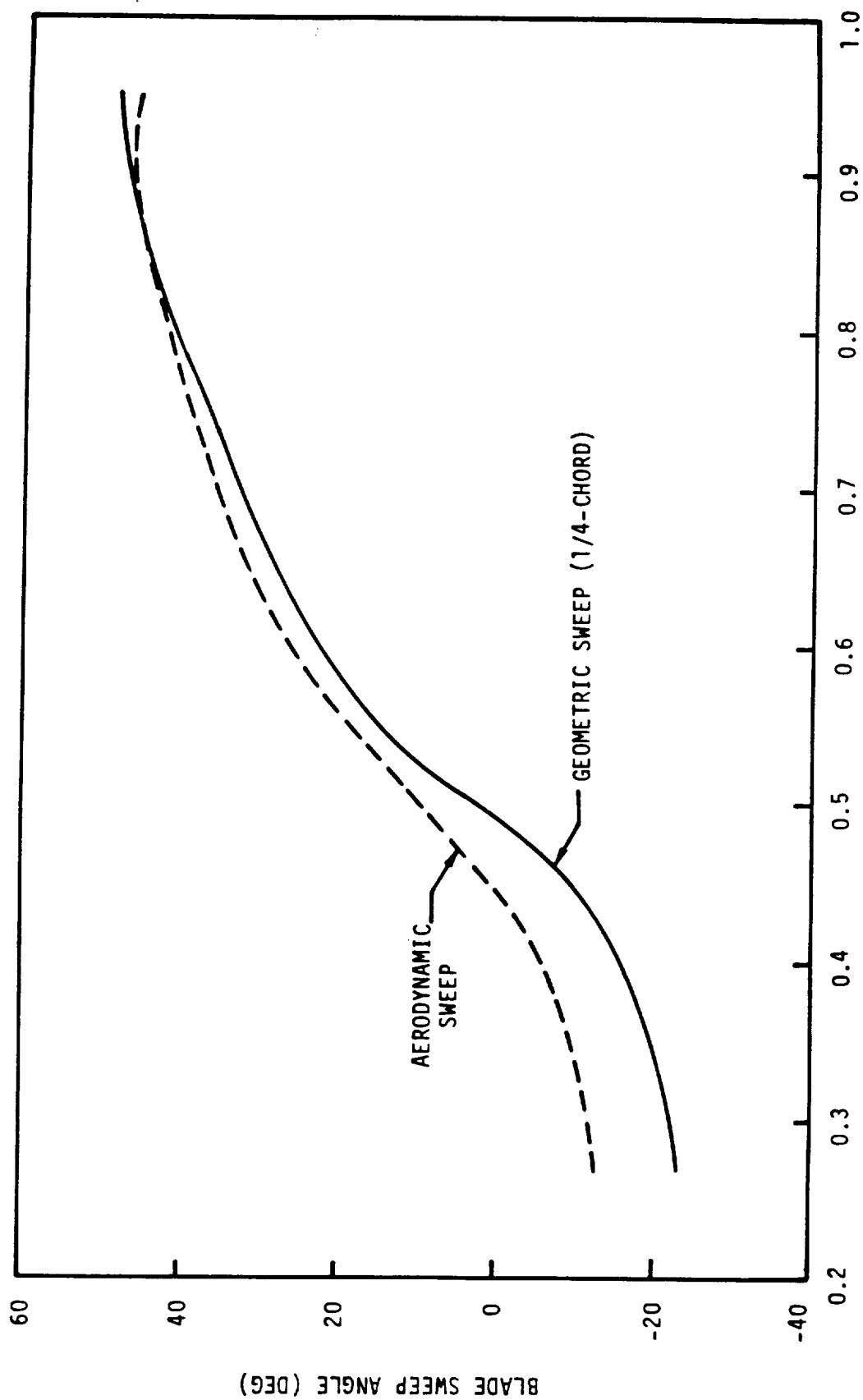


Figure 6.1-2. SR-3 Propeller Blade Characteristics



BLADE FRACTIONAL RADIUS,  $r/R$

Figure 6.1-3. Geometric Blade Sweep as a Function of Blade Fractional Radius

geometric sweep of the blade as a function of blade fractional radius. Due to the conical nature of the flow near the spinner, a difference exists between the effective aerodynamic sweep and the manufacturers geometric sweep (Figure 6.1-3). A three view sketch of the SR-3 showing in-plane and out-of-plane geometric sweep is shown in Figure 6.1-4.

The SR-3 propeller calculation was performed for the following operating conditions: (1) freestream Mach number  $M_\infty = 0.8$ ; (2) advance ratio  $J = 3.06$ ; (3) power coefficient,  $C_p = 1.71$ ; and (4) sea level altitude. The modules exercised during this calculation were (1) geometry generator; (2) Jumper; (3) AIR 23 and NACA 16 data banks, (4) Chang-Sullivan; (5) beam; and (6) TPN. Although the AIR 23 data bank is for a NACA 16 airfoil, it does not contain the moment coefficient. Thus, it was necessary to utilize the NACA 16 data bank to obtain this coefficient.

In the initial conception of GAPAS, the question arose of how to properly utilize the airfoil loading module for the cases of propellers that involve sweep. From classical inviscid two-dimensional swept wing theory, the lift depends on the normal Mach number and the airfoil section normal to the leading edge. In the actual SR-3 propeller, the flow is three-dimensional since the blade is swept both in-plane and out-of-plane as well as being tapered (Figure 6.1-4) and is being generated from airfoil sections that are not uniform along the blade. Without the aid of a detailed three-dimensional Euler code capability for propellers, it was recommended that the airfoil section be determined by a slice normal to the quarter-chord at any particular radial station. An example of such a cut is shown in Figures 6.1-5 through 6.1-7. Figure 6.1-5 shows the actual camber line that is obtained by taking a slice perpendicular to the quarter-chord line at  $r/R = 0.5837$ . For the NACA 16 airfoil, the coordinates of the camber line can be described by specifying the design lift coefficient,  $C_{L_D}$ . The dashed line shows the shape of the camber line of a NACA 16 airfoil obtained by matching the value of the maximum ordinate of the camber line. Note that results indicate that that airfoil obtained by a slice perpendicular to the quarter-chord is nearly a NACA 16 airfoil section. Figure 6.1-2 shows the input distribution of  $C_{L_D}$  for the airfoil sections along the blade. Since these airfoils are almost laid in along

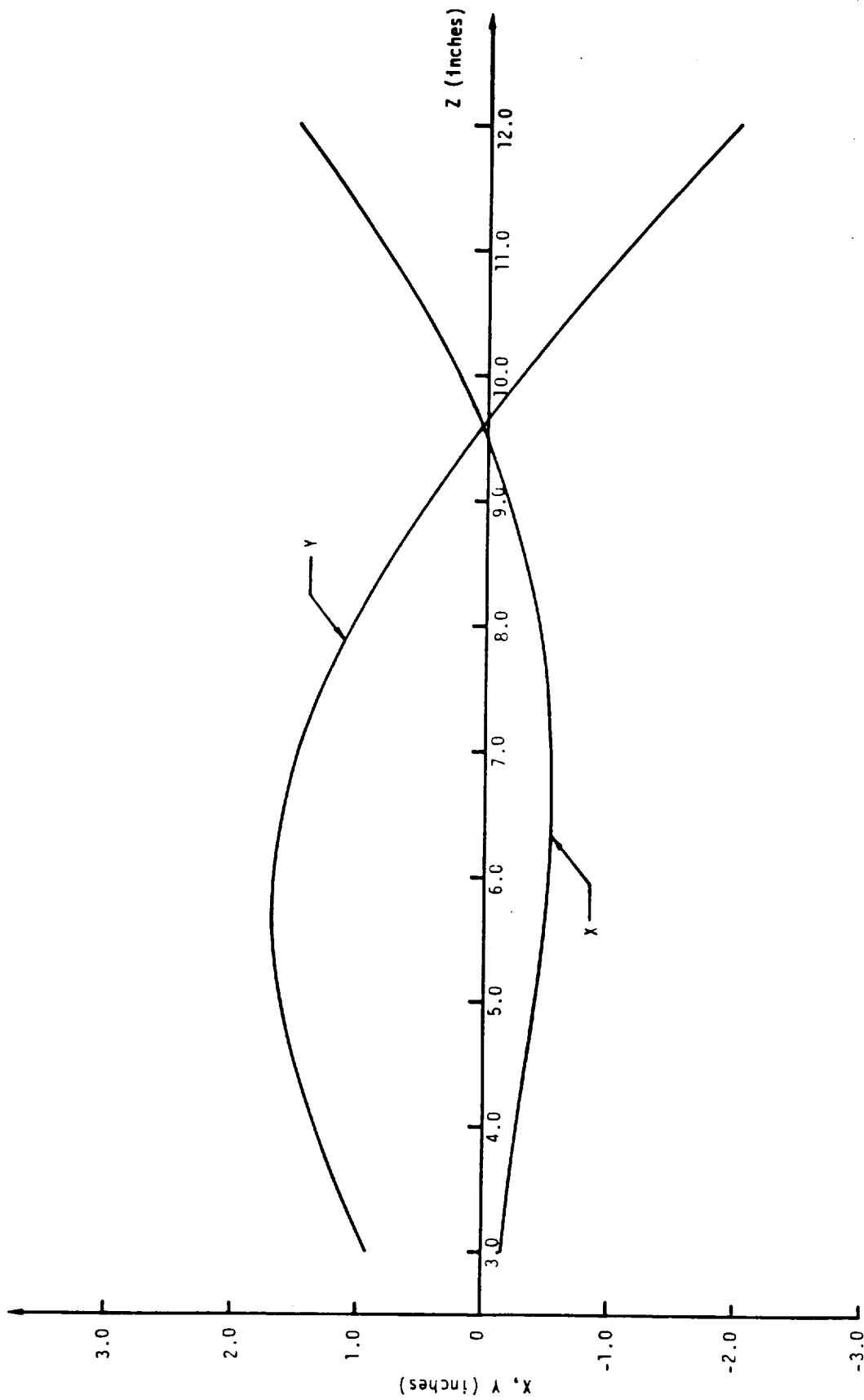


Figure 6.1-4. SR-3 1/4 Chord Geometry

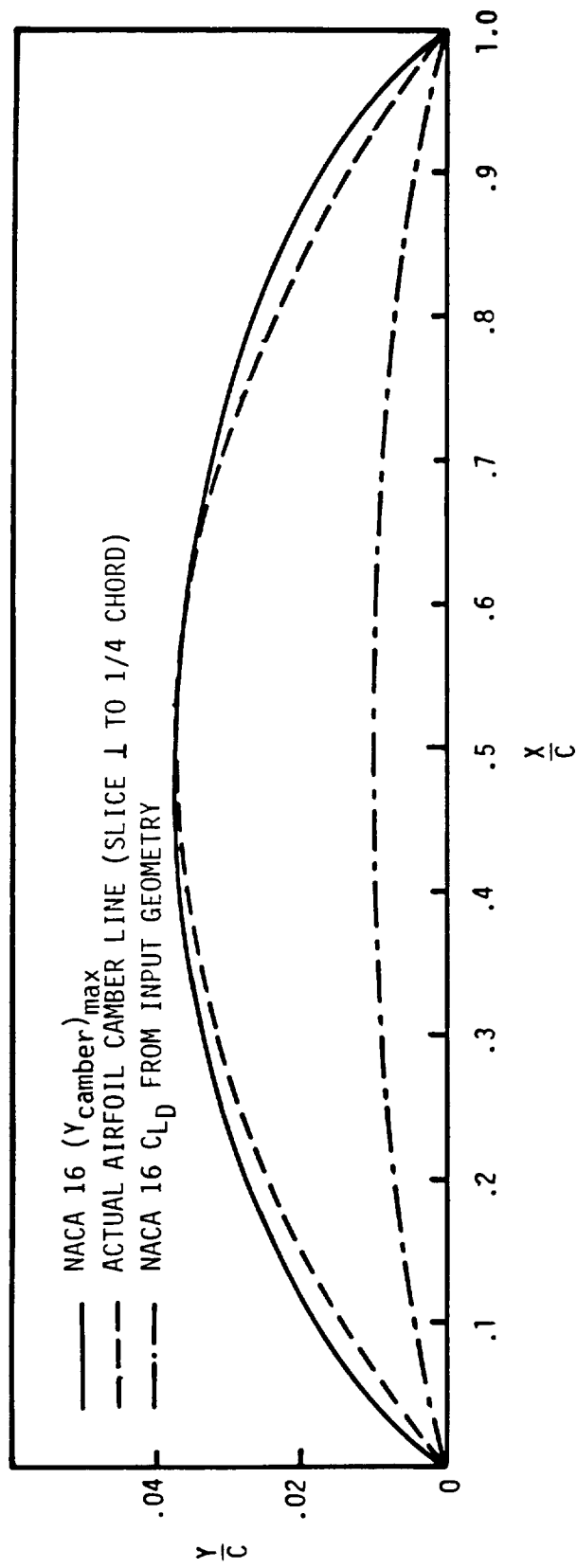


Figure 6.1-5. SR-3 Camber Line from Airfoil Loading Module ( $Z/C = 0.5837$ )

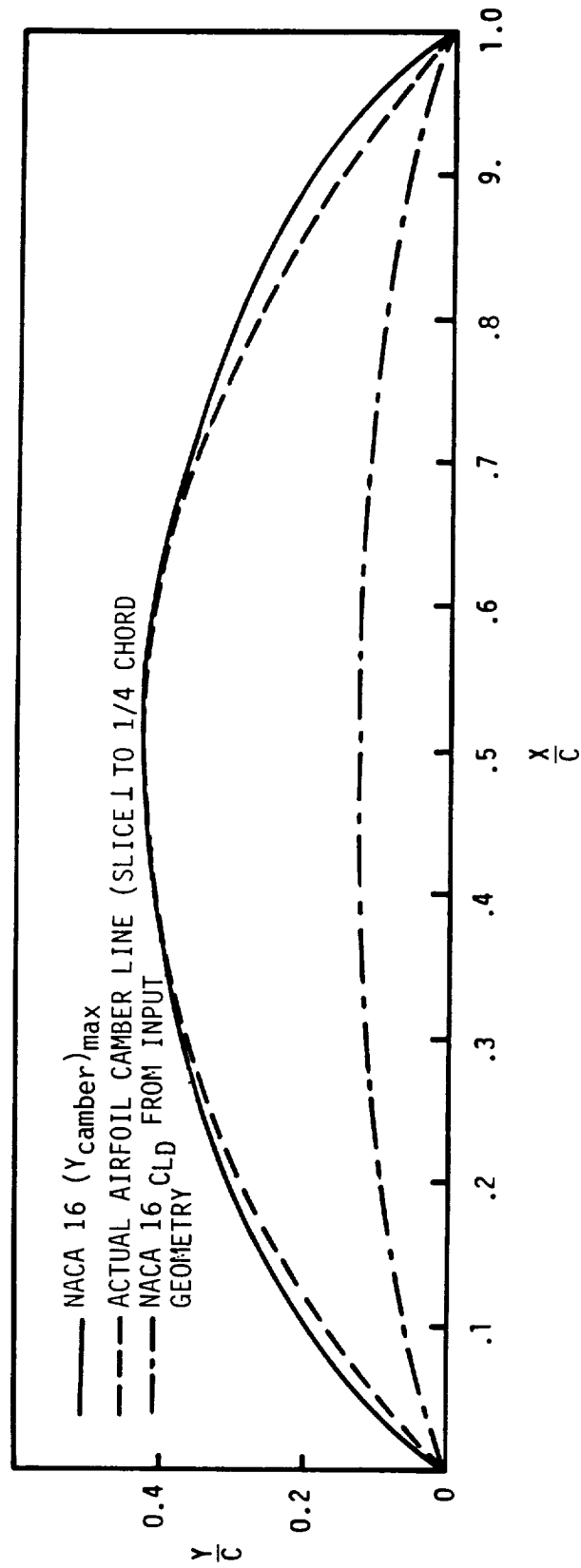


Figure 6.1-6. SR-3 Camber Line from Airfoil Loading Module ( $Z/C = 0.7673$ )



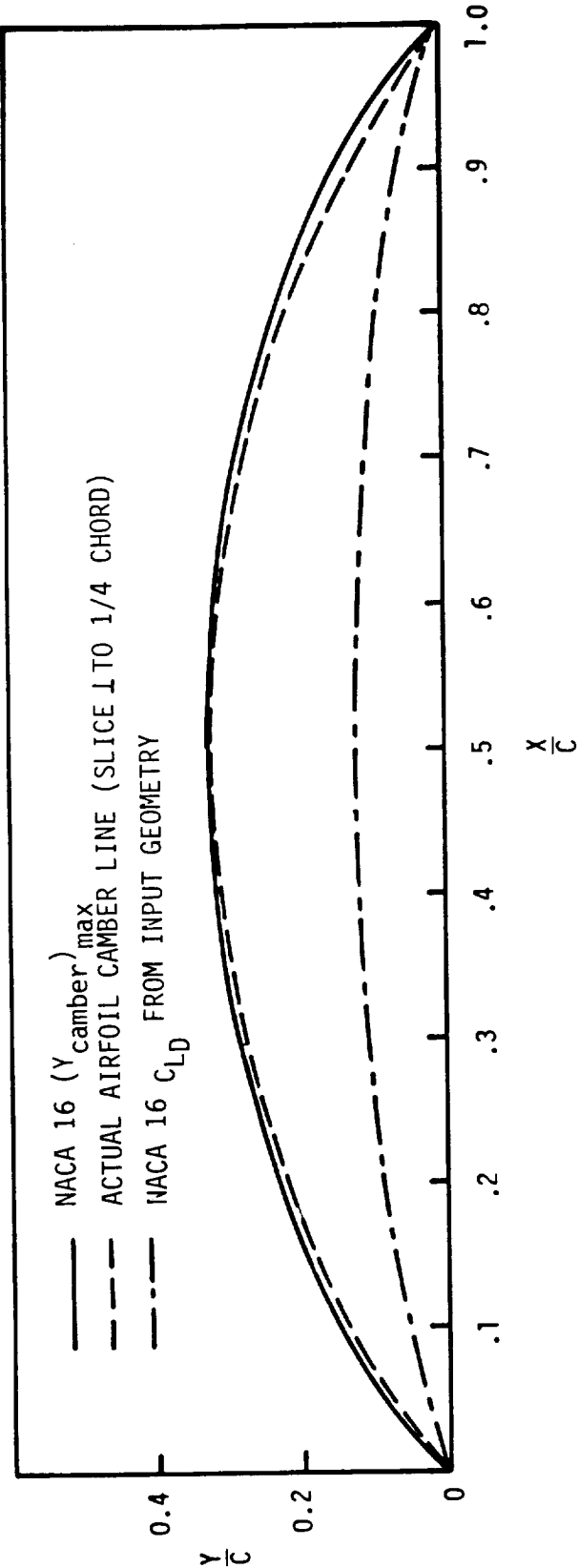


Figure 6.1-7. SR-3 Camber Line from Airfoil Loading Module ( $Z/C = 0.955$ )

cylindrical surfaces, the actual airfoil section laid in is shown by the second dashed line in Figure 6.1-5. Thus, it is apparent that significantly different  $C_L$  and  $C_D$  will be computed depending on how the cut is made. Figures 6.1-6 and 6.1-7 show similar results at  $r/R = 0.7673$  and  $r/R = 0.855$ . The fact that the resulting airfoil sections obtained by taking slices perpendicular to the quarter-chord are nearly NACA 16 sections may be fortuitous and requires further investigation. The usual increase in both camber and thickness to chord ratio of an airfoil normal to the quarter chord line due to the shortened chord has been substantially increased here and is primarily attributed to the twist of the SR-3 propeller blade.

Due to the uncertainty in the correct manner of choosing the airfoil section, it was decided to use the AIR 23 data banks specifying the value of  $C_{L,D}$  as in Figure 6.1-1. However, if the proper airfoil section were known, TRANSEP would have provided a more accurate calculation of  $C_L$ ,  $C_D$  and  $C_M$ .

Once the propeller geometry is set up, the blade pitch angle at the  $3/4$  span station,  $\beta_{3/4}$ , is specified. For this calculation  $\beta_{3/4}$  was set to 61.3 degrees. With the nacelle geometry specified the Jumper code is used to calculate the flow field in the plane of the propeller. Figure 6.1-8 shows the results of the calculation for the SR-3. Here,  $W$  represents the axial flow component and  $V$  is the radial flow component. As expected, the results show the largest radial velocities to be in the hub region. The resultant flow field in the plane of the propeller is then used as input to the Chang-Sullivan performance module.

The Chang-Sullivan code was run using  $\beta_{3/4} = 61.3^\circ$ . The resultant  $C_p$  did not exactly match the prescribed  $C_p = 1.71$ . Thus, the  $\beta_{3/4}$  was perturbed until a match on  $C_p$  was attained. A  $\Delta\beta$  of  $-0.8^\circ$  produced this match. However, a sensitivity study was performed in which the number of trailing vortices were varied in order to determine the error in not utilizing sufficient bound vortex segments. Originally 11 trailing vortices were used and then calculations using 13 and 16 trailing vortices were

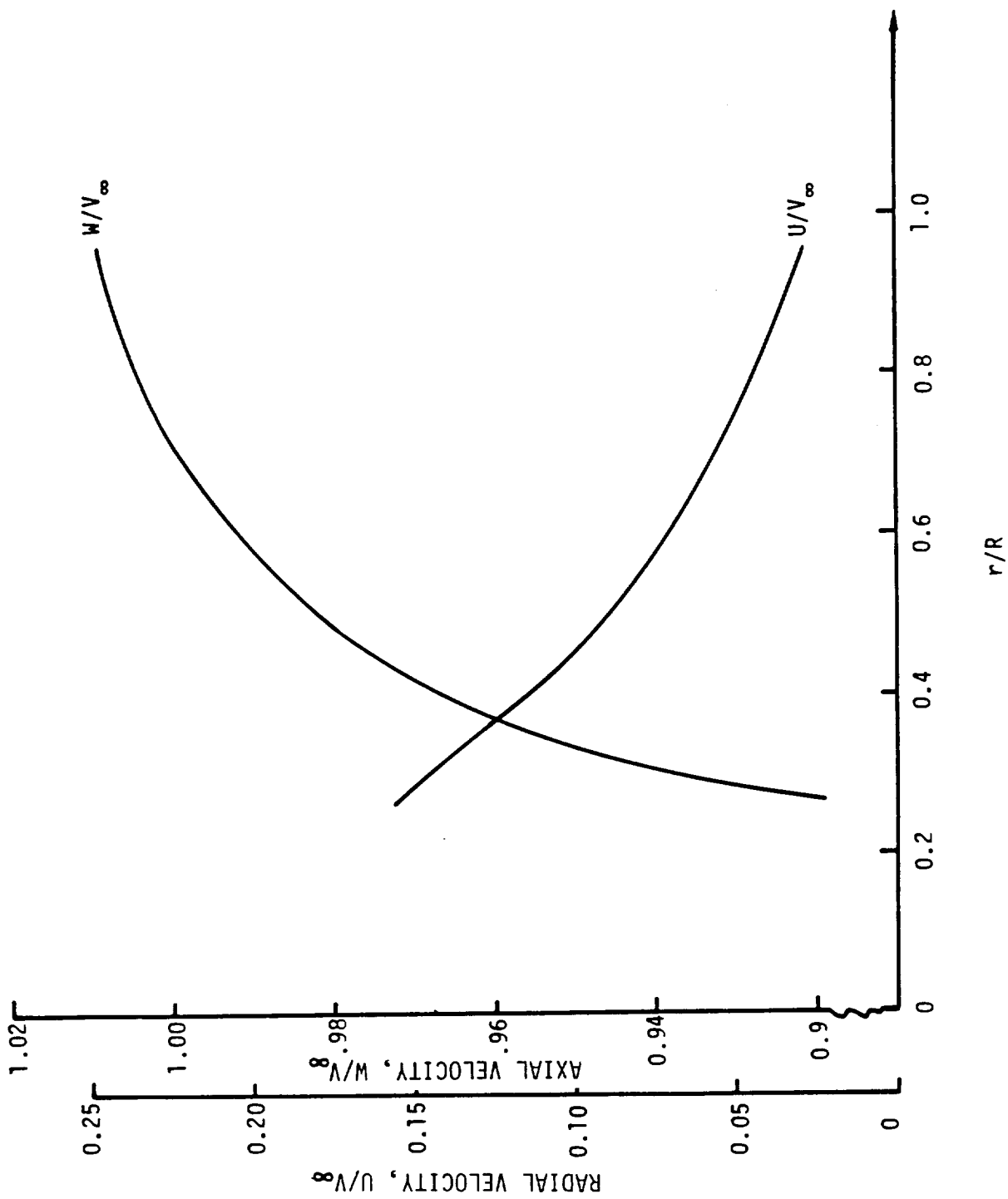
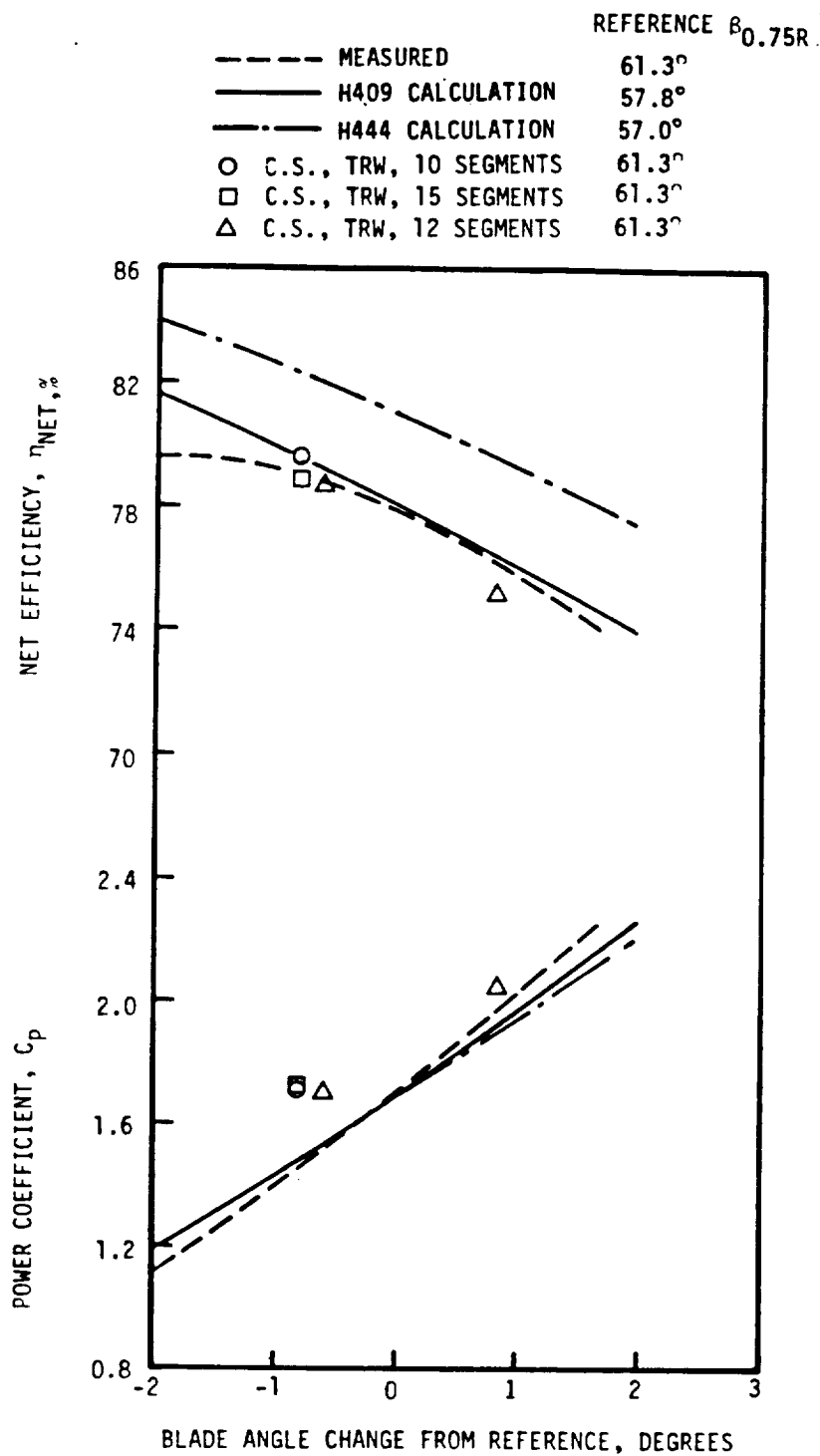


Figure 6.1-8. Velocity in Propeller Plane of SR-3

performed. The additional trailing vortices were incorporated in the region of large curvature (i.e., in the region from forward sweep to rearward sweep). The results of the calculations are shown in Figures 6.1-9 through 6.1-12. Figure 6.1-9 shows the resultant efficiency and power coefficient as a function of  $\Delta\beta$  measured from various reference values of  $\beta_{3/4}$ . The Chang-Sullivan results are referenced to the  $\beta_{3/4} = 61.3^\circ$ . The terminology, number of segments, relates to the number of bound vortex segments and is thus one less than the number of trailing vortices. The results show that a sufficient number of trailing vortices are required to produce reasonably accurate results. A change in the number of segments not only changes the  $\Delta\beta$  to match  $C_p$ , but the efficiency as well. Fifteen segments match the power coefficient with a  $\Delta\beta = -0.8$ , and match the efficiency to within a few tenths of a percent. Note that 10 segments match the  $C_p$  but the efficiency obtained is higher. Figures 6.1-10 and 6.1-11 show the calculated normal Mach number,  $C_L$  and  $C_D$  distribution as a function of blade spanwise position. Although the Mach number distribution appears to vary substantially over the outer 50% of the blade, the scale in Figure 6.1-10 has been expanded to cover the range of Mach numbers in the outer portion of the blade between 0.76 and 0.88. In addition a comparison of the elemental thrust coefficient ( $dC_T/dx$ ) and elemental power coefficient ( $dC_p/dx$ ) between the Chang-Sullivan results and that of the Goldstein methodology is shown in Figure 6.1-12.

In the non-interactive mode, the calculation first proceeds to the acoustic module and then to the structural module. In the interactive mode, the procedure is to proceed from the Chang-Sullivan module to the structural module and back to the Chang-Sullivan module. This procedure continues until a converged solution is obtained. At this point, the calculation proceeds to the acoustic module to calculate the acoustic signature. The results of both modes of operation are discussed below.

In the non-interactive mode the calculation for the acoustic signature was performed using TPN. This was necessary because the helical tip Mach number was supersonic. Due to the uncertainty in the correct airfoil shapes to use in the case of highly swept and twisted propellers, it was decided to utilize the NACA 16 airfoil data banks instead of TRANSEP. In



(B) ADVANCE RATIO = 3.06; MACH NUMBER = 0.80

Figure 6.1-9. SR-3 Power Coefficient and Efficiency Comparison of Calculations and Experiment as a Function of  $\Delta\beta$

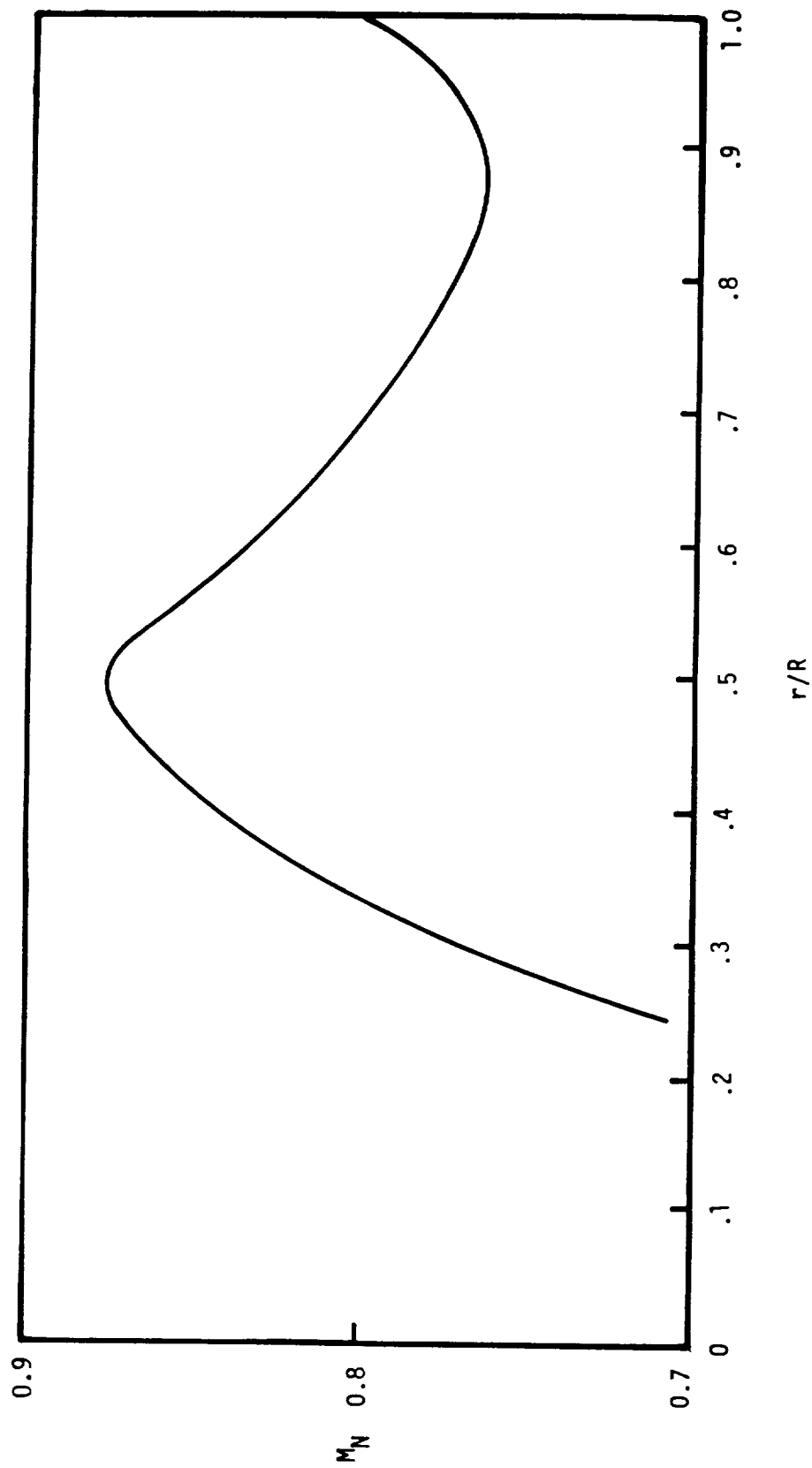


Figure 6.1-10. Normal Mach Number vs. Radial Distance for SR-3 Propeller  
 $M_O = 0.8$ ,  $J = 3.06$ ,  $C_p = 1.71$

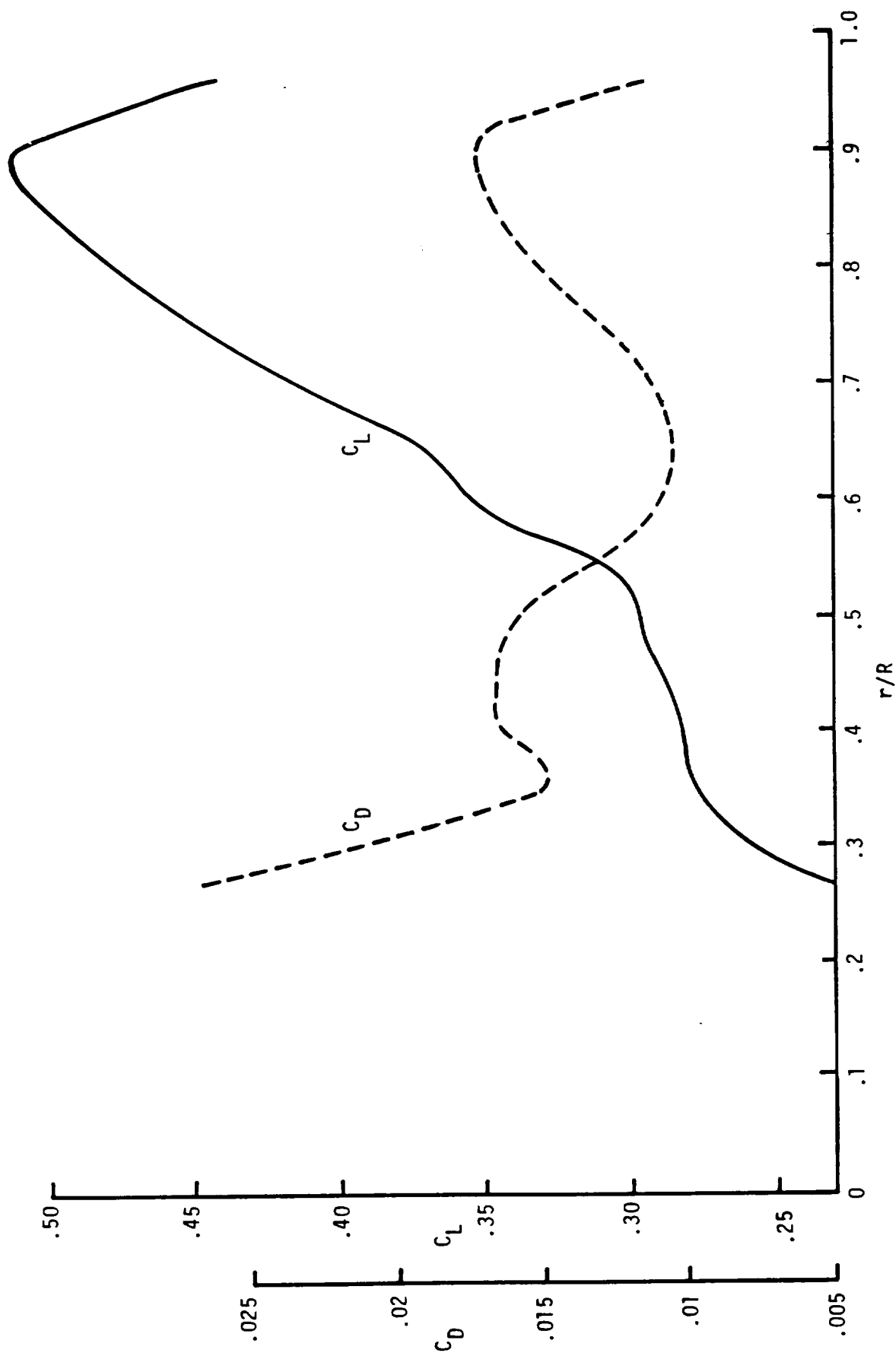


Figure 6.1-11. Variation of Lift and Drag Coefficients with Radial Location for SR-3 Propeller  
 $M_0 = 0.8$ ,  $J = 3.06$ ,  $C_p = 1.71$

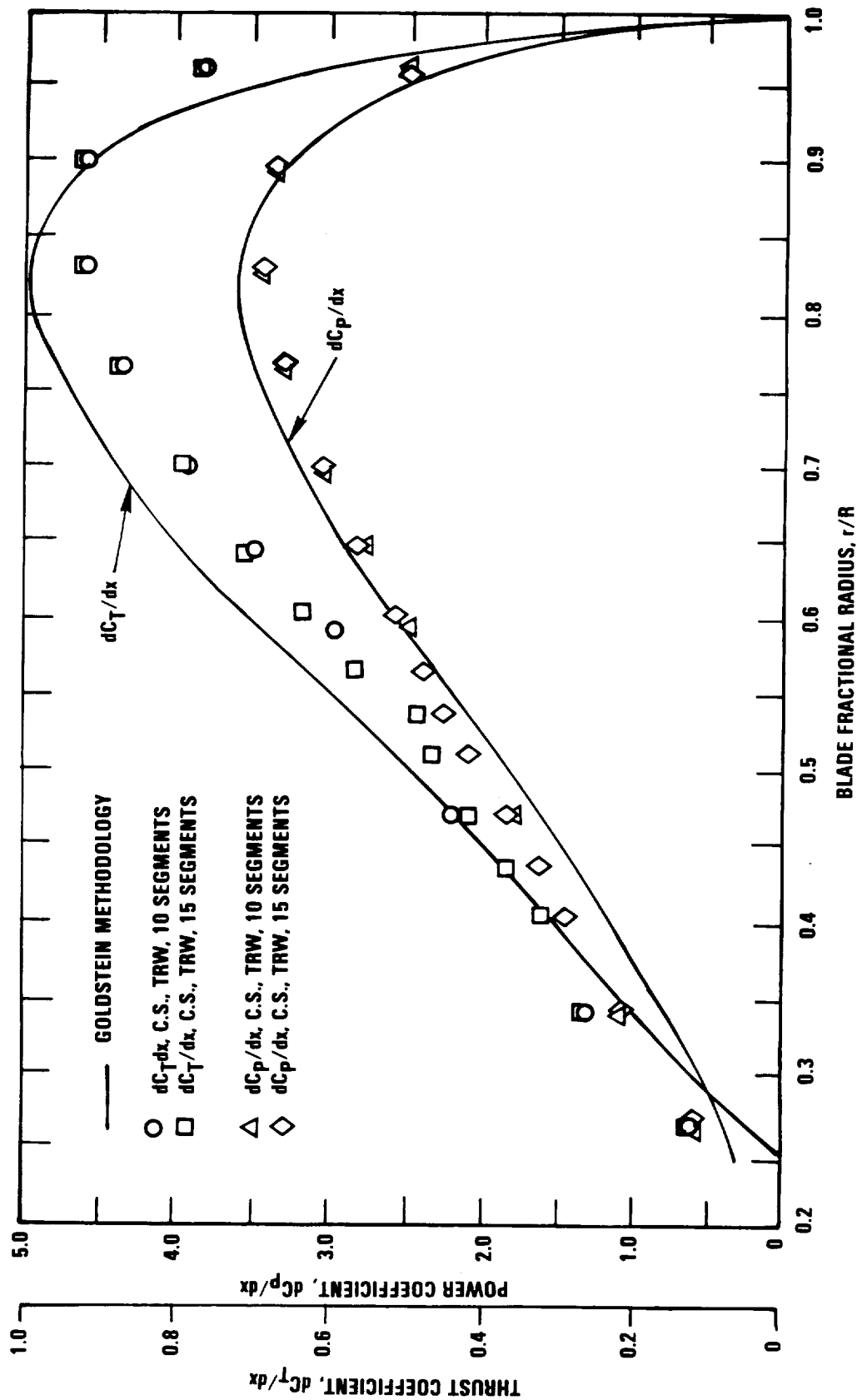


Figure 6.1-12. Variation of Calculated Thrust and Power Coefficient Gradients with Blade Fractional Radius  
 $M_0 = 0.80$ ,  $J = 3.06$ ,  $C_p = 1.71$ ,  $B = 8$



addition this would allow the airfoil data bank module to be checked for proper data transfers. The use of the airfoil data banks poses somewhat of a problem because only the  $C_L$ ,  $C_D$ , and  $C_m$  are stored. Therefore, in order to compute the required loading distribution, a simple parameterization was developed. In this analysis the design lift coefficient is used to determine the  $C_p$  based on the assumption that  $(C_p)_{upper} = -(C_p)_{lower} = \text{constant}$ . This establishes the pressure distribution on the lower surface. The total loading is defined in terms of a blade loading parameter,  $a$ , as shown in Figure 6.1-13. Using the computed values of  $C_L$ , the upper surface  $C_p$  distribution is obtained. The calculation of the acoustic signature used various values of the parameter  $a$  to determine the sensitivity to how the loading was distributed. It is important to mention that the current version of TPN in GAPAS does not include the contribution of the skin friction to the acoustic signature. It is suspected that this would not be a major contribution at the higher Mach numbers. However, although this contribution is contained in the SPN code which is also part of GAPAS, the current version of GAPAS does not transfer the skin friction to the acoustic module.

Acoustic results for the helical tip Mach number 1.14 SR-3 near-field case as calculated using the TPN acoustic module for the four pressure transducer locations depicted in Figure 6.1-14 are shown in Figures 6.1-15 through 6.1-23. Figures 6.1-15 through 6.1-22 show acoustic pressure signatures and overall noise spectra at each of the four transducer locations. The 11 and 13 station blade description notations refer to the number of spanwise stations utilized to calculate the blade loading, and the parameter,  $a$ , define the assumed camber-line loading distribution (see Section 6.1.1). Note that the results for the pressure signature at Station No. 1 (Figure 6.1-15) does not show a single sinusoidal-type cyclic behavior over one period as noted at the other stations (Figures 6.1-17, 6.1-19, 6.1-21) and theoretically anticipated. This is due to difficulties with the iterative method utilized in TPN to solve the retarded time equation. Instances in which this method results in an incorrect solution are shown in Figures 6.1-24 and 6.1-25. Figure 6.1-24 exhibits a situation wherein the initial guess for the solution was -3.40312 and the method picks the oscillating root at -7.8999 as the solution after the iteration

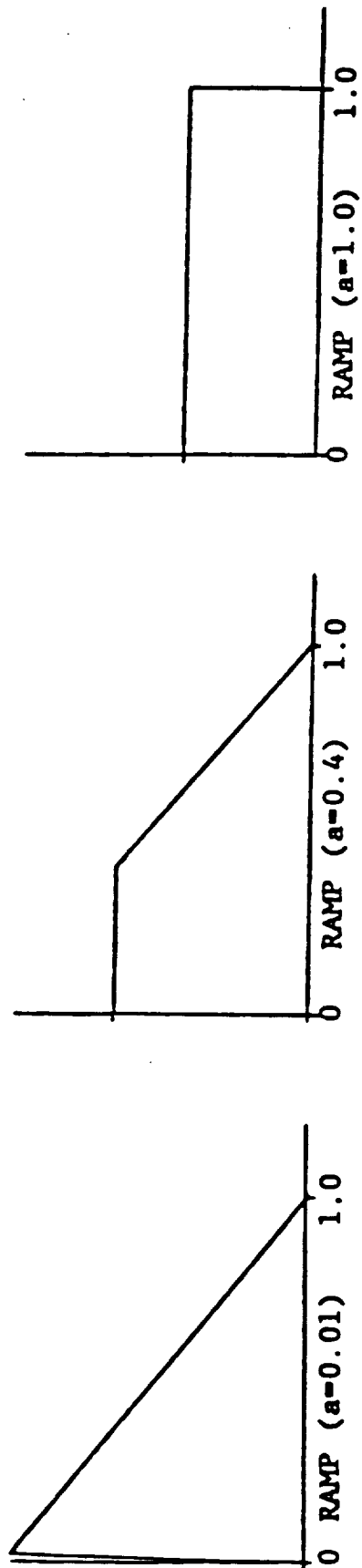
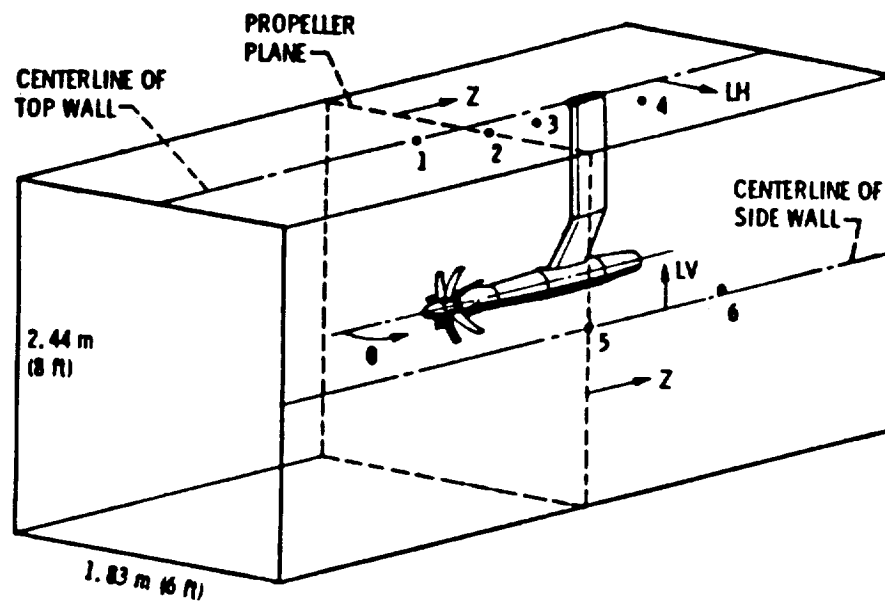


Figure 6.1-13. Meaning of Camber-Line Loading Parameter,  $a$



TRANSDUCER POSITIONS, cm/in.

POSITIONS	1		2		3		4	
Z	-27.7	-10.9	0.953	0.375	45.2	17.8	104.4	41.1
LH	2.54	1.0	10.2	4.0	7.62	3.0	31.5	12.4
LV	121.9	48.0	121.9	48.0	121.9	48.0	121.9	48.0
NOMINAL ANGLE, θ	77°		90°		110°		130°	

Figure 6.1-14. Pressure Transducer Positions, SR-3 Propeller

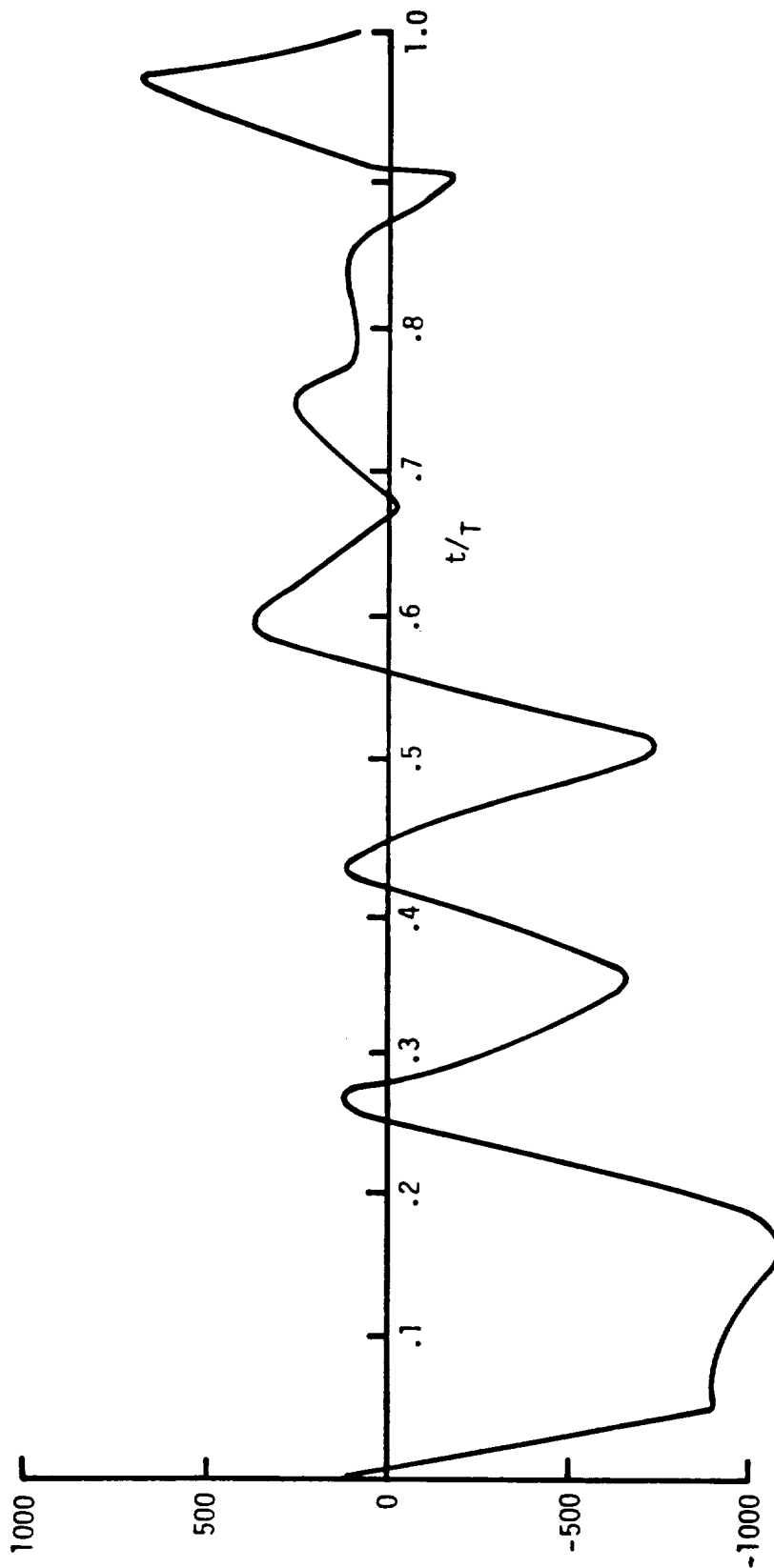


Figure 6.1-15. Acoustic Pressure Signature SR-3 Propeller Near Field  
(Station No. 1) ( $M_0 = 0.80$ ,  $J = 3.06$ ,  $C_p = 1.71$ ,  $B = 8$ ,  
 $M_{TH} = 1.14$ ,  $a = 1$ )

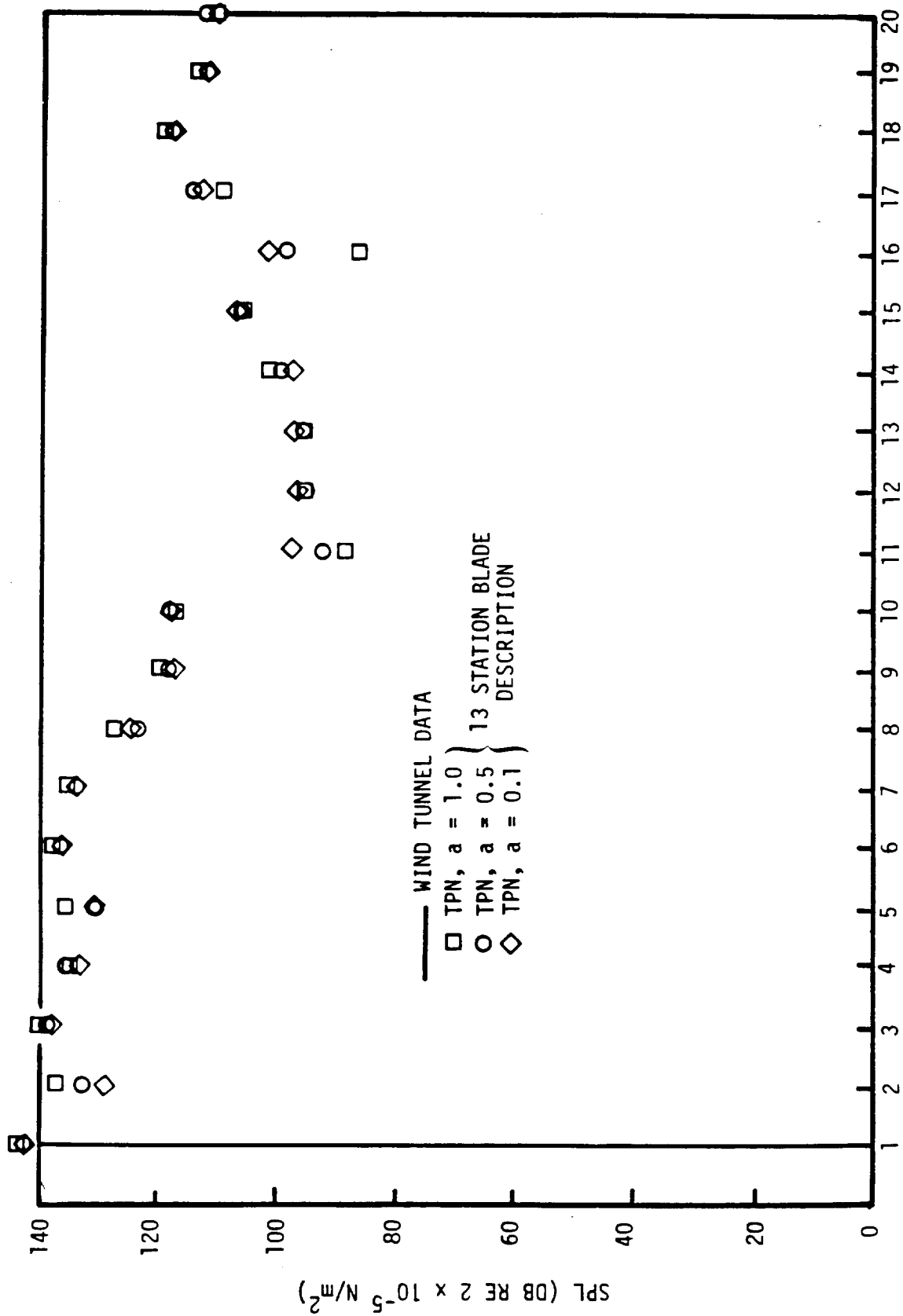


Figure 6.1-16. Overall Noise Spectra SR-3 Propeller Near Field  
(Station No. 1) ( $M_0 = 0.80$ ,  $J = 3.06$ ,  $C_p = 1.71$ ,  
 $B = 8$ ,  $M_{TH} = 1.14$ ,  $a = 1$ )

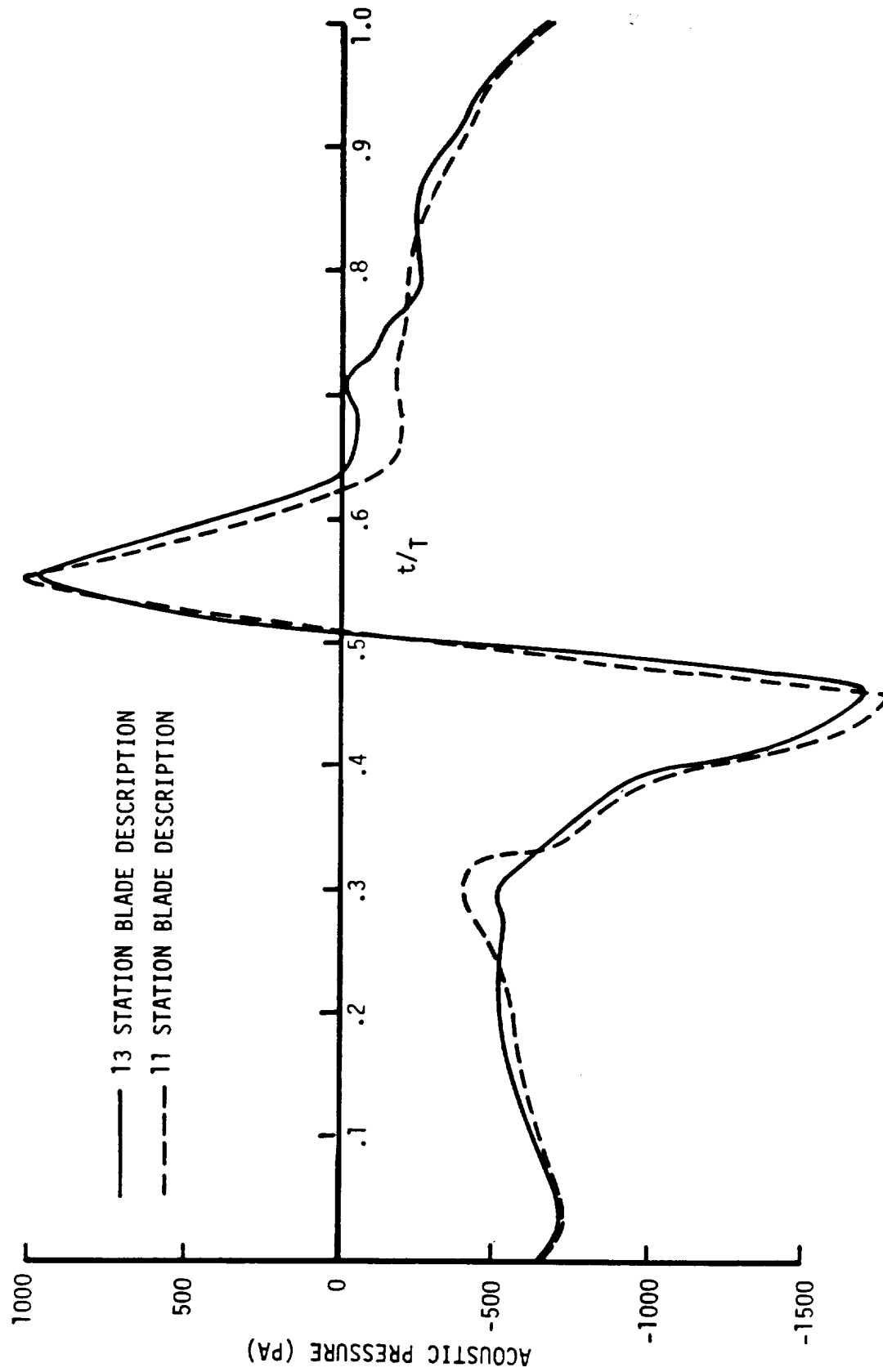


Figure 6.1-17. Acoustic Pressure Signature SR-3 Propeller Near Field  
 (Station No. 2) ( $M_0 = 0.80$ ,  $J = 3.06$ ,  $C_p = 1.71$ ,  $B = 8$ ,  
 $M_{TH} = 1.14$ ,  $a = 1$ )

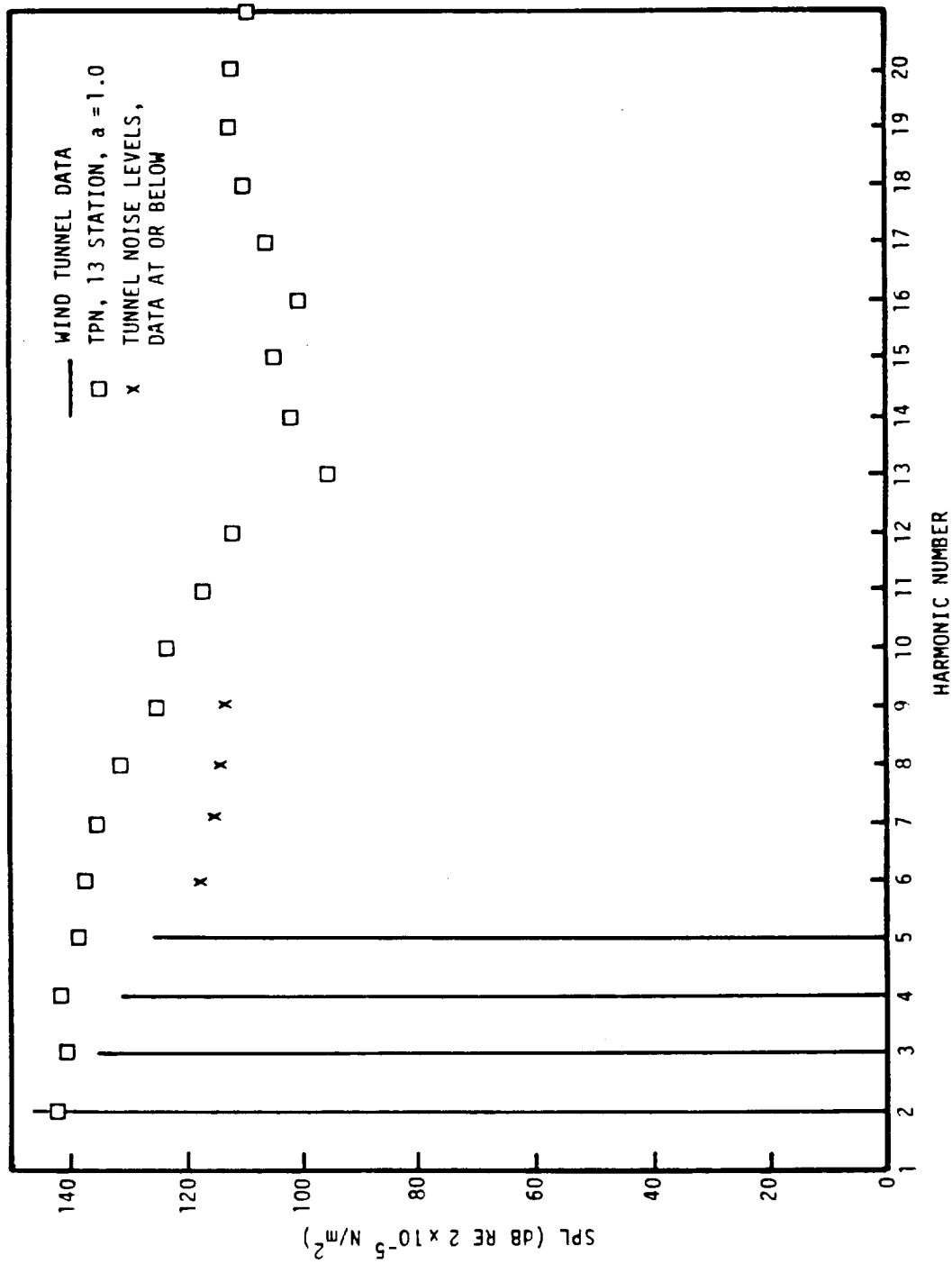


Figure 6.1-18. Overall Noise Spectra SR-3 Propeller Near Field (Station No. 2) ( $M_0 = 0.80$ ,  $J = 3.06$ ,  $C_p = 1.71$ ,  $B = 8$ ,  $M_{TH} = 1.14$ ,  $a = 1.0$ )

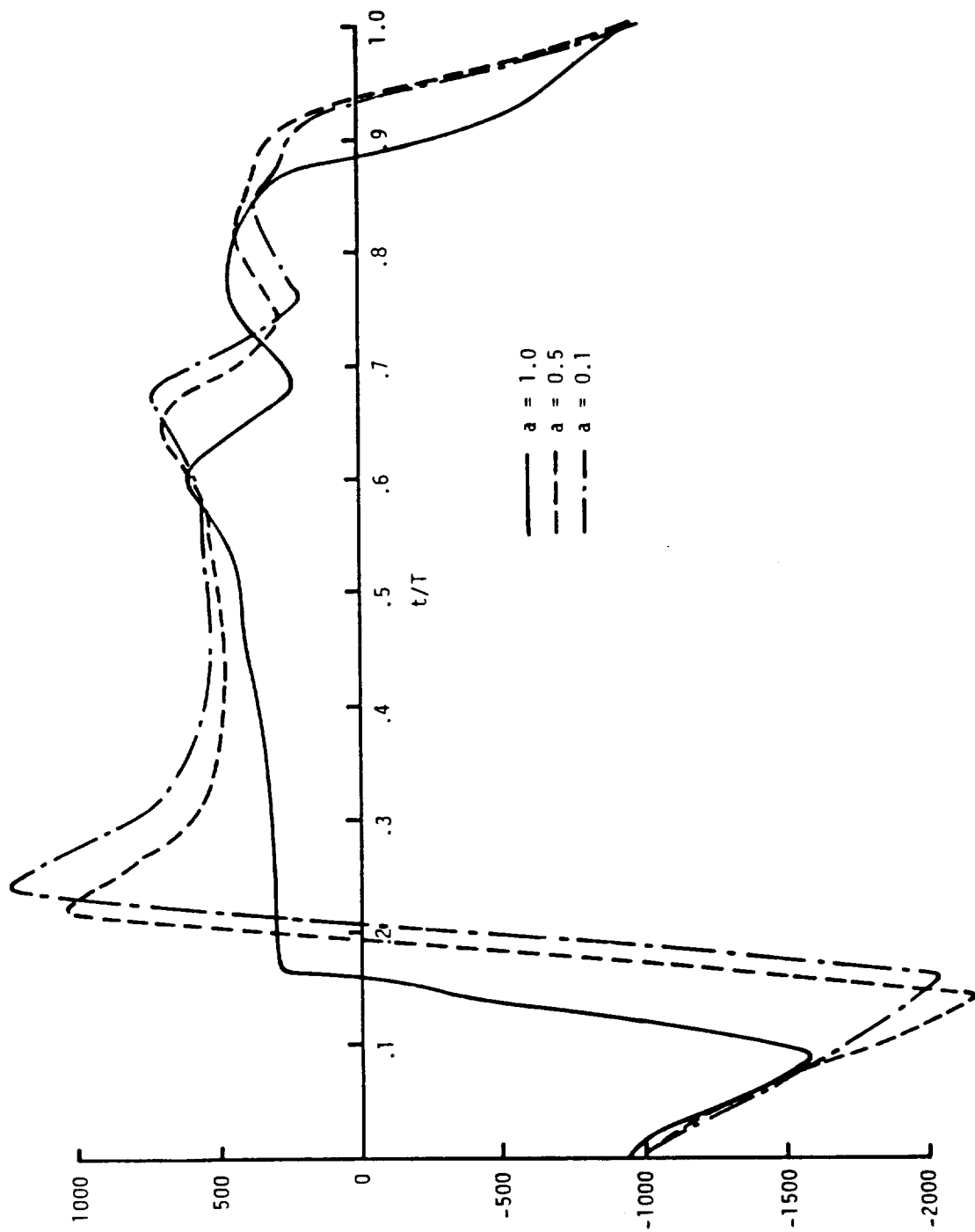


Figure 6.1-19. Acoustic Pressure Signature SR-3 Propeller Near Field  
(Station No. 3) ( $M_0 = 0.80$ ,  $J = 3.06$ ,  $C_p = 1.71$ ,  $B = 8$ ,  
 $M_{TH} = 1.14$ ,  $a = 1.0$ )



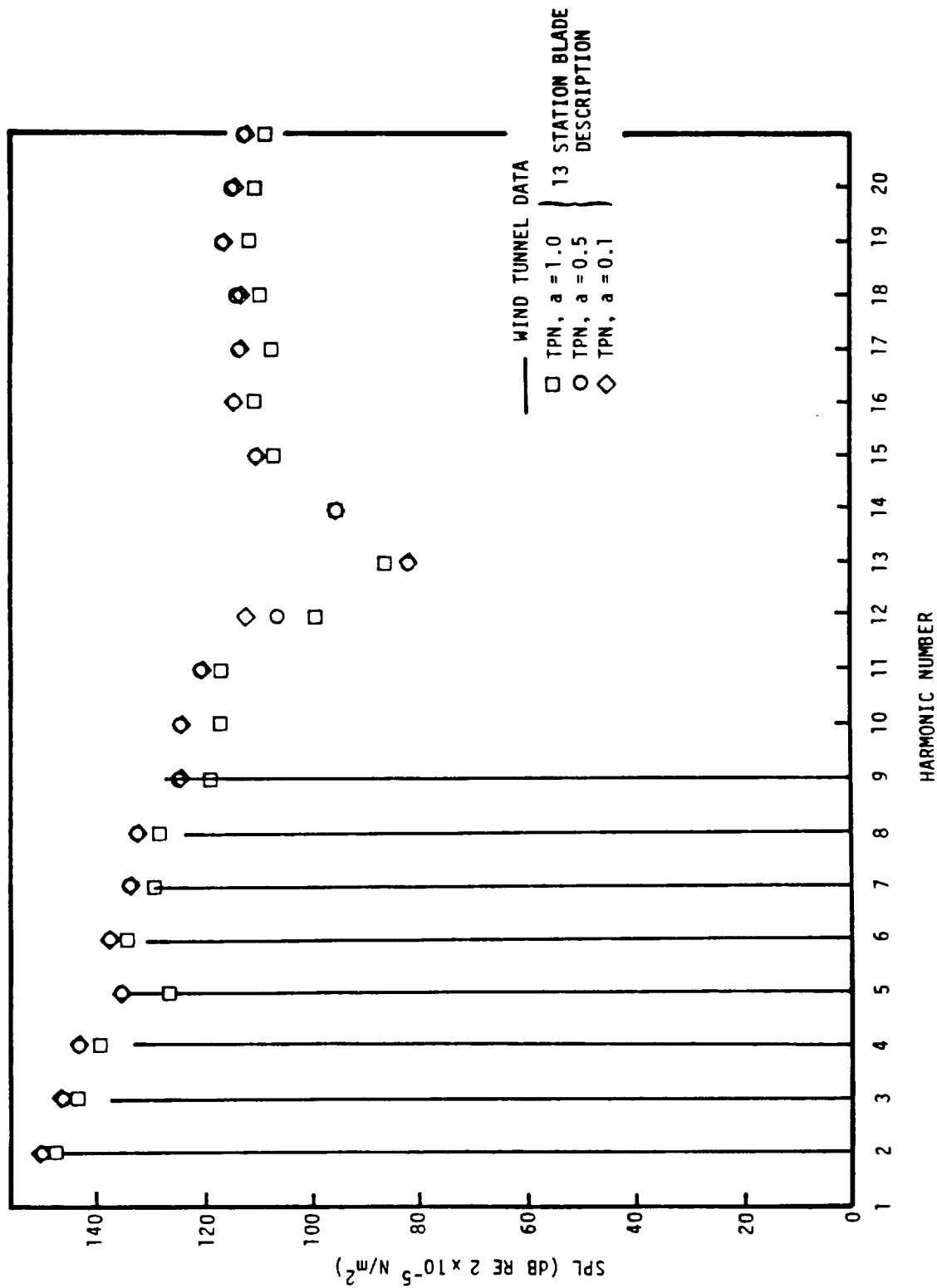


Figure 6.1-20. Overall Noise Spectra SR-3 Propeller Near Field (Station No. 3) ( $M_0 = 0.80$ ,  $J = 3.06$ ,  $C_p = 1.71$ ,  $B = 8$ ,  $M_{TH} = 1.14$ ,  $a = 1.0$ )

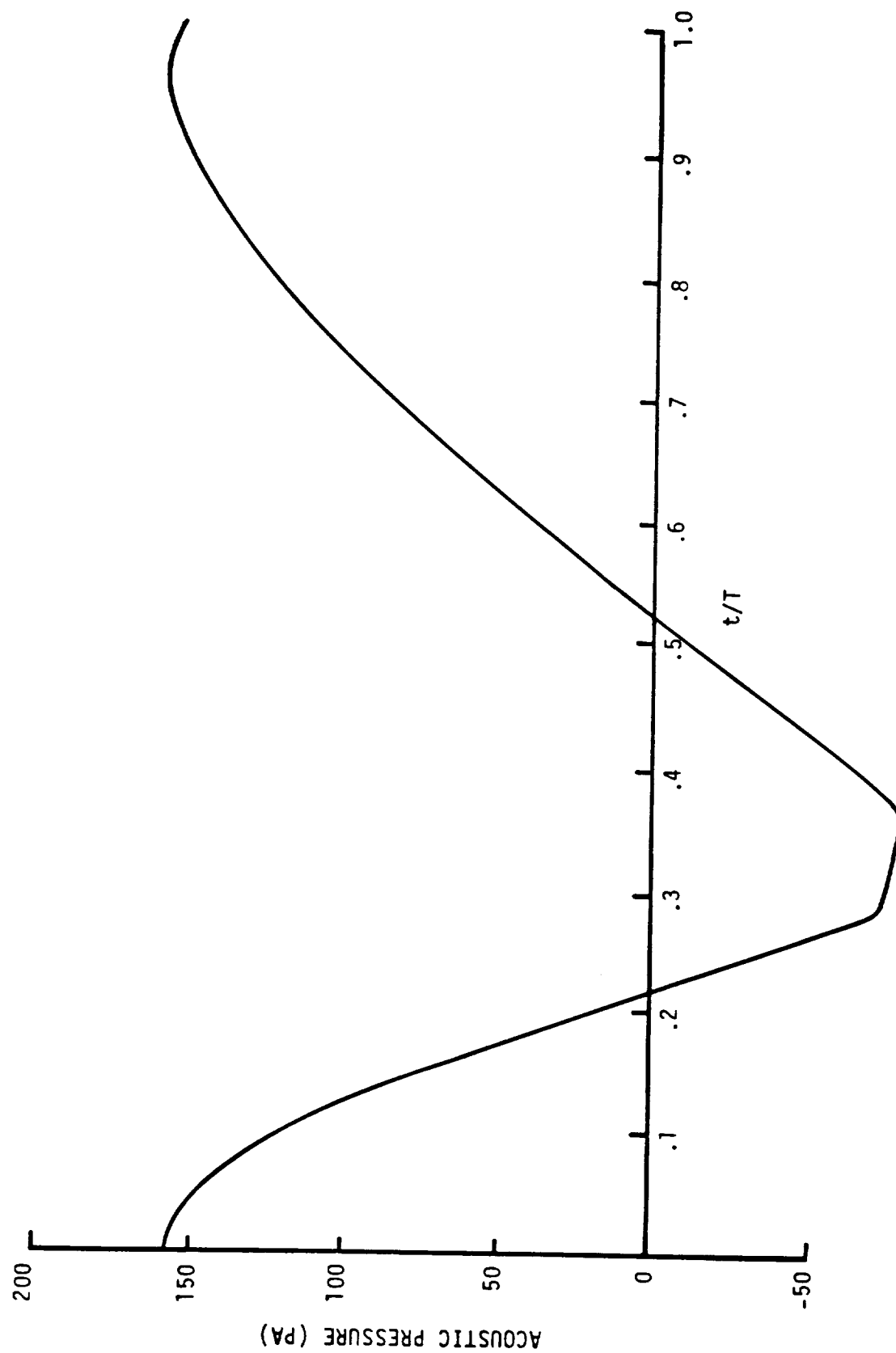


Figure 6.1-21. Acoustic Pressure Signature SR-3 Propeller Near Field  
( $M_0 = 0.80$ ,  $J = 3.06$ ,  $C_p = 1.71$ ,  $B = 8$ ,  $M_{TH} = 1.14$ ,  
 $\bar{a} = 1$ )

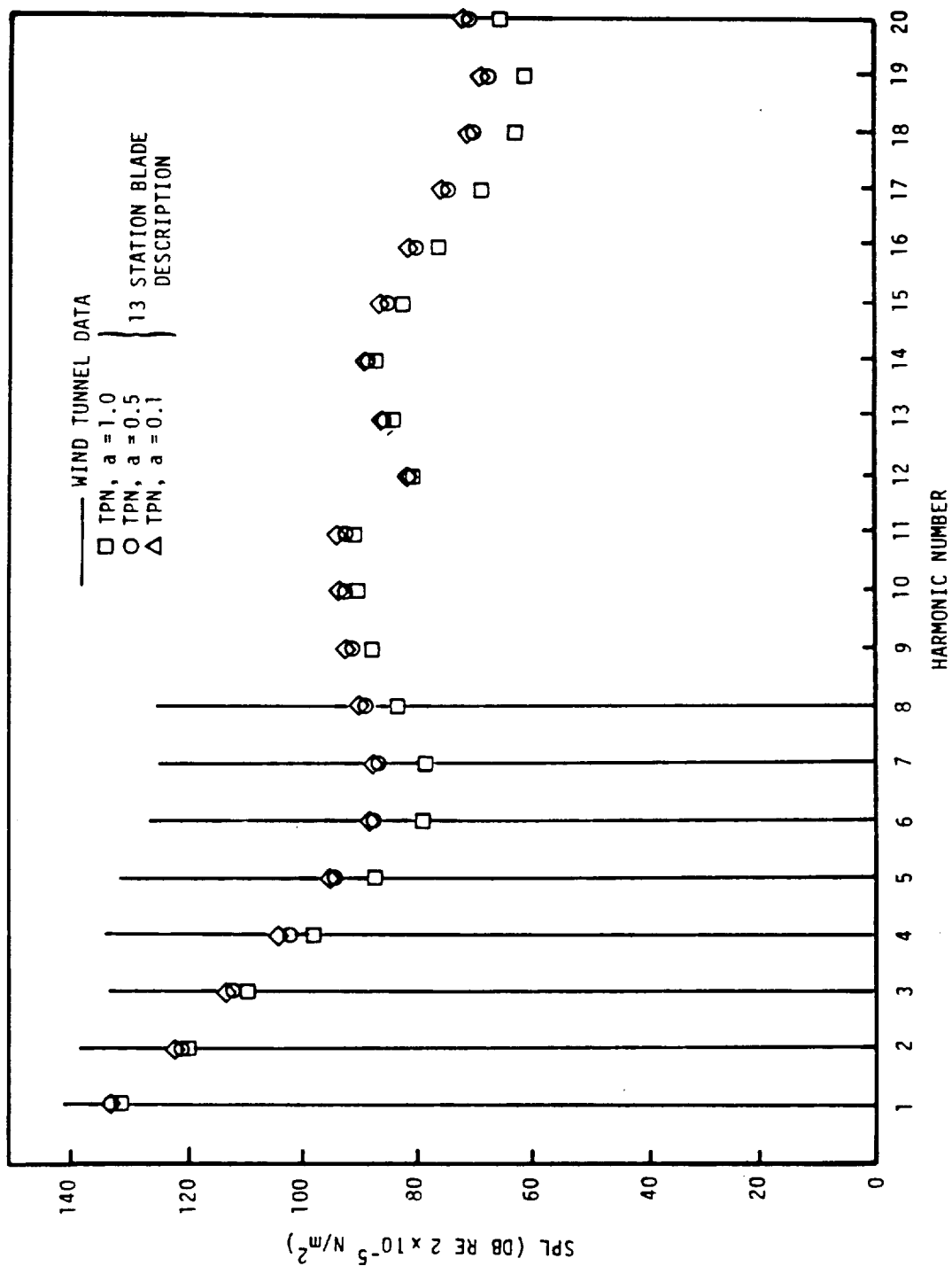
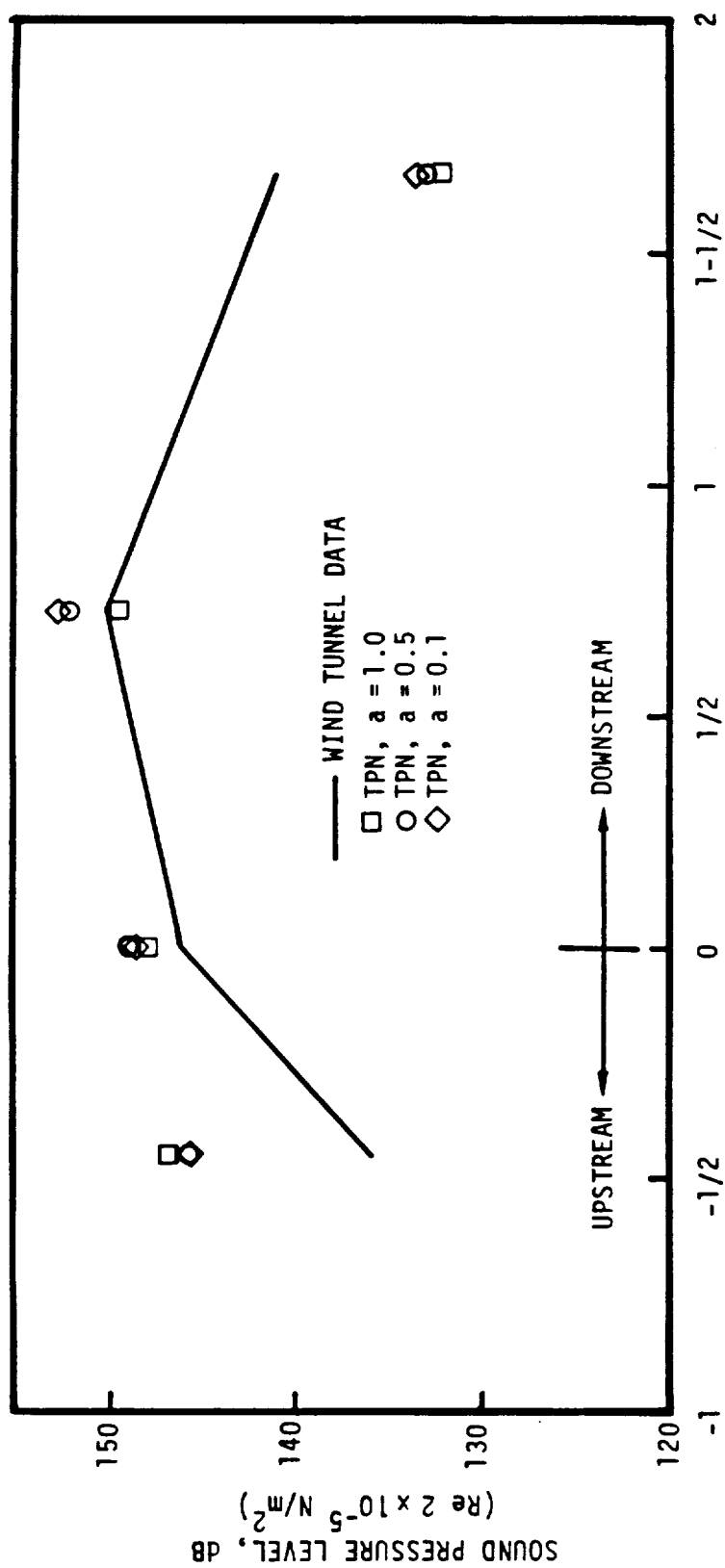


Figure 6.1-22. Overall Noise Spectra SR-3 Propeller Near Field (Station No. 4) ( $M_0 = 0.80$ ,  $J = 3.06$ ,  $C_p = 1.71$ ,  $B = 8$ ,  $M_{TH} = 1.14$ ,  $a = 1.0$ )



FORE AND AFT LOCATION IN PROP-FAN DIAMETERS

Figure 6.1-23. Overall Sound Pressure Level SR-3 Propeller Near Field  
 $(M_0 = 0.80, J = 3.06, C_p = 1.71, n = 8495 \text{ rpm},$   
 $M_{TH} = 1.14, a = 1.0)$

# RETARDED TIME-EQUATION

$$F(X) = AX^2 + BX + C + \cos(X+D) = 0$$

$$A = 0.787974$$

$$B = 0.253942$$

$$C = -2.492615$$

$$D = -.378825$$

$$\text{INITIAL GUESS} = -3.40312$$

FINAL SOLUTION BY TPN = NO SOLUTION AFTER  
20 ITERATIONS (-7.8999)

$$\text{GRAPHIC SOLUTION} = -6.40$$

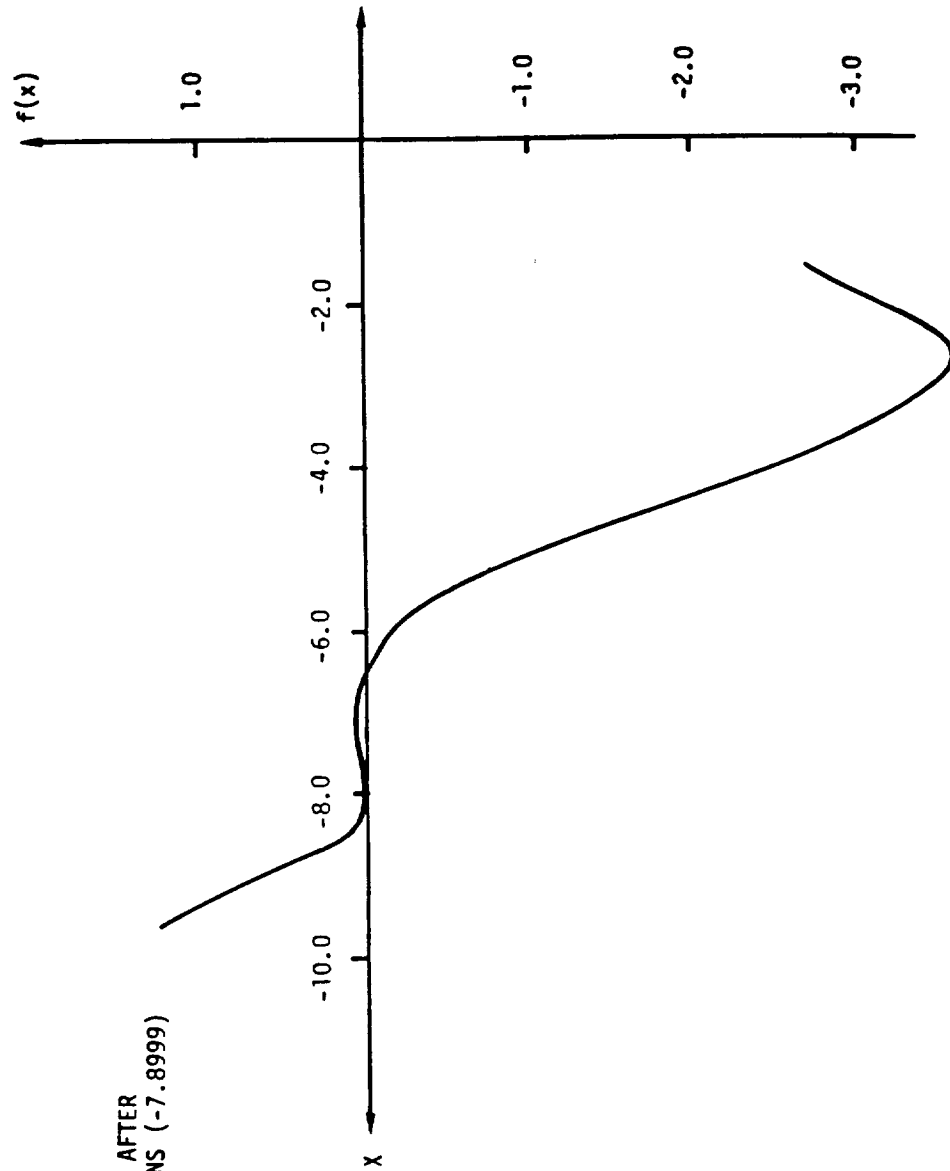


Figure 6.1-24. Solution Results of Retarded Time Equation

# RETARDED TIME EQUATION

$$F(X) = AX^2 + BX + C + \cos(X+D) = 0$$

A = .070389

B = 0.26577

C = -2.28989

D = .398626

INITIAL GUESS = -3.7717

FINAL SOLUTION = 4.2245 BY TPN

GRAPHIC SOLUTION = -5.55

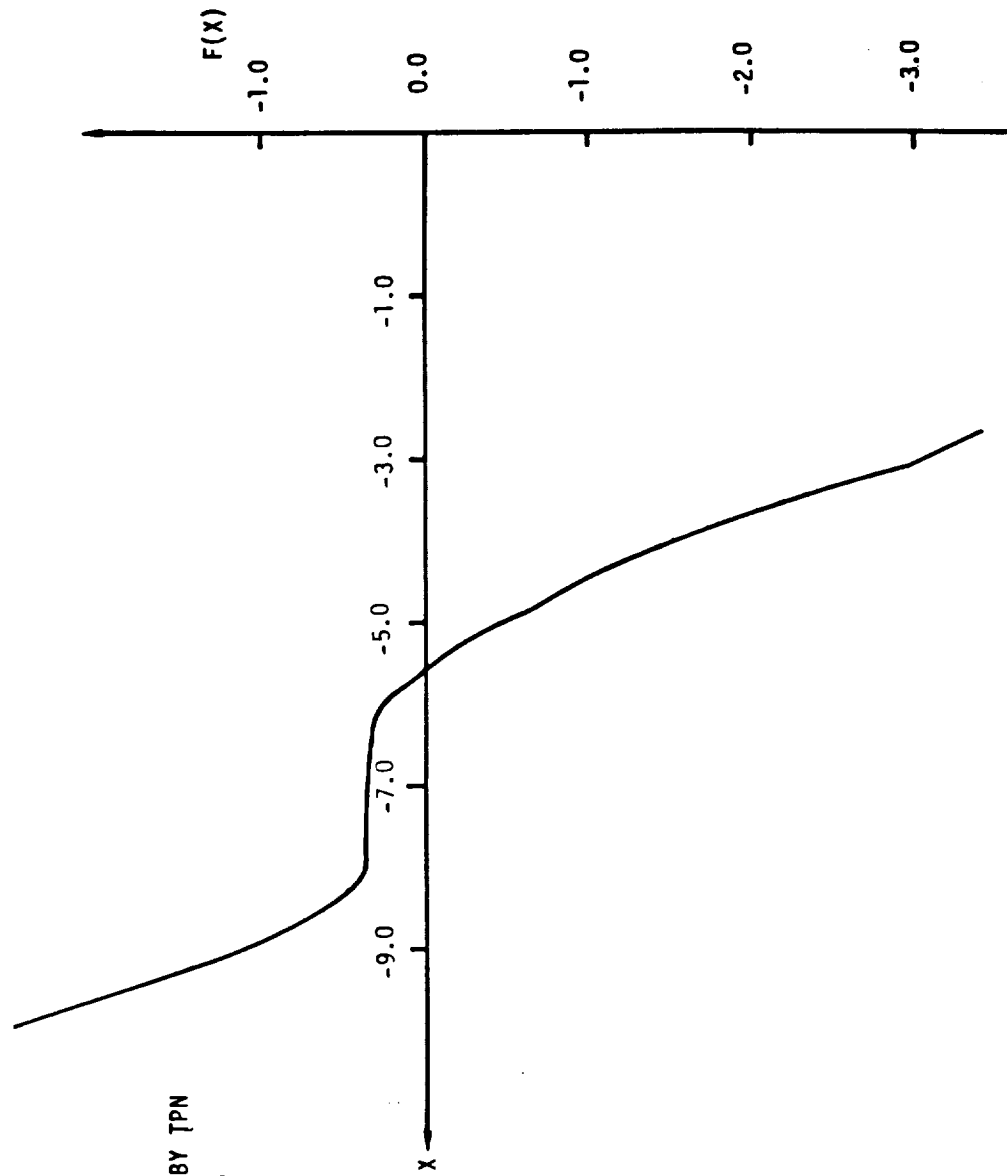


Figure 6.1-25. Solution Results of Retarded Time Equation

limit is reached, whereas the correct solution root is -6.40. Figure 6.1-25 depicts a case where, even through the initial guess for the solution was -3.7717, the method yields a final solution of +4.2245, whereas the graphical solution is shown to be -5.55. Clearly, refinement of the solution method is needed. Note however, that even though the pressure signature is incorrectly predicted at Station 1, the first-harmonic sound-pressure level is within about 2% of the measured data (Figure 6.1-16).

Difficulties in solving the retarded-time equation were not encountered at Stations 2, 3, and 4, and these results (Figures 6.1-17 through 6.1-22) show well-behaved pressure signatures. Comparison of predicted noise-spectra with data show fair to good agreement for Stations 1, 2, and 3 (less than 15 dB), however Station 4 predictions show poor comparison with data for harmonics 3-8.

In addition, the overall sound-pressure levels predicted by TPN (Figure 6.1-23) show good-to-fair agreement with data depending on station location, and are relatively insensitive to blade-loading parameters. Errors of 3-4 dB may be noted at the first two stations downstream at the propeller plane (Stations 2 and 3, Figure 2.5-20), whereas errors on the order of 10 dB are noted at the upstream and far downstream station (Stations 1 and 4, respectively).

The structural dynamics characteristics of SR-3 propeller were also analyzed. The SR3 propeller is composed of titanium, and the calculated line of shear centers consists of a three-dimensional space curve (Figures 6.1-26 through 6.1-28). Three of the cross section profiles, which are perpendicular to the line of shear centers, are presented in Figures 6.1-29 through 6.1-32. The finite element model consisted of 12 beam elements (Figure 6.1-28).

The accuracy of the beam model depends on the line of shear centers and the structural properties of the blade cross sections. Thus, errors involved with the calculation of the structural constants will directly affect the results of the structural dynamic analysis. The line of shear centers was determined by fitting a polynomial through all of the computed shear center locations. Results of the predictions are compared with modal

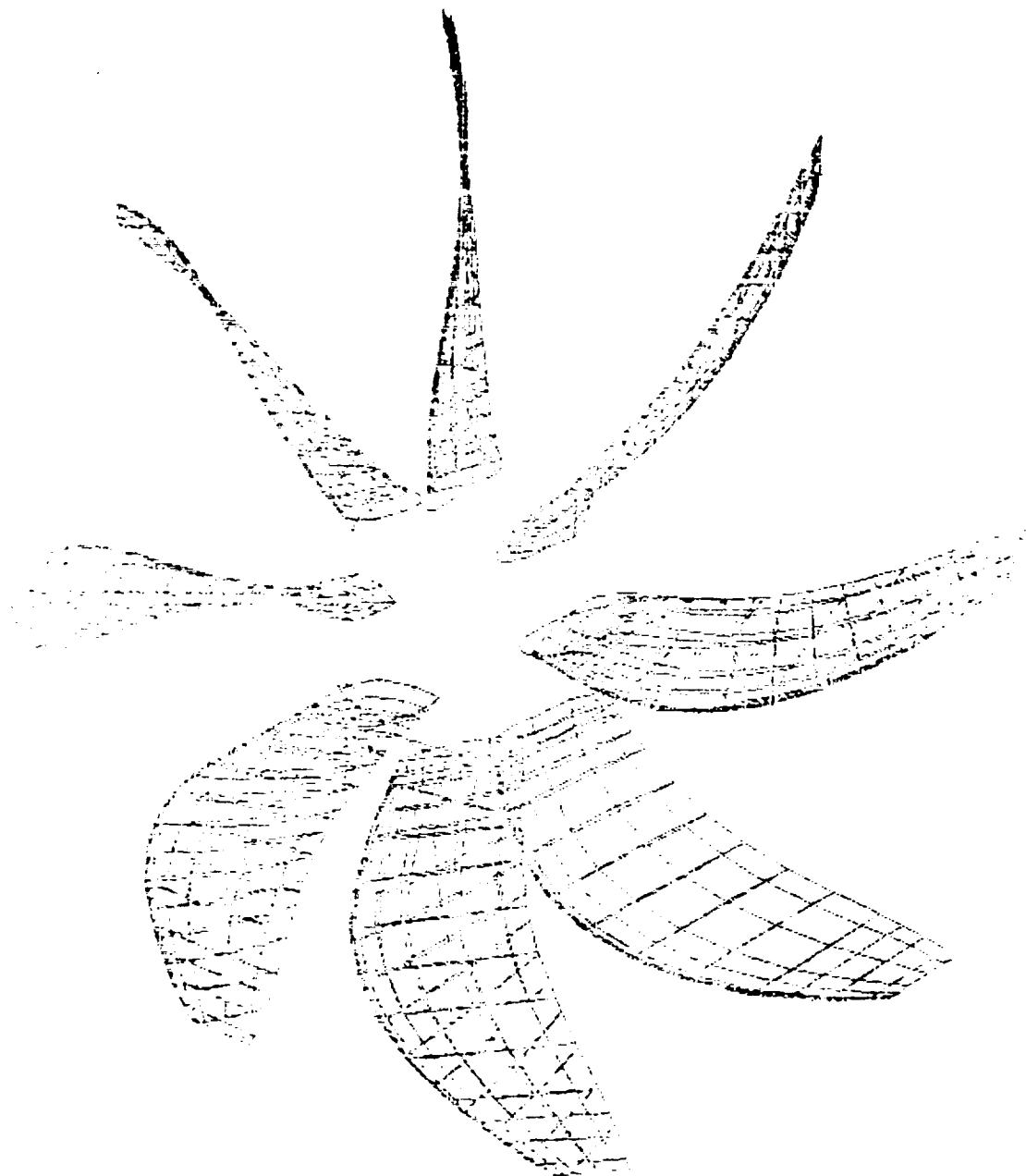


Figure 6.1-26. NASA SR-3 Advanced Turbopropeller



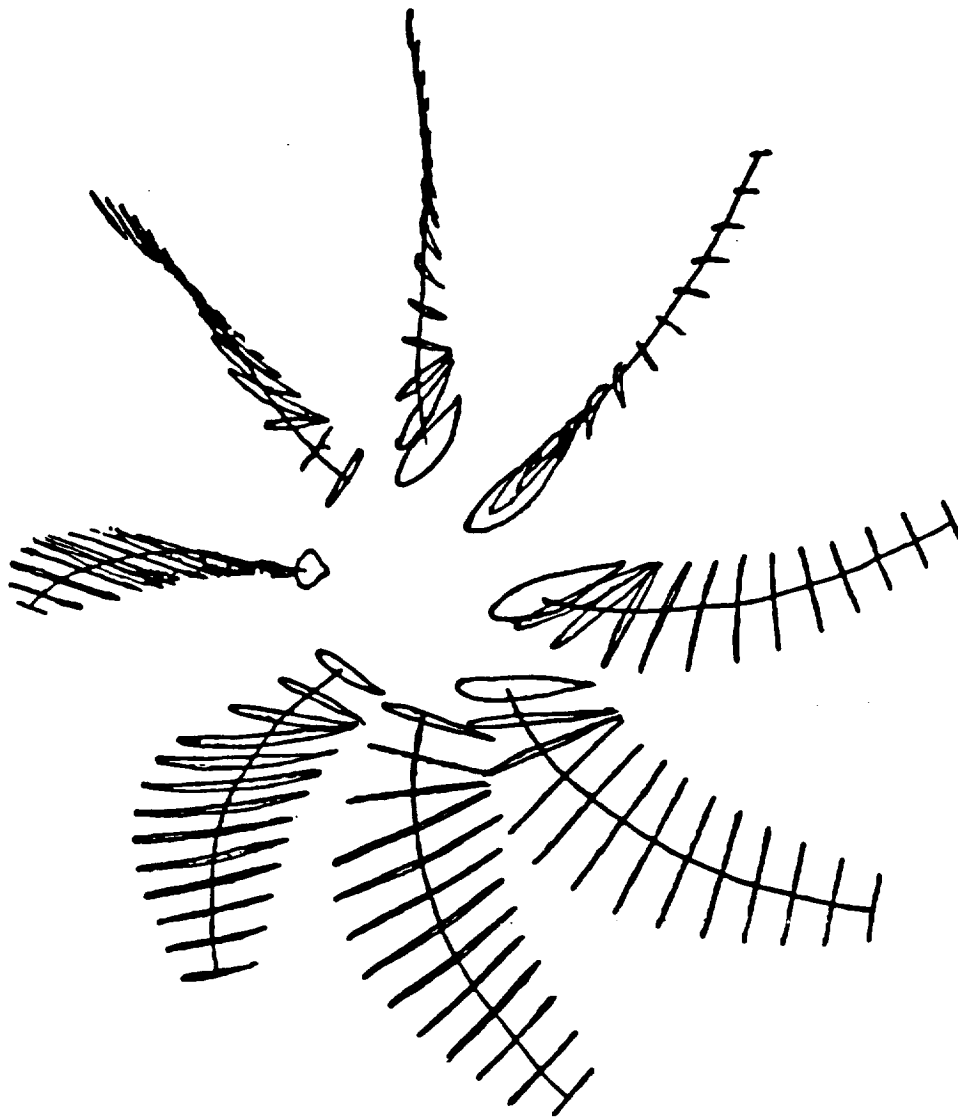
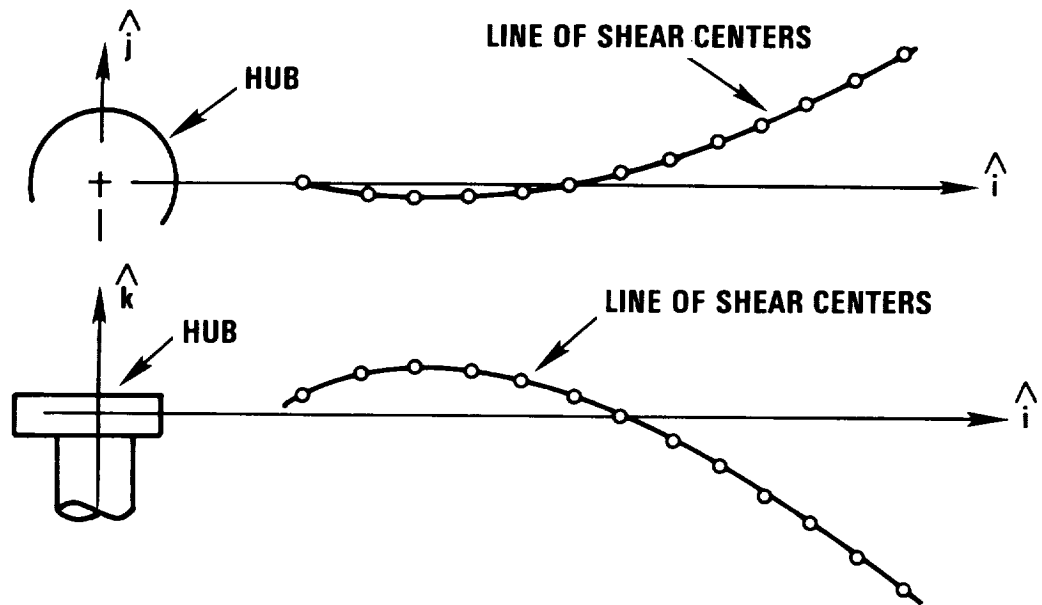
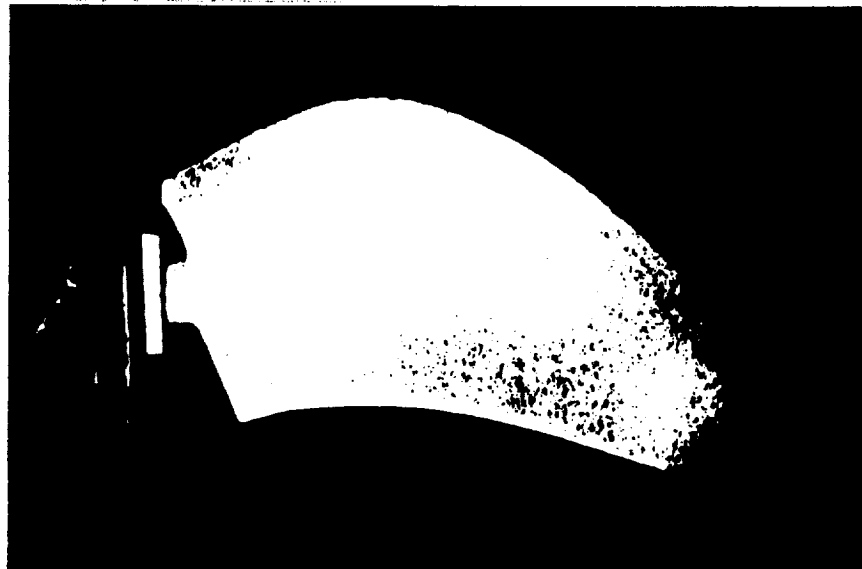


Figure 6.1-27. SR-3 Structural Model Line of Shear Centers and Profiles Perpendicular to line of Shear Centers



**A) FINITE ELEMENT MODEL OF THE UNDEFORMED LINE OF SHEAR CENTERS (12 ELEMENTS)**



**B) TEST SETUP OF ADVANCED PROPELLER**

Figure 6.1-28. Finite Element Model and Test Setup of NASA SR-3 Propeller

**CHORD:** 4.620 in.  
**CENTROID:**  $x = 2.077$  in.  
 $y = 0.04756$  in.  
**SHEAR CENTER:**  $x = 1.938$  in.  
 $y = 0.06923$  in.  
**AREA:** 0.9319 in.<sup>2</sup>  
**MOMENTS OF INERTIA:**  
 $I_{pp} = 0.00491$  in.<sup>4</sup>  
 $I_{qq} = 1.034$  in.<sup>4</sup>  
 $\theta_p = 0.1312^\circ$   
**TORSION CONSTANT, J:** 0.02053 in.<sup>4</sup>

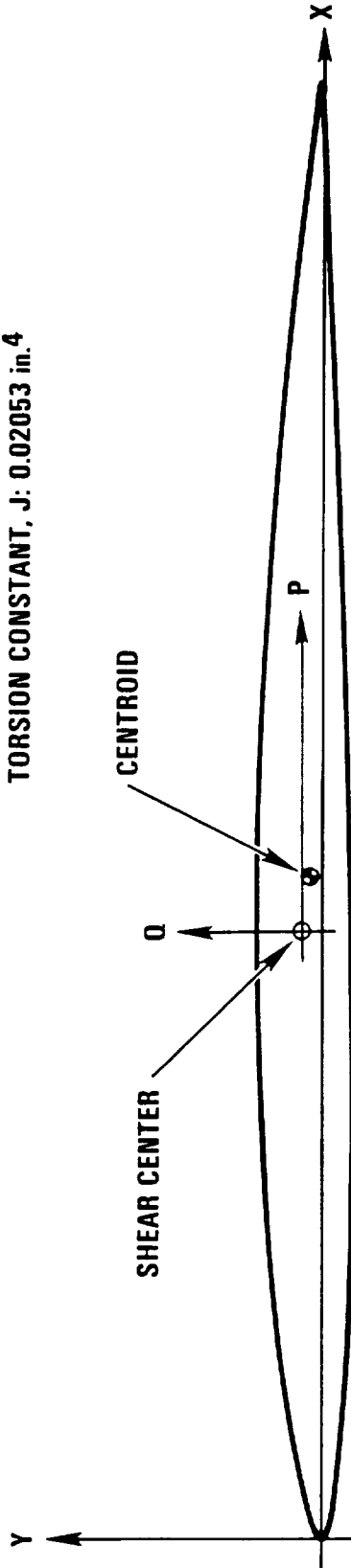


Figure 6.1-29. Analysis of a NASA SR-3 Advanced Propeller Cross Section Located at a Point 25% from Blade Root

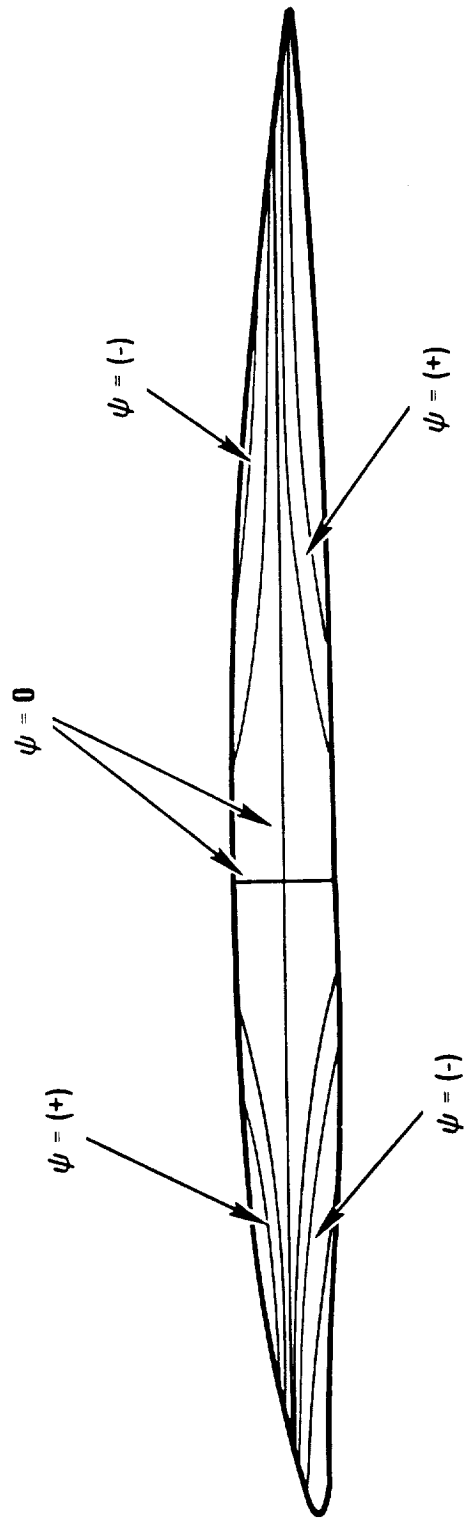


Figure 6.1-30. Warping Function Distribution of a NASA SR-3 Cross Section Located at a Point 25% from Blade Root

CHORD: 4.039 in.

AREA: 2.103 in<sup>2</sup>

CENTROID:

X = 1.722 in.

Y = -0.0845 in.

MOMENTS OF INERTIA:

$I_{pp} = 0.07628 \text{ in.}^4$

$I_{qq} = 1.716 \text{ in.}^4$

SHEAR CENTER:

X = 1.520 in.

Y = -0.1164 in.

$\theta_p = -0.2058^\circ$

TORSION CONSTANT,  $J = 0.2896 \text{ in.}^4$

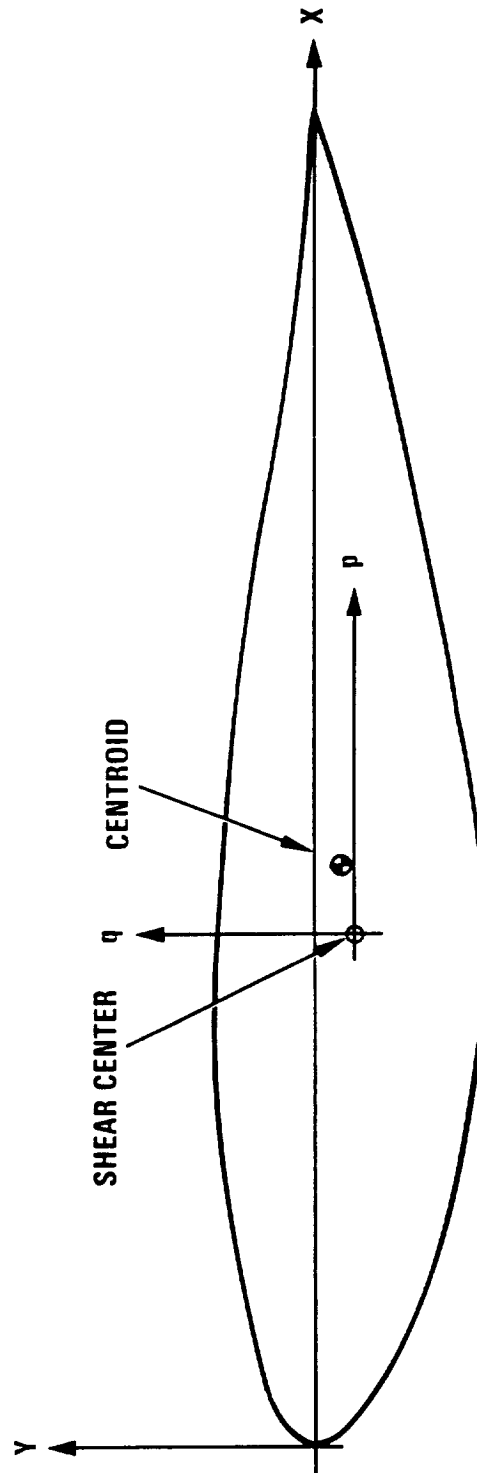


Figure 6.1-31. Analysis of a NASA SR-3 Advanced Propeller Root Cross Section

**CHORD:** 1.675 in.  
**CENTROID:**  $x = 0.7836$  in.  
 $y = 0.03617$  in.  
**SHEAR CENTER:**  $x = 0.7196$  in.  
 $y = 0.05071$  in.  
**AREA:**  $0.05309 \text{ in.}^2$   
**MOMENTS OF INERTIA:**  
 $I_{pp} = 1.06 \times 10^{-5} \text{ in.}^4$   
 $I_{qq} = 8.206 \times 10^{-3} \text{ in.}^4$   
 $\theta_p = 0.1165^\circ$   
**TORSION CONSTANT, J:**  $3.926 \times 10^{-5} \text{ in.}^4$

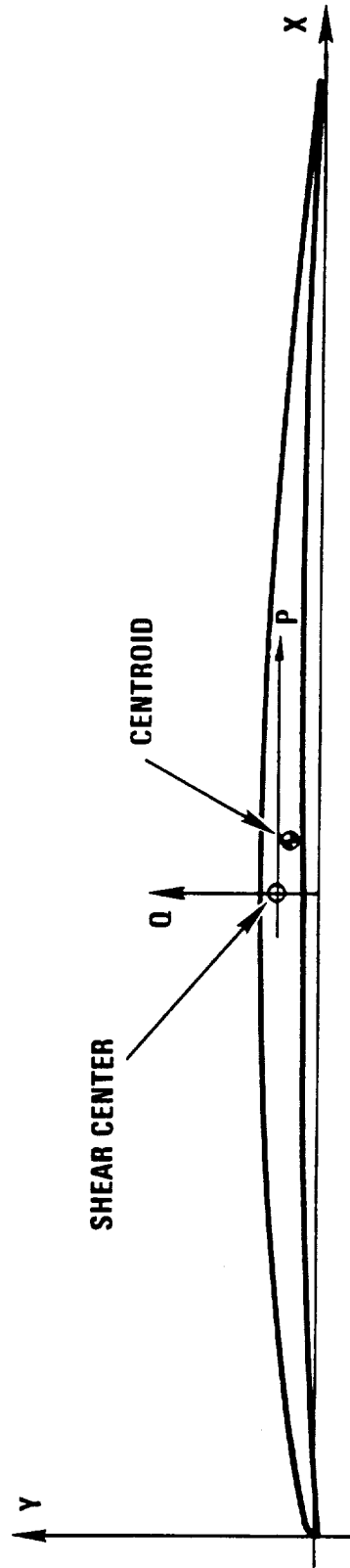
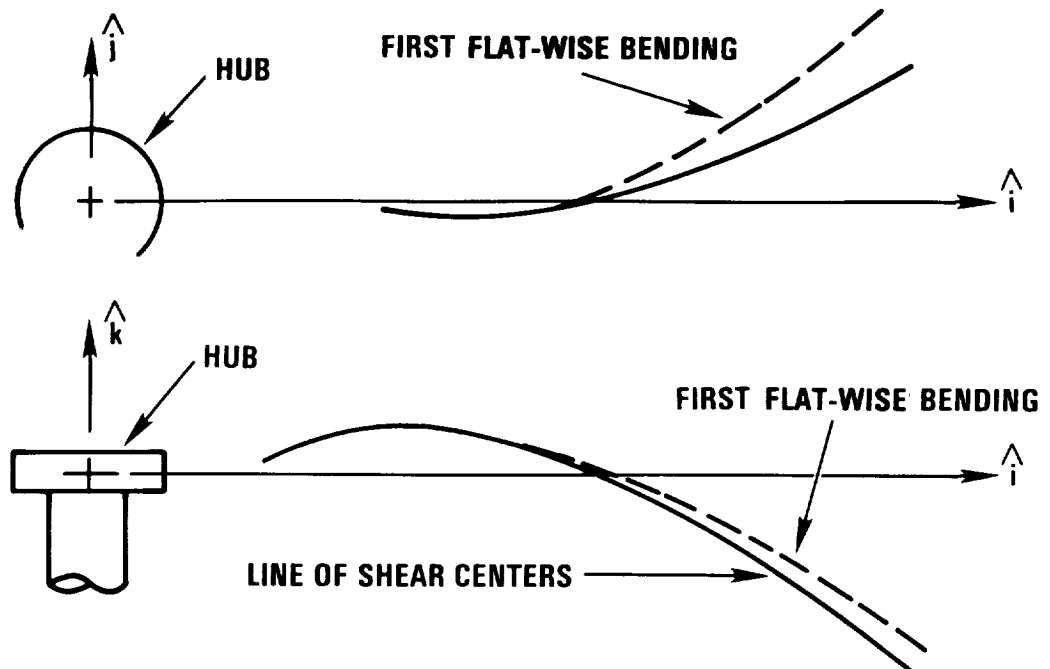


Figure 6.1-32. Analysis of a NASA SR-3 Advanced Propeller Tip Cross Section

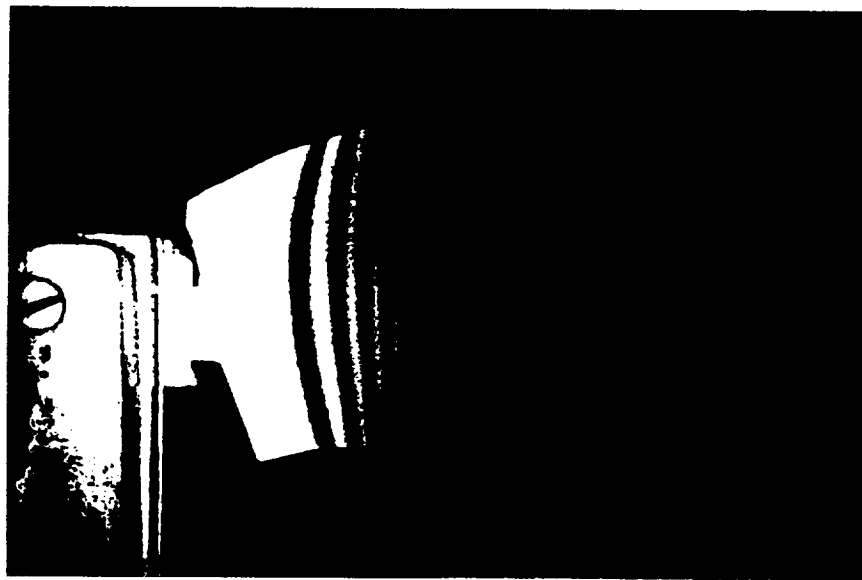
tests of the SR-3 propeller. The modal test is based on using laser holography techniques where the fringe patterns that appear on the blade are the lines of constant displacement of the mode. The undeformed blade, which is illuminated by laser light is shown in Figure 6.1-28.

The first four analytically derived (current finite element results) and experimentally determined mode shapes are presented in Figures 6.1-33 through 6.1-36. The first two modes that were predicted using the finite element model are the first and second flapwise bending modes of the SR-3 (6.1-33a, 6.1-34a). These calculated modes have the correct shape without any twisting or edgewise bending effects coupled in. The first two experimental modes (6.1-33b, 6.1-34b) clearly show the same type of behavior, where the nodal line of the second mode is in the same approximate location as the finite element prediction. The third mode that was predicted via the finite element method was the first torsion mode of the blade (6.1-35a). This mode has almost no deformation of the line of shear centers, as seen in the figure, only relative twisting about this line of shear centers, which cannot be seen in the figure. Similarly, the third experimental mode (6.1-35b) is the first torsion mode of the SR-3, where the blade is twisting about a nodal curve that runs along the length of the blade. At the blade root, there appears to be additional deformation which is a result of chordwise bending which cannot be predicted by the current beam-type model. The fourth analytical mode (6.1-36a) can be described as the third flapwise bending, where the blade has two nodal lines in addition to the fixed root region. The experimental (6.1-36b) fourth mode is clearly the third flapwise bending mode which has no tip twisting, but it also has additional chordwise bending near the hump and root. These additional effects cannot be predicted with the current beam-type model.

A comparison of the predicted natural frequencies and the experimental results for different operating speeds is presented in the Campbell diagram in Figure 6.1-37. For the condition of the nonrotating blade, the experimental results are in agreement with the predicted results for the first three modes. The experimental results for the higher modes do not match as well due to the effects of chordwise bending that cannot be



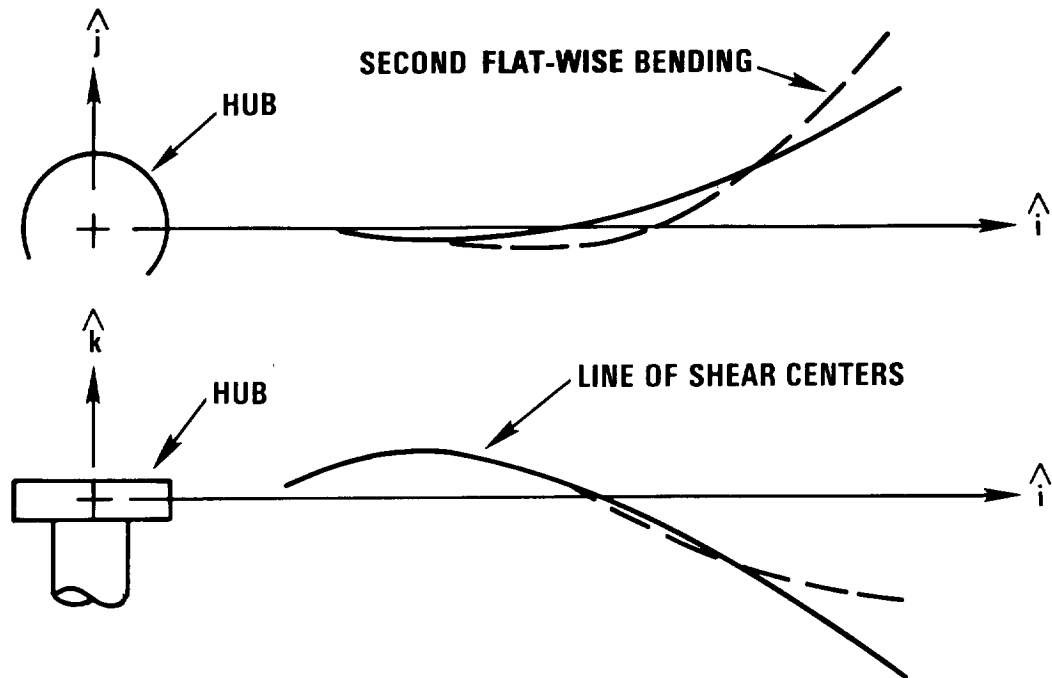
**A) CALCULATED FIRST MODE SHAPE**



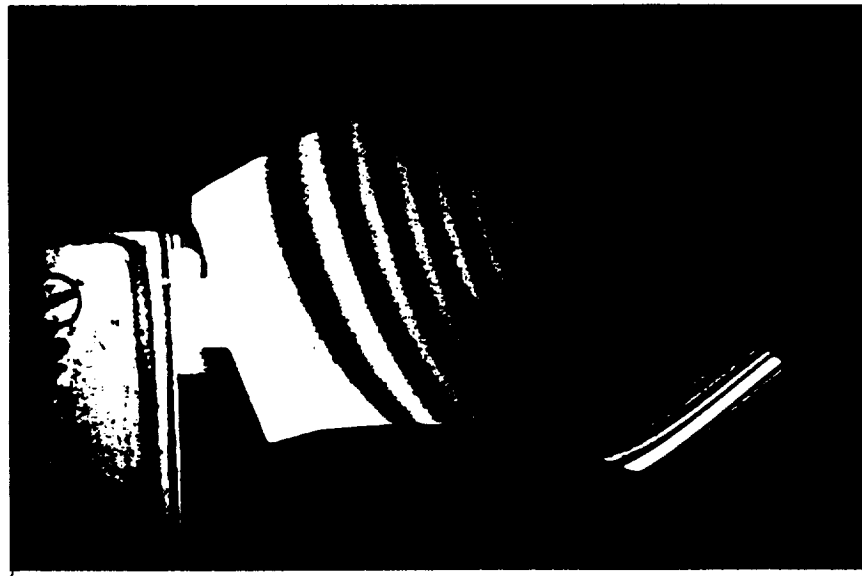
**B) EXPERIMENTALLY OBTAINED FIRST MODE SHAPE**

Figure 6.1-33. Comparison of Current Finite Element Predictions and Experimental Results for the First Mode Shape of NASA SR-3 Propeller



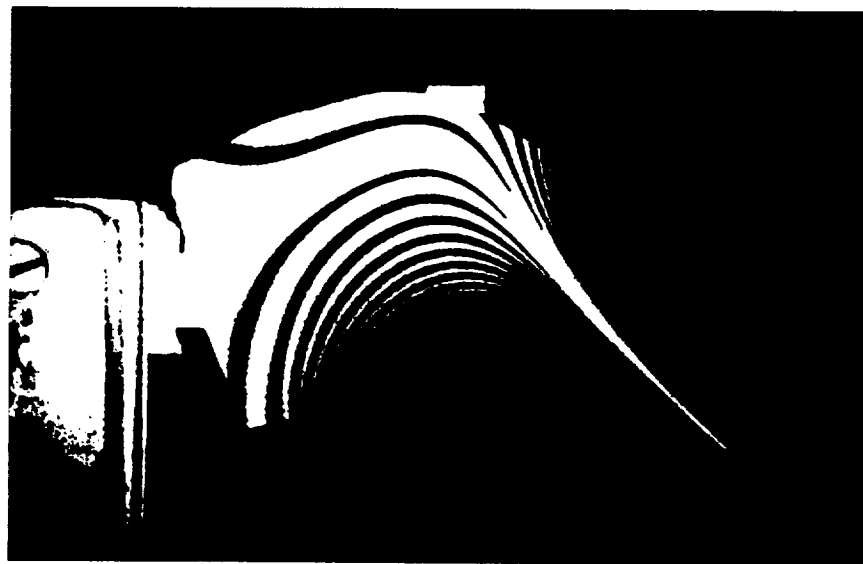
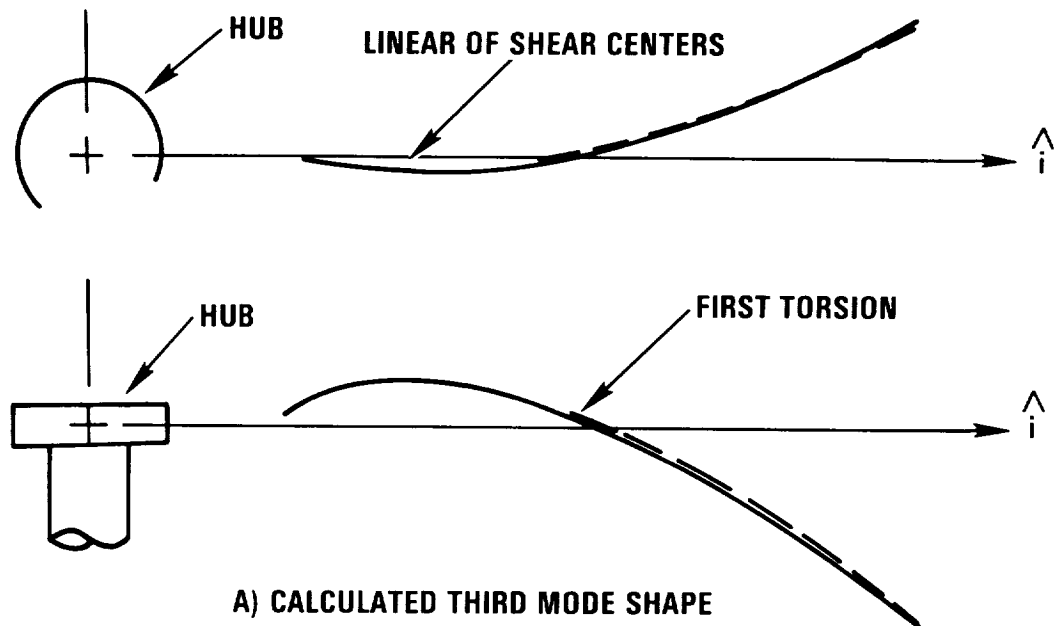


**A) CALCULATED SECOND MODE SHAPE**



**B) EXPERIMENTALLY OBTAINED SECOND MODE SHAPE**

Figure 6.1-34. Comparison of Current Finite Element Predictions and Experimental Results for the Second Mode Shape of NASA SR-3 Propeller



**B) EXPERIMENTALLY OBTAINED THIRD MODE SHAPE**

Figure 6.1-35. Comparison of Current Finite Element Predictions and Experimental Results for the Third Mode Shape of the NASA SR-3 Propeller

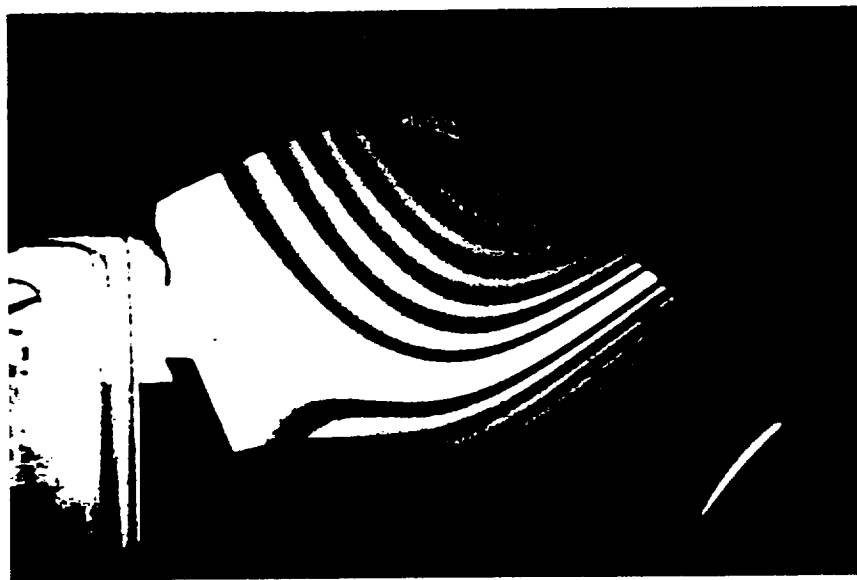
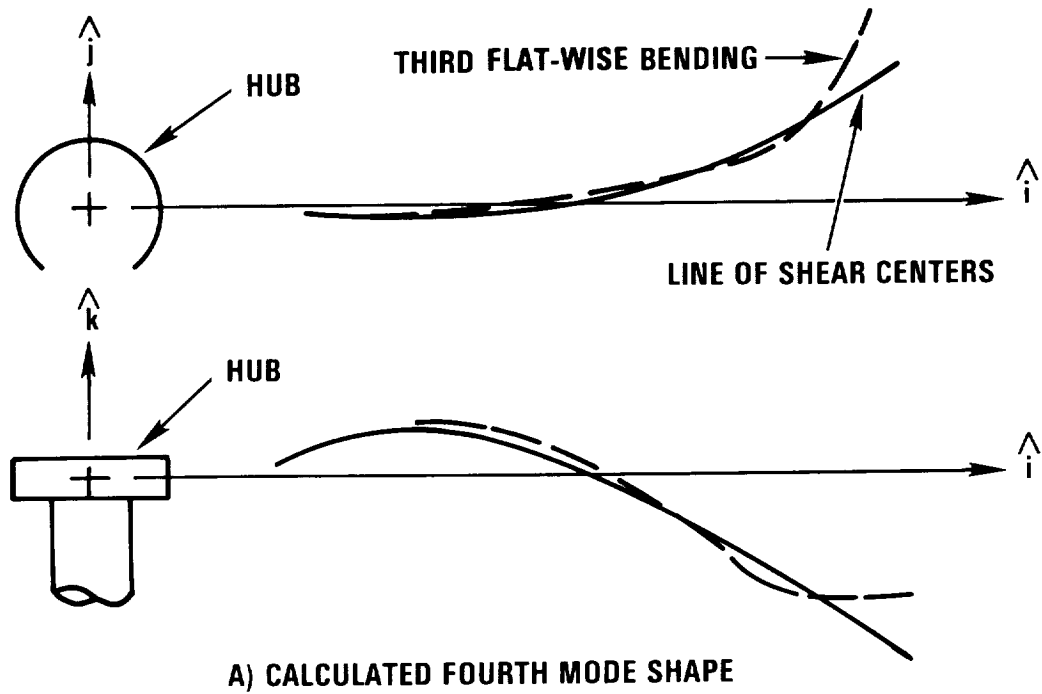


Figure 6.1-36. Comparison of Current Finite Element Predictions and Experimental Results for the Fourth Mode Shape of the NASA SR-3 Propeller

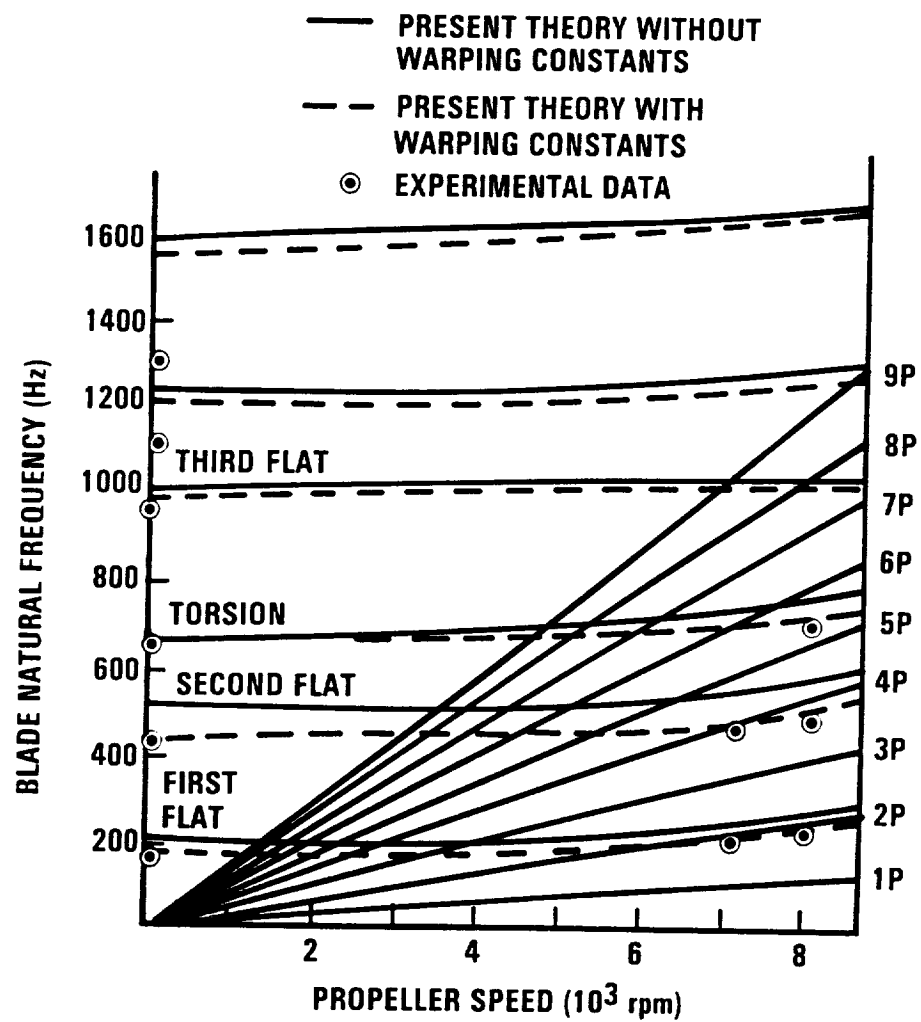


Figure 6.1-37. Comparison of Test and Predicted Natural Frequencies for the NASA SR-3 (Campbell Diagram)

accounted for with this finite element model. The effects of cross section warping play an important part in correctly predicting the natural frequencies of the blade. These warping effects lower the predicted natural frequencies of the blade and are important for modeling the thin cross sections. The experimental results of the rotating blade (7000 and 8000 rpm) also show very good correlation with the finite element model when the effects of warping are included.

The results of the SR-3 calculations described above are based on the single-pass mode of operation. In order to verify the interactive mode of operation, the above calculation was repeated using the aerodynamic/structural interaction option. In this mode, the method utilizes the calculated structural deformation to generate a new propeller geometry. This geometry is then utilized to calculate a new aerodynamic loading which cycles back to the structural module for a new structural deformation. This procedure continues until the deflected shape of the line of shear centers does not change with iteration. In this mode, the geometry generator, Chang-Sullivan, and the structural beam model are coupled in the iteration process.

Figure 6.1-38 shows the results of the SR-3 propeller calculation using the interaction mode. The calculations were run for three iterations before being terminated due to non-convergence problems. The convergence problem appears to be related to the reconstruction of the propeller in the tip region during each iteration. Further investigation is necessary to determine the exact cause of the problem. Therefore, at this time, the interactive mode should not be utilized for propeller analysis.

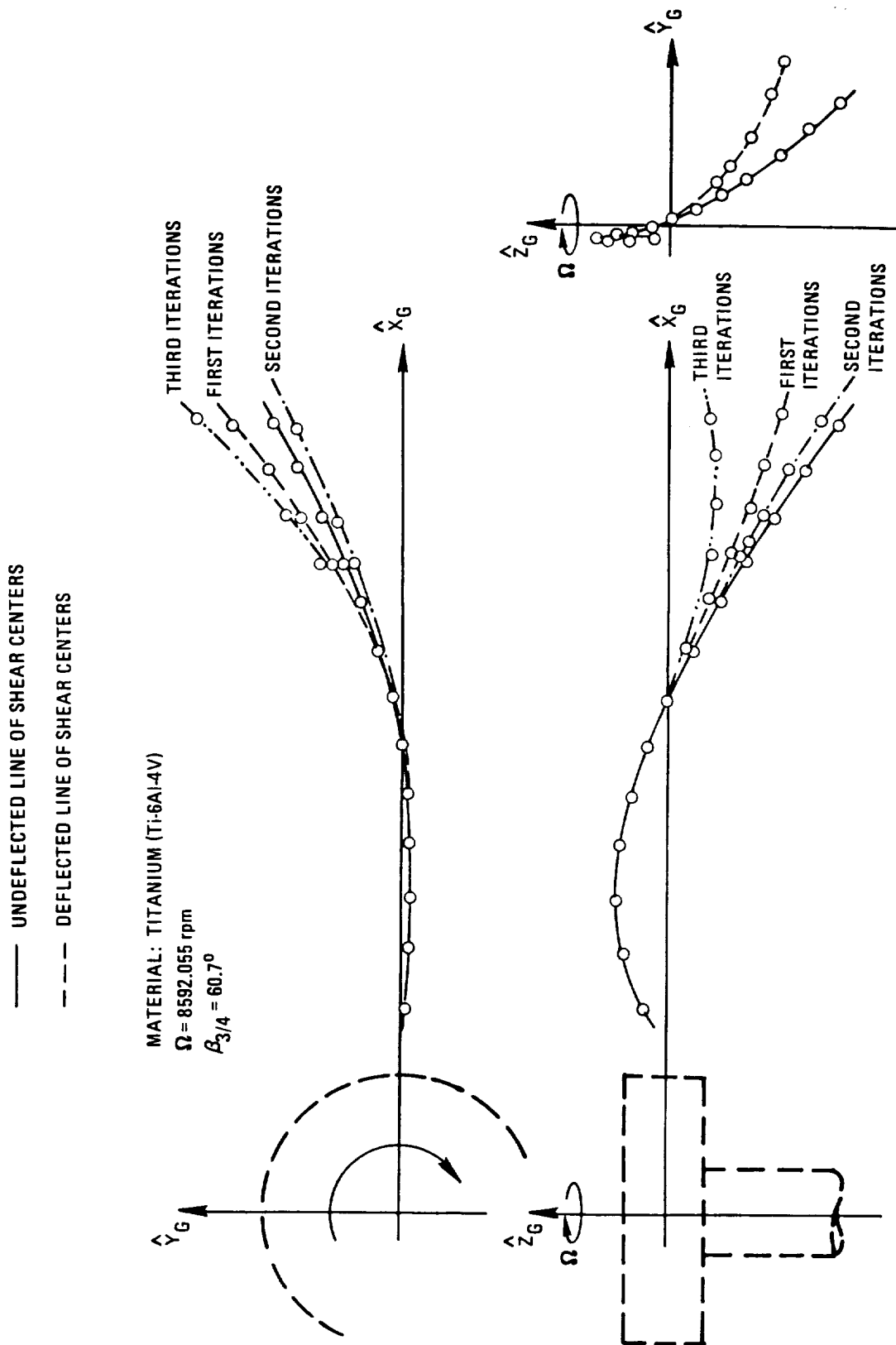


Figure 6.1-38. Undelected and Deflected Line of Shear Centers for the SR-3 Propeller

## 6.2 HARTZELL PROPELLER TEST CASE

As a second test case for the verification of GAPAS, a Hartzell 101/16 3-bladed propeller was utilized. The characteristics of this propeller are shown in Figure 6.2-1. The propeller is generated using NACA 16 airfoils sections in the outer region, Modified Clark Y sections in the mid-region, and NACA 65 C/A sections in the hub region. The data available for use in constructing the geometry of the propeller were limited. A scaled version of the 101/16 propeller was used for generating the geometry. Seven spanwise stations were provided. These stations were 0.175 m (6.901-inch), 0.261 m (10.282-inch), 0.347 m (13.662-inch), 0.433 m (17.042-inch), 0.519 m (20.423-inch), 0.604 m (23.803-inch), 0.690 m (27.183-inch). The radius of the scaled propeller is 0.762 m (30 inch). Thus, the complete propeller could not be generated, that is, nearly 0.076 m (3 inches) were missing near the tip, while about 0.051 m (2 inches) were missing near the hub. Since the acoustic data were available on the full-scale propeller 1.349 m (53-inch radius), all the dimensions were scaled up by the ratio 53/30, and the calculations performed for this configuration. Therefore, the only comparison between predictions and data will be for the acoustic signature. However, results will be presented for the non-interactive case for the structural prediction.

The operating conditions for this comparison were: (1)  $M_\infty = 0.317$ ; (2)  $J = 1.52$ ; (3)  $C_p = 0.244$ ; (4)  $N = 1591$  rpm; (5)  $\beta_{3/4} = 39.3^\circ$ ; (6) 10000 feet altitude. These conditions correspond to a helical tip Mach number of 0.727. For this case, the airfoil data banks were replaced with TRANSEP, wherein, the airfoil shape was obtained by taking cuts perpendicular to the pitch change axis. In addition, SPN was used in place of TPN since the flow over the blade was essentially subsonic.

The results of the acoustic calculation for the OASPL for the 101/16 propeller near-field conditions for the microphone location given in Figure 3.5-1 are shown in Figure 6.2-2. Here a comparison is shown between flight data and the results of SPN using both Langley aerodynamics and GAPAS aerodynamics. The OASPL results with the GAPAS aerodynamics are not in as close agreement as that obtained using the Langley aerodynamics. There are two basic differences between the aerodynamic modules. The first is that

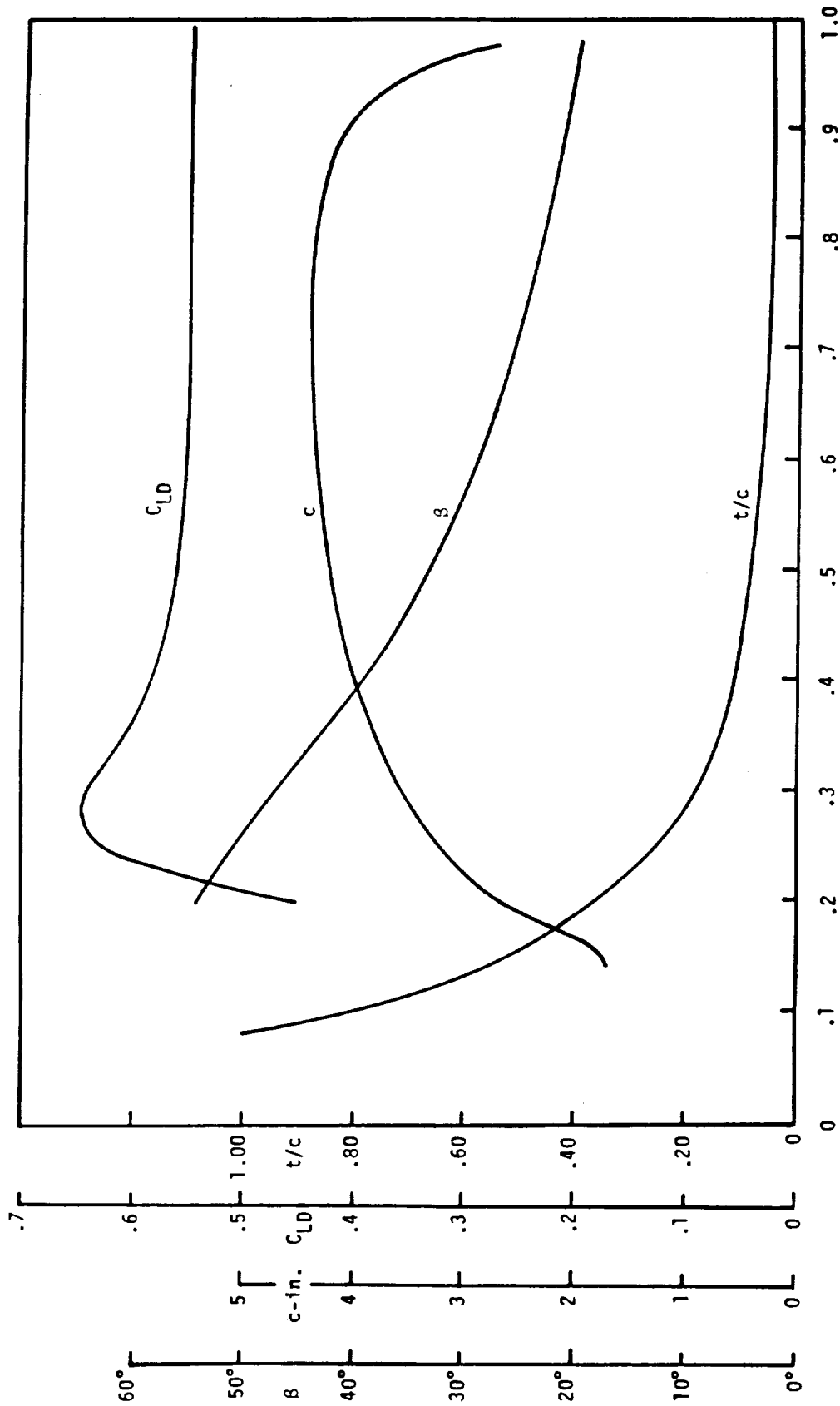


Figure 6.2-1. Hartzell 101/16 Propeller Blade Characteristics



$M_0=0.317$ ,  $J=1.52$ ,  $R = 1.346$  M.(53 IN.),  $B=3$ ,  $N=1591$  RPM,  $M_{TH}=0.727$

$$(OASPL = 10 \log_{10} \sum_{N=1}^N (P_{RMS}/P_{REF})^2); N = \text{TOTAL NUMBER OF HARMONICS}$$

RUN NO. 11

( $X_3=-11$  IN.)

FLIGHT DATA	131.15 DB
SPN (LANGLEY AERO)	131.54 DB
WOAN-GREGOREK	126.85 DB
SPN (GAPAS AERO)	128.55 DB

RUN NO. 12

( $X_3=-16$  IN.)

FLIGHT DATA	130.86 DB
SPN (LANGLEY AERO)	130.67 DB
WOAN-GREGOREK	129.18 DB
SPN (GAPAS AERO)	128.21 DB

RUN NO. 13

( $X_3=-22$  IN.)

FLIGHT DATA	130.95 DB
SPN (LANGLEY AERO)	129.96 DB
WOAN-GREGOREK	127.66 DB
SPN (GAPAS AERO)	127.37 DB

Figure 6.2-2. OASPL Results - 101/16 Propeller Near Field Conditions

GAPAS replaces classical vortex theory with a vortex-lattice methodology. The second is that the airfoil loading Theodorsen methodology is replaced with a transonic airfoil loading methodology. Since the match on power coefficient in GAPAS is determined by a varying  $\beta_{3/4}$ , the  $\beta_{3/4}$  obtained using the Langley aerodynamics will not agree with the  $\beta_{3/4}$  obtained from the GAPAS aerodynamics. Since no aerodynamic data on  $\beta_{3/4}$  for the full scale propeller was available, an uncertainty exists in knowing which method provides the more accurate  $\beta_{3/4}$ . In addition, the pressure and skin friction as determined using both methods will not be in complete agreement. Therefore, the above difference in methodology can lead to the differences in OASPL as shown in Figure 6.2-2. Further comparisons with available data are necessary to determine the accuracy of GAPAS aerodynamic methodology.

Using the aerodynamic loading as previously calculated for the acoustic results, the structural dynamics of the 101/16 propeller blade was computed. The 101/16 is a straight conventional propeller blade that is made out of 2025-T6 aluminum. The blade was modeled using 12 beam finite elements that were placed along the straight line of shear centers, Figure 6.2-3. The line of shear centers and the modal test setup are shown in Figure 6.2-4. Due to problems uncovered in the interactive mode for the SR-3 propeller, it was decided to utilize the single pass mode only.

The first three mode shapes of the actual blade and those predicted by the finite element model are presented in Figures 6.2-5 through 6.2-7. Figures 6.2-5 and 6.2-6 clearly show excellent agreement between the predicted first and second flap modes and the experimental results. The reason that the predicted modes appear in both views of the propeller is that the blade is defined with a pitch angle that is not coincident with the hub coordinates. The third mode that was predicted by the finite element method is the first torsion mode of the blade and this is in agreement with the experimental results. A Campbell diagram is presented in Figure 6.2-8 to show a comparison of the predicted natural frequencies and the experimental results. The experimental data and the predicted results are in very good agreement for the nonrotating blade. Experimental results do not currently exist for the rotating blade.

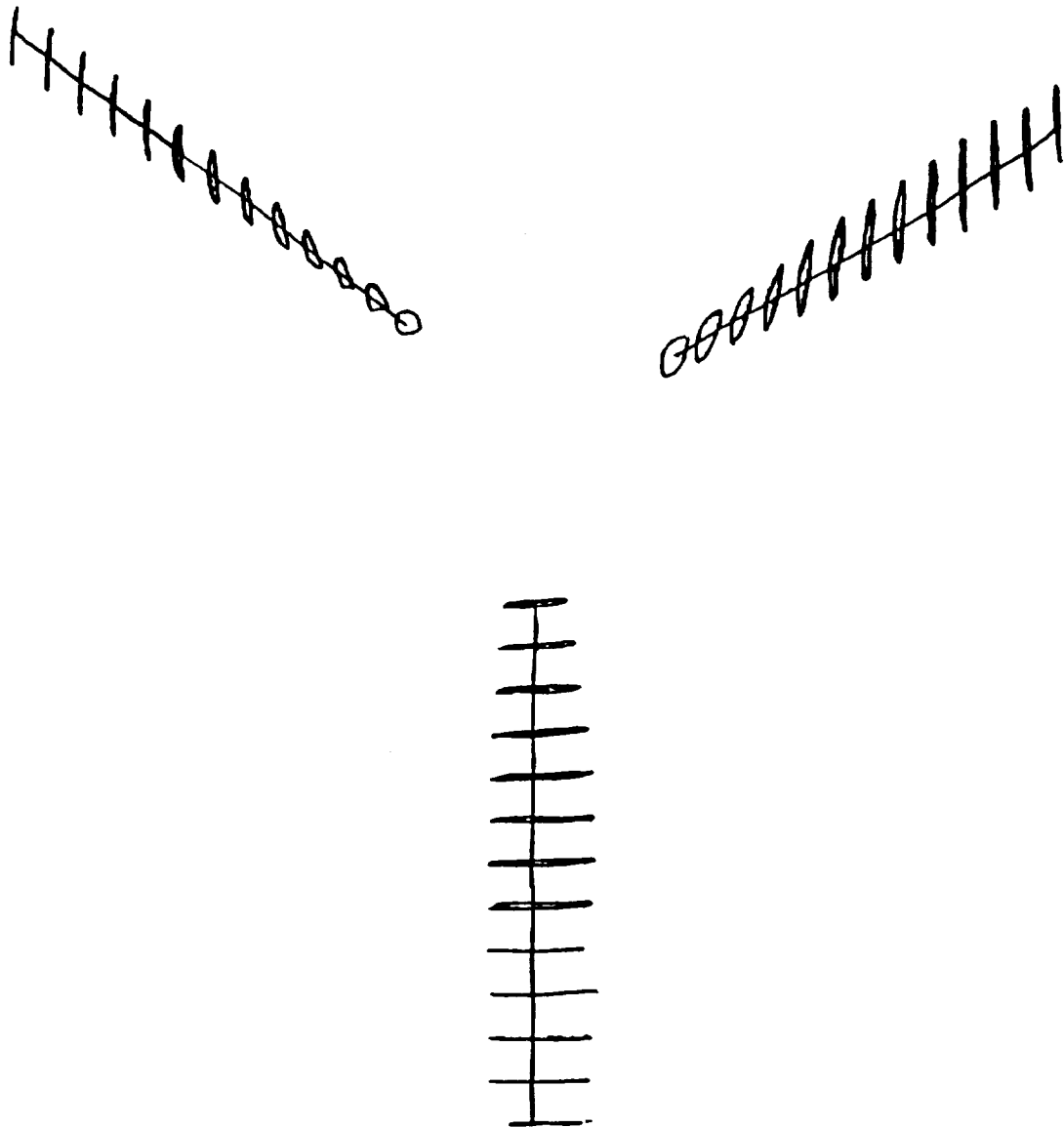
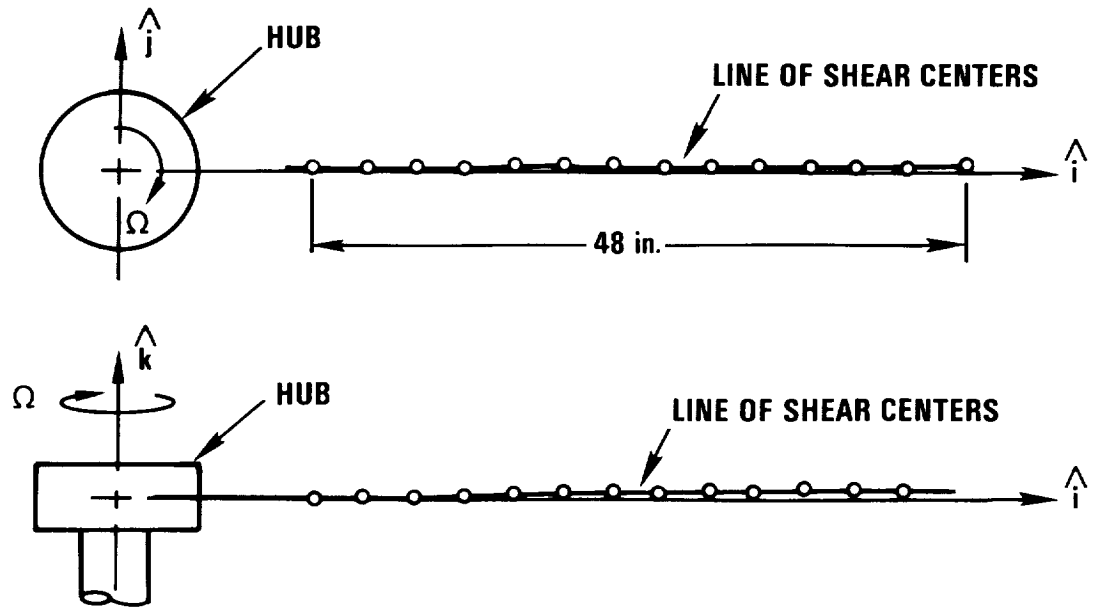


Figure 6.2-3. TRW-Hartzell 101/16 Structural Model Line of Shear Centers and Profiles Perpendicular

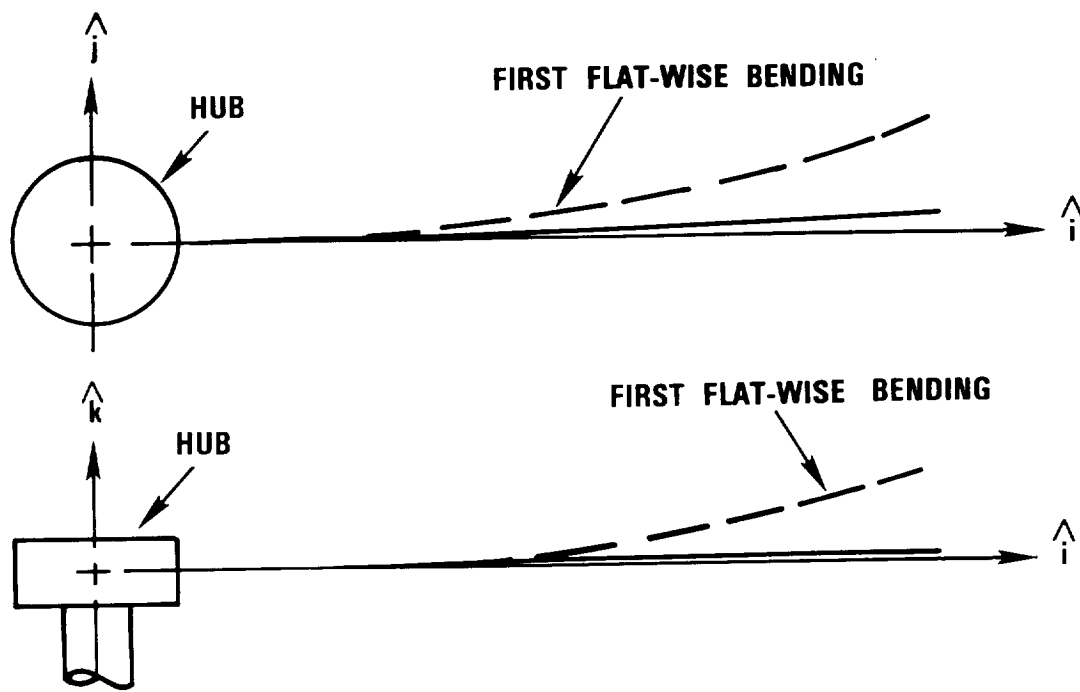


**A) FINITE ELEMENT MODEL OF THE UNDEFORMED LINE OF SHEAR CENTERS (12 ELEMENTS)**



**B) TEST SETUP OF UNDEFORMED PROPELLER**

Figure 6.2-4. Finite Element Model and Test Setup of Hartzell 101/16 Propeller

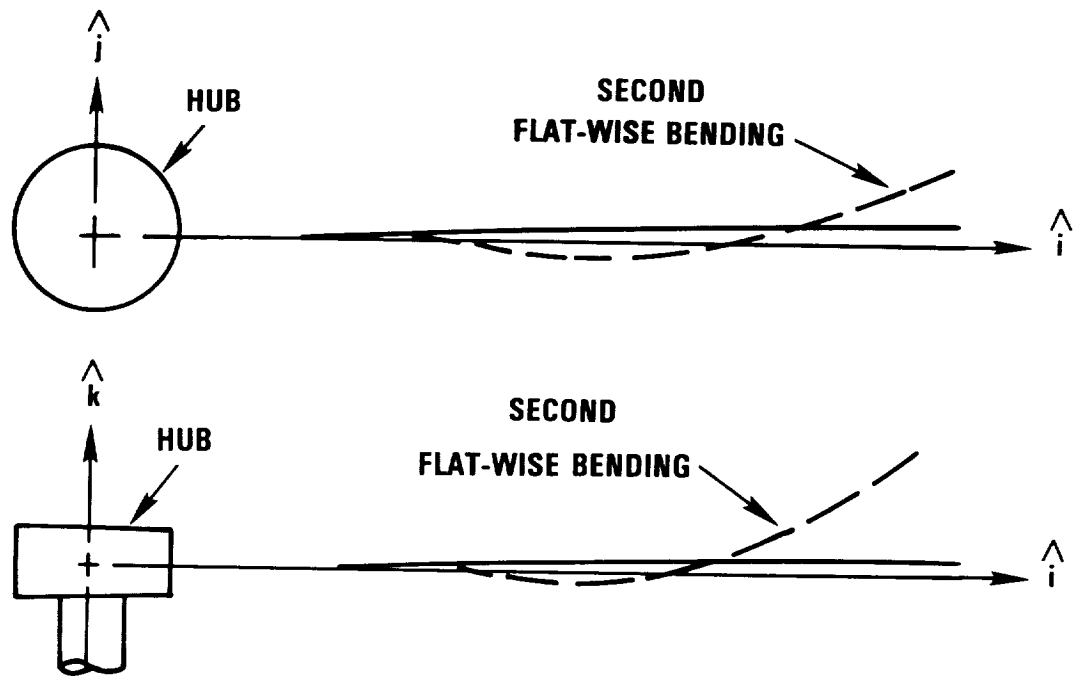


**A) FIRST MODE SHAPE BY THE FINITE ELEMENT MODEL**



**B) EXPERIMENTALLY OBTAINED FIRST MODE SHAPE**

Figure 6.2-5. Comparison of Predicted and Experimental of First Mode Shape for the Hartzell 101/16 Propeller

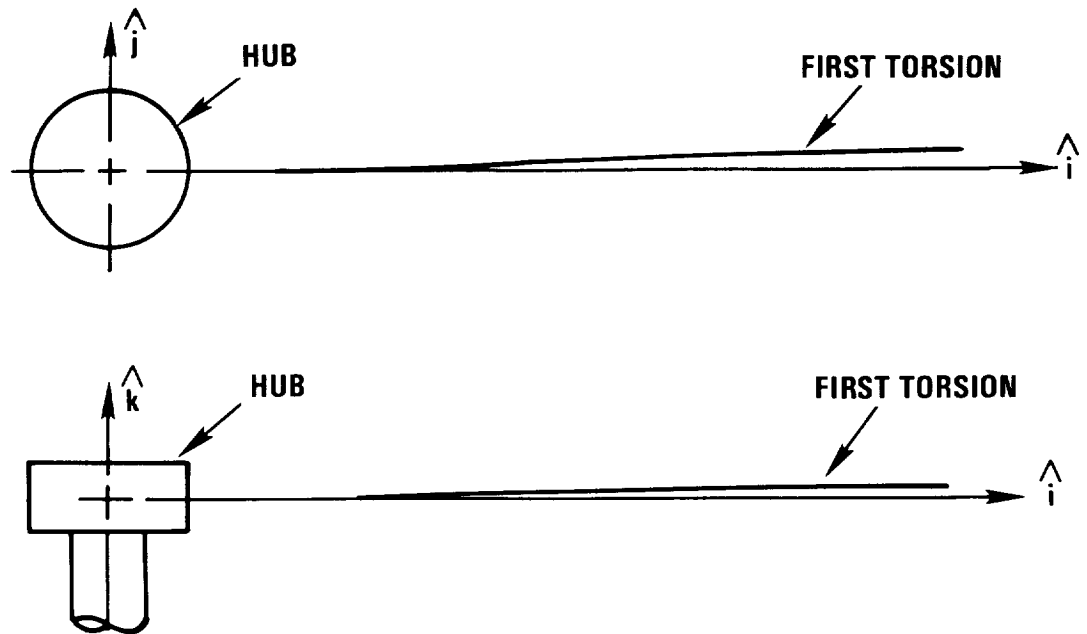


**A) SECOND MODE SHAPE BY THE FINITE ELEMENT MODEL**



**B) EXPERIMENTALLY OBTAINED SECOND MODE SHAPE**

Figure 6.2-6. Comparison of Predicted and Experimental Second Mode Shape for Hartzell 101/16 Propeller



**A) THIRD MODE SHAPE BY THE FINITE ELEMENT MODEL**



**B) EXPERIMENTALLY OBTAINED THIRD MODE SHAPE**

Figure 6.2-7. Comparison of Predicted and Experimental Third Mode Shape for Hartzell 101/16 Propeller

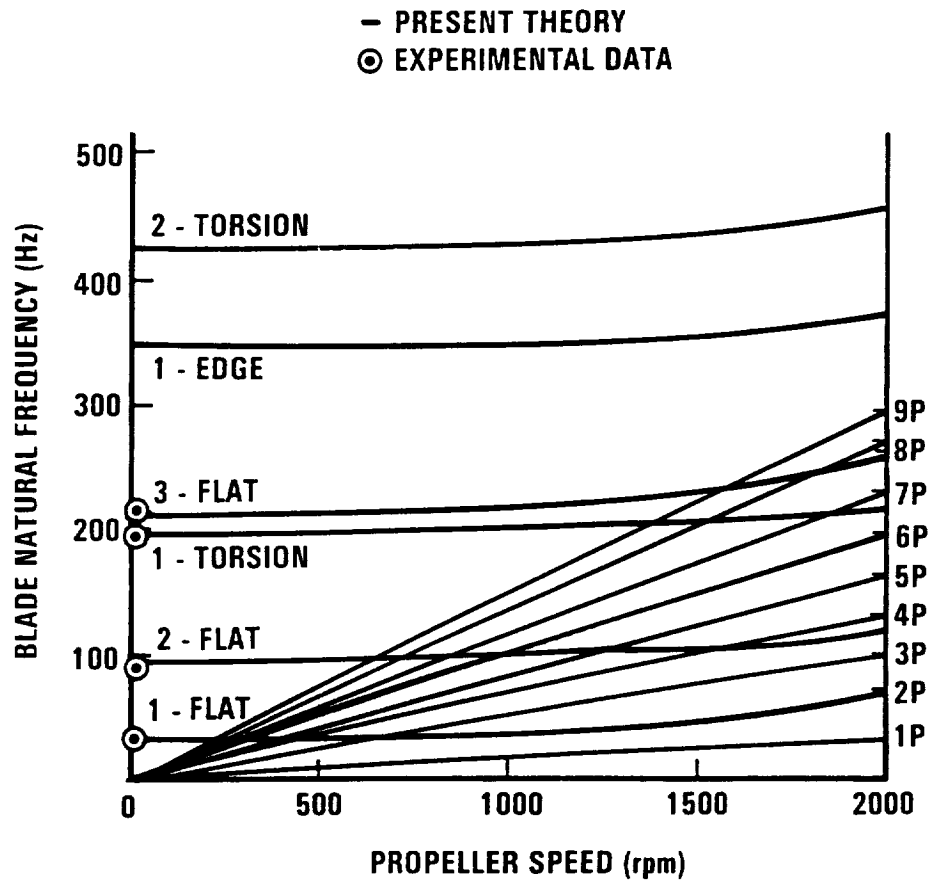


Figure 6.2-8. Comparison of Test and Predicted Natural Frequencies for the Hartzell 101/16 (Campbell Diagram)



### 6.3 COMPUTER RESOURCES REQUIREMENTS

System verification has focused on the NASA-Hamilton Standard SR-3 propeller operating at  $M_{\infty} = 0.8$  and the Hartzell 101/16 propeller operating at  $M_{\infty} = 0.317$ . Computer resource requirements, namely CPU time and core storage, are arrived at based on these studies. Table 6.3-1 summarizes these requirements. As mentioned previously, GAPAS is developed to operate on the CDC computer under the NOS operating system. The total memory requirement is 340K octal words which includes the executive system routines, functional module, system routines, intrinsic functions, etc. Processing the SR-3 and H101/16 test cases under similar conditions (i.e., single pass, 13 spanwise stations and same number of observers for acoustics calculations) requires approximately 400 and 800 seconds of execution, respectively. The basic difference in CPU time is due to the fact that the airfoil data bank is used to build the drag polar for the SR-3 case, while for the H101/16, TRANSEP is utilized to construct the drag polar. It should be pointed out that the estimate for SR-3 is based on the assumption that TPN runs without retarded time equation problems.

Table 6.2-1. GAPAS Limitations and Requirements

#### COMPUTER SYSTEM:

- CDC - NOS OPERATING SYSTEM
- MEMORY ~340,000 OCTAL WORDS
- CPU TIME (SEC) ~400 (SR3, SINGLE PASS)  
13 STATIONS  
~800 (H101/16, SINGLE PASS)  
13 STATIONS

#### FUNCTIONAL MODULE REQUIREMENT:

<u>MODULE</u>	<u>CPU(SEC)</u>	<u>MEMORY (OCTAL WORDS)</u>
ATM	~1.0	~1,000
GEOGEN	113.0	101,000
JUMPER	70.0	50,000
NACA16	~2.0	41,000
TRANSEP	11.0	73,000
PROPCHG	30.0	36,000
STRUC (EIGEN)	48.0	67,000 (40,000)
PLD	3.0	40,000
RBS	4.0	40,000
SPN	40.0	47,000
TPN	20 - 120	43,000



## 7. RECOMMENDATIONS

The current version of GAPAS that has been installed on the NASA Langley CDC 7600 Computer has inherent limitations due to limitations of the analysis codes that have been incorporated in GAPAS. Although, all the pertinent data communication links exist between the modules, the primary concern is the inability of GAPAS to perform the aeroelastic analysis of the propeller. However, as the aeroelastic analysis tool becomes available it can be incorporated in GAPAS. It is also important to point out that over the 4 years that the GAPAS computer program was being developed, new analysis capabilities have become available. However, the intent of the GAPAS design was to address this issue by developing the code in modular form, such that, as newer inherently more sophisticated analysis tools became available, they could replace the existing ones.

### 7.1 MODULE IMPROVEMENTS

Recommendations for module improvements, as well as the need for additional calculations and experimental data for further verification of GAPAS, are discussed below.

#### 7.1.1 Geometry Generator Module

The current version of the module is applicable only to solid blades of one material. It is necessary to modify the code to include composites and hollow structures.

#### 7.1.2 Aircraft Flow Field Module

Although the Jumper code can calculate the 3-D flow field, it is an incompressible panel method code and must be modified to account for compressibility effects when analyzing propellers at high subsonic Mach numbers.

#### 7.1.3 Airfoil Loading Module

This module requires a study to determine the correct shape of the airfoils for use in the airfoil loading module. In the case of a swept propeller with varying airfoil sections, it is not clear as to how to perform the cut to obtain the airfoil to be analyzed. One method of resolving

this problem is to calculate the flow field around the propeller using a 3-D Euler methodology. These results would then be compared with the results of a 2-D Euler solver used along various cuts through the propeller at prescribed radial stations. This study would address the pressure distribution. The skin friction contribution can be calculated using the same methodology that is currently in GAPAS.

The current 2-D airfoil analysis code, TRANSEP, does not adequately calculate the trailing edge separation. Therefore, it is recommended that it be replaced with a 2-D Euler code, coupled to an integral boundary layer method (i.e., Green's Lag Entrainment method), which properly accounts for both strong and weak interaction effects, as well as being able to address massive separation (cf. Ref. 7.1-1 to 7.1-5).

Finally, new airfoil family data banks (i.e., four-digit series) need to be incorporated. Some of these can be developed using experimental data while others can be developed using sophisticated computational fluid dynamic analysis tools.

#### 7.1.4 Propeller Performance Module

The version of the Chang-Sullivan code currently in GAPAS does not include spinner-shank interference drag. In addition, the method is only valid for axisymmetric flow conditions. Modifications are required to incorporate the spinner-shank drag as well as a methodology such as in Aljabri to account for non-axisymmetric effects. Finally, the code requires modification to handle centerbodies as well as the incorporation of a domain of influence/domain of dependence methodology to account for supersonic effects.

#### 7.1.5 Propeller Acoustic Module

During the calculation of the acoustic signature using TPN, non-convergence problems arose in the retarded time equation. It is necessary to correct these problems in the methodology. In addition, it is necessary to incorporate the quadrupole noise source term in the basic equation. Although both TPN and SPN can address unsteady loading effects, it has not been checked out at this time. Finally, the effect on the noise signature due to the inclusion of the skin friction loading needs to be investigated.

### 7.1.6 Structural Analysis Module

The following are recommendations for the GAPAS beam-type structural model. These recommendations are divided into two groups. The first group is concerned with the verification of the current program. The second group outlines possible future modifications to the code.

#### Verification of the Current Model

The current version of the GAPAS beam-type structural program has undergone initial checkout by comparing model results with known exact analytical and experimental solutions. These test cases included static and dynamic, linear and nonlinear analyses of straight and curved beams. The following analytical studies are recommended to further exercise the program.

- (1) Sensitivity studies of the structural dynamic analysis of an advanced prop-fan. These studies would be used to assess the sensitivity of the calculated results and the experimental results to the following:
  - (a) Location of the line of shear centers: It is important to understand how small perturbations in the calculated line of shear centers affect the results. It is known that the magnitude of the applied forces (i.e., aerodynamic and centrifugal) and the structural behavior of the blade are directly dependent on this location, since the line of mass centers and the quarter-chord are referenced relative to this line. This study would be helpful in assessing the quality of the calculated results of the geometry generator/shear center program.
  - (b) Cross section warping: Since these blades are extremely wide and thin, there will be a sufficient amount of chord-wise bending and cross section warping during the blade deformation process. In order to use a one-dimensional beam-type model, warping constants are used to capture these effects. Studies done on thin flat plates by NASA Lewis (Kaza) have shown that these constants are important, but their model was not applied to cross sections of arbitrary shape.
  - (c) Cross section definition: The current model includes all effects for a blade with an arbitrary cross section. This was included because it was assumed that sections which are perpendicular to the line of shear centers may not resemble airfoil sections or any other expected section. Many terms

could be dropped from the program if it were determined that the blade was behaving with near-symmetric cross sections.

- (d) Second-order nonlinear effects: The assessment of the effects of the nonlinear terms would be an important study that should be considered. These nonlinear terms are responsible for coupling the in-plane centrifugal forces with the out-of-plane stiffening of the blade.
- (2) Comparison of the analytical results with experimental results for a straight propeller: The experimental results would include the following: (1) Measured deflections and stresses of a cantilevered propeller subjected to tip loads and tip moments. Two separate sets of tip forces should be applied so that the blade is loaded linearly and nonlinearly (i.e., small strains, finite rotations). These results would be used to assess the quality of the structural model (from the geometry generator/shear center program) and some of the nonlinear terms. (2) Measured mode shapes and frequencies of the cantilevered propeller can be used to assess the quality of the dynamic modeling capabilities of the code (i.e., checkout of dynamic portion of beam model and ability of the geometry generator to model the mass axis correctly). (3) Measured tip deflections and rotations, blade stresses, mode shapes, and natural frequencies of the rotating propeller in a vacuum chamber. This study can be used to check out the coupling of the nonlinear effects with the centrifugal forces without being concerned about the aerodynamic loads. (4) Apply aerodynamic loads to the rotating blade and measure deflections and rotations. This can be used to assess the effects of the aerodynamic forces and the calculated line of quarter-chords from the geometry generator.
- (3) Repeat Step (2) for a swept blade. This would check out the capability of the model to analyze swept propellers that include large geometric coupling effects.

#### Future Modifications to the Code

The current version of the beam-type structural model in the GAPAS program includes everything that is required for performing the static and structural dynamic analysis of any isotropic rotating blade with an arbitrary shape. The next step would be to include the capability of analyzing blades that are composed of generally anisotropic materials (i.e., composite construction). Since most of the materials that are being used in conventional and advanced propellers behave in a nonisotropic manner, it is important that the analysis procedure also includes these capabilities. The current beam-type program could be modified for composite material analysis by deriving the additional linear and nonlinear terms associated with the

nonisotropic material behavior. Anisotropic material coupling constants are used to describe the behavior of the blade. A composite shear center model that is capable of analyzing the composite blade cross sections is also required to generate the shear center location and all of the anisotropic material coupling constants. Both of these analysis procedures have already been derived by Kosmatka (Ref. 7.1-6). The geometry generator would have to be extensively modified to include additional input parameters such as ply angle definitions, number of composite wraps, spar location, etc.

#### 7.1.7 Aeroelasticity Module

Since GAPAS currently does not have an aeroelastic capability, this is the highest priority item in completing the unified analysis system. This will require the completion of the verification of the applicability of the G400 PROP code as a tool for analyzing advanced technology propellers. If G400 PROP proves to be unreliable for these propellers, a task should be undertaken to combine the existing beam theory with an unsteady aerodynamic model which will fit into GAPAS in the manner that the other modules are incorporated.

#### 7.1.8 Option Module

Incorporation of a limited design option module is necessary to design propellers subject to specified constraints.

### 7.2 ADDITIONAL CALCULATIONS

The verification of GAPAS undertaken in Task 5 was limited due to available resources. It is necessary to investigate other operating conditions of the SR-3 propeller wherein aerodynamic, acoustic and structural/aeroelastic data are available, as well as other propellers for which various data exist (i.e., SR-2, SR-5).

Problems still exist in obtaining a converged solution in the interactive mode. Additional calculations are required to correct this deficiency.

The current beam-type finite element analysis program will accurately predict the deflections and vibration modes of straight and moderately

swept propellers (high aspect ratios), however, it cannot predict chordwise deformation and local edge stresses which are clearly important for blades with low aspect ratios or high activity factors (prop-fans). This is a result of the blade being modeled with a one-dimensional moderate deflection structural theory that takes into account the warping of the cross section in an approximate manner. In order to accurately analyze low aspect blades, a plate- or shell-type finite element approach is required and is currently being developed. This model includes the following capability:

- (1) Full two-dimensional moderate deflection structural theory that includes allowances for large rotational deflections (von Karman strains), transverse shear strains in either a first order (Mindlin, Reissner) or refined manner, and laminated composite materials.
- (2) Derivation of compatible aerodynamic and inertia loads, including the Coriolis and centrifugal effects, that are compatible with the nonlinear structural theory.
- (3) Development of the corresponding linear and nonlinear finite elements matrices, so that the resulting elements do not suffer from "shear locking" and are numerically stable (i.e., full numerical integration only). This is imperative for the modeling of low aspect blades where the elements must be extremely thick near the blade root and extremely thin at the tip. Elements are developed using an isoparametric formulation with a variable thickness at each node.
- (4) The resulting elements will be incorporated in the existing beam-type finite element program, where the code must be modified to allow for additional utility items (i.e., bandwidth minimizer, out-of-core solvers, etc.) and for the additional storage requirements associated with the large model sizes.
- (5) The current GAPAS geometry generator must be modified to correctly supply the blade information at specific spanwise and chordwise locations. This data would include the blade thickness, laminate ply definitions/structural properties, and airloads.
- (6) An appropriate aeroelastic module for the plate module could be developed by either expanding strip theory for the two-dimensional structural theory or more accurately by incorporating a double-lattice approach.



## REFERENCES

- 2.2-1. Jumper, S. J., "Computer Prediction of Three-Dimensional Potential Flow Fields in Which Aircraft Propellers Operate," Master of Science Thesis, Pennsylvania State University, 1982.
- 2.2-2. Jumper, S. J., "Computer Prediction of Three-Dimensional Potential Flow Fields in Which Aircraft Propellers Operate (Computer Program Description and User's Manual)," Pennsylvania State University, PSU-AERO-R-79/80-25, 1979.
- 2.2-3. Smith, A.M.O. and Pierce, J., "Exact Solution of the Neumann Problem. Calculation of Non-Circulatory Plane and Axially Symmetric Flows About or Within Arbitrary Boundaries," Douglas Aircraft Co., Report No. ES 26988, 106 pp.; also in Proceedings of the Third U.S. National Congress of Applied Mechanics, Brown University, 1958.
- 2.2-4. Hess, J.L., "Calculation of Potential Flow About Bodies of Revolution Having Axes Perpendicular to the Free-Stream Direction," J. Aerospace Sci, Vol. 29, No. 6, pp 726-742, June 1962.
- 2.2-5. Hess, J. L. and Smith, A. M. O., "Calculation of Potential Flow About Arbitrary Bodies," Progress in Aeronautical Sciences Vol. 8, Pergamon Press, Oxford, pp. 1-138, 1966.
- 2.2-6. Egolf, T.A., Anderson, O.L., Edwards, D.E., and Landgrebe, A.J., "Analysis for High Speed Propeller-Nacelle Aerodynamic Performance Prediction, Vol. I - Theory and Initial Application," UTRC Report R79-912949-19, 149 PP., 1979.
- 2.2-7. Woodward, F.A., "An Improved Method for the Aerodynamic Analysis of Wing-Body-Tail Configurations in Subsonic and Supersonic Flow," NASA CR-2228, 126 pp., 1973.
- 2.2-8. Carmichael, R.L. and Erickson, L.L., "Pan Air - A Higher Order Panel Method for Predicting Subsonic or Supersonic Linear Potential Flows About Arbitrary Configurations," Cosmic Publication, University Georgia, Athens, GA, 34 pp., 1980.
- 2.2-9. Morino, L., "A General Theory of Unsteady Compressible Potential Aerodynamics," NASA CR-2464, 1974.
- 2.2-10. Morino, L., "Steady, Oscillatory, and Unsteady Subsonic and Supersonic Aerodynamics - Production Version (SOUSSA-P1.1) Volume I - Theoretical Manual," NASA CR 159130, 1980.
- 2.2-11. Morino, L. and Kuo, C.C., "Subsonic Potential Aerodynamics for Complex Configurations: A General Theory," AIAA J., Vol. 12, No. 2, pp. 191-197, Feb 1974.

- 2.2-12 Smolka, S.A., Preuss, R.D., Tseng, K., and Morino, L., "Steady Oscillatory, and Unsteady Subsonic and Supersonic Aerodynamic Production Version 1.1 (SOUSSA-P1.1) Volume II - User/Programmer Manual," NASA CR 159131, 1980.
- 2.2-13. Clark, D.R. and Maskew, B., "An Analysis of Airframe/Rotor Interference in Forward Flight," Seventh European Rotorcraft and Powered Lift Aircraft Forum, Germany, Paper No. 50, 28 pp., Sept. 1981.
- 2.2-14. Clark, D.R. and Maskew, B., "Calculation of the Aerodynamic Characteristics of Configurations with Strong Component/Component Interference," Presented at 13th ICAS Meeting, Seattle, Washington, 11 pp., August 1982.
- 2.2-15. Maskew, B., "Prediction of Subsonic Aerodynamic Characteristics: A Case for Low-Order Panel Methods," J. Aircraft, Vol. 19, No. 2, pp. 157-163.
- 2.2-16. Maskew, B. and Rao, B.M., "Calculation of Vortex Flows on Complex Configurations," Presented at 13th ICAS Meeting, Seattle, Washington, 12 pp., August 1982.
- 2.2-17. Chang, L. K., "The Theoretical Performance of High Efficiency Propellers," Ph.D. Thesis Thesis, Purdue University, December 1980.
- 2.2-18. Aljabri, A.S., "Prediction of Propeller Performance and Loading in Uniform and Nonuniform Flowfields," M.S. Thesis, Pennsylvania State University Department of Aerospace Engineering, November 1978.
- 2.2-19 Crigler, J.L., "Application of Theodorsen's Theory to Propeller Design," NACA RM No. L8F30, July 1948.
- 2.2-20. Society of British Aircraft Constructors, "S.B.A.C. Standard Method of Propeller Performance Estimation," Society of British Aircraft Constructors, Ltd., London.
- 2.2-21. Theodorsen, T., "The Theory of Propellers," Parts, I, II, III, and IV, NACA Report Nos. 775, 776, 777, and 778, 1944.
- 2.2-22. Anderson, O.L. and Edwards, D.E., "Extensions to an Analysis of Turbulent Swirling Compressible Flow in Axisymmetric Ducts," UTRC Report No. R81-914720-18, February 1981.
- 2.2-23. Anderson, O.L., Hankins, G.B. Jr., and Edwards D.E., "Extensions to an Analysis of Turbulent Swirling Compressible Flow for Application to Axisymmetric Small Gas Turbine Ducts," UTRC Report No. R81-915395-12, December 1981.
- 2.2-24. Borst, H.V., "Summary of Propeller Design Procedures and Data," U.S. Army Air Mobility Research and Development Laboratory, USAMRDL TR 73-34A, November 1973.

- 2.2-25. Evvard, J.C., "Distribution of Wave Drag and Lift in the Vicinity of Wing Tips at Supersonic Speeds," NACA TN 1382, 1947.
- 2.2-26. Mellor, G.L., "A Combined Theoretical and Empirical Method of Axial Compressor Cascade Prediction," May 1970.
- 2.2-27. Egolf, T.A., Anderson, O.L., Edwards, D.E., and Landrebe, A.J., "An Analysis for High-Speed Propeller-Nacelle Aerodynamic Performance Prediction, Volume II, User's Manual for the Computer Program," United Technology Research Center Report No. R1279-91294-19, June 1979.
- 2.2-28. Sullivan, J. P., "The Effect of Blade Sweep on Propeller Performance," AIAA Preprint 77-716, June 1977.
- 2.2-29. Aljabri, A.S., "Prediction of Propeller Performance and Loading in Uniform and Nonuniform Flowfields," Computer Program Description and User's Manual, November 1978.
- 2.2-30. Bober, L. J. and Chang, L. K., "Factors Influencing the Predicted Performance of Advanced Propeller Designs," AIAA Preprint 81-1564, 1981.
- 2.2-31. Bober, L.J., and Mitchell, G.A., "Summary of Advanced Methods for Predicting High-Speed Propeller Performance," AIAA Preprint 80-0225, January 1980.
- 2.2-32. McCormick, B.W., Aerodynamics of V/STOL Flight, Academic Press, Inc., New York, 1967.
- 2.2-33. McCormick B.W., "The Effect of a Finite Hub on the Optimum Propeller," J. Aero, Sci. 22, No. 9, September 1955.
- 2.2-34. Thorsen, T.L., "Approximate Theory for the Optimum Circulation Distribution for Propellers with Very Large Hubs," Department of the Navy Technical Report 127-2, July 1962.
- 2.2-35. Bauer, F., Garabedian, P., and Korn, D., A Theory of Supercritical Wing Sections, with Computer Programs and Examples, Lecture Notes in Economics and Mathematical Systems, Vol. 66, Springer-Verlag, New York, 1972.
- 2.2-36. Bauer, F., Garbedian, P., Korn, D., and Jameson A., Supercritical Wing Sections II, A Handbook, Lecture Notes in Economics and Mathematical Systems, Vol. 108, Springer-Verlag, New York, 1975.
- 2.2-37. Bauer, F., Garabedian, P., and Korn, D., Supercritical Wing Sections III, Lecture Notes in Economics and Mathematical Systems, Vol. 150, Springer-Verlag, New York, 1977.

- 2.2-38. Carlson, L.A., "Transonic Airfoil Analysis and Design Using Cartesian Coordinates," *Journal of Aircraft*, Vol. 13, No. 5, pp. 349-356, May 1976.
- 2.2-39. Carlson, L.A., "TRANDES: A FORTRAN Program for Transonic Airfoil Analysis or Design," NASA CR-2821, June 1977.
- 2.2-40. Carlson, L.A., TRANSEP: A Program for High-Lift Separated Flow About Airfoils," NASA CR-3376, 1980.
- 2.2-41. Smetana, F.O., Summey, D.C., Smith, N.S., and Carden, R.K., "Light Aircraft Lift, Drag, and Moment Prediction - A Review and Analysis," NASA CR-2523, May 1975.
- 2.2-42. Stevens, W.A., Goradia, S.H., and Braden, J.A., "Mathematical Model for Two-Dimensional Multi-Component Airfoils in Viscous Flows," NASA CR-1843, July 1971.
- 2.2-43. Eppler, R., "Practical Calculation of Laminar and Turbulent Bled-Off Boundary Layers," NASA TM-75328, 1978. (Translated from *Ingenieur-Archiv*, Vol. 32, pp. 221-245, 1963).
- 2.2-44. Eppler, Richard; and Somers, Dan M., "Low Speed Airfoil Design and Analysis. Advanced Technology Airfoil Research - Volume I," NASA CP-2045, Part 1, pp. 73-99, 1979.
- 2.2-45. Eppler, R. (Francesca Neffgen, transl.), "Laminar Airfoils for Reynolds Numbers Greater than  $4 \times 10^6$ ," B-819-35, April 1969. (Available from NTIS as N69-28178.) (Translated from *Ingenieur-Archiv*, Vol. 38, pp. 232-240, 1969.)
- 2.2-46. Eppler, Richard, "Turbulent Airfoils for General Aviation," *J. Aircr.*, Vol. 15, No. 2, pp. 93-99, February 1978.
- 2.2-47. Nash, J.F. and Macdonald, A.G.J., "The Calculation of Momentum Thickness in a Turbulent Boundary Layer at Mach Numbers up to Unity," *Aero. Res. Council C.P. No. 963*, 1967.
- 2.2-48. South, J.C., Jr. and Jameson, A., "Relaxation Solutions for Inviscid Axisymmetric Transonic Flow over Blunt or Pointed Bodies," *Proc. AIAA Computational Fluid Dynamics Conf.*, Palm Springs, California, pp. 8-17, July 1973.
- 2.2-49. Schlichting, H., Boundary Layer Theory, McGraw Hill, 1968.
- 2.2-50. Squire, H.B., and Young, A.D., "The Calculation of the Profile Drag of Aerofoils," *R. & M. No. 1838*, British A.R.C., 1938.
- 2.2-51. Freuler, R.J., and Gregorek, G.M., "An Evaluation of Four Single Element Airfoil Analytic Methods," *Proceedings of the Advanced Technology Airfoil Research Conference*, NASA Langley Research Center, NASA Conference Publication 2046, 1979.

- 2.2-52. McGhee, R.J., and Beasley, W.D., "Effects of Thickness of an Initial Low-Speed Family of Airfoils for General Aviation Applications," NASA TM X-72843, June 1976.
- 2.2-53. Woan, C.J. and Gregorek, G.M., "The Exact Numerical Calculation of Propeller Noise," AIAA Preprint 78-1122, July 1978.
- 2.2-54. Farassat, F. and Succi, G.P., "A Review of Propeller Discrete Frequency Noise Prediction Technology with Emphasis on Two Current Methods for Time Domain Calculations," Journal of Sound and Vibration 71 (3), pp. 399-419, 1980.
- 2.2-55. Succi, G.P., "Computed and Experimental Spectra for a Wing-Mounted Microphone on a Light STOL Aircraft," NAS CR 165725, May 1978.
- 2.2-56. "Aircraft Noise Prediction Theoretical Manual, Part 3: Propeller Analysis Modules," NASA-Langley Research Center, February 1983; see also: Zorunski, W. E., and Weir, D. S., "Aircraft Noise Prediction Program Theoretical Manual; Part 3, Propeller Aerodynamics and Noise," NASA TM 83199, October 1984.
- 2.2-57. "Prediction Procedure for Near-Field and Far-Field Propeller Noise," Society of Automotive Engineers Aerospace Information Report No. AIR 1407, May 1977.
- 2.2-58. Korkan, K.D. and Ruff, G.A., "Near-Field and Far-Field Propeller Noise Prediction Method for Programmable Calculators based on SAC AIR 1407 (Version II)," Texas A&M Aerospace Engineering Department Report, 1982.
- 2.2-59. Houbolt, J.C., and Brooks, G.W., "Differential Equations of Motion for the Combined Flapwise Bending, Chordwise Bending, and Torsion of Twisted Nonuniform Rotor Blades," NACA Report 1346, October 1956.
- 2.2-60. Hodges, D.H., and Dowell, E.H., "Nonlinear Equations of Motion for the Elastic Bending and Torsion of Twisted Nonuniform Rotor Blades," NASA TN D-7818, December 1974.
- 2.2-61. Rosen, A., and Friedmann, P.P., "Nonlinear Equations of Equilibrium for Elastic Helicopter or Wind Turbine Blades Undergoing Moderate Deflection," NASA CR-159478, December 1978.
- 2.2-62. Kaza, K.R.V. and Kvaternik, R.G., "Nonlinear Aeroelastic Equations for Combined Flapwise Bending, Torsion, and Extension of Twisted Nonuniform Rotor Blades in Forward Flight," NASA TM-74059, 1977.
- 2.2-63. Kaza, K.R.V. and Kvaternik, R.G., "Aeroelastic Equations of Motion of a Darrieus Vertical-Axis Wind-Turbine Blade," NASA TM-79295, December 1979.
- 2.2-64. Rosen, A., and Abramovich, H., "Investigation of the Structural Behavior of the Blades of a Darrieus Wind Turbine," Fourth International Symposium on Wind Energy Systems, Paper H3, 1982.

- 2.2-65. Timoshenko, S. and Goodier, J.N., Theory of Elasticity, 1st edition, McGraw-Hill Book Co., New York, N.Y., 1951.
- 2.2-66. Straub, F.K. and Friedman, P.P., "Application of the Finite Element Method to Rotary-Wing Aeroelasticity," NASA CR-165854, February 1982.
- 2.2-67. Sivaneri, H.T., and Chopra, I., "Dynamic Stability of a Rotor Blade Using Finite Element Analysis," AIAA Journal, Vol. 20, No. 5, pp. 716-723, 1984.
- 2.2-68. Hong, C. and Chopra, I., "Aeroelastic Stability Analysis of a Composite Blade," Proceedings of the 40th Annual National Forum of the Helicopter Society, pp. 539-557, May 16-18, 1984.
- 2.2-69. Hodges, D.H., "Torsion of Pretwisted Beams Due to an Axial Loading," ASME Journal of Applied Mechanics, Vol. 47, pp. 393-397, June 1980.
- 2.2-70. Rosen, A., "The Effect of the Initial Twist on the Torsional Rigidity of Beams - Another Point of View," ASME Journal of Applied Mechanics, Vol. 47, pp. 389-392, June 1980.
- 2.2-71. Batoz, J.L., Bathe, K.J., and Ho, L.W., "A Study of Three Node Triangular Plate Bending Elements," International Journal of Numerical Methods in Engineering, Vol. 15, pp. 1771-1812, 1980.
- 2.2-72. Bielawa, R.L., Johnson, S.A., Chi, R.M., and Gangwani, S.T., "Aeroelastic Analysis of Propellers - Mathematical Formulations and Program User's Manual," NASA CR-3729, December 1983.
- 2.2-73. Houbolt, J.C., and Brooks, G.W., "Differential Equations of Motion for the Combined Flapwise Bending, Chordwise Bending, and Torsion of Twisted Nonuniform Rotor Blades," NACA Report 1346, October 1956.
- 2.2-74. Ganwani, S.T., "Prediction of Dynamic Stall and Unsteady Airloads for Rotor Blades," Proceedings of the 37th Annual Forum of the American Helicopter Society, New Orleans, pp. 1-17, May 1981.
- 2.2-75. Straub, F.K. and Friedmann, P.P., "Application of the Finite Element Method to Rotary-Wing Aeroelasticity," NASA CR-165854, February 1982.
- 3.3-1. Borst, H.V., "Wind Tunnel Tests of Four General Aviation Propellers Using Blades with Different Airfoil Sections," Volume II, Work Performed under Ohio State University Grant NSG-3247, August 1982.
- 3.3-2. "Low-Speed Aerodynamic Performance Data for SR-3 Propeller: Power Coefficient vs. Advance Ratio and Efficiency vs. Advance Ratio," NASA Lewis Research Center, September 1982.
- 3.3-3. Rohrbach, C., et al., "Evaluation of Wind Tunnel Performance Testing of an Advanced 45° Swept Eight-Bladed Propeller at Mach Numbers from 0.45 to 0.85," NASA CR-3505, March 1982.

- 3.4-1. Blascovich, J.D., "Characteristics of Separated Flow Airfoil Analysis Methods," M.S. Thesis, MIT, January 1983.
- 3.5-1. Zorumski, W.E., and Weir, D.S., "Aircraft Noise Prediction Program Theoretical Manual, Part 3, Propeller Aerodynamics and Noise," NASA TM 83199, October 1984.
- 3.5-2. Gregorek, G. M., "Five Case Studies of the Hartzell Baseline Propeller," work carried out under Ohio State University Grant NSG-3247, December 1982.
- 3.5-3. Dittmar, J.H. and Jeracki, R.J., "Additional Noise Data on the SR-3 Propeller," NASA TM-81736, May 1981.
- 3.5-4. Dittmar, J.H. and Lasagna, P.L., "A Preliminary Comparison Between the SR-3 Propeller Noise in Flight and in a Wind Tunnel," NASA TM-82805, April 1982.
- 3.5-5. Brooks, B.M. and Metzger, F.B., "Acoustic Test and Analysis of Three Advanced Turboprop Models," NASA CR-159667, January 1980.
- 3.6-1. Hodges, D.H., and Dowell, E.H., "Nonlinear Equations of Motion for the Elastic Bending and Torsion of Twisted Nonuniform Rotor Blades," NASA TN D-7818, December 1974.
- 3.6-2. Rosen, A., and Friedmann, P.P., "Nonlinear Equations of Equilibrium for Elastic Helicopter or Wind Turbine Blades Undergoing Moderate Deflection," NASA CR-159478, December 1978.
- 3.6-3. Love, A.E.H., A Treatise on the Mathematical Theory of Elasticity, 1st edition, Cambridge University Press, 1927.
- 3.6-4. Timoshenko, S., and Goodier, J.N., Theory of Elasticity, 1st edition, McGraw-Hill Book Co., New York, N.Y., 1951.
- 3.6-5. Wang, C.T., Applied Elasticity, 1st edition, McGraw-Hill Book Co., New York, N.Y., 1953.
- 3.6-6. Oden, J.T., and Ripperger, E.A., Mechanics of Elastic Structures, 2nd edition, McGraw-Hill Book Co., New York, N.Y., 1981
- 3.6-7. Boresi, A.P., Sidebottom, O.M, Seely, F.B., and Smith, J.O., Advanced Mechanics of Materials, 3rd edition, John Wiley and Sons, Inc., New York, N.Y., 1978.
- 3.6-8. Wempner, G., Mechanics of Solids With Applications to Thin Bodies, 1st edition, McGraw-Hill Book Co., New York, N.Y., 1973.
- 3.6-9. Tauchert, T.R., Energy Principles in Structural Mechanics, 1st edition, McGraw-Hill Book Co., New York, N.Y., 1974.

- 3.6-10. Oden, J.T., Finite Elements of Nonlinear Continua, 1st edition, McGraw-Hill Book Co., New York, N.Y., 1972.
- 3.6-11. Friedmann, P.P., and Straub, F.K., "Application of the Finite Element Method to Rotary Wing Aeroelasticity", Journal of the American Helicopter Society, Vol. 25, pp. 36-44, January 1980.
- 3.6-12. Straub, F.K., and Friedmann, P.P., "A Galerkin Type Finite Element for Rotary-Wing Aeroelasticity in Hover and Forward Flight," Vertica, Vol. 5, pp. 75-98, 1981.
- 3.6-13. Bathe, K., Finite Element Procedures in Engineering Analysis, 1st edition, Prentice-Hall, Inc., Englewood Cliffs, N.J., 1982.
- 3.6-14. Zienkiewicz, O.C., The Finite Element Method, McGraw-Hill Book Co., New York, N.Y., 1977.
- 3.6-15. Guyan, R., "Reduction of Stiffness and Mass Matrices", AIAA, Vol. 3, No.2, pp. 380, February 1965.
- 3.6-16. Tillerson, J.R., Stricklin, J.A., and Haisler, W.E., "Numerical Methods for the Solution of Nonlinear Problems in Structural Analysis," Numerical Solution of Nonlinear Structural Problems, ASME, 1973.
- 3.6-17. Meirovitch, L., "A New Method of Solution of the Eigenvalue Problem for Gyroscopic Systems," AIAA, Vol. 12, No. 10, 1337-1342, October 1974.
- 3.6-18. Roark, R.J., and Young, W.C., Formulas for Stress and Strain, 5th edition, McGraw-Hill Book Co., New York N.Y., 1975.
- 3.6-19. Blevins, R.D., Formulas for Natural Frequency and Mode Shape, Van Nostrand Reinhold Co., New York, N.Y., 1979.
- 3.6-20. Rosen, A., and Friedmann, P. P., "The Nonlinear Behavior of Elastic Slender Straight Beams Undergoing Small Strains and Moderate Rotations," Journal of Applied Mechanics, pp. 161-168, March 1979.
- 3.7-1. Bielawa, R.L., "Aeroelastic for Helicopter Rotor Blades with Time-Variable, Nonlinear Structural Twist and Multiple Structural Redundancy - Mathematical Derivation and Program User's Manual," NASA CR-2638, February 1976.
- 3.7-2. Bielawa, R.L., "Aeroelastic Analysis for Helicopter Rotors with Blade Appended Pendulum Vibration Absorbers - Mathematical Derivation and Program User's Manual," NASA CR-165896, June 1982.
- 3.7-3. Houbolt, J.C., and Brooks, G.W., "Differential Equations of Motion for the Combined Flapwise Bending, Chordwise Bending, and Torsion of Twisted Nonuniform Rotor Blades," NACA Report 1346, October 1956.



- 3.7-4. Hodges, D.H., and Dowell, E. H., "Nonlinear Equations of Motion for the Elastic Bending and Torsion of Twisted Nonuniform Rotor Blades," NASA TN D-7818, December 1974.
- 3.7-5. Rosen, A. and Friedmann, P. P., "Nonlinear Equations of Equilibrium for Elastic Helicopter or Wind Turbine Blades Undergoing Moderate Deflections," NASA CR-159478, December 1978.
- 3.7-6. Rosen, A., "The Effect of Initial Twist on the Torsional Rigidity of Beams - Another Point of View," ASME Journal of Applied Mechanics, Vol. 47, pp. 389-392, June 1980.
- 3.7-7. Hodges, D.H., "Torsion of Pretwisted Beams Due to Axial Loading," ASME Journal of Applied Mechanics, Vol. 47, pp. 393-397, June 1980.
- 3.7-8. Shield, R.T., "Extension and Torsion of Elastic Bars With Initial Twist," ASME Journal of Applied Mechanics, Vol. 49, pp. 779-786, December 1982.
- 3.7-9. Bielawa, R.L., Johnson, S.A., Chi, R.M., and Gangwani, S.T., "Aeroelastic Analysis of Propellers - Mathematical Formulations and Program User's Manual," NASA CR-3729, December 1983.
- 3.7-10. Gangwani, S.T., "Prediction of Dynamic Stall and Unsteady Airloads for Rotor Blades," Proceedings of the 37th Annual Forum of the American Helicopter Society, New Orleans, pp. 1-17, May 1981.
- 3.7-11. Dadone, L.U., "Two-Dimensional Wind Tunnel Test Data of an Oscillating Rotor Airfoil," Vol. II, NASA CR-2915, December 1977.
- 3.7-12. Gray, L. and Liiva, J., "Two-Dimensional Tests of Airfoils Oscillating Near Stall," Vol. II, USAAVLAB TR-68-13B, USAAMRDL, Ft. Eustis, VA, April 1968.
- 3.7-13. Vepa, R., "Finite State Modeling of Aeroelastic Systems," NASA CR-2779, February 1977.
- 3.7-14. Roark, R.J., and Young, W.C., Formulas for Stress and Strain, McGraw-Hill Book Company, Inc., New York, N.Y., p. 294, 1975.
- 7.1-1. Edwards, D.E., and Carter, J.E., "A Quasi-Simultaneous Finite Difference Approach for Strongly Interacting Flow," Third Symposium on Numerical and Physical Aspects of Aerodynamic Flows, Cal State University, Long Beach, January 1985.
- 7.1-2. LeBalleur, J.C., "Numerical Viscous-Inviscid Interaction in Steady and Unsteady Flows," Second Symposium on Numerical and Physical Aspects of Aerodynamic Flows, Cal State University, Long Beach, January 1983.

- 7.1-3. Melnik, R.E., "Theory of Viscous Transonic Flow Over Airfoils at High Reynolds Numbers," Computational Fluid Dynamics Workshop, Tullahoma, Tennessee, March 1984.
- 7.1-4. Whitfield, D.L., Thomas, J.L., Jameson, A., and Schmidt, W., "Computational of Transonic Viscous-Inviscid Interacting Flows," Second Symposium on Numerical and Physical Aspects of Aerodynamics Flows, Cal State University, Long Beach, January 1983.
- 7.1-5. Green, J.E., Weeks, D.J., Broome, J.W.F., "Prediction of Turbulent Boundary Layers and Wakes in Compressible Flow by a Lag Entrainment Method," RAE Technical Report, 72231, 1983.
- 7.1-6. Kosmatka, J., "Structural Dynamic Modeling of Advanced Composite Propellers by the Finite Element Method," University of California, Los Angeles PhD dissertation, 1986.



## Report Documentation Page

1. Report No. CR-185276		2. Government Accession No.		3. Recipient's Catalog No.	
4. Title and Subtitle Generalized Advanced Propeller Analysis System (GAPAS) - Volume 1 - Final Report				5. Report Date December 1986	
				6. Performing Organization Code	
7. Author(s) Leslie Glatt Donald R. Crawford John B. Kosmatka Rudy J. Swigart Eric W. Wong				8. Performing Organization Report No.	
				10. Work Unit No.	
9. Performing Organization Name and Address TRW Space & Defense Sector One Space Park Redondo Beach, CA 90278				11. Contract or Grant No. NAS3-22251	
				13. Type of Report and Period Covered Contractor Final Report	
12. Sponsoring Agency Name and Address National Aeronautics and Space Administration NASA Lewis Research Center Cleveland, Ohio 44135				14. Sponsoring Agency Code	
15. Supplementary Notes					
16. Abstract A Generalized Advanced Propeller Analysis System (GAPAS) has been developed under NASA Lewis Research Center Funding to provide a unified propeller analysis capability for analyzing advanced technology propellers. The technology areas incorporated in GAPAS include propeller aerodynamic performance, airfoil loading, acoustics, and structural analysis. These propeller analysis tools include the most fully developed technologies in a modular but unified system. GAPAS will treat multi-bladed propellers having straight or swept blades operating on aircraft up to Mach 0.8 and altitudes to 40,000 feet (12 km).					
17. Key Words (Suggested by Author(s)) Advanced Technology Propellers Unified Analysis System Aerodynamics Acoustics Structures			18. Distribution Statement		
19. Security Classif. (of this report) Unclassified		20. Security Classif. (of this page) Unclassified		21. No. of pages 343	
				22. Price	

